

Dissertation zur Erlangung des Doktorgrades der Naturwissenschaften vorgelegt  
beim Fachbereich 14  
der Johann Wolfgang Goethe – Universität in Frankfurt am Main

Metal ions as novel polarizing agents for  
dynamic nuclear polarization enhanced  
NMR spectroscopy

von  
Monu Kaushik  
aus Sonapat, Indien

Frankfurt am Main, November 7, 2017

D30



Accepted by Department 14: Biochemistry, Chemistry and Pharmacy  
of the Johann Wolfgang Goethe University as a dissertation for doctoral degree in natural  
sciences

First expert assessor:

Dr. Björn Corzilius

Second expert assessor:

Prof. Dr. Thomas F. Prisner

Dean:

Prof. Dr. Clemens Glaubitz

Date of Disputation:

.....



## Summary

High-spin complexes of  $\text{Gd}^{3+}$  and  $\text{Mn}^{2+}$  were introduced as polarizing agents (PAs) for solid-state dynamic nuclear polarization (DNP) in 2011. This dissertation was undertaken in 2013, with the intention of exploring these PAs further. Major goals of this work were to understand their DNP mechanism(s) and explore their application in biomolecular research. This cumulative thesis details the methods, advantages, and practical implications of using high-spin PAs for MAS DNP. Data from electron paramagnetic resonance (EPR) and NMR spectroscopy are discussed for a complete understanding of DNP mechanisms.

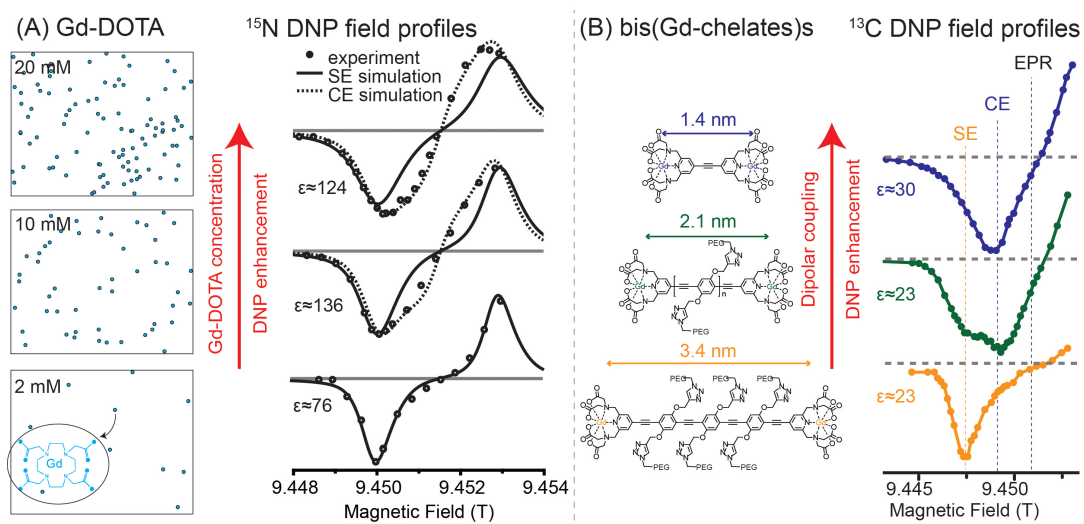
Out of the two main mechanisms—solid effect (SE) and cross effect (CE)—active under experimental conditions of solid-state DNP, commonly used nitroxide PAs evoke CE owing to their broad EPR spectra. On the other hand, DNP mechanisms evoked by high-spin metal ions seem non-trivial due to additional features (originating from spin-orbit coupling or zero field splitting) in their EPR spectra. The features of the EPR signal generally influence the shape of enhancement profiles. Therefore, the metal ion with a simpler EPR signal i.e.,  $\text{Gd}^{3+}$ , is chosen as the starting point for the investigation of DNP mechanisms. Varying concentrations (2, 10, 20 mM) of a water-soluble and stable complex Gd-DOTA was dissolved as the PA in a glycerol-water solution of  $^{13}\text{C}$ ,  $^{15}\text{N}$  - urea. Field profiles of DNP enhancement on each nuclear type ( $^1\text{H}$ ,  $^{13}\text{C}$ , and  $^{15}\text{N}$ ) establishes SE as the active DNP mechanism at the smallest PA concentration (2 mM). This confirms the theoretical predictions that narrow line width of the  $\text{Gd}^{3+}$  EPR signal arising from the central transition (CT,  $m_s = -1/2 \rightarrow 1/2$ ) allows for resolved SE DNP. However, that is no longer the case at higher PA concentrations of 10 and 20 mM. At higher  $\text{Gd}^{3+}$  concentrations, the CE mechanism contributes significantly and varies with nuclear Larmor frequency ( $\omega_n$ ) of the concerned nuclei. The enhancement maxima shifts towards the EPR resonance as the contribution from CE increases. This shift is evident in the field profiles of  $^{15}\text{N}$  and  $^{13}\text{C}$ , whereas that of  $^1\text{H}$  is least influenced. This observation can be explained by combining theoretical estimates with the experimental data; the CE is evoked by increased dipolar coupling ( $D_{ee}$ )—a prerequisite for CE—between neighboring  $\text{Gd}^{3+}$  spins as the statistical inter-spin distance shortens at elevated concentrations. This finding is important because the knowledge of active DNP mechanisms is essential for accurate interpretation of results from DNP experiments.

From the experiments on Gd-DOTA it becomes clear that concentration, inter-spin distances, and hence induced  $D_{ee}$  are intertwined. In order to explicitly address the influence of inter-spin distances on DNP mechanisms we started a collaboration with the group of Adelheid Godt (Bielefeld). In this collaborative project, bis-complexes of the type Gd(III)-spacer-Gd(III) with variable spacer lengths were investigated. These PAs provided an excellent model system where the influence of only inter-spin distances can be determined for a fixed  $Gd^{3+}$  concentration. A small PA concentration of 4 mM is used to ensure absence of significant inter-molecular dipolar interactions. A mono-Gd complex of similar geometry and chemistry is taken as a reference for SE DNP.

The mono-Gd complex yields enhancements arising from SE as expected from negligible inter-molecular  $D_{ee}$ . The contribution of CE increases as the inter-spin distances between  $Gd^{3+}$  ions become shorter going from 3.4 nm  $\rightarrow$  2.1 nm  $\rightarrow$  1.4 nm  $\rightarrow$  1.2 nm due to corresponding increase in  $D_{ee}$ . The extent of CE on  $\omega_n$  follows the same trend as for Gd-DOTA. Highest CE contribution is observed on nuclei with the smallest  $\omega_n$   $^{15}N$  because smaller  $\omega_n$  approaches the width of the EPR signal, this is an additional requirement for CE DNP. Representative observations on  $^{13}C$  nuclei are shown in the graphical abstract (B) where an enhancement doublet for bis(Gd-chelate) with 2.1 nm inter-spin distance marks the transition clearly with maxima corresponding to SE and CE each.

The field position for maximum DNP enhancement corresponding to Gd-DOTA, is used for DNP experiments on Ubiquitin with an attached Gd-tag as PA. The success of DNP on this sample illustrates the possibility of site-directed DNP with metal ions tags as PAs. As a perspective Gd-tags can be used to examine change in conformation of a protein that would give higher enhancements due to CE if two  $Gd^{3+}$  labeled domains are closer in space. In a separate project,  $Mn^{2+}$  ( $S = 5/2$ ) bound to the divalent site of a hammerhead ribozyme was used as a PA which resulted in the first demonstration of intra-complex DNP using an intrinsically bound metal ion PA.

## Graphical abstract



(A) Distribution of  $\text{Gd}^{3+}$  ions with respect to concentration is shown as a random distribution of blue dots;  $^{15}\text{N}$  DNP field profiles show an increased contribution from CE (dotted curves) as the concentration increases. (B)  $^{13}\text{C}$  DNP field profiles for bis(Gd-chelate)s corresponding to variable inter-spin distance indicate a transition from SE (positioned at the orange dotted line) to CE (positioned at the blue dotted line) mechanism.





# Contents

<b>Contents</b>	<b>i</b>
<b>List of Figures</b>	<b>iii</b>
<b>1 Introduction</b>	<b>1</b>
1.1 Motivation and aim . . . . .	3
1.2 List of publications and contributions . . . . .	5
1.3 List of conferences attended . . . . .	6
<b>2 Dynamic nuclear polarization</b>	<b>9</b>
2.1 DNP improves sensitivity . . . . .	9
2.2 Method and Instrumentation . . . . .	10
2.3 Quantization of enhancement . . . . .	12
2.4 Sample constitution . . . . .	13
2.5 DNP Mechanisms . . . . .	16
<b>3 EPR spectra and DNP profiles</b>	<b>21</b>
3.1 Shape of EPR spectra . . . . .	21
3.2 Estimation of field profiles . . . . .	26
<b>4 Metal ions in magnetic resonance</b>	<b>33</b>
4.1 Rise of metal ions for MAS DNP . . . . .	34
4.2 Advantages of metal ions . . . . .	35
4.3 Practical aspects . . . . .	38
<b>5 DNP with metal ions</b>	<b>41</b>
5.1 Endogenous Mn <sup>2+</sup> as PA in hammerhead ribozyme . . . . .	41
5.2 Active DNP mechanism(s) via Gd <sup>3+</sup> . . . . .	44
5.3 PA concentration vs inter-spin distance for CE DNP . . . . .	48
5.4 Conclusion . . . . .	50

<b>ii</b>	Contents	
	5.5 Outlook . . . . .	52
<b>6</b>	<b>Zusammenfassung</b>	<b>53</b>
<b>7</b>	<b>Glossary</b>	<b>59</b>
	<b>Bibliography</b>	<b>61</b>
	<b>Appendix publications</b>	
	<b>Acknowledgments</b>	
	<b>Curriculum Vitae</b>	

## List of Figures

2.1	Schematic representation of a MAS DNP experimental setup . . . . .	10
2.2	Direct and indirect DNP pulse sequences . . . . .	11
2.3	An example of DNP experiment on hammerhead ribozyme sample . . . . .	12
2.4	Overview of polarizing agents . . . . .	15
2.5	DNP mechanisms and their prerequisites . . . . .	17
2.6	Energy level diagram of SE and CE . . . . .	18
3.1	Simulated EPR spectra of nitroxide and Gd-DOTA . . . . .	21
3.2	Spin energy splitting of $Gd^{3+}$ . . . . .	25
3.3	Effect of various parameters on EPR spectra . . . . .	26
3.4	Estimation of SE DNP field profiles . . . . .	28
3.5	SE DNP field profiles of MnDOTA . . . . .	29
3.6	Estimation of CE DNP field profiles . . . . .	31
4.1	Stable metal complexes of $Gd^{3+}$ and $Mn^{2+}$ . . . . .	33
4.2	$Mn^{2+}$ and $Gd^{3+}$ tags for direct DNP . . . . .	35
4.3	DNP with globally distributed PAs vs site-targeted DNP . . . . .	36
4.4	DNP field profiles with TOTAPOL vs Gd-DOTA . . . . .	37
4.5	EPR spectra of various PAs at 140 GHz and 275 GHz . . . . .	37
4.6	Microwave power dependence of enhanced NMR signal . . . . .	40
5.1	Intra-complex DNP via $Mn^{2+}$ ion bound to inactivated hammerhead ribozyme . .	42
5.2	EPR spectra vs DNP field profiles of Gd-DOTA . . . . .	45
5.3	Gd-DOTA and bis-(Gd-complex)es as PAs . . . . .	47
5.4	Transition from SE to CE DNP in bis-(Gd-complex)es . . . . .	49
5.5	Comparison of optimum inter-spin distance between nitroxide and $Gd^{3+}$ for CE DNP . . . . .	50



## Chapter 1

### **Introduction**

The central theme of structural biology is that structure defines the function. Understanding structure is vital to understand the function of individual units in biomolecules. The same applies to materials as well, where arrangements of atoms control the physical properties of the material [Wilder et al., 1998]. In order to scrutinize structure, choosing the right characterization techniques from the available toolbox is imperative. Surface and bulk characterization techniques are often utilized in synergy to determine the structure of materials and biomolecules. Solid-state nuclear magnetic resonance (NMR) with magic angle spinning (MAS) is one of the widely used techniques. It has played a major role in biomolecular structural determination, catalysis and materials optimization, and innovation in chemical industry [Watts, 2005]. The signals arising from nuclear spins reveal information about their electronic and chemical environment. Solid-state NMR is especially applicable to study large and insoluble biomolecules which cannot be studied in solution form. MAS NMR also surpasses X-ray crystallography for biomolecules that do not crystallize, intrinsically disordered proteins, and other amorphous samples. Solid-state NMR has made possible to tackle various challenges in structural biology such as the arrangement of amyloidogenic peptides [Quinn and Polenova, 2017], proteins with (proto-)fibrils [Jaroniec et al., 2004], and membrane proteins in their native lipidic environment [Kaur et al., 2016]. Efforts have been made towards achieving in-cell application of MAS NMR for investigation of such species within cells and viruses [Selenko and Wagner, 2007]. In materials science, MAS NMR has been used to understand catalyst qualities, explore glasses, functional materials, energy materials, biomass, soil sediments, polymers, hybrid biomaterials, sol-gel material, micro or macroporous materials among others [Ashbrook and Dawson, 2016; Ashbrook and Sneddon, 2014; M. and E., 2012].

Evidently, solid-state NMR is a powerful spectroscopic method and has applications in various fields of research. However, one limitation of this technique is inherently low sen-

sitivity. Sensitivity is directly correlated to the gyromagnetic ratio ( $\gamma$ ) of the spin system. For example, nuclear spins have smaller  $\gamma$  than electron spins, therefore, NMR is less sensitive than electron paramagnetic resonance (EPR). One way to improve the sensitivity/signal intensity of NMR experiments is by transferring spin polarization from highly polarized electron spins under microwave irradiation. The method based on such polarization transfer is called dynamic nuclear polarization (DNP). With DNP over two- to three-fold magnitude of signal enhancements can be achieved leading to a significant shortening of experimental time. This is especially relevant for multi-dimensional experiments that become prohibitively long with added dimensions [Donovan et al., 2017]. By the virtue of signal gain obtained by DNP, solid-state NMR has found applications in areas of research otherwise inaccessible due to limited sensitivity. Employing DNP has made the investigation of important and challenging biological systems feasible [Smith et al., 2015].

The extent of sensitivity gain promoted by DNP relies on various factors, the source of electron spin polarization being a major contributor. Paramagnetic species, called polarizing agents (PAs) are doped uniformly in a matrix of analyte nuclear spins in prepared DNP samples. Biomolecules can also be spin labeled with PAs at specific sites/positions [Maly et al., 2012]. The integration of PAs, their stability, and mechanism(s) of polarization transfer are other factors that contribute to the efficacy of DNP.

Uniformly distributed PAs improve the sensitivity of nuclear spins inside their sphere of influence. Alternative schemes for selectively enhancing the signal from certain nuclear species can yield invaluable structural information. Along with improved signal quality, the prospect of obtaining site-specific information by DNP has inspired interest and effort in the search for labels that can be attached or bound to intended molecular sites [Wylie et al., 2015]. Utilization of such endogenous PAs offers multifaceted benefits including enhancement of NMR signal of desired nuclear spins and maintained the integrity of the biomolecule in its natural state. Endogenous semiquinone radical produced through reduction of native flavin mononucleotide in a flavodoxin protein has been shown to obtain enhanced polarization of  $^1\text{H}$  spins [Maly et al., 2012]. In many cases, enhanced polarization from PAs is lost in the matrix by spin diffusion, such polarization losses can be avoided by site-directed spin labeling (SDSL). For example, nitroxide bi-radical tag bound covalently to

a small protein dihydrofolate reductase has been shown to give better signal enhancement on the protein, as compared to the classically co-dissolved bi-radical [Rogawski et al., 2017]. Loss of polarization to the matrix can be avoided by perdeuteration. However, this approach is expensive and has limited physiological relevance, for instance, perdeuteration is toxic in-vivo [Money and Myles, 1974]. Moreover, addition of solvent matrix and potential phase separation is also circumvented in such sample preparation.

Plenty of paramagnetic species occur naturally in biomolecules, such as  $Mn^{2+}$  ions in arginase– the final enzyme of the urea cycle. Native diamagnetic ions can also be replaced by paramagnetic ones owing to their similar coordination properties. Site-specifically bound metal ions make a unique situation for DNP where the sample is stoichiometrically unadulterated and the spatial confinement of the paramagnetic ion is defined.

## 1.1 Motivation and aim

Improved quality of multi-dimensional correlation spectroscopy of low- $\gamma$  nuclei is highly sought-after as it reveals vital information about the structure of biomolecular sites under investigation. Immobilized paramagnetic species bound to the biomolecule of interest facilitate and even broaden the scope of information that can be obtained by DNP enhanced NMR spectroscopy. Localization of polarization lays the foundation of extracting site and state-specific information. DNP with nitroxide bi-radicals leads to non-selective enhancement of  $^1H$  and  $^{13}C$ , i.e., both resonances are simultaneously polarized [Maly et al., 2010b]. Sometimes polarization is lost in the sample matrix by spin-diffusion through  $^1H$  network. Deuteration schemes are employed in such cases. For example, an endogenous flavin in its reduced semiquinone radical form has been shown to localize polarization within the protein molecule in absence of highly-protonated spin-diffusion promoting matrix [Maly et al., 2012]. In another study, the use of covalently attached bi-radical, and the absence of proton containing matrix was proposed as a way to “contain” the polarization locally [Rogawski et al., 2017].

Protons in the sample promote spreading of polarization via a strong  $^1H$  network and thus signal decay due to relaxation. Such a situation can be avoided by directly polarizing low- $\gamma$  nuclei ( $^{13}C$  and  $^{15}N$ ). This can be achieved either by perdeuteration or utilizing PAs that can

selectively polarize low- $\gamma$  nuclei. PAs with narrow EPR linewidths (e.g., high spin metal ions) are suitable for such applications. Stable complexes of high-spin metal ions are additionally advantageous over nitroxides due to their non-toxicity under physiological conditions. For that reason,  $Gd^{3+}$  complexes with 1,4,7,10-tetraazacyclododecane-1,4,7,10-tetraacetic acid (DOTA) and its derivatives are often used as contrast agents in magnetic resonance imaging (MRI). Besides forming stable tags for SDSL,  $Gd^{3+}$  can also replace naturally occurring diamagnetic ions of similar size. Use of  $Mn^{2+}$  tags and  $Mn^{2+}$  substituted in place of  $Mg^{2+}$  is prevalent in dipolar spectroscopy due to the equivalence of coordination properties of  $Mn^{2+}$  and  $Mg^{2+}$  [Shannon, 1976]. The work presented in this thesis focuses on  $Gd^{3+}$  and  $Mn^{2+}$  complexes as PAs for MAS DNP.

DNP mechanisms for this relatively new class of PAs are non-trivial due to starkly different electron paramagnetic resonance (EPR) properties, in contrast to well-studied nitroxide radicals ( $S = 1/2$ ). A challenge facing utilization of high-spin metal ions as PAs is the limited availability of sweepable DNP hardware. Experimental results from EPR and DNP are to be interpreted incongruence to deduce active DNP mechanisms. Therefore, EPR experiments at corresponding frequency are required for complete understanding of DNP mechanisms. Available infrastructure at BMRZ (Frankfurt) and TU Darmstadt was used for EPR and DNP experiments.

A simple model for estimation of DNP profiles w.r.t. the magnetic field was developed and tested against experimental data. A stable complex of  $Gd^{3+}$  (Gd-DOTA) was chosen as the starting point for comprehensive analysis of DNP mechanisms in the context of high-spin metal ions. Findings from investigation of Gd-DOTA inspired extension of model PA molecule. The scope of mono-Gd complex was therefore extended to bis-(Gd-complex)es, in order to probe the effect of inter-spin distance on cross effect DNP. Direct DNP on  $^{13}C$  and  $^{15}N$  nuclei with slow polarization build-up times were aimed in this project, since it facilitates selective enhancement of these insensitive nuclei and localization of polarization onto the molecular region of interest.

Possibility of using  $Gd^{3+}$  and  $Mn^{2+}$  as PA for biomolecules was also explored. Therefore, various  $Gd^{3+}$  binding tags were tested on a small protein–Ubiquitin. Owing to the potential of



Mn<sup>2+</sup> to replace native Mg<sup>2+</sup> ions, a molecule that naturally binds a Mg<sup>2+</sup> ion was chosen as the analyte system. A Hammerhead ribozyme macromolecule with a single available divalent site for Mg<sup>2+</sup> or Mn<sup>2+</sup> binding was thus investigated. The optimum signal enhancement condition caused by polarization from Mn<sup>2+</sup> ion within the ribozyme was determined by using theoretical estimates developed earlier from simpler experiments on Gd-DOTA.

## 1.2 List of publications and contributions

1) P. Wenk, **M. Kaushik**, D. Richter, M. Vogel, B. Suess, and B. Corzilius. "Dynamic Nuclear Polarization of Ribonucleic Acid with Endogenously Bound Manganese." *J. Biomol. NMR* 63, 97-109 (2015).

The author contribution was performance of DNP experiments with Mn<sup>2+</sup> and AMUPol samples, and critical reading of the manuscript.

2) **M. Kaushik**, T. Bahrenberg, T. V. Can, M. A. Caporini, R. Silvers, J. Heiliger, A. A. Smith, H. Schwalbe, R. G. Griffin, and B. Corzilius. "Gd(III) and Mn(II) complexes for dynamic nuclear polarization: small molecular chelate polarizing agents and applications with site-directed spin labeling of proteins." *Phys. Chem. Chem. Phys.* 18, 27205-27218 (2016).

The author contribution was performance of EPR and DNP experiments on Gd-DOTA samples of various concentrations, data analysis, and writing and critical reading of the manuscript.

3) **M. Kaushik**, M. Qi, A. Godt, B. Corzilius. "Bis-Gadolinium Complexes for Solid Effect and Cross Effect Dynamic Nuclear Polarization." *Angew. Chem.* 134, 4359-4363 (2017); *Angew. Chem. Int. Ed.* 56, 4295-4299 (2017)

The author contribution was performance of EPR and DNP experiments, data analysis and presentation, as well as writing and critical reading of the manuscript.

4) A.L. Lilly Thankamony, J. J. Wittmann, **M. Kaushik**, B. Corzilius. "Dynamic nuclear polarization for sensitivity enhancement in modern solid-state NMR." *Prog. Nucl. Magn. Reson. Spectr.* 102-103, 120-195 (2017)

The author contribution was literature research, consultation about content, writing sections of this review, and critical reading of the manuscript.

### 1.3 List of conferences attended

#### Oral presentations

- (Invited) 39<sup>th</sup> Joint Conference of the French and German Magnetic Resonance Societies, September 2017, Bayreuth (Germany)
- 10<sup>th</sup> Alpine conference on solid-state NMR, September 2017, Chamonix-Mont Blanc (France)
- (Invited) Ringberg Meeting 2016: Connecting EPR, ssNMR and DNP for the study of complex biomolecules, December 2016, Kreuth (Germany)
- Sonderforschungsbereich SFB Conference 2016: RNA Structural Biology, November 2016, Bad Homburg vor der Höhe (Germany)
- 38<sup>th</sup> FGMR Discussion Meeting of the German Magnetic Resonance Society, September 2016, Düsseldorf (Germany)
- (Selected) 58<sup>th</sup> Annual Rocky Mountain Conference on Magnetic Resonance, July 2016, Breckenridge (Colorado, USA)
- 5<sup>th</sup> International DNP symposium, August 2015, Egmond aan Zee (The Netherlands)
- RNA Sonderforschungsbereich SFB09 winter school, February 2015, Obergurgl (Austria)

#### Poster presentations

- 9<sup>th</sup> BMRZ symposium, June 2017, Bad Homburg vor der Höhe (Germany)
- 58<sup>th</sup> Annual Rocky Mountain Conference on Magnetic Resonance, July 2016, Breckenridge (Colorado, USA)
- 37<sup>th</sup> FGMR Discussion Meeting of the German Magnetic Resonance Society, September 2015, Darmstadt (Germany)
- 5<sup>th</sup> international DNP symposium, August 2015, Egmond aan Zee (The Netherlands)
- COST Summer School on Hyperpolarisation, June 2015, Hampshire (United Kingdom)

- European congress on Magnetic Resonance (EUROMAR), July 2014, Zürich (Switzerland)
- COST Annual Meeting: Spin Hyperpolarisation in NMR and MRI, June 2014, Zürich (Switzerland)
- EMBO practical course: solution and solid-state NMR of paramagnetic molecule, July 2014, Sesto Fiorentino (Italy)



## Chapter 2

# Dynamic nuclear polarization

### 2.1 DNP improves sensitivity

The low intrinsic sensitivity of NMR is caused by the small thermal population differences of the spin states ( $\alpha$  and  $\beta$ ), determined by Boltzmann distribution (equation 2.1).

$$\frac{N_\alpha - N_\beta}{N_\alpha + N_\beta} = \tanh\left(\frac{\gamma\hbar B_0}{2kT}\right) \quad (2.1)$$

where  $N_\alpha$  and  $N_\beta$  are the populations of respective spin states,  $\hbar$  is Dirac constant,  $B_0$  is the external magnetic field,  $k$  is the Boltzmann constant, and  $T$  is the temperature, and  $\gamma$  is the gyromagnetic ratio of the spin system. The thermal signal-to-noise can be improved, to a certain extent, by employing lower experimental temperatures and/or higher external magnetic fields. However, the gain in thermal population, recovered by variation of  $B_0$  and  $T$  is small. Significantly large non-thermal population gain can be achieved with hyperpolarization techniques. The signal enhancement ( $\varepsilon$ ) is quantified as the ratio of signal intensities with and without hyperpolarization. Theoretical maximum enhancement factor ( $\varepsilon_{max}$ ), obtained by transferring polarization from spin  $S$  to  $I$  is given by:

$$\varepsilon_{max} = \frac{\gamma_S}{\gamma_I} \quad (2.2)$$

The  $\gamma_e$  of electron spins is several orders of magnitude higher than  $\gamma_n$  of nuclear spins, for example,  $\gamma_e \approx 658 \times \gamma(^1H)$ ;  $\gamma_e \approx 2620 \times \gamma(^{13}C)$ ; and  $\gamma_e \approx 6510 \times \gamma(^{15}N)$ . This makes hyperpolarization techniques especially relevant for low- $\gamma$  nuclei (e.g.,  $^{13}C$ ,  $^{15}N$ ). Hyperpolarization techniques such as para-hydrogen induced polarization (PHIP) [Duckett and Mewis, 2012], chemically-induced dynamic nuclear polarization (CIDNP) [Lawler, 1972], spin-exchange optical pumping (SEOP) [Walker, 2011], and dynamic nuclear polarization (DNP) [Ardenkjaer-Larsen, 2016] benefit from improved sensitivity using this method.

Longer relaxation times in solids, often limit the repetition rates and the number of scans practicable within reasonable experimental times. However, with an enhanced signal,

spectra of better quality can be recorded with the same or even shorter acquisition time. Thus DNP when combined with MAS NMR, alleviates the restriction that low sensitivity puts on potential applications of MAS NMR.

## 2.2 Method and Instrumentation

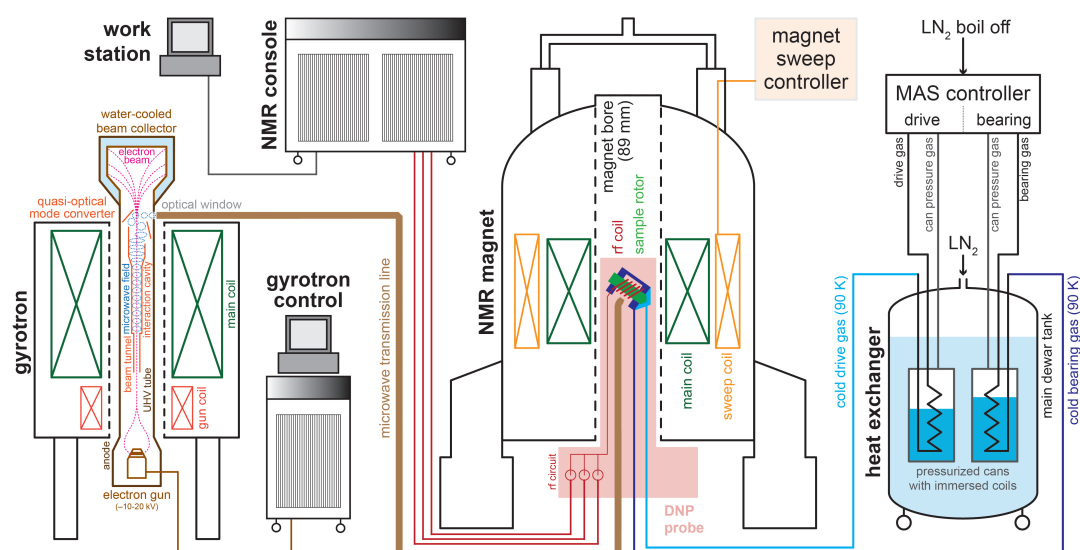


**Figure 2.1** Schematic representation of an experimental setup for DNP MAS NMR spectroscopy. MAS unit is coupled with a control unit and a cryogenic setup for low-temperature experiments. High power microwave (mw) source is coupled to the sample chamber by a corrugated waveguide. A typical MAS NMR magnet is augmented by additional sweep coil for a small variation in  $B_0$ . (Adapted from [Thankamony et al., 2017])

DNP Instrumentation requires three main components i.e., a high-field NMR magnet, coupled high-power microwave source, and a cryogenic MAS probe. Therefore, extensive and expensive modifications are made to the existing MAS NMR setup. Figure 2.1 shows schematic of such a setup.

High power mw source is required for DNP, partly due to the absence of resonance cavity in MAS NMR setup, and partly due to the forbidden nature of DNP transitions. Additionally, high-frequency mw sources are required in accordance with high magnetic fields. This was the restricting factor for high-field DNP in 1990's. Solid state sources available for EPR spectroscopy at the time offered inadequate output power (in mW) in contrast to tens of watts required for DNP. High-frequency, high-power microwave sources were introduced for DNP by combined efforts from groups of Temkin and Griffin [Becerra et al., 1993]. These

electron cyclotron maser devices, called gyrotrons, produce microwaves by the acceleration of annular shaped high-energy electron beam in a longitudinal magnetic field. Custom built MAS DNP set-ups had largely been used for research. Subsequently, gyrotrons were made commercially available by Bruker Biospin in 2009 [Rosay et al., 2010]. In a DNP setup, continuous microwave irradiation from gyrotron source is coupled to NMR magnet through a corrugated waveguide to minimize power losses. For specialized applications of DNP where the external magnetic field is to be varied, an additional sweep coil is coupled to the main magnetic field. Instruments working at higher fields of 14.1 and 18.8 T have also been developed to extend the scope and application of MAS DNP [Matsuki et al., 2010].

Cryogenic probes have been developed for low temperatures DNP and nitrogen is the most commonly used cryogenic gas for temperatures of about 110 K. Lower temperatures (25 K) can be achieved by employing specialized instrumentation such as heat exchangers, helium cooling, closed loop circuit of gas flow [Lee et al., 2016; Thurber et al., 2013].

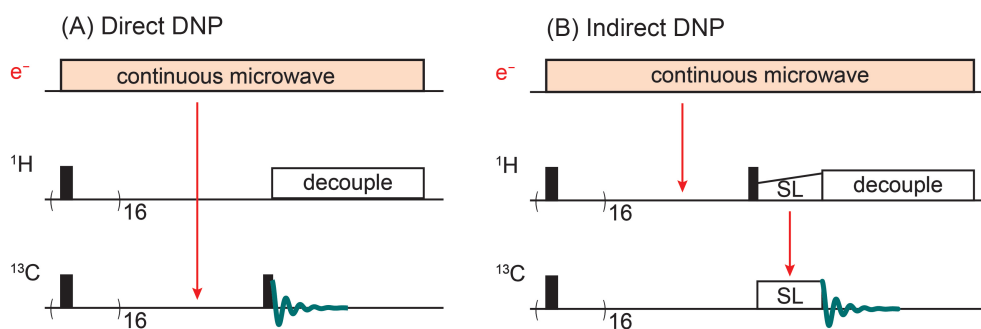


**Figure 2.2** Schematic of pulse sequences used for DNP experiments. Continuous microwave irradiation (pale orange block) drives electron polarization. Conventional (A) direct excitation and (B) cross-polarization pulse sequences are employed with a pre-saturation pulse sequence of 16  $\pi/2$  pulses. Red arrows indicate pathway of polarization transfer.

Execution of MAS DNP experiments is practically the same as standard MAS NMR experiments. Major differences between these two are — spinning at cryogenic temperatures, the presence of microwaves, and paramagnetic doping of the sample. Paramagnetic relaxation effects caused by doping, are to be considered while setting up a DNP NMR experiment. Therefore, delay times are optimized accordingly. Figure 2.2 shows pulse sequences for direct and indirect (cross polarization via  $^1\text{H}$ ) DNP on  $^{13}\text{C}$  nuclei. Standard NMR pulse sequences are preceded by a pre-saturation pulse train consisting of 16 flip pulses (of  $90^\circ$

each) and a subsequent polarization delay during which (enhanced) polarization can build up. This allows for reproducible and quantitative measurement, especially in cases where reaching a quasi-equilibrium using dummy scans is not possible due to long build-up times.

### 2.3 Quantization of enhancement

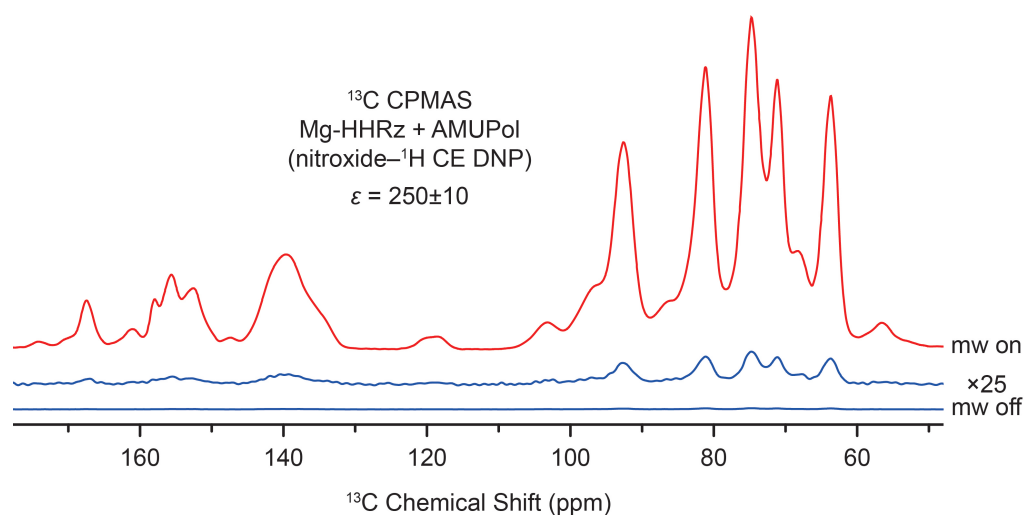


**Figure 2.3**  $^1\text{H}$  to  $^{13}\text{C}$  cross polarization spectra of a hammerhead ribozyme (HHRz), with (red) and without (blue) DNP from AMUPol bi-radical. The spectra are recorded on a 400 MHz DNP spectrometer from Bruker Biospin, with a gyrotron operating at 263 GHz. (Data taken from [Wenk et al., 2015])

Signal enhancement ( $\epsilon$ ) by DNP is reported as the ratio of signal intensity of the NMR spectrum with 'mw on' (DNP) and 'mw off' (without DNP). An example of DNP MAS NMR spectra is shown in Figure 2.3,  $\epsilon$  of about 250 is observed for a Hammerhead ribozyme sample with AMUPol as the polarizing agent. An enhancement of  $\epsilon$  corresponds to the time-savings of  $\epsilon^2$ -fold, which is exceptionally advantageous for time-consuming multi-dimensional correlation spectroscopy [Takahashi et al., 2013]. For most practical purposes this is a valid and practical measure of effectiveness of DNP. However, in order to evaluate and rationalize the true sensitivity gain obtained by DNP, all other contributing factors must be considered [Takahashi et al., 2012].

The absolute sensitivity ratio (ASR) is calculated by accounting for differences in NMR and DNP experiments. Some factors lead to increase in sensitivity with DNP, for example, lower temperatures reduce thermal noise and boost magnetization due to the Boltzmann distri-



bution. Paramagnetic relaxation in a DNP sample due to doped electron spins, shortens the nuclear longitudinal relaxation times ( $T_{1n}$ ), thus facilitating shorter recycle decay and faster repetition of the experiment [Takahashi et al., 2012]. On the other hand, some factors may worsen the ASR, for example, paramagnetic relaxation leads to very fast signal decay of nuclear spins in direct contact with the electron spin, thus said nuclear spins become unobservable by NMR. Signal bleaching and line broadening due to paramagnetic centers also affect the ASR. Reduction in analyte volume to accommodate for glass forming matrix and PAs might be of concern. In addition to that, magnetic field strengths, performance of respective probes, and efficiency of pulse sequences etc. also influence the sensitivity gain [Barnes et al., 2008]. Development of NMR instrumentation, pulsed microwave sources, helium cooling set-up, new methods and applications, sample preparation techniques, and investigation of DNP mechanisms are constantly being improved for better sensitivity gains from DNP as a technique [Thankamony et al., 2017].

## 2.4 Sample constitution

The information extracted from DNP experiments is to be viewed in the light of sample-constitution for accurate interpretation of the data. Clearly, sample preparation plays a crucial role in the success of an experiment. In a DNP experiment, the electron polarization to nuclear spins of analyte is provided by unpaired electrons from radicals, or metal ions with open shell configuration. PA is often uniformly dispersed in the analyte-containing solvent matrix. In the frozen state, the solvent matrix can crystallize and cause phase separation of the PA from the analyte molecules, resulting in diminished enhancements [Ong et al., 2013]. For this reason, good glass-forming solvent mixtures, glycerol-water and Dimethylsulfoxide-water are often used in aqueous samples [Baudot, 1998]. These mixtures additionally offer cryoprotection of the analyte upon freezing. The presence of significant amounts of cryoprotectant causes a reduction in sample filling factor and consequently reduction in signal intensity. Alternative sample preparation approaches have been developed to counter such situations, for example, matrix-free approach [Takahashi et al., 2013] - where the solvent is dried out of the sample, leaving PA in the analyte; and wetness impregnation [Lesage et al., 2010] - where minimum volume of solvent is used to wet the sample, is specifically suitable for porous samples insoluble in the PA-bearing solvent.

Other sample preparation techniques are co-sedimentation of large biomolecules [Ravera et al., 2014] by centrifugation, co-condensation of nitroxide radicals in a post-synthesis step with mesoporous silica [Thankamony et al., 2012], film casting of polymers by evaporation of excess solvent [Le et al., 2014], or co-milling of solid samples with a cryoprotecting matrix-forming agent [Elisei et al., 2015].

Polarizing agents are an integral part of sample preparation for DNP, therefore, development of efficient PAs has been one of the focal points in DNP research. Novel PAs have been synthesized by considering all contributing factors for optimum DNP performance, such as, their stability in the sample, solubility in the glass forming matrix, and DNP efficiency by the desired mechanism (see section 2.5). As a result, the library of PA has expanded over the years owing to the collective efforts of synthetic chemistry groups.

#### 2.4.1 Overview of polarizing agents

Generally, PAs can be categorized based on several criteria such as, EPR line widths, DNP mechanisms evoked, chemical properties, number of radical moieties etc. An overview of PAs used for MAS DNP are presented in Figure 2.4, classified according to these criteria. 1,3-bisdiphenylene-2-phenylallyl (BDPA) was the first stable radical PA utilized for DNP under MAS [Koelsch, 1957]. This narrow EPR linewidth radical- BDPA, is chemically stable and dilute easily in polystyrene. BDPA-doped polystyrene was used as ideal sample in early investigations of DNP mechanisms [Hwang et al., 1967]. Even though BDPA is an excellent PA, its biological applications are limited due to its lack of solubility in aqueous mixtures. The potential biological applications of BDPA were facilitated by synthesis of a highly water-soluble and air-stable derivate, sulfonated-BDPA (SA-BDPA) [Haze et al., 2012].

Another group of water-soluble PAs with narrow EPR line width, that has contributed significantly to the development of MAS DNP is- triphenylmethyl (trityl) based radicals. Trityl derivative- OX063, has hydrophilic functional groups substituting aromatic hydrogens. This chemical modification provides chemical stability by steric hindrance and water-solubility to the trityl based radical [Ardenkjaer-Larsen et al., 1998]. In contrast to another prominent trityl derivative, Finland trityl CT-03 [Dhimitruka et al., 2010], OX063 does not contain

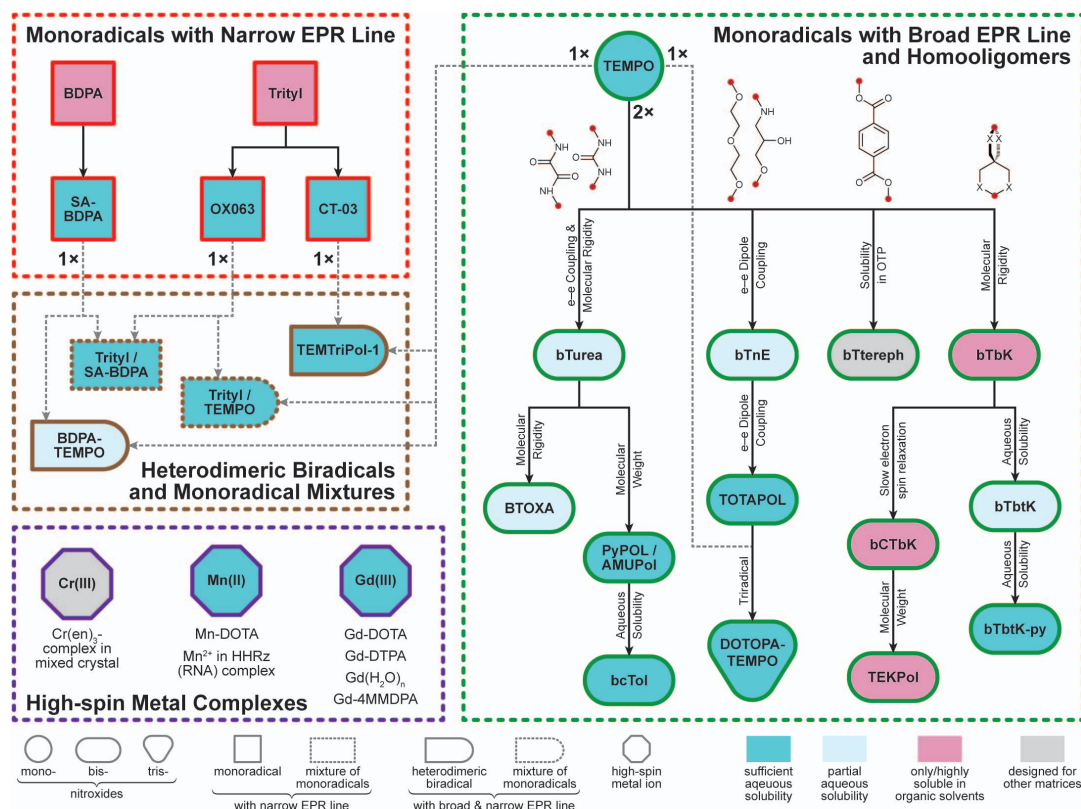


**Figure 2.4** Schematic classification of PAs used for MAS DNP. The type of radical is represented by the shape of the box, red and green box distinguishes between EPR line-shapes and the number of unpaired electrons per PA molecule. Solubility of the individual families is color-coded by shades of blue, darker shades indicate higher solubility. Factors accompanying dashed arrows indicate type and number of mono-radicals which are chemically bonded to form bi- and tri-radicals. Chemical structures with red filled circles indicate the connecting position with the TEMPO moieties on molecular tethers. Figure adapted from [Thankamony et al., 2017]

relaxation-promoting methyl groups, which alleviates the need for deuteration in order to reduce the homogeneous EPR linewidth.

BDPA and trityl based mono-radicals feature narrow and homogeneous EPR line widths, a prerequisite for solid effect (SE) DNP (see section 2.5). OX063 is a versatile PA for MAS DNP ( $\epsilon(^1\text{H}) = 91$ ), and is especially suitable for low- $\gamma$  nuclei, such as,  $^2\text{H}$  ( $\epsilon \geq 700$ ) [Maly et al., 2010a],  $^{13}\text{C}$  ( $\epsilon \geq 480$ ) [Michaelis et al., 2013b] and  $^{17}\text{O}$  ( $\epsilon \geq 115$ ) [Michaelis et al., 2013a]. For such low- $\gamma$  nuclei, the EPR linewidth is of a similar magnitude as the nuclear Larmor frequencies, allowing for a more efficient DNP mechanism- cross effect (CE) to be active (see section 2.5).

Due to the better performance CE DNP, PAs with broad and inhomogeneous EPR linewidths

gained popularity. Early DNP experiments with nitroxide mono-radicals were performed with 2,2,6,6-tetramethyl-1-piperidiny-1-oxyl (TEMPO), that gave higher signal enhancements at higher concentrations [Hall et al., 1997]. However, for general applications of DNP, high PA concentration is undesired due to paramagnetic quenching and line broadening in NMR spectra. This hurdle was surpassed with introduction of bis-nitroxides [Hu et al., 2004]. In a series of bis-TEMPO-*n*-ethyleneglycol (BTnE) bi-radicals, two TEMPO moieties were linked by poly-glycol units, and PAs with shorter linker performed better.  $^1\text{H}$  enhancement of  $\sim 175$  was obtained with 5 mM concentration of BTnE ( $n = 2$ ) PA. One drawback of the BTnE series was limited solubility in aqueous solutions. The bi-radical PA design was improved by conception of water-soluble TOTAPOL [Song et al., 2006] in 2006. Further improvement to DNP PAs has been brought about by groups of Ouari and Tordo (Aix-Marseille), and Sigurdsson (Reykjavik) by developing AMUpol [Sauvée et al., 2013] and BcTol [Jagtap et al., 2016] respectively. Tremendous efforts had been made in order to optimize the linker length, rigidity, stability, and solubility in organic and inorganic solvents [Kubicki et al., 2016]. It is to be noted that many commonly used modern bi-radicals are refined and tailored form of bis-nitroxides. A detailed survey of PA development is provided in the appendix [Thankamony et al., 2017].

Aforementioned mono- and bi-radicals are typically included in the sample as uniformly distributed exogenous PAs. Lately, endogenous PAs have been successfully used for MAS DNP. DNP with endogenous radicals in proteins and, nitroxides covalently-attached to biomolecules has been shown to yield moderate  $^1\text{H}$  enhancement factors of  $\sim 10$ . In the very first demonstration, endogenous flavin in its reduced semiquinone form was used as a PA, for  $^1\text{H}$  DNP on the flavodoxin protein [Maly et al., 2012]. DNP with immobilized nitroxide based PAs has been performed on proteins and lipids [de Alba et al., 2015; Smith et al., 2015; Wylie et al., 2015]. This work contributes to the extension of DNP with endogenous PAs, using high-spin metal ions,  $\text{Gd}^{3+}$  and  $\text{Mn}^{2+}$  (see section 5.4).

## 2.5 DNP Mechanisms

Mechanism of polarization transfer from electron spins to nuclear spins relies on their individual interaction with the external magnetic field, and their mutual interaction. Therefore, the theory of DNP is an extension of combined knowledge from EPR and NMR. The sample

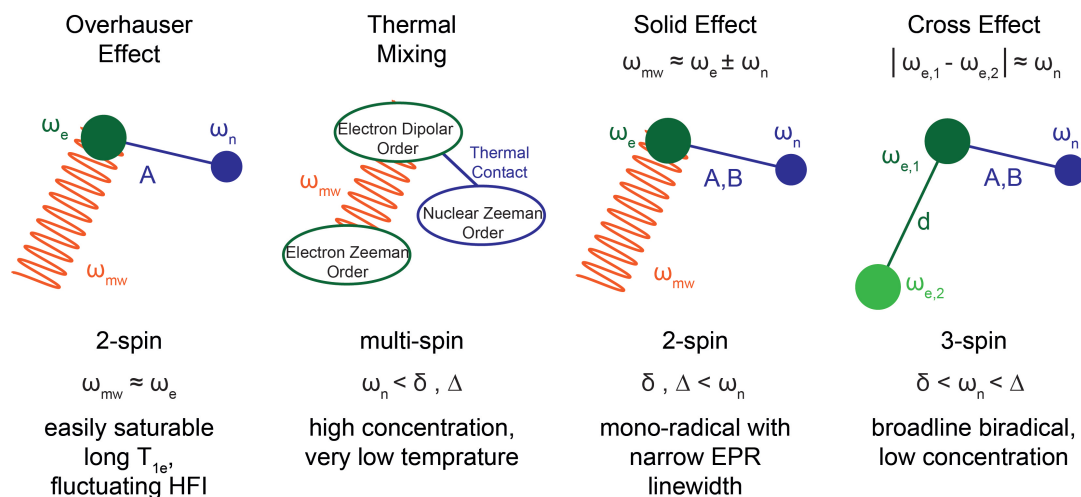


**Figure 2.5** An overview of possible DNP mechanisms with a conceptual schematic of prerequisites and conditions.

constitution and experimental conditions certainly influence the feasibility of DNP mechanisms whose respective prerequisites are illustrated in figure 2.5. The first DNP mechanism was predicted and discovered in 1953 as a result of experiments on metals. A. W. Overhauser predicted that the saturation of the conduction electrons in metals can simultaneously increase the population difference between the nuclear Zeeman levels thus increasing NMR signal several fold [Overhauser, 1953]. Soon after this prediction, Carver and Slichter published experimental results on lithium that confirmed the Overhauser effect (OE) [Carver and Slichter, 1953].

In solid dielectrics, as concerned for MAS DNP, the DNP mechanisms that mediate the polarization transfer also include solid effect (SE), cross effect (CE), and thermal mixing (TM). The SE and the CE can be modeled quantum mechanically with a system consisting of two and three spins, respectively [Hu et al., 2011]. In cases where significant electron dipolar interaction is present between two electron spins, either CE or TM can occur. TM is a macroscopic phenomenon that requires a network of coupled spins and is only active at very low temperatures (typically  $\leq 4$  K). As MAS NMR experiments are conducted at  $\sim 100$  K, this mechanism does not play a role and will not be discussed further. Clearly, the nature of DNP mechanism depends on the sample system and experimental parameters. In the context of MAS DNP, SE and CE are the most relevant DNP mechanisms and these will be discussed explicitly in the following.

## 2.5.1 Solid effect (SE)

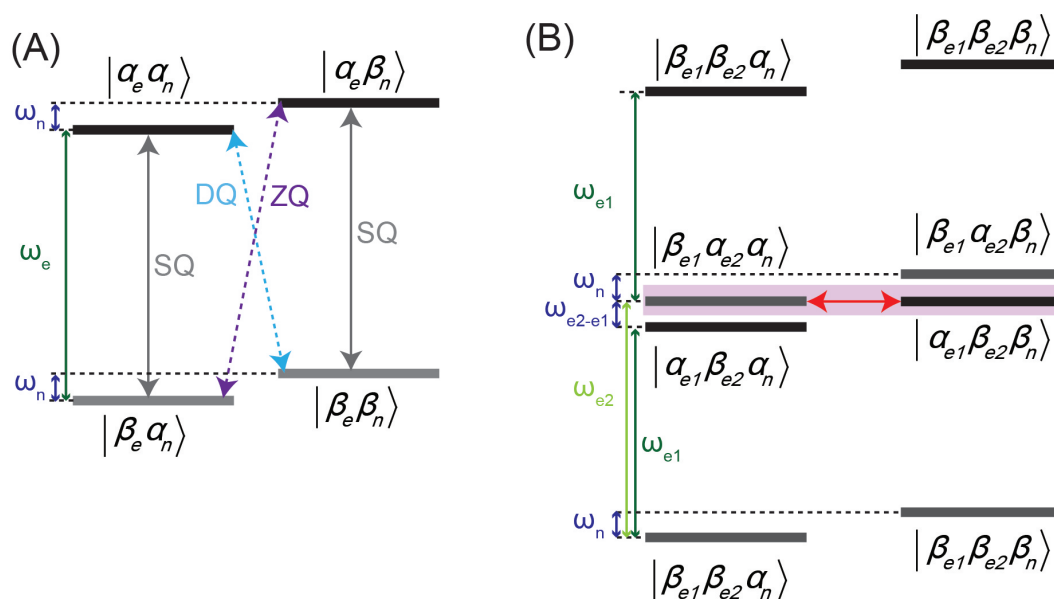


**Figure 2.6** Energy level diagram for (A) solid effect and (B) cross effect.

A prerequisite for SE DNP on a nuclear spin from a PA with electron spin is that the homogeneous ( $\delta$ ) and inhomogeneous ( $\Delta$ ) line widths of the EPR signal from the PA are smaller than the nuclear Larmor frequency ( $\omega_n$ ) of the said nuclear spin (i.e.,  $\omega_n > \delta, \Delta$ ). PAs based on BDPA and trityl mono-radicals are known to evoke SE DNP due to their narrow EPR signals.

Solid effect is the oldest known mechanism for MAS DNP and has been described as a simple two-spin model consisting of an electron spin and a nuclear spin [Abragam and Goldman, 1978; Wind et al., 1985]. The energy level diagram for this spin system, electron spin  $S = 1/2$  and nuclear spin  $I = 1/2$ , is shown in figure 2.6 (A). The optimum microwave frequency  $\omega_{mw}$  for SE is determined by the respective electron and nuclear Larmor frequencies,  $\omega_e, \omega_n$  (equation 2.3).

$$\omega_{mw} = \omega_e \pm \omega_n \quad (2.3)$$

Irradiation at  $\omega_{mw}$  leads to simultaneous flipping of electron and nuclear spins in zero quantum, ZQ (i.e.,  $\beta_e \alpha_n \leftrightarrow \alpha_e \beta_n$ ) or double quantum, DQ ( $\beta_e \beta_n \leftrightarrow \alpha_e \alpha_n$ ) which results in enhanced polarization on nuclear spin. The SE Hamiltonian ( $\hat{H}_{SE}$ ) for this two spin system consists of independent electron and nuclear Zeeman terms as well as electron-nuclear

hyperfine interaction terms.

$$\hat{H}_{SE} = \omega_e \hat{S}_z - \omega_n \hat{I}_z + A \hat{S}_z \hat{I}_z + B \hat{S}_z \hat{I}_x \quad (2.4)$$

$\hat{S}_z$  and  $\hat{I}_z$  denote z-axis vector components of the electron and nuclear spin operators  $\vec{S}$  and  $\vec{I}$ , respectively, and  $A$  and  $B$  represent the secular and non-secular terms of the electron-nuclear hyperfine coupling [Hu et al., 2011]. The non-secular HFI term  $B$  leads to mixing of spin states, partially-allowing the nominally forbidden transitions under SE matching condition (equation 2.3). The ZQ and DQ transitions are about  $10^{-4} - 10^{-8}$  times less probable than the single quantum (SQ) transitions (i.e.,  $\beta_e \alpha_n \leftrightarrow \alpha_e \alpha_n$  and  $\beta_e \beta_n \leftrightarrow \alpha_e \beta_n$ ). The forbidden transitions can be excited by high mw powers, typically tens of watts provided by gyrotrons.

Maximum enhancements of positive and negative signs are observed at the resonance condition for ZQ and DQ transitions, respectively. Enhancements of opposite signs can cancel each other out if DQ and ZQ are not well separated due to small  $\gamma$  or broad homogeneous EPR linewidth. Thus resulting enhancement profiles resemble the first-order spectral derivative, termed as differential solid effect [Wenckebach, 2008].

### 2.5.2 Cross effect (CE)

The theoretical description of CE DNP is considerably complex in comparison to that of SE. The simplest explanation of CE DNP requires a minimum of three spins— two electron spins with dipolar coupling ( $D_{ee}$ ) and a nuclear spin which is hyperfine coupled to at least one of the electrons. Fulfillment of these prerequisites relies on the matching conditions given by equation 2.5, where the difference in effective Larmor frequencies ( $\omega_{e1}, \omega_{e2}$ ) of the two electron spins equals the nuclear Larmor frequency while at the same time one of the two electron spins is on resonance with the incident mw frequency.

$$\omega_n \approx |\omega_{e2} - \omega_{e1}| \quad \wedge \quad \omega_{mw} = \omega_{e2} \quad \vee \quad \omega_{e1} \quad (2.5)$$

where,  $\omega_{e1}, \omega_{e2}, \omega_n$  are Larmor frequencies of first and second electron spin  $e1, e2$  and the nuclear spin  $n$ , respectively. The energy level diagram for CE mechanism is shown in figure 2.6 (B). Simultaneous flip-flop-flip of  $e1$  and  $e2$  with the nuclear spin  $n$  occurs as a result of degeneracy of energy levels  $|\beta_{e1} \alpha_{e2} \alpha_n\rangle$  and  $|\alpha_{e1} \beta_{e2} \beta_n\rangle$  or  $|\alpha_{e1} \beta_{e2} \alpha_n\rangle$  and  $|\beta_{e1} \alpha_{e2} \beta_n\rangle$

when  $\omega_n$  equals  $|\omega_{e2-e1}|$ .

The possibility of finding two electron spin packets with the difference in Larmor frequencies matching the nuclear Larmor frequency is rare considering PAs with narrow EPR line widths. Mixtures of narrow EPR linewidth radicals (BDPA- and trityl- type, TEMPO and trityl- type) have been shown to evoke CE [Hu, 2011; Michaelis et al., 2013b]. PAs with broad and anisotropic EPR spectra are commonly used where CE is evoked from two electron spin packets lying within the inhomogeneously broadened EPR spectra. Nitroxides and bis-nitroxides with broad inhomogeneous line width ( $\delta < \omega_n < \Delta$ ) are widely utilized as PAs for CE DNP.

It was considered for a long time that irradiation by mw is essential for DNP effect to take place, which is only partially true because mw irradiation is required for SE DNP. Through rigorous quantum mechanical treatment, it has been established that mw irradiation is indeed not essential for CE DNP [Thurber and Tycko, 2014]. In this scenario, CE DNP is driven by state-mixing due to modulation of spin states during the rotor period under MAS. Soon after, it was demonstrated experimentally that the NMR signal gained by CE DNP varied with the spinning frequency in a MAS NMR experiment without microwave irradiation [Mentink-Vigier et al., 2015]. Nevertheless, the magnitude of this effect is much smaller than DNP with mw irradiation. Practical and useful enhancements have been observed only with mw irradiation [Mentink-Vigier et al., 2015].



## Chapter 3

# EPR spectra and DNP profiles

### 3.1 Shape of EPR spectra

The EPR spectra of organic radicals and metal ions with the same spin ( $S = 1/2$ ) are starkly different because the latter often has higher spin-orbit coupling. The electron spin-lattice relaxation time ( $T_{1e}$ ) of metal ions are much shorter than organic radicals. Often low-temperature measurements are required to thermally lengthen  $T_{1e}$  for the observable signal. In this section, PAs are treated separately as  $S = 1/2$  system such as nitroxides; and metal ions with half-integer spin ( $S > 1/2$ ) such as  $Gd^{3+}$  and  $Mn^{2+}$ . The effects of spin interactions are discussed to explain the EPR properties of these paramagnetic species.

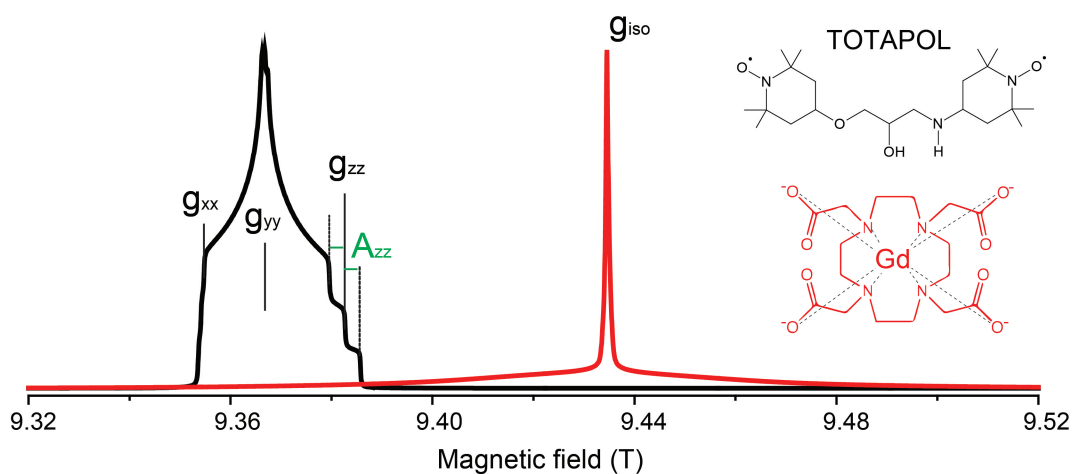


**Figure 3.1** EPR spectra of nitroxide (in black) ( $S = 1/2$ ,  $g = 2.0088, 2.0061, 2.0027$ ) and Gd-DOTA (in red) ( $S = 7/2$ ,  $g = 1.9917$ ) simulated by easyspin [Stoll and Schweiger, 2006] at microwave frequency of 263.4 GHz. Chemical structure of the paramagnetic species are correspondingly color coded.

The EPR spectrum of unpaired electrons at high magnetic fields arises primarily from electron Zeeman (EZ) interaction (i.e., interaction of electron spins with the external magnetic field  $B_0$ ) under simultaneous microwave irradiation. The electron Zeeman resonance condition for an electron spin in  $B_0$  under microwave irradiation of  $\omega_{mw}$  frequency is given by

the following equation:

$$\hbar\omega_{mw} = g_e\beta_e B_0 \quad (3.1)$$

where  $\beta_e$  is the Bohr magneton, and  $g_e$  is a dimensionless quantity that is characteristic of the electron spin ( $g$  can be defined for a general, non-specified spin). The implication of difference in  $g$ -factor can be seen in figure 3.1, for TOTAPOL, the  $g$ -value is anisotropic with components  $g_{xx}$ ,  $g_{yy}$ ,  $g_{zz}$  while for Gd-DOTA it has only one isotropic component  $g_{iso}$ . Additionally, the resonance field is determined by the magnitude of the  $g$ -factor. A complete description of the EPR spin Hamiltonian  $\hat{H}$  contains the field dependent terms such as the interaction of electron and nuclear spin magnetic dipole moments with the external magnetic field  $B_0$ , and field independent spin-spin interactions [Schweiger and Jeschke, 2001; Weil and Bolton, 2007]. Various interactions contribute to the overall spin Hamiltonian given by equation 3.2, each component will be explained separately in the following.

$$\hat{H} = \hat{H}_{EZ} + \hat{H}_{NZ} + \hat{H}_{HF} + \hat{H}_{ee} + \hat{H}_{ZFS} \quad (3.2)$$

Electron and nuclear spin magnetic dipole moments interact with the external magnetic field  $B_0$ , contributing the EZ term  $\hat{H}_{EZ}$  and the nuclear Zeeman term  $\hat{H}_{NZ}$ .

$$\hat{H}_{EZ} = g_e\beta_e B_0 \hat{S}_z \quad (3.3)$$

$$\hat{H}_{NZ} = -g_n\beta_n B_0 \hat{I}_z \quad (3.4)$$

where,  $g_e$  and  $g_n$  correspond to electron and nuclear spins and  $\beta_n$  is the nuclear magneton. The dimensionless  $g_n$  can be positive (e.g.,  $^1\text{H}$ ) or negative (e.g.,  $^{15}\text{N}$ ), in the following text  $g_n$  is defined as negative.  $\hat{S}$  and  $\hat{I}$  are spin operators of electron and nuclear spins, respectively. The third term equation 3.2 is the hyperfine interaction between electron and nuclear spins ( $I \neq 0$ ) is field independent and is represented by  $\hat{H}_{HF}$  in the spin Hamiltonian. This interaction gives rise to a  $(2I + 1)$ -fold splitting in the EPR signal. The separation between hyperfine lines is a measure of the hyperfine coupling constant given by hyperfine tensor  $\mathbf{A}$ . In general case,  $\hat{H}_{HF}$  term contains two contributions: isotropic or Fermi contact interaction ( $\hat{H}_F$ ) and the spatial interaction between electron and nuclear magnetic dipoles ( $\hat{H}_{en}$ ).

$$\hat{H}_{HF} = \hat{S}\mathbf{A}\hat{I}, \quad \hat{H}_{HF} = \hat{H}_F + \hat{H}_{en} \quad (3.5)$$

$$\text{where,} \quad \hat{H}_F = a_{iso}\hat{I}_z\hat{S}_z, \quad \text{and} \quad \hat{H}_{en} = (3\cos^2\theta + 1)a_{ani}$$

$a_{iso}$  and  $a_{ani}$  are isotropic and anisotropic components of  $\mathbf{A}$ , and  $\theta$  is the angle between  $B_0$  and the vector joining electron and nuclear spin. The dipolar interaction  $\hat{H}_{ee}$  between

paramagnetic centers  $e1$  and  $e2$  through space must be considered in the spin Hamiltonian when these spins are located close together.

$$\hat{H}_{ee} = \hat{S}_{e1} D_{ee} \hat{S}_{e2} \quad (3.6)$$

Organic radicals generally feature EPR spectra dominated by  $g$  anisotropy, hyperfine anisotropy, and dipolar interactions. When more than one nuclear spins (say  $m$ ) interact with the electron spin(s), the terms in nuclear spin operators  $\hat{I}_k$  become additive and the relevant components of the  $S = I_k = 1/2$  spin Hamiltonian from equation 3.2 are given as the following:

$$\hat{H}_{S=1/2} = g_e \beta_e B_0 \hat{S} - \sum_{k=1}^m g_{n,k} \beta_n B_0 \hat{I}_k + \sum_{k=1}^m \hat{S} \mathbf{A}_k \hat{I}_k + \sum_{k=1}^m \hat{S}_{e1} D_{ee} \hat{S}_{e2} \quad (3.7)$$

Other possible interactions are neglected in the above equation for the sake of simplicity and relevance. These interactions include exchange electron-electron interactions due to delocalization, nuclear quadrupole interactions originating from the interaction of nuclear spin  $I \geq 1$  with the electric field gradient, and interactions between two nuclear spins.

Spin-Hamiltonian corresponding to zero field splitting (ZFS) is only discussed for spin systems with  $S > 1/2$  such as metal ions  $\text{Gd}^{3+}$  ( $S = 7/2$ ) and  $\text{Mn}^{2+}$  ( $S = 1/2$ ). Spin properties of metal ions are largely influenced by the nature and symmetry of coordinating ligands, and thus induced ZFS. For  $S > 1/2$ , the ZFS interaction Hamiltonian  $\hat{H}_{ZFS}$  must be described in equation 3.2.

$$\begin{aligned} \hat{H}_{ZFS} &= D \left( \hat{S}_z^2 - \frac{1}{3}(S(S+1))\hat{1} \right) + E(\hat{S}_x^2 - \hat{S}_y^2) \\ D &= \frac{3}{2} D_{zz} \\ E &= \frac{1}{2}(D_{xx} - D_{yy}) \end{aligned} \quad (3.8)$$

$D$  is the anisotropy component of the magnetic dipole-dipole interaction, and  $E$  is the asymmetry component. ZFS parameters are non-existent in a cubic symmetry i.e.,  $D = E = 0$ . In the presence of a ligand field, the ZFS tensor assume values for axial ( $D \neq 0, E = 0$ ) or lower ( $D \neq E \neq 0$  for rhombic, tetragonal) symmetries. Depending on the spin system and symmetry of the ligand field, the parameter  $D$  can vary from a few hundred MHz to GHz [Raitsimring et al., 2005], whereas, the maximum possible value of  $E \leq D/3$ .

### 3.1.1 EPR properties of $Gd^{3+}$

Gadolinium lies in the middle of f-block rare earth metals and favors +3 oxidation state. Electronic configuration of  $Gd^{3+}$  ( $[Xe]6s^04f^7$ ) has half-filled f-orbitals that lead to  $S = 7/2$ . The valence electrons occupy 4f-orbitals which are deeply buried in the ion and are largely shielded by higher 5s-orbitals. As a result, negligible spin-orbit interaction yields a nearly isotropic ( $g = 1.99$ ). As a consequence of higher spin-multiplicity, the EPR signal consists of the central transition (CT) originating from  $m_s = -1/2 \leftrightarrow +1/2$  transition, and additional satellite transitions (STs) originating from  $m_s = -7/2 \leftrightarrow -5/2$ ,  $-5/2 \leftrightarrow -3/2$ ,  $-3/2 \leftrightarrow -1/2$ ,  $+1/2 \leftrightarrow +3/2$ ,  $+3/2 \leftrightarrow +5/2$ ,  $+5/2 \leftrightarrow +7/2$ . However, the CT is notably intense as compared to the STs which are often not visible in EPR spectrum of frozen solution (see figure 3.1). This is partly because of high transition probability of CT. For a spin system with isotropic  $g$  and linearly polarized microwave field along the x-axis, transition probability  $P_{m_s}$  is given by:

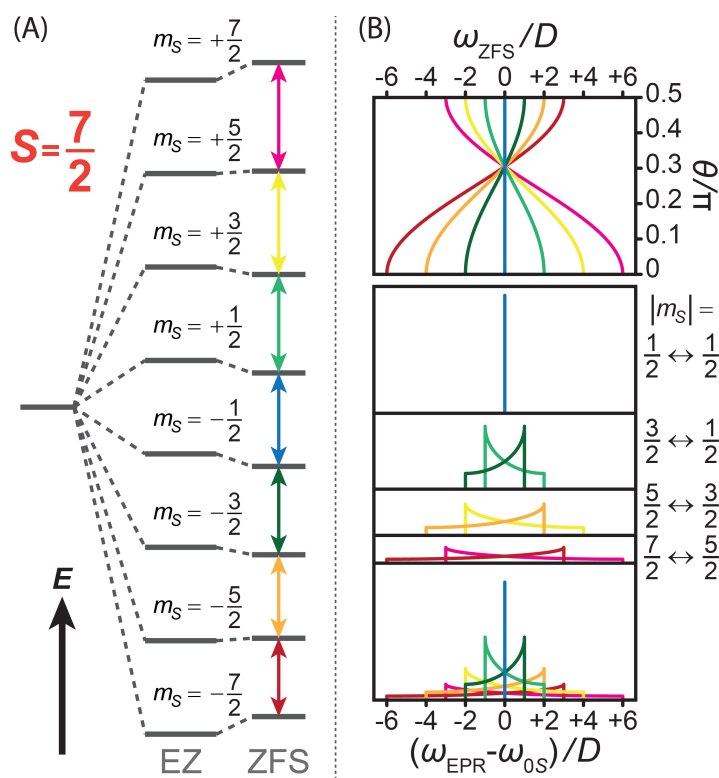
$$P_{m_s} = [S(S+1) - (m_s - 1)m_s] \cdot (g_e \beta_e B_x)^2 \quad (3.9)$$

According to the equation above,  $P_{m_{1/2}}$  is 16/7 times larger than  $P_{m_{7/2}}$ . Higher intensity of the CT line is also contributed by the sharpness of the line-shape. ZFS has a dominant contribution to the width of the EPR spectra of the high-spin systems because it leads to broadening of fine structure lines. The width of EPR lines arising from each transition is influenced mainly by ZFS anisotropy to first and/or second order. The influence of EZ and ZFS on the energy levels of  $Gd^{3+}$  is depicted in figure 3.1.1 (A). The directional character of ZFS leads to pake pattern of each ST as a result of random molecular orientations shown in figure 3.1.1 (B). First order approximation can be applied if  $\beta_e g_e B_0 \gg D$  (high-field approximation) and  $g_e$  is isotropic. The EPR resonance condition contains ZFS Hamiltonian terms of following nature:

$$\hat{H}_{ZFS}^{(1)} \propto (D(3\cos^2\theta - 1) + 3E\sin^2\theta\cos 2\phi) \left(m_s - \frac{1}{2}\right) \quad (3.10)$$

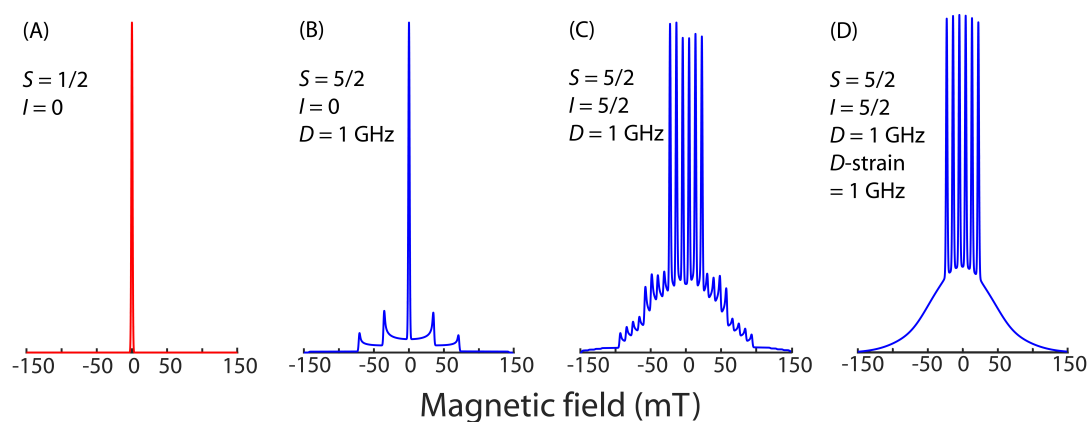
$\theta$ , and  $\phi$  are Euler angles between the molecular frame and  $B_0$ . Clearly, this term has a finite value for  $m_s \neq 1/2$  (ST) and vanishes for  $m_s = 1/2$  (CT). Thus broadening due to first order ZFS applies only to STs. This approximation is not valid for very high  $D$  parameter typically observed for  $Gd^{3+}$  and higher order correction terms are to be included. A second-order correction term  $\hat{H}_{ZFS}^{(2)}$  (equation 3.11) contributes to all transitions, although the magnitude of  $\hat{H}_{ZFS}^{(2)}$  is generally small.

$$\hat{H}_{ZFS}^{(2)} \propto \frac{D^2}{\beta_e g_e B_0} \quad (3.11)$$



**Figure 3.2** (A) Spin energy splitting of an  $Gd^{3+}$  ( $S = 7/2$ ) system with axially symmetric ZFS ( $D \neq 0$ ). Note that EZ and ZFS interactions are not to scale. The magnitude of EZ is almost twice the magnitude of ZFS at high field. (B) Angular dependence of EPR transitions shifted by the first-order ZFS and resulting shape of the EPR line as deduced from individual EPR transitions. (Adapted from [Corzilius, 2016] with permission)

The CT is only broadened by small  $\hat{H}_{ZFS}^{(2)}$  whereas ST broadens by first as well as second order effects. Consequently, CT is rather sharp and intense as compared to STs. In amorphous samples, the statistical distribution of ZFS parameters ( $D$ -strain) of  $Gd^{3+}$  is often as large as the ZFS parameter itself. Therefore, the STs are smeared out as a broad feature from infinite molecular orientations. The statistical distribution of ZFS parameter  $D$  for  $Gd^{3+}$  varies in the range of 0.6 to 2.2 GHz in complexes with water-soluble polydentate ligands [Benmelouka et al., 2009; Goldfarb, 2014; Raitsimring et al., 2005]. ZFS dominates the shape of the EPR spectra if the magnitude of  $g$ -anisotropy (if any) and hyperfine coupling to nuclear isotopes is small. For example, gadolinium isotopes  $^{157}Gd$  and  $^{159}Gd$  ( $I = 3/2$ , about 15% natural abundance each) feature a hyperfine coupling of nearly 15 MHz [Goldfarb, 2014]. The dipolar coupling can also be observed from EPR spectrum of  $Gd^{3+}$  as the CT broadens as a result of the spin-spin interaction.

3.1.2 EPR properties of  $\text{Mn}^{2+}$ 

**Figure 3.3** EPR spectra simulated with easyspin [Stoll and Schweiger, 2006] for spin systems with (A)  $S = 1/2$ , (B)  $S = 5/2$  and  $D = 1$  GHz, (C)  $S = I = 5/2$ ,  $D = 1$  GHz, (D)  $S = I = 5/2$ ,  $D = D\text{-strain} = 1$  GHz. In (C) and (D) a hyperfine coupling  $A = 250$  is considered. In a symmetric environment such as DOTA, the EPR signal from STs appear as broad baseline under intense signal from CT. Sextet pattern is typical for  $\text{Mn}^{2+}$  due to hyperfine coupling from  $^{55}\text{Mn}$  nucleus ( $S = I = 5/2$ ).

The EPR Hamiltonian of  $\text{Mn}^{2+}$  shares the high-spin characteristics of  $\text{Gd}^{3+}$ . A spin system with  $S = 5/2$  would give rise to 5 peaks, comprising of CT  $m_s = -1/2 \leftrightarrow +1/2$  and STs from  $\text{mod } m_s = 3/2, 5/2$ . Unlike  $\text{Gd}^{3+}$ ,  $\text{Mn}^{2+}$  has  $I = 5/2$  due to 100% abundant  $^{55}\text{Mn}$  nucleus. Due to that, each transition splits into six lines ( $2I + 1$  rule) separated by isotropic hyperfine coupling (about  $\sim 250$  MHz in Mn-DOTA).  $\text{Mn}^{2+}$  tends to form octahedral complexes that are highly symmetric and have negligible second order ZFS contribution. Two specific points of distinction between  $\text{Gd}^{3+}$  and  $\text{Mn}^{2+}$  are as follows: firstly, even though the effective breadth of CT is  $5 \times 254$  MHz due to the sextet pattern, each individual line is relatively narrow. Secondly, splitting into six lines decreases the net intensity of each constituent line of by  $1/6$ . Figure 3.3 shows the manifestation of high spin multiplicity and ZFS on the EPR spectra. Symmetric  $\text{Mn}^{2+}$  complexes such as Mn-DOTA give well resolved EPR spectra at high fields, with intense CT and obscured STs (see figure 3.3(D)).

## 3.2 Estimation of field profiles

In the context of DNP mechanisms, the main point of difference between classical organic PAs and high-spin metal ions come from the EPR line-shapes caused by  $g$ -anisotropy and ZFS parameters. Metal ions with broad flattened EPR signal are not suitable for DNP as the matching conditions become non-specific and unachievable with the available hardware.

Metal ions with nearly isotropic  $g$ -factor and negligible spin-orbit coupling are a suitable choice for DNP PAs.  $\text{Mn}^{2+}$  and  $\text{Gd}^{3+}$  are two such PAs with nearly isotropic  $g$  values centered at 2.00 and 1.99, respectively, as shown in the experimental EPR spectra in appendix [Kaushik et al., 2016].

Polarization transfer from electron spins to nuclear spins can only take place at appropriate resonance conditions defined by the DNP mechanisms. This can be achieved in two ways: either the magnetic field is shifted such that the electron and nuclear Zeeman interactions fulfill the matching condition with a fixed microwave frequency, or the mw frequency can directly be adjusted if a tunable microwave source is available. Thus obtained profiles of field- or frequency-dependent enhancement factors are commonly referred to as DNP field or frequency profiles. Both of these methods yield profiles that are equivalent for practical purposes. The information contained in such profiles is used to investigate DNP mechanisms and optimize DNP experiments. Initial development of DNP theory is based on *frequency profiles* obtained from experiments on static-sample where an EPR spectrometer equipped with an NMR coil is used to detect enhanced NMR signals [Feintuch et al., 2011]. For fixed-frequency gyrotron sources utilized for MAS DNP, *field profiles* are recorded with sweepable NMR magnets [Becerra et al., 1995].

### 3.2.1 Solid effect

A simple yet effective method for semi-quantitative analysis of SE DNP profiles has been presented by Shimon et al. [Shimon et al., 2012], where the spectral shape of DQ and ZQ transitions is derived from the EPR spectral shape function  $G_{EPR}(B_0)$ . The spectral shape function of SE DNP profile,  $G_{SE}(B_0)$  can be approximated by extension of SE DNP condition (equation 2.3) [Hovav et al., 2010]. DQ and ZQ peaks are modeled by shifting the EPR spectral function to the corresponding direction by  $\frac{\omega_n}{\gamma_e}$ . The difference of spectral density function of DQ and ZQ transitions according to the equation 2.3 results in estimated SE DNP field profile.

$$G_{SE}(B_0) = \underbrace{G_{EPR}\left(B_0 + \frac{\omega_n}{\gamma_e}\right)}_{G_{ZQ}(B_0)} - \underbrace{G_{EPR}\left(B_0 - \frac{\omega_n}{\gamma_e}\right)}_{G_{DQ}(B_0)} \quad (3.12)$$

This method can easily be applied if the experimental cw EPR spectrum is available at the same microwave frequency used for DNP because in an echo-detected EPR spectrum

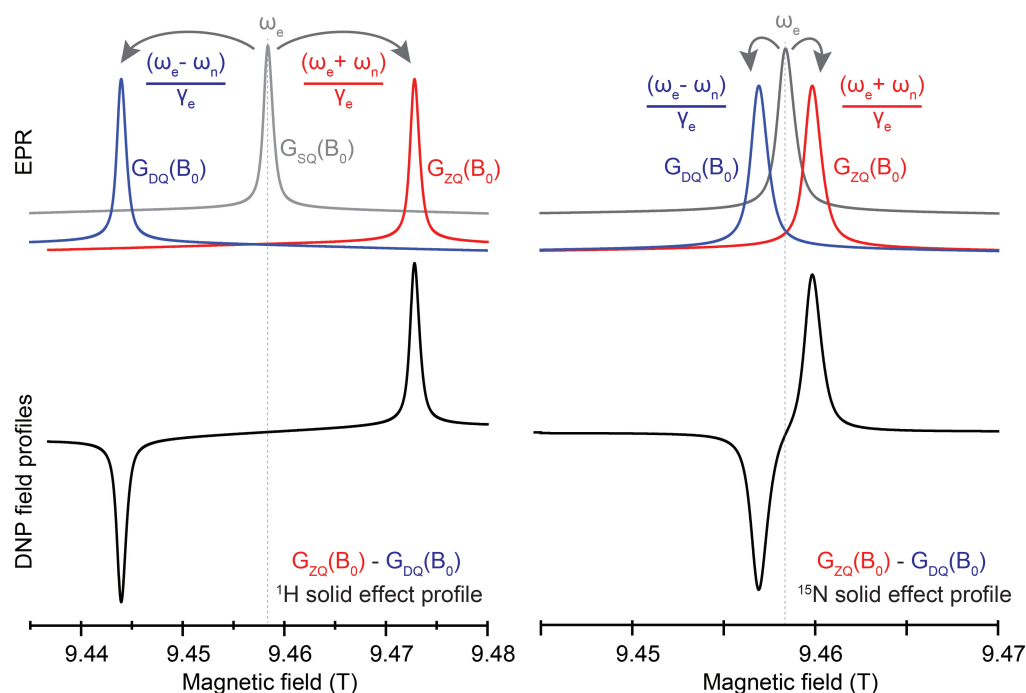


**Figure 3.4** Spectral estimation of SE DNP field profiles (black) based on difference of ZQ (red) and DQ (blue) transitions.  $\gamma(^1\text{H}) > 0$  and  $\gamma(^{15}\text{N}) < 0$  so DQ and ZQ transitions are defined accordingly.

broader components with short phase memory are filtered out and under-represented [Erilov et al., 2004]. These spectral components, however, do contribute to DNP mechanisms and should not be overlooked. SE simulations by equation 3.12 have proven useful in the identification of active DNP mechanisms and their relative contributions (if any) for static as well as MAS DNP [Corzilius et al., 2014; Shimon et al., 2012]. Estimation of SE DNP field profiles based on EPR spectrum of Gd-DOTA is shown in figure 3.4. The effect of  $\omega_n$  on DNP field profile is manifested as separation of positive and negative lobes for each nucleus. It also shows that DNP effect can be observed on the nuclei of choice by utilizing a PA with very narrow EPR signal. For a narrow EPR spectrum, ZQ and DQ transitions are sufficiently separated and the positive and negative DNP enhancement peaks are separated by  $2\omega_n$ . ZQ and DQ transitions tend to overlap if the overall EPR spectrum is broader than  $\omega_n$ . Such overlap causes differential solid effect (DSE) where mutual cancellation of positive and negative enhancements occur in addition to ineffective excitation of electron spin packets. Consequently, the separation between the maxima of positive and negative DNP peaks becomes smaller than  $2\omega_n$  [Corzilius, 2016; Wenckebach, 2008].

Inhomogeneous broadening of EPR spectra by Zeeman anisotropy, unresolved HFI, or ZFS



anisotropy affects the DNP field profiles and possible maximum enhancement factors. Even when ZQ and DQ transitions are well separated, the monochromatic microwave frequency can only excite a limited number of spin packets out of an ensemble that can evoke SE. In high-spin system ( $\text{Gd}^{3+}$ ,  $\text{Mn}^{2+}$ ) directionally sensitive ZFS and/or anisotropic hyperfine interaction modulates the position of CT. As the sample orientation changes these interactions during a rotor period, more spin ensembles are exposed to SE matching [Mentink-Vigier et al., 2012]. Therefore, SE MAS DNP enhancements are the sum of contributions from all possible individual spin packets that fulfill SE matching condition (equation 2.3). In a similar way, far-spread spin packets contribute to DNP enhancements during frequency modulation where DNP resonance condition is achieved by changes in mw frequency [Hovav et al., 2014]. Spectral estimation seems simple and straightforward when extended

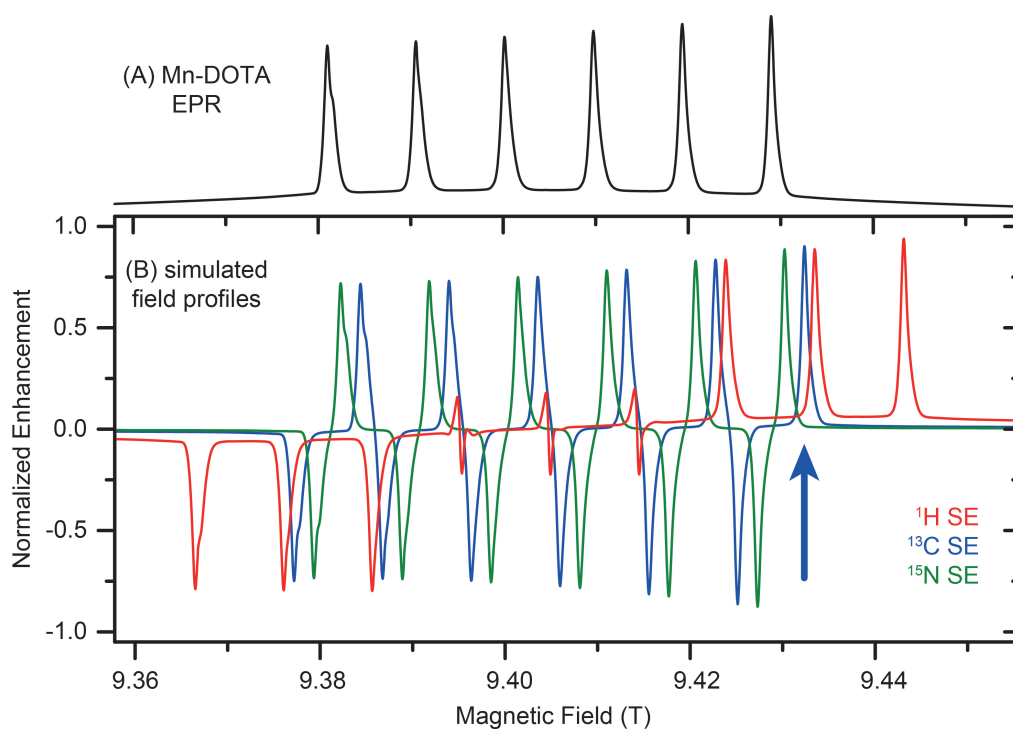


**Figure 3.5** (A) Simulated EPR spectrum of Mn-DOTA at 263 GHz. (B)  $^1\text{H}$ ,  $^{13}\text{C}$ ,  $^{15}\text{N}$  DNP field profiles of Mn-DOTA estimated from EPR spectrum of Mn-DOTA according to equation 3.13.  $\gamma(^1\text{H}) > 0$  and  $\gamma(^{15}\text{N}) < 0$  so DQ and ZQ transitions are defined accordingly. Blue arrow signifies  $^{13}\text{C}$  direct DNP condition, DNP experiments are performed at the field position corresponding to the maximum DNP enhancement for respective nuclei. Adapted from [Wenk et al., 2015] with permission.

from an EPR spectrum with one major spectral feature. It becomes complicated in the case of  $\text{Mn}^{2+}$ . Sextet pattern of  $\text{Mn}^{2+}$  EPR spectrum shows up in the SE field profile as intertwined positive and negative lobes for each line. The separation between hyperfine-split  $\text{Mn}^{2+}$  lines (about 250 MHz for Mn-DOTA) exceeds the  $\omega_n$  of  $^1\text{H}$  (212 MHz at 5 T and 400 MHz at 9.4 T).

The SE feature rising from one individual line inter-crosses that of the other one resulting in a cancellation of positive and negative enhancements. This complication is evident from estimated field profiles at 9.4 T (depicted in figure 3.5(B)) and experimental field profiles of  $^1\text{H}$  and  $^{13}\text{C}$  at 5 T [Kaushik et al., 2016].

Recording full field profiles is often not practical or even possible with biological samples. The limitation is time and resources due to often small signal and requirement of small field increment steps with narrow DNP matching conditions. A compromise to this situation is to use estimated field profile (similar to figure 3.5) as guidance. This approach was used for the first demonstration of intra-complex DNP using  $\text{Mn}^{2+}$  Wenk et al. [2015].

### 3.2.2 Cross effect

PAs with broad and anisotropic EPR spectra evoke CE mechanism, given sufficient inter- or intra-molecular e–e dipole coupling is present. The shape of the CE field profile caused by such an inhomogeneous EPR line is difficult to understand or predict. In principle, CE can be evoked in a fictitious three spin system featuring two narrow EPR lines separated by  $\omega_n$ . In this case, the field profile would consist of two DNP peaks of different relative signs, separated by  $\frac{\omega_n}{\gamma_e}$ . Spectral shape function of CE DNP profile,  $G_{CE}(B_0)$  can be approximated according to equation 3.13 and step-by-step illustration is shown in figure 3.6 for  $^1\text{H}$  and  $^{15}\text{N}$  CE DNP field profiles.

$$G_{CE}(B_0) = \underbrace{G_{EPR}(B_0)}_{G_{SQ}(B_0)} \times \underbrace{G_{EPR}\left(B_0 + \frac{\omega_n}{\gamma_e}\right)}_{G_{ZQ}(B_0)} - \underbrace{G_{EPR}(B_0)}_{G_{SQ}(B_0)} \times \underbrace{G_{EPR}\left(B_0 - \frac{\omega_n}{\gamma_e}\right)}_{G_{DQ}(B_0)} \quad (3.13)$$

CE DNP enhancement peaks coincide with the two EPR absorption lines. Saturation (excitation) of either the low- or high-frequency EPR transition would result in a three-spin-flip CE process. Such idealized systems are difficult to design due to the limitations on  $g$ -factor variation of available radicals. For example, a mixture of trityl and BDPA-type radicals is shown to mimic such a scenario for DNP of low- $\gamma$  nuclei [Michaelis et al., 2013b]. However, even in this case, the breadth of the trityl spectrum is of the same order as  $\omega_n$  of  $^{13}\text{C}$ , which leads to anisotropy in CE matching.

The experimental field profiles of PAs known to evoke CE (bis-nitroxide, TOTAPOL) look very different from figure 3.6 [Kaushik et al., 2016]. This is because the broad EPR signal fulfills the

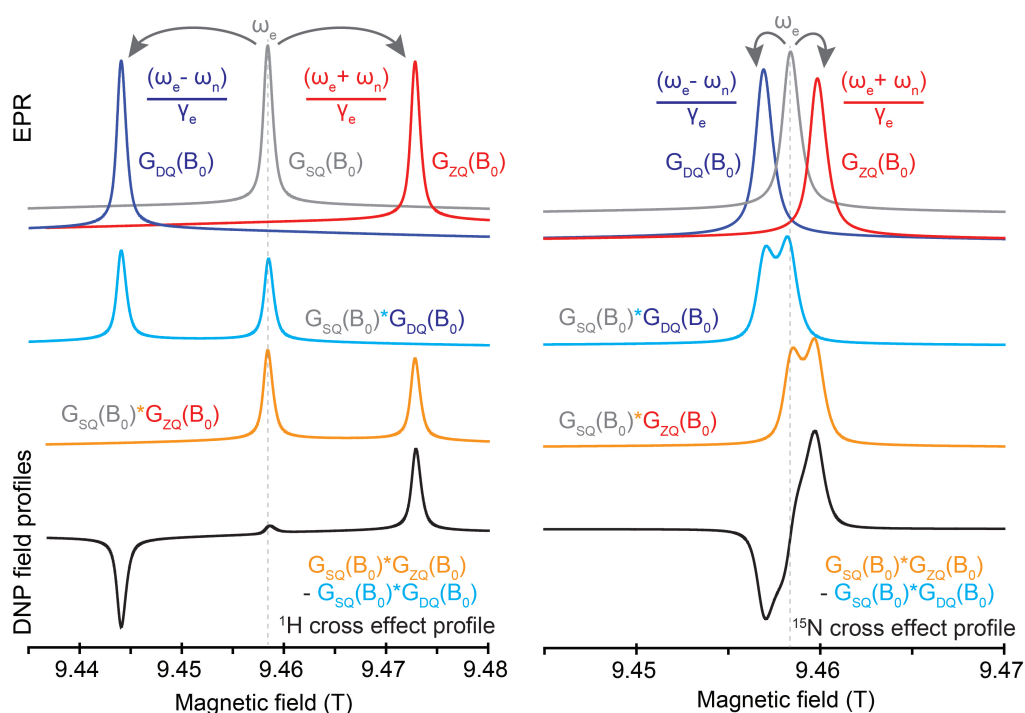


**Figure 3.6** Estimation of CE DNP field profiles for  $^1\text{H}$  and  $^{15}\text{N}$  as per equation 3.13. Mathematical product of ZQ and SQ subtracted from product of SQ and DQ gives CE DNP field profile for corresponding spin packets.

CE matching condition by statistical probability of containing two spin packets separated by  $\omega_n$  throughout its spread. In a static case, the requirement for matching of CE condition of dipolar coupling and simultaneous coupling with nuclear spin restricts the number spin pairs that can actively contribute to CE enhancements. Under MAS, the spin energy eigenstates are modulated during the rotation period due to strong anisotropic interactions in nitroxides. As a result, a majority of the randomly oriented PA molecules can contribute to DNP at some point or other during the rotor period [Mentink-Vigier et al., 2012; Thurber and Tycko, 2014]. The experimental field profile is a summation of all individual constructive or destructive contributions that either add up or cancel out the enhancement from neighboring spin packets [Hu et al., 2007].



## Chapter 4

### Metal ions in magnetic resonance

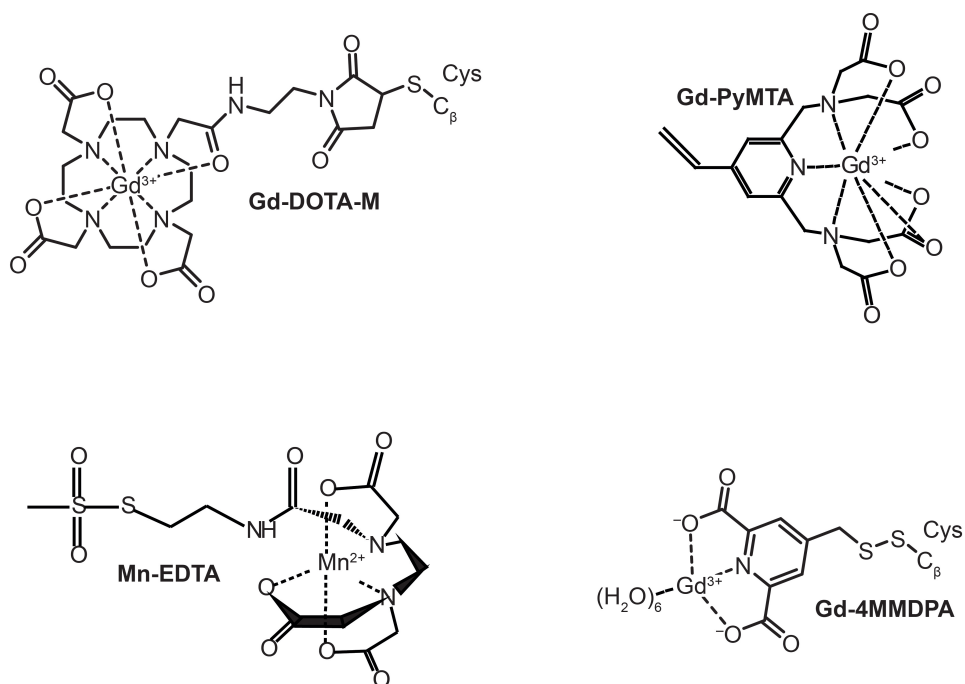


**Figure 4.1** Stable metal complexes of  $Gd^{3+}$  and  $Mn^{2+}$  used for EPR spectroscopy.  $Gd^{3+}$  complexes have also been used for MAS DNP.

Paramagnetic species find crucial roles in different domains of magnetic resonance, for example, these are used as contrast agents in MRI studies, as labels in EPR spectroscopy, and as a source of polarization in DNP techniques. Biological samples can be labeled at specific positions with paramagnetic tags for determination of distances between biomolecular domains by dipolar spectroscopy [Hubbell et al., 2013]. Lanthanide-binding tags can be attached to biomolecules via binding with cysteine residue by SDSL. The abundance of cysteines in biological systems such as peptides, proteins, DNA, and RNA makes this method particularly suitable. Paramagnetic metal ions  $Mn^{2+}$ ,  $Gd^{3+}$  have been gaining popularity in last decade for such applications [Klare, 2012]. Heterocyclic polydentate ligands or chelators for stable complexes with the metal ions with higher binding affinity than a col-

lection of similar non-chelating (monodentate) ligands [Yang et al., 2013]. For example, 1,4,7,10-tetraazacyclododecane-1,4,7,10-tetraacetate (DOTA) is an octadentate ligand that forms a very stable complex with  $Gd^{3+}$  through binding four amine and four carboxylate groups. The large  $Gd^{3+}$  ion (radius 0.12 nm) can accommodate eight coordinating atoms from DOTA and an exchangeable water ligand from the bulk solution. More examples of metal -complex used in magnetic resonance are shown in figure 4.1.  $Gd^{3+}$  chelates with 1,4,7,10-tetraazacyclododecane-1,4,7-tris-acetic acid 10-maleimidoethylacetamide (DOTA-M); pyridine-2,6-diyl)bismethylenenitrilo tetrakis acetate (pyMTA); and 4-Mercaptomethyl dipicolinic acid (4MMDPA) labels have been used in EPR spectroscopy as labeled tags [Dalaloyan et al., 2015; Song et al., 2011]. Complexes of  $Mn^{2+}$  such as with ethylenediaminetetraacetic acid (EDTA) have also been utilized for multi-frequency EPR spectroscopy [Stich et al., 2007]. In a limited number of novel and promising studies, similar tags are used for MAS DNP, where paramagnetic species act as PAs.

#### 4.1 Rise of metal ions for MAS DNP

Experimental observation of DNP followed quickly after its postulation by Overhauser in 1953 [Overhauser, 1953]. The very first DNP experiments were reported on metallic  $Li^+$  by Carver and Slichter [Carver and Slichter, 1953]. Metal ions were used as PAs further with the discovery of SE in 1967. Abraham et al. explored  $Ce^{3+}$  as PA within  $Ce_2Mg_3(NO_3)_{12} \cdot 24H_2O$ , and as impurity in diamagnetic  $La_2Mg_3(NO_3)_{12} \cdot 24H_2O$  (LMN) and  $CaF_2$  [Hwang et al., 1967]. These studies led to the conception of CE DNP. Metal ions such as  $Cr^{3+}$  within  $\alpha-Al_2O_3$  and ferric impurities within  $K_3Co(CN)_6$  yielded small but significant enhancement factors [Abragam et al., 1962; Abraham et al., 1959]. Later,  $Cr^{5+}$  produced by in situ reduction of  $Cr^{6+}$  was used as PA in complexes with diols and glycerol for spin-polarized targets in scattering experiments [Garif'yanov et al., 1968]. Notably, these experiments were performed at low magnetic field (< 2.5 T) and liquid-Helium temperatures, unlike conventional MAS DNP.

After these early DNP experiments and discoveries, the involvement of metal ions for DNP stayed latent for decades mainly due to instrumental limitations. The DNP resonance condition for metal ions is not matched in DNP set-up typically including a gyrotron with a fixed-frequency output. Advancement of technology and gyrotron devices at Massachusetts Insti-

tute of Technology enabled the use of metal ions as PAs. Gadopentetic acid (Gd-DTPA) and DOTA complexes of  $Gd^{3+}$  and  $Mn^{2+}$  were introduced as PAs for MAS DNP in 2011 [Corzilius et al., 2011] using a custom-built 211 MHz/140 GHz DNP set-up. Later, crystalline compound  $Co[(en)_3Cl_3]_2 \cdot NaCl \cdot 6H_2O$  (en = ethylenediamine,  $C_2H_8N_2$ ) was investigated with  $Cr^{3+}$  paramagnetic doping, using the same setup [Corzilius et al., 2014]. It is an ideal system that features a trigonal symmetry of the metal site for  $Cr^{3+}$  and  $Co^{3+}$  that are structurally interchangeable due to the similar ionic radii [Shannon, 1976]. It was observed that enhancement of direct  $^{13}C$  and  $^{59}Co$  NMR signals depend strongly on doping ratios [Corzilius et al., 2014]. Findings from this study established the possibility of direct  $^{13}C$ , and  $Co^{3+}$  DNP in crystalline materials; and an indication of CE DNP at higher dopant concentrations.

## 4.2 Advantages of metal ions

Conventional DNP experiments require exogenous PAs uniformly dispersed in a cryoprotecting matrix and the maximum possible NMR resonances are enhanced non-selectively. The use of metal ions as PAs offer special benefits in the context of biomolecular research as summarized in the following text.

### 4.2.1 Endogenous PA

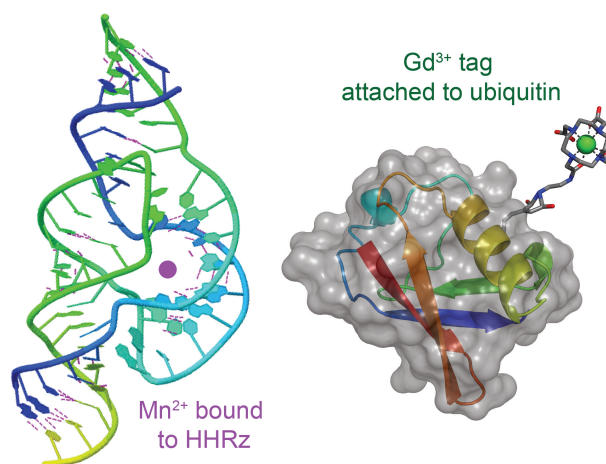


**Figure 4.2**  $Mn^{2+}$  ion embedded in place of intrinsic  $Mg^{2+}$  ion in a full-length hammerhead ribozyme (PDB entry: 3ZP8) and  $Gd^{3+}$  tag attached to Ubiquitin (PDB entry: 1ubq) for direct DNP.

Many enzymes bind magnesium as a cofactor in their natural state.  $Mn^{2+}$  occurs naturally in a number of metalloproteins and biomolecules, and therefore, can be used as intrinsic PA

without the requirement of further sample modification [Lawrence et al., 1998].  $\text{Mg}^{2+}$  and  $\text{Mn}^{2+}$  have similar covalent radii (141 pm and 139 pm) and ionic radii (72 pm and 83 pm), so, diamagnetic  $\text{Mg}^{2+}$  can readily be replaced by paramagnetic  $\text{Mn}^{2+}$  and used as endogenous PA [Shannon, 1976]. Figure 4.2 shows examples of high spin metal ions as local PAs. The prospect of metal ions as endogenous PAs is especially alluring for DNP in the cellular milieu where limited stability of nitroxides is an issue. Furthermore, endogenous PAs eliminate the need of a dispersing matrix thus facilitating more sample volume for the analyte.

#### 4.2.2 Site-targeted DNP

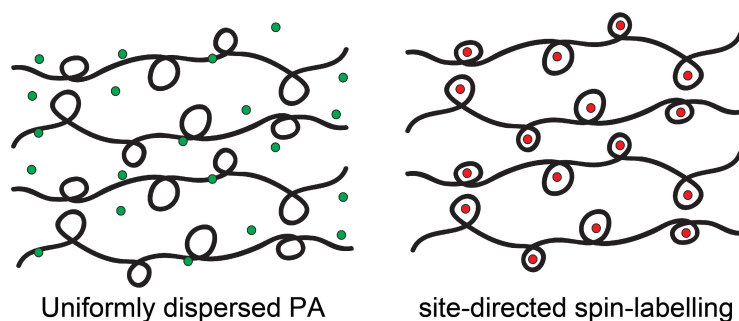


**Figure 4.3** Cartoon representation of biomolecules (black curves) with uniformly dispersed PA (filled green circles) in glass forming solvent matrix, and site-directed spin labeling (filled red circles).

Generally, the enhancements obtained from nitroxide PAs are global. Localization of the PA to a specific site (see figure 4.2.2) of interest can be utilized to obtain structural information by solid-state NMR DNP. Recently,  $\text{Gd}^{3+}$  spin label (with a lanthanide binding tag) has been produced in-vivo and used for in-cell distance measurements by EPR spectroscopy [Mascali et al., 2016]. Successful execution of DNP experiments with paramagnetic  $\text{Cr}^{3+}$  ions (0.3% to 1%) replacing  $\text{Co}^{3+}$  in a lattice has been reported [Corzilius et al., 2014] for direct DNP of low- $\gamma$  nuclei. Similarly,  $\text{Gd}^{3+}$  binding tags localized in a specific biomolecular site can be used to explore the site of interest by DNP.

#### 4.2.3 Selective and direct DNP

The broad linewidth of commonly used nitroxide radicals prohibits selective enhancement of  $^1\text{H}$  and  $^{13}\text{C}$  resonances. DNP enhancement profiles of  $^1\text{H}$  and  $^{13}\text{C}$  given by PAs with broad linewidths overlap and thus both the nuclear species are enhanced simultaneously. Some organic radicals such as BDPA, and trityl, as well as high-spin PAs, investigated in this work



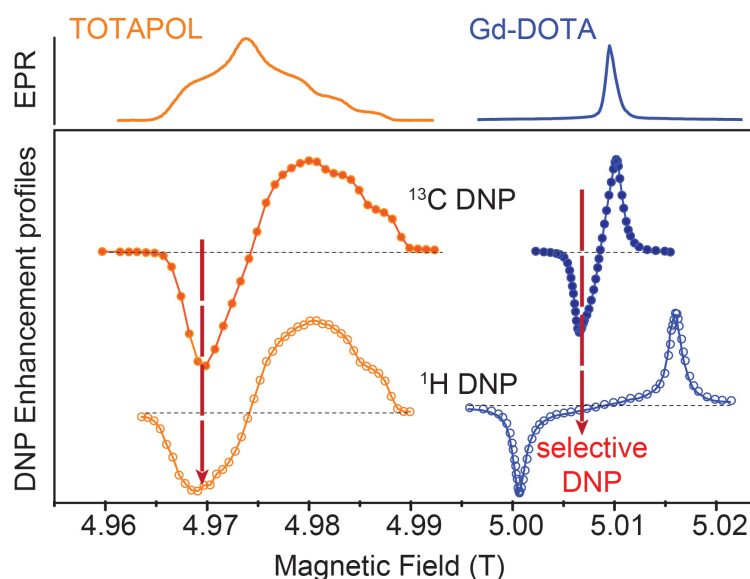


**Figure 4.4**  $^1\text{H}$  (open circles) and  $^{13}\text{C}$  (filled circles) DNP field profiles of TOTAPOL (in orange) and Gd-DOTA (in blue) along-with to their respective EPR spectra at 5 T. Data taken from [Kaushik et al., 2016]

have narrow linewidth  $\delta$  and therefore, non-overlapping DNP enhancement profiles. With such PAs, either one of the the nuclear types can be enhanced by tuning  $B_0$  in MAS DNP experiments as shown in figure 4.4 by comparison of DNP field profiles of TOTAPOL with Gd-DOTA. Furthermore, it is possible to selectively evoke DNP mechanism of choice (either SE or CE) by tuning  $B_0$  for specific PA design.

#### 4.2.4 Suitability for high field applications

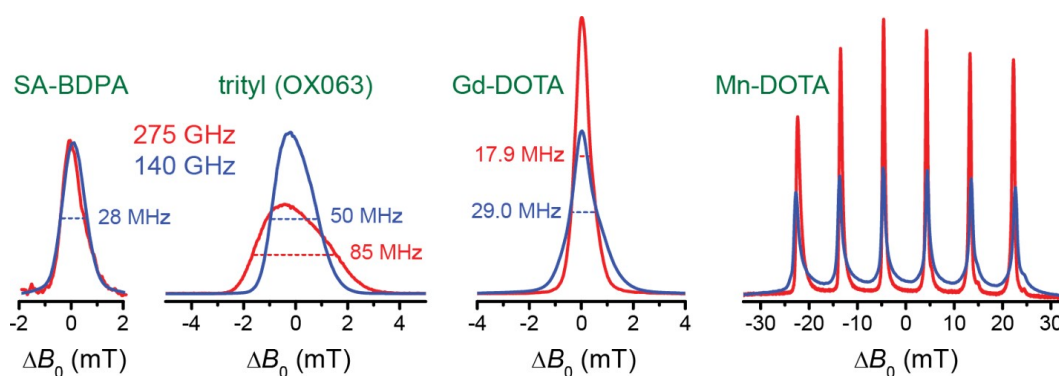


**Figure 4.5** Comparison of EPR lineshapes between various PAs namely- sulfonated-BDPA, trityl, Gd-DOTA, and Mn-DOTA at 140 GHz (blue) and 275 GHz (red). Data taken from [Kaushik et al., 2016]

High-field (over 5 T) MAS DNP is generally used with fast MAS for structural studies because resolution ( $R$ ) and sensitivity ( $S$ ) of homogeneous NMR signals typically improve with the

magnetic field strength (i.e.,  $R \propto B_0$  and  $S \propto B_0^{3/2}$ ) [Moser et al., 2017]. However, the effect of  $B_0$  on lineshapes of EPR signal cannot be generalized. Figure 4.5 demonstrates the change in the EPR line shapes of several PAs compared at two magnetic field strengths, 5 T (140 GHz) and 9.8 T (275 GHz) [Kaushik et al., 2016]. The effect of magnetic field strength on SA-BDPA is hardly observable, whereas, the EPR signal of trityl is symmetrically broadened due to axially symmetric  $g$ -anisotropy. In contrast to the organic radicals (SA-BDPA and trityl), the EPR signal (visible CT) of  $Gd^{3+}$  and  $Mn^{2+}$ -DOTA complexes narrow down at higher field because the second-order effects due to ZFS—which is responsible for the apparent narrowing of the CT—scales inversely proportional with respect to  $B_0$  (section 3.1).

Unfortunately the efficacy of SE and CE mechanisms decrease at higher magnetic fields [Hu et al., 2011]. Therefore, suitable PAs with narrow EPR linewidths are to be considered in order to achieve reasonable signal enhancements with SE DNP. Decrease in SE efficiency can partially be compensated by increased EPR signal of CT of high-spin PAs. Narrower EPR signal of high-spin PAs avoids loss of DNP signal caused by differential SE especially for low- $\gamma$  nuclei.

### 4.3 Practical aspects

Even though metal ions provide access to unique information by MAS DNP, their use in regular DNP experiments is limited mainly due to the lack of specialized instrumentation. Extensive technology development is undergoing in various research groups to overcome these limitations. Frequency-sweep mw sources and High-power gyrotrons are under development [Barnes, 2017; Idehara, 2017] for advancement of terahertz technology and pulsed DNP [Golota et al., 2017; Idehara and Sabchevski, 2017]. Practical constraints that exist due to historical reasons and still-developing mw technology are described in the following.

#### 4.3.1 Requirement of field/frequency sweep

The DNP resonance condition is given by equation 2.3 for SE and equation 2.5 for CE mechanism, establishing that the required microwave frequency scales with the nuclear Larmor frequency. As a result of this relationship, a commercially available MAS DNP spectrometer employs a gyrotron operating at the resonance mw frequency with respect to an NMR magnet of a certain magnetic field strength  $B_0$ . For instance, for optimum CE DNP using bis-

nitroxides, 400 MHz and 800 MHz MAS-DNP spectrometers have gyrotrons operating at mw frequency of 263 GHz and 527 GHz, respectively. The design of commercially available MAS DNP spectrometers is such that the gyrotron frequency, and the magnetic field strength of corresponding NMR magnet are fixed (optimized for CE DNP resonance of nitroxides). A comparison of EPR spectrum of  $Gd^{3+}$  with that of a nitroxide shows distinct resonance field positions (see figure 4.4) for each PA. Metal ions feature a variation in  $g$ -factor and  $g$ -anisotropy thus the resonance condition is no longer fulfilled by the available instrumentation. DNP with such metal ions can only be possible by changing either the mw frequency or the magnetic field strength.

Specialized versions of the commercially available MAS DNP spectrometers are equipped with a "sweepable" NMR magnets [Rosay et al., 2010]. In the design by Bruker Biospin,  $B_0$  is varied with the help of an additional sweep coil that adds to or deducts a fraction from the external magnetic field strength (figure 2.1). A 400 MHz MAS DNP magnet (9.4 T) from Bruker can be swept to  $\pm 75$  mT, corresponding to a coil current of  $\pm 20$  A. Even though technological advancement promotes the use of metal ions for DNP, the constraint is not completely circumvented. PAs with pronounced spin-orbit coupling and resulting  $g$ -factors significantly different from the free electron cannot be utilized. For example, the magnetic field of currently available NMR magnets can not varied to the extent of resonance condition for  $Cu^{2+}$  or  $Fe^{3+}$  complexes. The PAs investigated in this work (complexes of  $Gd^{3+}$  and  $Mn^{2+}$ ) exhibit nearly isotropic  $g$ -values similar to free electron that can be attained by minor changes in  $B_0$ .

#### 4.3.2 Inadequacy of available microwave power

Generally, enhancements obtained from DNP increases with mw power until a saturation limit is reached depending on the PA and DNP mechanism. The output mw power of commercially available gyrotrons can be optimized for organic radicals simply by varying the gun current. We experimentally tested two state-of-art commercial DNP spectrometers for optimum microwave power for metal ions and found that the available mw is grossly insufficient for metal ions. In figure 4.6, the DNP enhancements increase up to three-fold almost linearly within the variable range of the gun current that determines the magnitude of output mw power from the gyrotron. The increase in  $^{13}C$  enhancement from Gd-DOTA (figure 4.6

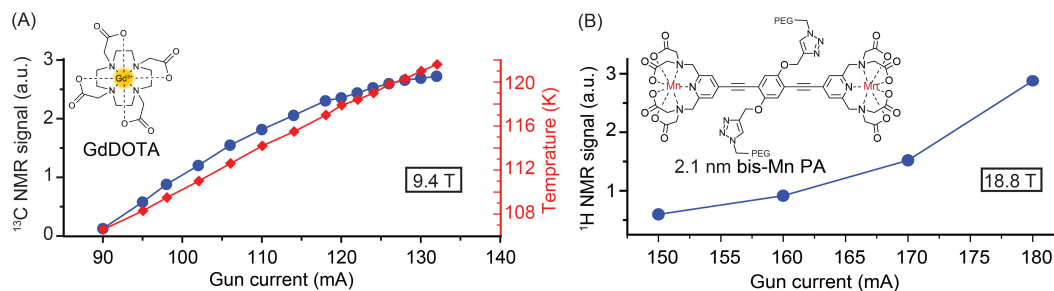


**Figure 4.6** Microwave power dependence of DNP enhancements obtained on (A) 9.4 T MAS DNP spectrometer for Gd-DOTA, (B) 18.8 T MAS DNP spectrometer for a bis(Mn-complex) with inter-Mn distance of 2.1 nm. Clearly, the maximum possible DNP Enhancements are not achieved for the metal ions with the available mw power (Unpublished data).

(A) is seemingly gradual. The rise in temperature with the incident mw power is measured through a thermocouple located near the spinning rotor. Sample heating caused by absorption of microwaves is inevitable in the commercial experimental setup. Even though the rise in temperature undermines the Boltzmann distribution and hence obtainable signal gain, the enhancements from Gd-DOTA shows an increasing trend till the last recorded data point. Evidently higher enhancement factors can be obtained with higher microwave power and better temperature control. Figure 4.6 (B) shows a similar correlation of  $^1\text{H}$  NMR signal arising from DNP with bis(Mn-complex) as PA. This correlation is recorded on a state-of-art 800 MHz Bruker spectrometer using upto maximum mw power specification. The slope of signal increment is visibly steep which underlines that higher enhancements can be achieved with metal ion PAs. The limited range of mw power stems from historical use of organic PAs and the lack of a resonance cavity in the MAS DNP setup. A new generation of gyrotrons are expected to yield hundreds of watts of mw power that is required for advanced DNP techniques [Golota et al., 2017].

## Chapter 5

### DNP with metal ions

High-spin complexes of  $\text{Gd}^{3+}$  and  $\text{Mn}^{2+}$  were introduced as PAs for MAS DNP in 2011 [Corzilius et al., 2011]. This dissertation was undertaken in 2013, with the intention of exploring these PAs further. Major goals for this work were to understand their DNP mechanisms and explore their application as PAs in biomolecular research using MAS DNP enhanced NMR spectroscopy.

#### 5.1 Endogenous $\text{Mn}^{2+}$ as PA in hammerhead ribozyme

The investigated system is an inactivated version of a full-length uniformly labeled hammerhead ribozyme. The hammerhead ribozyme (HHRz) is a construct found in virusoids and viroids and act as a self-cleaving structural element [Boots et al., 2008]. The self-cleavage reaction takes place in presence of a divalent metal ion as co-factor. It was found that all hammerhead ribozyme varieties have a catalytic core region which contains several binding sites for divalent ions [Scott et al., 1995], one such example is shown in figure 5.1(A). The conformational change brought by binding of a divalent ion ( $\text{Mn}^{2+}$  or  $\text{Mg}^{2+}$ ) to one of these sites results in the self-cleavage reaction changing the hammerhead conformation (figure 5.1 (B)) to Y-shaped conformation (figure 5.1 (C)). However, the exact position of the specific binding site for  $\text{Mn}^{2+}$  or  $\text{Mg}^{2+}$  is still unclear [Martick and Scott, 2006]. Additional less specific metal binding sites present in the HHRz show an affinity towards monovalent ions and are completely saturated under excess ( $>1$  M)  $\text{Na}^+$  concentrations. The HHRz is inactivated, i.e., prevented from self-cleavage, by mutating adenosine to guanosine at position 53 in the sequence [Yen et al., 2004]. Ribonuclease (RNase) present in the environment can cause degradation of the RNA, therefore the absence of RNase is ensured at all times during sample handling. The dissociation constant ( $K_D \approx 4$  mM) of  $\text{Mn}^{2+}$  binding to HHRz was determined by spin-counting experiments on an X-band (9.3 GHz) EPR spectrometer.

In preliminary experiments, AMUPol was used as the PA to obtain high-sensitivity in two

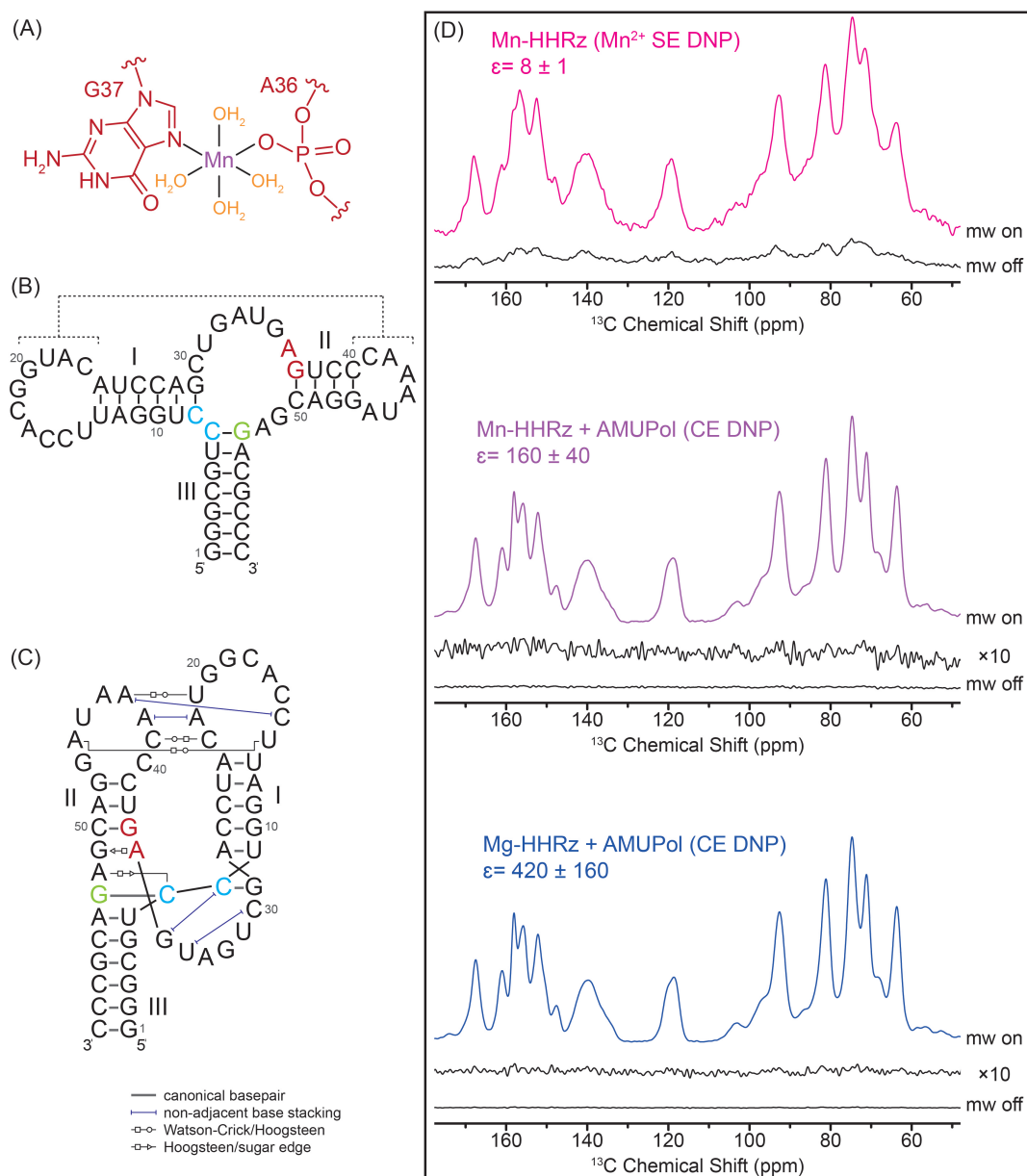


**Figure 5.1** (A) Complex geometry of the binding site, where  $\text{Mn}^{2+}$  forms coordination bonds with the investigated HHRz [Morrissey et al., 2000; Wang et al., 1999]. (B) Predicted secondary structure of the investigated full-length HHRz (inactivated). Base mutation A-to-G (marked in green) at position 53 prevents self-cleavage between two cytidines (marked in blue). Canonical base pairing interactions are shown with black lines within stems. The proposed selective binding site for divalent ions ( $\text{Mg}^{2+}$  or  $\text{Mn}^{2+}$ ) is marked in red. Dashed lines indicate tertiary loop-loop interactions. (C) A depiction of the same structure (as (B)) showing possible tertiary interactions between stem-loops II and III as observed in the active construct [Martick and Scott, 2006]. Black elongated lines show sequence continuity. (D) Comparison of directly-detected  $^{13}\text{C}$  MAS NMR spectra obtained with and without DNP where either  $\text{Mn}^{2+}$  or AMUPol, or both PAs are present in the sample. SE DNP is evoked with 0.4 mM Mn-HHRz complex utilizing  $\text{Mn}^{2+}$  as PA (top), CE DNP from nitroxide is evoked by 5 mM AMUPol present in 0.4 mM Mn-HHRz complex (middle), as well as in 0.4 mM Mg-HHRz complex (bottom).

dimensional MAS NMR experiments. DNP enhancements of  $^1\text{H}$  obtained (via  $^{13}\text{C}$ -CP) with 5 mM AMUPol in Mg-HHRz sample was  $\epsilon = 250 \pm 10$  (figure 2.3) which significantly surpasses previously observed  $\epsilon$  on protein solutions even with larger bi-radical concentrations under similar conditions. Generally,  $\epsilon$  is two to three times smaller for proteins as compared to model systems (for example,  $\epsilon(^1\text{H}) = 235$  for proline [Sauvée et al., 2013] and drops further with increasing complexity of the environment in biological systems [Renault et al., 2012]). We attribute the observed large enhancement to the absence of relaxation-inducing methyl groups in the HHRz molecule. Further DNP experiments with and without  $\text{Mn}^{2+}$  gave an insight into DNP in regard to the presence of additional paramagnet in the sample. The effect of  $\text{Mn}^{2+}$  on  $^1\text{H}$  DNP are negligible except for slightly faster rates of NMR signal build-up. The need for better sensitivity for multi-dimensional experiments was highlighted by a MAS NMR study of a smaller (26 nucleotides) RNA within a protein complex [Marchanka et al., 2015]. With the sensitivity boost by DNP, we are able to record  $^{13}\text{C}$ - $^{13}\text{C}$  and  $^{15}\text{N}$ - $^{13}\text{C}$  correlation spectra for Mn-HHRz and Mg-HHRz, and assign a consistent set of resonances to the atoms in each constituting nucleotide. All expected intra-nucleotide correlations, as well as several inter-nucleotide resonances due to base-pairing or stacking, are identified. High sensitivity by MAS DNP offers optimistic idea of recording higher dimension spectra for peak assignment using advanced strategies [Marchanka et al., 2015].

Direct  $^{13}\text{C}$  enhancements of  $\sim 420$  and  $\sim 160$  were obtained from Mg-HHRz and Mn-HHRz samples, respectively, with AMUPol as active PA. The reduced enhancement can easily be explained by faster spin-lattice relaxation induced by the paramagnetic  $\text{Mn}^{2+}$  ion.  $B_0$  needs to be optimized for direct  $^{13}\text{C}$  SE DNP by  $\text{Mn}^{2+}$  ion. Here, DNP simulations play an important role in finding the optimum  $B_0$ . The intensity of NMR signal from MnHHRZ without DNP is very small for a field profile to be feasible in a reasonable measurement time. Higher concentration (2 M) of a labeled sample is required for such experimental field profiles. At the calculated optimum  $B_0$ , the direct  $^{13}\text{C}$  enhancement,  $\epsilon = 8$  is recorded by  $\text{Mn}^{2+}$  ions as PA. For quantitative comparison, it must be noted that concentration of AMUPol in the sample is  $> 12$  times the concentration of  $\text{Mn}^{2+}$ . In addition to the higher enhancements yielded by a higher concentration of PA, the presence of highly efficient CE DNP evoked by AMUPol, is to be considered.

## 5.2 Active DNP mechanism(s) via $Gd^{3+}$

Since high-spin metal ions are relatively new and unexplored PA for MAS DNP, the interest towards investigating their mechanisms is self-explanatory. Owing to their high-spin properties, understanding DNP via  $Gd^{3+}$  and  $Mn^{2+}$  adds on to the established knowledge of DNP mechanisms as well. One of these ions was to be chosen as the starting point for such an investigation. The sextet of  $Mn^{2+}$  and resulting overlap of ZQ, DQ, and SQ transitions in DNP field profiles makes ambiguous assignment of DNP mechanism thus evoked somewhat challenging (section 3.2). On the contrary,  $Gd^{3+}$  has negligible hyperfine coupling and exhibits simpler EPR spectra. EPR spectrum of  $Gd^{3+}$  in near-symmetric ligand-field features one narrow peak of CT at high fields. Well separated DQ and ZQ transitions as a consequence of narrow CT EPR spectra lead to well resolved positive and negative DNP conditions that allow for *selective enhancement* on  $^1H$ ,  $^{13}C$ , or  $^{15}N$  resonances. Therefore,  $Gd^{3+}$  is the preferred choice for studying DNP mechanisms of this new PA class. We chose a stable and water-soluble complex, Gd-DOTA, for such studies. From the perspective of applications,  $Gd^{3+}$ -tags can be used to label biomolecules for potential site-specific studies via SDSL.

conc. (mM)	$r_B$ (nm)	$D_{ee}$ (MHz)	$\epsilon$ ( $^1H$ )	$\epsilon$ ( $^{13}C$ )	$\epsilon$ ( $^{15}N$ )
20	2.4	3.8	-8	-42	-124
10	3.0	1.9	-10	-40	-136
2	5.2	0.4	-4	-25	-76

**Table 5.1** Summary of experimental enhancements,  $\epsilon(^1H, ^{13}C, ^{15}N)$  and calculated ( $r_B, D_{ee}$ ) parameters for 2 mM, 10 mM, 20 mM concentration of Gd-DOTA.

Three concentrations of Gd-DOTA, 2 mM, 10 mM, and 20 mM, were used as PA, in 60/40 vol% glycerol/ $H_2O$  solution of 2 M labeled  $^{13}C, ^{15}N$ -Urea. Field profiles of all three concentrations are shown for  $^1H, ^{13}C$ , and  $^{15}N$  in figure 5.2. The EPR spectra and DNP field profiles, were recorded at about 9.4 T and microwave frequency of 263 GHz. The DNP field profiles shown in figure 5.2 are limited to the negative DNP region. The extent of reachable field is restrained by limit on maximum sustainable current in the sweep coil of the NMR magnet. Maximum enhancements are reported at the negative DNP maxima. Negative sign of enhancement only indicates that the DNP enhanced NMR spectra are inverted (phase



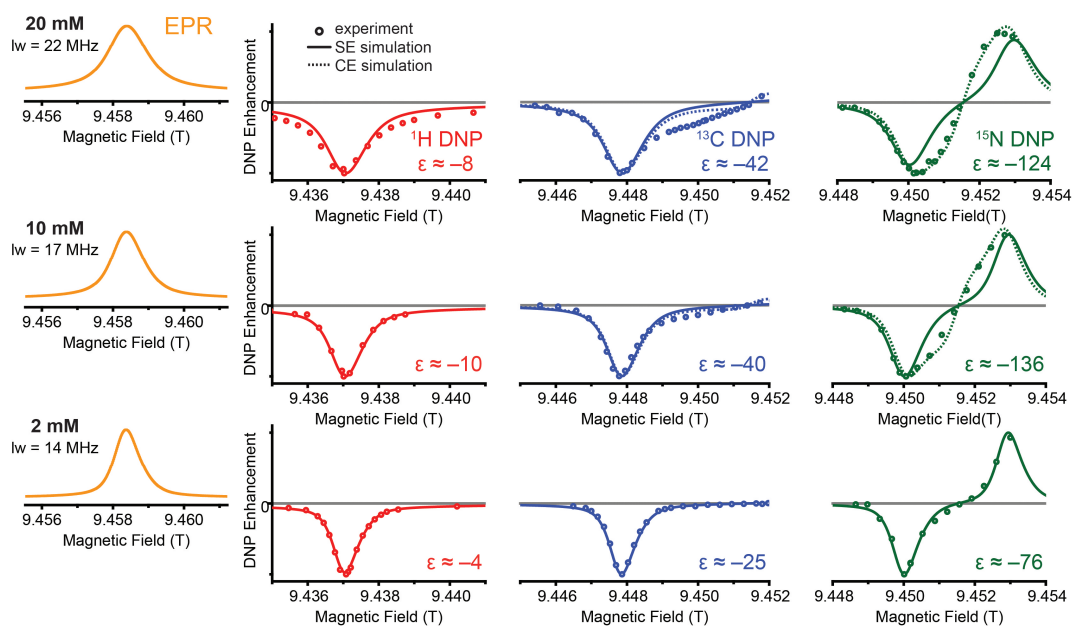


**Figure 5.2** First column: EPR spectra of 2 mM, 10 mM, and 20 mM Gd-DOTA are obtained by simulating experimental 263 GHz cw (field-modulated) EPR spectra using easyspin in order to avoid artifacts by integration. Respective columns: Normalized DNP enhancement of <sup>1</sup>H, <sup>13</sup>C, and <sup>15</sup>N at for 2 mM, 10 mM, and 20 mM (open circles) measured at sweepable 9.4 T MAS NMR magnet. Solid lines represent SE estimations according to equation 3.12; dashed lines represent CE simulations according to equation 3.13. Enhancement factors given in the figure correspond to the field of maximum enhancement. Data taken from [Kaushik et al., 2016]

difference of  $\pi$ ), w.r.t. NMR spectra without mw irradiation.

As the concentration of paramagnetic ions increase in the sample, naturally, their inter-spin separation ( $r_B$ ) becomes smaller. Average nearest-neighbour distance can be estimated by a statistical model [Chandrasekhar, 1943] (equation 5.1) and dipolar couplings,  $D_{ee}$  are calculated by easyspin toolbox [Stoll and Schweiger, 2006].

$$r_B = \frac{0.554}{c^{1/3}}, \quad (5.1)$$

$$D_{ee} = \frac{\mu_0 \gamma^2 \hbar}{4\pi r_B^3} \quad (5.2)$$

where,  $c$  is the concentration of Gd<sup>3+</sup> spins, and other symbols have their usual meaning (defined earlier). At small Gd<sup>3+</sup> concentration, dipolar coupling between Gd<sup>3+</sup> ions is negligible (0.4 MHz) (see table 5.1) so SE is the only active mechanism. Overlap of experimental data with estimated SE field profiles for all three nuclei support this expectation. Broadening of EPR spectra at higher concentrations is indicative of increased dipolar couplings. Theo-

retically it facilitates CE mechanism, however, the linewidths of CT are relatively narrow as compared to classical CE-inducing PAs. The experimentally observed  $\epsilon$ , in the light of field profiles shown in figure 5.2 do indicate the contribution of CE at higher concentrations.

Observation of CE contribution is evident for  $^{15}\text{N}$  field profile where, deviation from SE estimation is noticeable already at 10 mM and intensifies at 20 mM. In fact, the experimental  $^{15}\text{N}$  profile overlaps with estimated CE field profile (see figure 5.2). The contribution of CE DNP varies among all three nuclei studied and scales according to their Larmor frequencies. The reason for this is the probability of finding spin packets matching the CE condition ( $\Delta\omega_e \approx \omega_n$ ) lying within the intense CT of the EPR spectrum. The contribution of CE in  $^{13}\text{C}$  field profile can be seen as an asymmetric feature on right side, which increase with concentration from moderate to high.

In contrast, the  $^1\text{H}$  field profiles seem to be unaffected by the change in PA concentration. The distinctive trait of  $^1\text{H}$  is the similarity of estimated SE and CE field profiles. The estimated SE and CE field profiles for  $^1\text{H}$  differ only at the center and remain similar in the experimentally observed region (compare figure 3.4 and figure 3.6). In conclusion, low  $\text{Gd}^{3+}$  concentration (2 mM) evoke SE whereas higher concentrations evoke CE for low- $\gamma$  nuclei. The fact that biological samples endogenously contain very small concentration ( $\ll 2$  mM) of PAs, knowing that SE is the active DNP mechanism ensures unambiguous data interpretation.

In order to use  $\text{Gd}^{3+}$  as PA in biological samples, several Gd-binding chelator tags were tested. Ubiquitin serves as an excellent model system to bind the  $\text{Gd}^{3+}$  -tag with owing to its over-expression efficiency, and biochemical robustness under different environmental conditions. Ubiquitin can compatibly bind to other larger proteins and larger complexes via ubiquitylation and is suitable for site-selective DNP applications. We use Gd-DOTA-M and Gd-4MMDPA tags bound to ubiquitin for preliminary experiments. These tags yield rather small direct  $^{13}\text{C}$  SE enhancement on the order of 1 to 3 respectively, for 1 mM ubiquitin in 60/36/4(vol%) of  $\text{D}_8\text{-}^{12}\text{C}_3\text{-glycerol/D}_2\text{O/H}_2\text{O}$ . Interestingly, enhancement increased up to 9 by omitting glycerol in the sample. The reason for this observed increase in enhancement is unclear. A possible explanation could be phase separation or precipitation of protein in

the non-ideal glass. Nevertheless, this observation emphasizes the scope of optimization of sample preparation and labeling schemes.

The enhancements shown in figure 5.2 on  $^{13}\text{C}$  and  $^{15}\text{N}$  are detected by direct excitation pulse sequence. Thus, these preliminary experiments establish the possibility of selective direct DNP of low- $\gamma$  nuclei ( $^{13}\text{C}$ ,  $^{15}\text{N}$ ) using  $\text{Gd}^{3+}$  as PA. The direct enhancements on  $^{13}\text{C}$  resonances of Ubiquitin with attached PA tags are numerically small but its conceptual implication is significant. This is a promising example that proteins labeled with  $\text{Gd}^{3+}$ -binding chelator tags could themselves be used as polarizing agents.

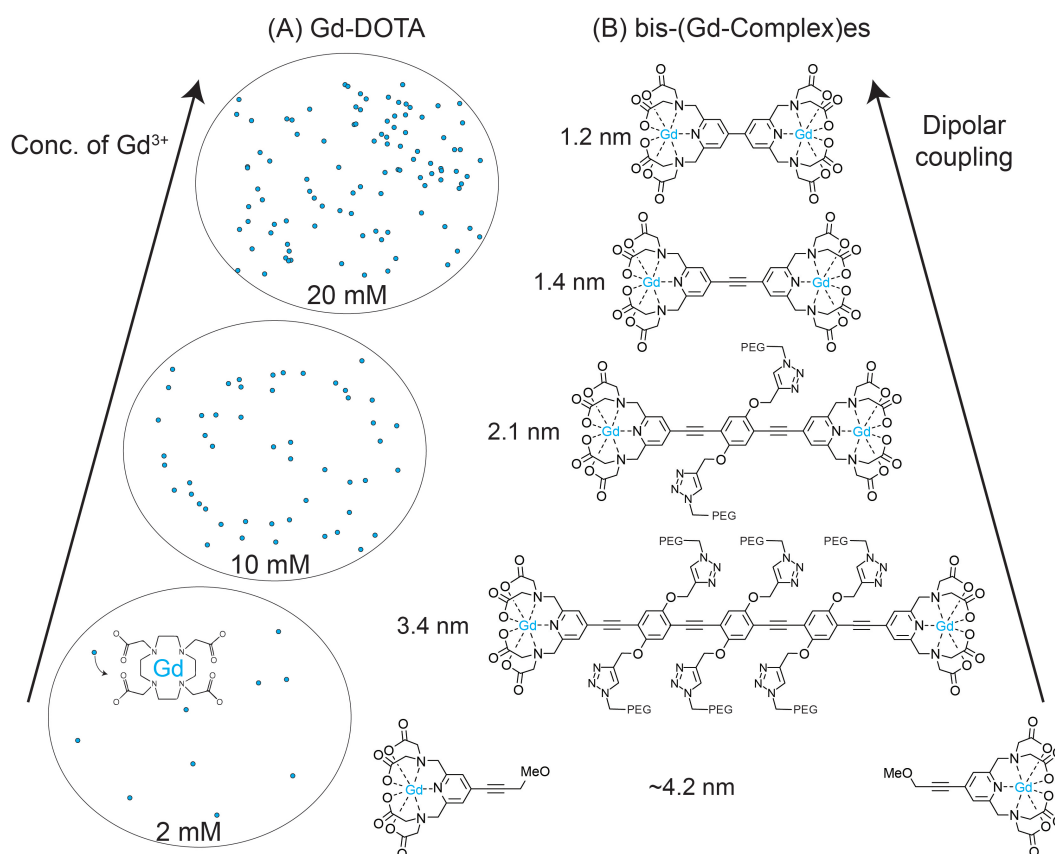


**Figure 5.3** (A) Random distribution of points (extracted from matlab function) representing distribution of 2 mM, 10 mM, and 20 mM Gd-DOTA in frozen solution. (B) Bis-(Gd-Complex)es used for MAS DNP, here the inter-spin distance is well defined between 1.2 to 3.4 nm for bis-complexes and 4.2 nm is estimated  $r_B$  for 4 mM mono-complex.

### 5.3 PA concentration vs inter-spin distance for CE DNP

The effect of concentration and inter-spin distances are intertwined in aforementioned experiments with Gd-DOTA. These two factors are co-dependent in a solution of uniformly distributed electron spins. As described in the section 3.2, both of these factors influence the active DNP mechanisms. In order to better understand CE via high spin metal ions, the relevance of inter-spin distances needs to be addressed explicitly. Therefore, varying the distance of  $Gd^{3+}$  ions while keeping the spin concentration constant should separate these factors. This can be achieved by utilizing bis-metal complexes with varying range of separation between metal ions. Gd-spacer-Gd type complexes are used as 'molecular-rulers' in EPR spectroscopy to determine the distance between two labeled sites of a molecule or molecular aggregates [Qi et al., 2016]. The rigidity of such rulers provides a basis for accurate distance measurement [Dalaloyan et al., 2015]. We have specifically tailored Bis-metal complexes, with reasonable inter-spin distances ( $r_B < 4$  nm) for DNP applications. Due to the stiffness of the spacer backbone and the tetherless attachment of the Gd-containing moiety Gd-PyMTA, their inter-  $Gd^{3+}$  distances are well defined (see figure 5.3) and are reliable for DNP [Qi et al., 2016]. The bis(Gd-chelate)s contain branched polyethylene glycol chains to mask the hydrophobic spacer backbone and achieve solubility in aqueous solvents. Bis-complexes, where intra-molecular  $Gd^{3+}$  ions are expected to evoke CE DNP, are compared to a mono-complex of similar geometry and chemical nature as a reference. Equal  $Gd^{3+}$  concentration was used in DNP samples, i.e., 2 mM for bis-complexes and 4 mM for mono-complex. This small PA concentration ensures negligible inter-molecular interaction.

EPR spectra of Gd-complexes are dominated by the CT of the high-spin ( $S=7/2$ ) system and broad components arising from STs are barely noticeable.  $D_{ee}$  increases significantly from 1.3 MHz to 32.4 MHz as inter-spin distance varies from 3.4 nm to 1.2 nm. As a consequence of  $D_{ee}$ , broadening is observed in the cw EPR spectra. In the DNP field profiles of  $^{13}C$  and  $^{15}N$ , it is reflected as a transition from the SE to the CE mechanism with decreasing inter-spin distance. For the reference compound, mono-complex, and the bis(Gd-complex) with  $r_B$  of 3.4 nm, the DNP field profile resembles inverted EPR spectra at the respective matching condition for SE. At inter-spin distances of 1.2 nm and 2.1 nm, CE mechanism dominates  $^{13}C$  and  $^{15}N$  profiles respectively. The onset of CE contribution is marked by a significant increase in DNP enhancement despite the increasing dipolar broadening of the EPR spec-

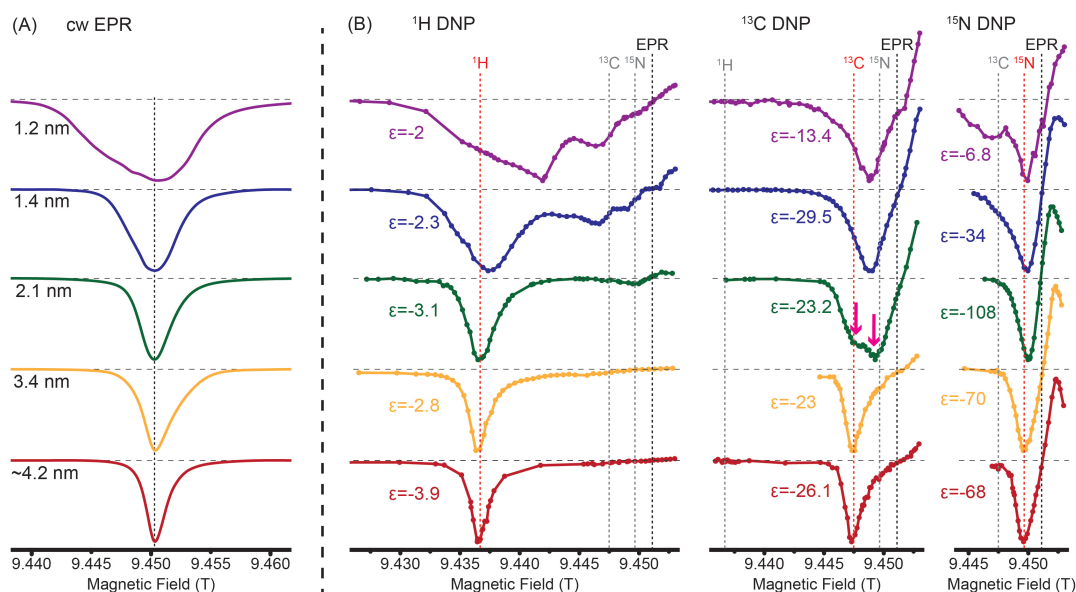


**Figure 5.4** (A) 263 GHz EPR spectra of frozen solutions of 4 mM mono(Gd-chelate) and 2 mM bis(Gd-chelate)s dissolved in 60/30/10 (vol%)  $D_8$ -glycerol/ $D_2O$ / $H_2O$  solution of  $^{13}\text{C}$ ,  $^{15}\text{N}$  2-urea (2 M), recorded at 100 K. cw EPR absorption spectra shown here are obtained by integration of as-recorded cw spectra and subsequent baseline correction. The spectra are inverted for visual comparison with  $^1\text{H}$  DNP field profile. The vertical dotted line indicates the central resonance field and is marked as EPR in (B). (B)  $^1\text{H}$ ,  $^{13}\text{C}$ , and  $^{15}\text{N}$  DNP field profiles of the same samples as in (a), acquired by sweeping the NMR field and recording the  $^1\text{H}$ - $^{13}\text{C}$  cross-polarization intensity as well as direct  $^{13}\text{C}$  or  $^{15}\text{N}$  signal intensity during microwave irradiation. Horizontal dashed lines indicate the baseline ( $\epsilon = 1$ ) for each normalized DNP profile. Respective field position of maximum negative SE DNP enhancement for each nucleus is shown by a red dotted line. Bold pink arrows indicate doublet arising from SE and CE. Data taken from [Kaushik et al., 2017].

trum. If SE mechanism was to be active, enhancements would decrease due to less efficient excitation by monochromatic microwaves as the EPR signal intensity decreases due to dipolar broadening. Furthermore, the shift from SE to CE with decreasing inter-spin distance is indicated by a shift of the negative maxima in the DNP field profile towards the EPR resonance field. For the expected symmetric field profile, the peak separation of positive and negative DNP becomes  $<2\omega_N$ . The transition is prominent for the bis(Gd-complex) with  $r_B = 2.1$  nm for which  $^{13}\text{C}$  SE and CE field profile peaks are separated within a *doublet* (shown by pink arrows in figure 5.4) and the mechanism of choice can be evoked rather selectively by tuning  $B_0$ . A transition from SE to CE can be seen for  $^1\text{H}$  DNP as well. A comparison of the  $^1\text{H}$  DNP field profiles of bis(Gd-complex)es with  $r_B = 1.2$  nm and 3.4 nm shows the difference in DNP mechanisms evoked. In  $^1\text{H}$  field profiles of PAs with 1.2 nm and 1.4 nm inter-spin distances, additional features occur closer to the EPR resonance frequency. CE matching conditions including STs might lead to such features. However, due to the fact

that these features are centered around the SE field positions of  $^{13}\text{C}$  and  $^{15}\text{N}$  these could arise from multiple nuclei undergoing consorted DNP. Another interesting finding is that the widths of the  $^{13}\text{C}$  and  $^{15}\text{N}$  DNP field profiles remain constant despite significant broadening of the EPR spectra for shorter inter- $\text{Gd}^{3+}$  distances. EPR spectral width is a result of effective variation in spin precession frequency caused by the distribution of ZFS and electron-electron dipolar coupling for a slightly varied geometry of PA molecules. DNP field profiles, on the other hand, are a result of CE matching conditions. Since not all molecular geometries and/or initial spin states are expected to contribute equally to DNP enhancement, the effective widths of EPR spectra and field profiles deviate. The shape of the field profiles is attributed to molecular degrees of freedom of the spacer, that enables a set of CE matching events during sample rotation. It is illustrated that Gd-spacer-Gd type bis(Gd-complex)es can be used as effective CE PAs for direct DNP on low- $\gamma$   $^{13}\text{C}$  and  $^{15}\text{N}$ . The enabling of CE at rather low concentrations is highly useful for biological applications.

## 5.4 Conclusion

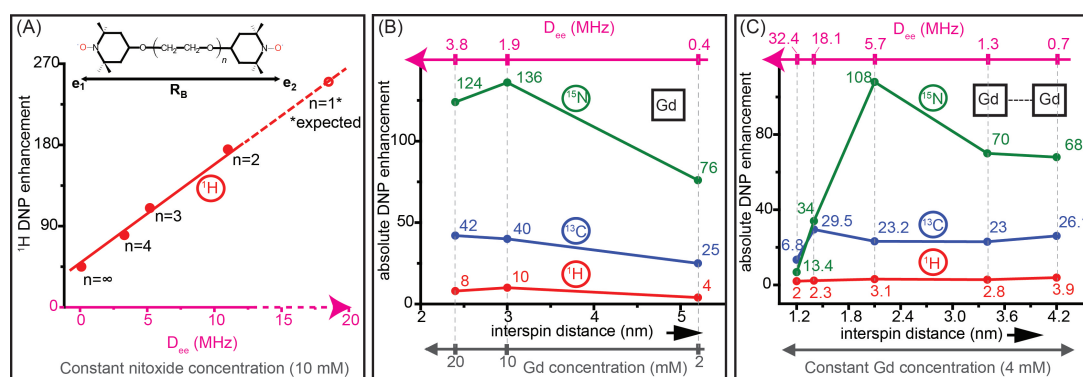


**Figure 5.5** (A)  $^1\text{H}$  DNP enhancement as a function of  $D_{ee}$  for a series of BTnE bis-nitroxides (Data taken from Hu et al. [Hu et al., 2004]). (B) DNP enhancements for  $^1\text{H}$ ,  $^{13}\text{C}$ , and  $^{15}\text{N}$  as a function of inter-spin distance,  $D_{ee}$ , and  $\text{Gd}^{3+}$  concentration. (C) DNP enhancements obtained from bis-Gd complexes with varying  $D_{ee}$  while keeping  $\text{Gd}^{3+}$  concentration constant.

Understanding DNP mechanisms have been one of the major contributing development in the optimization of PAs [Hwang et al., 1967]. Introduction of biradicals for MAS DNP [Hu et al., 2004] and superior performance of TOTAPOL revolutionized the design of PAs developed thereafter [Sauvée et al., 2016, 2013]. Rigidity and relative orientation of the nitroxide moieties were later optimized for a series of PAs [Kubicki et al., 2016]. High-performance bis-nitroxides such as bcTol are formulated accordingly for efficient CE DNP [Jagtap et al.,

2016]. Every new bit of information about the theory of DNP mechanisms and performance of PAs advances the state of DNP technique. For example, recently, the observation of depolarization effects during MAS DNP has inspired research on hetero-dimeric PAs that evoke minimum depolarization and perform better at higher spinning frequencies. Unequivocally, the development of PAs for MAS DNP is a collective effort from various groups. With this work, we have extended the understanding and scope of high-spin metal ions as PAs.

This is the very-first exploration of DNP mechanisms with high-spin metal ions. Figure 5.5 illustrates the DNP performance of BTnE series ( $n = 1 - 4$ ), in comparison of Gd-DOTA and bis(Gd-complex)es. The most noticeable difference between these PAs is on  $^1\text{H}$  enhancements. CE mediated enhancements via biradical (figure 5.5 (A)) increase significantly with  $D_{ee}$  (up to  $\approx 11$  MHz), whereas for bis(Gd-complex)es (figure 5.5 (C)), the change is barely noticeable within  $D_{ee}$  varying from about  $\approx 1$  MHz to  $\approx 32$  MHz. In stark contrast to that,  $^{13}\text{C}$  and  $^{15}\text{N}$  enhancements from  $\text{Gd}^{3+}$  PAs vary notably with variation in  $D_{ee}$ . An abrupt increase in enhancements for  $^{13}\text{C}$  and  $^{15}\text{N}$  at 1.4 nm and 2.1 nm, respectively, mark the onset of CE DNP via each nuclear species.  $^{13}\text{C}$  CE DNP field profile of bis-nitroxides are known to overlap with that of  $^1\text{H}$  profiles, therefore, such a distinction is generally not seen with bis-nitroxide PAs.

Even though  $\text{Gd}^{3+}$  PAs seem to be ineffective for  $^1\text{H}$  CE DNP, their quality to selectively evoke CE on low- $\gamma$  nuclei is valuable and oftentimes preferred for applications. Similar behavior of CE DNP on low- $\gamma$  nuclei is observed by varying concentration of uniformly dispersed Gd-DOTA (figure 5.5 (B)). Increase in  $^1\text{H}$  enhancement at 10 mM  $\text{Gd}^{3+}$  concentration is most likely due to more efficient SE DNP. As an indirect result of these observations and discussions that followed, a detailed theoretical description of SE and CE via high-spin metal ions has also been published from our group [Corzilius, 2016].

Our demonstration of intra-complex DNP, where the intrinsically bound  $\text{Mn}^{2+}$  polarized the  $\text{Mn}^{2+}$  containing hammerhead ribozyme, serves as an example for future application of such an approach. We also showed the possibility of utilizing  $\text{Gd}^{3+}$  tags as site-directed spin labels for biomolecules.

## 5.5 Outlook

The demonstrated applicability of  $Gd^{3+}$  and  $Mn^{2+}$  based PAs can be extended to a variety of biological systems. For example, bone material contains trace amounts of  $Mn^{2+}$  that has been observed by EPR spectroscopy [Mayer et al., 1993]. Direct DNP from endogenous  $Mn^{2+}$  could reveal key differences between healthy and diseased bones, by MAS NMR spectroscopy.

Paramagnetic substitution of catalytic sites in materials can be done for DNP SENS (Surface Enhanced NMR Spectroscopy) [Rossini et al., 2013], for example,  $Gd^{3+}$  can replace other lanthanide ions or  $Ca^{2+}$ . Recently, preliminary results on battery research using  $Mn^{2+}$  as PA, were presented [Leskes, 2017]. At the same time, MAS DNP with other metal ions ( $S = 1/2$ ) for materials research, was also discussed [Gordon and group, 2017]. This shows that metal ions do hold potential as viable PAs for MAS DNP and are interesting to a broader scientific community.

Beyond what we have demonstrated, these metal ions can undoubtedly be included as PAs in other biological systems. Complicated processes such as ATP hydrolysis in membrane proteins could be probed using MAS DNP by substituting naturally present  $Mg^{2+}$  with  $Mn^{2+}$ . Short-range information thus obtained could be combined with information about domain-domain interaction, obtained from dipolar EPR spectroscopy, in order to envision a clearer picture of the process [Collauto et al., 2017]. The possibility of evoking CE DNP with  $Gd^{3+}$  ions bound to protein subunits in close spatial proximity, could be used to investigate different conformations of the biomolecule. Only closed conformation could be singled out due to increased DNP enhancements.

Relative arrangement or folding of  $Gd^{3+}$ -containing small proteins could be estimated by probing inter-molecular transfer of polarization. Using  $Gd^{3+}$  as PA offers the possibility of selectively enhancing  $^{13}C$  resonances, and "containing" the enhanced polarization within the molecule, which is lost due to spin-diffusion in the case of non-selective DNP. This could result in simplified correlation spectra even without perdeuteration of the sample.



## Chapter 6

### Zusammenfassung

Die dynamische Kernpolarisation (engl.: Dynamic Nuclear Polarization, DNP) hat sich in Verbindung mit Festkörper-NMR zu einer leistungsfähigen Technik in der Strukturbiologie entwickelt. Die Verstärkung der NMR-Signale und der daraus resultierende Zeitgewinn ermöglichen die Durchführung neuer Experimente und damit die Untersuchung anspruchsvoller Systeme. Hierdurch hat diese Methode mittlerweile Anwendung in Forschungsbereichen gefunden, die andernfalls aufgrund begrenzter Empfindlichkeit der Festkörper-NMR unzugänglich wären. Das Maß des Empfindlichkeitsgewinns durch DNP hängt von einer Vielzahl Faktoren ab, wie zum Beispiel dem Ursprung der Elektronenspinpolarisation. Paramagnetische Spezies, die Polarisationsmittel genannt werden, können entweder gleichmäßig in der Probe verteilt sein oder in Form von Spinmarkern an einer spezifischen Position des Analyten angebracht werden. Die chemische Struktur von Polarisationsmitteln, deren Stabilität und die Mechanismen des Polarisationstransfers sind einige Faktoren, die Einfluss auf die DNP-Effizienz haben. Unkonventionelle Herangehensweisen zur selektiven Verstärkung des Signals ausgewählter Kernspins mittels DNP können wertvolle, strukturelle Informationen liefern. Zusammen mit einer erhöhten Signalqualität hat die Aussicht auf die Gewinnung ortsspezifischer Informationen durch DNP das Interesse und die Bemühungen in der Suche nach Markern, die ortsspezifisch angebracht werden können, verstärkt. Eine Vielzahl an paramagnetischen Spezies kommt von Natur aus in biologischen Systemen vor. Beispiele hierfür sind: reduzierbare Flavin-Semichinone im DNA-Reparaturenzym Photolyase oder  $Mn^{2+}$ -Ionen in der Arginase, dem finalen Enzym des Harnstoffzyklus, welcher ubiquitär in allen Lebensbereichen vorkommt. Zudem können natürlich vorkommende diamagnetische Ionen durch paramagnetische Ionen mit ähnlichen Koordinationseigenschaften ersetzt werden. Stabile Komplexe von High-Spin-Metallionen sind vorteilhaft gegenüber radikalischen Nitroxid-Polarisationsmitteln, da sie unter physiologischen Bedingungen nicht-toxisch sind und eine lange Lebensdauer aufweisen. Die Verwendung von  $Mn^{2+}$ -basierten Polarisationsmitteln ist aufgrund der vergleichbaren Koordinationseigenschaften von  $Mn^{2+}$  und  $Mg^{2+}$ -Ionen

innerhalb der dipolaren EPR-Spektroskopie weit verbreitet. Der Fokus dieser Arbeit liegt in der Etablierung von  $\text{Gd}^{3+}$  und  $\text{Mn}^{2+}$  Komplexen als Polarisationsmittel für DNP in der Festkörper-NMR in Verbindung mit der „Magic-Angle Spinning“ (MAS) Methode. Im Folgenden werden die untersuchten Probensysteme beschrieben.

### **Natürlich komplexiertes Mn als Polarisationsmittel im Hammerkopf-Ribozym**

Das untersuchte System ist ein inaktiviertes, uniform  $^{13}\text{C}$ ,  $^{15}\text{N}$  -isotopenmarkiertes Voll-längenkonstrukt des Hammerkopf-Ribozyms (HHRz). Die Selbstspaltungs-Reaktion findet unter Anwesenheit von divalenten Metallionen, die als Co-Faktoren dienen, statt. Weitere weniger spezifische Metallbindungsstellen im HHRz zeigen eine Affinität für monovalente Ionen und sind bei einem Überschuss von  $\text{Na}^+$  (>1 M) vollständig gesättigt. In grundlegenden Experimenten wurde AMUPol als Polarisationsmittel verwendet, um eine hohe Empfindlichkeit in zweidimensionalen MAS NMR Experimenten zu erhalten. Die Zugabe von 5 mM AMUPol bei einem  $^1\text{H}$  -DNP-Experiment ( $^{13}\text{C}$  -CPMAS) an der  $\text{Mg}^{2+}$ -HHRz Probe führte zu einem Verstärkungsfaktor von 250. Die große Signalverstärkung schreiben wir der Abwesenheit von relaxationsinduzierenden Methylgruppen im HHRz zu. Durch den Empfindlichkeitsgewinn mittels DNP war es möglich,  $^{13}\text{C}$  - $^{13}\text{C}$  und  $^{15}\text{N}$  - $^{13}\text{C}$  Korrelationsspektren von  $\text{Mn}^{2+}$ -HHRz und  $\text{Mg}^{2+}$ -HHRz aufzunehmen und konsistente Zuordnungen zwischen Resonanzen und Atomen in den Nucleotidtypen zu generieren. Direkte  $^{13}\text{C}$  -DNP-Experimente mittels AMUPol als Polarisationsmittel wurden für  $\text{Mg}^{2+}$ -HHRz und  $\text{Mn}^{2+}$ -HHRz aufgenommen und Verstärkungsfaktoren von jeweils 420 bzw. 160 wurden erzielt. Die verringerte Verstärkung im Falle von  $\text{Mn}^{2+}$ -HHRz lässt sich leicht mit einer schnelleren Spin-Gitter-Relaxation durch das paramagnetische  $\text{Mn}^{2+}$ -Ion erklären. Für ein direktes  $^{13}\text{C}$  -DNP-Experiment mittels  $\text{Mn}^{2+}$  durch den solid effect (SE) – der aktive DNP-Mechanismus bei isolierten paramagnetischen Zentren – musste das externe Magnetfeld variiert werden. Hierfür spielten DNP-Simulationen eine wichtige Rolle; für die Aufnahme eines vollständigen Feldprofils, durch welches das optimale Magnetfeld experimentell bestimmt werden kann, war die Intensität des NMR-Signals von  $\text{Mn}^{2+}$ -HHRz zu gering. Höhere Konzentrationen (2 M) von isotopenmarkiertem Analyten sind normalerweise für solche Experimente nötig. Am berechneten Optimum des Magnetfeldes wurde experimentell ein Verstärkungsfaktor von  $\epsilon = 8$  für  $\text{Mn}^{2+}$  als Polarisationsmittel erreicht. Dieser Verstärkungsfaktor ist signifikant, auch wenn er viel kleiner ist als der durch AMUPol erzielte. Diese

Studie bringt uns der angestrebten ortsspezifischen DNP einen bedeutenden Schritt näher. Für eine quantitative Gegenüberstellung muss berücksichtigt werden, dass die AMUPol-Konzentration zwölfmal höher war im Vergleich zur  $\text{Mn}^{2+}$ -Konzentration. Zusätzlich zu der durch die höhere Konzentration verursachten Signalverstärkung muss der von AMUPol hervorgerufene hocheffiziente cross effect (CE), der DNP-Mechanismus bei zwei dipolar gekoppelten paramagnetischen Zentren, in Betracht gezogen werden.

### **Aktive DNP Mechanismen durch $\text{Gd}^{3+}$**

Drei unterschiedliche Konzentrationen (2, 10 und 20 mM) der Gadotersäure (Gd-DOTA) wurden als Polarisationsmittel mit  $^{13}\text{C}$ ,  $^{15}\text{N}$ -isotopenmarkiertem Harnstoff in einer glasbildenden Mischung aus Glycerin/Wasser (60/40 vol%) verwendet. Mit steigender Konzentration der paramagnetischen Ionen sinkt statistisch der mittlere Abstand zwischen den Elektronenspins. Im Falle kleiner  $\text{Gd}^{3+}$  Konzentration ist die dipolare Kopplung zwischen den Ionen mit 0.4 MHz vernachlässigbar, so dass der SE-Mechanismus der einzige aktive DNP-Mechanismus ist. Die Verbreiterung der EPR-Spektren bei höheren Konzentrationen deutet auf eine Zunahme der dipolaren Kopplung hin. Theoretisch würde diese den CE-Mechanismus begünstigen, jedoch sind die EPR-Linienbreiten des zentralen Spin-Übergangs (engl.: central transition, CT) relativ schmal im Vergleich zu klassischen CE-induzierenden Polarisationsmitteln. Die experimentell beobachteten Verstärkungsfaktoren deuten auf eine Beteiligung des CE-Mechanismus bei höheren Konzentrationen hin. Der CE-Beitrag variiert für die drei untersuchten Kerne und skaliert mit deren Larmorfrequenzen. Der Grund hierfür ist die Wahrscheinlichkeit, dass ein Spin-Paket, welches innerhalb des intensiven zentralen Übergangs des EPR-Spektrums liegt, die CE-Bedingungen erfüllt. Abschließend lässt sich sagen, dass kleine  $\text{Gd}^{3+}$ -Konzentrationen (2 mM) den SE-Mechanismus hervorrufen, wohingegen höhere Konzentrationen bei Kernen mit geringem gyromagnetischem Verhältnis bevorzugt den CE-Mechanismus auslösen. Die Tatsache, dass biologische Systeme für gewöhnlich niedrige Konzentrationen (<2 mM) an Polarisationsmitteln enthalten, und das Wissen, dass in diesem Fall der SE der aktive DNP-Mechanismus ist, erlaubt eine eindeutige Interpretation der experimentellen Daten an biologischen Systemen. Um  $\text{Gd}^{3+}$  als Polarisationsmittel in biologischen Proben nutzen zu können, wurden verschiedene  $\text{Gd}^{3+}$ -bindende Chelat-Marker getestet. Für vorläufige DNP-Experimente wurden Gd-Komplexe mit 1,4,7,10-Tetraazacyclododecan-1,4,7-tris-

essigsäure-10-maleimidoethylacetamid (DOTA-M) und 4-Mercaptomethyldipicolinsäure (4MMDPA) an Ubiquitin gebunden. Diese Marker erzeugten relativ kleine direkte  $^{13}\text{C}$ -SE-Verstärkungen in der Größenordnung von 1 bis 3 für 1 mM Ubiquitin in einer Mischung von Glycerin/Wasser (60/36/4 vol%).

### **Bis-Gd-Komplexe für CE-DNP**

Der Einfluss der Konzentration und des Interspin-Abstandes der aktiven Polarisationsmittelzentren sind in den vorher gezeigten Experimenten an Gd-DOTA miteinander verflochten. Diese beiden Faktoren beeinflussen die hervorgerufenen DNP-Mechanismen. Um ein besseres Verständnis der aktiven Mechanismen bei High-Spin-Metallionen zu erlangen, muss der relevante Interspin-Abstand explizit eingestellt werden. Dies konnte durch Bis-Metall-Komplexe mit unterschiedlichem Abstand zwischen den Metallzentren erreicht werden. Ähnliche Bis-Metall-Komplexe mit größerem Interspin-Abstand sind bereits in der EPR-Spektroskopie etabliert und werden als sogenannte „molekulare Lineale“ verwendet, um Abstände zwischen zwei Marker-Positionen in einem Molekül oder einem molekularen Komplex zu ermitteln. Die Starrheit dieser Bis-Metall-Komplexe stellt die Basis für eine akkurate Distanzbestimmung dar. Für DNP-Experimente wurden die Bis-Metall-Komplexe so entworfen, dass der Interspin-Abstand für DNP-Anwendungen verkürzt wurde, die Verbindung zwischen den Metallen besonders rigide ist und die Metallionen besonders fest gebunden sind. Ferner wurden verzweigte Polyethylenglycol-Ketten eingeführt, um zum einen Löslichkeit zu erhöhen und zum anderen eine stabile Streckung des Moleküls zu gewährleisten, so dass der Interspin-Abstand sehr gut definiert und verlässlich für Distanzbestimmungen ist. Die Bis-Metall-Komplexe, mit Abständen kleiner 4 nm, wurden mit dem Mono-Metall-Komplex mit vergleichbarer chemischer Geometrie verglichen, wobei die gleiche  $\text{Gd}^{3+}$ -Konzentrationen verwendet wurde. Vernachlässigbare intermolekulare Wechselwirkungen wurden durch eine kleine gewählte Konzentration an Polarisationsmittel gewährleistet.

EPR-Spektren von  $\text{Gd}^{3+}$ -Komplexen werden durch den Zentralübergang des High-Spin-Systems ( $S = 7/2$ ) dominiert und breite Komponenten, die durch die Sattelitenübergänge (engl.: satellite transition, ST) hervorgerufen werden, sind kaum wahrnehmbar. Die interelektronische dipolare Kopplungskonstante ( $D_{ee}$ ) steigt bei Verringerung des Interspin-Abstands von 3,4 nm auf 1,2 nm erwartungsgemäß von 1,3 MHz auf 32,4 MHz an; dies

wird als Verbreiterung im EPR Spektrum beobachtet. In den DNP-Feldprofilen von  $^{13}\text{C}$  und  $^{15}\text{N}$  ist dieser Effekt durch den Übergang vom SE- zum CE-Mechanismus mit sinkendem Interspin-Abstand sichtbar. Für den Mono-Gd-Komplex und den Bis-Gd-Komplex mit einem Inter-Spin-Abstand von 3,4 nm zeigen DNP-Feldprofile einen Verlauf, der charakteristisch für den SE-Mechanismus zu erwarten ist. Bei Interspin-Abständen von 1,2 und 2,1 nm ist erkennbar, dass der CE-Mechanismus die  $^{13}\text{C}$ - und  $^{15}\text{N}$ -Feldprofile dominiert. Einsetzende CE-Beteiligung wird durch einen signifikanten Anstieg des DNP-Verstärkungsfaktors trotz der steigenden dipolaren Verbreiterung des EPR-Spektrums markiert. Bei dem SE-Mechanismus würde die Verstärkung auf Grund der weniger effizienten Anregung des verbreiteten Spektrums durch monochromatische Mikrowellen abnehmen. Des Weiteren wird die Verlagerung vom SE- zum CE-Mechanismus für abnehmende Interspin-Abstände durch eine Verschiebung des Minimums des DNP-Feldprofils hin zum EPR-Resonanzfeld erkennbar. Für das erwartete symmetrische Feldprofil beträgt die Separation des positiven und negativen DNP-Effekts weniger als das Zweifache der Kern-Larmor-Frequenz. Der Übergang von SE auf CE ist für den Bis-Gd-Komplex mit einem Abstand von 2,1 nm besonders auffällig, da hier die  $^{13}\text{C}$ -SE und -CE-Feldprofilbeiträge in einem Duplett separiert sind und ein ausgewählter Mechanismus selektiv durch die Abstimmung des Magnetfeldes hervorgerufen werden kann. Ein Übergang vom SE- zu CE-Mechanismus wurde auch für  $^1\text{H}$  beobachtet. Ein Vergleich des DNP-Feldprofils der Bis-Gd-Komplexe mit Abständen von 1,2 und 3,4 nm zeigt den Unterschied im aktiven DNP-Mechanismus. Im Falle der  $^1\text{H}$ -Feldprofile der Polarisationsmittel mit 1,2 und 1,4 nm Interspin-Abständen wurden zusätzliche Merkmale nahe des EPR-Resonanzfelds beobachtet. Diese Merkmale liegen auf der SE Feldposition von  $^{13}\text{C}$  und  $^{15}\text{N}$  und könnten von konzertierter DNP mehrerer Kerne hervorgerufen werden.

### Schlussfolgerung

Dies ist die erste ausgeprägte Untersuchung der DNP-Mechanismen von High-Spin-Metallionen. Die DNP-Leistungsfähigkeit von Gd-DOTA und Bis-Gd-Komplexen wurde mit den Biradikalen einer bis-TEMPO-*n*-ethylenglycol-(BTnE)-Serie ( $n = 1-4$ ) verglichen. Der bemerkenswerteste Unterschied zwischen den Polarisationsmitteln wurde bei  $^1\text{H}$  Verstärkungen beobachtet. Die Verstärkung durch den CE Mechanismus, welcher durch Biradikale verursacht wird, steigt signifikant mit steigender dipolarer Kopplung bis 11

MHz, wohingegen dieser bei den Bis-Gd-Komplexen in einem Bereich von 1 MHz bis 32 MHz kaum wahrnehmbar ist. In besonders starkem Gegensatz hierzu stehen die  $^{13}\text{C}$ - und  $^{15}\text{N}$ -Verstärkungen der Bis-Gd-Komplexe als Polarisationsmittel bei Abständen von 1,4 nm und 2,1 nm.  $^{13}\text{C}$ -CE-DNP-Feldprofile von bis-Nitroxiden sind für ihre Überlappung mit den  $^1\text{H}$ -Feldprofilen bekannt, daher wird hier eine generelle Unterscheidung im Falle von bis-Nitroxid Polarisationsmitteln nicht beobachtet. Für  $\text{Gd}^{3+}$ -Polarisationsmittel hingegen, für die der  $^1\text{H}$ -CE-DNP-Mechanismus ineffektiv zu sein scheint, ist es jedoch möglich selektiv den CE-Mechanismus an Kernen mit einem geringen gyromagnetischen Verhältnis  $\gamma$  wie ( $^{13}\text{C}$  und  $^{15}\text{N}$ ) separat hervorzurufen. Weiter wurde beobachtet, dass durch Erhöhung der Konzentration von gleichmäßig verteiltem Gd-DOTA eine Vergrößerung der  $^1\text{H}$ -Verstärkung für  $\text{Gd}^{3+}$ -Konzentration größer 2 mM auftritt. Dies ist höchstwahrscheinlich auf einen effizienteren SE-DNP-Mechanismus zurückzuführen.

## Chapter 7

### Glossary

AMUPol	Aix-Marseille Université polarizing agent
ASR	absolute sensitivity ratio
bCTbK	bis-cyclohexyl-TEMPO-bisketal
BDPA	1,3-bisdiphenylene-2-phenyl allyl
BT2E	bis-TEMPO-2-ethyleneglycol
bTbK	bis-TEMPO-bisketal
bTbtK	bis-TEMPO-bis-thioketal
bTbtK-py	bis-TEMPO-bis-thioketal-tetra-tetrahydropyran
BTnE	bis-TEMPO-n-ethyleneglycol
BTOXA	bis-TEMPO-oxalyl amide
bTtereph	bis-TEMPO terephthalate
bTurea	bis-TEMPO-urea
CE	cross effect
CIDNP	chemically induced dynamic nuclear polarization
CP	cross polarization
CT	central transition
cw	continuous wave
DNP	dynamic nuclear polarization
DOTA	1,4,7,10-tetraazacyclododecane-1,4,7,10-tetraacetic acid
DOTOPA-TEMPO	4-[N,N-di-(2-hydroxy-3-(TEMPO-4'-oxy)-propyl)]-amino-TEMPO
DQ	double quantum
EPR	electron paramagnetic resonance
HFI	hyperfine interaction
LMN	lanthanum magnesium double nitrate
MAS	magic-angle spinning
4-MMDPA	4-Mercaptomethyl Dipicolinic Acid

MRI	magnetic resonance imaging
NMR	nuclear magnetic resonance
OE	Overhauser effect
OTP	ortho-terphenyl
PA	polarizing agent
PEG	polyethyleneglycole
PHIP	para-hydrogen induced polarization
rf	radio frequency
SA-BDPA	sulfonated BDPA
SDSL	site-directed spin labeling
SE	solid effect
SEOP	spin-exchange optical pumping
SN-BDPA	sulfonamide BDPA
SQ	single quantum
ST	satellite transition
TAM	triarylmethyl
TEKPol	tetrakis(phenylcyclohexyl) TEMPO-bisketal
TEMPO	2,2,6,6-tetramethyl-1-piperidiny-1-oxyl
TEMPOL	4-Hydroxy-TEMPO
TEMTriPol	TEMPO/trityl polarizing agent
TM	thermal mixing
TOTAPOL	1-(TEMPO-4-oxy)-3-(TEMPO-4-amino)propan-2-ol
VT	variable temperature
ZFS	zero-field splitting
ZQ	zero quantum
mw	microwave



## Bibliography

- Abragam, A., Borghini, M., Catillon, P., Coustham, J., Roubeau, P., and Thirion, J. (1962). Diffusion de protons polarisés de 20 mev par une cible de protons polarisés et mesure préliminaire du paramètre  $\rho$ . *Physics Letters*, 2(7):310–311.
- Abragam, A. and Goldman, M. (1978). Principles of dynamic nuclear polarisation. *Reports on Progress in Physics*, 41(3):395.
- Abraham, McCausland, M. A. H., and Robinson, F. N. H. (1959). Dynamic nuclear polarization. *Phys. Rev. Lett.*, 2:449–451.
- Ardenkjaer-Larsen, J., Laursen, I., Leunbach, I., Ehnholm, G., Wistrand, L.-G., Petersson, J., and Golman, K. (1998). Epr and dnp properties of certain novel single electron contrast agents intended for oximetric imaging. *Journal of Magnetic Resonance*, 133(1):1–12.
- Ardenkjaer-Larsen, J. H. (2016). On the present and future of dissolution-DNP. *Journal of Magnetic Resonance*, 264:3–12.
- Ashbrook, S. E. and Dawson, D. M. (2016). NMR spectroscopy of minerals and allied materials. In *Nuclear Magnetic Resonance*, pages 1–52. Royal Society of Chemistry.
- Ashbrook, S. E. and Sneddon, S. (2014). New methods and applications in solid-state NMR spectroscopy of quadrupolar nuclei. *Journal of the American Chemical Society*, 136(44):15440–15456.
- Barnes, A. (2017). Gyrotron technology. Research Group.
- Barnes, A., De Paëpe, G., Van Der Wel, P., Hu, K.-N., Joo, C.-G., Bajaj, V., Mak-Jurkauskas, M., Sirigiri, J., Herzfeld, J., Temkin, R., et al. (2008). High-field dynamic nuclear polarization for solid and solution biological nmr. *Applied magnetic resonance*, 34(3):237–263.
- Baudot, B. (1998). Glass-forming tendency and stability of aqueous solutions of diethylformamide and dimethylformamide. *Cryobiology*, 32:187–199.
- Becerra, L., Gerfen, G., Bellew, B., Bryant, J., Hall, D., Inati, S., Weber, R., Un, S., Prisner, T., Mcdermott, A., Fishbein, K., Kreisler, K., Temkin, R., Singel, D., and Griffin, R. (1995). A spectrometer for dynamic nuclear polarization and electron paramagnetic resonance at high frequencies. *Journal of Magnetic Resonance, Series A*, 117(1):28–40.

- Becerra, L. R., Gerfen, G. J., Temkin, R. J., Singel, D. J., and Griffin, R. G. (1993). Dynamic nuclear polarization with a cyclotron resonance maser at 5 t. *Physical Review Letters*, 71(21):3561–3564.
- Benmelouka, M., Van Tol, J., Borel, A., Nellutla, S., Port, M., Helm, L., Brunel, L.-C., and Merbach, A. (2009). Multiple-frequency and variable-temperature epr study of gadolinium(iii) complexes with polyaminocarboxylates: Analysis and comparison of the magnetically dilute powder and the frozen-solution spectra. *Helvetica Chimica Acta*, 92(11):2173–2185.
- Boots, J. L., Canny, M. D., Azimi, E., and Pardi, A. (2008). Metal ion specificities for folding and cleavage activity in the schistosoma hammerhead ribozyme. *RNA*, 14(10):2212–2222.
- Carver, T. R. and Slichter, C. P. (1953). Polarization of nuclear spins in metals. *Physical Review*, 92(1):212–213.
- Chandrasekhar, S. (1943). Stochastic problems in physics and astronomy. *Reviews of Modern Physics*, 15(1):1–89.
- Collauto, A., Mishra, S., Litvinov, A., Mchaourab, H. S., and Goldfarb, D. (2017). Direct spectroscopic detection of ATP turnover reveals mechanistic divergence of ABC exporters. *Structure*.
- Corzilius, B. (2016). Theory of solid effect and cross effect dynamic nuclear polarization with half-integer high-spin metal polarizing agents in rotating solids. *Phys. Chem. Chem. Phys.*, 18(39):27190–27204.
- Corzilius, B., Michaelis, V. K., Penzel, S. A., Ravera, E., Smith, A. A., Luchinat, C., and Griffin, R. G. (2014). Dynamic nuclear polarization of <sup>1</sup>h, <sup>13</sup>c, and <sup>59</sup>co in a tris(ethylenediamine)cobalt(III) crystalline lattice doped with cr(III). *Journal of the American Chemical Society*, 136(33):11716–11727.
- Corzilius, B., Smith, A. A., Barnes, A. B., Luchinat, C., Bertini, I., and Griffin, R. G. (2011). High-field dynamic nuclear polarization with high-spin transition metal ions. *Journal of the American Chemical Society*, 133(15):5648–5651.
- Dalaloyan, A., Qi, M., Ruthstein, S., Vega, S., Godt, A., Feintuch, A., and Goldfarb, D. (2015). Gd(iii)–gd(iii) EPR distance measurements – the range of accessible distances and the impact of zero field splitting. *Phys. Chem. Chem. Phys.*, 17(28):18464–18476.
- de Alba, C. F., Takahashi, H., Richard, A., Chenavier, Y., Dubois, L., Maurel, V., Lee, D., Hediger, S., and De Paëpe, G. (2015). Matrix-free DNP-enhanced NMR spectroscopy of liposomes using a lipid-anchored biradical. *Chemistry - A European Journal*, 21(12):4512–4517.

- Dhimitruka, I., Grigorieva, O., Zweier, J. L., and Khramtsov, V. V. (2010). Synthesis, structure, and epr characterization of deuterated derivatives of finland trityl radical. *Bioorganic & medicinal chemistry letters*, 20(13):3946–3949.
- Donovan, K. J., Silvers, R., Linse, S., and Griffin, R. G. (2017). 3d mas nmr experiment utilizing through-space 15n–15n correlations. *Journal of the American Chemical Society*.
- Duckett, S. B. and Mewis, R. E. (2012). Application of Parahydrogen induced polarization techniques in NMR spectroscopy and imaging. *Accounts of Chemical Research*, 45(8):1247–1257.
- Elisei, E., Filibian, M., Carretta, P., Serra, S. C., Tedoldi, E., Willart, J., Descamps, M., and Cesàro, A. (2015). Dynamic nuclear polarization of a glassy matrix prepared by solid state mechanochemical amorphization of crystalline substances. *Chemical Communications*, 51(11):2080–2083.
- Erilov, D. A., Bartucci, R., Guzzi, R., Marsh, D., Dzuba, S. A., and Sportelli, L. (2004). Echo-detected electron paramagnetic resonance spectra of spin-labeled lipids in membrane model systems. *The Journal of Physical Chemistry B*, 108(14):4501–4507.
- Feintuch, A., Shimon, D., Hovav, Y., Banerjee, D., Kaminker, I., Lipkin, Y., Zibzener, K., Epel, B., Vega, S., and Goldfarb, D. (2011). A dynamic nuclear polarization spectrometer at 95ghz/144mhz with EPR and NMR excitation and detection capabilities. *Journal of Magnetic Resonance*, 209(2):136–141.
- Garif'yanov, N. S., Kozyrev, B. M., and Fedotov, V. N. (1968). Width of the EPR Line of Liquid Solutions of Ethylene Glycol Complexes for Even and Odd Chromium Isotopes. *Soviet Physics Doklady*, 13:107.
- Goldfarb, D. (2014). Gadolinium spin labeling for distance measurements by pulse EPR spectroscopy. *Physical Chemistry Chemical Physics*, 16(21):9685.
- Golota, N., Scott, F., Saliba, E., Albert, B., and Barnes, A. (2017). Design and activation of frequency tunable 200ghz gyrotron.
- Gordon, C. and group, C. (2017). Dnp with metal ions. The Alpine Conference on solid-state NMR, in a scientific discussion.
- Hall, D. A., Maus, D. C., Gerfen, G. J., Inati, S. J., Becerra, L. R., Dahlquist, F. W., and Griffin, R. G. (1997). Polarization-enhanced nmr spectroscopy of biomolecules in frozen solution. *Science*, 276(5314):930–932.
- Haze, O., Corzilius, B., Smith, A. A., Griffin, R. G., and Swager, T. M. (2012). Water-soluble narrow-line radicals for dynamic nuclear polarization. *Journal of the American Chemical Society*, 134(35):14287–14290.

- Hovav, Y., Feintuch, A., and Vega, S. (2010). Theoretical aspects of dynamic nuclear polarization in the solid state – the solid effect. *Journal of Magnetic Resonance*, 207(2):176–189.
- Hovav, Y., Feintuch, A., Vega, S., and Goldfarb, D. (2014). Dynamic nuclear polarization using frequency modulation at 3.34t. *Journal of Magnetic Resonance*, 238:94–105.
- Hu, K.-N. (2011). Polarizing agents and mechanisms for high-field dynamic nuclear polarization of frozen dielectric solids. *Solid State Nuclear Magnetic Resonance*, 40(2):31–41.
- Hu, K.-N., Bajaj, V. S., Rosay, M., and Griffin, R. G. (2007). High-frequency dynamic nuclear polarization using mixtures of TEMPO and trityl radicals. *The Journal of Chemical Physics*, 126(4):044512.
- Hu, K.-N., Debelouchina, G. T., Smith, A. A., and Griffin, R. G. (2011). Quantum mechanical theory of dynamic nuclear polarization in solid dielectrics. *The Journal of Chemical Physics*, 134(12):125105.
- Hu, K.-N., Hua Yu, H., Swager, T. M., and Griffin, R. G. (2004). Dynamic nuclear polarization with biradicals. *Journal of the American Chemical Society*, 126(35):10844–10845.
- Hubbell, W. L., López, C. J., Altenbach, C., and Yang, Z. (2013). Technological advances in site-directed spin labeling of proteins. *Current Opinion in Structural Biology*, 23(5):725–733.
- Hwang, C. F., Hasher, B. A., Hill, D. A., and Markley, F. (1967). The use of chemically doped polystyrene as a polarized proton target material. *Nuclear Instruments and Methods*, 51(2):254–256.
- Idehara, T. (2017). Gyrotron technology. Research Group.
- Idehara, T. and Sabchevski, S. P. (2017). Gyrotrons for high-power terahertz science and technology at fir uf. *Journal of Infrared, Millimeter, and Terahertz Waves*, 38(1):62–86.
- Jagtap, A. P., Geiger, M.-A., Stöppler, D., Orwick-Rydmark, M., Oschkinat, H., and Sigurdsson, S. T. (2016). bcTol: a highly water-soluble biradical for efficient dynamic nuclear polarization of biomolecules. *Chem. Commun.*, 52(43):7020–7023.
- Jaroniec, C. P., MacPhee, C. E., Bajaj, V. S., McMahon, M. T., Dobson, C. M., and Griffin, R. G. (2004). High-resolution molecular structure of a peptide in an amyloid fibril determined by magic angle spinning nmr spectroscopy. *Proceedings of the National Academy of Sciences of the United States of America*, 101(3):711–716.
- Kaur, H., Lakatos-Karoly, A., Vogel, R., Nöll, A., Tampé, R., and Glaubitz, C. (2016). Coupled ATPase-adenylate kinase activity in ABC transporters. *Nature Communications*, 7:13864.
- Kaushik, M., Bahrenberg, T., Can, T. V., Caporini, M. A., Silvers, R., Heiliger, J., Smith, A. A., Schwalbe, H., Griffin, R. G., and Corzilius, B. (2016). Gd(III) and Mn(II) complexes for dynamic nuclear polarization: small molecular chelate polarizing agents and applications with site-directed spin labeling of proteins. *Phys. Chem. Chem. Phys.*, 18(39):27205–27218.

- Kaushik, M., Qi, M., Godt, A., and Corzilius, B. (2017). Bis-gadolinium complexes for solid effect and cross effect dynamic nuclear polarization. *Angewandte Chemie International Edition*, 56(15):4295–4299.
- Klare, J. P. (2012). Site-directed spin labeling and electron paramagnetic resonance (EPR) spectroscopy: A versatile tool to study protein-protein interactions. In *Protein Interactions*. InTech.
- Koelsch, C. F. (1957). Syntheses with triarylvinylmagnesium bromides.  $\alpha$ ,  $\gamma$ -bisdiphenylene- $\beta$ -phenylallyl, a stable free radical. *Journal of the American Chemical Society*, 79(16):4439–4441.
- Kubicki, D. J., Casano, G., Schwarzwälder, M., Abel, S., Sauvée, C., Ganesan, K., Yulikov, M., Rossini, A. J., Jeschke, G., Copéret, C., et al. (2016). Rational design of dinitroxide biradicals for efficient cross-effect dynamic nuclear polarization. *Chemical Science*, 7(1):550–558.
- Lawler, R. G. (1972). Chemically induced dynamic nuclear polarization (CIDNP). II. radical-pair model. *Accounts of Chemical Research*, 5(1):25–33.
- Lawrence, M. C., Pilling, P. A., Epa, V. C., Berry, A. M., Ogunniyi, A. D., and Paton, J. C. (1998). The crystal structure of pneumococcal surface antigen psaa reveals a metal-binding site and a novel structure for a putative abc-type binding protein. *Structure*, 6(12):1553–1561.
- Le, D., Casano, G., Phan, T. N. T., Ziarelli, F., Ouari, O., Aussenac, F., Thureau, P., Mollica, G., Gignes, D., Tordo, P., and Viel, S. (2014). Optimizing sample preparation methods for dynamic nuclear polarization solid-state nmr of synthetic polymers. *Macromolecules*, 47(12):3909–3916.
- Lee, D., Bouleau, E., Saint-Bonnet, P., Hediger, S., and De Paëpe, G. (2016). Ultra-low temperature mas-dnp. *Journal of Magnetic Resonance*, 264:116–124.
- Lesage, A., Lelli, M., Gajan, D., Caporini, M. A., Vitzthum, V., Miéville, P., Alauzun, J., Roussey, A., Thieuleux, C., Mehdi, A., Bodenhausen, G., Coperet, C., and Emsley, L. (2010). Surface enhanced nmr spectroscopy by dynamic nuclear polarization. *Journal of the American Chemical Society*, 132(44):15459–15461. PMID: 20831165.
- Leskes, M. (2017). Probing bulk materials properties and the electrode-electrolyte interface with exogenous and endogenous mas-dnp. Chamonix, France. The Alpine Conference on solid-state NMR.
- M., T. and E., J. (2012). HR-MAS NMR spectroscopy in material science. In *Advanced Aspects of Spectroscopy*. InTech.
- Maly, T., Andreas, L. B., Smith, A. A., and Griffin, R. G. (2010a). 2 h-dnp-enhanced 2 h- $^{13}\text{C}$  solid-state nmr correlation spectroscopy. *Physical Chemistry Chemical Physics*, 12(22):5872–5878.

- Maly, T., Cui, D., Griffin, R. G., and Miller, A.-F. (2012). 1h dynamic nuclear polarization based on an endogenous radical. *The Journal of Physical Chemistry B*, 116(24):7055–7065.
- Maly, T., Miller, A.-F., and Griffin, R. G. (2010b). In situ high-field dynamic nuclear polarization—direct and indirect polarization of  $^{13}\text{C}$  nuclei. *ChemPhysChem*, 11(5):999–1001.
- Marchanka, A., Simon, B., Althoff-Ospelt, G., and Carlomagno, T. (2015). RNA structure determination by solid-state NMR spectroscopy. *Nature Communications*, 6:7024.
- Martick, M. and Scott, W. G. (2006). Tertiary contacts distant from the active site prime a ribozyme for catalysis. *Cell*, 126(2):309–320.
- Mascali, F. C., Ching, H. Y. V., Rasia, R. M., Un, S., and Tabares, L. C. (2016). Using genetically encodable self-assembling GdIII Spin labels to make in-cell nanometric distance measurements. *Angewandte Chemie International Edition*, 55(37):11041–11043.
- Matsuki, Y., Takahashi, H., Ueda, K., Idehara, T., Ogawa, I., Toda, M., Akutsu, H., and Fujiwara, T. (2010). Dynamic nuclear polarization experiments at 14.1 T for solid-state nmr. *Physical Chemistry Chemical Physics*, 12(22):5799–5803.
- Mayer, I., Diab, H., Reinen, D., and Albrecht, C. (1993). Manganese in apatites, chemical, ligand-field and electron paramagnetic resonance spectroscopy studies. *Journal of materials science*, 28(9):2428–2432.
- Mentink-Vigier, F., Paul, S., Lee, D., Feintuch, A., Hediger, S., Vega, S., and Paëpe, G. D. (2015). Nuclear depolarization and absolute sensitivity in magic-angle spinning cross effect dynamic nuclear polarization. *Phys. Chem. Chem. Phys.*, 17(34):21824–21836.
- Mentink-Vigier, F., Ümit Akbey, Hovav, Y., Vega, S., Oschkinat, H., and Feintuch, A. (2012). Fast passage dynamic nuclear polarization on rotating solids. *Journal of Magnetic Resonance*, 224:13–21.
- Michaelis, V. K., Corzilius, B., Smith, A. A., and Griffin, R. G. (2013a). Dynamic nuclear polarization of  $^{17}\text{O}$ : Direct polarization. *The Journal of Physical Chemistry B*, 117(48):14894–14906. PMID: 24195759.
- Michaelis, V. K., Smith, A. A., Corzilius, B., Haze, O., Swager, T. M., and Griffin, R. G. (2013b). High-field  $^{13}\text{C}$  dynamic nuclear polarization with a radical mixture. *Journal of the American Chemical Society*, 135(8):2935–2938.
- Money, K. and Myles, W. (1974). Heavy water nystagmus and effects of alcohol. *Nature*, 247:404–405.
- Morrissey, S. R., Horton, T. E., and DeRose, V. J. (2000).  $\text{Mn}^{2+}$  sites in the hammerhead ribozyme investigated by epr and continuous-wave q-band endor spectroscopies. *Journal of the American Chemical Society*, 122(14):3473–3481.

- Moser, E., Laistler, E., Schmitt, E., and Kontaxis, G. (2017). Ultra-high field nmr and mri—the role of magnet technology to increase sensitivity and specificity. *Frontiers in Physics*, 5:33.
- Ong, Y. S., Lakatos, A., Becker-Baldus, J., Pos, K. M., and Glaubitz, C. (2013). Detecting substrates bound to the secondary multidrug efflux pump emre by dnp-enhanced solid-state nmr. *Journal of the American Chemical Society*, 135(42):15754–15762.
- Overhauser, A. W. (1953). Polarization of nuclei in metals. *Physical Review*, 92(2):411–415.
- Qi, M., Hülsmann, M., and Godt, A. (2016). Spacers for geometrically well-defined water-soluble molecular rulers and their application. *The Journal of Organic Chemistry*, 81(6):2549–2571.
- Quinn, C. M. and Polenova, T. (2017). Structural biology of supramolecular assemblies by magic-angle spinning NMR spectroscopy. *Quarterly Reviews of Biophysics*, 50.
- Raitsimring, A., Astashkin, A., Poluektov, O., and Caravan, P. (2005). High-field pulsed epr and endor of gd 3+ complexes in glassy solutions. *Applied Magnetic Resonance*, 28(3):281–295.
- Ravera, E., Corzilius, B., Michaelis, V. K., Luchinat, C., Griffin, R. G., and Bertini, I. (2014). DNP-enhanced MAS NMR of bovine serum albumin sediments and solutions. *The Journal of Physical Chemistry B*, 118(11):2957–2965.
- Renault, M., van Boxtel, R. T., Bos, M. P., Post, J. A., Tommassen, J., and Baldus, M. (2012). Cellular solid-state nuclear magnetic resonance spectroscopy. *Proceedings of the National Academy of Sciences*, 109(13):4863–4868.
- Rogawski, R., Sergeyev, I. V., Li, Y., Ottaviani, M. F., Cornish, V., and McDermott, A. E. (2017). Dynamic nuclear polarization signal enhancement with high-affinity biradical tags. *The Journal of Physical Chemistry B*, 121(6):1169–1175.
- Rosay, M., Tometich, L., Pawsey, S., Bader, R., Schauwecker, R., Blank, M., Borchard, P. M., Cauffman, S. R., Felch, K. L., Weber, R. T., Temkin, R. J., Griffin, R. G., and Maas, W. E. (2010). Solid-state dynamic nuclear polarization at 263 GHz: spectrometer design and experimental results. *Physical Chemistry Chemical Physics*, 12(22):5850.
- Rossini, A. J., Zagdoun, A., Lelli, M., Lesage, A., Copéret, C., and Emsley, L. (2013). Dynamic nuclear polarization surface enhanced NMR spectroscopy. *Accounts of Chemical Research*, 46(9):1942–1951.
- Sauvée, C., Casano, G., Abel, S., Rockenbauer, A., Akhmetzyanov, D., Karoui, H., Siri, D., Aussenac, E., Maas, W., Weber, R. T., Prisner, T., Rosay, M., Tordo, P., and Ouari, O. (2016). Tailoring of polarizing agents in the bTurea series for cross-effect dynamic nuclear polarization in aqueous media. *Chemistry - A European Journal*, 22(16):5598–5606.

- Sauvée, C., Rosay, M., Casano, G., Aussenac, F., Weber, R. T., Ouari, O., and Tordo, P. (2013). Highly efficient, water-soluble polarizing agents for dynamic nuclear polarization at high frequency. *Angewandte Chemie International Edition*, 52(41):10858–10861.
- Schweiger, A. and Jeschke, G. (2001). *Principles of Pulse Electron Paramagnetic Resonance*. Oxford University Press, USA, 1 edition.
- Scott, W. G., Finch, J. T., and Klug, A. (1995). The crystal structure of an aii-rnahammerhead ribozyme: A proposed mechanism for rna catalytic cleavage. *Cell*, 81(7):991–1002.
- Selenko, P. and Wagner, G. (2007). Looking into live cells with in-cell nmr spectroscopy. *Journal of structural biology*, 158(2):244–253.
- Shannon, R. D. (1976). Revised effective ionic radii and systematic studies of interatomic distances in halides and chalcogenides. *Acta Crystallographica Section A*, 32:751–767.
- Shimon, D., Hovav, Y., Feintuch, A., Goldfarb, D., and Vega, S. (2012). Dynamic nuclear polarization in the solid state: a transition between the cross effect and the solid effect. *Physical Chemistry Chemical Physics*, 14(16):5729.
- Smith, A. N., Caporini, M. A., Fanucci, G. E., and Long, J. R. (2015). A method for dynamic nuclear polarization enhancement of membrane proteins. *Angewandte Chemie International Edition*, 54(5):1542–1546.
- Song, C., Hu, K.-N., Joo, C.-G., Swager, T. M., and Griffin, R. G. (2006). Totapol: A biradical polarizing agent for dynamic nuclear polarization experiments in aqueous media. *Journal of the American Chemical Society*, 128(35):11385–11390. PMID: 16939261.
- Song, Y., Meade, T., Astashkin, A., Klein, E., Enemark, J., and Raitsimring, A. (2011). Pulsed dipolar spectroscopy distance measurements in biomacromolecules labeled with gd(III) markers. *Journal of Magnetic Resonance*, 210(1):59–68.
- Stich, T., Lahiri, S., Yeagle, G., Dicus, M., Brynda, M., Gunn, A., Aznar, C., DeRose, V., and Britt, R. (2007). Multifrequency pulsed epr studies of biologically relevant manganese (ii) complexes. *Applied magnetic resonance*, 31(1-2):321.
- Stoll, S. and Schweiger, A. (2006). EasySpin, a comprehensive software package for spectral simulation and analysis in EPR. *Journal of Magnetic Resonance*, 178(1):42–55.
- Takahashi, H., Hediger, S., and Paëpe, G. D. (2013). Matrix-free dynamic nuclear polarization enables solid-state NMR <sup>13</sup>c–<sup>13</sup>c correlation spectroscopy of proteins at natural isotopic abundance. *Chemical Communications*, 49(82):9479.



- Takahashi, H., Lee, D., Dubois, L., Bardet, M., Hediger, S., and De Paëpe, G. (2012). Rapid natural-abundance  $2d13c$ - $13c$  correlation spectroscopy using dynamic nuclear polarization enhanced solid-state NMR and matrix-free sample preparation. *Angewandte Chemie International Edition*, 51(47):11766–11769.
- Thankamony, A. S. L., Lafon, O., Lu, X., Aussenac, F., Rosay, M., Trébosc, J., Vezin, H., and Amoureux, J. P. (2012). Solvent-free high-field dynamic nuclear polarization of mesoporous silica functionalized with tempo. *Applied Magnetic Resonance*, 43:237–250.
- Thankamony, A. S. L., Wittmann, J. J., Kaushik, M., and Corzilius, B. (2017). Dynamic nuclear polarization for sensitivity enhancement in modern solid-state NMR. *Progress in Nuclear Magnetic Resonance Spectroscopy*.
- Thurber, K. R., Potapov, A., Yau, W.-M., and Tycko, R. (2013). Solid state nuclear magnetic resonance with magic-angle spinning and dynamic nuclear polarization below 25k. *Journal of Magnetic Resonance*, 226:100–106.
- Thurber, K. R. and Tycko, R. (2014). Perturbation of nuclear spin polarizations in solid state NMR of nitroxide-doped samples by magic-angle spinning without microwaves. *The Journal of Chemical Physics*, 140(18):184201.
- Walker, T. G. (2011). Fundamentals of spin-exchange optical pumping. *Journal of Physics: Conference Series*, 294:012001.
- Wang, S., Karbstein, K., Peracchi, A., Beigelman, L., and Herschlag, D. (1999). Identification of the hammerhead ribozyme metal ion binding site responsible for rescue of the deleterious effect of a cleavage site phosphorothioate. *Biochemistry*, 38(43):14363–14378. PMID: 10572011.
- Watts, A. (2005). Solid-state NMR in drug design and discovery for membrane-embedded targets. *Nature Reviews Drug Discovery*, 4(7):555–568.
- Weil, J. A. and Bolton, J. R. (2007). *Electron paramagnetic resonance: elementary theory and practical applications*. John Wiley & Sons.
- Wenkebach, W. T. (2008). The solid effect. *Applied Magnetic Resonance*, 34(3-4):227.
- Wenk, P., Kaushik, M., Richter, D., Vogel, M., Suess, B., and Corzilius, B. (2015). Dynamic nuclear polarization of nucleic acid with endogenously bound manganese. *Journal of Biomolecular NMR*, 63(1):97–109.
- Wilder, J. W., Venema, L. C., Rinzler, A. G., Smalley, R. E., and Dekker, C. (1998). Electronic structure of atomically resolved carbon nanotubes. *Nature*, 391(6662):59–62.

## Bibliography

- Wind, R., Duijvestijn, M., Van Der Lugt, C., Manenschijn, A., and Vriend, J. (1985). Applications of dynamic nuclear polarization in  $^{13}\text{C}$  nmr in solids. *Progress in Nuclear Magnetic Resonance Spectroscopy*, 17:33–67.
- Wylie, B. J., Dzikovski, B. G., Pawsey, S., Caporini, M., Rosay, M., Freed, J. H., and McDermott, A. E. (2015). Dynamic nuclear polarization of membrane proteins: covalently bound spin-labels at protein–protein interfaces. *Journal of Biomolecular NMR*, 61(3-4):361–367.
- Yang, Y., Li, Q.-F., Cao, C., Huang, F., and Su, X.-C. (2013). Site-specific labeling of proteins with a chemically stable, high-affinity tag for protein study. *Chemistry – A European Journal*, 19(3):1097–1103.
- Yen, L., Svendsen, J., Lee, J.-S., Gray, J. T., Magnier, M., Baba, T., D'Amato, R. J., and Mulligan, R. C. (2004). Exogenous control of mammalian gene expression through modulation of RNA self-cleavage. *Nature*, 431(7007):471–476.



## **Appendix publications**

# Dynamic nuclear polarization of nucleic acid with endogenously bound manganese

Patricia Wenk<sup>1,3</sup> · Monu Kaushik<sup>1</sup> · Diane Richter<sup>1</sup> ·  
Marc Vogel<sup>2</sup> · Beatrix Suess<sup>2</sup> · Björn Corzilius<sup>1</sup>

Received: 12 May 2015 / Accepted: 22 July 2015 / Published online: 29 July 2015  
© Springer Science+Business Media Dordrecht 2015

**Abstract** We report the direct dynamic nuclear polarization (DNP) of  $^{13}\text{C}$  nuclei of a uniformly [ $^{13}\text{C}$ ,  $^{15}\text{N}$ ]-labeled, paramagnetic full-length hammerhead ribozyme (HHRz) complex with  $\text{Mn}^{2+}$  where the enhanced polarization is fully provided by the endogenously bound metal ion and no exogenous polarizing agent is added. A  $^{13}\text{C}$  enhancement factor of  $\varepsilon = 8$  was observed by intra-complex DNP at 9.4 T. In contrast, “conventional” indirect and direct DNP experiments were performed using AMUPol as polarizing agent where we obtained a  $^1\text{H}$  enhancement factor of  $\varepsilon \approx 250$ . Comparison with the diamagnetic ( $\text{Mg}^{2+}$ ) HHRz complex shows that the presence of  $\text{Mn}^{2+}$  only marginally influences the (DNP-enhanced) NMR properties of the RNA. Furthermore two-dimensional correlation spectra ( $^{15}\text{N}$ – $^{13}\text{C}$  and  $^{13}\text{C}$ – $^{13}\text{C}$ ) reveal structural inhomogeneity in the frozen, amorphous state indicating the coexistence of several conformational states. These demonstrations of intra-complex DNP using an endogenous metal ion as well as DNP-enhanced MAS NMR of

RNA in general yield important information for the development of new methods in structural biology.

**Keywords** Dynamic nuclear polarization (DNP) · Solid-state NMR · EPR · RNA · Transition metal · Polarizing agent

## Introduction

Solid-state magic-angle spinning (MAS) NMR applications to nucleic acid including ribonucleic acid (RNA) are scarce (Abramov and Goldbourt 2014; Cherepanov et al. 2010; Huang et al. 2012; Marchanka et al. 2015), especially when compared to the abundance of solution-state NMR techniques in RNA structural biology (Bothe et al. 2011; Fürtig et al. 2003; Rinnenthal et al. 2011; Sripakdeevong et al. 2014). On the other hand, MAS NMR is invaluable for structural investigations of biomolecules which has been demonstrated in wide-spread applications to protein structural biology (Bayro et al. 2010; Castellani et al. 2002; Wasmer et al. 2008). MAS NMR has advantages over solution NMR when large molecules or molecular complexes are studied since their rotational tumbling is too slow for standard solution NMR. Additionally, the quantitative determination of dipole (through-space) couplings can yield precise internuclear distances. However, short decoherence times as well as incomplete dynamic averaging of local fields often result in intrinsically larger line widths and lower sensitivity.

Because RNA contains only four chemically similar nucleotides—each comprised of a ribose moiety and either a purine (adenine, guanine) or pyrimidine (cytosine, uracil) nucleobase—there is a large potential for spectral overlap of resonances arising from equal or similar

**Electronic supplementary material** The online version of this article (doi:10.1007/s10858-015-9972-1) contains supplementary material, which is available to authorized users.

✉ Björn Corzilius  
corzilius@em.uni-frankfurt.de

<sup>1</sup> Institute of Physical und Theoretical Chemistry, Institute of Biophysical Chemistry und Center for Biomolecular Magnetic Resonance (BMRZ), Goethe University, Max-von-Laue-Str. 7-9, 60438 Frankfurt am Main, Germany

<sup>2</sup> Department of Biology, Technical University Darmstadt, Schnittpahnstraße 10, 64287 Darmstadt, Germany

<sup>3</sup> Present Address: Werner Siemens Imaging Center and Department of Preclinical Imaging and Radiopharmacy, University of Tübingen, Röntgenweg 13, 72076 Tübingen, Germany

nucleobases. Furthermore, resonance assignment based on scalar couplings is complicated because the connecting, generic ribofuranose phosphodiester groups put unique nucleobases at distances of >10 chemical bonds. Here, solid-state NMR has the advantage of generally being able to utilize dipolar (through-space) instead of scalar (through-bond) couplings which allows for direct determination of contacts between nuclei of neighboring nucleobases in the same RNA strand (Marchanka et al. 2015).

Dynamic nuclear polarization (DNP) has been introduced to overcome the MAS NMR sensitivity issue by increasing the intensity of signals by several orders of magnitude (Becerra et al. 1993; Hall et al. 1997; Overhauser 1953). During irradiation with microwaves (mw) of appropriate frequency the large electron spin polarization of a paramagnetic polarizing agent is transferred to surrounding nuclear spins in a frozen solution at cryogenic temperatures of ~100 K. The polarization increase is quantified by the enhancement factor,  $\varepsilon$ , which is the ratio of the NMR intensity under mw irradiation (mw on),  $I_{\text{on}}$ , with that under thermal equilibrium conditions (mw off),  $I_{\text{off}}$ :

$$\varepsilon = \frac{I_{\text{on}}}{I_{\text{off}}} \quad (1)$$

The theoretical maximum is given by the ratio of the electron and nuclear gyromagnetic ratios,  $\gamma_S$  and  $\gamma_I$ , respectively, and reaches 660 for  $^1\text{H}$  and 2620 for  $^{13}\text{C}$ . DNP can be performed indirectly by hyperpolarizing  $^1\text{H}$  and successively transferring the enhanced nuclear polarization to the nuclear species of interest, or by directly hyperpolarizing the nuclei to be detected (Maly et al. 2010). The former method leads to a uniform enhancement of all proton spins within a few seconds of polarization build-up due to efficient  $^1\text{H}$ – $^1\text{H}$  spin diffusion; the latter is often limited by slow diffusion between heteronuclei, especially when nuclei with small abundance are to be polarized (Maly et al. 2010). Nevertheless, slow spin-diffusion can potentially be utilized in order to control the spatial distribution of enhanced polarization.

Most typically, small paramagnetic molecules being dissolved in the cryoprotecting matrix are used as polarizing agents (Hu 2011). Bis-nitroxide biradicals provide for highly efficient cross effect (CE) DNP by evoking a three-spin mechanism within the anisotropic electron paramagnetic resonance (EPR) spectrum under MAS (Hu et al. 2004; Kessenikh et al. 1963). This makes CE the mechanism-of-choice for uniform, indirect DNP (Ni et al. 2013). For intramolecular or intra-complex DNP with endogenous polarizing agents CE is often unfeasible due to the reliance on strong inter-electronic couplings (Hovav et al. 2012; Hu et al. 2011). Therefore, a simpler mechanism—which is

easier to analyze quantitatively—is provided by the solid effect (Abragam and Proctor 1958; Corzilius et al. 2012; Hovav et al. 2010; Jeffries 1957, 1960; Smith et al. 2012; Wenckebach 2008). In short, the solid effect (SE) can be selectively evoked for any nucleus by selective irradiation of the electron–nuclear zero or double quantum transition with a microwave frequency of

$$\omega_{\text{mw}} = \omega_{0S} \pm \omega_{0I}, \quad (2)$$

where  $\omega_{0S}$  and  $\omega_{0I}$  are the electron and nuclear Larmor frequencies, respectively. This leads to the requirement of paramagnetic species with extremely narrow lines, especially for direct SE of nuclei with small gyromagnetic ratio such as  $^{13}\text{C}$  or  $^{15}\text{N}$ .

We have shown earlier that—for the SE—a quantitative analysis of DNP efficiency can be performed by careful measurement of the DNP enhancement factor, the build-up time constant of enhanced nuclear polarization, as well as the nuclear longitudinal relaxation time constant without DNP (Corzilius et al. 2012). By knowledge of DNP enhancement and spin relaxation properties direct information about distance may be obtained after calibration with a model system of known electron–nuclear separation. Therefore our study shall serve as an early proof-of-concept for the feasibility of transferring electron spin polarization from an endogenous metal ion to nuclei within the same biomolecule, since such a transfer has never been demonstrated before.

DNP with endogenous radicals in proteins (Maly et al. 2012) as well as nitroxides covalently attached to lipids (Fernández-de-Alba et al. 2015; Smith et al. 2015) or proteins (Wylie et al. 2015) has already been demonstrated to yield moderate  $^1\text{H}$  enhancement factors of ~10. Nevertheless, fast  $^1\text{H}$ – $^1\text{H}$  spin diffusion limits the potential to directly extract structural information by these indirect DNP approaches. We have shown earlier that paramagnetic metal ions like  $\text{Gd}^{3+}$  or  $\text{Mn}^{2+}$  can be utilized as polarizing agents which makes them ideal candidates for intra-complex DNP of biomolecules (Corzilius et al. 2011).  $\text{Mn}^{2+}$  is highly abundant in biological systems or can often readily substitute diamagnetic  $\text{Mg}^{2+}$ . The central EPR transition ( $m_S = -\frac{1}{2} \leftrightarrow +\frac{1}{2}$ ) of the high-spin ( $S = \frac{5}{2}$ ) system often features narrow lines at high field. This allows for efficient polarization of nuclei with small gyromagnetic ratio such as  $^{13}\text{C}$  or  $^{15}\text{N}$  using SE. Although in the case of  $\text{Mn}^{2+}$  the electron spin is strongly hyperfine coupled to the 100 % abundant  $I = \frac{5}{2}$   $^{55}\text{Mn}$  nucleus significant  $^{13}\text{C}$  enhancement can be achieved as will be shown below.

The biomolecule we utilized as a model system belongs to the well-studied group of hammerhead ribozymes, of which the first construct has been discovered in the late 1980s as a self-cleaving structural element of virusoids and viroids (Forster and Symons 1987; Hutchins et al. 1986;

Prody et al. 1986). It was found early that the self-cleavage reaction strongly depends on the presence of a divalent metal ion as co-factor (Dahm and Uhlenbeck 1991). The structure of a ‘minimal’ HHRz construct has been solved early under several conditions (Pley et al. 1994; Scott et al. 1995); however, it has been shown later that tertiary contacts between stem loops—missing in the minimal structure—play an important role in ribozyme function (De la Peña et al. 2003; Khvorova et al. 2003). The ‘extended’ or ‘full-length’ construct includes those conserved loop regions and the structure was solved by XRD (Martick and Scott 2006). All hammerhead ribozyme (HHRz) varieties share a highly conserved catalytic core region which contains several binding sites for divalent ions such as  $Mg^{2+}$  or  $Mn^{2+}$  (Scott et al. 1995). Binding of a divalent ion to one of these sites triggers a conformational change and allows for the self-cleavage reaction to occur (Bassi et al. 1996; Murray et al. 1998; Scott et al. 1996). Additional less-specific metal binding sites show a similar affinity towards monovalent ions and are completely saturated under large  $Na^+$  concentrations ( $\geq 1$  M) (Horton et al. 1998; Schiemann et al. 2003). The core region is flanked by three stems which give HHRz a robust fold; nevertheless the core region features large internal dynamics. The combination of its moderate molecular size and internal dynamics make the full-length HHRz difficult to access using solution NMR methods—as can be seen when comparing the abundance of NMR studies on the minimal structure (Fürsting et al. 2008; Hammann et al. 2001; Osborne et al. 2009) with the absence of such studies on the full-length variant. Thus it serves as an ideal system for demonstration of DNP-enhanced MAS NMR.

In this study we investigated DNP-enhanced NMR spectroscopy on an inactive 18.0 kDa, 59-mer cis-acting full-length HHRz; the sequence and secondary structure prediction are shown in Fig. 1a and the proposed tertiary fold with loop–loop interactions in subplot b. To inactivate the HHRz the adenosine at position 53 was mutated to a guanosine (Yen et al. 2004). In-vivo functionality of the unmutated construct and effective inactivation due to this point-mutation has been shown in previous studies (Beilstein et al. 2015; Wittmann and Suess 2011). The position of the specific binding site for  $Mg^{2+}$  or  $Mn^{2+}$  is still heavily debated. In the minimal structure, selective binding of the divalent ion was found in XRD structures predominantly between the phosphate of an adenosine and neighboring guanosine (A36 and G37 in Fig. 1a) within the catalytic core on the opposite site of the cleavage position (between C7 and C8 in Fig. 1a) and the importance of this binding site was confirmed by a functional analysis upon base depletion; catalysis then requires the adaption of a transient conformational state with the divalent ion bridging to the scissile phosphate (Scott et al. 1995; Wang et al. 1999). The nature of

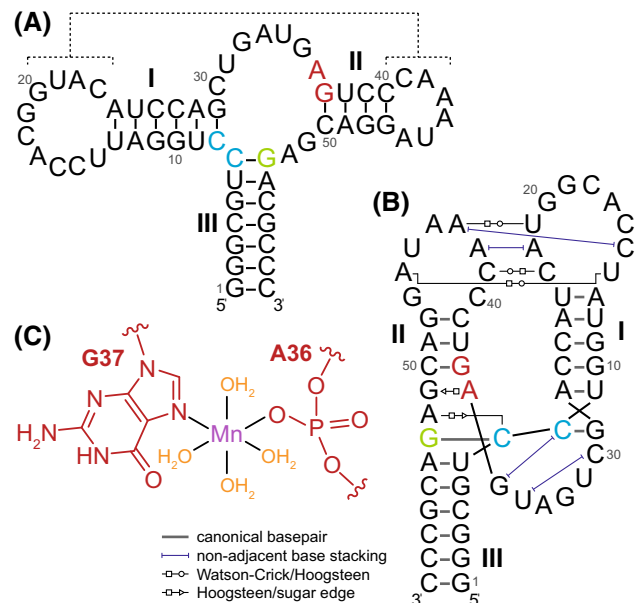


**Fig. 1** **a** Predicted secondary structure of the investigated full-length HHRz (inactivated). Canonical base pairing interactions are shown with *black lines* within stems. The A-to-G base mutation at position 53 (marked in *green*) is preventing self-cleavage between two cytidines marked in *blue*. The proposed selective binding site for divalent ions is marked in *red*. Tertiary loop–loop interactions are indicated by *dashed lines*. **b** Depiction of the same structure demonstrating possible tertiary interactions between stem-loops II and III as observed in the active construct (Martick and Scott 2006). *Black lines* show sequence continuity. **c** Proposed complex geometry of selective  $Mn^{2+}$  binding site (Morrissey et al. 2000; Wang et al. 1999)

the binding site has also been investigated with EPR spectroscopy (Morrissey et al. 1999, 2000). In the case of the extended or full-length HHRz the catalytically active structure is expected to allow for stable closing of the AG active binding site and the scissile phosphate in the cleavage site via a bridging divalent ion (Ward and DeRose 2012). However, in the XRD structure selective binding to only the AG active site has been observed, especially in the case of  $Mn^{2+}$  (Martick et al. 2008).

## Materials and methods

### Nucleic acid preparation

The inactivated full-length hammerhead ribozyme (HHRz) shown in Fig. 1 was transcribed in vitro using the *Sma*I linearized plasmid pHHI as template (the full plasmid sequence is available upon request). The plasmid codes for the T7 promoter followed by the HHRz. The in vitro transcription was carried out in a volume of 10 mL over night at 37 °C with a final concentration of 20 mM magnesium acetate, 0.2 M Tris–HCl (pH 8.0), 20 mM dithiothreitol

(DTT), 2 mM spermidine, 0.2 mg/mL plasmid, 7.5  $\mu\text{g/mL}$  T7 RNA polymerase (purified in the lab) and 4 mM of each nucleoside triphosphate (NTP); for uniformly [ $^{13}\text{C}$ ,  $^{15}\text{N}$ ] isotope labeled HHRz 3 mM of each uniformly  $^{13}\text{C}$ ,  $^{15}\text{N}$ -labeled NTP (Silantes) was used. The isotope labeled NTPs were purified by ethanol precipitation and resuspended in purified water prior to transcription. After the transcription the precipitated pyrophosphate was pelleted by centrifugation and EDTA was added to the supernatant to a final concentration of 10 % (v/v). After ethanol precipitation we performed a denaturing polyacrylamide gel electrophoresis (PAGE, 8 % PAA, 8 M urea). The RNA was detected by ultraviolet shadowing, cut out of the gel and eluted from the gel in 0.3 M sodium acetate (pH 6.5) at 4 °C overnight. Afterwards we filtered the supernatant to remove remaining gel slices using a 0.45  $\mu\text{m}$  filter (Sarstedt, Nürnberg, Germany). The RNA was again ethanol precipitated, dissolved in purified water and the concentration was determined via UV/Vis spectroscopy by a ND-1000 spectrophotometer (Thermo Fischer Scientific, Wilmington, DE). A native PAGE assay was used to confirm purity of the RNA (Fig. S1). The HHRz was then lyophilized for storage and further handling.

### EPR spectroscopy

For the determination of the Mn–HHRz dissociation constant ( $K_D$ ) solutions of 62.5  $\mu\text{M}$  HHRz with varying MnCl<sub>2</sub> content between 1  $\mu\text{M}$  and 0.2 mM were prepared in triethanolamine (TEA) buffer (40 mM, pH 7.5) with 0.2 M NaCl. In comparison, an additional set of samples was prepared without addition of HHRz in order to demonstrate applicability and linearity of the method. Continuous-wave (cw) EPR was performed using an X-band Bruker EleXsys E500 spectrometer with attached ER 4102ST resonator employing a TE<sub>102</sub> rectangular cavity. The sample ( $\sim 10$   $\mu\text{L}$ ) was contained inside a clear fused quartz (CFQ) capillary with 1.1 mm inner diameter (i.d.) in order to minimize penetration of the sample volume into the electric field region and reduce dielectric losses. Care was taken that each sample tube was positioned equally inside the resonator. Spectra were taken under 10 dB of microwave attenuation ( $\sim 20$  mW power). 100 kHz magnetic field modulation with 1.5 mT amplitude was applied. The field was swept with 82 ms conversion time over 1024 points and signal was integrated with a 41 ms time constant. Each spectrum was accumulated over 20 scans.

The confirmation of Mn<sup>2+</sup> binding to HHRz in DNP samples was performed directly on the samples used for DNP enhanced NMR spectroscopy as described below. The same instrumentation was used as for  $K_D$  determination. Spectra were taken under 20 dB of microwave attenuation ( $\sim 2$  mW power). 100 kHz magnetic field modulation with

0.4 mT amplitude was applied. The field was swept with 164 ms of conversion time over 1024 points and signal was integrated with a 164 ms time constant. Each spectrum was accumulated over 8 scans.

180 GHz EPR spectroscopy was performed using a custom-built spectrometer described elsewhere utilizing a cylindrical TE<sub>011</sub> cavity resonator (Rohrer et al. 2001). The samples were prepared by dissolving an equal amount of HHRz and MnCl<sub>2</sub> in TEA buffer (40 mM triethanolamine, 0.2 M NaCl) and subsequent addition of glycerol, so that a glycerol/water (60/40 vol.%) cryoprotecting mixture with 62.5  $\mu\text{M}$  final Mn–HHRz concentration was achieved. The sample was contained within a 0.4 mm i.d. quartz capillary. Experiments were performed at a temperature of 80 K. Pulse lengths (30 ns for 90° and 45 ns for 180°) and separation (200 ns) of the Hahn echo sequence were optimized for maximum signal intensity and the field-swept spectrum was detected by integrating over the full echo width and averaging over 400 shots with 0.7 ms repetition time in a single scan.

### DNP sample preparation

0.9 mg HHRz in lyophilized form was dissolved in 0.2 mL buffer solution containing 40 mM TEA and 0.2 M NaCl. The solution was split in three equal volume samples and lyophilized again. To each sample 40  $\mu\text{L}$  of cryoprotecting solution consisting of 60 %  $^{12}\text{C}_3, \text{d}_8$ -glycerol (99.95 %  $^{12}\text{C}$ , 98 % D; Euriso-Top), 30 % D<sub>2</sub>O (99.9 % D; Sigma-Aldrich), and 10 % H<sub>2</sub>O was added, together with an equimolar amount of MnCl<sub>2</sub> or MgCl<sub>2</sub> with respect to RNA. Final concentrations were 0.4 mM of RNA and MnCl<sub>2</sub> or MgCl<sub>2</sub>, 0.33 M NaCl. For CE DNP 5 mM AMUPol (SATT Sud-Est, Marseille, France) was added. For comparison of build-up dynamics (see Table 1) and as cw EPR reference for unbound Mn<sup>2+</sup> (see Figs. 6 and S3) 0.4 mM MnCl<sub>2</sub> and 225 mM  $^{13}\text{C}$ ,  $^{15}\text{N}_2$ -urea (99 %  $^{13}\text{C}$ , 98 %  $^{15}\text{N}$ ; CortecNet, Voisins-Le-Bretonneux, France) were dissolved in the  $^{12}\text{C}_3, \text{d}_8$ -glycerol/D<sub>2</sub>O/H<sub>2</sub>O mixture as described above.

### DNP-enhanced MAS NMR spectroscopy

For experiments using bis-nitroxide as polarizing agent we utilized a commercially available Bruker AVANCE II DNP spectrometer operating at 400.2 MHz  $^1\text{H}$  frequency with a Bruker Ultrashield 9.4 T widebore (89 mm) magnet. 263.4 GHz microwaves were produced by a Bruker gyrotron with 60 mA of beam current at which we found an optimum  $^1\text{H}$  enhancement for AMUPol. Experiments were performed at 112 K (mw on) or 104 K (mw off), read out via a thermocouple inside the MAS stator.

For direct DNP using Mn<sup>2+</sup> as polarizing agent we utilized a commercially available Bruker AVANCE III DNP



**Table 1**  $^{13}\text{C}$  enhancement factors and polarization build-up time constants

Sample	$T$ (K) <sup>a</sup>	$\varepsilon$	$T_{B,f}^{(^{13}\text{C})}$ (s) <sup>b</sup>	$T_{B,s}^{(^{13}\text{C})}$ (s) <sup>c</sup>	$\phi^d$
Mg–HHRz + AMUPol <sup>e</sup>	~112	420 ± 160	118	2840	0.38
Mn–HHRz + AMUPol <sup>e</sup>	~112	160 ± 40	96	1954	0.53
Mn–HHRz <sup>f</sup>	~114	8 ± 1	130	3043	1.13
$^{13}\text{C}$ , $^{15}\text{N}_2$ -urea + $\text{MnCl}_2^f$	~114	>4	215	5074	0.085

<sup>a</sup> Measured inside MAS stator. <sup>b</sup>Fast (short) component. <sup>c</sup>Slow (long) component. <sup>d</sup>Proportionality factor according to Eq. (3). <sup>e</sup>Measured at magnetic field optimized for cross effect DNP with nitroxides (9.40 T). <sup>f</sup>Measured at magnetic field optimized for  $^{13}\text{C}$  solid effect DNP with  $\text{Mn}^{2+}$  (9.434 T)

spectrometer operating at 401.7 MHz  $^1\text{H}$  frequency. The Bruker Ascent DNP magnet was centered at 9.40 T and contained a superconducting sweep coil with a range of  $\pm 70$  mT. The sweep coil was energized so that a field of 9.434 mT was reached. After the optimum DNP enhancement was achieved the sweep unit was put into persistent mode. The NMR frequencies were roughly re-calibrated using a  $^1\text{H}$  Bloch decay and further referenced on the RNA spectrum. 263.4 GHz microwaves were produced by a Bruker gyrotron operating at the maximum beam current of 115 mA. Experiments were performed at 114 K (mw on) or 105 K (mw off), read out via a thermocouple inside the MAS stator.

For all experiments radio frequency (rf) pulse powers were set to 100, 50, and 40 kHz for  $^1\text{H}$ ,  $^{13}\text{C}$ , and  $^{15}\text{N}$ , respectively;  $^1\text{H}$  power was matched to  $^{13}\text{C}$  or  $^{15}\text{N}$  during Hartmann-Hahn CP. SPINAL64 at 100 kHz was used for broadband decoupling of  $^1\text{H}$ . All one-dimensional spectra were measured after applying a pre-saturation pulse train and subsequent polarization delay; for the acquisition of build-up curves this delay was varied. The sample was contained within a 3.2 mm sapphire rotor (Bruker) and sealed with silicone soft plug and  $\text{ZrO}_2$  drive cap. Magic-angle spinning with a spinning frequency of 10 kHz was used for all experiments except proton-driven spin diffusion (PDS) correlation spectra where 10.8 kHz was utilized.

## Results and discussion

### EPR spectroscopy of the Mn–HHRz complex

The 180 GHz EPR spectrum of a frozen solution of the  $\text{Mn}^{2+}$  complex of HHRz (Mn–HHRz) is depicted in Fig. 2 and shows only minor differences to the hexaquo complex (not shown). This is in agreement with previous comparisons at X- and Q-band frequencies (Morrissey et al. 2000). The occurrence of a significantly larger electric field gradient in the HHRz complex and thus resulting zero-field splitting (electron quadrupole interaction) in combination with slow tumbling of the biopolymer leads to a very broad EPR spectrum in liquid solution. This allows for

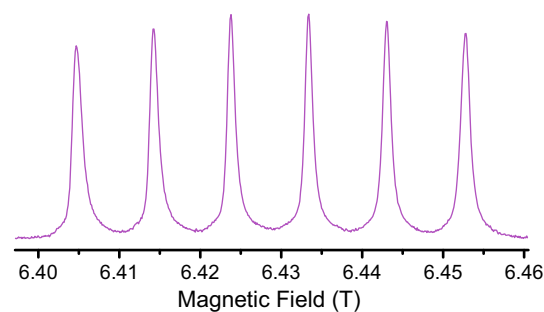


**Fig. 2** 180 GHz field-swept, electron spin echo detected EPR spectrum of Mn–HHRz in 60/40 (v/v) glycerol/water at 80 K

unambiguous and quantitative determination of “free” (i.e. not bound to HHRz)  $\text{Mn}^{2+}$  by titration. Using continuous-wave (cw) EPR spectroscopy at X-band frequency (9.4 GHz) we have confirmed binding of a single  $\text{Mn}^{2+}$  with a dissociation constant in agreement with the previously reported value of  $K_D \approx 4 \mu\text{M}$  (Horton et al. 1998; Schiemann et al. 2003) even at the relatively low NaCl concentration of 200 mM (Fig. S2). Because samples used for DNP-enhanced NMR spectroscopy are prepared with a large concentration of cryoprotecting glycerol we also verified quantitative binding of  $\text{Mn}^{2+}$  to HHRz in the same samples after recording of NMR spectra. We were unable to detect any unbound  $\text{Mn}^{2+}$  (see Fig. S3) and therefore estimate the ratio of “free”  $\text{Mn}^{2+}$  to overall added  $\text{Mn}^{2+}$  to be below 10 % which is in line with a dissociation constant in the low  $\mu\text{M}$  range.

By using these methods the error in estimated  $K_D$  is relatively large, and practically no conclusion can be drawn on the position and nature of the binding site. Nevertheless, these experiments confirm that the majority of HHRz is binding a single  $\text{Mn}^{2+}$ . This is the most important factor for the further analysis of direct, intra-complex DNP of  $^{13}\text{C}$  as well as the investigation of paramagnetic interactions by  $\text{Mn}^{2+}$  on indirect  $^1\text{H}$  DNP.

### Direct DNP of Mn–HHRz using endogenous $\text{Mn}^{2+}$

Since typically commercial DNP spectrometers are optimized for  $^1\text{H}$  cross effect DNP using bis-nitroxide

polarizing agents, it was required to shift the magnetic field to the  $^{13}\text{C}$  solid effect matching condition of  $\text{Mn}^{2+}$  for the first demonstration employing the endogenous, paramagnetic metal center as polarizing agent for a biomolecule. The matching condition was estimated based on a simulated EPR spectrum using Easyspin (Stoll and Schweiger 2006) and spectral superposition of the electron–nuclear double and zero quantum transitions (Shimon et al. 2012). The procedure is described in more detail in the SI where we also show the simulation (Fig. S3). For exact matching of the external magnetic field we utilized a special DNP-dedicated NMR magnet (Bruker Ascent DNP) featuring a superconducting sweep coil. After sweeping the magnet to the estimated position the field was optimized in order to maximize the intensity of the detected  $^{13}\text{C}$  spectrum evoked by Bloch-decay under mw irradiation. In Fig. 3 the obtained  $^{13}\text{C}$  spectrum is shown with and without mw irradiation. An enhancement factor of  $\varepsilon = 8$  is induced by intra-complex  $^{13}\text{C}$  SE DNP by  $\text{Mn}^{2+}$ .

### DNP of HHRz using AMUPol

In comparison, we also show spectra which have been obtained with a “conventional” DNP approach, that is by adding AMUPol as bis-nitroxide biradical polarizing agent and employing  $^1\text{H}$  (indirect) DNP prior to cross polarization to  $^{13}\text{C}$  or  $^{15}\text{N}$  (CPMAS). A rather small biradical

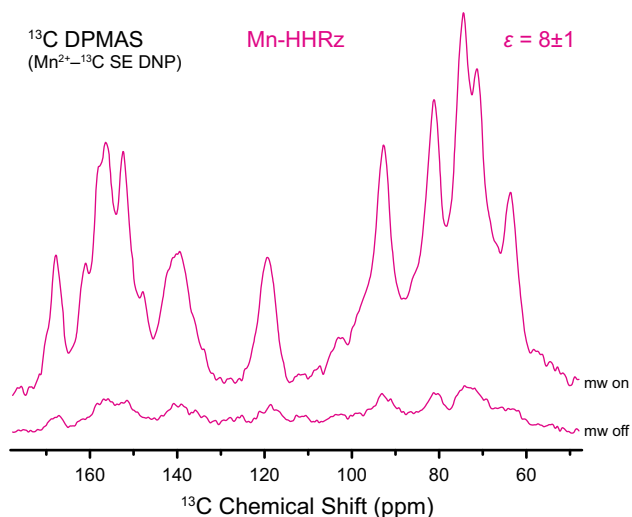


**Fig. 3**  $^{13}\text{C}$  DPMAS of Mn–HHRz, read-out via Bloch decay obtained by employing  $\text{Mn}^{2+}$  as only polarizing agent for SE at the matching field at 9.43 T; 0.75 ppm exponential line broadening was applied before Fourier transformation. On-spectra were obtained by co-adding 16 scans obtained with short (160 s) and 4 scans obtained with long (3276 s) polarization time, respectively. For the off-spectra we co-added 64 and 16 scans, respectively. Spectra are normalized with respect to number of scans. A complete compilation of individual direct-DNP enhanced spectra and their respective acquisition parameters is given in the SI (Fig. S5)

concentration of 5 mM was chosen in order to minimize potential signal quenching and/or broadening due to the nitroxide spins and to be able to observe effects induced by paramagnetic  $\text{Mn}^{2+}$ . The  $^1\text{H}$  DNP enhancement is unexpectedly large with  $\varepsilon = 240 \pm 10$  (Fig. 4) which significantly surpasses what has been observed on protein solutions—even with larger biradical concentrations—under otherwise similar conditions. Even though enhancement factors as large as 235 have been observed with AMUPol in the case of a simple proline solution (Sauvée et al. 2013),  $\varepsilon$  is usually reduced within a protein by a factor of 2–3; this loss of polarization can be recovered by complete deuteration of non-exchangeable hydrogens (Akbej et al. 2010). Also, in highly biologically relevant mixtures such as cell envelopes or even whole cells the enhancement factor drops significantly with increasing complexity of environment (Renault et al. 2012). Therefore, we attribute the large enhancement in RNA to the absence of side-chain dynamics and most profoundly methyl groups which provide for a dominant mechanism of  $^1\text{H}$  longitudinal relaxation by reorientation under similar conditions in proteins or lipids (Glowinkowski et al. 1997; Gutsche et al. 2004; Nozirov et al. 2006).

The large  $^1\text{H}$  enhancement obtained with AMUPol seems to overshadow the relatively small enhancement factor of 8 induced by  $\text{Mn}^{2+}$  at first sight. Nonetheless, the demonstration of intra-complex DNP with an endogenously bound metal ion is an important step towards alternative approaches using internal polarizing agents. This becomes even clearer when this factor is compared to similar approaches where nitroxide labels covalently bound to lipids or proteins have been employed (Smith et al. 2015; Wylie et al. 2015). In these cases the observed enhancement factors were of the same magnitude.

We also prepared a diamagnetic RNA complex using  $\text{Mg}^{2+}$  as diamagnetic reference in order to assess the effects of paramagnetic  $\text{Mn}^{2+}$  on the NMR spectrum. The  $^1\text{H}$ -DNP-enhanced  $^{13}\text{C}$  and  $^{15}\text{N}$  CPMAS spectra of this Mg–HHRz is shown in Fig. 4 in direct comparison with that of Mn–HHRz. Moderate reduction in signal amplitude is observed in the presence of  $\text{Mn}^{2+}$  for both  $^{13}\text{C}$  and  $^{15}\text{N}$  CPMAS. Nuclear resonance quenching depended mainly on the chemical environment: for  $^{13}\text{C}$  directly bonded to  $^1\text{H}$  we observed a  $\sim 12$ – $14$  % reduction in peak height, while carbons not carrying hydrogen experienced a  $\sim 20$ – $30$  % signal decrease; in the  $^{15}\text{N}$  case the values converge to  $\sim 16$  and  $19$ – $22$  % presumably due to longer required CP contact times. We tentatively attribute this signal reduction without apparent broadening to a  $T_{1\rho}$ -dominated paramagnetic relaxation mechanism during Hartmann-Hahn contact. Accelerated coherence decay and signal reduction by paramagnets in DNP samples has been observed in earlier studies (Corzilius et al. 2014; Lange et al. 2012;

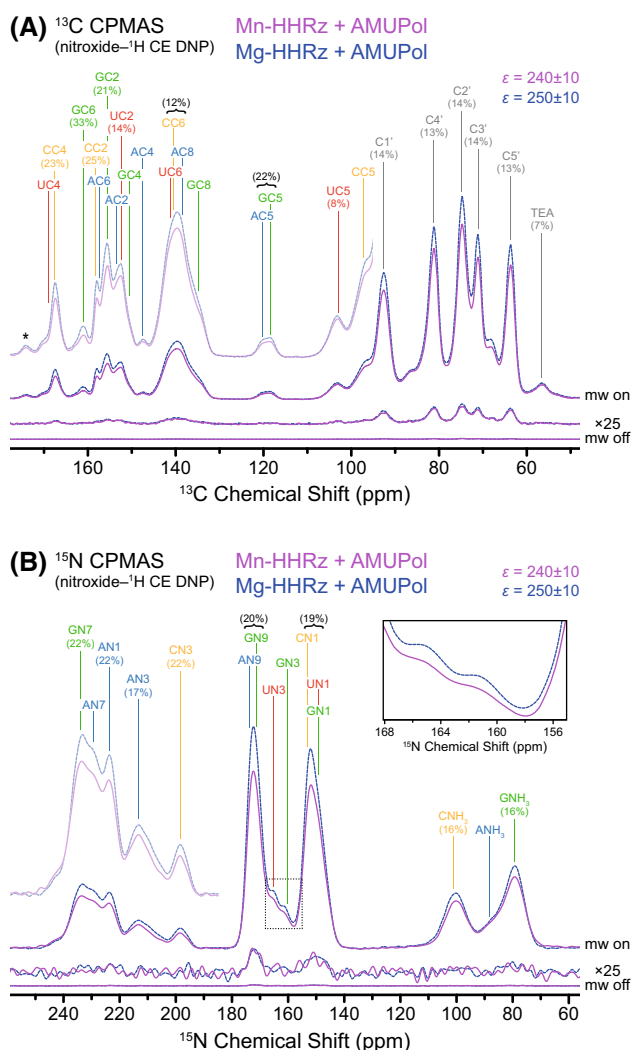


**Fig. 4** DNP-enhanced  $^{13}\text{C}$  (a) and  $^{15}\text{N}$  (b) CPMAS spectra of Mn-HHRz (solid magenta line) and Mg-HHRz (blue dashed line) recorded with 16 scans and 64 scans, respectively; non-enhanced spectra (lower trace, ‘mw off’) are 512 scans in both cases. On- and off-spectra are normalized with respect to number of scans. Recycle delays were 9 and 10 s for the Mn- and the Mg-HHRz, respectively. The off-signal was also multiplied with a factor 25 (middle trace) for better visibility. Resonances have been assigned to nucleotide atoms based on two-dimensional spectra (see below); a MAS sideband from C5’ is marked with an asterisk and a  $^{13}\text{C}$  signal from TEA buffer in natural abundance is occurring around 57 ppm. Values in parentheses represent relative signal loss due to presence of  $\text{Mn}^{2+}$ ; absolute intensities of spectra have been normalized by sample weight to correct for slightly different rotor filling. The lighter spectra are vertical magnifications with a factor 2.5 for better visibility of weaker signals. The inset shows the area marked by the dotted box

Rossini et al. 2012), but no difference has been observed between different nuclear environments in a biomolecule and a clear identification of the major mechanism to  $T_{1\rho}$  relaxation has not been attempted. In order to investigate this effect further, CP build-up and/or  $T_{1\rho}$  relaxation

experiments on these HHRz samples are clearly of great interest and are planned in our lab.

The TEA signal at 57 ppm—which arises from homogeneously dispersed buffer molecules and therefore is expected to show the smallest effect due to  $\text{Mn}^{2+}$ —experienced only  $\sim 7\%$  signal reduction. Thus, the direct binding of  $\text{Mn}^{2+}$  to HHRz is reflected by a selective and significantly stronger quenching of RNA resonances.

### Analysis of polarization build-up dynamics

The  $^1\text{H}$  polarization build-up constant was determined by saturation recovery. The data could be fitted perfectly with a single exponential function and yielded  $T_B^{\text{H}} = 7.1$  s. In the diamagnetic Mg-HHRz the time constant was slightly increased to 8.0 s (build-up curves are shown in the SI, Fig. S6). This is accompanied by a slightly increased  $\epsilon$  of  $\sim 250$  due to less efficient thermal contact of the  $^1\text{H}$  spin bath to the lattice. The effects of  $\text{Mn}^{2+}$  on  $^1\text{H}$  DNP are negligible which can be expected when extrapolating studies on paramagnetic effects to small paramagnet concentrations of  $<0.5$  mM (Corzilius et al. 2014).

Direct polarization (DPMAS) read-out of  $^{13}\text{C}$  using Bloch decay can potentially be a quantitative measure of polarization since it is not influenced by differences in  $^1\text{H}$  environment. However, at cryogenic temperatures the longitudinal relaxation times of  $^{13}\text{C}$  become prohibitively long for full recovery of longitudinal magnetization between scans. In fact, we observed large enhancements and a bi-exponential build-up behavior for both Mn- and Mg-HHRz (see Table 1 for details; a full overview of spectra and build-up curves is given in the SI, Figures S5 and S7). Using the fitting function

$$I(t) \propto \varphi \left[ 1 - \exp\left(-\frac{t}{T_{B,f}}\right) \right] + \left[ 1 - \exp\left(-\frac{t}{T_{B,s}}\right) \right], \quad (3)$$

a fast (f) and a slow (s) build-up time constant have been determined which lie in the range of  $\sim 100$  s and  $\sim 2000$ – $3000$  s, respectively, for all samples. We tentatively ascribe the fast and slow build-up components to a direct contact between  $^{13}\text{C}$  and the electron spin(s) as well as relayed contact involving  $^{13}\text{C}$ – $^{13}\text{C}$  spin-diffusion through the  $^{13}\text{C}$  depleted matrix (see details below). Furthermore,  $^{13}\text{C}$  DPMAS spectra show visible broadening depending on the chosen pre-polarization delay (Fig. S5). This is caused by non-statistical weighting of resonances from nuclei in close proximity to the polarizing agent by fast longitudinal build-up and/or large DNP enhancements. The presence of  $\text{Mn}^{2+}$  again has a negligible impact on the observable spectrum. This might seem surprising, but can be explained by the relatively large concentration of AMUPol; at 5 mM each HHRz of about  $\sim 6$  nm globular

diameter is surrounded statistically by  $\sim 4$  AMUPol molecules (accordingly 8 nitroxide spins) within 1 nm distance. This could also explain the highly efficient direct  $^{13}\text{C}$  DNP in the isotope-depleted matrix; however, unspecific interactions between RNA and AMUPol cannot be excluded at the present time. The single  $\text{Mn}^{2+}$  at the defined binding position on the other hand leaves many nuclei at a distance of 3 nm and larger. Nevertheless, we observed a significant reduction in  $^{13}\text{C}$  enhancement from  $\sim 420$  in Mg-HHRz to  $\sim 160$  in Mn-HHRz, leaving us with the conclusion that  $\varepsilon$  is significantly reduced by more efficient nuclear spin–lattice relaxation induced by the paramagnetic metal ion.

Build-up time constants for direct  $\text{Mn}^{2+}$ - $^{13}\text{C}$  SE DNP are similar to time constants measured for the Mg-HHRz samples including AMUPol and are significantly longer than those for Mn-HHRz including AMUPol (the latter two were measured under  $^{13}\text{C}$  CE DNP). This seems natural because paramagnetic relaxation rates induced by  $\text{Mn}^{2+}$  and AMUPol are additive in first order. Interestingly, the relative contribution of the fast and slow build-up components are inverted compared to both AMUPol containing samples. We explain this by the occurrence of parallel, competing relaxation modes, namely a direct as well as a relayed polarization transfer pathway via  $^{13}\text{C}$ - $^{13}\text{C}$  spin diffusion. By depletion of the  $^{13}\text{C}$  abundance in glycerol to 0.05 % not only a significant background signal is diminished but—more importantly—the  $^{13}\text{C}$ - $^{13}\text{C}$  spin-diffusion between RNA molecules is suppressed. Therefore, directly bound  $\text{Mn}^{2+}$  can transfer polarization more efficiently through the direct pathway while AMUPol—though a more efficient polarizing agent due to cross effect—relies on spin-diffusion through the matrix. In order to confirm this hypothesis we prepared a reference sample comprised of 225 mM  $^{13}\text{C}$ ,  $^{15}\text{N}_2$ -urea and 0.4 mM  $\text{MnCl}_2$  dissolved in the same glycerol/water mixture. This sample provides concentrations of  $^{13}\text{C}$  and  $\text{Mn}^{2+}$  which are equal to those in the Mn-HHRz solution; although both  $^{13}\text{C}$  and  $\text{Mn}^{2+}$  are now homogeneously dispersed within the glassy matrix. In contrast to Mn-HHRz the bi-exponential polarization build-up features only a minor contribution of a fast component while the majority of spin polarization built up with a time constant of  $\sim 5000$  s, as can be seen in Table 1 and Fig. 5. This confirms our initial assignment of polarization build-up modes due to the absence of any efficient direct DNP transfer pathway from  $\text{Mn}^{2+}$  to  $^{13}\text{C}$  in combination with slow spin-diffusion through the diluted  $^{13}\text{C}$  network. For DNP with AMUPol an intermediate situation is encountered: the large molar excess of biradicals leads to a high probability of sufficiently close RNA–nitroxide contacts and opens the direct polarization pathway, nevertheless, in significantly lower extend as compared to the endogenous polarizing agent.

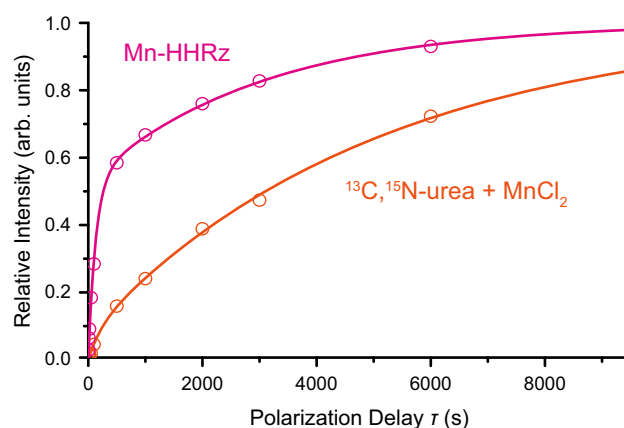


**Fig. 5** Direct  $^{13}\text{C}$  DNP build-up curves for 0.4 mM Mn-HHRz complex (magenta) and 0.4 mM  $\text{MnCl}_2$  with 225 mM  $^{13}\text{C}$ ,  $^{15}\text{N}_2$ -urea (orange) both using  $\text{Mn}^{2+}$ - $^{13}\text{C}$  SE DNP. Curves were obtained by pre-saturation of  $^{13}\text{C}$  and following polarization delay of varying time  $\tau$  and normalized to the extrapolated polarization at infinite time

Given the rather long polarization delays used for direct  $\text{Mn}^{2+}$ - $^{13}\text{C}$  SE DNP (160 and 3276 s), enhanced magnetization can efficiently exchange throughout the uniformly labeled biomolecule by  $^{13}\text{C}$ - $^{13}\text{C}$  spin diffusion. Therefore, a site-selective enhancement cannot be expected. Nevertheless, we notice slight differences in relative peak intensities, most visible in the spectral area between 150 and 160 ppm. This might indicate selective resonance quenching/broadening and/or non-uniform enhancements of nuclei in the direct vicinity of  $\text{Mn}^{2+}$ . For further investigation of these sought-after effects, experiments using specifically isotope-labeled RNA are required in order to not only suppress equilibration of polarization by spin-diffusion but also to allow for unambiguous assignment of resonances to atomic sites in the large nucleic acid molecule.

## Two-dimensional correlation spectroscopy

The large  $^1\text{H}$  enhancements allowed us to obtain two-dimensional  $^{13}\text{C}$ - $^{13}\text{C}$  and  $^{15}\text{N}$ - $^{13}\text{C}$  correlation spectra with excellent signal-to-noise ratio in short time, as shown in Fig. 6. Since both techniques utilize  $^1\text{H}$  magnetization with an initial  $^1\text{H}$ - $^{13}\text{C}$  or  $^1\text{H}$ - $^{15}\text{N}$  CP step, the enhancement factors measured by simple CP read-out also apply for the correlation spectra. Proton-driven spin diffusion (PDS) was allowed for 100 ms mixing time for magnetization transfer over distances significantly longer than a C–C bond (Bloembergen 1949; Szeverenyi et al. 1982). In another experiment, transferred-echo double resonance (TEDOR) with a mixing time of 1.6 ms was utilized for recoupling of  $^{15}\text{N}$ - $^{13}\text{C}$  pairs in relatively close distance comparable to typically one to two bonds (Hing et al. 1992;

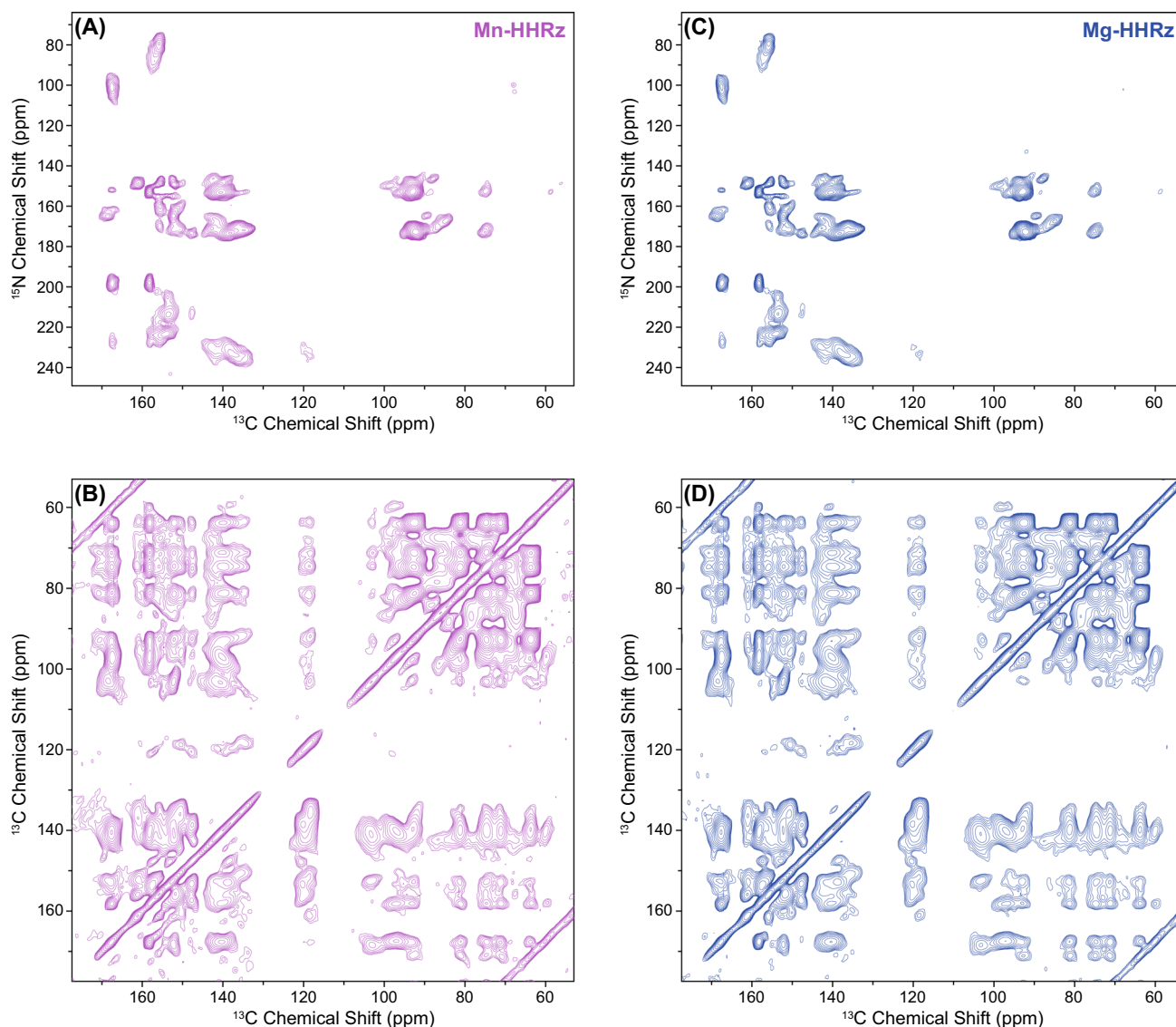


**Fig. 6** DNP-enhanced  $^{15}\text{N}$ - $^{13}\text{C}$  TEDOR (a) and  $^{13}\text{C}$ - $^{13}\text{C}$  PDS (b) correlation spectra of Mn-HHRz, and the respective TEDOR (c) and PDS (d) spectra of Mg-HHRz. TEDOR spectra were recorded with 1.6 ms mixing time, 56  $t_1$  slices with 100  $\mu\text{s}$  increment and 64 scans each (representing two 32-step phase cycles). Recycle delays of 8 and 9 s were used for Mn-HHRz and Mg-HHRz, respectively, resulting in 8 and 9 h acquisition time. A sine bell window function was applied in both dimensions and the spectra were

Fourier-transformed after zero filling to  $4096 \times 1024$  points. PDS spectra were recorded with 100 ms mixing time, 128  $t_1$  slices with 44  $\mu\text{s}$  increment and one 16-step phase cycle. A recycle delay of 9 s was used for both Mn-HHRz and Mg-HHRz, resulting in 5 h acquisition time. A sine bell window function was applied in both dimensions and the spectra were Fourier-transformed after zero filling to  $4096 \times 1024$  points. All resonances above 170 ppm or below 62 ppm  $^{13}\text{C}$  chemical shift are attributable to spinning sidebands

Jaroniec et al. 2002). Despite an overall intensity loss comparable to that observed in simple CP experiments, the effect of  $\text{Mn}^{2+}$  is minimal: only a very minor broadening can be observed in Mn-HHRz; additionally, several cross peaks show slightly larger relative intensity presumably due to more efficient recoupling by faster transverse relaxation during longitudinal mixing.

The combination of short range  $^{15}\text{N}$ - $^{13}\text{C}$  and long range  $^{13}\text{C}$ - $^{13}\text{C}$  correlations allowed us to assign a consistent set of resonances to the atoms in each nucleotide type (see SI,

Tables S1 and S2, and Fig. S8). Every expected intra-nucleotide correlation has been clearly observed and assigned; additionally several inter-nucleotide resonances are visible and indicate close contacts due to base pairing or nucleotide stacking. Especially the resonances of cytidine-C5 and uridine-C5 show the largest number of unambiguous inter-nucleotide couplings due to their very large relative CP signal intensity caused by the directly bonded  $^1\text{H}$  in combination with little spectral overlap. For the C6 atoms of the same nucleotides a similar situation is

expected, but mutual spectral overlap between cytidine-C6 and uridine-C6 and additional overlap with adenosine-C8 impedes unambiguous assignments. Also it is noteworthy that several nucleobase resonances feature a large chemical shift dispersion which is often correlated with a shift of a coupled resonance potentially allowing for the identification of structural elements given single-site resolution can be achieved by higher-dimensional correlation spectroscopy or selective isotope labeling.

In Fig. 7 we present slices taken out of the two-dimensional correlation spectra in order to demonstrate the impressive signal-to-noise ratio obtained by DNP. Clearly the enhanced signal intensity is sufficient to extend the space into three or even more dimensions for increased chemical shift dispersion selectivity and/or for peak assignment using more sophisticated strategies (Marchanka et al. 2013). Some broadening induced by  $Mn^{2+}$  seems to occur in the down-field shifted region above 140 ppm as is visible in the PDS slice. This might arise from direct magnetic interactions between the electron spin of  $Mn^{2+}$  and the aromatic carbons of nucleobases close to the binding site. The large spectral overlap in the unselective one-dimensional CP experiment masks this broadening in Fig. 4.

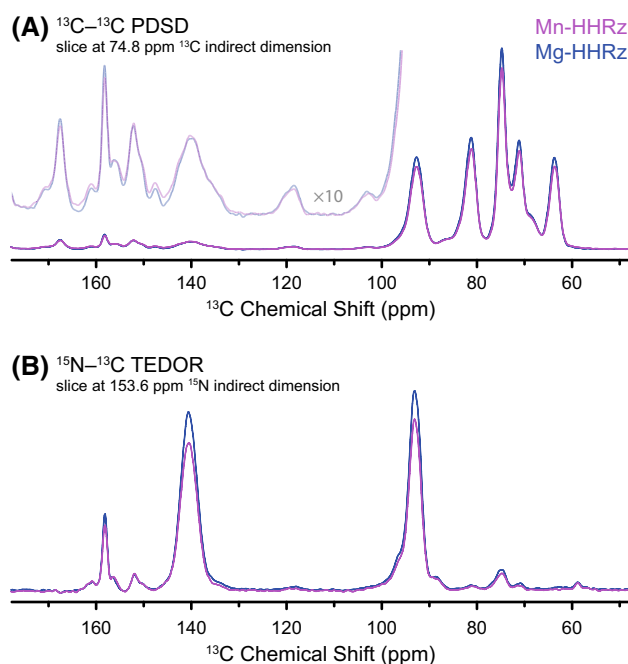


**Fig. 7** One-dimensional slices of correlation spectra of Mn-HHRz and Mg-HHRz. **a** Slice taken out of PDS (Fig. 6) at a  $^{13}C$  chemical shift of 74.8 ppm corresponding to C2' resonance of all nucleotides. The *light lines* are a vertical magnification by a factor 10 for better visibility of the low-intensity aromatic regions. **b** Slice taken out of TEDOR (Fig. 6) at a  $^{15}N$  chemical shift of 153.6 ppm corresponding to cytidine-N1 resonance. No apodization (window function) was applied in the direct dimension of both spectra to allow for demonstration of signal/noise ratio

Even though the intrinsically strong overlap of resonances in large nucleic acid molecules in the solid state often does not allow for assignment of individual nucleotides (Abramov and Goldbourt 2014), we can nevertheless identify several interesting, distinct spectral features not observed in solution NMR spectra of RNA. For example, we observe the occurrence of several  $^{15}N$  correlation peaks to cytidine-C4 centered at a  $^{13}C$  chemical shift of 167.3 ppm (see Fig. 8). A rather narrow but intense peak is found at a  $^{15}N$  chemical shift of 198.2 ppm which we attribute to cytidine-N3 due to the sole coupling to cytidine-C2 at 158.2 ppm (besides C4). However, this resonance typically is reported to occur around 210 ppm with a narrow distribution. We found a broader resonance of smaller peak intensity at 227.3 ppm which is also coupled to cytidine-C2, -C4, and additionally to guanosine-C2 (although coupling to guanosine-C6 has not been observed). We tentatively attribute this to an alternative conformation of cytidine, which might be stabilized by Watson-Crick base pairing to guanosine. Fast exchange between these conformations in liquid state leads to coalescence of the resonances and occurrence of a single peak at the mean chemical shift of  $\sim 210$  ppm. Please note that the simple analysis of peak intensities of the correlation spectra does not allow for the determination of conformational populations. A (tentatively assigned) third correlation resonance between cytidine-N3 and -C4 can be found at a  $^{15}N$  chemical shift of 152.2 ppm. This significant upfield shift by  $\sim 50$  ppm—together with observed coupling to  $^{13}C$  resonances at 158.2 ppm (cytidine-C2) and  $\sim 134$  ppm (guanosine-C8)—could be

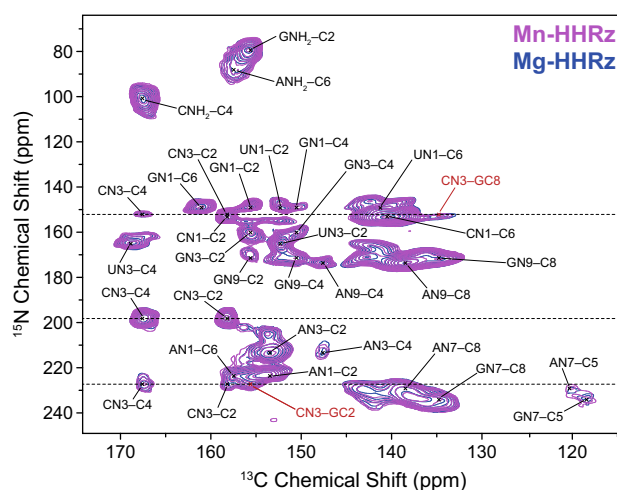


**Fig. 8** Section of  $^{15}N$ - $^{13}C$  correlation spectrum showing heterogeneous splitting of cytidine-N3 into three resonances (marked with *dashed lines*). Resonances are labeled with nucleotide type (i.e. A, G, C, and U) and atom label according to Fig. S8. For inter-nucleotide contacts (*red*) both nucleotides are given in the label; for intra-nucleotide contacts (*black*) the nucleotide is given only as first character of the label

explained by protonation of cytidine-N3 and base pairing to guanosine in a Hoogsteen-type conformation. The occurrence of Hoogsteen-type base pairs in the tertiary structure of HHRz has been observed (Chi et al. 2008; Martick and Scott 2006). In order to vet this tentative conformational analysis further experiments are clearly required. Nevertheless, these preliminary findings clearly guide the way for future investigations.

## Conclusion

In conclusion, uniformly isotope-labeled RNA can be efficiently polarized in a cryoprotecting frozen solution. The endogenously bound  $\text{Mn}^{2+}$  in HHRz can be used as polarizing agent for  $^{13}\text{C}$  DNP of ribonucleic acid as we have shown in this first demonstration of direct, intracomplex DNP transfer in a biomolecule. Even though the enhancement factor is moderate and equilibration of enhanced polarization most probably occurs over the course of several tens or hundreds of seconds during build-up in uniformly  $^{13}\text{C}$ -labeled biomolecules, the analysis of build-up dynamics in combination with potentially non-uniform enhancements in sparsely or selectively labeled samples might allow for the observation of site-selective DNP and may bear invaluable information for structural biology problems. Furthermore, with typical bis-nitroxide polarizing agents,  $^1\text{H}$  enhancement factors of up to 250 have been observed which surpass those commonly observed in proteins due to the absence of fast-reorienting methyl groups. Furthermore, the presence of an endogenously bound paramagnetic  $\text{Mn}^{2+}$  ion only marginally influences the enhancement and linewidth as far as the analysis of overlapping resonances in the 59-mer allows. Analysis of two-dimensional  $^{15}\text{N}$ - $^{13}\text{C}$  and  $^{13}\text{C}$ - $^{13}\text{C}$  correlation spectra indicate the occurrence of multiple distinct conformations which would be interconverting in the liquid state but are trapped in the frozen solution. Therefore, MAS DNP in the cryogenic solid state allows for direct access of these otherwise “hidden” states as opposed to indirect detection methods in solution (Nikolova et al. 2011). During the preparation of this manuscript, Marchanka et al. have demonstrated nearly complete atomic site assignments of a small (26 nucleotides) RNA within a protein complex by MAS NMR (Marchanka et al. 2015). Extension of MAS NMR spectra to three or more spectral dimensions—not possible without the outstanding signal-to-noise ratio evoked by DNP (Marchanka et al. 2015)—would aid the development of efficient assignment protocols similar to those already available for proteins (Franks et al. 2007; Li et al. 2007; Pauli et al. 2001) and adapted for RNA structural biology by Marchanka et al. (Marchanka et al. 2013). This could establish DNP-enhanced MAS

NMR as a valuable addition to the already existing toolbox for the structural biology of nucleic acids.

## Additional information

**Supporting Information.** Native PAGE assay, dissociation constant determination, EPR confirmation of  $\text{Mn}^{2+}$  binding in DNP samples,  $\text{Mn}^{2+}$ - $^{13}\text{C}$  SE simulation, full set of direct  $^{13}\text{C}$  DNP spectra, build-up curves, and resonance assignment.

**Acknowledgments** This work was supported by the Deutsche Forschungsgemeinschaft (DFG) via Emmy Noether Grant CO802/2-1 issued to B.C. as well as DFG collaborative research center (Sonderforschungsbereich) 902, and by the Center for Biomolecular Magnetic Resonance (BMRZ). We thank J. Becker-Baldus and T. Gutmann for access to DNP spectrometers and technical assistance. Help from D. Akhmetzyanov during 180 GHz EPR experiments is gratefully acknowledged. We thank T. Prisner for proposing HHRz as the target system of this study, as well as H. Schwalbe and J. Wöhnert for helpful discussions. The sweepable MAS DNP NMR spectrometer was granted to G. Buntkowsky (Darmstadt) via DFG Grant BU911/20-1.

**Funding** Deutsche Forschungsgemeinschaft (DFG) Grants CO802/2-1, SFB902, and BU911/20-1; Center for Biomolecular Magnetic Resonance (BMRZ).

## Compliance with ethical standards

**Conflict of interest** The authors declare that they have no conflict of interest.

## References

- Abragam A, Proctor WG (1958) Une nouvelle méthode de polarisation dynamique des noyaux atomiques dans les solides. *CR Hebd Acad Sci* 246:2253–2256
- Abramov G, Goldbourt A (2014) Nucleotide-type chemical shift assignment of the encapsulated 40 kbp dsDNA in intact bacteriophage T7 by MAS solid-state NMR. *J Biomol NMR* 59:219–230
- Akbey Ü, Franks WT, Linden A, Lange S, Griffin RG, van Rossum BJ, Oschkinat H (2010) Dynamic nuclear polarization of deuterated proteins. *Angew Chem Int Ed* 49:7803–7806
- Bassi GS, Murchie AI, Lilley DM (1996) The ion-induced folding of the hammerhead ribozyme: core sequence changes that perturb folding into the active conformation. *RNA* 2:756–768
- Bayro MJ, Maly T, Birkett NR, MacPhee CE, Dobson CM, Griffin RG (2010) High-resolution MAS NMR analysis of PI3-SH3 amyloid fibrils: backbone conformation and implications for protofilament assembly and structure. *Biochemistry* 49:7474–7484
- Becerra LR, Gerfen GJ, Temkin RJ, Singel DJ, Griffin RG (1993) Dynamic nuclear polarization with a cyclotron resonance maser at 5T. *Phys Rev Lett* 71:3561–3564
- Beilstein K, Wittmann A, Grez M, Suess B (2015) Conditional control of mammalian gene expression by tetracycline-dependent hammerhead ribozymes. *ACS Synth Biol* 4:526–534

- Bloembergen N (1949) On the interaction of nuclear spins in a crystalline lattice. *Physica* 15:386–426
- Bothe JR, Nikolova EN, Eichhorn CD, Chugh J, Hansen AL, Al-Hashimi HM (2011) Characterizing RNA dynamics at atomic resolution using solution-state NMR spectroscopy. *Nat Methods* 8:919–931
- Castellani F, van Rossum B, Diehl A, Schubert M, Rehbein K, Oschkinat H (2002) Structure of a protein determined by solid-state magic-angle-spinning NMR spectroscopy. *Nature* 420:98–102
- Cherepanov AV, Glaubitz C, Schwalbe H (2010) High-resolution studies of uniformly  $^{13}\text{C}$ ,  $^{15}\text{N}$ -labeled RNA by solid-state NMR spectroscopy. *Angew Chem Int Ed* 49:4747–4750
- Chi Y-I, Martick M, Lares M, Kim R, Scott WG, Kim S-H (2008) Capturing hammerhead ribozyme structures in action by modulating general base catalysis. *PLoS Biol* 6:2060–2068
- Corzilius B, Smith AA, Barnes AB, Luchinat C, Bertini I, Griffin RG (2011) High-Field dynamic nuclear polarization with high-spin transition metal ions. *J Am Chem Soc* 133:5648–5651
- Corzilius B, Smith AA, Griffin RG (2012) Solid Effect in magic angle spinning dynamic nuclear polarization. *J Chem Phys* 137:054201
- Corzilius B, Andreas LB, Smith AA, Ni QZ, Griffin RG (2014) Paramagnet-induced signal quenching in MAS-DNP experiments on frozen homogeneous solutions. *J Magn Reson* 240:113–123
- Dahm SC, Uhlenbeck OC (1991) Role of divalent metal ions in the hammerhead RNA cleavage reaction. *Biochemistry* 30:9464–9469
- De la Peña M, Gago S, Flores R (2003) Peripheral regions of natural hammerhead ribozymes greatly increase their self-cleavage activity. *EMBO J* 22:5561–5570
- Fernández-de-Alba C et al (2015) Matrix-free DNP-enhanced NMR spectroscopy of liposomes using a lipid-anchored biradical, chemistry. *Eur J* 21:4512–4517
- Forster AC, Symons RH (1987) Self-cleavage of virusoid RNA is performed by the proposed 55-nucleotide active site. *Cell* 50:9–16
- Franks WT, Kloepper K, Wylie B, Rienstra C (2007) Four-dimensional heteronuclear correlation experiments for chemical shift assignment of solid proteins. *J Biomol NMR* 39:107–131
- Fürtig B, Richter C, Wöhnert J, Schwalbe H (2003) NMR spectroscopy of RNA. *ChemBioChem* 4:936–962
- Fürtig B, Richter C, Schell P, Wenter P, Pitsch S, Schwalbe H (2008) NMR-spectroscopic characterisation of phosphodiester bond cleavage catalyzed by the minimal hammerhead ribozyme. *RNA Biol* 5:41–48
- Glowinkowski S, Jurga S, Suchanski W, Szczesniak E (1997) Local and global dynamics in the glass-forming di-isobutyl phthalate as studied by  $^1\text{H}$  NMR. *Solid State Nucl Magn Reson* 7:313–317
- Gutsche P, Rinsdorf M, Zimmermann H, Schmitt H, Haeblerl U (2004) The shape and information content of high-field solid-state proton NMR spectra of methyl groups. *Solid State Nucl Magn Reson* 25:227–240
- Hall DA, Maus DC, Gerfen GJ, Inati SJ, Becerra LR, Dahlquist FW, Griffin RG (1997) Polarization-enhanced NMR spectroscopy of biomolecules in frozen solution. *Science* 276:930–932
- Hammann C, Norman DG, Lilley DMJ (2001) Dissection of the ion-induced folding of the hammerhead ribozyme using 19F NMR. *Proc Natl Acad Sci U S A* 98:5503–5508
- Hing AW, Vega S, Schaefer J (1992) Transferred-echo double-resonance NMR. *J Magn Reson* 96:205–209
- Horton TE, Clardy DR, DeRose VJ (1998) Electron paramagnetic resonance spectroscopic measurement of  $\text{Mn}^{2+}$  binding affinities to the hammerhead ribozyme and correlation with cleavage activity. *Biochemistry* 37:18094–18101
- Hovav Y, Feintuch A, Vega S (2010) Theoretical aspects of dynamic nuclear polarization in the solid state—the solid effect. *J Magn Reson* 207:176–189
- Hovav Y, Feintuch A, Vega S (2012) Theoretical aspects of dynamic nuclear polarization in the solid state—the cross effect. *J Magn Reson* 214:29–41
- Hu KN (2011) Polarizing agents and mechanisms for high-field dynamic nuclear polarization of frozen dielectric solids. *Solid State Nucl Magn Reson* 40:31–41
- Hu KN, Yu HH, Swager TM, Griffin RG (2004) Dynamic nuclear polarization with biradicals. *J Am Chem Soc* 126:10844–10845
- Hu KN, Debelouchina GT, Smith AA, Griffin RG (2011) Quantum mechanical theory of dynamic nuclear polarization in solid dielectrics. *J Chem Phys* 134:19
- Huang W, Bardaro MF Jr, Varani G, Drobny GP (2012) Preparation of RNA samples with narrow line widths for solid state NMR investigations. *J Magn Reson* 223:51–54
- Hutchins CJ, Rathjen PD, Forster AC, Symons RH (1986) Self-cleavage of plus and minus RNA transcripts of avocado sunblotch viroid. *Nucleic Acids Res* 14:3627–3640
- Jaroniec CP, Filip C, Griffin RG (2002) 3D TEDOR NMR experiments for the simultaneous measurement of multiple carbon-nitrogen distances in uniformly C-13, N-15-labeled solids. *J Am Chem Soc* 124:10728–10742
- Jeffries CD (1957) Polarization of nuclei by resonance saturation in paramagnetic crystals. *Phys Rev* 106:164–165
- Jeffries CD (1960) Dynamic orientation of nuclei by forbidden transitions in paramagnetic resonance. *Phys Rev* 117:1056–1069
- Kessenikh AV, Lushchikov VI, Manenkov AA, Taran YV (1963) Proton polarization in irradiated polyethylenes. *Sov Phys-Sol State* 5:321–329
- Khvorova A, Lescoute A, Westhof E, Jayasena SD (2003) Sequence elements outside the hammerhead ribozyme catalytic core enable intracellular activity. *Nat Struct Mol Biol* 10:708–712
- Lange S, Linden AH, Akbey Ü, Franks WT, Loening NM, van Rossum B-J, Oschkinat H (2012) The effect of biradical concentration on the performance of DNP-MAS-NMR. *J Magn Reson* 216:209–212
- Li Y, Berthold DA, Frericks HL, Gennis RB, Rienstra CM (2007) Partial  $^{13}\text{C}$  and  $^{15}\text{N}$  chemical-shift assignments of the disulfide-bond-forming enzyme DsbB by 3D magic-angle spinning NMR spectroscopy. *ChemBioChem* 8:434–442
- Maly T, Miller AF, Griffin RG (2010) In situ high-field dynamic nuclear polarization-direct and indirect polarization of C-13 nuclei. *ChemPhysChem* 11:999–1001
- Maly T, Cui D, Griffin RG, Miller A-F (2012)  $^1\text{H}$  dynamic nuclear polarization based on an endogenous radical. *J Phys Chem B* 116:7055–7065
- Marchanka A, Simon B, Carlomagno T (2013) A suite of solid-state NMR experiments for RNA intranucleotide resonance assignment in a 21 kDa protein–RNA complex. *Angew Chem Int Ed* 52:9996–10001
- Marchanka A, Simon B, Althoff-Ospelt G, Carlomagno T (2015) RNA structure determination by solid-state NMR spectroscopy. *Nat Commun* 6:7024
- Martick M, Scott WG (2006) Tertiary contacts distant from the active site prime a ribozyme for catalysis. *Cell* 126:309–320
- Martick M, Lee T-S, York DM, Scott WG (2008) Solvent structure and hammerhead ribozyme catalysis. *Chem Biol* 15:332–342
- Morrissey SR, Horton TE, Grant CV, Hoogstraten CG, Britt RD, DeRose VJ (1999)  $\text{Mn}^{2+}$ -nitrogen interactions in RNA probed by electron spin-echo envelope modulation spectroscopy: application to the hammerhead ribozyme. *J Am Chem Soc* 121:9215–9218
- Morrissey SR, Horton TE, DeRose VJ (2000)  $\text{Mn}^{2+}$  sites in the hammerhead ribozyme investigated by EPR and continuous-wave Q-band ENDOR spectroscopies. *J Am Chem Soc* 122:3473–3481
- Murray JB, Terwey DP, Maloney L, Karpeisky A, Usman N, Beigelman L, Scott WG (1998) The structural basis of hammerhead ribozyme self-cleavage. *Cell* 92:665–673



- Ni QZ et al (2013) High frequency dynamic nuclear polarization. *Acc Chem Res* 46:1933–1941
- Nikolova EN, Kim E, Wise AA, O'Brien PJ, Andricioaei I, Al-Hashimi HM (2011) Transient Hoogsteen base pairs in canonical duplex DNA. *Nature* 470:498–502
- Nozirov F, Nazirov A, Jurga S, Fu R (2006) Molecular dynamics of poly(l-lactide) biopolymer studied by wide-line solid-state  $^1\text{H}$  and  $^2\text{H}$  NMR spectroscopy. *Solid State Nucl Magn Reson* 29:258–266
- Osborne EM, Ward WL, Ruehle MZ, DeRose VJ (2009) The identity of the nucleophile substitution may influence metal interactions with the cleavage site of the minimal hammerhead ribozyme. *Biochemistry* 48:10654–10664
- Overhauser AW (1953) Polarization of nuclei in metals. *Phys Rev* 92:411–415
- Pauli J, Baldus M, van Rossum B, de Groot H, Oschkinat H (2001) Backbone and side-chain  $^{13}\text{C}$  and  $^{15}\text{N}$  signal assignments of the  $\alpha$ -spectrin SH3 domain by magic angle spinning solid-state NMR at 17.6 Tesla. *ChemBioChem* 2:272–281
- Pley HW, Flaherty KM, McKay DB (1994) Three-dimensional structure of a hammerhead ribozyme. *Nature* 372:68–74
- Prody GA, Bakos JT, Buzayan JM, Schneider IR, Bruening G (1986) Autolytic processing of dimeric plant virus satellite RNA. *Science* 231:1577–1580
- Renault M et al (2012) Solid-state NMR spectroscopy on cellular preparations enhanced by dynamic nuclear polarization. *Angew Chem Int Ed* 51:2998–3001
- Rinntenthal J, Buck J, Ferner J, Wacker A, Fürtig B, Schwalbe H (2011) Mapping the landscape of RNA dynamics with NMR spectroscopy. *Acc Chem Res* 44:1292–1301
- Rohrer M, Brüggemann O, Kinzer B, Prisner TF (2001) High-field/high-frequency EPR spectrometer operating in pulsed and continuous-wave mode at 180 GHz. *Appl Magn Reson* 21:257–274
- Rossini AJ et al (2012) One hundred fold overall sensitivity enhancements for Silicon-29 NMR spectroscopy of surfaces by dynamic nuclear polarization with CPMG acquisition. *Chem Sci* 3:108–115
- Sauvée C, Rosay M, Casano G, Aussenac F, Weber RT, Ouari O, Tordo P (2013) Highly efficient, water-soluble polarizing agents for dynamic nuclear polarization at high frequency. *Angew Chem Int Ed* 52:10858–10861
- Schiemann O, Fritscher J, Kisseleva N, Sigurdsson ST, Prisner TF (2003) Structural investigation of a high-affinity MnII binding site in the hammerhead ribozyme by EPR spectroscopy and DFT calculations. Effects of neomycin B on metal-ion binding. *ChemBioChem* 4:1057–1065
- Scott WG, Finch JT, Klug A (1995) The crystal structure of an AII-RNA hammerhead ribozyme: a proposed mechanism for RNA catalytic cleavage. *Cell* 81:991–1002
- Scott WG, Murray JB, Arnold JRP, Stoddard BL, Klug A (1996) Capturing the structure of a catalytic RNA intermediate: the hammerhead ribozyme. *Science* 274:2065–2069
- Shimon D, Hovav Y, Feintuch A, Goldfarb D, Vega S (2012) Dynamic nuclear polarization in the solid state: a transition between the cross effect and the solid effect. *Phys Chem Chem Phys* 14:5729–5743
- Smith AA, Corzilius B, Barnes AB, Maly T, Griffin RG (2012) Solid effect dynamic nuclear polarization and polarization pathways. *J Chem Phys* 136:015101
- Smith AN, Caporini MA, Fanucci GE, Long JR (2015) A method for dynamic nuclear polarization enhancement of membrane proteins. *Angew Chem Int Ed* 54:1542–1546
- Sripakdeevong P et al (2014) Structure determination of noncanonical RNA motifs guided by  $^1\text{H}$  NMR chemical shifts. *Nat Methods* 11:413–416
- Stoll S, Schweiger A (2006) EasySpin, a comprehensive software package for spectral simulation and analysis in EPR. *J Magn Reson* 178:42–55
- Szeverenyi NM, Sullivan MJ, Maciel GE (1982) Observation of spin exchange by two-dimensional fourier transform  $^{13}\text{C}$  cross polarization-magic-angle spinning. *J Magn Reson* 47:462–475
- Wang S, Karbstein K, Peracchi A, Beigelman L, Herschlag D (1999) Identification of the hammerhead ribozyme metal ion binding site responsible for rescue of the deleterious effect of a cleavage site phosphorothioate. *Biochemistry* 38:14363–14378
- Ward WL, DeRose VJ (2012) Ground-state coordination of a catalytic metal to the scissile phosphate of a tertiary-stabilized hammerhead ribozyme. *RNA* 18:16–23
- Wasmer C, Lange A, Van Melckebeke H, Siemer AB, Riek R, Meier BH (2008) Amyloid fibrils of the HET-s(218–289) prion form a beta solenoid with a triangular hydrophobic core. *Science* 319:1523–1526
- Wenckebach WT (2008) The solid effect. *Appl Magn Reson* 34:227–235
- Wittmann A, Suess B (2011) Selection of tetracycline inducible self-cleaving ribozymes as synthetic devices for gene regulation in yeast. *Mol Biosyst* 7:2419–2427
- Wylie BJ, Dzikovski BG, Pawsey S, Caporini M, Rosay M, Freed JH, McDermott AE (2015) Dynamic nuclear polarization of membrane proteins: covalently bound spin-labels at protein–protein interfaces. *J Biomol NMR* 61:361–367
- Yen L et al (2004) Exogenous control of mammalian gene expression through modulation of RNA self-cleavage. *Nature* 431:471–476

## Supporting Information

### Dynamic Nuclear Polarization of Nucleic Acid with Endogenously Bound Manganese

Patricia Wenk,<sup>†,§</sup> Monu Kaushik,<sup>†</sup> Diane Richter,<sup>†</sup> Marc Vogel,<sup>‡</sup> Beatrix Suess,<sup>‡</sup> and Björn Corzilius<sup>†,\*</sup>

<sup>†</sup> Institute of Physical and Theoretical Chemistry, Institute of Biophysical Chemistry and Center for Biomolecular Magnetic Resonance (BMRZ), Goethe University, Max-von-Laue-Str. 7-9, 60438 Frankfurt am Main (Germany).

<sup>‡</sup> Department of Biology, Technical University Darmstadt, Schnittspahnstraße 10, 64287 Darmstadt (Germany).

<sup>§</sup> present address: Werner Siemens Imaging Center and Department of Preclinical Imaging and Radiopharmacy, University of Tübingen, Röntgenweg 13, 72076 Tübingen (Germany).

#### Content

<b>Native PAGE assay</b> .....	<b>2</b>
<b>Confirmation of Mn<sup>2+</sup> binding to HHRz and determination of dissociation constant</b>	
Determination of dissociation constant in aqueous buffer solution .....	3
Confirmation of Mn <sup>2+</sup> binding to HHRz in glycerol/water DNP samples .....	4
<b>Estimation of the Mn<sup>2+</sup>-<sup>13</sup>C solid effect matching condition</b> .....	<b>5</b>
<b>MAS NMR spectra</b>	
Direct <sup>13</sup> C DNP enhanced spectra (Bloch decay) .....	6
Build-up curves of enhanced <sup>1</sup> H polarization .....	7
Build-up curves of enhanced <sup>13</sup> C polarization .....	7
Assignment of NMR resonances .....	8
<b>References</b> .....	<b>11</b>

## Native PAGE assay



**Figure S1.** Native polyacrylamide gel electrophoresis (PAGE) assay performed in order to confirm purity of the RNA after purification. An 8% polyacrylamide (PAA) gel was used with 650  $\mu\text{g}$  of RNA. Two purified transcription products from separate preparations are shown; the product on the right was used for all MAS DNP experiments in this work. No marker was used.

## Confirmation of Mn<sup>2+</sup> binding to HHRz and determination of dissociation constant

### Determination of dissociation constant in aqueous buffer solution

For determination of  $K_D$  we determined the relative intensity of the isotropic Mn<sup>2+</sup> EPR spectrum in aqueous solution. Due to binding of Mn<sup>2+</sup> to HHRz the rotational correlation time increases dramatically, thus the severely broadened spectrum of Mn<sup>2+</sup> in a complex with HHRz cannot be detected with conventional solution EPR. This allows us to determine the relative concentration of “free” (unbound) Mn<sup>2+</sup> ( $[Mn^{2+}]$ ) as a function of overall added  $[Mn^{2+}]_0$  from MnCl<sub>2</sub> (Fig. S2).

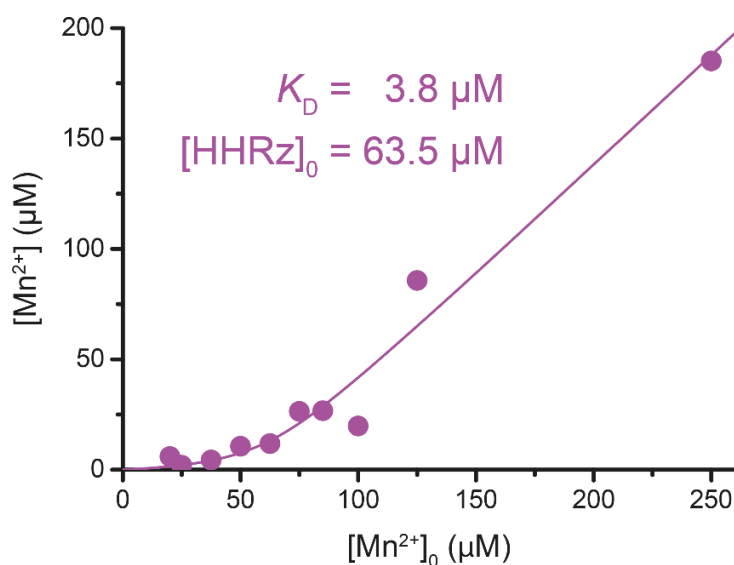


**Figure S2.** Determination of dissociation constant  $K_D$  for Mn-HHRz complex.

The data was fitted with a simple dissociation kinetics according to



The dissociation constant is defined as

$$K_D = \frac{[Mn^{2+}][HHRz]}{[Mn-HHRz]} \quad (1.2)$$

where  $[HHRz]$  is the concentration of the “free” HHRz without bound Mn<sup>2+</sup>, and  $[Mn-HHRz]$  is the concentration of the complex. Under the condition that both Mn<sup>2+</sup> as well as HHRz exist only in their free or complex bound form, this can be rearranged as

$$[Mn^{2+}] = \frac{[Mn^{2+}]_0 - [HHRz]_0 - K_D}{2} + \sqrt{\left(\frac{-[Mn^{2+}]_0 + [HHRz]_0 + K_D}{2}\right)^2 + K_D [Mn^{2+}]_0} . \quad (1.3)$$

The fit yielded a dissociation constant of  $K_D \approx 4 \mu\text{M}$  which is in good agreement with earlier studies<sup>[2]</sup> and confirms selective binding of a single Mn<sup>2+</sup> to HHRz at NaCl concentration at or above 100 mM and Mn<sup>2+</sup> concentration of up to 250  $\mu\text{M}$ .

## Confirmation of Mn<sup>2+</sup> binding to HHRz in glycerol/water DNP samples

In order to confirm the binding of Mn<sup>2+</sup> to HHRz in the samples used for DNP the solution was transferred to 1.1 mm i.d. CFQ EPR tubes after DNP experiments. The small diameter tubes were placed inside a 4 mm o.d. EPR tube for reduction of dielectric losses inside the aqueous solution. The cw EPR spectra were recorded at X-band and room temperature under equal conditions within the same day to ensure quantitative comparability. Sample tubes were filled with comparable sample volumes resulting in ~10 mm sample height, however, an uncertainty of ±20% in signal amplitude is assumed due to unavoidable variations in cavity tuning and matching, dielectric loss, as well as sample tube placement. Spectra are shown in Fig. S3.

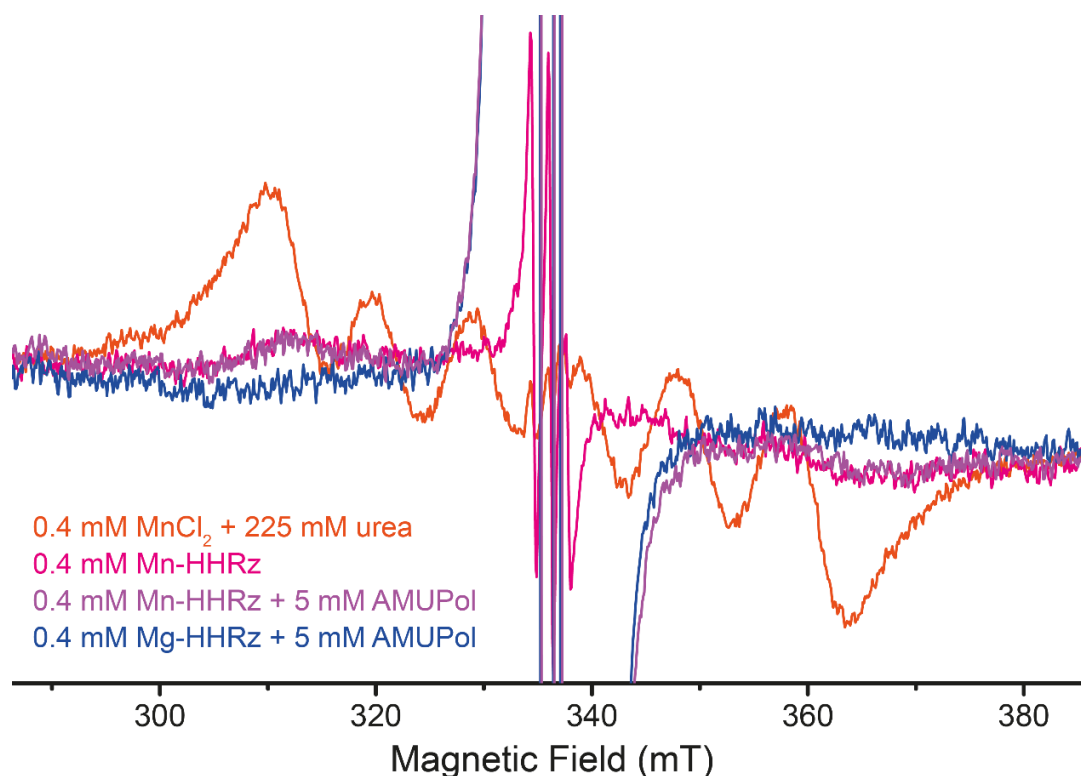


**Figure S3.** EPR spectra used for confirmation of Mn<sup>2+</sup> binding to HHRz in DNP samples. For all samples the same solvent mixture of 60/40 (vol.-%) glycerol/water was used as described in the experimental section. Nitroxide signals (between 330 and 342 mT) are clipped for better visibility of Mn<sup>2+</sup> signals). A negligible contamination with a nitroxide impurity of low  $\mu\text{M}$  concentration is visible for samples without intentional addition of AMUPol, probably due to contamination of reused sealing silicone soft plugs. This small concentration should have virtually no effect on DNP.

Without HHRz a typical Mn<sup>2+</sup> sextet spectrum is observed; the linewidth is larger than typically observed in water due to larger viscosity of the glycerol/water mixture. The rather large concentration of urea has no visible influence on the spectrum as we have confirmed by measurement of a sample excluding urea (not shown).

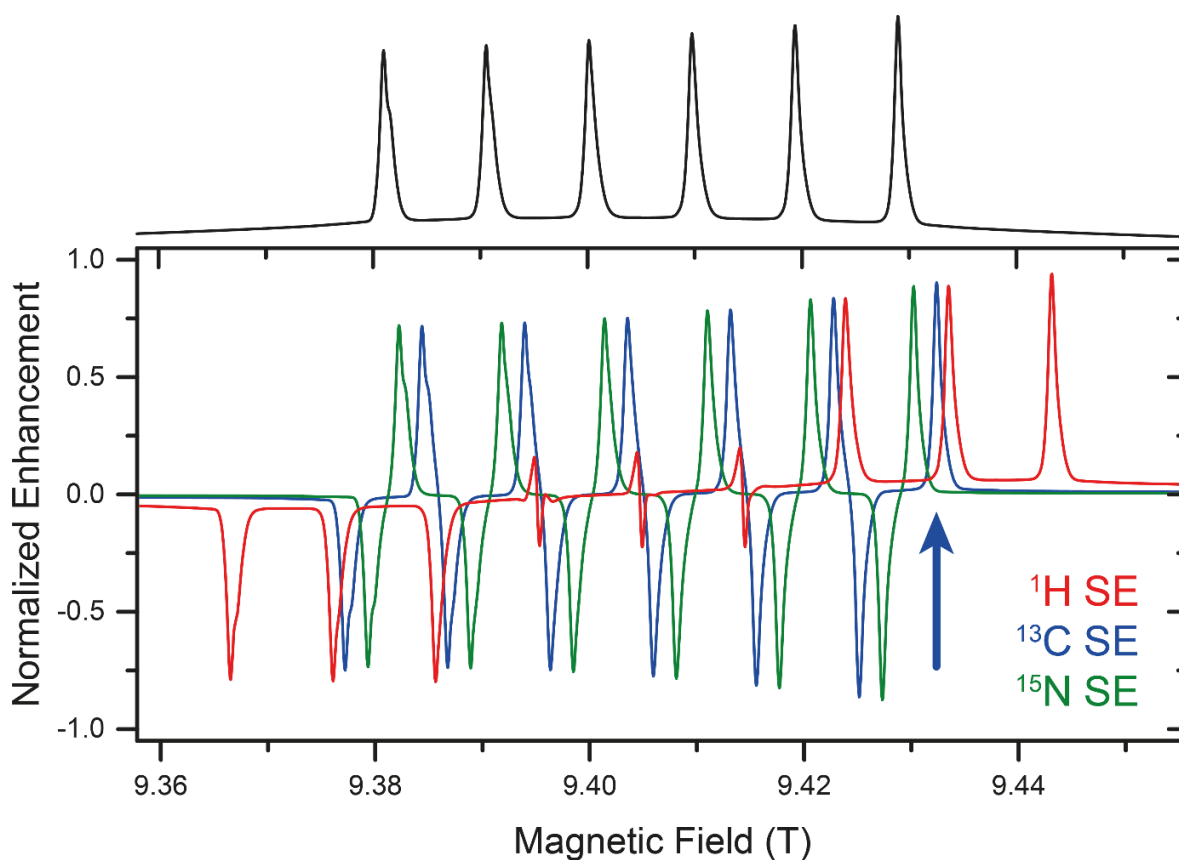
The presence of HHRz leads to a clear reduction of cw EPR signal amplitude of Mn<sup>2+</sup> due to longer rotational correlation times; the linewidth is dramatically increased and the typical sextet structure is barely visible. No difference is observed due to presence of nitroxide. We therefore conclude that ~90% or more of Mn<sup>2+</sup> is bound to HHRz which is in perfect agreement with a  $K_D$  in the low  $\mu\text{M}$  range.

## Estimation of the $\text{Mn}^{2+}$ - $^{13}\text{C}$ solid effect matching condition

For the estimation of the required field position for  $\text{Mn}^{2+}$ - $^{13}\text{C}$  solid effect matching we simulated an EPR spectrum with parameters obtained from 180 GHz EPR spectra of Mn-HHRz using Easyspin.<sup>[3]</sup> Note that only the position of the lines is significant; the detailed lineshape and width of each hyperfine line was not optimized. The SE field profiles were simulated by spectral overlap of positive and negative enhancements at the zero and double quantum transitions according to

$$\varepsilon_{\text{SE}}(B_0) \propto g_{\text{EPR}}\left(B_0 - \frac{\omega_{\text{H}}}{\gamma_S}\right) - g_{\text{EPR}}\left(B_0 + \frac{\omega_{\text{H}}}{\gamma_S}\right). \quad (1.4)$$

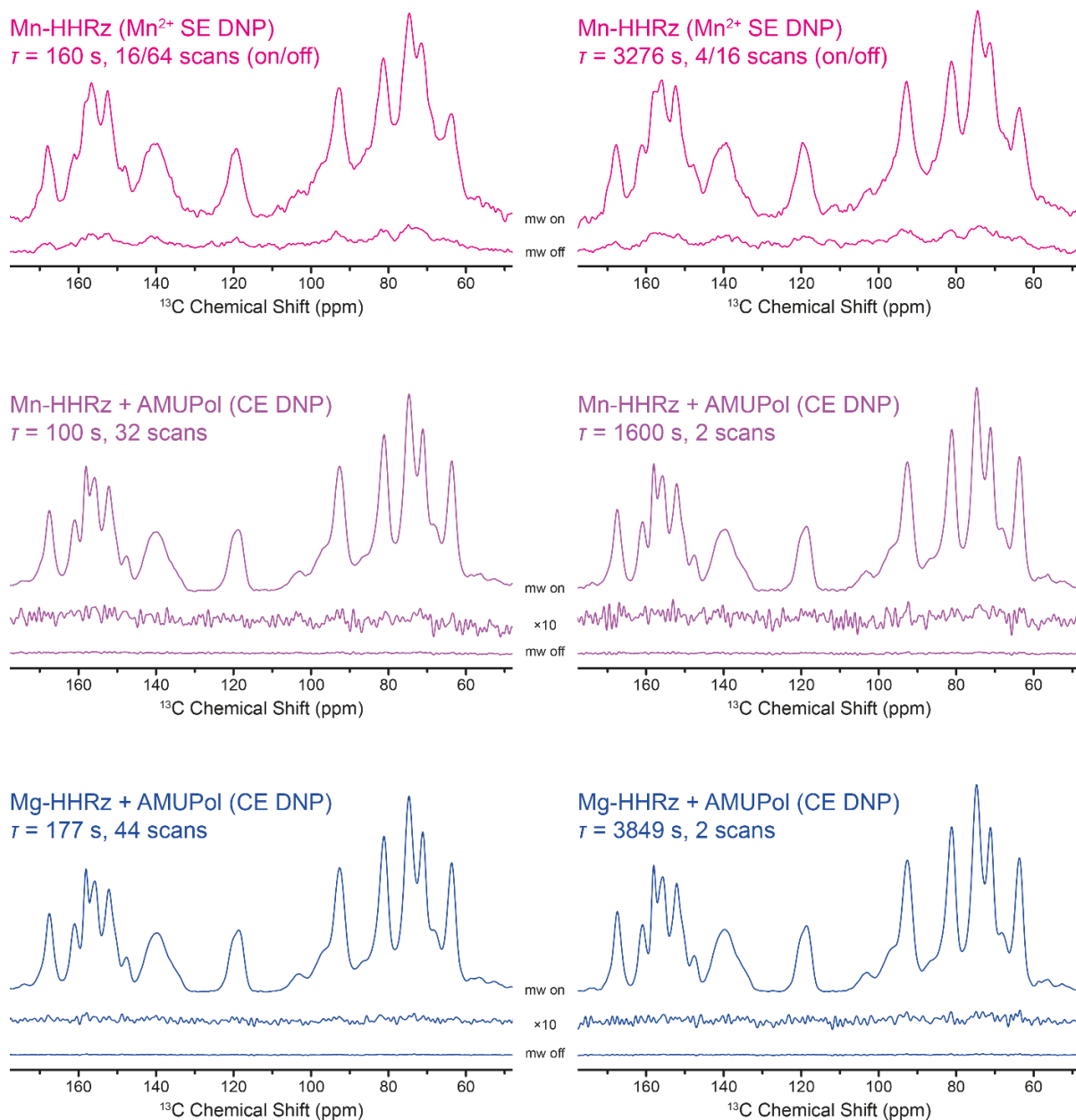
similar to what has been described by Shimon et al.<sup>[4]</sup> In Figure S4 the resulting DNP spectra are shown. After setting the field to the estimated position a  $^{13}\text{C}$  enhancement was immediately observed and allowed for optimization of the enhancement by varying the field in small increments.



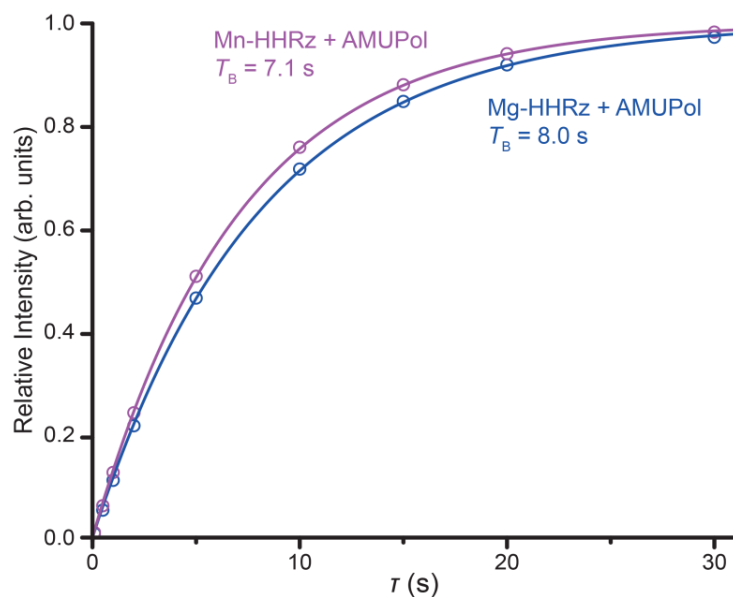
**Figure S4.** Estimation of  $^1\text{H}$  (red),  $^{13}\text{C}$  (blue), and  $^{15}\text{N}$  (green) matching conditions for SE DNP using  $\text{Mn}^{2+}$  as polarizing agent. The simulated EPR spectrum is shown on top of the graph in black. The field positions used for DNP is marked with a blue arrow.

## MAS NMR spectra

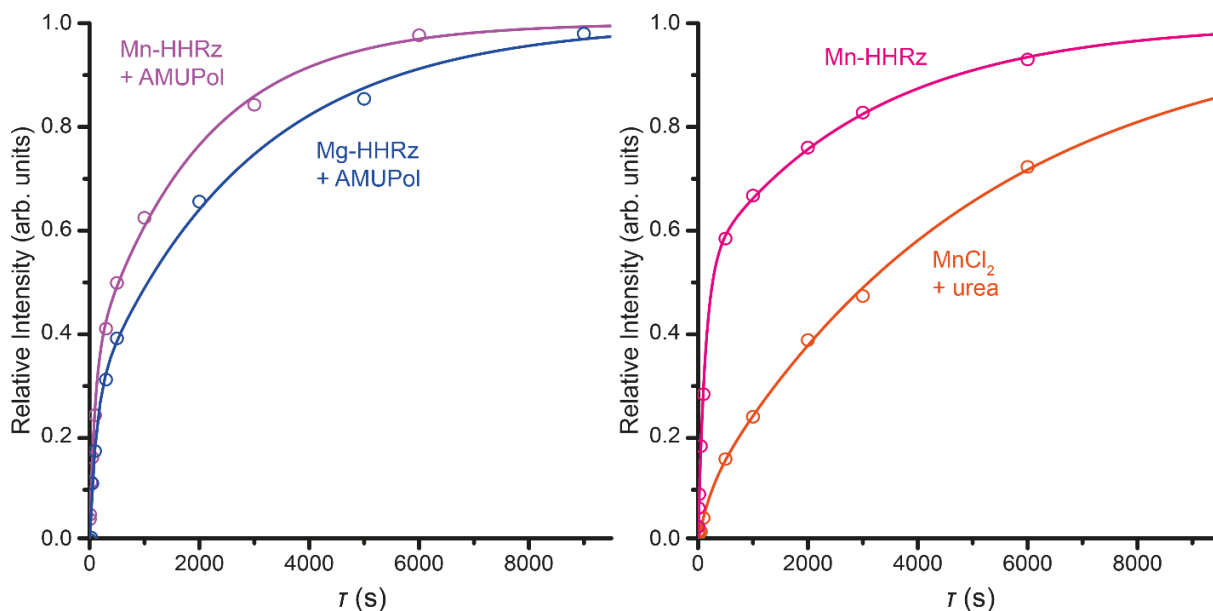
### Direct $^{13}\text{C}$ DNP enhanced spectra (Bloch decay)



**Figure S5.** Direct Polarization  $^{13}\text{C}$  MAS NMR spectra of 0.4 mM Mn-HHRz complex utilizing  $\text{Mn}^{2+}$  SE condition (top), of 0.4 mM Mn-HHRz complex containing 5 mM AMUPol utilizing nitroxide CE condition (middle), and 0.4 mM Mg-HHRz complex containing 5 mM AMUPol utilizing nitroxide CE condition (bottom). For each sample a spectrum representative of the fast build-up component (left) and the slow build-up component (right) is shown. Polarization times and numbers of scans are given in the figure. The top spectra are Fourier-transformed using a 0.75 ppm (75 Hz) exponential line broadening, while for the middle and bottom spectra no line broadening window function was applied. DNP-enhanced spectra (mw on) are shown in direct comparison with non-enhanced spectra (mw off) and 10-fold vertically magnified spectra ( $\times 10$ ) for samples containing AMUPol. Enhancement factors are given in Table 1 in the main text. All spectra are normalized to maximum intensity of the DNP-enhanced spectrum.

Build-up curves of enhanced  $^1\text{H}$  polarization

**Figure S6.** Indirect  $^1\text{H}$  DNP build-up curves for 0.4 mM Mg-HHRz complex (blue) and 0.4 mM Mn-HHRz complex (violet) with 5 mM AMUPol measured via cross polarization to  $^{13}\text{C}$ . Curves were obtained by pre-saturation of  $^1\text{H}$  with a following polarization delay of varying time  $\tau$  and were normalized to the extrapolated polarization at infinite time.

Build-up curves of enhanced  $^{13}\text{C}$  polarization

**Figure S7.** Left: Direct  $^{13}\text{C}$  DNP build-up curves for 0.4 mM Mg-HHRz complex (blue) and 0.4 mM Mn-HHRz complex (violet) with 5 mM AMUPol. Right: Direct  $^{13}\text{C}$  DNP build-up curves for 0.4 mM Mn-HHRz complex (magenta) and 0.4 mM  $\text{MnCl}_2$  with 225 mM  $^{13}\text{C}$ ,  $^{15}\text{N}_2$ -urea (orange) both using  $\text{Mn}^{2+}$  solid effect. Curves were obtained by pre-saturation of  $^{13}\text{C}$  with a following polarization delay of varying time  $\tau$  and were normalized to the extrapolated polarization at infinite time.



## Assignment of NMR resonances

Resonances have been assigned starting from clearly identifiable resonances, which are the amines as well as the C4 of pyrimidines which feature the largest downfield shift. This allowed for a complete assignment of all resonances without ambiguities. We generated a single consistent set of resonances which is compiled in Table S1 and used for labeling of two-dimensional correlation peaks in Fig. S8. We observed multiple peaks we attributed to cytidine-N3 as is described in detail in the main manuscript. A matrix with observed  $^{13}\text{C}$ – $^{13}\text{C}$  correlation peaks is shown in Table S2. All intra-nucleotide correlation have been observed with the exception of a few resonances originating from guanosine-C4, -C5, and -C6, as well as adenosine-C5. Note that these atoms do not carry a single proton along the directly connected carbon chain and therefore feature extremely small CP efficiency. Nevertheless, all expected resonances have been observed in the direct dimension. Chemical shift dispersion and peak doubling has been observed experimentally for several resonances, however, unambiguous assignment was not possible due to spectral overlap.

**Table S1.** List of assigned resonances and chemical shift used for generation of a single consistent set for peak assignment.

nucleobase atom	$^{15}\text{N}$ chemical shift (ppm)	nucleobase atom	$^{13}\text{C}$ chemical shift (ppm)	ribose atom	$^{13}\text{C}$ chemical shift (ppm)
A N1	223.6	A C2	153.5	A C1'	92.7
A N3	213.4	A C4	147.6	A C2'	75.1
A N7	229.2	A C5	120.3	A C3'	71.5
A N9	173.7	A C6	157.5	A C4'	81.5
A NH <sub>2</sub>	88.1	A C8	138.5	A C5'	63.6
G N1	149.1	G C2	155.6	G C1'	92.2
G N3	160.1	G C4	150.5	G C2'	74.5
G N7	234.1	G C5	118.4	G C3'	71.3
G N9	171.4	G C6	161.0	G C4'	81.7
G NH <sub>2</sub>	79.4	G C8	134.8	G C5'	63.5
C N1	153.1	C C2	158.2	C C1'	92.9
C N3	198.2	C C4	167.3	C C2'	74.7
(C N3)	(227.3)	C C5	97.2	C C3'	71.1
(C N3)	(152.2)	C C6	140.5	C C4'	81.1
C NH <sub>2</sub>	100.1			C C5'	63.6
U N1	149.3	U C2	152.3	U C1'	93.4
U N3	165.1	U C4	168.9	U C2'	74.5
		U C5	103.0	U C3'	71.1
		U C6	141.2	U C4'	81.4
				U C5'	63.6

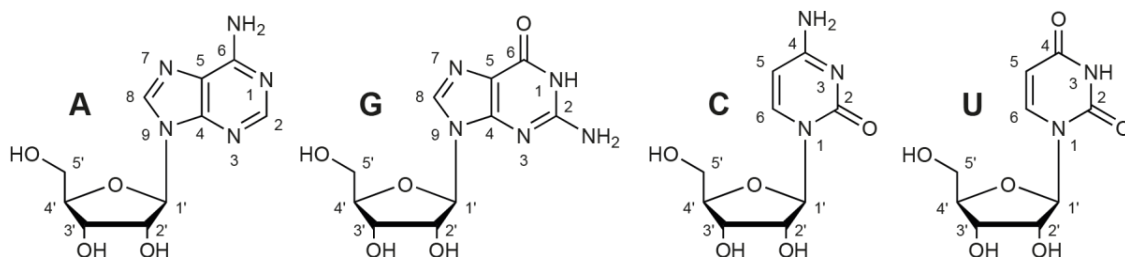


**Figure S8.** Chemical structures of nucleosides adenosine (A), guanosine (G), cytidine (C), and uridine (U) with atomic numbering

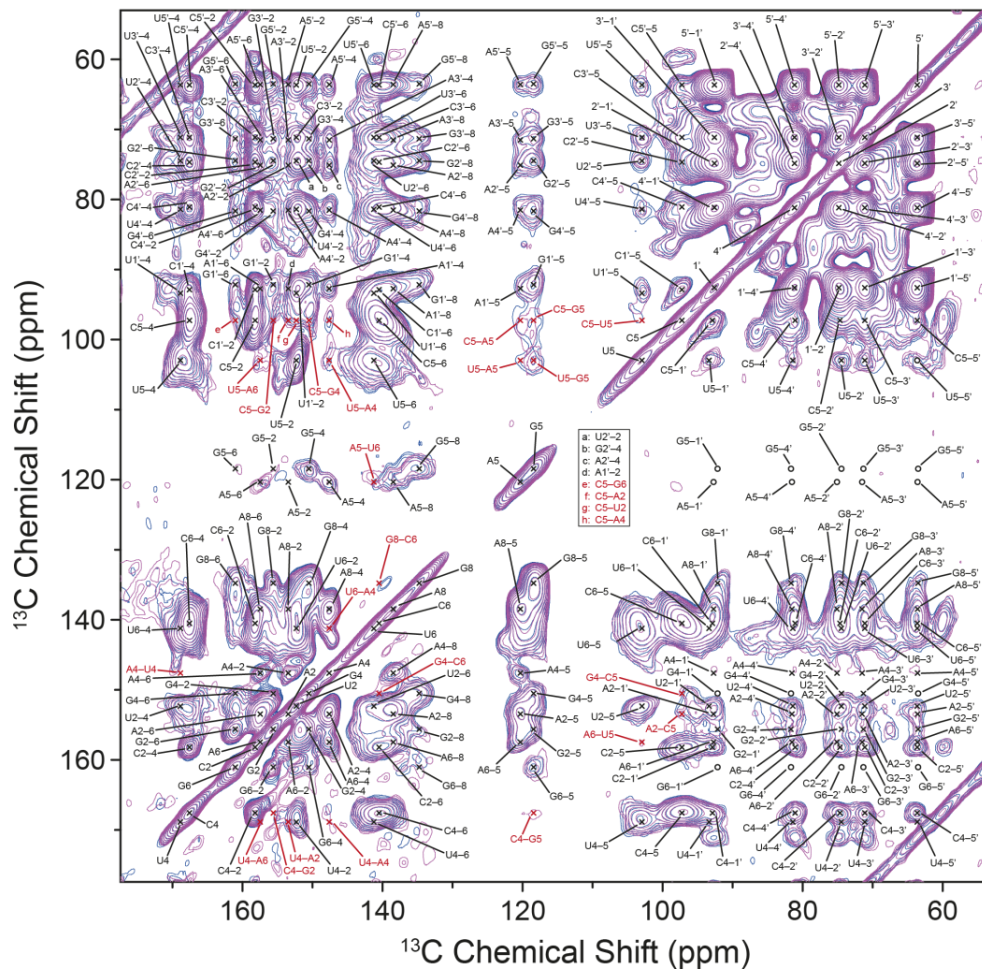
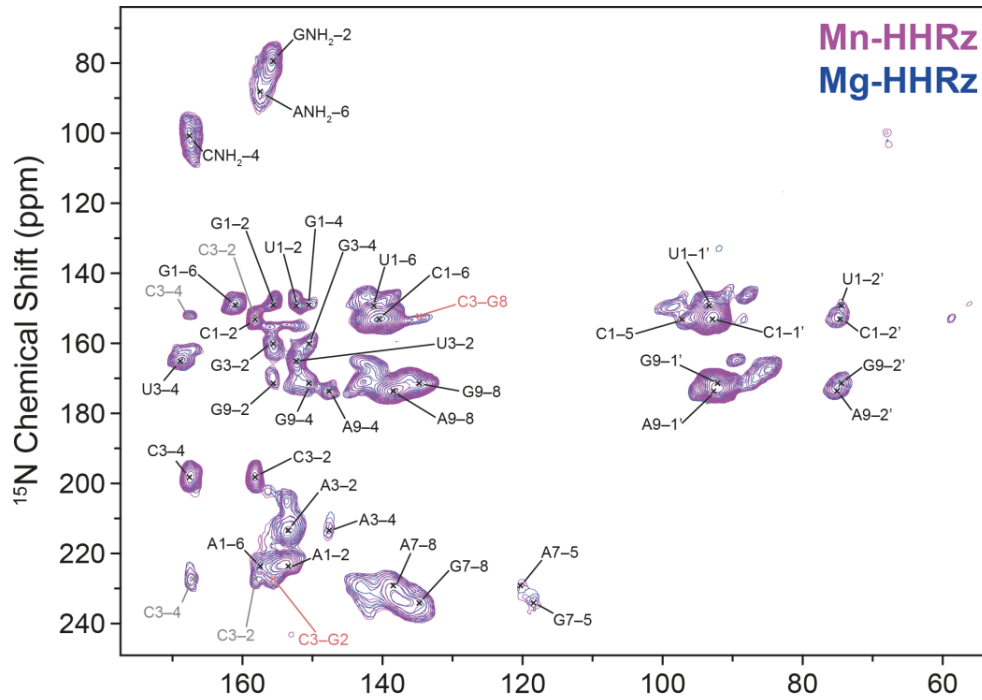


**Figure S9 (previous page).** Nucleotide-type specific resonance assignments of  $^{15}\text{N}$ - $^{13}\text{C}$  TEDOR (top) and  $^{13}\text{C}$ - $^{13}\text{C}$  PDSD (bottom) correlation spectra. For simplicity only nucleotide type (i.e. A, G, C, U) and atom number (1-9 for nucleobase and 1'-5' for ribose) are used for labeling. Amines are labeled as such ( $\text{NH}_2$ ); nucleus type (C or N) has been omitted. For atom numbering see Fig. S8. Tentative inter-nucleotide contacts are labeled in red; correlations of alternative conformations are labeled with gray or light red.

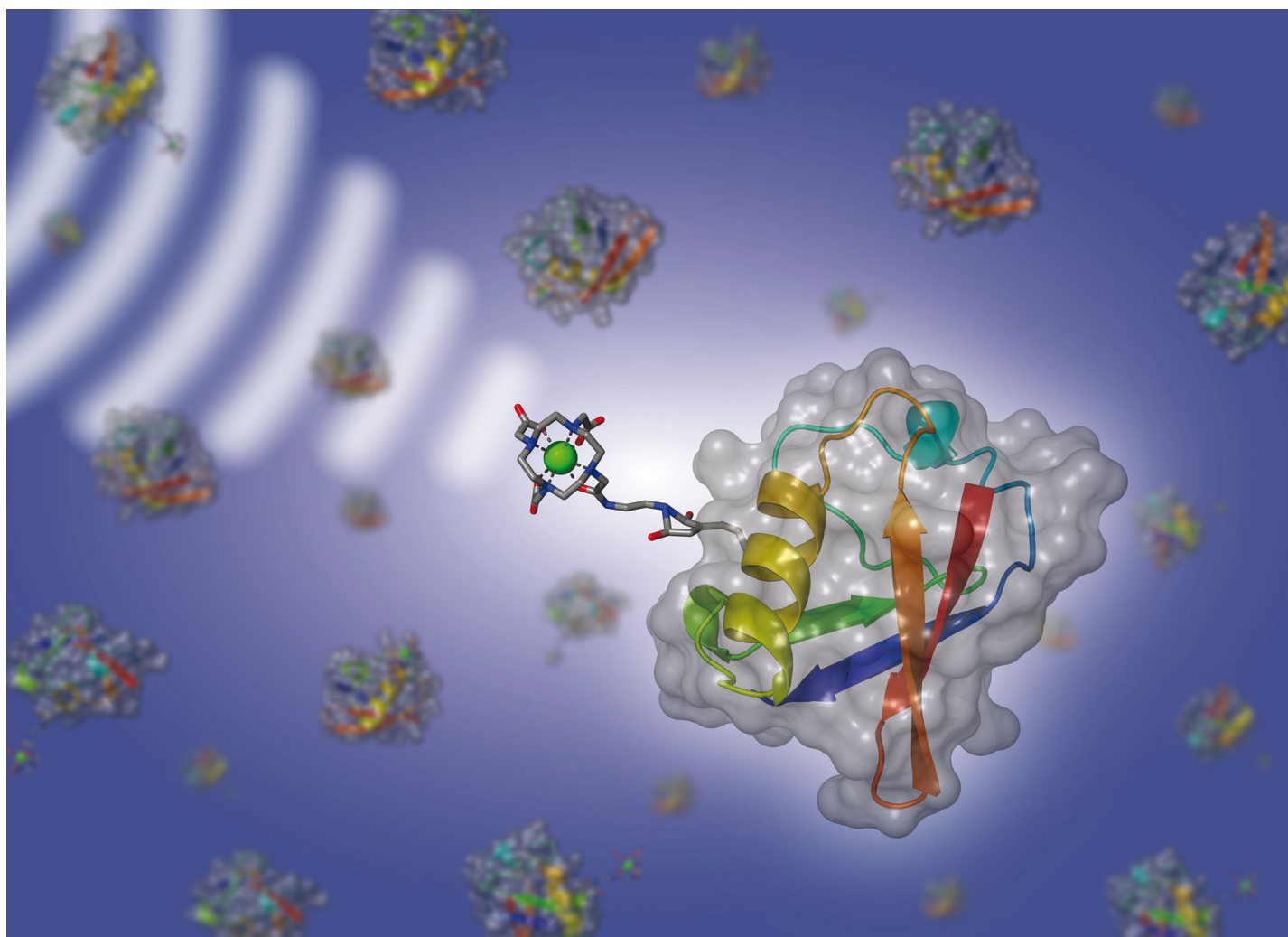
**Table S2.** Matrix representation of observed and assigned  $^{13}\text{C}$ - $^{13}\text{C}$  correlation peaks. Columns and rows represent direct and indirect dimensions (i.e. horizontal and vertical frequency axes) of the PDSD experiment.

	C2	C4	C5	C6	U2	U4	U5	U6	G2	G4	G5	G6	G8	A2	A4	A5	A6	A8	1'	2'	3'	4'	5'
C2	<b>X</b>	X	X	X															X	X	X	X	X
C4	X	<b>X</b>	X	X					X		X								X	X	X	X	X
C5	X	X	<b>X</b>	X	X		X		X	X	X	X		X	X	X			X	X	X	X	X
C6	X	X	X	<b>X</b>															X	X	X	X	X
U2					<b>X</b>	X	X	X											X	X	X	X	X
U4					X	<b>X</b>	X	X						X	X		X		X	X	X	X	X
U5					X	X	<b>X</b>	X			X				X	X	X		X	X	X	X	X
U6					X	X	X	<b>X</b>							X				X	X	X	X	X
G2									<b>X</b>	X	X	X	X						X	X	X	X	X
G4			X	X					X	<b>X</b>	X	X	X							X	X		
G5									X	X	<b>X</b>	X	X										
G6									X	X	X	<b>X</b>	X										
G8				X					X	X	X	X	<b>X</b>						X	X	X	X	X
A2			X											<b>X</b>	X	X	X	X	X	X	X	X	X
A4						X								X	<b>X</b>	X	X	X	X	X	X	X	X
A5								X						X	X	<b>X</b>	X	X					
A6							X							X	X	X	<b>X</b>	X	X	X	X	X	X
A8														X	X	X	X	<b>X</b>	X	X	X	X	X
1'	X	X	X	X	X	X	X	X	X	X	X	X	X	X	X	X	X	X	<b>X</b>	X	X	X	X
2'	X	X	X	X	X	X	X	X	X	X	X	X	X	X	X	X	X	X	X	X	<b>X</b>	X	X
3'	X	X	X	X	X	X	X	X	X	X	X	X	X	X	X	X	X	X	X	X	X	<b>X</b>	X
4'	X	X	X	X	X	X	X	X	X	X	X	X	X	X	X	X	X	X	X	X	X	X	<b>X</b>
5'	X	X	X	X	X	X	X	X	X	X	X	X	X	X	X	X	X	X	X	X	X	X	<b>X</b>

## References

- [1] M. Rohrer, O. Brüggmann, B. Kinzer, T. F. Prisner, *Appl. Magn. Reson.* **2001**, *21*, 257-274.
- [2] a) T. E. Horton, D. R. Clardy, V. J. DeRose, *Biochemistry* **1998**, *37*, 18094-18101; b) O. Schiemann, J. Fritscher, N. Kisseleva, S. T. Sigurdsson, T. F. Prisner, *ChemBioChem* **2003**, *4*, 1057-1065.
- [3] S. Stoll, A. Schweiger, *J. Magn. Reson.* **2006**, *178*, 42-55.
- [4] D. Shimon, Y. Hovav, A. Feintuch, D. Goldfarb, S. Vega, *Phys. Chem. Chem. Phys.* **2012**, *14*, 5729-5743.





Showcasing work from the laboratories of Dr Björn Corzilius and collaborators at Goethe University Frankfurt and Massachusetts Institute of Technology.

Title: Gd(III) and Mn(II) complexes for dynamic nuclear polarization: small molecular chelate polarizing agents and applications with site-directed spin labeling of proteins

In this work paramagnetic ions of Gd(III) and Mn(II) are investigated as polarizing agents for sensitivity enhancement of solid-state magic-angle spinning (MAS) NMR by dynamic nuclear polarization (DNP). Signal enhancement factors of up to 136-fold are reported at a magnetic field of 9.4 T. Chelate complexes of these ions can be dissolved in the sample, or can be attached to proteins for targeted DNP as is shown in the above illustration for ubiquitin. The paper investigates several experimental scenarios and is accompanied by a detailed theoretical derivation of the underlying mechanisms (B. Corzilius, *Phys. Chem. Chem. Phys.*, 2016, DOI: 10.1039/c6cp04621e).

As featured in:



See Björn Corzilius et al.,  
*Phys. Chem. Chem. Phys.*,  
2016, **18**, 27205.



[www.rsc.org/pccp](http://www.rsc.org/pccp)

Registered charity number: 207890


 Cite this: *Phys. Chem. Chem. Phys.*,  
2016, 18, 27205

# Gd(III) and Mn(II) complexes for dynamic nuclear polarization: small molecular chelate polarizing agents and applications with site-directed spin labeling of proteins†

 Monu Kaushik,<sup>ab</sup> Thorsten Bahrenberg,<sup>‡ab</sup> Thach V. Can,<sup>c</sup> Marc A. Caporini,<sup>§d</sup>  
Robert Silvers,<sup>bce</sup> Jörg Heiliger,<sup>ab</sup> Albert A. Smith,<sup>¶c</sup> Harald Schwalbe,<sup>be</sup>  
Robert G. Griffin<sup>c</sup> and Björn Corzilius<sup>\*abc</sup>

We investigate complexes of two paramagnetic metal ions Gd<sup>3+</sup> and Mn<sup>2+</sup> to serve as polarizing agents for solid-state dynamic nuclear polarization (DNP) of <sup>1</sup>H, <sup>13</sup>C, and <sup>15</sup>N at magnetic fields of 5, 9.4, and 14.1 T. Both ions are half-integer high-spin systems with a zero-field splitting and therefore exhibit a broadening of the  $m_s = -1/2 \leftrightarrow +1/2$  central transition which scales inversely with the external field strength. We investigate experimentally the influence of the chelator molecule, strong hyperfine coupling to the metal nucleus, and deuteration of the bulk matrix on DNP properties. At small Gd-DOTA concentrations the narrow central transition allows us to polarize nuclei with small gyromagnetic ratio such as <sup>13</sup>C and even <sup>15</sup>N via the solid effect. We demonstrate that enhancements observed are limited by the available microwave power and that large enhancement factors of >100 (for <sup>1</sup>H) and on the order of 1000 (for <sup>13</sup>C) can be achieved in the saturation limit even at 80 K. At larger Gd(III) concentrations (≥10 mM) where dipolar couplings between two neighboring Gd<sup>3+</sup> complexes become substantial a transition towards cross effect as dominating DNP mechanism is observed. Furthermore, the slow spin-diffusion between <sup>13</sup>C and <sup>15</sup>N, respectively, allows for temporally resolved observation of enhanced polarization spreading from nuclei close to the paramagnetic ion towards nuclei further removed. Subsequently, we present preliminary DNP experiments on ubiquitin by site-directed spin-labeling with Gd<sup>3+</sup> chelator tags. The results hold promise towards applications of such paramagnetically labeled proteins for DNP applications in biophysical chemistry and/or structural biology.

 Received 2nd July 2016,  
Accepted 12th August 2016

DOI: 10.1039/c6cp04623a

www.rsc.org/pccp

## Introduction

### Dynamic nuclear polarization

Over the last two decades high field dynamic nuclear polarization (DNP) has emerged as a prominent field of research and has impacted approaches to solution NMR, solid-state or magic-angle spinning (MAS) NMR, electron paramagnetic resonance (EPR), and magnetic resonance imaging (MRI). Furthermore, DNP has spawned fundamental investigations and new applications in each of these areas. For example, the development of the instrumentation for MAS DNP at high magnetic fields<sup>1–4</sup> has catalyzed fundamental studies of quantum mechanical properties of spin-systems,<sup>5–14</sup> applications in materials science<sup>15–20</sup> and structural biology.<sup>21–30</sup>

### DNP polarizing agents and field profiles

Paramagnetic species act as polarizing agents by transferring the large electron spin polarization to nuclear spins upon irradiation with microwaves ( $\mu\text{w}$ ) of an appropriate frequency.

<sup>a</sup> Institute of Physical and Theoretical Chemistry and Institute of Biophysical Chemistry, Goethe University Frankfurt, Max-von-Laue-Str. 7-9, 60438 Frankfurt am Main, Germany. E-mail: corzilius@em.uni-frankfurt.de

<sup>b</sup> Center for Biomolecular Magnetic Resonance (BMRZ), Goethe University Frankfurt, Max-von-Laue-Str. 9, 60438 Frankfurt am Main, Germany

<sup>c</sup> Francis Bitter Magnet Laboratory and Department of Chemistry, Massachusetts Institute of Technology, 77 Massachusetts Avenue, Cambridge, Massachusetts 02139, USA

<sup>d</sup> Bruker Biospin Ltd., Billerica, Massachusetts 01821, USA

<sup>e</sup> Institute of Organic Chemistry and Chemical Biology, Goethe University Frankfurt, Max-von-Laue-Str. 7, 60438 Frankfurt am Main, Germany

† Electronic supplementary information (ESI) available. See DOI: 10.1039/c6cp04623a

‡ Present address: Department of Chemical Physics, Weizmann Institute of Science, 76100 Rehovot, Israel.

§ Present address: Amgen, Inc., 360 Binney Street, Cambridge, Massachusetts 02142, USA.

¶ Present address: Department of Chemistry and Applied Biosciences, Laboratory of Physical Chemistry, ETH-Zürich, CH-8093 Zürich, Switzerland.



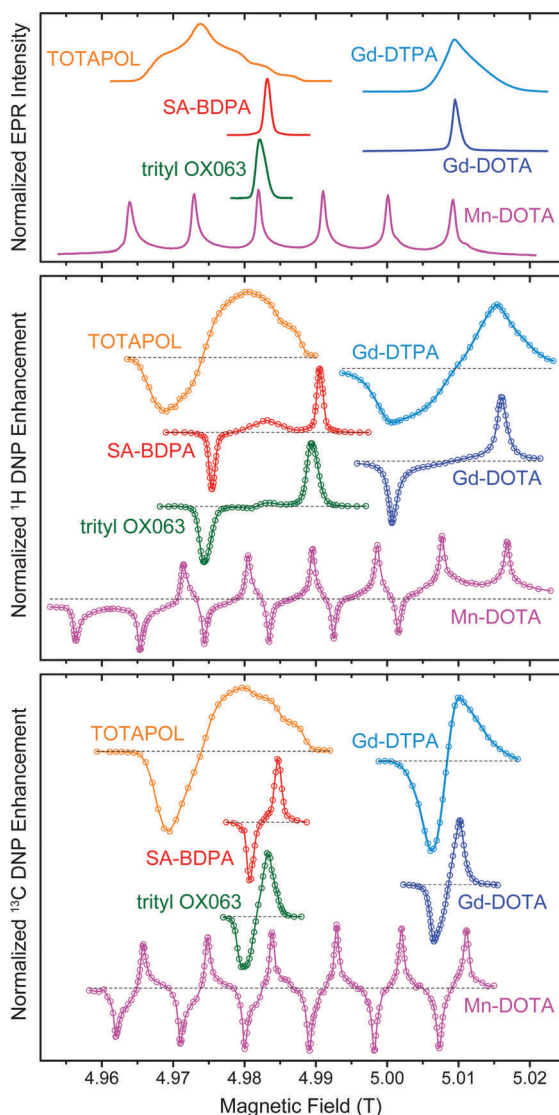


Fig. 1 EPR spectra (top) as well as field-dependent  $^1\text{H}$  (middle) and  $^{13}\text{C}$  (bottom) DNP profiles of various polarizing agents at 140 GHz  $\mu\text{w}$  frequency. TOTAPOL DNP data taken from ref. 32 ( $^1\text{H}$ ) and 33 ( $^{13}\text{C}$ ). SA-BDPA and trityl OX063 data from ref. 34 and 35, respectively, except  $^{13}\text{C}$  DNP profiles which were taken from ref. 36. Gd(III) and Mn(II) EPR spectra taken from ref. 37; DNP data from this work.

Microwave radiation is generated by either a solid-state source or—in the case of MAS DNP—by a gyrotron maser source due to the high power requirement in the absence of a  $\mu\text{w}$  resonance structure.<sup>31</sup> Since gyrotrons typically emit a fixed, narrow-band frequency the NMR magnetic field has to be adjusted if polarizing agents with varying EPR resonance fields are to be used or investigated.

In Fig. 1 we give an overview of several polarizing agents representing different classes of paramagnetic substances. TOTAPOL<sup>32</sup> is one of the most prominent examples of bis-nitroxide biradicals<sup>38,39</sup> which allow for efficient cross effect (CE) DNP of  $^1\text{H}$  and  $^{13}\text{C}$ .<sup>33</sup> Trityl OX063<sup>40</sup> and SA-BDPA<sup>34</sup> are water-soluble, persistent organic (carbon-based) radicals with rather narrow EPR resonances. At 5 T the linewidth of trityl ( $\sim 50$  MHz)

only allows for the solid effect (SE) of  $^1\text{H}$  with 212 MHz Larmor frequency,<sup>35,41</sup> while the smaller frequency of  $^{13}\text{C}$  (53 MHz) leads to efficient CE.<sup>7,36</sup> For SA-BDPA with 28 MHz linewidth both nuclei can only be polarized *via* the SE.<sup>34,36</sup> Paramagnetic metal complexes of  $\text{Gd}^{3+}$  and  $\text{Mn}^{2+}$  have been demonstrated as polarizing agents for  $^1\text{H}$  DNP earlier;<sup>37</sup> recently we have shown that  $\text{Mn}^{2+}$  naturally bound to RNA can be used to hyperpolarize  $^{13}\text{C}$  within a nucleic acid complex.<sup>42</sup> Even though the enhancement factors cannot compete quantitatively with the highly efficient bis-nitroxides, the natural occurrence in metalloproteins—in the case of  $\text{Mn}^{2+}$ —or the possibility to replace diamagnetic metal ions such as  $\text{Mg}^{2+}$  or  $\text{Ca}^{2+}$  make these high-spin metal ions interesting targets for further research.

### DNP with intrinsic polarizing agents

One aspect that has become of particular interest is the incorporation of polarizing agent with respect to the analyte. In “conventional” studies the polarizing agent—consisting of a paramagnetic molecule and providing the large electron polarization to be transferred to the nuclear spins—is dissolved in a cryoprotecting matrix. The matrix is highly deuterated with reduced proton abundance of  $\sim 10\%$  in order to optimize signal enhancement factors and transfer of enhanced polarization to the analyte *via* spin-diffusion.<sup>43</sup> This method has been successfully applied to several biological sample systems, including membrane proteins in native phospholipid environments as well as liposomes,<sup>22,26,44,45</sup> and dispersed micro/nano-crystalline proteins and peptides or amyloid fibrils.<sup>25,46–48</sup> A similar approach is used for microcrystalline materials<sup>49</sup> or by impregnation wetting of insoluble materials with polarizing agent solutions for surface-enhanced NMR spectroscopy.<sup>17</sup>

Immobilized paramagnetic species being covalently or non-covalently bound to or near the biomolecule to be investigated have recently attracted interest. In a first and elegant demonstration an endogenous flavin in its reduced semiquinone radical form has been used to polarize  $^1\text{H}$  within the protein.<sup>50</sup> Besides circumventing the addition of a solvent matrix and potential phase separation,<sup>51–54</sup> this approach is also aimed towards more efficient utilization of enhanced nuclear polarization near the site of interest at high magnetic field and fast MAS where spin-diffusion efficiency is limited,<sup>55</sup> and towards further structural insights by analysis of site- or state-specific DNP enhancement.<sup>56,57</sup> Furthermore, we have shown that endogenously bound, diamagnetic metal ions can be substituted with paramagnetic analogs in order to allow for DNP of ribonucleic acids.<sup>42</sup>

### Paramagnetic metal chelates in magnetic resonance

Gd(III) and Mn(II) chelate complexes are currently in the focus of several magnetic resonance techniques, including their use as efficient contrast agents in magnetic resonance imaging (MRI).<sup>58–61</sup> Spin labels based on Gd(III) have been demonstrated for distance measurements by dipolar EPR spectroscopy.<sup>62–69</sup> Additionally, both  $\text{Mn}^{2+}$  and  $\text{Gd}^{3+}$  have been used to study metal binding to biomolecules by paramagnetic relaxation enhancement of nuclear spins in solution NMR.<sup>70,71</sup> Similarly both ions





have been artificially attached to proteins by site-directed spin labeling with chelators for determination of structural constraints;<sup>72,73</sup> such applications have been demonstrated for magic-angle spinning (MAS) NMR as well.<sup>74,75</sup> Additionally, covalent labeling with Mn(II) or Gd(III) chelates allows for distance measurements by dipolar EPR spectroscopy.<sup>62,63,65,68,69</sup> Due to their chemical stability under redox-active conditions these complexes have proven extremely interesting for the investigation of in-cell EPR spectroscopy,<sup>67</sup> where nitroxide radicals suffer from chemical inactivation<sup>76,77</sup> and in-cell applications demand additional precautions.<sup>78,79</sup> Given these prospects in combination with the ubiquitous use of lanthanide chelate tags in NMR and the large availability of respective labeling techniques<sup>80</sup> we have earlier investigated the use of Mn(II) and Gd(III) chelate model compounds as polarizing agents for sensitivity-enhanced MAS NMR using dynamic nuclear polarization (DNP) of <sup>1</sup>H at a field of 5 T.<sup>37</sup> Here, we want to extend this investigation to fields of 9.4 T and up to 14.1 T. Furthermore, we focus on direct DNP of low- $\gamma$  nuclei <sup>13</sup>C and <sup>15</sup>N for which slower spin-diffusion might enable a site-selective DNP enhancement of resonances in biomolecules which contain a specifically-bound metal polarizing agent. Preliminary experiments obtained with chelator-labeled and uniformly isotope labeled ubiquitin yield promising results.

## Theory

### DNP mechanisms

Under the conditions relevant here DNP can occur *via* two different mechanisms: solid effect (SE) and cross effect (CE). SE enhancements are driven directly by  $\mu$ w excitation of nominally forbidden zero quantum (ZQ) and double quantum (DQ) electron–nuclear coherences.<sup>81</sup> Anisotropic hyperfine interaction (HFI) leads to partial state mixing of the nuclear substates; the respective ZQ and DQ SE matching conditions occur at the sum or difference combinations of the electron and nuclear Larmor frequencies. Due to the ZQ and DQ transitions leading to opposite nuclear enhancement and cancellation of the SE when excited equally, the polarizing agent has to feature a narrow EPR spectrum with an effective overall breadth smaller than the nuclear Larmor frequency.

The CE occurs when two electron spins are dipolar coupled. Upon  $\mu$ w saturation of one of the spins their polarization difference can be transferred to a coupled nuclear spin if the Larmor frequencies of the electron spins differ by the nuclear Larmor frequency:  $\Delta\omega_{0S} = \omega_{0r}$ .<sup>82</sup> In this case an energy-conserving three-spin flip–flop–flip process can occur. This process has been shown to be highly efficient for bis-nitroxide polarizing agents under MAS, where the variation in electron Larmor frequencies is achieved by significant  $g$  anisotropy, and the spin eigenstates undergo several level crossings during one sample rotational period.<sup>12,13</sup>

In the preceding article we have described the theoretical background in detail and have developed a model for CE with high-spin electrons with isotropic electron Zeeman interaction and significant ZFS such as Gd(III) and Mn(II).<sup>83</sup> We strongly

encourage the reader to refer to this work for theoretical background as basis of discussion of the experiments described here.

### Magnetic properties of Gd(III) and Mn(II)

The high-spin states of Gd(III) and Mn(II) lead to several peculiar properties which can be either advantageous or detrimental for applications in magnetic resonance. We have described these properties in detail in the preceding article;<sup>83</sup> nevertheless we want to briefly summarize these here. Even though the electron Zeeman interaction is isotropic with a  $g$  value close to that of the free electron the  $S = 7/2$  and  $S = 5/2$  states of Gd(III) and Mn(II), respectively, are subject to zero-field splitting (ZFS) most commonly caused by non-cubic ligand environment. In typical complexes this leads to an anisotropic broadening of the satellite transitions (ST)—where  $m_S$  changes its absolute value—by up to several GHz in total breadth. Due to the half-integer spin state a narrow central transition (CT)—where  $|m_S|$  is conserved—is observed which is not affected by ZFS in first-order; however, a second-order broadening occurs if the ZFS parameters are of significant magnitude with respect to the Zeeman splitting. Furthermore, Mn(II) underlies strong isotropic hyperfine interaction (HFI) to its core <sup>55</sup>Mn nucleus ( $I = 5/2$ ) with typical coupling constants  $\sim 250$  MHz, leading to a characteristic sextet pattern in EPR spectra. For Gd(III) small HFI to the minority magnetic nuclei <sup>157</sup>Gd and <sup>159</sup>Gd (both  $I = 3/2$  and 15% abundance each) can be neglected in most cases.

## Experimental

### EPR

Pulsed EPR spectra at 140 GHz and 275 GHz have been recorded using custom-built EPR spectrometers at a temperature of 80 K. Spectra were acquired by recording the field-swept intensity of a Hahn-echo of frozen solutions of each polarizing agent in 1 mM concentration in D<sub>8</sub>-glycerol/D<sub>2</sub>O (60/40 vol%) mixture. Detailed descriptions of the instruments can be found elsewhere.<sup>84–86</sup>

Continuous-wave EPR spectra of Gd(III)-labeled protein (see below) have been recorded using a Bruker EleXsys E780 spectrometer operating at 263 GHz and utilizing a sweepable Bruker Ascent DNP magnet (89 mm) centered at 9.40 T and contained a superconducting sweep coil with a nominal range of  $\pm 75$  mT. The Bruker magnet power supply is remotely controlled by the Bruker Xepr software used for data acquisition. The spin-labeled proteins were dissolved at concentrations between 2 and 4 mM in a D<sub>8</sub>-glycerol/D<sub>2</sub>O/H<sub>2</sub>O (60/30/10 vol%) mixture, packed into 0.2 mm (i.d.) clear fused quartz capillaries and frozen inside a custom-built TE<sub>011</sub> resonator. Experiments were performed at a temperature of 100 K inside an Oxford instruments flow cryostat using liquid Helium as cryogen. For detailed set of parameters see ESI.†

### DNP at 5 T (140 GHz)

DNP experiments at 5 T were performed on samples containing 10 mM Gd-DOTA (Macrocyclics, Dallas, TX), Gd-DTPA (gracious gift of E. Ravera and C. Luchinat, Florence), or GdCl<sub>3</sub> (Sigma-Aldrich,



St. Louis, MO) in a  $^{13}\text{C}_3$ -glycerol/ $\text{H}_2\text{O}$  (60/40 vol%) or a  $[\text{D}_8, ^{13}\text{C}_3]$ -glycerol/ $\text{D}_2\text{O}/\text{H}_2\text{O}$  (60/30/10 vol%) mixture.  $^{13}\text{C}$ -labeled glycerol was purchased from Cambridge Isotope Laboratories (Tewksbury, MA). All compounds were used as received without further purification. The custom-built spectrometer operating at 213 MHz  $^1\text{H}$  frequency is courtesy of D. Ruben. A custom-built MAS NMR probe was utilized which features a triple resonance rf circuit ( $^1\text{H}$ ,  $^{13}\text{C}$ ,  $^{15}\text{N}$ ) and efficient microwave coupling to the sample using overmoded corrugated waveguides (similar to a design published by Barnes *et al.*<sup>87</sup>). The probe was also equipped with a cryogenic sample exchange system. Microwaves were generated using a custom-built gyrotron oscillator operating at 139.65 GHz with a maximum output power of  $\sim 13$  W.<sup>2,31,88</sup> Sample temperature was measured *via* a fiber optical sensor (Neoptix, Québec City, Canada) outside the MAS stator and was maintained at about 84 K. Experiments were performed using a MAS frequency of  $\omega_r/2\pi = 5$  kHz. A detailed description of experiments is given in the ESI.†

### DNP at 9.4 T (263 GHz) and above

The comparison of  $^1\text{H}$  DNP at 9.4 T and 14.1 T was performed at Bruker BioSpin (Billerica, MA) on two different DNP/NMR spectrometers operating at 400 MHz/263 GHz and 600 MHz/395 GHz, respectively. The sample contained 10 mM Gd-DOTA and 100 mM [ $^{13}\text{C}$ ,  $^{15}\text{N}$ ]-proline dissolved in  $\text{D}_8$ -glycerol/ $\text{D}_2\text{O}/\text{H}_2\text{O}$  (60/30/10 vol%). The spectrometers are equipped with 3.2 mm H-X probes of which the X channels are tuned to  $^{13}\text{C}$ . The  $^{13}\text{C}$  NMR signals of proline were measured by CP pulse sequence with a pre-saturation period. The temperature of the sample was  $\sim 90$  K without microwave and  $\sim 100$  K with  $\sim 15$  W of microwave. The sample was spun at  $\omega_r/2\pi = 12.5$  kHz.

All other DNP experiments at 9.4 T were performed using a commercially available Bruker AVANCE III DNP spectrometer operating at 401.7 MHz  $^1\text{H}$  frequency. 2 M [ $^{13}\text{C}$ ,  $^{15}\text{N}_2$ ]-urea (CortecNet) was dissolved in a glass forming solvent of [ $\text{D}_8, ^{12}\text{C}_3$ ]-glycerol/ $\text{H}_2\text{O}$  (60/40 vol%). The glycerol depleted in  $^{13}\text{C}$  (99.95%  $^{12}\text{C}$ ) was purchased from Euriso-Top. Gd-DOTA- $\text{NH}_3$  (gracious gift of J. Plackmeyer, Frankfurt) was used as polarizing agent in concentrations of 2 mM, 10 mM and 20 mM. All compounds were used as purchased without further purification. A Bruker gyrotron yielding 263.4 GHz microwaves, operating at the maximum beam current of 115 mA was used.  $^1\text{H}$  enhancement was recorded using cross-polarization to  $^{13}\text{C}$ . Direct  $^{13}\text{C}$  and  $^{15}\text{N}$  enhancements were measured using Bloch decay. Microwave on and off experiments were performed at 114 K and 105 K respectively; this temperature was measured outside the stator. Sample heating due to  $\mu\text{W}$  irradiation was not quantified or controlled for. MAS of 8 kHz was employed. For further information see ESI.†

### Protein expression and labeling

A detailed description of protein expression, purification, and labeling is given in the ESI.† 4-Mercaptomethyl dipicolinic acid (4MMDPA) has been synthesized following the procedure published by Potapov *et al.*;<sup>63</sup> 1,4,7,10-tetraazacyclododecane-1,4,7-tris-acetic acid-10-maleimidoethylacetamide (DOTA-M) was

purchased from Macrocyclics, Inc. (Plano, TX). After recombinant expression, purification, labeling, and concentration, the uniformly [ $^{13}\text{C}$ ,  $^{15}\text{N}$ ]-labeled protein was transferred to an  $\text{NH}_4\text{OAc}$  buffer (pH = 7.0) for DNP with a final concentration of  $\sim 1$  mM ubiquitin in 60% (v/v) [ $\text{D}_8, ^{12}\text{C}_3$ ]-glycerol, 36%  $\text{D}_2\text{O}$ , and 4%  $\text{H}_2\text{O}$ . The labeling efficiency was quantified using cw spin-counting at X-band frequency at 80 K and was determined as  $\sim 90\%$  in the case of 4MMDPA and  $\sim 100\%$  for DOTA-M.

## Results and discussion

### EPR linewidth of the CT at different fields

With the introduction of several custom-built or commercially available DNP spectrometers operating at fields between 9.4 and 18.8 T considerable focus should be laid on the efficiency of polarizing agents with increasing fields. One important aspect in this context is the broadening of the EPR line and resulting excitation efficiency with a monochromatic microwave source.

In Fig. 2 we demonstrate the effect of increasing external magnetic field strength on the line shape of several polarizing agents with narrow EPR lines which have been utilized for SE at high field. While SA-BDPA shows no significant variation in linewidth between 140 GHz (5 T) and 275 GHz (9.8 T) due to negligible  $g$ -anisotropy and inhomogeneous broadening dominated by unresolved hyperfine couplings to  $^1\text{H}$ , the axially symmetric  $g$ -anisotropy of trityl leads to an increase of spectral

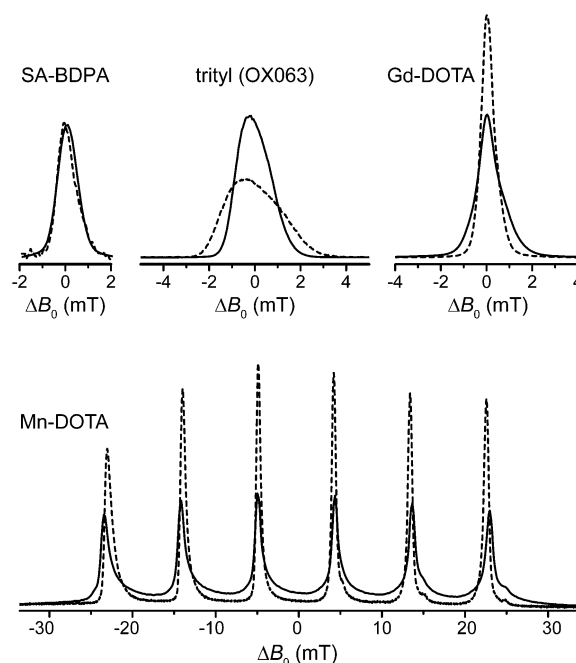


Fig. 2 140 GHz (solid lines) and 275 GHz (dashed lines) field-swept, echo-detected EPR spectra of SA-BDPA, trityl, Gd-DOTA, and Mn-DOTA demonstrating the narrowing of the high-spin CT at higher field. All spectra (except Mn-DOTA) were normalized to equal amplitude at 140 GHz. All 275 GHz spectra were scaled so that the respective integrals at the two frequencies are equal. Field offset in abscissa is given w.r.t. to the resonance field observed for the isotropic  $g$  value.



breadth proportional to the external field. The high-spin complexes of  $\text{Gd}^{3+}$  and  $\text{Mn}^{2+}$ , on the other hand, show an effective reduction in linewidth of the EPR CT with higher field which seems counterintuitive at first, but is explained by the occurrence of a second-order effect due to ZFS which scales inversely proportional with respect to the Zeeman strength. In the preceding article we have described in detail the unique properties of these high-spin metal ions regarding DNP;<sup>83</sup> here we will demonstrate these properties in DNP experiments performed on  $^1\text{H}$  and  $^{13}\text{C}$  at a field of 5 T. Further experiments conducted at high fields of 9.4 T and 14.1 T demonstrate the unique line-narrowing properties of Gd-DOTA and underline the potential of this class of polarizing agents under these high-field conditions, especially when compared to the efficiency of the SE with radical polarizing agents at these high field strengths.<sup>8</sup>

### Effect of different complex ligands on DNP

In Fig. 3 we compared several different chelate complexes of  $\text{Gd}^{3+}$  as polarizing agents for  $^1\text{H}$  and  $^{13}\text{C}$  DNP at 140 GHz, recorded at a  $\mu\text{W}$  power level of 6 W (at probe input). There is a clear correlation between EPR line width of each complex and induced DNP enhancement (given as relative difference in relation to thermal polarization, *i.e.*,  $\varepsilon - 1$ ) for  $^1\text{H}$  and  $^{13}\text{C}$ , see Table 1. While for Gd-DOTA and  $\text{GdCl}_3$  (the latter exists as an aquo complex in aqueous solution)<sup>89</sup> the positive and negative  $^1\text{H}$  SE legs are separated by a plateau area, they overlap for  $^{13}\text{C}$  even for the complex with the smallest linewidth due to mutual overlap of the ZQ and DQ electron-nuclear transitions. Interestingly, for  $\text{GdCl}_3$  two components with starkly different

Table 1 EPR and DNP properties of 10 mM Gd(III) complexes in  $^{13}\text{C}_3$ -glycerol/ $\text{H}_2\text{O}$  (60/40 vol%) at 5 T

Complex	ZFS parameters <sup>b</sup>			$\varepsilon_{\text{H}} - 1^a$	$\varepsilon_{\text{C}} - 1^a$
	$D$ (MHz)	$\Delta D$ (MHz)	EPR linewidth (MHz)		
Gd-DOTA	672	336	30 <sup>c</sup>	7.3 (−7.3)	44.0 (−38.5)
$\text{GdCl}_3^d$	784/2184 (1 : 2.8)	448/952	50 <sup>c</sup>	2.5 (−2.5)	16.5 (−14.5)
Gd-DTPA	1568	728	170 <sup>c</sup>	1.5 (−1.2)	6.0 (−8.5)

<sup>a</sup> Measured at  $\sim 6$  W  $\mu\text{W}$  power; values given at the field of max. positive enhancement, values in parentheses at field of max. magnitude of negative enhancement. <sup>b</sup> From ref. 90. <sup>c</sup> At 5 T, simulated from given ZFS parameters. <sup>d</sup> Two components contributing to the spectrum with relative weight given in parentheses.

ZFS parameters have been reported from EPR experiments.<sup>90</sup> We do not observe such a biphasic behavior; however, our observations only seem to show a contribution from the component with smaller  $D$  value. This might indicate that the complex species with large ZFS might not be effective as polarizing agent for DNP, or that its contribution to DNP is unproportionally small compared to the EPR contribution, as can also be seen by the  $\sim 3$ -fold reduction in enhancement w.r.t. Gd-DOTA while the apparent linewidth only increases by  $\sim 50\%$ .

$^{13}\text{C}$  enhancements are significant, with  $\sim 6$ – $7$  times larger values than for  $^1\text{H}$ . For Gd-DTPA this ratio is somewhat smaller, however, in this case the magnitude of the negative enhancement is larger than that of the positive leg, most probably due to complicated overlap of SE transitions and other mechanisms leading to opposing DNP effects. We did not detect any sign of solid-state Overhauser effect (OE) as has been reported on BDPA radicals.<sup>8,34</sup> Factors contributing to the OE in BDPA are the presence of significantly hyperfine-coupled  $^1\text{H}$  and slow spin-lattice relaxation of the electron spin, both of which are less favorable in  $\text{Gd}^{3+}$  complexes.

Experiments using Mn-DOTA reveal a very similar situation; the main difference being the splitting of the rather narrow CT into an almost equally spaced sextet caused by hyperfine coupling to  $^{55}\text{Mn}$  with a coupling constant of 254 MHz.<sup>37</sup> This leads to a complicated system of six individual SE features evoked by each EPR line as is shown in Fig. 4. For  $^1\text{H}$  these SE pairs are intricately intertwined due the  $^1\text{H}$  nuclear Zeeman frequency being larger than half the  $^{55}\text{Mn}$  HFI constant. For  $^{13}\text{C}$  we encounter the opposite situation and each EPR line's SE pair is individually resolved. Furthermore, the small EPR linewidth now allows for almost complete separation of positive and negative enhancement legs with little-to-none mutual cancellation. NMR intensity comparisons between  $\mu\text{W}$ -irradiation and non-irradiation allowed us to measure the enhancement factor for each EPR line (see red symbols in Fig. 4). Towards lower field slight deviations between the DNP-enhanced signal intensity and enhancement (obtained by on/off-comparison) occur which are due to lower efficiency of the spectrometer components (*i.e.*, preamplifiers, filters, *etc.*). Nevertheless, for  $^{13}\text{C}$  a symmetric variation of enhancement factors is observed which closely resembles the peak amplitude pattern of the EPR spectrum; for

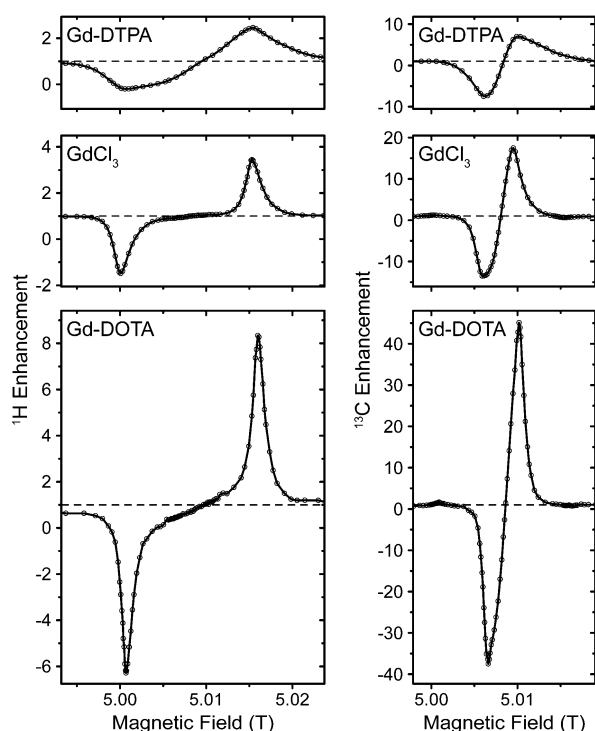


Fig. 3 Field dependent  $^1\text{H}$  and  $^{13}\text{C}$  DNP enhancement profiles of various Gd(III) complexes at 140 GHz.



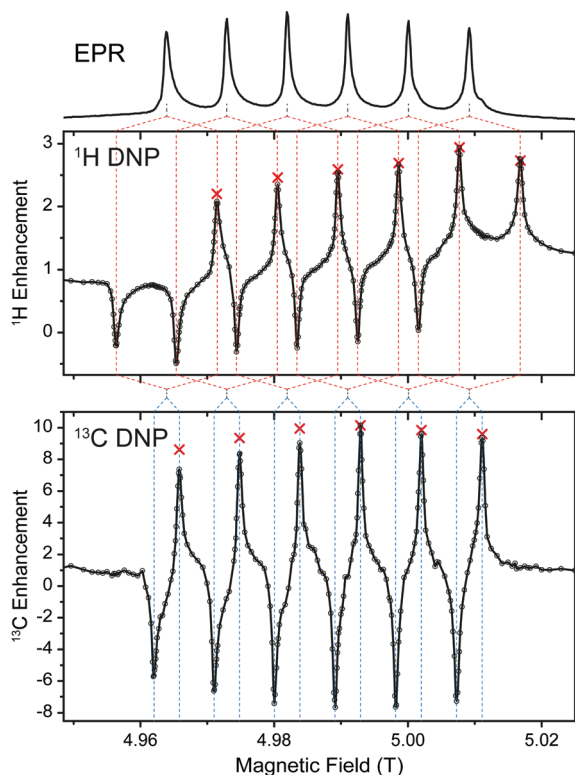


Fig. 4  $^1\text{H}$  (top graph) and  $^{13}\text{C}$  (bottom graph) DNP of  $^{13}\text{C}_3$ -glycerol/ $\text{H}_2\text{O}$  (60/40 vol%). Red crosses represent enhancement factors determined by explicit  $\mu\text{w}$  on vs.  $\mu\text{w}$  off measurements. Dashed lines serve as aides for correlation between EPR lines and DNP peaks.

$^1\text{H}$  slight overlap of SE conditions lead to an asymmetric variation with larger enhancements obtainable for the second-to-outermost lines. Destructive interference occurs when  $2\omega_{\text{OI}} = nA(^{55}\text{Mn})$ , where  $\omega_{\text{OI}}$  is the Larmor frequency of the nucleus to be enhanced,  $A(^{55}\text{Mn})$  is the isotropic hyperfine coupling constant to the metal nucleus and  $n$  is any integer between 1 and 5. In such a case a positive enhancement peak is canceled by a negative peak of another HFI peak; however, the  $n$  outermost (positive or negative) SE peaks are never canceled in such a way. Since peaks of equal sign cannot overlap, constructive interference of SE peaks is not possible. Nevertheless, when  $\omega_{\text{OI}} = nA(^{55}\text{Mn})$ , a ZQ/DQ peak can be on resonance with a SQ transition of another dipolar coupled  $\text{Mn}^{2+}$ . This situation might lead to efficient CE matching, for example at a magnetic field of 11.7 T (500 MHz), where  $\omega_{\text{OI}}(^1\text{H}) \approx 2A(^{55}\text{Mn})$ , and will be subject to further research.

### Influence of bulk protonation level

For Gd-DOTA we investigated the effect of solvent deuteration level on  $^{13}\text{C}$  DNP. Earlier studies have shown that slightly larger enhancement factors and faster polarization build-up can be achieved without matrix deuteration, in stark contrast to radical polarizing agents.<sup>35</sup> Here, we record a  $\sim 13\%$  larger enhancement of  $^{13}\text{C}$  for full protonation—with a maximum positive enhancement of 70—compared to 62 for typically utilized 12% protonation within “DNP juice” (*i.e.*, 60/30/10 vol% mixture of  $\text{D}_8$ -glycerol/ $\text{D}_2\text{O}/\text{H}_2\text{O}$ )

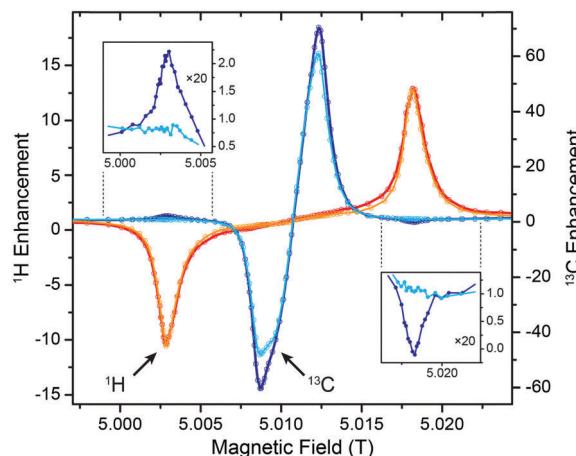


Fig. 5 Proton level dependence of  $^1\text{H}$  (red) and  $^{13}\text{C}$  (blue) DNP at 140 GHz using Gd-DOTA as polarizing agent. Darker profiles are recorded on  $^{13}\text{C}_3$ -glycerol/ $\text{H}_2\text{O}$  (60/40 vol%) as solvent, lighter profiles on  $[\text{D}_8, ^{13}\text{C}_3]$ -glycerol/ $\text{D}_2\text{O}/\text{H}_2\text{O}$  (60/30/10 vol%). The insets show 20-fold vertical magnifications of  $^{13}\text{C}$  enhancements in the respective field region where  $^1\text{H}$  SE condition is matched.

even though a slight broadening of the peaks within the field profile is visible (Fig. 5). This might be caused due to improved proton-driven spin diffusion and/or longer build-up and longitudinal relaxation time constants. A complete overview of  $^1\text{H}$  and  $^{13}\text{C}$  enhancements at various protonation levels can be found in the ESI† in Table S2.

An interesting effect occurs at the fields of most efficient (positive or negative)  $^1\text{H}$  enhancement. Here, we see a small, but significant  $^{13}\text{C}$  DNP enhancement of inverse sign with respect to  $^1\text{H}$ . The effect is observed with a fully protonated sample and does not occur with low  $^1\text{H}$  levels (see below and Fig. 5). Possible multi-spin flips, where  $^1\text{H}$  and  $^{13}\text{C}$  are excited at the same time are theoretically and experimentally expected, but would occur at offsets of nuclear combination frequencies with respect to the SQ (EPR) frequency.<sup>91,92</sup> We do not observe any splitting or shift of these features with respect to the  $^1\text{H}$  SE peaks. Therefore, we attribute this effect to heteronuclear cross relaxation.  $^1\text{H}$  populations—driven away from thermal equilibrium by SE DNP—may enhance  $^{13}\text{C}$  in a similar way to the classical nuclear Overhauser effect (NOE). Due to relaxation from a hyperpolarized state instead of simple saturation this would result in opposite sign of  $^{13}\text{C}$  enhancement with respect to that of  $^1\text{H}$ . Similar effects have been reported in samples after dissolution where molecular tumbling provides the required dynamics for relaxation.<sup>93</sup> In our case it is unclear which dynamical process enables this relaxation process in the solid. The reader should note that the effect is rather weak ( $\sim 2\%$  of maximum cross-relaxation enhancement); therefore even absolutely small variation of spectral density at the required sum and difference of nuclear Larmor frequencies might suffice for the observed effect to occur.

### Power dependence of DNP enhancement

The power dependence of DNP enhancements is perfectly linear in most cases, as seen in Table 2 and shown in Fig. S1 (ESI†).



Interestingly, the DNP efficiency which is given by polarization increase of the nucleus relative to the theoretical maximum is almost identical for  $^1\text{H}$  and  $^{13}\text{C}$ ; consequently enhancement factors scale inversely with the nuclear gyromagnetic factor.  $^{13}\text{C}$  DNP power dependence with Gd-DOTA shows a slight reduction of slope with larger power compared to the  $\text{Mn}^{2+}$  complex. The 'relayed' DNP enhancement of  $^{13}\text{C}$  caused by  $\mu\text{W}$  excitation at the field of  $^1\text{H}$  SE seems to indicate a more significant 'saturation' effect at larger powers, the reason for this is still unclear.

Also, a slight reduction of polarization time constant with increasing  $\mu\text{W}$  power is noticed (see Table 2). This trend is expected for SE,<sup>41</sup> and has been already observed for trityl on the same instrument where we have also experimentally excluded sample heating as the major cause.<sup>35</sup>

Furthermore, in order to assess the achievable DNP enhancement in the excess of  $\mu\text{W}$  field strength we have investigated a static sample inside a  $\mu\text{W}$  cavity resonator driven by low-power solid-state source. With this instrument a typical  $Q$  factors on the order of  $\sim 1000$  leads to an effective nutation frequency of  $\sim 16$  MHz for the CT of the  $S = 7/2$  spin; this allows for significant  $^1\text{H}$  DNP enhancement of  $>100$  as we have reported earlier.<sup>84</sup> Direct DNP of  $^{13}\text{C}$  under irradiation of the  $^{13}\text{C}$  SE transition leads to large absolute intensity of the enhanced NMR signal of  $^{13}\text{C}_3$ -glycerol, see Fig. S2 (ESI<sup>†</sup>). Due to the large  $\mu\text{W}$  field strength available we reach a near-saturation condition already at  $\sim 60\%$   $\mu\text{W}$  power; nevertheless a further reduction in polarization build-up time constant provides further sensitivity gains. A similar situation occurs for  $^1\text{H}$  DNP at lower temperature.<sup>84</sup> Unfortunately, we have been unable to measure the  $^{13}\text{C}$  enhancement factor because no signal could be observed without  $\mu\text{W}$  irradiation; analysis of the noise level allows us to provide a lower bound of  $\varepsilon$  of 400. For comparison we performed  $^{13}\text{C}$  CP experiment with  $^1\text{H}$  DNP enhancement (by irradiation at the  $^1\text{H}$  SE condition). We observe a 2.8-fold larger intensity of the direct polarization (DP) spectrum, indicating that the large, direct  $^{13}\text{C}$  SE enhancement easily overcompensates the up to 4-fold signal increase which can be achieved by  $^1\text{H}$  DNP and subsequent CP transfer to  $^{13}\text{C}$ . Reduced CP efficiency due to the inhomogeneously broadened resonances and the presence of the paramagnetic polarizing agent cannot completely be neglected. Nevertheless, considering the larger signal intensity of the non-DNP-enhanced CP spectrum with respect to the DP spectrum, it is clear that CP efficiency  $>1$ . We therefore conclude that for  $^{13}\text{C}$ ,  $\varepsilon \geq 400$ , with estimated factors of

800–1000 being much more likely. Enhancement factors of  $>700$  have been observed for 30 mM trityl solution by Banerjee *et al.* at 3.4 T but otherwise similar conditions.<sup>7</sup> Our observations indicate that very large enhancement factors can be observed with sufficient  $\mu\text{W}$  field strength which makes Gd-DOTA a promising target for further investigations under these conditions.

Reduction of temperature has been shown to be more favorable, leading to larger enhancement factors already with smaller  $\mu\text{W}$  power.<sup>84</sup> However, below a certain temperature (14 K at 5 T and increasing with larger fields) the depopulation of excited magnetic spin states of the  $S = 7/2$  system leads to reduced absolute population difference of the CT, rendering high-spin systems inactive as polarizing agents at low temperatures where  $k_{\text{B}}T < \gamma B_0$ . This situation could be alleviated by the employment of sophisticated adiabatic sweep or pulse schemes which are able to transfer population from the highly polarized ground state transition into the DNP-enabling CT.<sup>10,94</sup>

### Field dependence of $^1\text{H}$ DNP

5 T is an ideal testbed for DNP experiments due to its instrumental robustness in terms of magnet sweep capability and  $\mu\text{W}$  power availability in combination with rather straightforward scalability of results to higher fields. Nevertheless, experiments at the commercially accessible fields of 9.4 and 14.1 T are important to confirm predictions based on lower field experiments and might also yield unexpected observations. Therefore we conducted  $^1\text{H}$  DNP experiments using Gd-DOTA at these fields (Fig. 6). As expected, the matching field offset for positive and negative SE enhancement scale with the nuclear Larmor frequency and become more separated at higher field. Additionally, slight reduction in linewidth of the DNP peaks is observed with larger external field. This narrowing manifests when comparing the field dependence with that reported for BDPA,<sup>8</sup> where at 9.4 T a slightly larger  $\varepsilon$  was observed than for Gd-DOTA, however, at 14.1 T this ratio is inverse. Therefore we expect, that Gd-DOTA would significantly outperform BDPA at 18.8 T (reaching only vanishing  $\varepsilon \approx 2$ ).

The narrowing is less pronounced than would be expected from the  $B_0^{-1}$  dependence of the second-order ZFS. In fact a considerable amount of dipolar broadening of the Gd(III) EPR spectrum occurs within the 10 mM Gd-DOTA solution; when comparing DNP peak widths we found a reduction from 34.0 (30.8) MHz to 22.6 (22.0) MHz at 9.4 (14.1) T by lowering the Gd-DOTA concentration from 10 to 1 mM; we discuss this

**Table 2** DNP properties of 10 mM Gd-DOTA in  $^{13}\text{C}_3$ -glycerol/water (60/40 vol%) at various  $^1\text{H}$  concentrations at 5 T (140 GHz)

Solvent $\text{D}_8\text{-glyc.}/\text{H}_8\text{-glyc.} + \text{D}_2\text{O}/\text{H}_2\text{O}$ (vol%)	$^1\text{H}$ conc. (mol L <sup>-1</sup> )	$^1\text{H}$ ratio (%)	$\varepsilon^{(\text{H})}$ 5/9/14 W	$T_1^{(\text{H})}$ (s) no $\mu\text{W}$	$T_B^{(\text{H})}$ (s) 5/9/14 W	$\varepsilon^{(\text{C})a}$ 5/9/14 W	$T_1^{(\text{C})}$ (s) no $\mu\text{W}$	$T_B^{(\text{H})}$ (s) 5/9/14 W
0/60 + 0/40	111.9 <sup>a</sup>	100	8/13/19	3.2	3.1/3.0/2.8	45/71/103	86	85/83/80
0/60 + 40/0	66.3 <sup>a</sup>	59	—/—/— <sup>b</sup>	— <sup>b</sup>	—/—/— <sup>b</sup>	40/61/89	82	82/81/78
60/0 + 0/40	47.2 <sup>a</sup>	42	—/—/— <sup>b</sup>	— <sup>b</sup>	—/—/— <sup>b</sup>	39/59/90	56	57/55/55
60/0 + 30/10	13.0 <sup>a</sup>	12	8/13/18	5.2	5.1/5.1/5.0	41/61/91	55	52/50/48
60/0 + 40/0	$\sim 1.6^a$	$\sim 1.4$	5/8/12	12	12/14/13	41/64/93	51	50/49/48

Multiple values separated by slashes given for different  $\mu\text{W}$  power levels of 5, 9, and 14 W (measured at probe entrance). <sup>a</sup> Estimated from solvent composition. <sup>b</sup> Not measured.



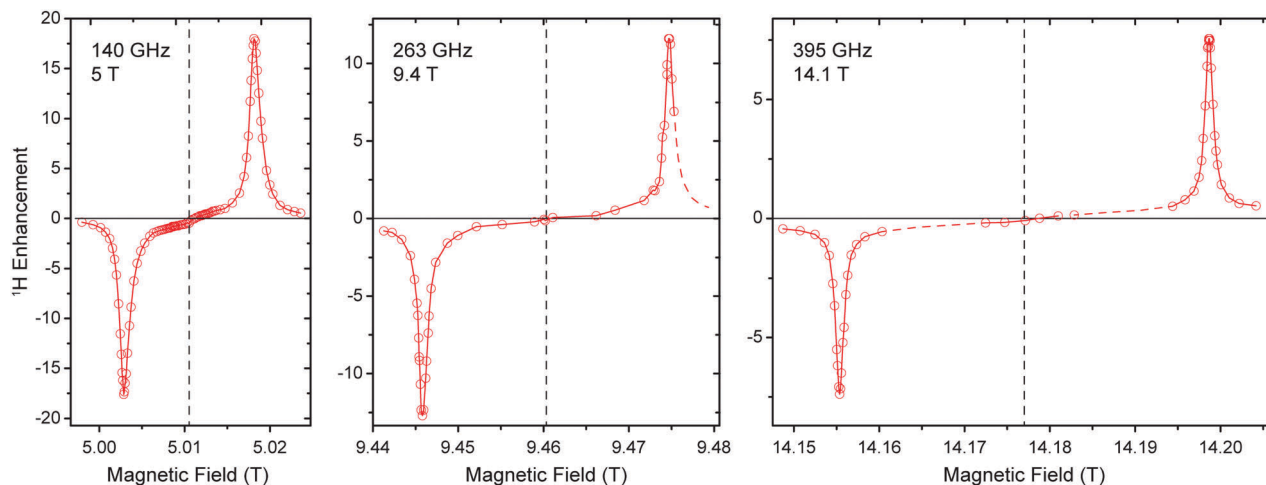


Fig. 6 Comparison between field-dependent  $^1\text{H}$  DNP profiles of 10 mM Gd-DOTA in  $\text{D}_8$ -glycerol/ $\text{D}_2\text{O}/\text{H}_2\text{O}$  (60 : 30 : 10 vol%) at 140, 263, and 395 GHz  $\mu\text{W}$  frequency. The EPR resonance fields are marked with dashed lines.

broadening in detail below. Nevertheless, we want to emphasize that a linewidth of 22 MHz at 395 GHz Larmor frequency corresponds to only 56 ppm, which is exceptionally small for a metal complex. For comparison, typical low-spin complexes such as  $\text{Cu}^{2+}$  feature  $g$  anisotropy of  $\sim 20\%$ .

Power dependence and build-up dynamics at 9.4 and 14.1 T are both similar to what we observed at 5 T. With larger  $\mu\text{W}$  power the  $^1\text{H}$  enhancement shows a nearly linear increase at all fields; build-up times become slightly longer at higher field ( $\sim 3$  s at 5 T,  $\sim 4$  s at 9.4 T,  $\sim 5$  s at 14.1 T).

#### Effect of inter-complex couplings on direct DNP of $^{13}\text{C}$ and $^{15}\text{N}$

Stimulated by the observed broadening of the DNP field profiles above, we have performed a detailed analysis of DNP enhancements of  $^1\text{H}$ ,  $^{13}\text{C}$ , and  $^{15}\text{N}$  in comparison with EPR spectra for Gd-DOTA concentrations between 2 and 20 mM at a  $\mu\text{W}$  frequency of 263 GHz and a field of 9.4 T (Fig. 7). Due to technical reasons the DNP magnet used could only be swept slightly past the EPR resonance field of the CT, therefore we were only able to record the negative enhancement of all nuclei except  $^{15}\text{N}$ . Note the reduced EPR linewidth compared to 5 T (15 MHz vs. 25 MHz) due to the less pronounced second-order ZFS acting on the CT. This narrowing in combination with larger separation of the electron-nuclear ZQ and DQ transitions leads to positive and negative  $^{13}\text{C}$  SE legs being now fully separated. A similar central plateau region occurs as seen for  $^1\text{H}$  at 5 T because of similar ratios between nuclear Zeeman frequency and inhomogeneous linewidth. Even for  $^{15}\text{N}$  we observe the occurrence of a distinctive reduction of slope around the inflection point between the positive and negative legs, indicative of nearly complete separation of opposing enhancement regions. This is—to our knowledge—the first example of a well-resolved SE profile for such a low- $\gamma$  nucleus reported in literature.

The SE field profile can relatively simply be approximated by an approach based on the EPR spectral shape. Superposition of modeled ZQ and DQ peaks (*i.e.*, by shifting the EPR spectral function by the field corresponding to the nuclear Zeeman

frequency) of opposite sign allows for generation of a simulated SE DNP profile:<sup>11</sup>

$$G_{\text{SE}}(B_0) = G_{\text{EPR}}(B_0 - \omega_{0I_n}/\gamma_S) - G_{\text{EPR}}(B_0 + \omega_{0I_n}/\gamma_S), \quad (1)$$

where  $G(B_0)$  is the spectral shape function of SE DNP profile or the EPR spectrum. These simulations are shown as solid lines in Fig. 7B. At a low concentration of 2 mM such an approximation generated from cw EPR spectra recorded at the same frequency of 263 GHz show excellent congruence with experimental DNP enhancement factors. We have observed that simulated field profile based on cw EPR spectra match the experimental DNP profiles much more closely than those based on pulsed (field-swept, echo-detected) EPR spectra; in the latter case broader spectral components with short phase-memory time constant are filtered out, but obviously still contribute to DNP. When increasing the Gd-DOTA concentration to 10 or even 20 mM we observe an incipient mismatch between EPR spectra and DNP profiles. For  $^1\text{H}$  and 10 mM the DNP peak and the EPR spectrum still show good agreement, while at 20 mM a significant broadening of the DNP peak is visible. The reason for this is unclear and requires further experiments for elucidation.

For  $^{13}\text{C}$  we observe an additional shoulder emerging in the DNP profile on the inner side of the negative SE peak, decreasing in magnitude with a constant slope towards the central inflection point. In the case of  $^{15}\text{N}$  the effect is even more pronounced; leading to a shift of the field of max. DNP enhancement towards the CT. Interestingly, we have succeeded in fitting the latter feature (see dashed lines in Fig. 7B) using a different approach based on a CE-type matching probability analysis:<sup>11</sup>

$$G_{\text{CE}}(B_0) = G_{\text{EPR}}(B_0 - \omega_{0I_n}/\gamma_S) \times G_{\text{EPR}}(B_0) - G_{\text{EPR}}(B_0 + \omega_{0I_n}/\gamma_S) \times G_{\text{EPR}}(B_0) \quad (2)$$

Here, we determine the statistical probability of finding a pair of EPR resonances fulfilling the CE matching condition  $\Delta\omega_L = \omega_{0I_n}$ . For  $^{15}\text{N}$  DNP using 20 mM Gd-DOTA there is an excellent agreement between such a simple simulation and experimental data indicating a relatively large contribution of CE besides SE.



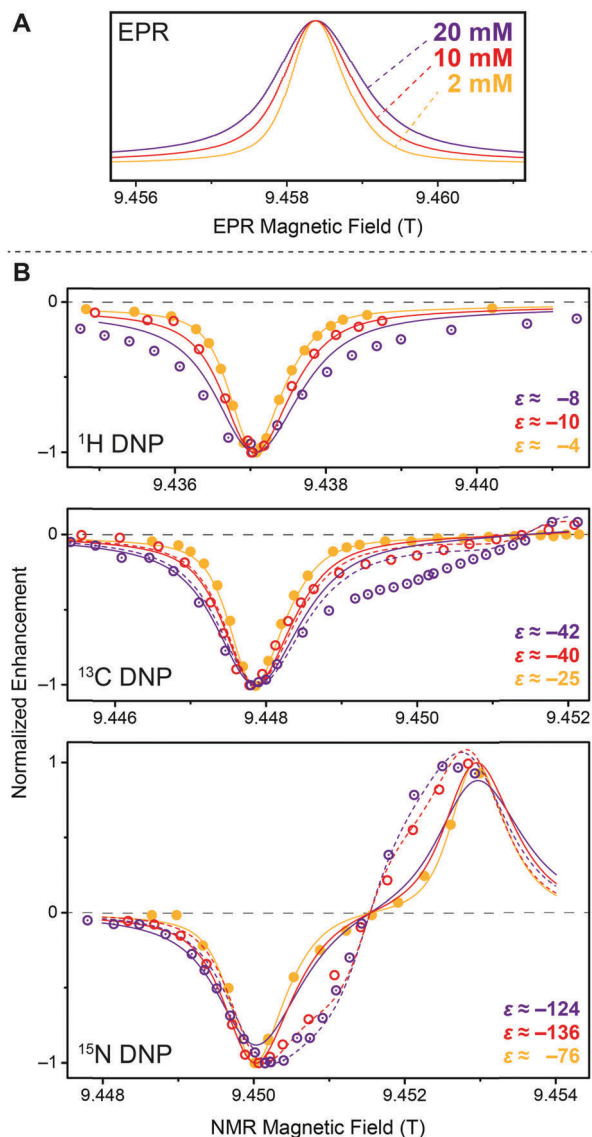


Fig. 7 (A) EPR spectra of 2 mM (orange), 10 mM (red), and 20 mM (purple) Gd-DOTA at 263 GHz. Curves were obtained by simulating experimental cw (field-modulated) EPR spectra using Easyspin<sup>95</sup> in order to avoid artifacts by integration. (B) Normalized DNP enhancement of  $^1\text{H}$ ,  $^{13}\text{C}$ , and  $^{15}\text{N}$  at 263 GHz at 2 mM (filled circles), 10 mM (open circles), and 20 mM (dotted open circles). Solid lines represent SE simulations according to eqn (1); dashed lines CE simulations according to eqn (2). Enhancement factors given are taken at field of maximum magnitude enhancement.

This is due to the inhomogeneous broadening allowing energy-conserving CE transitions within the CT which is not possible for nuclei with larger gyromagnetic ratio. The large Gd(III) concentration provides for sufficient electron–electron couplings. Based on a statistical model<sup>96</sup> the average nearest-neighbor distance amongst Gd<sup>3+</sup> is  $\sim 2.4$  nm at 20 mM concentration, yielding a dipole coupling constant of  $\sim 3.8$  MHz at this distance. At 10 mM the average distance increases to 3.0 nm (1.9 MHz); significant CE contribution is visible, albeit less pronounced. At 2 mM no contribution of CE can be found due to vanishing dipolar coupling at the average distance of 5.2 nm (0.4 MHz). Even though

we have not succeeded in reproducing the asymmetric feature of the  $^{13}\text{C}$  profile with this simple model we tentatively ascribe the occurrence to a similar cause. We assume that—due to operation of the  $^{13}\text{C}$  CE outside of the CT—more complicated dependences on mutual orientations between neighboring Gd-DOTA and potential selection of highly CE-supportive pairs inhibit the application of such a simple model as eqn (2), whereas for  $^{15}\text{N}$  efficient mixing of the relevant states within the CT leads to CE irrespective of the orientation of the molecular frame.<sup>83</sup>

### Observation of enhanced polarization spreading by spin-diffusion

When directly polarizing  $^{13}\text{C}$  or  $^{15}\text{N}$  of isotope-labeled urea using 20 mM Gd-DOTA through the glycerol/water matrix depleted in  $^{13}\text{C}$  we observe an interesting behavior: while for very short polarization times the NMR signal shows significant homogeneous broadening, this broadening is reduced when more time is available for enhanced polarization to build up as can be seen in Fig. S3 (ESI<sup>†</sup>). We explain this with a non-uniform spatial distribution of nuclear polarization where large enhancement is quickly generated for nuclei in close proximity to the paramagnetic ion. For polarization to spread further out towards less paramagnetically influenced nuclei spins, spin-diffusion has to occur through the bulk. Due to the small concentration of  $^{13}\text{C}$  and  $^{15}\text{N}$  with an average nearest-neighbor distance of  $\sim 0.5$  nm, spin diffusion constants are small and we observe overall build-up time constants on the order of  $\sim 400$  s and  $\sim 1000$  s for bridging the distance of  $\sim 2.4$  nm between polarizing agent centers. A complete set of build-up time constants for  $^{13}\text{C}$  and  $^{15}\text{N}$  at various Gd-DOTA concentrations is given in Table 3. Our experiments here also confirm an earlier observations, where we had measured through-bulk build-up time constants in excess of 5000 s even for  $^{13}\text{C}$  when both the urea and polarizing agent concentration were considerably smaller.<sup>42</sup>

### DNP with Gd(III) chelate tags attached to protein

In a series of preliminary experiments we attached Gd<sup>3+</sup>-binding chelator tags to ubiquitin using site-directed spin labeling. Ubiquitin is an excellent model system due to typically large overexpression efficiency, and biochemical robustness under different environmental conditions. Furthermore, spin-labeled ubiquitin could potentially be utilized as a protein tag targeting other proteins in larger complexes *via* ubiquitylation for site-selective DNP applications, a route we plan to investigate in the near future.

We carried out experiments using three different single-site mutations of ubiquitin where in each case one cysteine residue was introduced by mutagenesis. We selected phenylalanine F4, alanine A28, as well as glycine G75 as favorable targets for mutation because these sites possess large surface accessibility and are situated in differing secondary structure elements (*i.e.*, beta sheet, alpha helix, and terminal loop, respectively). Furthermore, the varying flexibility of the sites (*e.g.*, G75 being situated in the flexible C-terminal tail region) might lead to



**Table 3** DNP properties of Gd-DOTA at various concentrations in  $^{12}\text{C}_3$ -glycerol/ $\text{H}_2\text{O}$  at 9.4 T (263 GHz)

$C_{\text{Gd-DOTA}}$ ( $\text{mol L}^{-1}$ )	$\epsilon^{(\text{H})}$	$T_{\text{B}}^{(\text{H})}$ (s)	$\epsilon^{(\text{C})}$	$T_{\text{B,f}}^{(\text{C})a}$ (s)	$T_{\text{B,s}}^{(\text{C})b}$ (s)	$\phi^{(\text{C})c}$	$\epsilon^{(\text{N})}$	$T_{\text{B,f}}^{(\text{N})a}$ (s)	$T_{\text{B,s}}^{(\text{N})b}$ (s)	$\phi^{(\text{N})c}$
2	-4	17	-25	1213	3471	0.314	-76	296	2990	0.198
10	-10	4.6	-40	$^d$	$^d$	$^d$	-136	$^d$	$^d$	$^d$
20	-8	2.2	-42	113	396	0.351	-124	114	1003	0.721

<sup>a</sup> Fast component of bi-exponential build-up. <sup>b</sup> Slow component of bi-exponential build-up. <sup>c</sup> Ratio between contribution of fast and slow component to overall signal as described by Wenk *et al.*<sup>42</sup> <sup>d</sup> Not measured.

different conformational inhomogeneity during freezing. 4MMDPA and DOTA-M were chosen as promising chelator tags as described by Goldfarb and co-workers.<sup>63,67</sup>

In Fig. 8 we show the direct DNP-enhancement of  $^{13}\text{C}$  within uniformly [ $^{13}\text{C}$ ,  $^{15}\text{N}$ ]-labeled A28C ubiquitin mutant with each attached Gd(III) tag, a comparison with the direct polarization  $^{13}\text{C}$  MAS NMR spectrum of unlabeled A28C, the chemical structures of the tags and a model of the protein showing the single point mutation sites investigated. Within these preliminary experiments we have observed a rather small  $^{13}\text{C}$  DNP enhancement by  $\text{Gd}^{3+}$  SE on the order between approximately -1 to -3 when [ $\text{D}_8$ ,  $^{12}\text{C}_3$ ]-glycerol/ $\text{D}_2\text{O}$  mixture was used as solvent. We have not been able to observe significant differences between the different mutation sites so far. We assume that intra-molecular spin diffusion is sufficiently fast within the uniformly  $^{13}\text{C}$ -labeled protein, so that any variation in DNP efficiency is averaged after a few seconds of longitudinal magnetization build-up. Depletion of  $^{13}\text{C}$  in the matrix below natural abundance strongly attenuates intermolecular spin-diffusion so that enhanced polarization is mostly maintained within the protein also carrying the Gd(III) polarization source as we have demonstrated with endogenously bound  $\text{Mn}^{2+}$ .<sup>42</sup>

DNP enhancements are larger and build-up times are faster for Gd-4MMDPA labeled protein. EPR spectra of the Gd-labeled proteins at the same frequency (263 GHz) show a ~2 times larger linewidth of the CT in 4MMDPA as in DOTA-M caused by the lower symmetry and larger ZFS in the former complex (Fig. S4, ESI<sup>†</sup>). Therefore we would also expect lower efficiency of DNP according to Fig. 3 in this case. The opposite finding is likely explained by the shorter tether between chelator moiety and protein. We observe significant broadening of  $^{13}\text{C}$  resonances especially with Gd-4MMDPA due to similar reasons. Also, upon  $\mu\text{w}$  irradiation and hence DNP enhancement ( $\mu\text{w}$  on), additional broadening occurs as compared to the spectra acquired using thermal polarization ( $\mu\text{w}$  off). All these observations indicate more favorable DNP enhancement of  $^{13}\text{C}$  nuclei in close distance to the paramagnetic ion.

We have determined labeling efficiencies between 90% (for 4MMDPA) and 100% (for DOTA-M) by cw EPR spin counting; both values can be interpreted as quantitative within the experimental error. Therefore we assume that a significant contribution of unlabeled protein—which could lead to similar observations—is rather unlikely. Due to the rather short

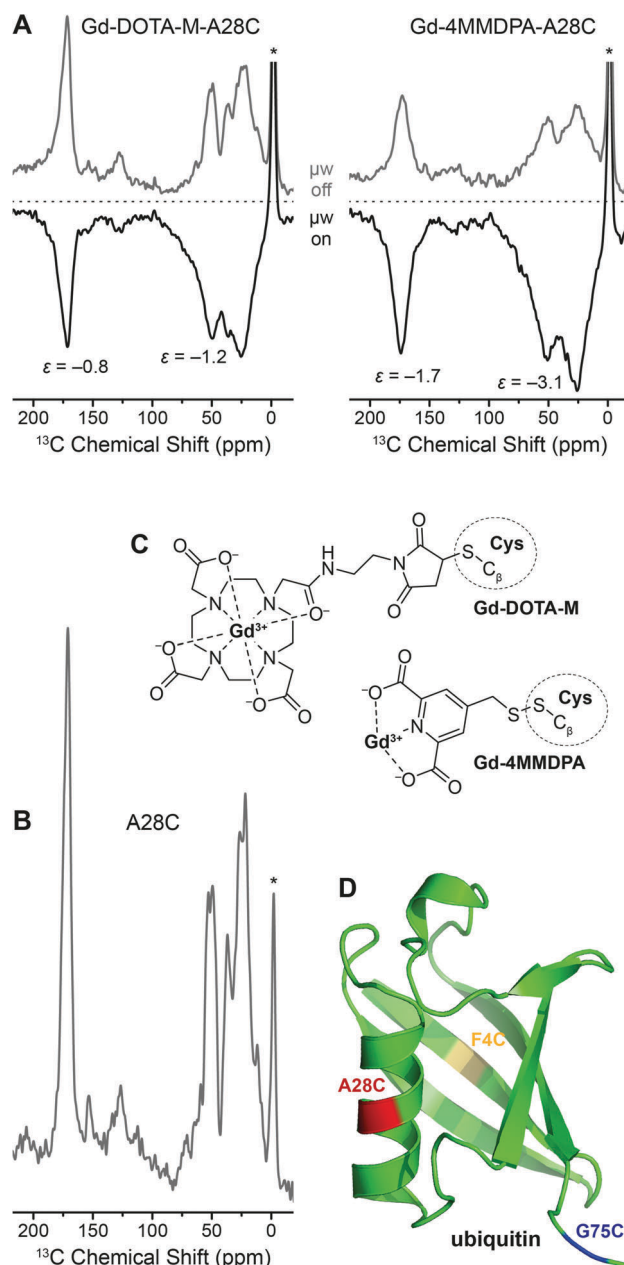


**Fig. 8** (A) Direct  $^{13}\text{C}$  DNP enhancement of uniformly [ $^{13}\text{C}$ ,  $^{15}\text{N}$ ]-labeled ubiquitin mutant A28C using site-directed spin labeling with Gd-DOTA-M and Gd-4MMDPA tags at 9.4 T. The field was optimized for  $\text{Gd}^{3+}$   $^{13}\text{C}$  SE resulting in negative signal enhancement. Read-out was performed via Bloch decay with 6 and 2.3 s polarization delay, respectively. (B)  $^{13}\text{C}$  MAS spectrum of A28C ubiquitin (without attached spin label), read-out via Bloch decay and 16 s polarization delay. Asterisks mark signals from silicone plugs. (C) Chemical structures of Gd-4MMDPA and Gd-DOTA-M spin labels connected to cysteine residues. (D) Ribbon structure of ubiquitin (PDB ID 1UBQ) with F4C, A28C, and G75C single-site mutations marked in yellow, red, and blue, respectively.

spin-lattice relaxation of  $^{13}\text{C}$  in the fully protonated (diamagnetic) protein with  $T_{1n}$  of about 10 s we expect the enhancement to drastically improve upon deuteration (fully or selectively of methyl-carrying amino acids); such experiments are currently pursued.





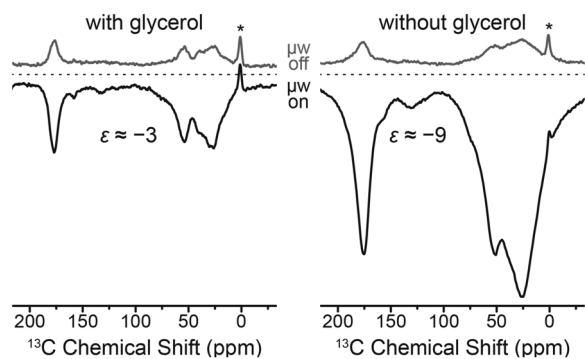


Fig. 9 Direct DNP enhancement of uniformly  $^{13}\text{C}$ ,  $^{15}\text{N}$ -labeled ubiquitin mutant F4C with and without added glycerol using site-directed spin labeling with Gd-DOTA-M tags at 9.4 T. The field was optimized for  $\text{Gd}^{3+}$   $^{13}\text{C}$  SE resulting in negative signal enhancement. Read-out was performed via Bloch decay with 4 s polarization delay. Asterisks mark signals from silicone plugs.

An unexpected phenomenon was observed when the cryoprotectant was absent from the aqueous buffer solution. Since the paramagnetic label is covalently attached to the biomolecule, separation of the polarizing agent and protein in different phases—which reportedly inhibits DNP<sup>51</sup>—cannot occur. DNP enhancement factors improved three-fold to about  $-9$  while at the same time strong line broadening occurs. This is shown in Fig. 9 on the F4C mutant labeled with Gd-DOTA-M; we have observed very similar effects with other point mutation/chelate tag combinations as well. We explain this by agglomeration of paramagnetically labeled ubiquitins and hence a local increase in  $\text{Gd}(\text{III})$  concentration. This is supported by shorter build-up time constants in the cryoprotectant-free samples.

Of course, the increase in linewidth in the small globular protein due to the presence of  $\text{Gd}^{3+}$  complicates the extraction of structural information in the typical way. However, such approaches might be fruitful with respect to specifically labeled proteins or ligands where spectral resolution is less important, or for problems in larger biomolecular systems where, for example, contacts between subunits are of interest. In fact, the occurrence of additional polarization pathways—including CE enabled by direct dipolar contact between  $\text{Gd}^{3+}$  of different proteins—bears an interesting prospect for future studies including multiply-labeled proteins and singly-labeled subunits within protein complexes, enabling efficient CE only upon direct contact of their constituents. Similar concepts have been demonstrated with nitroxides.<sup>56</sup> This could allow for filtering towards a minority of bound species in co-existence next to the majority of unbound components; a situation which poses a significant problem in biophysical chemistry or structural biology.

## Conclusion

While the indirect enhancement of  $^{13}\text{C}$  NMR spectra via  $^1\text{H}$  DNP using complexes of  $\text{Gd}^{3+}$  and  $\text{Mn}^{2+}$  has already been demonstrated in principle,<sup>37</sup> we have now extended the investigation especially for direct  $^{13}\text{C}$  DNP.  $^1\text{H}$  DNP enhancements of up to 20 have been measured which are yet unable to compete

with those factors obtained by more efficient bis-nitroxide polarizing agents on model systems. However, paramagnetic metal ions still offer various other interesting properties especially in the context of biomolecular DNP. We have shown that deuteration of the matrix—which is rather difficult in cellular milieu—is not required because it does not lead to larger enhancement factors in model systems. Furthermore, many biomolecules are routinely investigated with paramagnetic NMR using lanthanide probes where paramagnetic relaxation enhancements (PREs) and pseudocontact shifts (PCSs) are analyzed for structural constraints in solution.<sup>80,97</sup> MAS DNP could be able to contribute additional information without further modification of the sample. This is especially interesting in regards to highly efficient direct DNP of  $^{13}\text{C}$  or  $^{15}\text{N}$  with enhancement factors of  $\sim 100$  and larger. While at low polarizing agent concentrations SE is the dominating DNP mechanism for these nuclei, at large concentrations we observed a significant contribution of the CE which is achieved by electron spin frequency offsets caused by ZFS.

Direct DNP of low- $\gamma$  nuclei allows for a better control of spreading of enhanced polarization due to small spin-diffusion rates in environments with small isotope concentration. Furthermore, we have demonstrated in preliminary experiments that proteins labeled with  $\text{Gd}^{3+}$ -binding chelator tags could themselves be used as polarizing agents. This approach could in the future be extended in order to investigate protein-protein interactions, allowing enhanced polarization to spread from one domain to another only when a close contact is maintained.

## Acknowledgements

P. Gast (Leiden University) has kindly acquired the 275 GHz EPR spectra. Access to the 9.4 and 14.1 T DNP spectrometers has been generously provided by Bruker Biospin (Billerica, MA) for acquisition of data presented in Fig. 6. All other data at 9.4 T has been measured at Technical University Darmstadt with access provided by G. Buntkowsky and technical support from T. Gutmann. V. Denysenkov (Frankfurt) has helped with the acquisition of 263 GHz EPR spectra. We acknowledge help from F. Sochor (Frankfurt) regarding protein expression and J. Knauer (Frankfurt) for synthesis of 4MMDPA, for which A. Heckel (Frankfurt) has kindly provided laboratory space. We thank M. Reese (formerly MIT) for helpful discussions. RGG acknowledges funding by the National Institutes of Health (NIH) projects EB-002026 and EB-002804. BC has been funded by the Deutsche Forschungsgemeinschaft (DFG) through Emmy Noether grant CO802/2-1. RS is funded by a DFG research fellowship (SI2105/1-1). BC and HS acknowledge financial and technical support as well as spectrometer access from the Center for Biomolecular Magnetic Resonance (BMRZ).

## References

- 1 D. A. Hall, D. C. Maus, G. J. Gerfen, S. J. Inati, L. R. Becerra, F. W. Dahlquist and R. G. Griffin, *Science*, 1997, **276**, 930–932.



- 2 L. R. Becerra, G. J. Gerfen, R. J. Temkin, D. J. Singel and R. G. Griffin, *Phys. Rev. Lett.*, 1993, **71**, 3561–3564.
- 3 G. J. Gerfen, L. R. Becerra, D. A. Hall, R. G. Griffin, R. J. Temkin and D. J. Singel, *J. Chem. Phys.*, 1995, **102**, 9494–9497.
- 4 V. S. Bajaj, M. K. Hornstein, K. E. Kreischer, J. R. Sirigiri, P. P. Woskov, M. L. Mak-Jurkauskas, J. Herzfeld, R. J. Temkin and R. G. Griffin, *J. Magn. Reson.*, 2007, **189**, 251–279.
- 5 K. N. Hu, G. T. Debelouchina, A. A. Smith and R. G. Griffin, *J. Chem. Phys.*, 2011, **134**, 19.
- 6 E. A. Chekhovich, M. N. Makhonin, A. I. Tartakovskii, A. Yacoby, H. Bluhm, K. C. Nowack and L. M. K. Vandersypen, *Nat. Mater.*, 2013, **12**, 494–504.
- 7 D. Banerjee, D. Shimon, A. Feintuch, S. Vega and D. Goldfarb, *J. Magn. Reson.*, 2013, **230**, 212–219.
- 8 T. V. Can, M. A. Caporini, F. Mentink-Vigier, B. Corzilius, J. J. Walish, M. Rosay, W. E. Maas, M. Baldus, S. Vega, T. M. Swager and R. G. Griffin, *J. Chem. Phys.*, 2014, **141**, 064202.
- 9 Y. Hovav, A. Feintuch and S. Vega, *J. Magn. Reson.*, 2010, **207**, 176–189.
- 10 I. Kaminker, A. Potapov, A. Feintuch, S. Vega and D. Goldfarb, *Phys. Chem. Chem. Phys.*, 2009, **11**, 6799–6806.
- 11 D. Shimon, Y. Hovav, A. Feintuch, D. Goldfarb and S. Vega, *Phys. Chem. Chem. Phys.*, 2012, **14**, 5729–5743.
- 12 K. R. Thurber and R. Tycko, *J. Chem. Phys.*, 2012, **137**, 084508.
- 13 F. Mentink-Vigier, Ü. Akbey, Y. Hovav, S. Vega, H. Oschkinat and A. Feintuch, *J. Magn. Reson.*, 2012, **224**, 13–21.
- 14 D. Mance, P. Gast, M. Huber, M. Baldus and K. L. Ivanov, *J. Chem. Phys.*, 2015, **142**, 234201.
- 15 A. S. Lilly Thankamony, C. Lion, F. Pourpoint, B. Singh, A. J. Perez Linde, D. Carnevale, G. Bodenhausen, H. Vezin, O. Lafon and V. Polshettiwar, *Angew. Chem., Int. Ed.*, 2015, **54**, 2190–2193.
- 16 D. Lee, G. Monin, N. T. Duong, I. Z. Lopez, M. Bardet, V. Mareau, L. Gonon and G. De Paëpe, *J. Am. Chem. Soc.*, 2014, **136**, 13781–13788.
- 17 A. Lesage, M. Lelli, D. Gajan, M. A. Caporini, V. Vitzthum, P. Miéville, J. Alauzun, A. Roussey, C. Thieuleux, A. Mehdi, G. Bodenhausen, C. Copéret and L. Emsley, *J. Am. Chem. Soc.*, 2010, **132**, 15459–15461.
- 18 P. Wolf, M. Valla, A. J. Rossini, A. Comas-Vives, F. Núñez-Zarur, B. Malaman, A. Lesage, L. Emsley, C. Copéret and I. Hermans, *Angew. Chem., Int. Ed.*, 2014, **53**, 10179–10183.
- 19 L. Zhao, W. Li, A. Plog, Y. Xu, G. Buntkowsky, T. Gutmann and K. Zhang, *Phys. Chem. Chem. Phys.*, 2014, **16**, 26322–26329.
- 20 T. Gutmann, J. Liu, N. Rothermel, Y. Xu, E. Jaumann, M. Werner, H. Breitzke, S. T. Sigurdsson and G. Buntkowsky, *Chem. – Eur. J.*, 2015, **21**, 3798–3805.
- 21 M. Rosay, J. C. Lansing, K. C. Haddad, W. W. Bachovchin, J. Herzfeld, R. J. Temkin and R. G. Griffin, *J. Am. Chem. Soc.*, 2003, **125**, 13626–13627.
- 22 M. L. Mak-Jurkauskas, V. S. Bajaj, M. K. Hornstein, M. Belenky, R. G. Griffin and J. Herzfeld, *Proc. Natl. Acad. Sci. U. S. A.*, 2008, **105**, 883–888.
- 23 V. S. Bajaj, M. L. Mak-Jurkauskas, M. Belenky, J. Herzfeld and R. G. Griffin, *Proc. Natl. Acad. Sci. U. S. A.*, 2009, **106**, 9244–9249.
- 24 A. B. Barnes, B. Corzilius, M. L. Mak-Jurkauskas, L. B. Andreas, V. S. Bajaj, Y. Matsuki, M. L. Belenky, J. Lugtenburg, J. R. Sirigiri, R. J. Temkin, J. Herzfeld and R. G. Griffin, *Phys. Chem. Chem. Phys.*, 2010, **12**, 5861–5867.
- 25 G. T. Debelouchina, M. J. Bayro, A. W. Fitzpatrick, V. Ladizhansky, M. T. Colvin, M. A. Caporini, C. P. Jaroniec, V. S. Bajaj, M. Rosay, C. E. MacPhee, M. Vendruscolo, W. E. Maas, C. M. Dobson and R. G. Griffin, *J. Am. Chem. Soc.*, 2013, **135**, 19237–19247.
- 26 L. B. Andreas, A. B. Barnes, B. Corzilius, J. J. Chou, E. A. Miller, M. Caporini, M. Rosay and R. G. Griffin, *Biochemistry*, 2013, **52**, 2774–2782.
- 27 I. Gelis, V. Vitzthum, N. Dhimole, M. Caporini, A. Schedlbauer, D. Carnevale, S. Connell, P. Fucini and G. Bodenhausen, *J. Biomol. NMR*, 2013, **56**, 85–93.
- 28 E. J. Koers, E. A. W. van der Crujisen, M. Rosay, M. Weingarh, A. Prokofyev, C. Sauvée, O. Ouari, J. van der Zwan, O. Pongs, P. Tordo, W. E. Maas and M. Baldus, *J. Biomol. NMR*, 2014, **60**, 157–168.
- 29 Y. Su, L. Andreas and R. G. Griffin, *Annu. Rev. Biochem.*, 2015, **84**, 465–497.
- 30 A. Potapov, W.-M. Yau, R. Ghirlando, K. R. Thurber and R. Tycko, *J. Am. Chem. Soc.*, 2015, **137**, 8294–8307.
- 31 L. R. Becerra, G. J. Gerfen, B. F. Bellew, J. A. Bryant, D. A. Hall, S. J. Inati, R. T. Weber, S. Un, T. F. Prisner, A. E. McDermott, K. W. Fishbein, K. E. Kreischer, R. J. Temkin, D. J. Singel and R. G. Griffin, *J. Magn. Reson., Ser. A*, 1995, **117**, 28–40.
- 32 C. Song, K.-N. Hu, C.-G. Joo, T. M. Swager and R. G. Griffin, *J. Am. Chem. Soc.*, 2006, **128**, 11385–11390.
- 33 T. Maly, A. F. Miller and R. G. Griffin, *ChemPhysChem*, 2010, **11**, 999–1001.
- 34 O. Haze, B. Corzilius, A. A. Smith, R. G. Griffin and T. M. Swager, *J. Am. Chem. Soc.*, 2012, **134**, 14287–14290.
- 35 B. Corzilius, A. A. Smith and R. G. Griffin, *J. Chem. Phys.*, 2012, **137**, 054201.
- 36 V. K. Michaelis, A. A. Smith, B. Corzilius, O. Haze, T. M. Swager and R. G. Griffin, *J. Am. Chem. Soc.*, 2013, **135**, 2935–2938.
- 37 B. Corzilius, A. A. Smith, A. B. Barnes, C. Luchinat, I. Bertini and R. G. Griffin, *J. Am. Chem. Soc.*, 2011, **133**, 5648–5651.
- 38 K. N. Hu, H. H. Yu, T. M. Swager and R. G. Griffin, *J. Am. Chem. Soc.*, 2004, **126**, 10844–10845.
- 39 C. Sauvée, M. Rosay, G. Casano, F. Aussenac, R. T. Weber, O. Ouari and P. Tordo, *Angew. Chem., Int. Ed.*, 2013, **52**, 10858–10861.
- 40 J. H. Ardenkjær-Larsen, I. Laursen, I. Leunbach, G. Ehnholm, L. G. Wistrand, J. S. Petersson and K. Golman, *J. Magn. Reson.*, 1998, **133**, 1–12.
- 41 A. A. Smith, B. Corzilius, A. B. Barnes, T. Maly and R. G. Griffin, *J. Chem. Phys.*, 2012, **136**, 015101.
- 42 P. Wenk, M. Kaushik, D. Richter, M. Vogel, B. Süss and B. Corzilius, *J. Biomol. NMR*, 2015, **63**, 97–109.
- 43 M. Rosay, V. Weis, K. E. Kreischer, R. J. Temkin and R. G. Griffin, *J. Am. Chem. Soc.*, 2002, **124**, 3214–3215.



- 44 T. Jacso, W. T. Franks, H. Rose, U. Fink, J. Broecker, S. Keller, H. Oschkinat and B. Reif, *Angew. Chem., Int. Ed.*, 2012, **51**, 432–435.
- 45 J. Becker-Baldus, C. Bamann, K. Saxena, H. Gustmann, L. J. Brown, R. C. D. Brown, C. Reiter, E. Bamberg, J. Wachtveitl, H. Schwalbe and C. Glaubitz, *Proc. Natl. Acad. Sci. U. S. A.*, 2015, **112**, 9896–9901.
- 46 P. C. A. van der Wel, K. N. Hu, J. Lewandowski and R. G. Griffin, *J. Am. Chem. Soc.*, 2006, **128**, 10840–10846.
- 47 G. T. Debelouchina, M. J. Bayro, P. C. A. van der Wel, M. A. Caporini, A. B. Barnes, M. Rosay, W. E. Maas and R. G. Griffin, *Phys. Chem. Chem. Phys.*, 2010, **12**, 5911–5919.
- 48 M. J. Bayro, G. T. Debelouchina, M. T. Eddy, N. R. Birkett, C. E. MacPhee, M. Rosay, W. E. Maas, C. M. Dobson and R. G. Griffin, *J. Am. Chem. Soc.*, 2011, **133**, 13967–13974.
- 49 A. J. Rossini, A. Zagdoun, F. Hegner, M. Schwarzwälder, D. Gajan, C. Copéret, A. Lesage and L. Emsley, *J. Am. Chem. Soc.*, 2012, **134**, 16899–16908.
- 50 T. Maly, D. Cui, R. G. Griffin and A.-F. Miller, *J. Phys. Chem. B*, 2012, **116**, 7055–7065.
- 51 T.-C. Ong, M. L. Mak-Jurkauskas, J. J. Walish, V. K. Michaelis, B. Corzilius, A. A. Smith, A. M. Clausen, J. C. Cheetham, T. M. Swager and R. G. Griffin, *J. Phys. Chem. B*, 2013, **117**, 3040–3046.
- 52 C. Fernández-de-Alba, H. Takahashi, A. Richard, Y. Chenavier, L. Dubois, V. Maurel, D. Lee, S. Hediger and G. De Paëpe, *Chem. – Eur. J.*, 2015, **21**, 4512–4517.
- 53 M. A. Voinov, D. B. Good, M. E. Ward, S. Milikisiyants, A. Marek, M. A. Caporini, M. Rosay, R. A. Munro, M. Ljumovic, L. S. Brown, V. Ladizhansky and A. I. Smirnov, *J. Phys. Chem. B*, 2015, **119**, 10180–10190.
- 54 H. Takahashi, S. Hediger and G. De Paëpe, *Chem. Commun.*, 2013, **49**, 9479–9481.
- 55 A. N. Smith, M. A. Caporini, G. E. Fanucci and J. R. Long, *Angew. Chem., Int. Ed.*, 2015, **54**, 1542–1546.
- 56 B. J. Wylie, B. G. Dzikovski, S. Pawsey, M. Caporini, M. Rosay, J. H. Freed and A. E. McDermott, *J. Biomol. NMR*, 2015, **61**, 361–367.
- 57 E. A. W. van der Cruisjes, E. J. Koers, C. Sauvée, R. E. Hulse, M. Weingarth, O. Ouari, E. Perozo, P. Tordo and M. Baldus, *Chem. – Eur. J.*, 2015, **21**, 12971–12977.
- 58 V. M. Runge, R. G. Stewart, J. A. Clanton, M. M. Jones, C. M. Lukehart, C. L. Partain and A. E. James, *Radiology*, 1983, **147**, 789–791.
- 59 J. A. Koutcher, C. T. Burt, R. B. Lauffer and T. J. Brady, *J. Nucl. Med.*, 1984, **25**, 506–513.
- 60 R. H. Knop, J. A. Frank, A. J. Dwyer, M. E. Girton, M. Naeyege, M. Schrader, J. Cobb, O. Gansow, M. Maegerstadt, M. Brechbiel, L. Baltzer and J. L. Doppman, *J. Comput. Assist. Tomogr.*, 1987, **11**, 35–42.
- 61 P. Hermann, J. Kotek, V. Kubicek and I. Lukes, *Dalton Trans.*, 2008, 3027–3047.
- 62 A. M. Raitsimring, C. Gunanathan, A. Potapov, I. Efremenko, J. M. L. Martin, D. Milstein and D. Goldfarb, *J. Am. Chem. Soc.*, 2007, **129**, 14138–14139.
- 63 A. Potapov, H. Yagi, T. Huber, S. Jergic, N. E. Dixon, G. Otting and D. Goldfarb, *J. Am. Chem. Soc.*, 2010, **132**, 9040–9048.
- 64 H. Yagi, D. Banerjee, B. Graham, T. Huber, D. Goldfarb and G. Otting, *J. Am. Chem. Soc.*, 2011, **133**, 10418–10421.
- 65 D. Banerjee, H. Yagi, T. Huber, G. Otting and D. Goldfarb, *J. Phys. Chem. Lett.*, 2012, **3**, 157–160.
- 66 D. T. Edwards, Z. Ma, T. J. Meade, D. Goldfarb, S. Han and M. S. Sherwin, *Phys. Chem. Chem. Phys.*, 2013, **15**, 11313–11326.
- 67 A. Martorana, G. Bellapadrona, A. Feintuch, E. Di Gregorio, S. Aime and D. Goldfarb, *J. Am. Chem. Soc.*, 2014, **136**, 13458–13465.
- 68 P. Lueders, G. Jeschke and M. Yulikov, *J. Phys. Chem. Lett.*, 2011, **2**, 604–609.
- 69 D. Akhmetzyanov, J. Plackmeyer, B. Endeward, V. Denysenkov and T. F. Prisner, *Phys. Chem. Chem. Phys.*, 2015, **17**, 6760–6766.
- 70 J. Eisinger, R. G. Shulman and W. E. Blumberg, *Nature*, 1961, **192**, 963–964.
- 71 A. Cavé, M.-F. Daures, J. Parello, A. Saint-Yves and R. Sempere, *Biochimie*, 1979, **61**, 755–765.
- 72 A. Dvoretzky, V. Gaponenko and P. R. Rosevear, *FEBS Lett.*, 2002, **528**, 189–192.
- 73 M. D. Vlasie, C. Comuzzi, A. M. C. H. van den Nieuwendijk, M. Prudêncio, M. Overhand and M. Ubbink, *Chem. – Eur. J.*, 2007, **13**, 1715–1723.
- 74 P. S. Nadaud, J. J. Helmus, S. L. Kall and C. P. Jaroniec, *J. Am. Chem. Soc.*, 2009, **131**, 8108–8120.
- 75 I. Sengupta, P. S. Nadaud, J. J. Helmus, C. D. Schwieters and C. P. Jaroniec, *Nat. Chem.*, 2012, **4**, 410–417.
- 76 W. R. Couet, R. C. Brasch, G. Sosnovsky and T. N. Tozer, *Magn. Reson. Imaging*, 1985, **3**, 83–88.
- 77 S. Belkin, R. J. Mehlhorn, K. Hideg, O. Hankovsky and L. Packer, *Arch. Biochem. Biophys.*, 1987, **256**, 232–243.
- 78 I. Krstić, R. Hänsel, O. Romainczyk, J. W. Engels, V. Dötsch and T. F. Prisner, *Angew. Chem., Int. Ed.*, 2011, **50**, 5070–5074.
- 79 A. P. Jagtap, I. Krstic, N. C. Kunjir, R. Hänsel, T. F. Prisner and S. T. Sigurdsson, *Free Radical Res.*, 2015, **49**, 78–85.
- 80 G. Otting, *Annu. Rev. Biophys.*, 2010, **39**, 387–405.
- 81 C. D. Jeffries, *Phys. Rev.*, 1960, **117**, 1056–1069.
- 82 C. F. Hwang and D. A. Hill, *Phys. Rev. Lett.*, 1967, **19**, 1011–1014.
- 83 B. Corzilius, *Phys. Chem. Chem. Phys.*, 2016, DOI: 10.1039/c6cp04621e.
- 84 A. A. Smith, B. Corzilius, J. A. Bryant, R. DeRocher, P. P. Woskov, R. J. Temkin and R. G. Griffin, *J. Magn. Reson.*, 2012, **223**, 170–179.
- 85 H. Blok, J. A. J. M. Disselhorst, S. B. Orlinskii and J. Schmidt, *J. Magn. Reson.*, 2004, **166**, 92–99.
- 86 G. Mathies, H. Blok, J. A. J. M. Disselhorst, P. Gast, H. van der Meer, D. M. Miedema, R. M. Almeida, J. J. G. Moura, W. R. Hagen and E. J. J. Groenen, *J. Magn. Reson.*, 2011, **210**, 126–132.
- 87 A. B. Barnes, M. L. Mak-Jurkauskas, Y. Matsuki, V. S. Bajaj, P. C. A. van der Wel, R. DeRocher, J. Bryant, J. R. Sirigiri,



- R. J. Temkin, J. Lugtenburg, J. Herzfeld and R. G. Griffin, *J. Magn. Reson.*, 2009, **198**, 261–270.
- 88 C. D. Joye, R. G. Griffin, M. K. Hornstein, H. Kan-Nian, K. E. Kreischer, M. Rosay, M. A. Shapiro, J. R. Sirigiri, R. J. Temkin and P. P. Woskov, *IEEE Trans. Plasma Sci.*, 2006, **34**, 518–523.
- 89 C. Cossy, L. Helm, D. H. Powell and A. E. Merbach, *New J. Chem.*, 1995, **19**, 27–35.
- 90 A. M. Raitsimring, A. V. Astashkin, O. G. Poluektov and P. Caravan, *Appl. Magn. Reson.*, 2005, **28**, 281–295.
- 91 A. A. Smith, B. Corzilius, O. Haze, T. M. Swager and R. G. Griffin, *J. Chem. Phys.*, 2013, **139**, 214201.
- 92 D. Shimon, Y. Hovav, I. Kaminker, A. Feintuch, D. Goldfarb and S. Vega, *Phys. Chem. Chem. Phys.*, 2015, **17**, 11868–11883.
- 93 K. J. Donovan, A. Lupulescu and L. Frydman, *ChemPhysChem*, 2014, **15**, 436–443.
- 94 A. Doll, S. Pribitzer, R. Tschaggelar and G. Jeschke, *J. Magn. Reson.*, 2013, **230**, 27–39.
- 95 S. Stoll and A. Schweiger, *J. Magn. Reson.*, 2006, **178**, 42–55.
- 96 S. Chandrasekhar, *Rev. Mod. Phys.*, 1943, **15**, 1–89.
- 97 K. Barthelmes, A. M. Reynolds, E. Peisach, H. R. A. Jonker, N. J. DeNunzio, K. N. Allen, B. Imperiali and H. Schwalbe, *J. Am. Chem. Soc.*, 2011, **133**, 808–819.



## Supplementary Information

### **Gd(III) and Mn(II) complexes for dynamic nuclear polarization: small molecular chelate polarizing agents and applications with site-directed spin labeling of proteins**

Monu Kaushik<sup>1,2</sup>, Thorsten Bahrenberg<sup>1,2,§</sup>, Thach V. Can<sup>3</sup>, Marc A. Caporini<sup>4,†</sup>, Robert Silvers<sup>2,3,5</sup>, Jörg Heiliger<sup>1,2</sup>, Albert A. Smith<sup>3,‡</sup>, Harald Schwalbe<sup>2,5</sup>, Robert G. Griffin<sup>3</sup>, and Björn Corzilius<sup>1,2,3,\*</sup>

<sup>1</sup>*Institute of Physical and Theoretical Chemistry and Institute of Biophysical Chemistry, Goethe University Frankfurt, Max-von-Laue-Str. 7-9, 60438 Frankfurt am Main, Germany*

<sup>2</sup>*Center for Biomolecular Magnetic Resonance (BMRZ), Goethe University Frankfurt, Max-von-Laue-Str. 9, 60438 Frankfurt am Main, Germany*

<sup>3</sup>*Francis Bitter Magnet Laboratory and Department of Chemistry, Massachusetts Institute of Technology, 77 Massachusetts Avenue, Cambridge, Massachusetts 02139, USA*

<sup>4</sup>*Bruker Biospin Ltd., Billerica, Massachusetts 01821, United States*

<sup>5</sup>*Institute of Organic and Biological Chemistry, Goethe University Frankfurt, Max-von-Laue-Str. 7, 60438 Frankfurt am Main, Germany*

\* *corresponding author: [corzilius@em.uni-frankfurt.de](mailto:corzilius@em.uni-frankfurt.de)*

§ *present address: Department of Chemical Physics, Weizmann Institute of Science, 76100 Rehovot, Israel*

† *present address: Amgen, Inc., 360 Binney Street, Cambridge, Massachusetts 02142, United States*

‡ *present address: Department of Chemistry and Applied Biosciences, Laboratory of Physical Chemistry, ETH-Zürich, CH-8093 Zürich, Switzerland*

# Detailed Experimental Section

## EPR at 263 GHz

24  $\mu$ W  $\mu$ w power were used and the field was modulated with a frequency of 5 kHz at 0.1 mT amplitude. For 4MMDPA tag the field was swept by 40 mT over 2024 points at a conversion time of 196 ms; for DOTAM-M respective parameters were 10 mT, 801 points, and 250 ms. The integration time constant was fixed to the conversion time.

## DNP at 5 T (140 GHz)

A superconducting sweep coil with a range of  $\pm 75$  mT allowed for adjusting the field and recording field-dependent DNP profiles using Bloch decay (single-pulse) FID detection. After optimization of the maximum enhancement field position for the respective nucleus the magnet was set to persistent mode and enhancement factors were determined by comparison of NMR intensity with and without  $\mu$ w irradiation using cross-polarization (A. Pines, M. G. Gibby and J. S. Waugh, *J. Chem. Phys.*, 1972, **56**, 1776-1777) to  $^{13}\text{C}$  (in case of  $^1\text{H}$ ) or direct read-out of  $^{13}\text{C}$  polarization via Bloch decay (F. Bloch, W. W. Hansen and M. Packard, *Phys. Rev.*, 1946, **69**, 680-680). For all experiments radio frequency (rf) pulse amplitudes were set to a nutation frequency of 100 kHz for both  $^1\text{H}$  and  $^{13}\text{C}$ . TPPM was used for broadband decoupling of  $^1\text{H}$  (A. E. Bennett, C. M. Rienstra, M. Auger, K. V. Lakshmi and R. G. Griffin, *J. Chem. Phys.*, 1995, **103**, 6951-6958). Samples were contained in a 4 mm o.d. sapphire MAS rotor from Insaco (Quakertown, PA). Pulse sequences were preceded by a pre-saturation pulse train consisting of 16 flip ( $90^\circ$ ) pulses separated by 5 ms and a subsequent polarization delay during which (enhanced) polarization can build up. For the acquisition of build-up curves the polarization delay was varied; all other experiments were

performed using a fixed polarization delay close to  $1.26 \times T_B$  (with  $T_B$  being the DNP build-up time constant), thus allowing for optimal sensitivity in a given experimental time.

### **DNP at 9.4 T (263 GHz) and above**

#### **Comparison of $^1\text{H}$ DNP at 9.4 T and 14.1 T performed at Bruker BioSpin (Billerica, MA):**

The DNP field profiles were obtained by measuring the enhancements at each magnetic field position. The RF field strength on  $^1\text{H}$  was 50 kHz during CP and 100 kHz otherwise including TPPM decoupling during acquisition. The DNP enhancements were determined by comparing the NMR signals with and without microwave irradiation. The magnetic field of the NMR magnets were varied by superconducting sweep coils as well as room temperature shim stacks. The sweep ranges of the superconducting coils are 75 mT and 128 mT at 9.4 T and 14.1 T, corresponding to  $\sim 8,000$  ppm and  $\sim 9,000$  ppm, respectively. The shim stacks provide fine adjustments to the magnetic field within the range of 240 ppm and 150 ppm at 9.4 T and 14.1 T, respectively.

**All other DNP experiments at 9.4 T:** The sweepable Bruker Ascent DNP magnet (89 mm) was centered at 9.40 T and contained a superconducting sweep coil with a nominal range of  $\pm 75$  mT. The sweep coil was energized step-wise to sweep the magnetic field and record DNP field profiles for  $^1\text{H}$ ,  $^{13}\text{C}$ , and  $^{15}\text{N}$  nuclei. After careful optimization of the respective optimum field position the sweep coil was put into persistent operation and enhancement factors were determined by comparison of NMR intensity with and without  $\mu\text{w}$  irradiation. Temperature was read out via a thermocouple inside the MAS stator during experiments. For all experiments radio frequency (rf) pulse amplitudes were set to 100 kHz, 50 kHz, and 40 kHz for  $^1\text{H}$ ,  $^{13}\text{C}$ , and  $^{15}\text{N}$ , respectively;  $^1\text{H}$  amplitude was set for to  $^{13}\text{C}$  or  $^{15}\text{N}$  Hartmann-Hahn matching during CP (S. R. Hartmann and E. L. Hahn, *Phys. Rev.*, 1962, **128**, 2042-2053). SPINAL64 at 100 kHz was used for broadband

decoupling of  $^1\text{H}$  (B. M. Fung, A. K. Khitrin and K. Ermolaev, *J. Magn. Reson.*, 2000, **142**, 97-101). Bruker 3.2 mm sapphire rotors sealed with silicone soft plug and  $\text{ZrO}_2$  drive cap were used.

All pulse sequences were preceded by a presaturation pulse train consisting of 16 flip ( $90^\circ$ ) pulses separated by 5 ms and a subsequent polarization delay during which (enhanced) polarization can build up. This allowed for reproducible measurement of polarization in a quantitative manner, especially when reaching a quasi-equilibrium using dummy scans was not possible due to extremely long build-up times. For the acquisition of build-up curves the polarization delay was varied; all other experiments were performed with fixed polarization delays between 10 and 60 s unless given otherwise.

### **Protein expression and labeling**

pet-21a plasmids carrying the F4C, A28C, and G75C mutation of human ubiquitin were created using site-directed mutagenesis and were verified by sequencing. The proteins were expressed recombinantly from *E. coli* strain BL21(DE3) in M9 minimal medium containing  $^{13}\text{C}$ -glucose and  $^{15}\text{NH}_4\text{Cl}$  as exclusive carbon and nitrogen sources. Purification was performed uniformly for all mutants using the following protocol: cells were resuspended in 25 ml of 50 mM  $\text{NH}_4\text{OAc}$  buffer (pH = 7.0) containing 10 mM 2-mercaptoethanol, lysed, and the lysate acidified to pH = 5 with acetic acid. The lysate was centrifuged and subsequently heated to 85 °C for 15 minutes while inverting several times. After cooling to r.t., the cloudy solution was centrifuged at 10,000 g for 30 minutes. A HiTrap SP HP column was equilibrated with 5 column volumes of 50 mM  $\text{NH}_4\text{OAc}$  buffer (pH = 5.0). The supernatant was loaded, washed with 5 column volumes of the same buffer, and eluted by applying a concentration gradient to 500 mM  $\text{NH}_4\text{OAc}$  buffer (pH = 5.0). For further purification, the sample was loaded to a HiLoad 26/600 gel filtration column and eluted with 50 mM  $\text{NH}_4\text{OAc}$  buffer (pH = 5.0). At the end of the procedure, the buffer was exchanged to



50 mM NH<sub>4</sub>OAc buffer (pH = 7.0) for increased stability. Typical yields were about 30 mg per liter of medium used.

For site-directed labeling, 5 equivalents (relative to protein) of 4-mercaptomethyl dipicolinic acid (4MMDPA) or 15 equivalents of 1,4,7,10-tetraazacyclododecane-1,4,7-tris-acetic acid-10-maleimidoethylacetamide (DOTA-M) were added to 0.5 ml of 1 mM protein solution and rocked for 24 h at room temperature. The solution was placed in a PD-10 desalting column and eluted with 50 mM NH<sub>4</sub>OAc (pH = 7.0) to remove excess spin label.

## Supplementary Figures

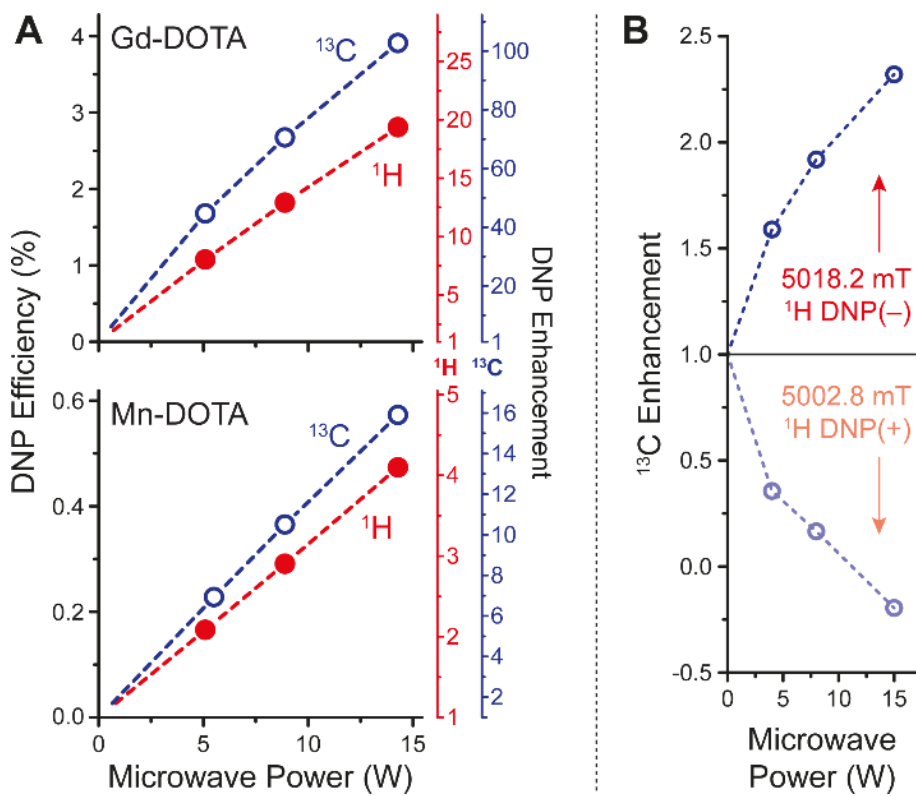


**Figure S1.** (A) Power dependence of  $^1\text{H}$  (full circles, red) and  $^{13}\text{C}$  (open circles, blue) DNP with Gd-DOTA. Left abscissa represents DNP efficiency relative to the theoretical maximum for each nucleus; right abscissas are  $^1\text{H}$  (red) and  $^{13}\text{C}$  (blue) enhancement factors. (B) Power dependence of “indirect”  $^{13}\text{C}$  enhancement at optimum (positive or negative)  $^1\text{H}$  enhancement.

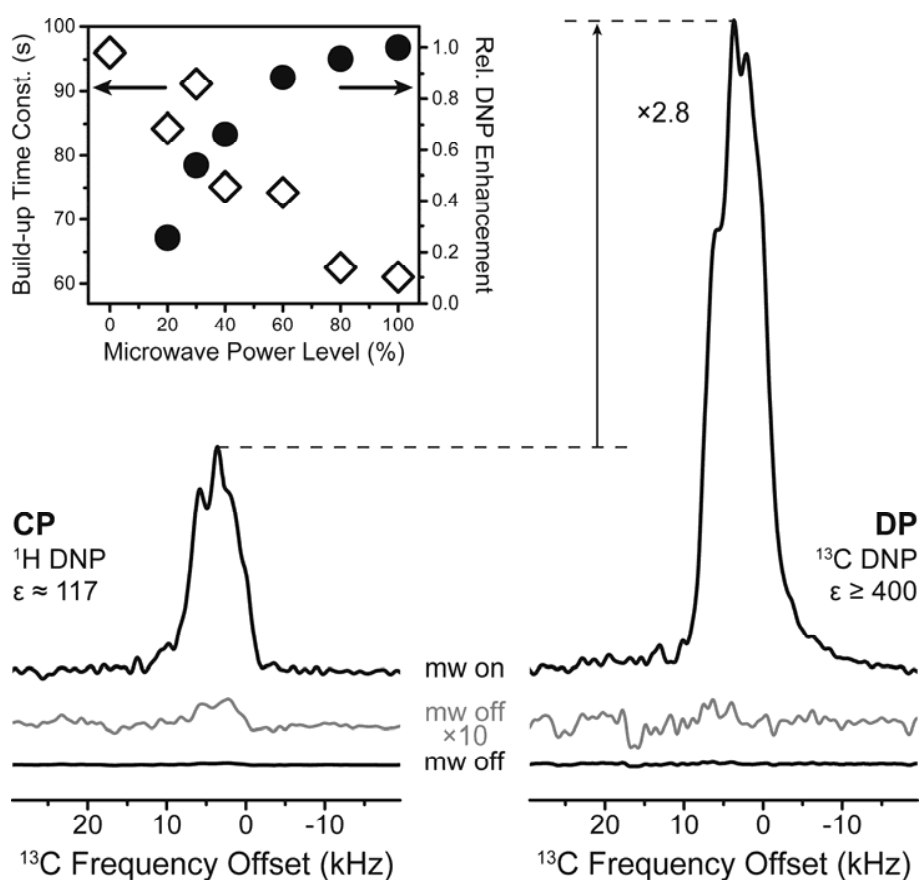


**Figure S2.**  $^1\text{H}$ - $^{13}\text{C}$  cross polarization (CP, left) and  $^{13}\text{C}$  direct polarization (DP, right) spectra of 60%  $^{13}\text{C}_3$ -glycerol in a mixture with 40%  $\text{H}_2\text{O}$  with DNP enhancement by irradiation of 10 mM Gd-DOTA at the appropriate SE field with 120 mW of 140 GHz microwave irradiation at 80 K and under static conditions. To increase  $\mu\text{w}$  field strength a  $\text{TE}_{011}$  resonator was used. 4.2 s and 120 s polarization time was used for CP and DP, respectively. For better visibility the ‘ $\mu\text{w}$  off’ spectra have been multiplied by a factor 10 (gray line). Spectra were averaged over 128 (CP,  $\mu\text{w}$  on), 31,104 (CP,  $\mu\text{w}$  off), 64 (DP,  $\mu\text{w}$  on), and 3,808 (DP,  $\mu\text{w}$  off) scans, respectively, and normalized for direct comparability of signal intensity. The inset shows  $^{13}\text{C}$  build-up time constant (open diamonds) and relative  $^{13}\text{C}$  DNP enhancement (filled circles) as function of  $\mu\text{w}$  power level relative to 120 mW.

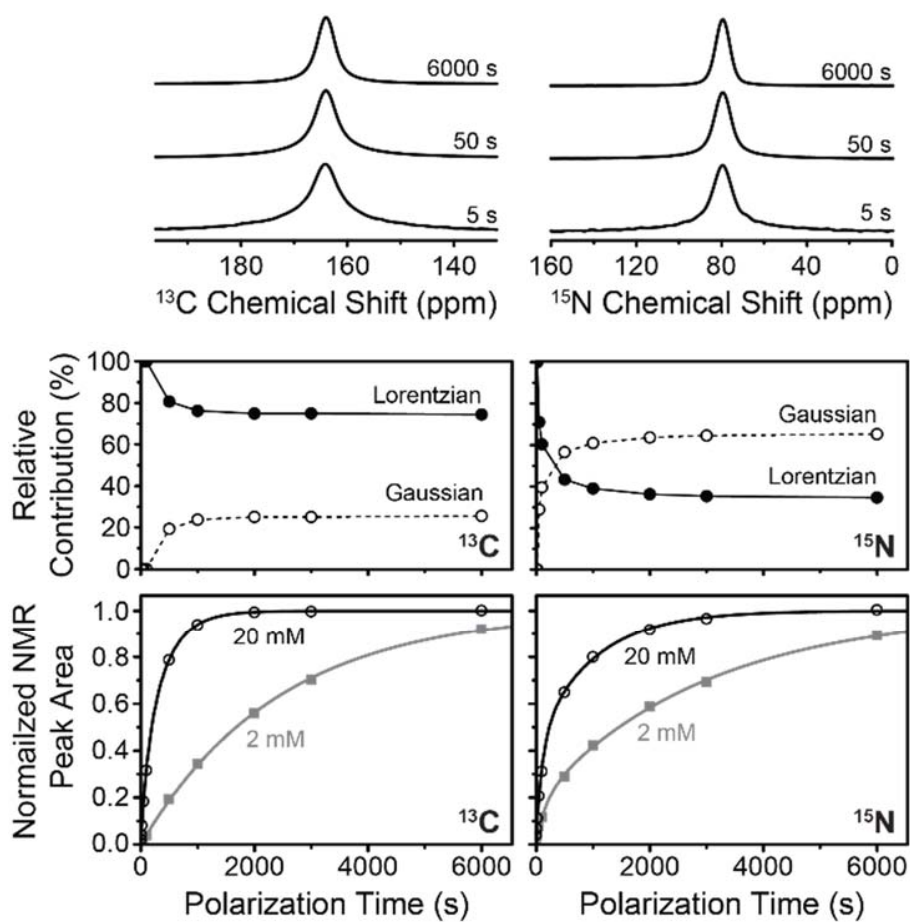


**Figure S3.** DNP-enhanced  $^{13}\text{C}$  (left) and  $^{15}\text{N}$  (right) spectra of  $^{13}\text{C},^{15}\text{N}$ -urea showing larger degree of broadening at shorter polarization times for a frozen solution containing 20 mM Gd-DOTA. The middle panel shows the relative contribution of homogeneous (Lorentzian) broadening and inhomogeneous (Gaussian) broadening, obtained by fitting with a linear combination of a Lorentzian and a Gaussian line. The lower graphs show the build-up of enhanced polarization obtained by integration over the whole NMR peak in comparison with that of a 2 mM Gd-DOTA solution.

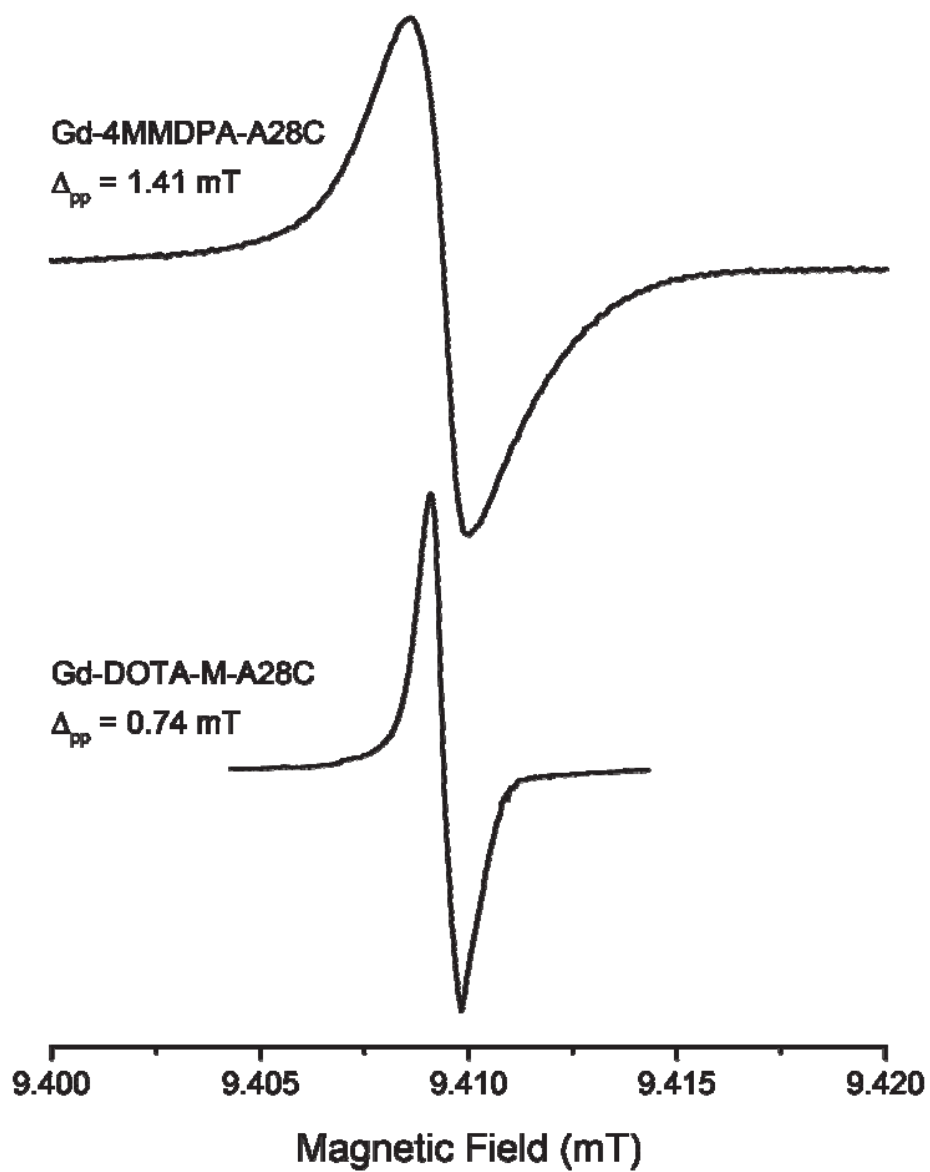


**Figure S4.** Cw EPR spectra of frozen DNP-solutions of Gd-4MMDPA-labeled and Gd-DOTA-M-labeled A28C mutant of ubiquitin measured at a  $\mu$ w frequency of 263 GHz and a temperature of 100 K.  $\Delta_{pp}$  is the peak-to-peak linewidth of the cw spectra (*i.e.*, first derivative of the absorption spectra).

## Polarizing Agents

International Edition: DOI: 10.1002/anie.201612388

German Edition: DOI: 10.1002/ange.201612388

## Bis-Gadolinium Complexes for Solid Effect and Cross Effect Dynamic Nuclear Polarization

Monu Kaushik, Mian Qi, Adelheid Godt,\* and Björn Corzilius\*

**Abstract:** High-spin complexes act as polarizing agents (PAs) for dynamic nuclear polarization (DNP) in solid-state NMR spectroscopy and feature promising aspects towards biomolecular DNP. We present a study on bis(Gd-chelate)s which enable cross effect (CE) DNP owing to spatial confinement of two dipolar-coupled electron spins. Their well-defined Gd...Gd distances in the range of 1.2–3.4 nm allowed us to elucidate the Gd...Gd distance dependence of the DNP mechanism and NMR signal enhancement. We found that Gd...Gd distances above 2.1 nm result in solid effect DNP while distances between 1.2 and 2.1 nm enable CE for  $^1\text{H}$ ,  $^{13}\text{C}$ , and  $^{15}\text{N}$  nuclear spins. We compare 263 GHz electron paramagnetic resonance (EPR) spectra with the obtained DNP field profiles and discuss possible CE matching conditions within the high-spin system and the influence of dipolar broadening of the EPR signal. Our findings foster the understanding of the CE mechanism and the design of high-spin PAs for specific applications of DNP.

Dynamic nuclear polarization (DNP) has experienced widespread application in structural biology and materials research for sensitivity enhancement of magic-angle spinning (MAS) NMR spectroscopy.<sup>[1]</sup> By transferring the large electron spin polarization to the surrounding nuclear spins through microwave ( $\mu\text{W}$ ) irradiation of a frozen solution, the NMR signal intensity can be increased by up to three orders of magnitude.<sup>[2]</sup> Polarizing agents (PAs), typically based on nitroxides, provide the electron spin polarization.<sup>[3]</sup> Lately, complexes of the high-spin metal ions  $\text{Gd}^{\text{III}}$  or  $\text{Mn}^{\text{II}}$  have been introduced as alternative PAs.<sup>[4]</sup> A recent, intriguing development is the utilization of PAs site-directedly bound to biomolecules. Owing to the limited distance between PA and biomolecule, hyperpolarization can be selectively transferred to the site(s) of interest.<sup>[5]</sup> Loss of polarization to the bulk can be prevented either by matrix perdeuteration in the

case of (indirect)  $^1\text{H}$  DNP,<sup>[6]</sup> or by utilizing direct DNP of nuclei with small natural abundance in the matrix (e.g.,  $^{13}\text{C}$ ,  $^{15}\text{N}$ ) so that spin-diffusion pathways are limited.<sup>[7]</sup> For the latter case the development of PAs with properties tailored for efficient, direct DNP of  $^{13}\text{C}$  and  $^{15}\text{N}$  is crucial. Bis-nitroxide tags can provide sufficient  $^1\text{H}$  polarization but fail to provoke direct  $^{13}\text{C}$  DNP,<sup>[6]</sup> while direct  $^{13}\text{C}$  DNP was demonstrated with tags based on the paramagnetic metal ions  $\text{Mn}^{\text{II}}$  or  $\text{Gd}^{\text{III}}$ .<sup>[7,8]</sup> Furthermore, in contrast to nitroxides,  $\text{Gd}^{\text{III}}$  and  $\text{Mn}^{\text{II}}$  complexes are stable within cellular environments, which makes them suitable PAs for in-cell studies.<sup>[9]</sup>

In the context of MAS NMR, two DNP mechanisms have been exploited so far: the solid effect (SE)<sup>[10]</sup> and the cross effect (CE).<sup>[11]</sup> The SE can be evoked by irradiating a nominally forbidden electron-nuclear double- or zero-quantum transition. For the CE, two dipolar-coupled electron spins need to be present and their frequency difference,  $\Delta\omega_{0\text{S}}$ , is required to match the nuclear Larmor frequency,  $\omega_{0\text{I}}$  [Eq. (1)]:

$$\Delta\omega_{0\text{S}} = \pm\omega_{0\text{I}} \quad (1)$$

DNP occurs with positive or negative sign of nuclear hyperpolarization. A separation between the field of (+)- and (-)-DNP maxima corresponding to (at least)  $2\omega_{0\text{I}}$  is observed for SE, whereas for CE, all DNP matching conditions have to be encompassed within the inhomogeneously broadened envelope of the EPR spectrum.<sup>[12]</sup> This difference allows for clear identification of DNP mechanisms based on analysis of DNP field profiles.<sup>[8,13]</sup>

Besides the frequency matching, CE relies strongly on the effective coupling strength between the two electron spins. Off-diagonal coupling elements introduce state mixing of the magnetic spin levels which in turn allows the transfer of polarization to the nuclear spin. Equation (1) is strictly valid only if the dipolar coupling is small compared to  $\omega_{0\text{I}}$ . In this case, CE efficiency increases with dipolar coupling strength due to the responsible transition moment being proportional to  $D_0/\omega_{0\text{I}}$ , where  $D_0$  is the effective off-diagonal coupling element.<sup>[14]</sup> However, once the magnitude of this coupling becomes comparable to the nuclear Larmor frequency, the efficiency of CE can decrease as was shown in theory and experiment.<sup>[15]</sup>

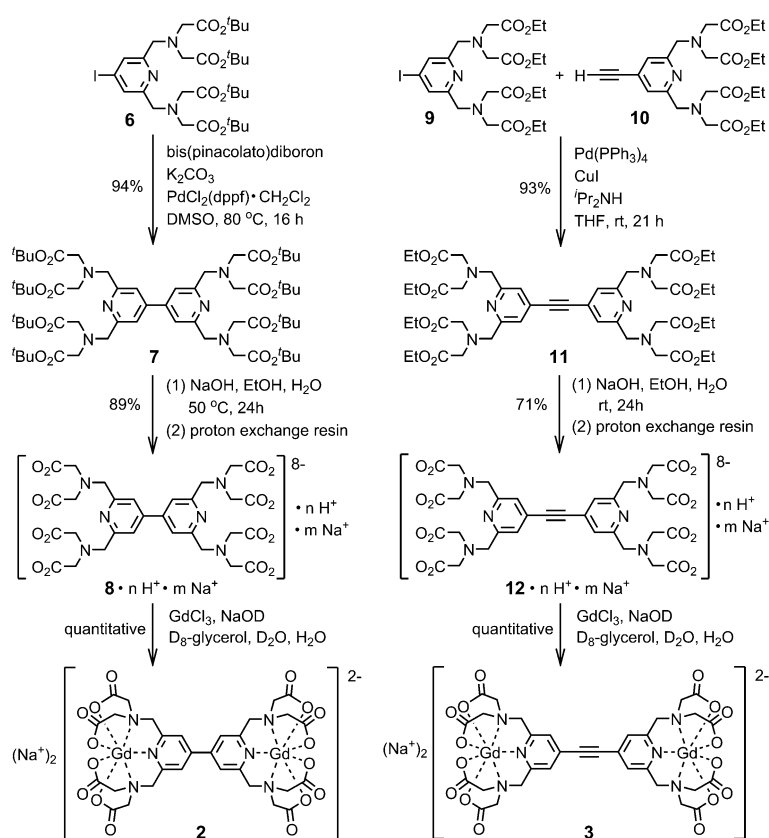
Dipolar coupling between electron spins, as needed for CE, can be provided by means of inter-molecular nearest-neighbor interactions in a frozen solution of PAs with one paramagnetic site.<sup>[16]</sup> This requires a high concentration of the PA. For nitroxides, a major improvement was the interconnection of two TEMPO moieties giving a biradical that

[\*] M. Sc. M. Kaushik, Dr.-Ing. B. Corzilius  
Goethe-Universität Frankfurt am Main  
Institut für Physikalische und Theoretische Chemie, Institut für Biophysikalische Chemie und Biomolekulares Magnetresonanzzentrum (BMRZ)  
Max-von-Laue-Strasse 7–9, 60438 Frankfurt am Main (Germany)  
E-mail: corzilius@em.uni-frankfurt.de  
Dr. M. Qi, Prof. Dr. A. Godt  
Fakultät für Chemie und Centrum für Molekulare Materialien (CM<sub>2</sub>)  
Universität Bielefeld  
Universitätsstrasse 25, 33615 Bielefeld (Germany)  
E-mail: godt@uni-bielefeld.de

Supporting information and the ORCID identification number(s) for the author(s) of this article can be found under:  
<http://dx.doi.org/10.1002/anie.201612388>.

allowed for sufficient dipolar coupling even at low PA concentration.<sup>[17]</sup>

Earlier, we have demonstrated that complexes of Gd<sup>III</sup> and Mn<sup>II</sup> act as PAs for <sup>13</sup>C and <sup>15</sup>N direct DNP.<sup>[8]</sup> However, high concentrations of up to 20 mM are needed to achieve CE. Therefore, we became interested to investigate bis(Gd-complexes)<sup>[18]</sup> as PAs. Additionally, Gd<sup>III</sup> is an ideal test system for the biologically highly relevant Mn<sup>II</sup> ion because it features very similar EPR/DNP properties, but does not suffer from strong hyperfine interaction to the metal nucleus.<sup>[8]</sup> The bis(Gd-complexes) used in this study, bis(Gd-chelate)s **2–5**, are presented in Figure 1. Due to the stiffness of the spacer backbone<sup>[19]</sup> and the tetherless attachment of the Gd-containing moiety Gd-PyMTA, their Gd...Gd distances are well defined. They range from 1.2–3.4 nm as was calculated taking into account the experimentally determined stiffness and the glass transition temperature of the solvent mixture used for the experiments.<sup>[20]</sup> The bis(Gd-chelate)s **4** and **5** are furnished with branched polyethylene glycol chains to mask the hydrophobic spacer backbone and therefore achieve solubility in protic solvents including water. The bis(Gd-chelate)s **2** and **3** miss such chains. Nevertheless, they dissolve in glycerol/water, probably because of the two polar and charged Gd-PyMTA units. As a reference for inter-



Scheme 1. Syntheses of **2** and **3**. For details see Supporting Information.

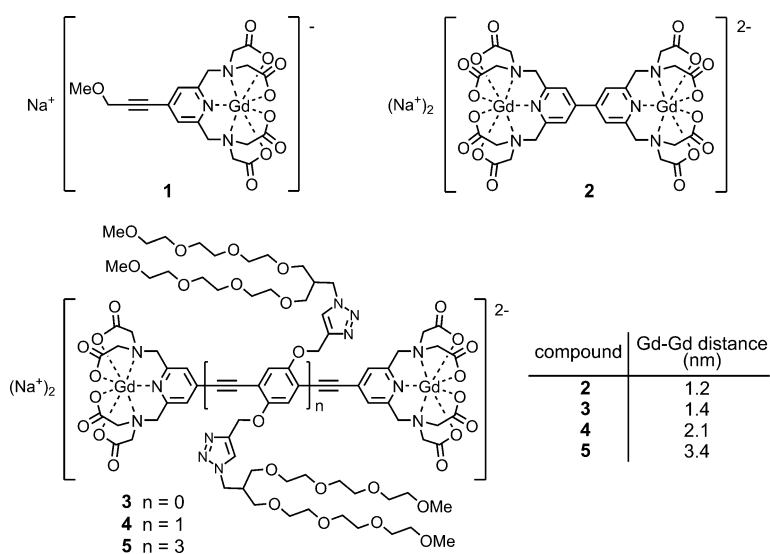


Figure 1. Structural formulae and calculated Gd...Gd distances of the compounds in this study.

molecular dipolar coupling, the mono(Gd-chelate) **1** was used. The syntheses of bis(Gd-chelate)s **2** and **3** are shown in Scheme 1 and details are given in the supporting information. The syntheses of bis(Gd-chelate)s **4** and **5** have been reported elsewhere.<sup>[18]</sup>

For the EPR and DNP experiments a Gd<sup>III</sup> ion concentration of 4 mM was used in order to favor intra-molecular

dipolar coupling within the bis(Gd-chelate)s over inter-molecular interactions. All samples were equal in Gd ion concentration, that is, we used a 4 mM solution of mono(Gd-chelate) **1** and 2 mM solutions of bis(Gd-chelate)s **2–5**. Besides the PA in 60/30/10 (vol%) of [<sub>8</sub>D]-glycerol/D<sub>2</sub>O/H<sub>2</sub>O, <sup>13</sup>C, <sup>15</sup>N<sub>2</sub>-urea was present at a concentration of 2 M for direct read-out of <sup>13</sup>C and <sup>15</sup>N polarization and for indirect read-out of <sup>1</sup>H polarization via cross polarization to <sup>13</sup>C.

Figure 2A shows the EPR spectra of compounds **1–5**, limited to the  $m_S = -1/2 \leftrightarrow +1/2$  central transition (CT) region of the high-spin ( $S = 7/2$ ) system. We have inverted the spectra for better visual comparison with the <sup>1</sup>H, <sup>13</sup>C, and <sup>15</sup>N DNP field profiles shown in Figure 2B. Both, EPR spectra and DNP field profiles, were recorded at the  $\mu$ w frequency of 263 GHz. The DNP field profiles are limited to the (–)-DNP region due to limited sweep range of the instrumental set-up used. Nevertheless, using (–)-DNP with inversion of the recorded emissive NMR spectrum is practically equivalent to the more common utilization of (+)-DNP.<sup>[21]</sup> In the following, we will refer to absolute values when discussing relative changes (increase/decrease) of enhancement between bis(Gd-chelate)s.

The increasing dipolar coupling, with constants ranging from 0.7 to 32 MHz (Table 1), upon decreasing Gd...Gd distance is manifested clearly by broadening of the CT line in

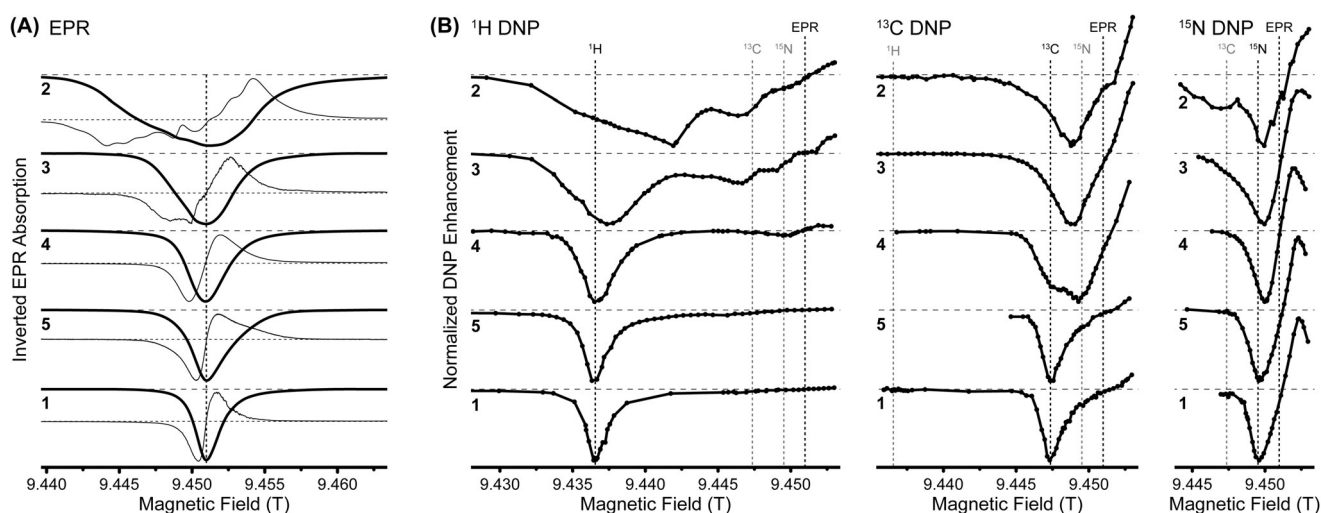


**Figure 2.** A) 263 GHz EPR spectra of frozen solutions of mono(Gd-chelate) **1** (4 mM) and bis(Gd-chelate)s **2–5** (2 mM) in 60/30/10 (vol%) [D<sub>8</sub>]-glycerol/D<sub>2</sub>O/H<sub>2</sub>O recorded at 100 K. The samples also contained <sup>13</sup>C,<sup>15</sup>N<sub>2</sub>-urea (2 M) for detection of <sup>1</sup>H, <sup>13</sup>C, and <sup>15</sup>N polarization in DNP experiments. As-recorded continuous-wave (cw) EPR spectra (i.e., absorption derivative) are shown as thin lines with dotted zero line. Thick lines are absorption spectra obtained by integration of cw spectra and subsequent baseline correction. The vertical dotted line indicates the central resonance field for direct comparison with field profiles (marked as EPR) in (B). B) 263 GHz <sup>1</sup>H, <sup>13</sup>C, and <sup>15</sup>N DNP field profiles of the same samples as in (A), acquired by sweeping the NMR field and recording the <sup>1</sup>H–<sup>13</sup>C cross-polarization intensity as well as direct <sup>13</sup>C or <sup>15</sup>N signal intensity during μw irradiation. The profiles were normalized to the respective maximum (–)DNP enhancement. Horizontal dashed lines indicate the baseline ( $\epsilon = 1$ ) for each profile. Vertical dotted lines mark the central EPR resonance field [equal to the dotted line in (A)], as well as the field position of maximum (–)SE DNP enhancement for each nucleus.

**Table 1:** DNP enhancement factors  $\epsilon$  of <sup>1</sup>H, <sup>13</sup>C, and <sup>15</sup>N signals obtained with mono(Gd-chelate) **1** and the bis(Gd-chelate)s **2–5**.

Compound	Gd...Gd distance [nm]	Dipolar coupling [MHz] <sup>[c]</sup>	$\epsilon(^1\text{H})$ <sup>[d]</sup>	$\epsilon(^{13}\text{C})$ <sup>[d]</sup>	$\epsilon(^{15}\text{N})$ <sup>[d]</sup>
<b>1</b>	4.2 <sup>[a]</sup>	0.7	–3.9(1)	–26.1(9)	–68(7)
<b>2</b>	1.2 <sup>[b]</sup>	32.4	–2.0(1)	–13.4(3)	–6.8(6)
<b>3</b>	1.4 <sup>[b]</sup>	18.1	–2.3(1)	–29.5(8)	–34(3)
<b>4</b>	2.1 <sup>[b]</sup>	5.7	–3.1(1)	–23.2(6)	–108(7)
<b>5</b>	3.4 <sup>[b]</sup>	1.3	–2.8(1)	–23(1)	–70(7)

[a] Average nearest neighbor Gd...Gd distance calculated<sup>[24]</sup> for a homogeneous solution of mono(Gd-chelate) **1**. [b] Calculated<sup>[20]</sup> Gd...Gd distances at the glass-transition temperature of 165 K of the solvent mixture. [c] Coupling constants calculated by point-dipole approximation. [d] Determined at the respective field of maximum negative enhancement. Values in parentheses are the uncertainty in the last significant digit determined by signal/noise analyses of the NMR spectra.

the EPR spectrum. Because of the  $1/r^3$  dependency of the line width of the CT, with  $r$  being the Gd...Gd distance,<sup>[22]</sup> exchange interaction can be neglected. This is explained by the full localization of spin density on the Gd<sup>III</sup> ion.<sup>[23]</sup> The shape of DNP field profiles reveals the type of DNP mechanism being active for each nucleus and PA.<sup>[8,13]</sup> Although in the high-spin system several transitions can fulfil the CE matching condition under MAS,<sup>[12]</sup> we can explain most of our findings by only considering the CT. This seems logical because all other (satellite) transitions are subject to strong angular dependence due to zero-field splitting anisotropy and should therefore contribute to a much smaller degree. We observe a transition in the <sup>13</sup>C

and <sup>15</sup>N DNP field profiles from the SE to the CE mechanism with decreasing Gd...Gd distance. A clear signature of SE is observed for the reference compound, mono(Gd-chelate) **1**, and the bis(Gd-chelate) **5** with the largest Gd...Gd separation. At Gd...Gd distances of 1.4 nm [bis(Gd-chelate) **3**] and 2.1 nm [bis(Gd-chelate) **4**] we propose dominance of the CE mechanism for <sup>13</sup>C and <sup>15</sup>N polarization, respectively. The onset of CE contribution is marked by a significant increase in DNP enhancement (Table 1) despite the increasing dipolar broadening of the EPR spectrum which—on its own—would lead one to expect a decreasing enhancement by SE due to less efficient excitation by monochromatic μw.<sup>[4]</sup> The transition from SE to CE with decreasing Gd...Gd distance is accompanied by a shift of the maximum of the (–)enhancement peak in the DNP field profile towards the EPR resonance field, resulting in (+)DNP and (–)DNP peak separation of  $< 2\omega_{0f}$ . The transition is impressively obvious for bis(Gd-chelate) **4**, for which <sup>13</sup>C SE and CE field profile peaks are distinguishable within a “doublet” and the mechanism of choice can be evoked rather selectively by tuning the external magnetic field.

A SE to CE shift occurs for <sup>1</sup>H DNP as well, as is clearly visible from a comparison of the <sup>1</sup>H DNP field profiles of bis(Gd-chelate)s **5** and **2**. However, no increase in the enhancement factor is observed. Nevertheless, the reduction from  $\epsilon = -4$  to  $\epsilon = -2$  is less than expected based on the amplitude reduction of the EPR signal due to line broadening.<sup>[4]</sup> Interestingly, some of the <sup>1</sup>H DNP field profiles show additional features close to the center of the EPR resonance. They are barely visible at 2.1 nm [bis(Gd-chelate) **4**], but highly prominent at shorter Gd...Gd distances. These might arise from several matching conditions including satellite



transitions within the high-spin system.<sup>[12]</sup> However, these features seem to be centered at the <sup>13</sup>C and <sup>15</sup>N Larmor frequency offsets which suggest cross-talk between the polarizations of different nuclear species,<sup>[8,25]</sup> or might be a sign of multiple nuclei undergoing concerted DNP transitions. Earlier studies have shown such features to occur at field offsets corresponding to nuclear combination frequencies,<sup>[26]</sup> a situation not given in this case. Another explanation might be an “indirect excitation” of one Gd<sup>III</sup> ion by <sup>13</sup>C or <sup>15</sup>N SE which leads to partial saturation of the electron spin and subsequently drives <sup>1</sup>H CE.<sup>[27]</sup>

Another interesting finding is that, despite the significant broadening of the EPR CT line with shorter Gd...Gd distances, the width of the <sup>13</sup>C and <sup>15</sup>N DNP field profiles remains rather constant. This is striking when comparing the <sup>13</sup>C and <sup>15</sup>N field profiles of bis(Gd-chelate)s **2–4** (neglecting the additional <sup>13</sup>C SE feature of the latter) in light of the drastic differences in their EPR spectra. The reason for this is unclear but might be found by closer inspection of the CE matching condition [Eq. (1)], keeping in mind the molecular geometry and that it is a high-spin system. For the bis(Gd-chelate)s, effective variation in spin precession frequency is caused by ZFS and electron-electron dipolar coupling.<sup>[12]</sup> Therefore, the naturally occurring distribution of ZFS parameters,<sup>[28]</sup> deviations of the tensors from collinearity caused by molecular bending,<sup>[19]</sup> and the orthorhombicity of the ZFS of Gd-PyMTA in combination with rotation around the C–C single bonds of the spacer axis lead to CE matching conditions for different molecular orientations during MAS experiments.<sup>[12]</sup> At the same time, the EPR spectral envelope is the result of a multitude of possible spin states within the coupled high-spin system. Since not all molecular geometries and/or initial spin states are expected to contribute equally to DNP enhancement, the effective widths of EPR spectra and field profiles deviate. An in-depth theoretical analysis, possibly in combination with an experimental study on a variety of bis(Gd-complex)es differing in their ligand, would be very useful in elaborating the cause of the observed effects.

We found the largest <sup>13</sup>C and <sup>15</sup>N signal enhancements with the bis(Gd-chelate)s with Gd...Gd distances of 1.4 and 2.1 nm, respectively, while for shorter distances efficiencies are lower for both nuclei. Especially for <sup>15</sup>N, enhancement is dramatically reduced at 1.2 nm. Besides the trivial excitation penalty due to broadening of the EPR signal, this might be caused by the rather large ratio between dipolar coupling constant (32 MHz) and nuclear Larmor frequency (42 MHz). While dipolar coupling is a requirement for CE transfer, large ratios inhibit CE.<sup>[15]</sup>

Summarizing, bis(Gd-chelate)s with stiff spacers between the Gd<sup>III</sup> ions can be used as effective CE PAs for <sup>13</sup>C and <sup>15</sup>N direct DNP. The enabling of CE at rather low concentrations is caused by mutual spatial confinement of two ions as an electron spin pair. The comparison of bis(Gd-chelate)s with Gd...Gd distances between 3.4 and 1.2 nm indicate that the Gd...Gd coupling required for transition from SE to CE DNP correlates with the gyromagnetic ratio of the nucleus polarized. Furthermore, the two Gd...Gd distances corresponding to the largest <sup>13</sup>C and <sup>15</sup>N enhancements show a similar correlation. No boost in <sup>1</sup>H enhancement as compared to the

mono(Gd-chelate) has been observed. The widths of the <sup>13</sup>C and <sup>15</sup>N DNP field profiles remain constant although the line width of the EPR CT is increasing with decreasing Gd...Gd distance. To explain this finding, molecular geometry and/or initial spin state of the coupled high-spin system are suggested to influence the CE. Based on this, we propose theoretical studies in combination with an investigation of bis(Gd-complex)es of different molecular symmetries. This would allow for an in-depth understanding of the effects and might give a guideline for improving CE efficiency and for the use of the biologically highly relevant Mn<sup>II</sup> ion as PA. Our study opens the field to special applications, for example under conditions where nitroxides are chemically unstable. Biomolecules could be labeled with bis(metal-chelate)-based tags, or intermolecular contacts between subunits labeled with one metal ion each could be probed.

### Experimental Section

A sweepable Bruker Avance III DNP spectrometer operating at 400 MHz <sup>1</sup>H frequency was used to record all DNP field profiles. 263 GHz Bruker EleXsys E780 spectrometer was used to record cw EPR spectra. Detailed instrumental and experimental description as well as sample preparation are given in the Supporting Information.

### Acknowledgements

We thank Dr. T. Gutmann and Prof. Dr. G. Buntkowsky (TU Darmstadt) for access to the DNP spectrometer. We thank H. P. Dette (Bielefeld University) for the determination of the glass transition temperature. B.C. acknowledges funding by the Deutsche Forschungsgemeinschaft (DFG) through an Emmy Noether project (CO 802/2-1) as well as support from the Center for Biomolecular Magnetic Resonance (BMRZ). A.G. acknowledges DFG (SPP1601, GO 555/6-2) as funding source.

### Conflict of interest

The authors declare no conflict of interest.

**Keywords:** cross effect · dynamic nuclear polarization · gadolinium complexes · polarizing agent · solid-state NMR spectroscopy

**How to cite:** *Angew. Chem. Int. Ed.* **2017**, *56*, 4295–4299  
*Angew. Chem.* **2017**, *129*, 4359–4363

- 
- [1] a) A. N. Smith, J. R. Long, *Anal. Chem.* **2016**, *88*, 122–132; b) Q. Z. Ni, E. Daviso, T. V. Can, E. Markhasin, S. K. Jawla, T. M. Swager, R. J. Temkin, J. Herzfeld, R. G. Griffin, *Acc. Chem. Res.* **2013**, *46*, 1933–1941.  
[2] J.-H. Ardenkjaer-Larsen, G. S. Boebinger, A. Comment, S. Duckett, A. S. Edison, F. Engelke, C. Griesinger, R. G. Griffin, C. Hilty, H. Maeda, G. Parigi, T. Prisner, E. Ravera, J. van Bentum, S. Vega, A. Webb, C. Luchinat, H. Schwalbe, L. Frydman, *Angew. Chem. Int. Ed.* **2015**, *54*, 9162–9185; *Angew. Chem.* **2015**, *127*, 9292–9317.

- [3] a) C. Song, K.-N. Hu, C.-G. Joo, T. M. Swager, R. G. Griffin, *J. Am. Chem. Soc.* **2006**, *128*, 11385–11390; b) C. Sauvée, M. Rosay, G. Casano, F. Aussenac, R. T. Weber, O. Ouari, P. Tordo, *Angew. Chem. Int. Ed.* **2013**, *52*, 10858–10861; *Angew. Chem.* **2013**, *125*, 11058–11061.
- [4] B. Corzilius, A. A. Smith, A. B. Barnes, C. Luchinat, I. Bertini, R. G. Griffin, *J. Am. Chem. Soc.* **2011**, *133*, 5648–5651.
- [5] a) T. Maly, D. Cui, R. G. Griffin, A.-F. Miller, *J. Phys. Chem. B* **2012**, *116*, 7055–7065; b) B. J. Wylie, B. G. Dzikovski, S. Pawsey, M. Caporini, M. Rosay, J. H. Freed, A. E. McDermott, *J. Biomol. NMR* **2015**, *61*, 361–367; c) M. A. Voinov, D. B. Good, M. E. Ward, S. Milikisoyants, A. Marek, M. A. Caporini, M. Rosay, R. A. Munro, M. Ljumovic, L. S. Brown, V. Ladizhansky, A. I. Smirnov, *J. Phys. Chem. B* **2015**, *119*, 10180–10190; d) E. A. W. van der Crujisen, E. J. Koers, C. Sauvée, R. E. Hulse, M. Weingarth, O. Ouari, E. Perozo, P. Tordo, M. Baldus, *Chem. Eur. J.* **2015**, *21*, 12971–12977.
- [6] T. Viennet, A. Viegas, A. Kuepper, S. Arens, V. Gelev, O. Petrov, T. N. Grossmann, H. Heise, M. Etzkorn, *Angew. Chem. Int. Ed.* **2016**, *55*, 10746–10750; *Angew. Chem.* **2016**, *128*, 10904–10908.
- [7] P. Wenk, M. Kaushik, D. Richter, M. Vogel, B. Suess, B. Corzilius, *J. Biomol. NMR* **2015**, *63*, 97–109.
- [8] M. Kaushik, T. Bahrenberg, T. V. Can, M. A. Caporini, R. Silvers, J. Heiliger, A. A. Smith, H. Schwalbe, R. G. Griffin, B. Corzilius, *Phys. Chem. Chem. Phys.* **2016**, *18*, 27205–27218.
- [9] a) A. Martorana, G. Bellapadrona, A. Feintuch, E. Di Gregorio, S. Aime, D. Goldfarb, *J. Am. Chem. Soc.* **2014**, *136*, 13458–13465; b) M. Qi, A. Groß, G. Jeschke, A. Godt, M. Drescher, *J. Am. Chem. Soc.* **2014**, *136*, 15366–15378.
- [10] a) E. Erb, J. L. Motchane, J. Uebbersfeld, *C. R. Hebd. Seances Acad. Sci.* **1958**, *246*, 2121–2123; b) M. Abraham, R. W. Kedzie, C. D. Jeffries, *Phys. Rev.* **1957**, *106*, 165–166; c) A. Abragam, W. G. Proctor, *C. R. Hebd. Seances Acad. Sci.* **1958**, *246*, 2253–2256.
- [11] a) A. V. Kessenikh, V. I. Lushchikov, A. A. Manenkov, Y. V. Taran, *Sov. Phys. Sol. State* **1963**, *5*, 321–329; b) C. F. Hwang, D. A. Hill, *Phys. Rev. Lett.* **1967**, *19*, 1011–1014; c) C. F. Hwang, D. A. Hill, *Phys. Rev. Lett.* **1967**, *18*, 110–112.
- [12] B. Corzilius, *Phys. Chem. Chem. Phys.* **2016**, *18*, 27190–27204.
- [13] D. Shimon, Y. Hovav, A. Feintuch, D. Goldfarb, S. Vega, *Phys. Chem. Chem. Phys.* **2012**, *14*, 5729–5743.
- [14] K. N. Hu, G. T. Debelouchina, A. A. Smith, R. G. Griffin, *J. Chem. Phys.* **2011**, *134*, 19.
- [15] G. Mathies, M. A. Caporini, V. K. Michaelis, Y. Liu, K.-N. Hu, D. Mance, J. L. Zweier, M. Rosay, M. Baldus, R. G. Griffin, *Angew. Chem. Int. Ed.* **2015**, *54*, 11770–11774; *Angew. Chem.* **2015**, *127*, 11936–11940.
- [16] K. N. Hu, *Solid State Nucl. Magn. Reson.* **2011**, *40*, 31–41.
- [17] K. N. Hu, H. H. Yu, T. M. Swager, R. G. Griffin, *J. Am. Chem. Soc.* **2004**, *126*, 10844–10845.
- [18] M. Qi, M. Hülsmann, A. Godt, *J. Org. Chem.* **2016**, *81*, 2549–2571.
- [19] G. Jeschke, M. Sajid, M. Schulte, N. Ramezani, A. Volkov, H. Zimmermann, A. Godt, *J. Am. Chem. Soc.* **2010**, *132*, 10107–10117.
- [20] A. Dalaloyan, M. Qi, S. Ruthstein, S. Vega, A. Godt, A. Feintuch, D. Goldfarb, *Phys. Chem. Chem. Phys.* **2015**, *17*, 18464–18476.
- [21] A. B. Barnes, E. Markhasin, E. Daviso, V. K. Michaelis, E. A. Nanni, S. K. Jawla, E. L. Mena, R. DeRocher, A. Thakkar, P. P. Woskov, J. Herzfeld, R. J. Temkin, R. G. Griffin, *J. Magn. Reson.* **2012**, *224*, 1–7.
- [22] J. A. Clayton, M. Qi, A. Godt, D. Goldfarb, S. Han, M. Sherwin, *Phys. Chem. Chem. Phys.* **2017**, *19*, 5127–5136.
- [23] A. Collauto, A. Feintuch, M. Qi, A. Godt, T. Meade, D. Goldfarb, *J. Magn. Reson.* **2016**, *263*, 156–163.
- [24] S. Chandrasekhar, *Rev. Mod. Phys.* **1943**, *15*, 1–89.
- [25] D. Daube, V. Aladin, J. Heiliger, J. J. Wittmann, D. Barthelmes, C. Bengs, H. Schwalbe, B. Corzilius, *J. Am. Chem. Soc.* **2016**, *138*, 16572–16575.
- [26] D. Shimon, Y. Hovav, I. Kaminker, A. Feintuch, D. Goldfarb, S. Vega, *Phys. Chem. Chem. Phys.* **2015**, *17*, 11868–11883.
- [27] Y. Hovav, D. Shimon, I. Kaminker, A. Feintuch, D. Goldfarb, S. Vega, *Phys. Chem. Chem. Phys.* **2015**, *17*, 6053–6065.
- [28] A. M. Raitsimring, A. V. Astashkin, O. G. Poluektov, P. Caravan, *Appl. Magn. Reson.* **2005**, *28*, 281–295.

Manuscript received: December 21, 2016

Final Article published: March 20, 2017

Supporting Information

**Bis-Gadolinium Complexes for Solid Effect and Cross Effect Dynamic Nuclear Polarization**

*Monu Kaushik, Mian Qi, Adelheid Godt,\* and Björn Corzilius\**

anie\_201612388\_sm\_miscellaneous\_information.pdf

# Table of Contents

<b>Supplementary results and discussion.....</b>	<b>S2</b>
Comments on the syntheses of bis(Gd-chelate)s <b>2</b> and <b>3</b> .....	S2
Figure S1. Apparatus used for the preparation of ester <b>11</b> .....	S2
DNP build-up dynamics .....	S3
Figure S2. Build-up curves of <sup>1</sup> H, <sup>13</sup> C, and <sup>15</sup> N DNP .....	S3
Table S1. Build-up time constants of <sup>1</sup> H, <sup>13</sup> C, and <sup>15</sup> N DNP .....	S3
<b>Experimental part.....</b>	<b>S4</b>
Instrumentation and details of EPR and DNP experiments .....	S4
Sample preparation.....	S4
DNP experiments .....	S4
EPR experiments .....	S4
Glass transition temperature determination .....	S5
Syntheses procedures.....	S5
General .....	S5
Mono(Gd-chelate) <b>1</b> .....	S6
Ester <b>7</b> .....	S6
Bisligand <b>8</b> •n H <sup>+</sup> •m Na <sup>+</sup> .....	S6
Bis(Gd-chelate) <b>2</b> .....	S7
Ester <b>11</b> .....	S7
Bisligand <b>12</b> •n H <sup>+</sup> •m Na <sup>+</sup> .....	S7
Bis(Gd-chelate) <b>3</b> .....	S8
<b>References.....</b>	<b>S8</b>
<b>Appendix: Supplementary NMR spectra.....</b>	<b>S8</b>
Figure S3a. <sup>1</sup> H NMR spectrum of ester <b>7</b> .....	S9
Figure S3b. <sup>13</sup> C NMR spectrum of ester <b>7</b> .....	S10
Figure S3c. <sup>13</sup> C DEPT 135 NMR spectrum of ester <b>7</b> .....	S11
Figure S4a. <sup>1</sup> H NMR spectrum of bisligand <b>8</b> •n H <sup>+</sup> •m Na <sup>+</sup> .....	S12
Figure S4b. <sup>1</sup> H NMR spectrum of bisligand <b>8</b> •n H <sup>+</sup> •m Na <sup>+</sup> (including MeOH) .....	S13
Figure S4c. <sup>13</sup> C NMR spectrum of bisligand <b>8</b> •n H <sup>+</sup> •m Na <sup>+</sup> .....	S14
Figure S4d. <sup>13</sup> C DEPT 135 NMR spectrum of bisligand <b>8</b> •n H <sup>+</sup> •m Na <sup>+</sup> .....	S15
Figure S4e. HMQC NMR spectrum of bisligand <b>8</b> •n H <sup>+</sup> •m Na <sup>+</sup> .....	S16
Figure S4f. HMBC NMR spectrum of bisligand <b>8</b> •n H <sup>+</sup> •m Na <sup>+</sup> .....	S17
Figure S5a. <sup>1</sup> H NMR spectrum of ester <b>11</b> .....	S18
Figure S5b. <sup>13</sup> C NMR spectrum of ester <b>11</b> .....	S19
Figure S5c. <sup>13</sup> C DEPT 135 NMR spectrum of ester <b>11</b> .....	S20
Figure S5d. HMQC NMR spectrum of ester <b>11</b> .....	S21
Figure S5e. HMBC NMR spectrum of ester <b>11</b> .....	S22
Figure S6a. <sup>1</sup> H NMR spectrum of bisligand <b>12</b> •n H <sup>+</sup> •m Na <sup>+</sup> .....	S23
Figure S6b. <sup>13</sup> C NMR spectrum of bisligand <b>12</b> •n H <sup>+</sup> •m Na <sup>+</sup> .....	S24
Figure S6c. <sup>13</sup> C DEPT 135 NMR spectrum of bisligand <b>12</b> •n H <sup>+</sup> •m Na <sup>+</sup> .....	S25
Figure S6d. HMQC NMR spectrum of bisligand <b>12</b> •n H <sup>+</sup> •m Na <sup>+</sup> .....	S26
Figure S6e. HMBC NMR spectrum of bisligand <b>12</b> •n H <sup>+</sup> •m Na <sup>+</sup> .....	S27

## Supplementary results and discussion

### Comments on the syntheses of bis(Gd-chelate)s **2** and **3**

As presented in scheme 1 (main text), Pd- and Pd/Cu-catalysed carbon-carbon cross couplings were used to connect the two Gd(III) ligating moieties of the bis(Gd-chelate)s **2** and **3**. In the following we address details of these reactions.

The two PyMTA moieties of bis(Gd-chelate) **2** were joined by a Suzuki coupling with in-situ formed boronic acid ester,<sup>[S1]</sup> employing bis(pinacolato)diboron in a slight excess of 3 mol%. The removal of residual bis(pinacolato)diboron from the coupling product, ester **7**, through column chromatography was incomplete. However, this compound did not interfere with the next step, the ester hydrolysis of ester **7** which gave bisligand **8**·n H<sup>+</sup>·m Na<sup>+</sup>. Furthermore, the <sup>1</sup>H NMR spectrum of bisligand **8**·n H<sup>+</sup>·m Na<sup>+</sup> did not reveal the presence of pinacol or a derivative thereof. We assume that under the conditions of ester hydrolysis, the bis(pinacolato)diboron was hydrolysed and, because of working in air, it was additionally oxidised giving pinacol and boric acid. Pinacol was, as concluded from the <sup>1</sup>H NMR spectrum, removed during the washing of the aqueous phase with organic solvents. However, boric acid is expected to have stayed in the aqueous phase and thus is assumed as an additional component in the solution of bis(Gd-chelate) **2**.

On the way to bis(Gd-chelate) **3** a Sonogashira-Hagihara coupling was used to obtain ester **11**. A typical byproduct of this coupling is a butydiyne formed through oxidative dimerisation (Glaser coupling) of the alkyne. The oxidative dimer of 4-ethynyl-PyMTA ethyl ester **10** and the targeted coupling product, ester **11**, were expected to be chromatographically hardly separable, if at all. Therefore, several measures were taken to minimize the oxidative alkyne dimerisation: (1) Using Pd(PPh<sub>3</sub>)<sub>4</sub> instead of the usually used Pd(PPh<sub>2</sub>)<sub>2</sub>Cl<sub>2</sub>. (2) Using an excess of 4-iodo-PyMTA ethyl ester **9**, so as to avoid residual alkyne which dimerises upon exposure of the reaction mixture to air during work-up. (3) Avoiding to open the flask for adding the catalysts after degassing of the solution of 4-iodo-PyMTA ethyl ester **9** and 4-ethynyl-PyMTA ethyl ester **10**. For this purpose, an apparatus consisting of a Schlenk flask and a bent tube as shown in figure S1 were used. The catalysts were placed in the bent tube and the solution of the coupling partners was prepared in the Schlenk flask. After degassing of the solution through several freeze-pump-thaw cycles, turning of the tube made the catalysts slide into the solution.



**Figure S1.** Apparatus used for the preparation of ester **11**. Through turning the bent tube the catalysts are brought to the degassed solution of 4-iodo-PyMTA ethyl ester **9** and 4-ethynyl-PyMTA ethyl ester **10** without opening the apparatus.

## DNP build-up dynamics

Build-up curves of bis(Gd-chelate)s **2-5** and mono(Gd-chelate) **1** have been measured for  $^1\text{H}$ ,  $^{13}\text{C}$ , and  $^{15}\text{N}$  DNP at the respective magnetic field of maximum (negative) enhancement. For all compounds, a similar build-up behavior was observed. We explain this by dominance of spin-diffusion, especially in the case of  $^{13}\text{C}$  and  $^{15}\text{N}$  DNP where rather small isotope concentration is present. Build-up curves are shown in Figure S2, time constants obtained by exponential fitting are given in Table S1.

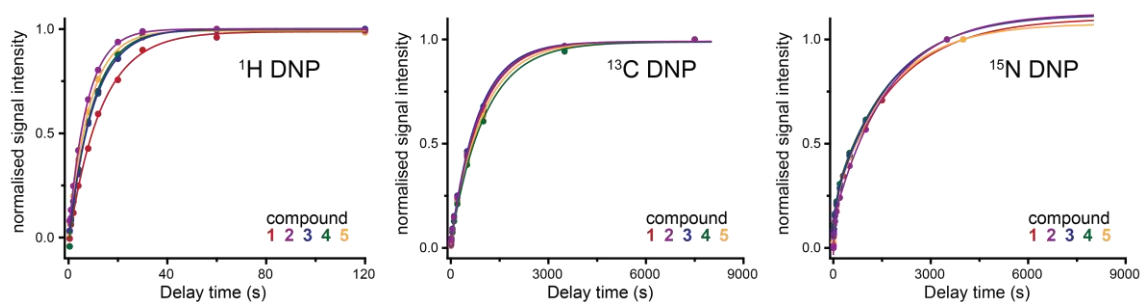


**Figure S2.** Build-up curves of  $^1\text{H}$ ,  $^{13}\text{C}$ , and  $^{15}\text{N}$  DNP obtained with mono(Gd-chelate) **1** and the bis(Gd-chelate)s **2-5**.

**Table S1.** DNP build-up time constants of  $^1\text{H}$ ,  $^{13}\text{C}$ , and  $^{15}\text{N}$  NMR signals obtained with mono(Gd-chelate) **1** and the bis(Gd-chelate)s **2-5**.

Compound	Gd–Gd distance [nm]	Dipolar coupling [MHz]	$T_B(^1\text{H})$ (s)	$T_B(^{13}\text{C})$ (s)	$T_B(^{15}\text{N})^{[a]}$ (s)	$\xi(^{15}\text{N})^{[b]}$
<b>1</b>	4.2	0.7	13.0	894	1874/98	5.51
<b>2</b>	1.2	32.4	7.4	882	1695/31	6.21
<b>3</b>	1.4	18.1	10.0	841	1728/85	5.65
<b>4</b>	2.1	5.7	9.2	1041	1751/85	5.26
<b>5</b>	3.4	1.3	8.2	962	1643/80	5.02

<sup>[a]</sup> Bi-exponential build-up was observed and two constants are given. For bis(Gd-chelate) **2** (1.2 nm) no complete saturation was observed; for this compound data points were shifted accordingly so that only the time-dependent component was fitted. <sup>[b]</sup> Ratio between slow and fast component of  $^{15}\text{N}$  build-up.

## Experimental part

### Instrumentation and details of EPR and DNP experiments

**Sample preparation.** 2 M  $^{13}\text{C}$ ,  $^{15}\text{N}_2$ -urea (99%  $^{13}\text{C}$ , 98%  $^{15}\text{N}$ , CortecNet) was dissolved in a 60/30/10 (vol.-%) mixture of  $\text{D}_8$ -glycerol/ $\text{D}_2\text{O}$ / $\text{H}_2\text{O}$  containing 4 mM mono(Gd-chelate) **1** or 2 mM of bis(Gd-chelate)s **2-5**.  $\text{D}_8$ -glycerol (98 % D) was purchased from CortecNet;  $\text{D}_2\text{O}$  (99.9 % D) was purchased from Sigma-Aldrich, and double distilled  $\text{H}_2\text{O}$  was used. All chemicals were used as received. The same samples were used for DNP and EPR experiments.

All complexes presented here are readily soluble in 60/30/10 (vol.-%) mixture of  $\text{D}_8$ -glycerol/ $\text{D}_2\text{O}$ / $\text{H}_2\text{O}$ . Samples for DNP (and EPR) were prepared from stock solutions of 40 mM mono(Gd-chelate) **1** or of 20 mM of bis(Gd-chelate)s **2-5**.

**DNP experiments.** A sweepable Bruker Avance III DNP spectrometer operating at 400 MHz  $^1\text{H}$  frequency was used to record all DNP field profiles. Bruker gyrotron operating at the maximum beam current of 115 mA produced corresponding microwave frequency of 263.4 GHz. The Bruker Ascent 400 DNP magnet was centred at 9.40 T and contained a superconducting sweep coil with a range of  $\pm 75$  mT. The sweep coil was controlled externally by a power supply with  $\pm 20$  A range. The sweep coil was energized step-wise to sweep the magnetic field and record DNP field profiles for  $^1\text{H}$ ,  $^{13}\text{C}$ , and  $^{15}\text{N}$  nuclei. After careful optimization of the respective optimum field position the sweep coil was put into persistent operation and enhancement factors were determined by comparison of NMR intensity with and without  $\mu\text{W}$  irradiation. Bruker 3.2 mm sapphire rotors sealed with silicone soft plug and  $\text{ZrO}_2$  drive cap were used. All DNP experiments were performed with MAS frequency of 8 kHz at cryogenic temperatures of  $\sim 119$  K and  $\sim 108$  K with and without microwaves respectively. Temperature was read out via a thermocouple inside the MAS stator during experiments, heating due to microwaves was not quantified. For all experiments radio frequency (rf) pulse amplitudes were set to 100 kHz, 50 kHz, and 40 kHz for  $^1\text{H}$ ,  $^{13}\text{C}$ , and  $^{15}\text{N}$ , respectively;  $^1\text{H}$  amplitude was set for  $^{13}\text{C}$  or  $^{15}\text{N}$  Hartmann-Hahn matching during CP.<sup>[S2]</sup> SPINAL64 at 100 kHz was used for broadband decoupling of  $^1\text{H}$ .<sup>[S3]</sup>

All spectra were preceded by a pre-saturation pulse train consisting of 16 flip ( $90^\circ$ ) pulses separated by 5 ms and subsequent polarisation delay during which (enhanced) polarization can build up. This allowed for reproducible measurement of polarization in a quantitative manner, especially when reaching a quasi-equilibrium using dummy scans was not possible due to long build-up times

**EPR experiments.** 263 GHz Bruker EleXsys E780 spectrometer was used to record continuous wave EPR spectra. Sample and probe temperature was maintained at 100 K with a LHe flow cryostat (Oxford Instruments). Bruker Ascent DNP magnet (89 mm) centered at 9.40 T with a superconducting sweep coil with a nominal range of  $\pm 75$  mT was employed. The sweep coil power supply is remotely controlled between -20 A and +20 A by the Bruker Xepr software used for data acquisition. EPR spectrum of compound **2** was recorded with a home-built resonator (with 5 kHz modulation frequency and 0.15 mT modulation amplitude) while all others were recorded with a Bruker resonator (with 100 kHz modulation frequency and 0.1 mT modulation amplitude), both operating in  $\text{TE}_{011}$  mode. Attenuation of 28 dB corresponding to nominally 23.7  $\mu\text{W}$  microwave power was used for all measurements. For all experiments, field was swept at the rate of 0.1 mT/s.

## Glass transition temperature determination

The glass transition temperature ( $T_g$ ) of the 60/30/10 (vol.-%) mixture of D<sub>8</sub>-glycerol/D<sub>2</sub>O/H<sub>2</sub>O was determined through differential scanning calorimetry (DSC) using a differential scanning heat-flow calorimeter (Q100, TA Instruments). About 10 mg of the mixture was placed into an aluminum pan and the pan was sealed hermetically. The sample was shock-frozen through dipping the filled pan into liquid nitrogen. Finally, the pan was transferred into the calorimeter. Measurements were performed with an empty pan as a reference. The  $T_g$  of the sample was determined in the heating mode at 10 K min<sup>-1</sup> using the onset of the glass transition signal, i.e. the intersection between the extrapolated baseline and a line of maximum slope in the heat flow signal, following the convention of Angell.<sup>[S4]</sup> The  $T_g$  of the mixture of D<sub>8</sub>-glycerol/D<sub>2</sub>O/H<sub>2</sub>O 60/30/10 (vol.-%) was determined to be 165 K ± 2 K.

## Syntheses procedures

**General.** Unless otherwise stated, reactions were performed under ambient conditions and with commercial solvents and reagents, except THF (HPLC grade) which was distilled from sodium/benzophenone prior to use. For the preparation of the aqueous solutions, deionized water was used. The argon was passed through anhydrous CaCl<sub>2</sub> prior to use. The solvents used for extraction and chromatography were of technical grade and were distilled prior to their use. The proton-exchange resin (Dowex 50WX4 hydrogen form, 91 g) was subsequently washed with THF (3 × 200 mL), EtOH (2 × 100 mL), H<sub>2</sub>O (2 × 150 mL), and EtOH (200 mL) and then dried over P<sub>4</sub>O<sub>10</sub> at 0.05 mbar for 5 days to obtain a pure and dry proton exchange resin (30 g).

The temperatures given for the reactions refer to the bath temperatures. Solvents were removed at a bath temperature of ~40 °C and reduced pressure. The products were dried at room temperature at ~0.05 mbar. The pH/pD values of the solutions were determined using pH indicator strips (resolution: 0.3 pH).

Column chromatography was carried out on silica gel 60 (0.035–0.070 mm) applying slight pressure. In the procedures reported below, the size of the column is given as diameter × length. The material was loaded onto the column dissolved in a small quantity of the eluent. Thin layer chromatography was performed on silica gel 60 containing fluorescent indicator F254. The solid support for the silica gel layer was aluminum foil. Unless otherwise stated, the spots were detected with UV light of  $\lambda = 254$  and 366 nm. The compositions of solvent mixtures are given in volume ratios.

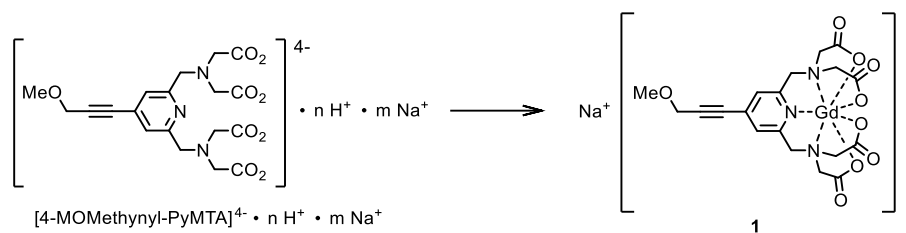
For centrifugation, a centrifuge with a relative centrifugal force of 6500rpm/4000g was used.

NMR spectra were calibrated using the solvent signal as an internal standard [CDCl<sub>3</sub>:  $\delta(^1\text{H}) = 7.25$ ,  $\delta(^{13}\text{C}) = 77.0$ ; D<sub>2</sub>O:  $\delta(^1\text{H}) = 4.79$ ]. For <sup>13</sup>C{<sup>1</sup>H} NMR experiments in D<sub>2</sub>O a drop of MeOH was added as the internal standard [ $\delta(^{13}\text{C})_{\text{MeOH}} = 49.5$ ]. Signal assignments are supported by DEPT-135, HMBC, and HMQC experiments.

Accurate MS experiments were performed using an FT-ICR mass spectrometer interfaced to an external ESI ion source.

The ratio of the components in a mixture was determined by <sup>1</sup>H NMR spectroscopy and is given as molar ratio.





**Mono(Gd-chelate) 1.** [4-MOMethynyl-PyMTA]<sup>4-</sup> · n H<sup>+</sup> · m Na<sup>+</sup>[<sup>S5</sup>] (8.19 mg, containing 16.8 μmol of the structural motif [4-MOMethynyl-PyMTA]<sup>4-</sup>) was dissolved in D<sub>2</sub>O (30 μL) and H<sub>2</sub>O (42 μL). A solution of GdCl<sub>3</sub> in D<sub>2</sub>O (500 mM, 33 μL, 16.5 μmol), a solution of NaOD in D<sub>2</sub>O (1.0 M, 50 μL, 50 μmol), and D<sub>8</sub>-glycerol (345.8 mg) were added successively. The solution was mixed well. The pD of the solution was 8.2. The solution was diluted with D<sub>2</sub>O (13 μL) to obtain a 40 mM solution of mono(Gd-chelate) **1** in a mixture of D<sub>8</sub>-glycerol/D<sub>2</sub>O/H<sub>2</sub>O with a volume ratio of 6:3:1. Due to the way of preparation this solution contained NaCl (49.5 μmol). MS (ESI) *m/z* = 590.9 [M - Na]<sup>-</sup>. Accurate MS (ESI) calculated for [M - Na]<sup>-</sup> C<sub>19</sub>H<sub>19</sub>GdN<sub>3</sub>O<sub>9</sub>: 591.03724; found 591.03593. Please note: The ESI-MS experiments of the sample in D<sub>8</sub>-glycerol/D<sub>2</sub>O/H<sub>2</sub>O (6:3:1) failed because of the high boiling point of D<sub>8</sub>-glycerol. The MS reported here was recorded with a sample, which had been prepared as described above, however without adding D<sub>8</sub>-glycerol.

**Ester 7.** This reaction was performed in dried glassware under argon using the Schlenk technique. A suspension of 4-iodo-PyMTA *tert*-butyl ester **6**[<sup>S6</sup>] (435 mg, 605 μmol), bis(pinacolato)diboron (79.3 mg, 311 μmol) and anhydrous K<sub>2</sub>CO<sub>3</sub> (247 mg, 1.79 mmol) in DMSO (8 mL) was degassed through three consecutive cycles consisting of reducing the pressure to 10 mbar and filling the flask with argon. To the pale brown suspension PdCl<sub>2</sub>(dppf)·CH<sub>2</sub>Cl<sub>2</sub> (20.0 mg, 23.6 μmol) was added. The color of the suspension changed to dark red. The suspension was heated to 80 °C, whereupon the reaction mixture became a brown-black suspension. The suspension was stirred at 80 °C for 16 h and then cooled to room temperature. Et<sub>2</sub>O (15 mL) was added and then H<sub>2</sub>O (15 mL) was added slowly (caution: exothermic reaction; Cooling with an ice bath is strongly recommended.). The organic and the aqueous phases were separated, and the aqueous phase was extracted with Et<sub>2</sub>O (3 × 10 mL). To the combined organic phases metal scavenger QuadraPure TU (241 mg) was added. The suspension was stirred at room temperature for 2.5 h, whereupon the color of the metal scavenger changed from yellow to brown. This suspension was dried with Na<sub>2</sub>SO<sub>4</sub> and filtered. The filter cake was washed with Et<sub>2</sub>O (100 mL), and the solvent of the combined filtrates was removed. Column chromatography (3.5 cm × 32 cm, CH<sub>2</sub>Cl<sub>2</sub>/EtOH 20:1) of the residual brown-black oil gave a yellow viscous oil (338 mg) consisting of ester **7** (94% yield; *R<sub>f</sub>* = 0.25) and a trace of bis(pinacolato)diboron (about 3 mol %). <sup>1</sup>H NMR (500 MHz, CDCl<sub>3</sub>): Signals assigned to ester **7**: δ = 7.68 (s, 4H, ArH), 4.09 (s, 8H, ArCH<sub>2</sub>), 3.50 (s, 16H, CH<sub>2</sub>C=O), 1.42 (s, 72H, <sup>t</sup>Bu); signal assigned to bis(pinacolato)diboron: δ = 1.23 (s, 24H, CH<sub>3</sub>). <sup>13</sup>C NMR (125 MHz, CDCl<sub>3</sub>): Signals assigned to ester **7**: δ = 170.3 (C=O), 159.4 (C<sub>Ar</sub> ortho to N), 147.7 (C<sub>Ar</sub> para to N), 119.3 (C<sub>Ar</sub>H), 80.8 (CMe<sub>3</sub>), 59.6 (ArCH<sub>2</sub>), 55.6 (CH<sub>2</sub>C=O), 28.1 (CMe<sub>3</sub>); signals assigned to bis(pinacolato)diboron: δ = 74.8 (OCMe<sub>2</sub>), 24.7 (OCMe<sub>2</sub>). MS (ESI) *m/z* = 1207.7 [M + Na]<sup>+</sup>, 1185.7 [M + H]<sup>+</sup>. Accurate MS (ESI) calcd. for [M + Na]<sup>+</sup> C<sub>62</sub>H<sub>100</sub>N<sub>6</sub>O<sub>16</sub>Na<sup>+</sup>: 1207.70880; found 1207.70907.

**Bisligand 8 · n H<sup>+</sup> · m Na<sup>+</sup>.** Ester **7** (229 mg, 193 μmol) was dissolved in EtOH (10 mL) at 50 °C. An aqueous solution of NaOH (125 mg in 5 mL H<sub>2</sub>O) was added and the pale yellow solution was stirred at 50 °C for 2h. H<sub>2</sub>O (5 mL) was added and the solution was stirred at 50

°C for another 22 h, whereupon the color of the solution changed from pale yellow to pale brown. Removal of the solvents gave a pale brown solid (270 mg). The pale brown solid was dissolved in H<sub>2</sub>O (15 mL) and then proton exchange resin (Dowex 50 WX4 hydrogen form) was added to reduce the pH of the solution to ca. 3.3. The solution was separated from the proton exchange resin by filtration through a syringe filter (PDVF, 13 mm, w/0.45 μm), and the resin was washed with H<sub>2</sub>O (3 × 5 mL). The combined filtrates were washed with CH<sub>2</sub>Cl<sub>2</sub> (3 × 5 mL) and Et<sub>2</sub>O (10 mL). The solvent of the aqueous phase was removed. Bisligand **8**•n H<sup>+</sup>•m Na<sup>+</sup> (218 mg, 89% yield) was obtained as a pale brown solid. The content of bisligand **8** was determined by quantitative <sup>1</sup>H NMR spectroscopy<sup>[S6]</sup> with maleic acid as the internal standard to be 57.3 wt%. Please note: Though both, bisligand **8**•n H<sup>+</sup>•m Na<sup>+</sup> and maleic acid, are soluble in water, their mixture possesses a very poor solubility in water. Moreover, bisligand **8**•n H<sup>+</sup>•m Na<sup>+</sup> is insoluble in methanol. Therefore, a solution of NaOD in D<sub>2</sub>O (0.5 M) was used as solvent for the quantitative <sup>1</sup>H NMR spectroscopy. <sup>1</sup>H NMR (500 MHz, D<sub>2</sub>O): δ = 8.46 (s, 4H, ArH), 4.81 (s, 8H, ArCH<sub>2</sub>), 3.99 (s, 16H, CH<sub>2</sub>C=O). <sup>13</sup>C NMR (125 MHz, D<sub>2</sub>O): 170.8 (C=O), 151.8 (C<sub>Ar</sub> ortho to N), 148.0 (C<sub>Ar</sub> para to N), 123.7 (C<sub>Ar</sub>H), 58.9 (ArCH<sub>2</sub>), 57.8 (CH<sub>2</sub>C=O). MS (ESI) *m/z* = 389.0 [**8** + 4H<sup>+</sup> + 2Na<sup>+</sup>]<sup>2-</sup>, 378.1 [**8** + 5H<sup>+</sup> + Na<sup>+</sup>]<sup>2-</sup>, 367.1 [**8** + 6H<sup>+</sup>]<sup>2-</sup>, 251.6 [**8** + 4H<sup>+</sup> + Na<sup>+</sup>]<sup>3-</sup>, 244.3 [**8** + 5H<sup>+</sup>]<sup>3-</sup>, 183.0 [**8** + 4H<sup>+</sup>]<sup>4-</sup>.

**Bis(Gd-chelate) 2.** Bisligand **8**•n H<sup>+</sup>•m Na<sup>+</sup> (20.35 mg, containing 16.0 μmol of bisligand **8**) was dissolved in D<sub>2</sub>O (50 μL) and H<sub>2</sub>O (80 μL). A solution of GdCl<sub>3</sub> in D<sub>2</sub>O (500 mM, 64 μL, 32.0 μmol), a solution of NaOD in D<sub>2</sub>O (1.0 M, 50 μL, 50 μmol), and D<sub>8</sub>-glycerol (659.0 mg) were added successively. The solution was well mixed. A solution of NaOD in D<sub>2</sub>O (1.0 M, 20 μL, 20 μmol) was added to raise the pD of the solution to 8.2. D<sub>2</sub>O (56 μL) was added to obtain a 20 mM solution of bis(Gd-chelate) **2** in a mixture of D<sub>8</sub>-glycerol/D<sub>2</sub>O/H<sub>2</sub>O with a volume ratio of 6:3:1. Due to the way of preparation this solution contained NaCl. MS (ESI) *m/z* = 522.0 [M - 2Na]<sup>2-</sup>. Accurate MS (ESI) calcd. for [M - 2Na]<sup>2-</sup> C<sub>30</sub>H<sub>28</sub>N<sub>6</sub>O<sub>16</sub>Gd<sub>2</sub><sup>2-</sup>: 522.00351; found 522.00293. Please note: The ESI-MS experiments with the sample in D<sub>8</sub>-glycerol/D<sub>2</sub>O/H<sub>2</sub>O (6:3:1) failed because of the high boiling point of D<sub>8</sub>-glycerol. The MS reported here was obtained with a sample, which had been prepared as described above, however without adding D<sub>8</sub>-glycerol.

**Ester 11.** This reaction was performed in dried glassware under argon using the Schlenk technique. 4-Iodo-PyMTA ethyl ester **9**<sup>[S6]</sup> (126 mg, 207 μmol) and 4-ethynyl-PyMTA ethyl ester **10**<sup>[S7]</sup> (104 mg, 206 μmol) were dissolved in <sup>i</sup>Pr<sub>2</sub>NH (1.4 mL, 9.99 mmol) and THF (3 mL). This solution was degassed through three freeze-pump-thaw cycles. Then Pd(PPh<sub>3</sub>)<sub>4</sub> (4.33 mg, 3.74 μmol) and CuI (1.36 mg, 7.14 μmol) were added. Shortly after the addition of the catalysts a precipitate formed. The suspension was stirred at room temperature for 21 h. Then all volatiles were removed. The residual mixture of a yellow oil and a solid was suspended in CH<sub>2</sub>Cl<sub>2</sub>/EtOH (15:1). The suspension was filtered through silica gel (2 cm × 8 cm) and the silica gel was rinsed with CH<sub>2</sub>Cl<sub>2</sub>/EtOH (15:1). The filtrates were combined and the solvents were removed. Chromatography (3.0 cm × 35 cm, CH<sub>2</sub>Cl<sub>2</sub>/EtOH 15:1) of the residual yellow viscous oil gave ester **11** (189 mg, 93%; *R<sub>f</sub>* = 0.42) as a yellow viscous oil. <sup>1</sup>H NMR (500 MHz, CDCl<sub>3</sub>): δ = 7.60 (s, 4H, ArH), 4.16 (q, <sup>3</sup>*J* = 7.2 Hz, 16H, CH<sub>2</sub>CH<sub>3</sub>), 4.04 (s, 8H, ArCH<sub>2</sub>), 3.61 (s, 16H, CH<sub>2</sub>C=O), 1.26 (t, <sup>3</sup>*J* = 7.2 Hz, 24H, CH<sub>2</sub>CH<sub>3</sub>). <sup>13</sup>C NMR (125 MHz, CDCl<sub>3</sub>): 171.0 (C=O), 158.8 (C<sub>Ar</sub> ortho to N), 131.5 (C<sub>Ar</sub>C≡C), 123.1 (C<sub>Ar</sub>H), 90.8 (C≡C), 60.5 (CH<sub>2</sub>CH<sub>3</sub>), 59.5 (ArCH<sub>2</sub>), 54.9 (CH<sub>2</sub>C=O), 14.1 (CH<sub>2</sub>CH<sub>3</sub>). MS (ESI) *m/z* = 1007.6 [M + Na]<sup>+</sup>, 985.6 [M + H]<sup>+</sup>, 515.3 [M + 2Na]<sup>2+</sup>, 504.3 [M + Na + H]<sup>2+</sup>. Accurate MS (ESI) calcd. for [M + 2Na]<sup>2+</sup> C<sub>48</sub>H<sub>68</sub>N<sub>6</sub>O<sub>16</sub>Na<sub>2</sub><sup>2+</sup>: 515.22381; found 515.22232. Elemental analysis calcd (%) for C<sub>48</sub>H<sub>68</sub>N<sub>6</sub>O<sub>16</sub> (984.469): C, 58.52; H, 6.96; N, 8.53. Found C, 57.96; H, 7.22; N, 8.47.

**Bisligand 12**•n H<sup>+</sup>•m Na<sup>+</sup>. Ester **11** (84 mg, 85.3 μmol) was dissolved in EtOH (1.5 mL). An aqueous solution of NaOH (2.0 M, 427 μL, 854 μmol) and then H<sub>2</sub>O (1.5 mL) were added,

whereupon a mixture of two liquid phases formed. During 5 min of stirring at room temperature, the mixture became a pale yellow one phase solution. The pale yellow solution was stirred at room temperature for another 24 h. Proton exchange resin was added to reduce the pH of the solution to ca. 3, whereupon a colorless precipitate formed. The solution was separated from the proton exchange resin and the precipitate through centrifugation. The proton exchange resin and the colorless precipitate were washed with H<sub>2</sub>O (6 × 5 mL), whereupon the colorless precipitate dissolved completely in H<sub>2</sub>O. The aqueous solutions were combined. After removal of the solvents bisligand **12**·n H<sup>+</sup>·m Na<sup>+</sup> (62 mg, 71% yield) was obtained as a colorless solid. Its content of bisligand **12** was 73 wt%, as determined by quantitative <sup>1</sup>H NMR spectroscopy<sup>[3]</sup> in D<sub>2</sub>O. <sup>1</sup>H NMR (500 MHz, D<sub>2</sub>O): δ = 7.75 (s, 4H, ArH), 4.76 (s, 8H, ArCH<sub>2</sub>), 4.04 (s, 16H, CH<sub>2</sub>C=O). <sup>13</sup>C NMR (125 MHz, D<sub>2</sub>O): 170.5 (C=O), 151.2 (C<sub>Ar</sub> ortho to N), 133.6 (C<sub>Ar</sub>-C≡C), 127.5 (C<sub>Ar</sub>H), 91.6 (C≡C), 58.8 (ArCH<sub>2</sub>), 57.4 (CH<sub>2</sub>C=O). MS (ESI) *m/z* = 759.1 [**12** + 7H<sup>+</sup>], 390.9 [**12** + 5H<sup>+</sup> + Na<sup>+</sup>]<sup>2-</sup>, 378.9 [**12** + 6H<sup>+</sup>]<sup>2-</sup>, 252.2 [**12** + 5H<sup>+</sup>]<sup>3-</sup>, 188.8 [**12** + 4H<sup>+</sup>]<sup>4-</sup>.

**Bis(Gd-chelate) 3.** Bisligand **12**·n H<sup>+</sup>·m Na<sup>+</sup> (8.50 mg, containing 8.07 μmol of bisligand **12**) was dissolved in a solution of NaOD in D<sub>2</sub>O (1.0 M, 50 μL, 50 μmol). D<sub>2</sub>O (38 μL), H<sub>2</sub>O (40 μL), D<sub>8</sub>-glycerol (331.3 mg), and a solution of GdCl<sub>3</sub> in D<sub>2</sub>O (500 mM, 31.7 μL, 15.84 μmol) were added successively. The solution was well mixed to obtain a 20 mM solution of bis(Gd-chelate) **3** in a mixture of D<sub>8</sub>-glycerol/D<sub>2</sub>O/H<sub>2</sub>O with a volume ratio of 6:3:1. Due to the way of preparation this solution contained NaCl. The pD value of this solution was ca. 8.0. Accurate MS (ESI) calcd. for [M - 2Na]<sup>2-</sup> C<sub>32</sub>H<sub>28</sub>N<sub>6</sub>O<sub>16</sub>Gd<sub>2</sub><sup>2-</sup>: 534.00274; found 534.00281. Please note: The ESI-MS experiments with the sample in D<sub>8</sub>-glycerol/D<sub>2</sub>O/H<sub>2</sub>O (6:3:1) failed because of the high boiling point of D<sub>8</sub>-glycerol. The MS reported here was obtained with a sample, which had been prepared as described above, however without adding D<sub>8</sub>-glycerol.

## References

- [S1] C. F. Nising, U. K. Schmid, M. Nieger, S. Bräse, *J. Org. Chem.* **2004**, *69*, 6830-6833.
- [S2] S. R. Hartmann, E. L. Hahn, *Phys. Rev.* **1962**, *128*, 2042-2053.
- [S3] B. M. Fung, A. K. Khitrin, K. Ermolaev, *J. Magn. Reson.* **2000**, *142*, 97-101.
- [S4] C. A. Angell, *Chem. Rev.* **2002**, *102*, 2627-2650.
- [S5] K. Keller, M. Zalibera, M. Qi, V. Koch, J. Wegner, H. Hintz, A. Godt, G. Jeschke, A. Savitsky, M. Yulikov, *Phys. Chem. Chem. Phys.* **2016**, *18*, 25120-25135.
- [S6] M. Qi, M. Hülsmann, A. Godt, *Synthesis* **2016**, *48*, 3773-3784.
- [S7] M. Qi, M. Hülsmann, A. Godt, *J. Org. Chem.* **2016**, *81*, 2549-2571.

## Appendix: Supplementary NMR spectra

The solution NMR spectra of ester **7**, bisligand **8**·n H<sup>+</sup>·m Na<sup>+</sup>, ester **11**, and bisligand **12**·n H<sup>+</sup>·m Na<sup>+</sup> are listed on the following pages.

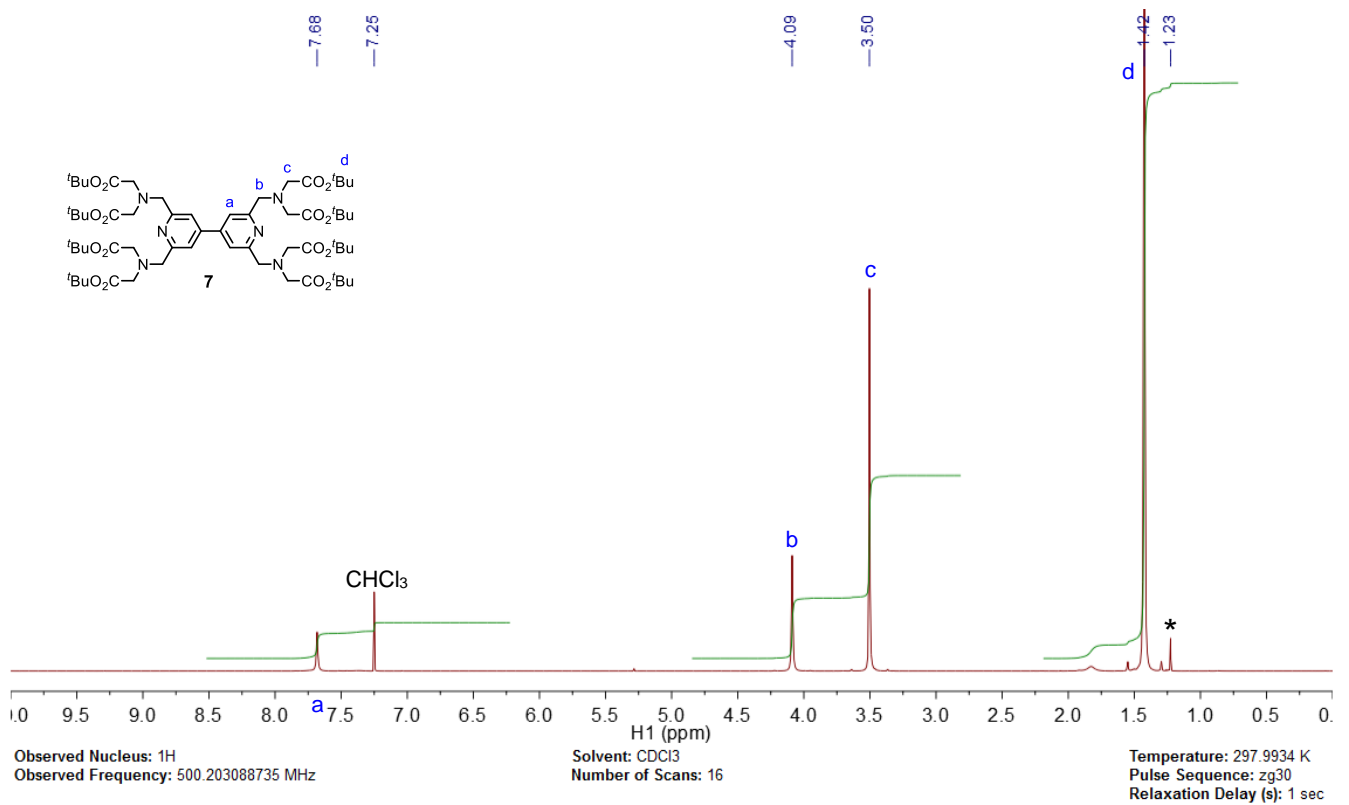


**Figure S3a.** <sup>1</sup>H NMR spectrum of ester **7**. \*Signal of bis(pinacolato)diboron.

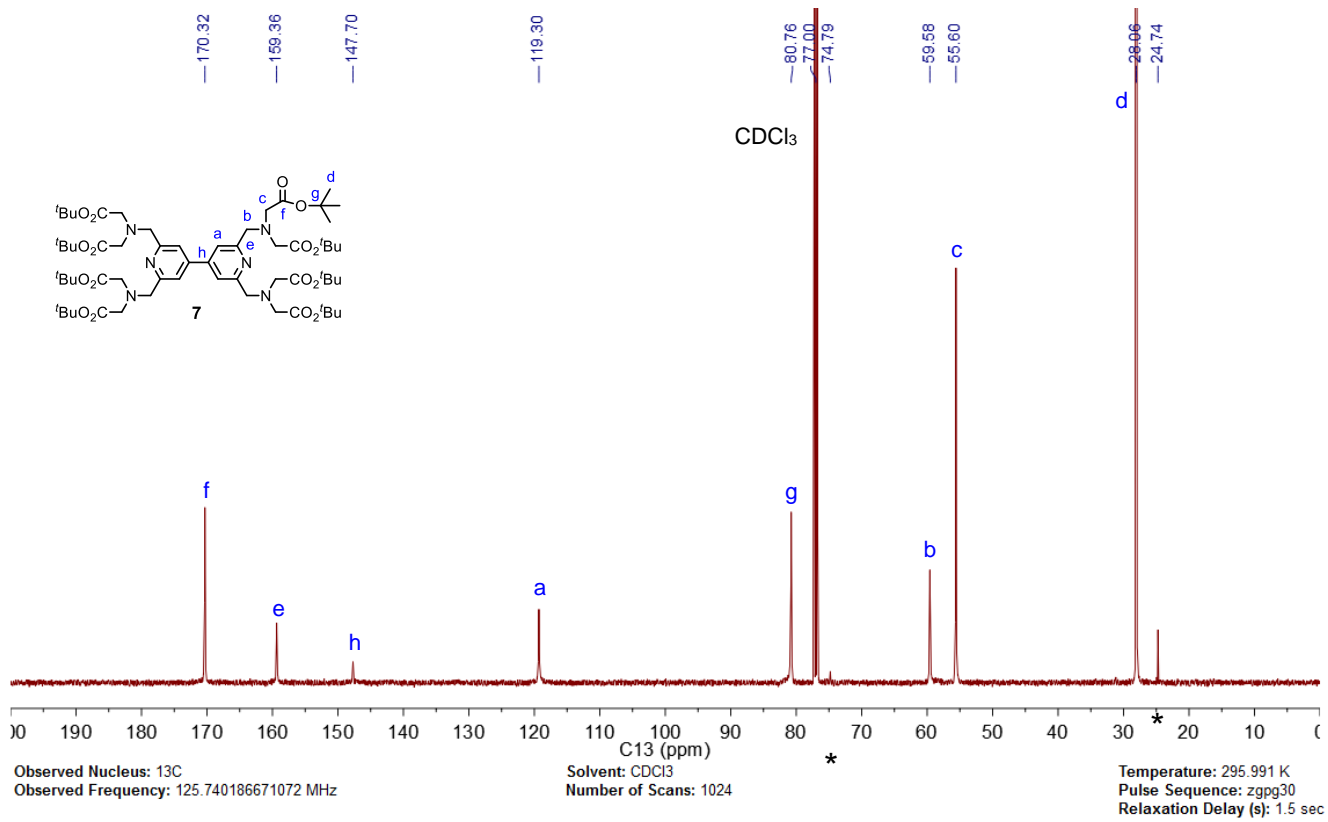


**Figure S3b.** <sup>13</sup>C NMR spectrum of ester **7**. \*Signals of bis(pinacolato)diboron.

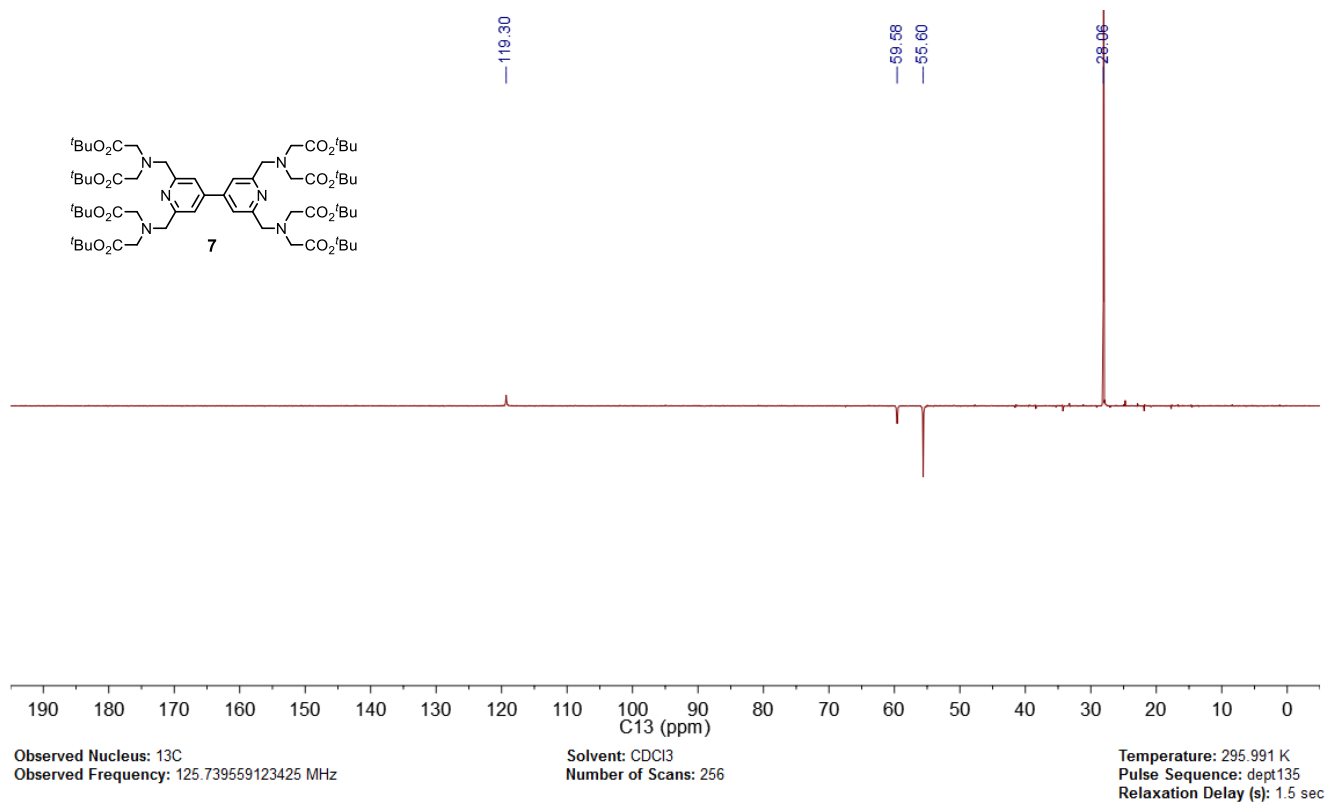


**Figure S3c.**  $^{13}\text{C}$  DEPT 135 NMR spectrum of ester **7**.

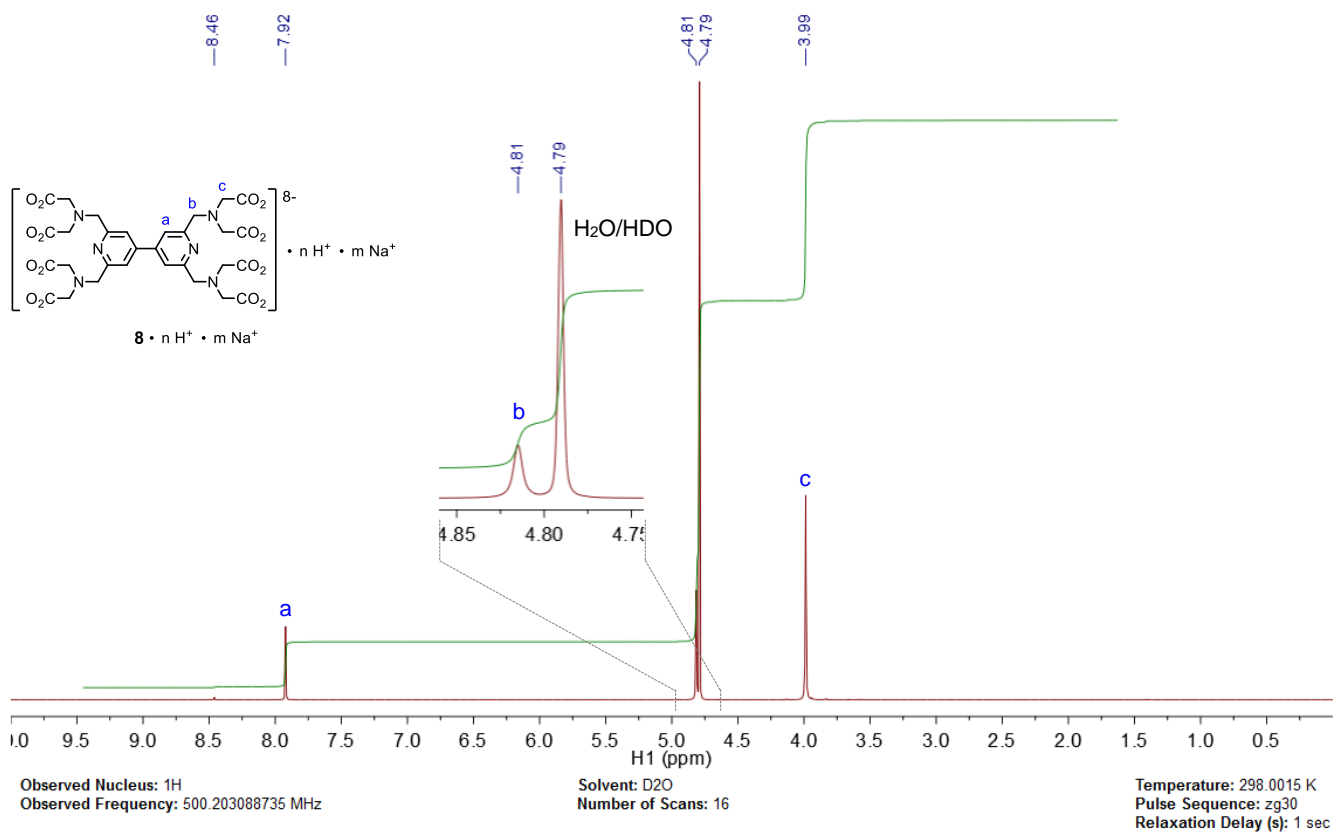


**Figure S4a.**  $^1H$  NMR spectrum of bisligand  $8 \cdot n H^+ \cdot m Na^+$ .

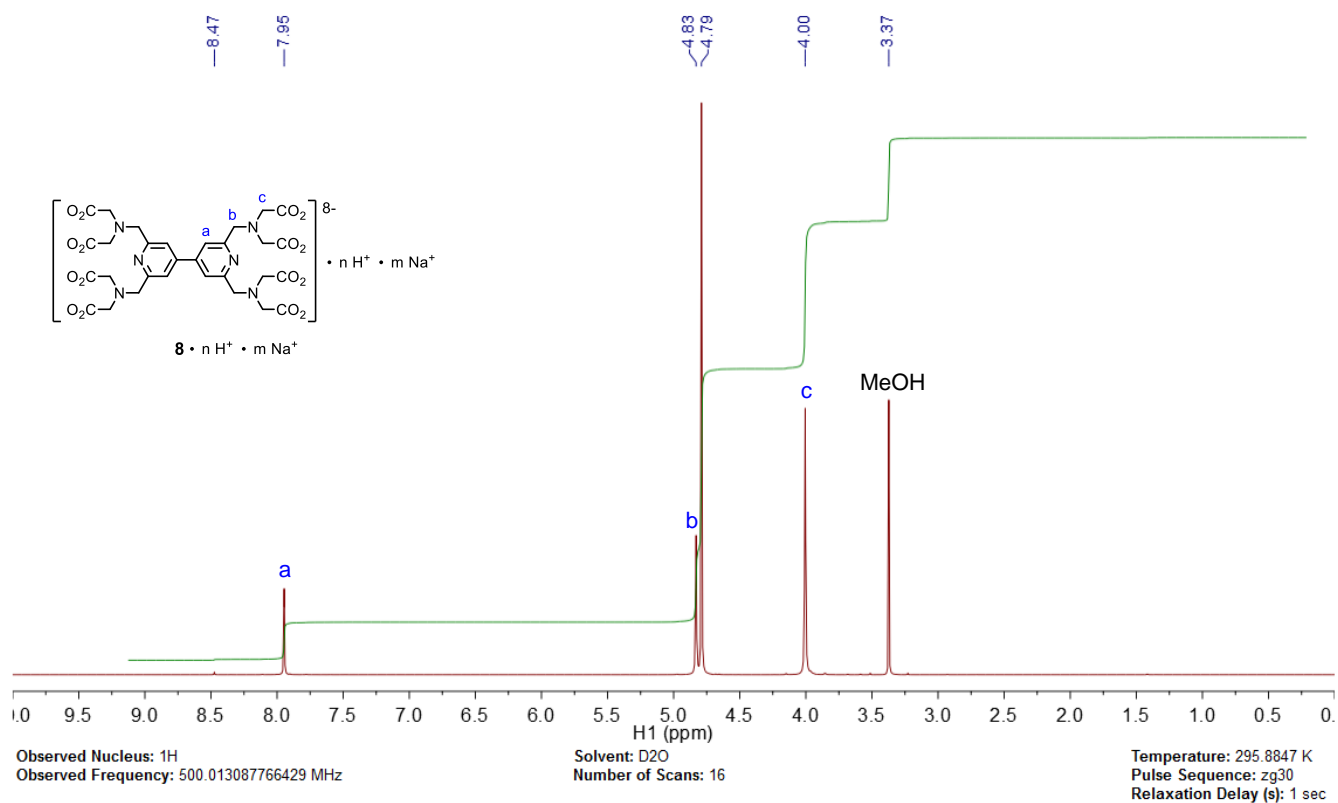


**Figure S4b.**  $^1\text{H}$  NMR spectrum of bisligand  $8 \cdot n \text{H}^+ \cdot m \text{Na}^+$ . A drop of MeOH was added as reference for the chemical shift.



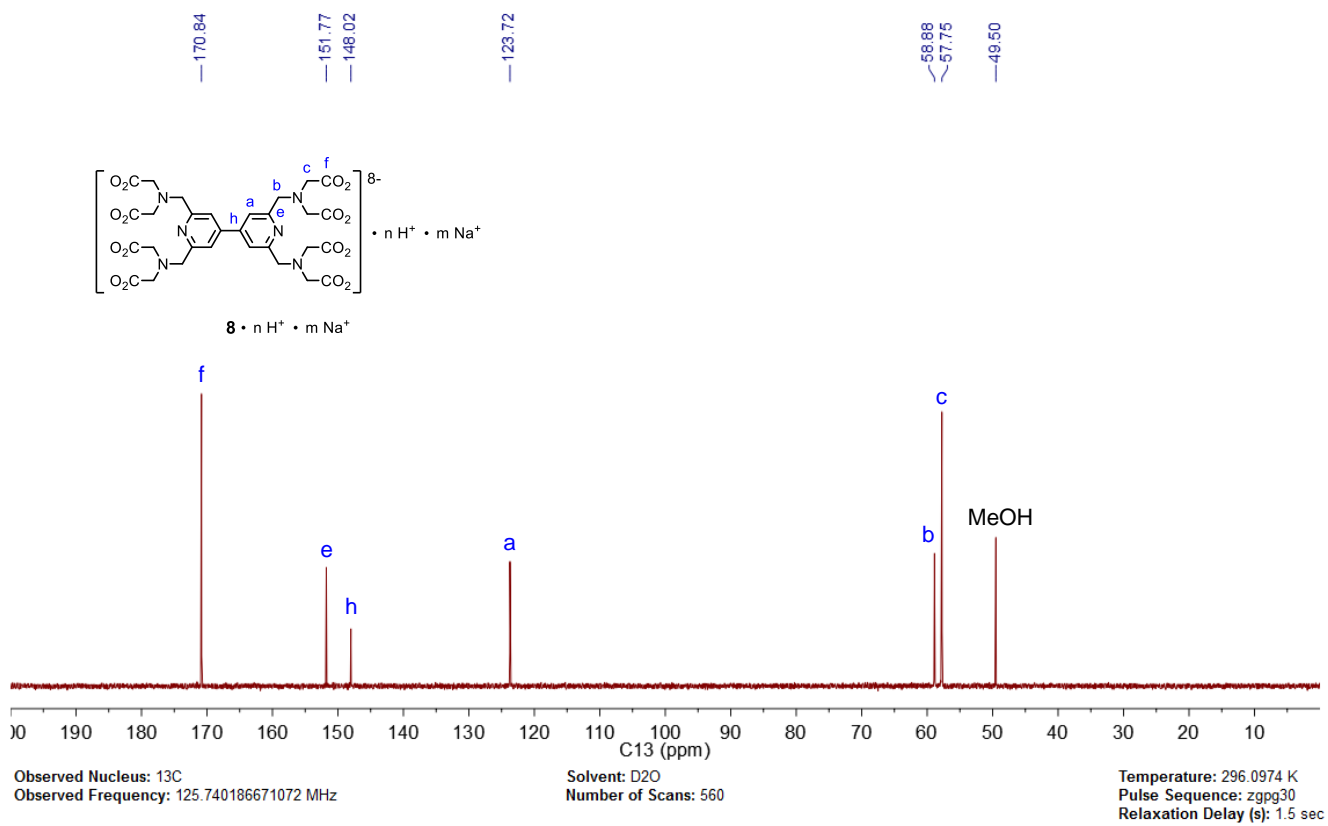


**Figure S4c.**  $^{13}\text{C}$  NMR spectrum of bisligand **8**·n H<sup>+</sup>·m Na<sup>+</sup>. A drop of MeOH was added as reference for the chemical shift.

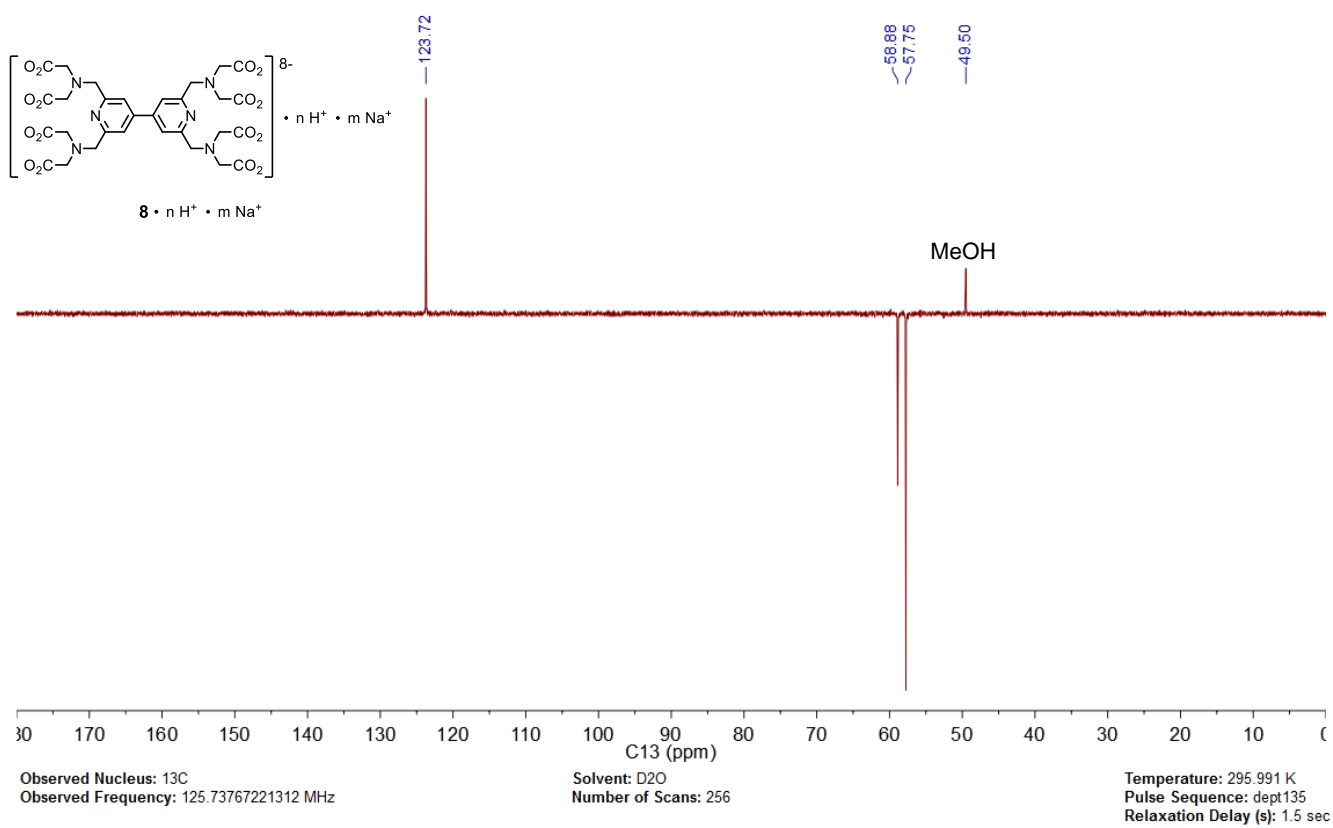


**Figure S4d.** <sup>13</sup>C DEPT 135 NMR spectrum of bisligand **8**·n H<sup>+</sup>·m Na<sup>+</sup>. A drop of MeOH was added as reference for the chemical shift.

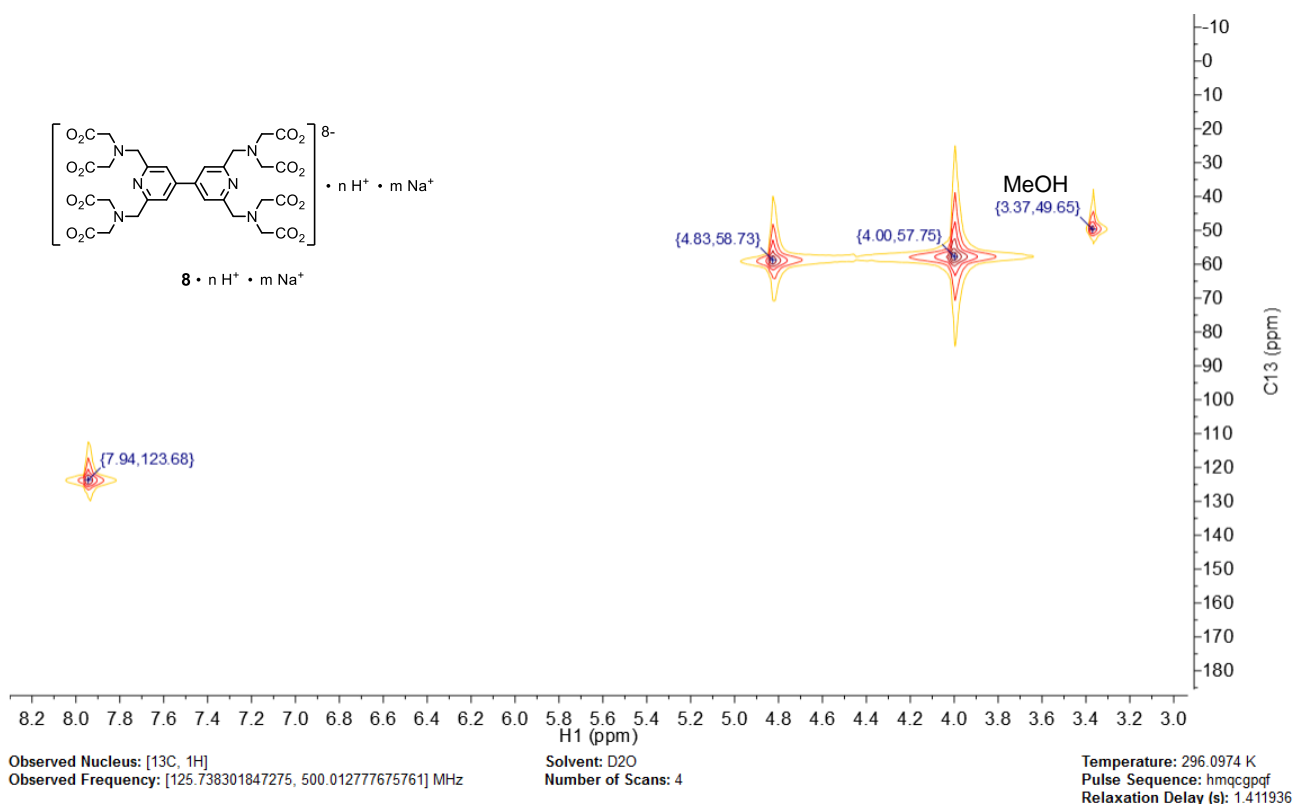


**Figure S4e.** HMPC NMR spectrum of bisligand  $8 \cdot n \text{H}^+ \cdot m \text{Na}^+$ . A drop of MeOH was added as reference for the chemical shift.

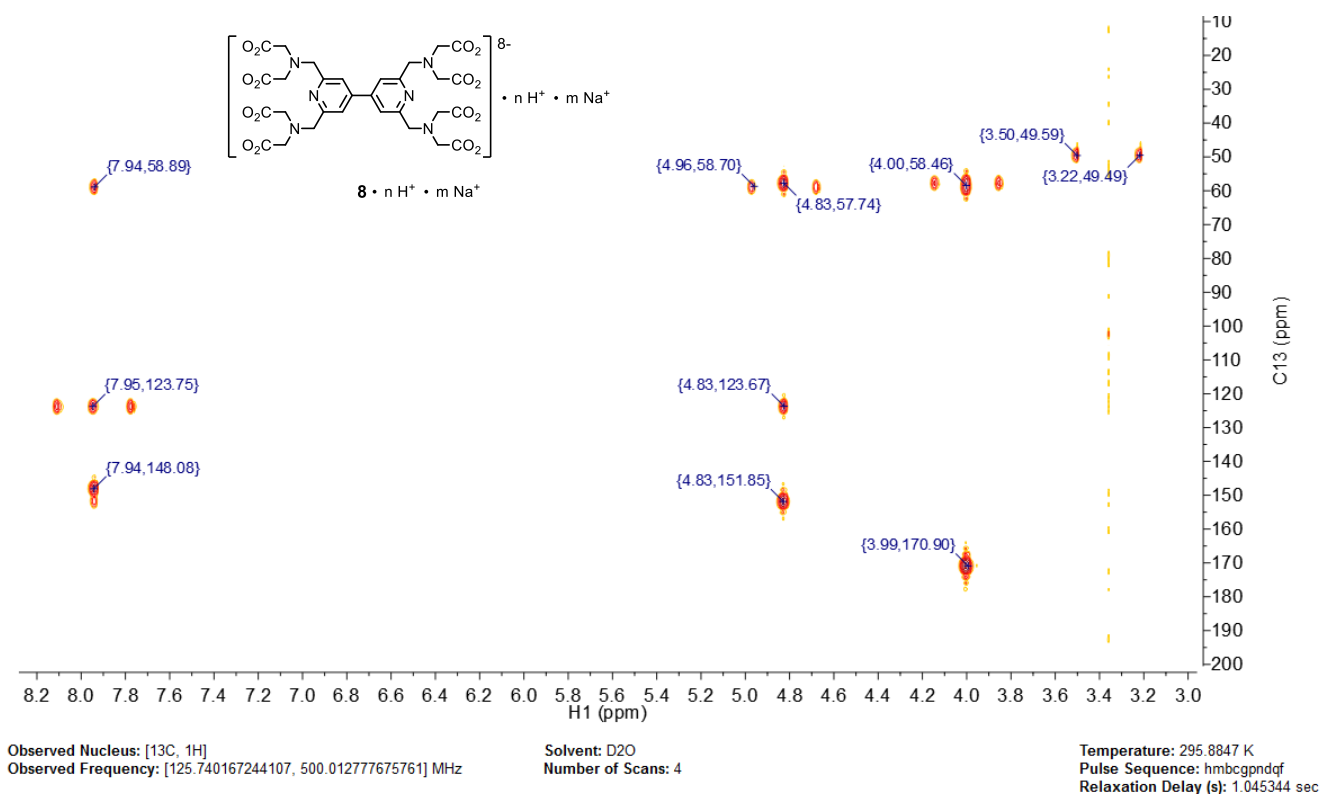


**Figure S4f.** HMBC NMR spectrum of bisligand  $8 \cdot n H^+ \cdot m Na^+$ . A drop of MeOH was added as reference for the chemical shift.

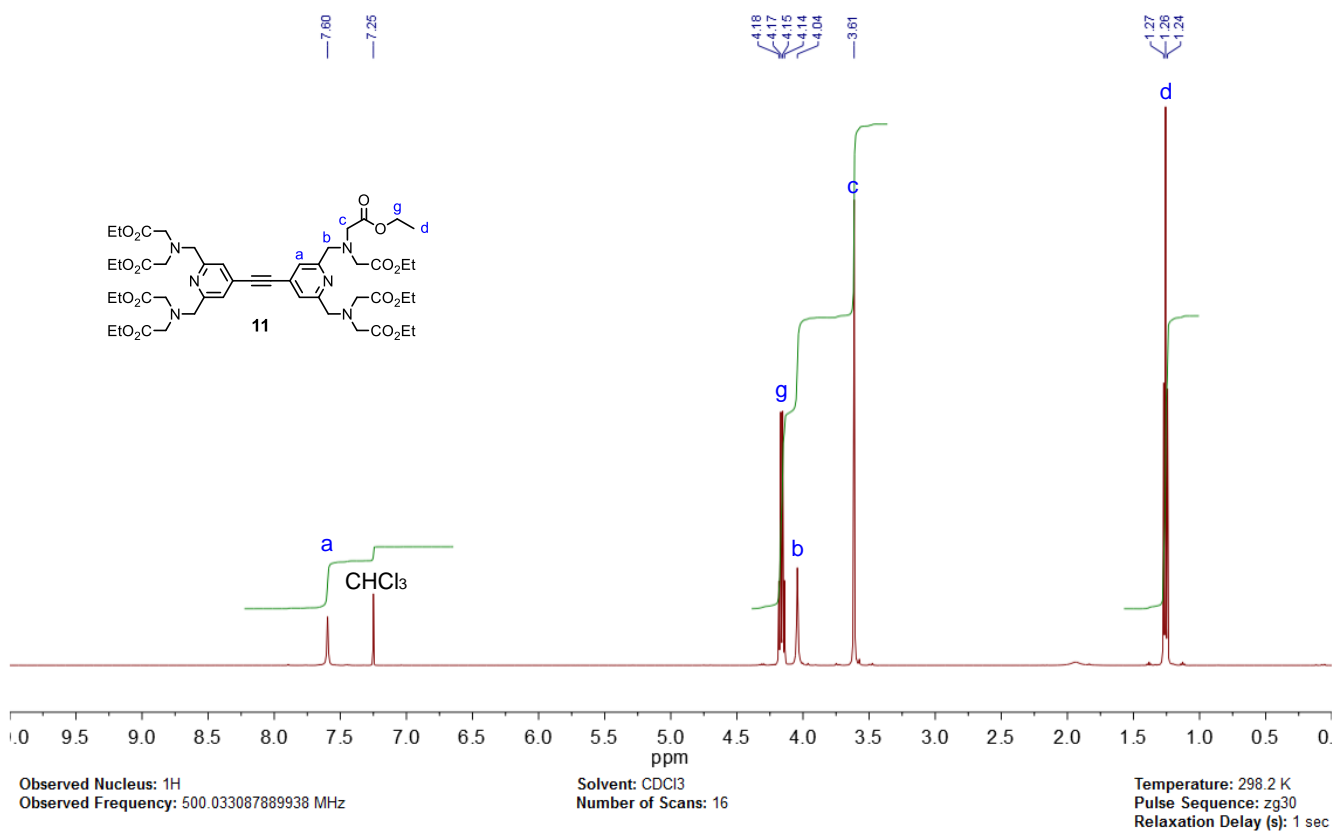


**Figure S5a.** <sup>1</sup>H NMR spectrum of ester **11**.

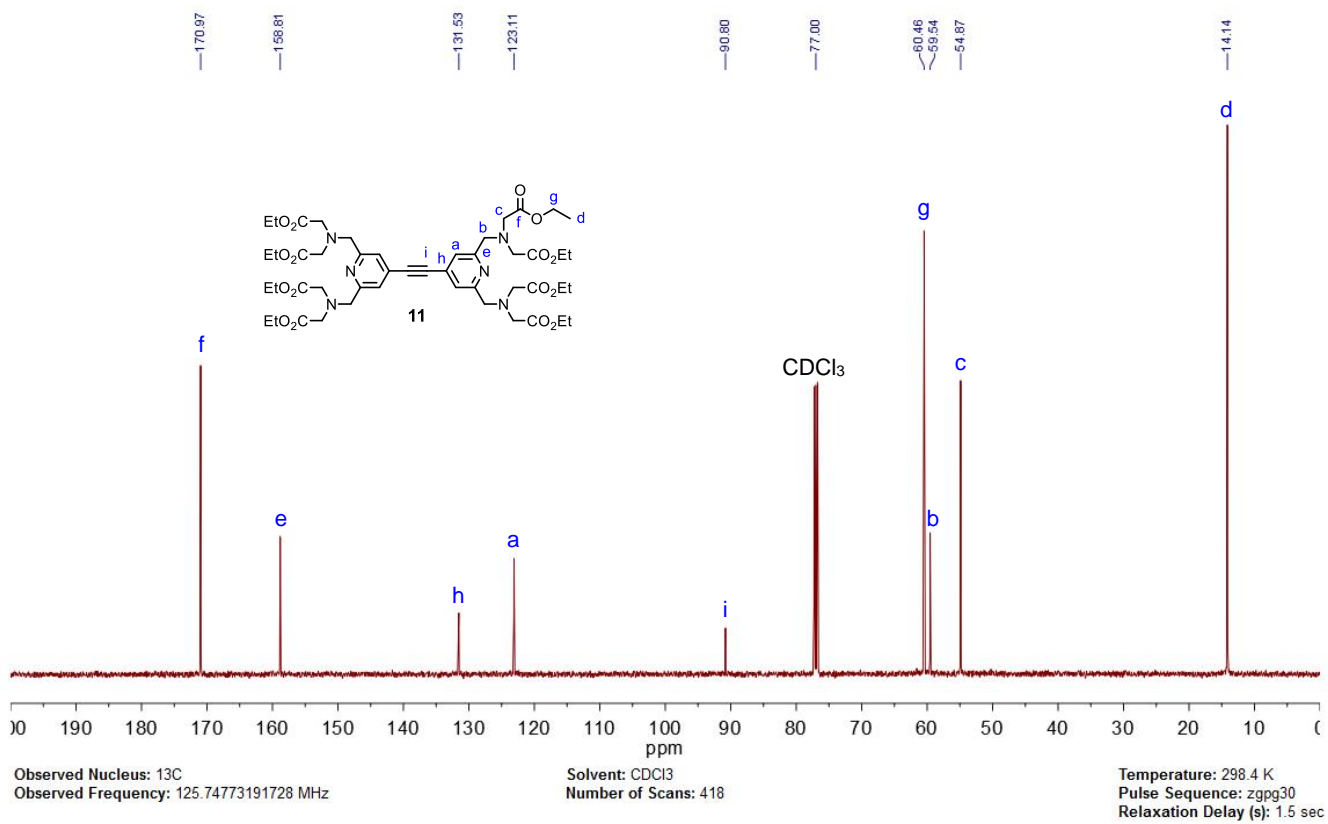


**Figure S5b.**  $^{13}\text{C}$  NMR spectrum of ester **11**.

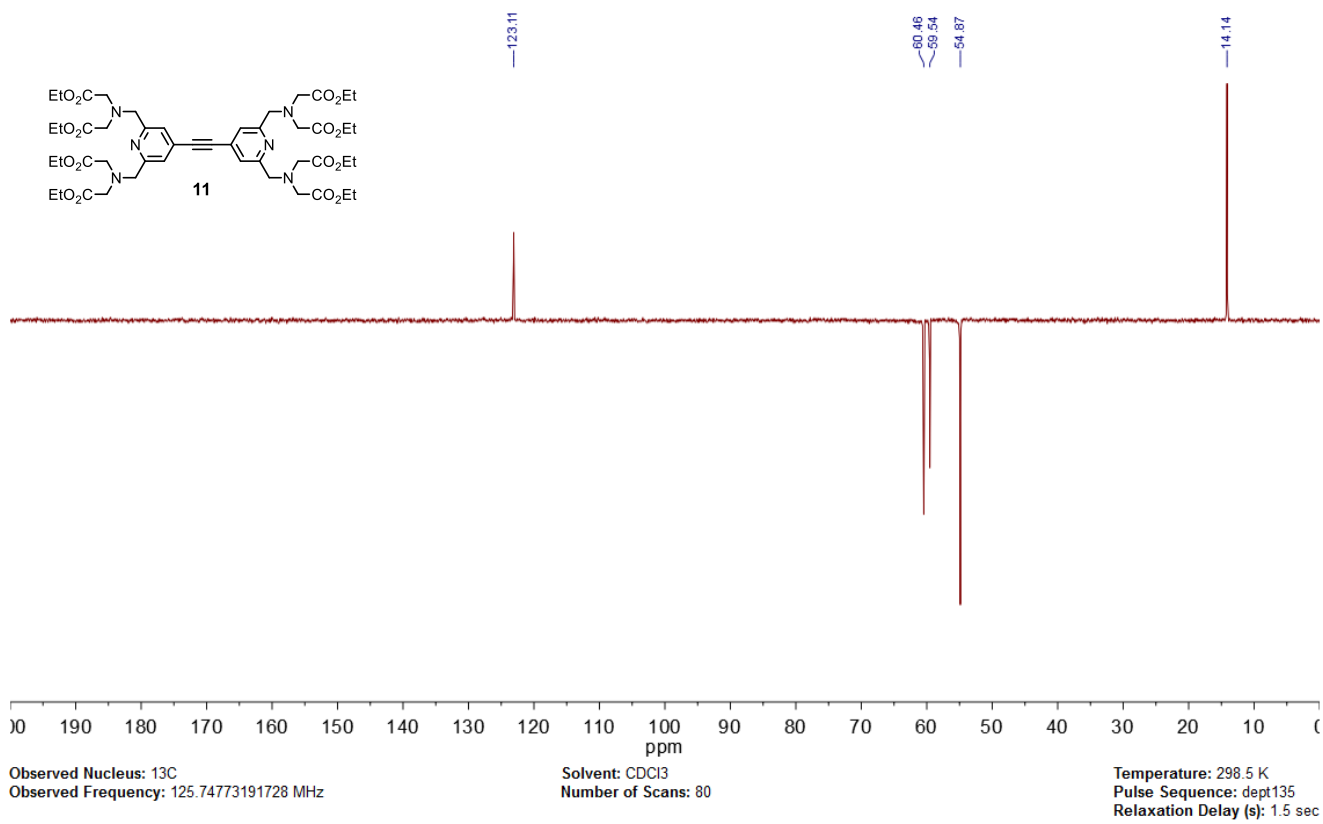


**Figure S5c.** <sup>13</sup>C DEPT 135 NMR spectrum of ester **11**.

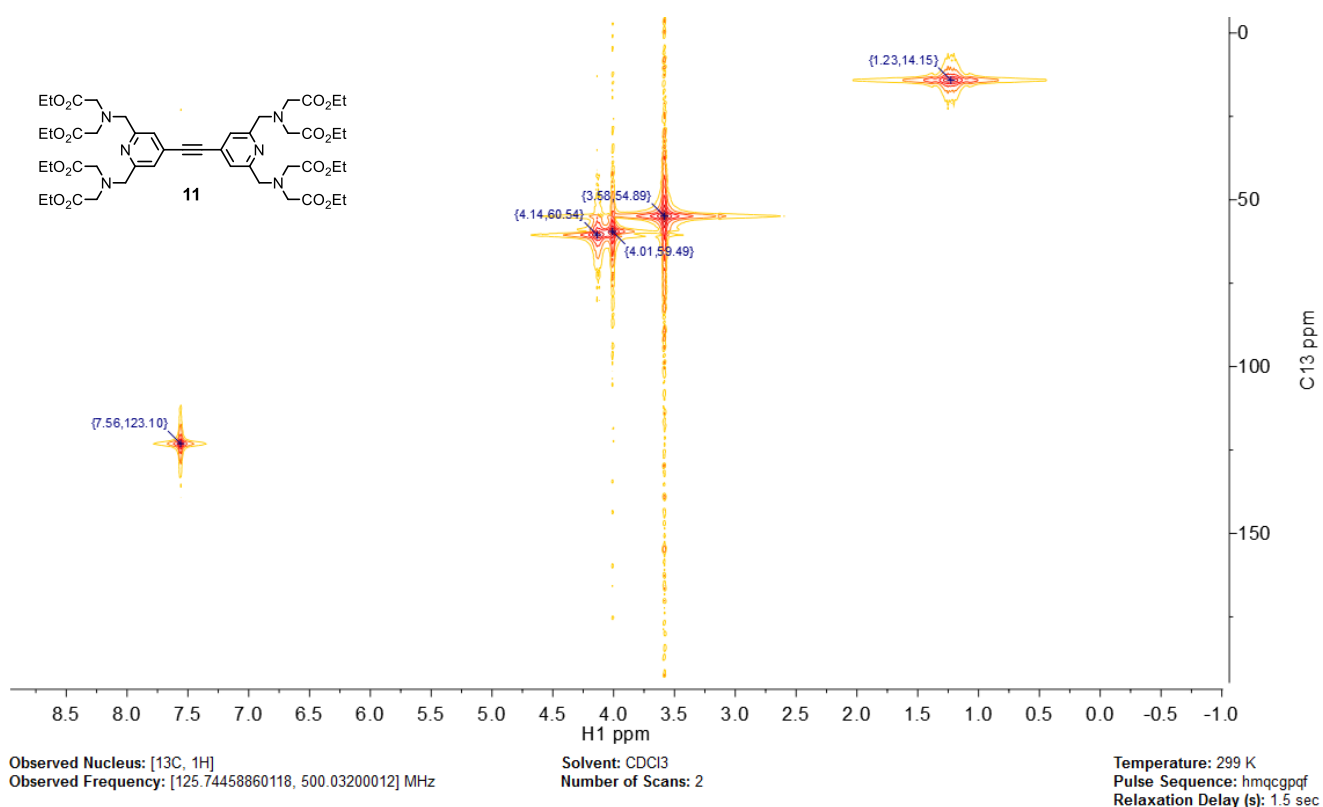


Figure S5d. HMBC NMR spectrum of ester **11**.



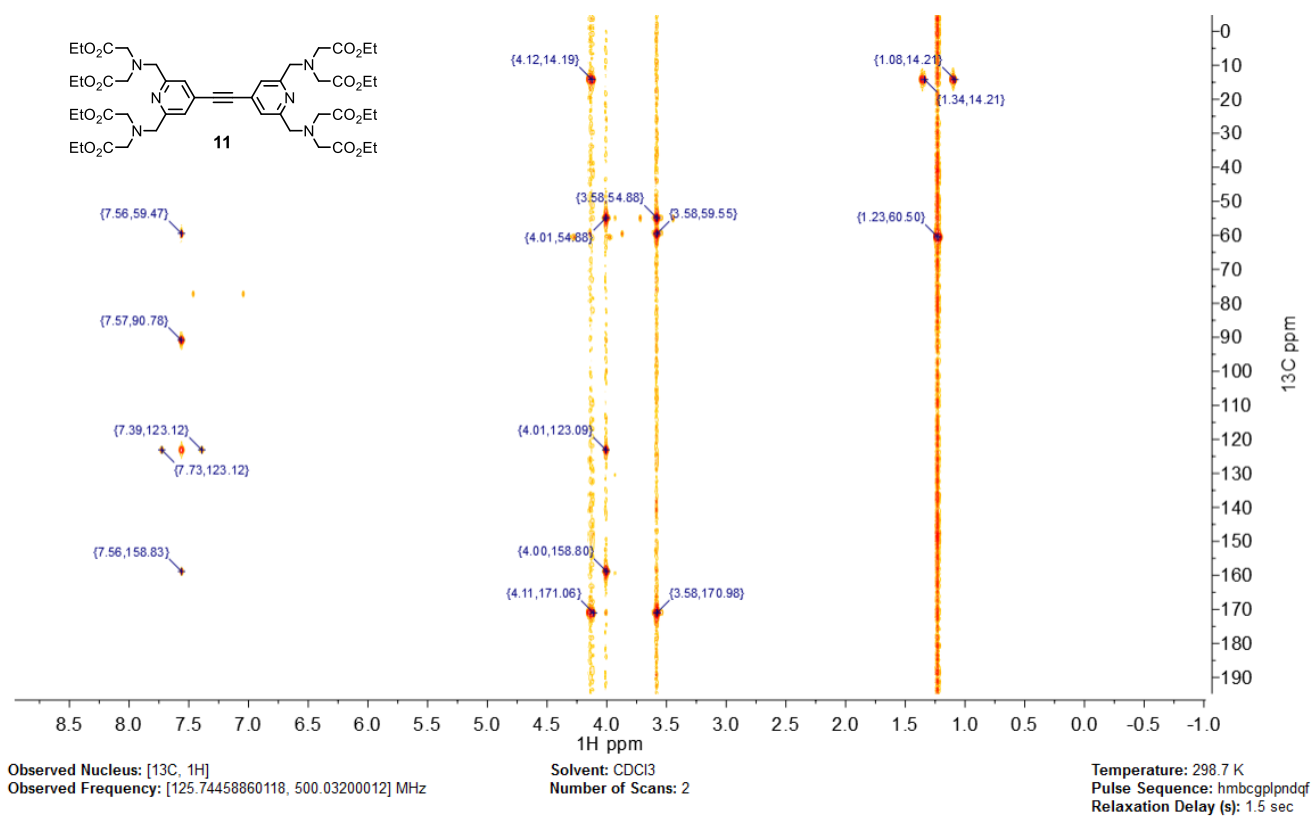
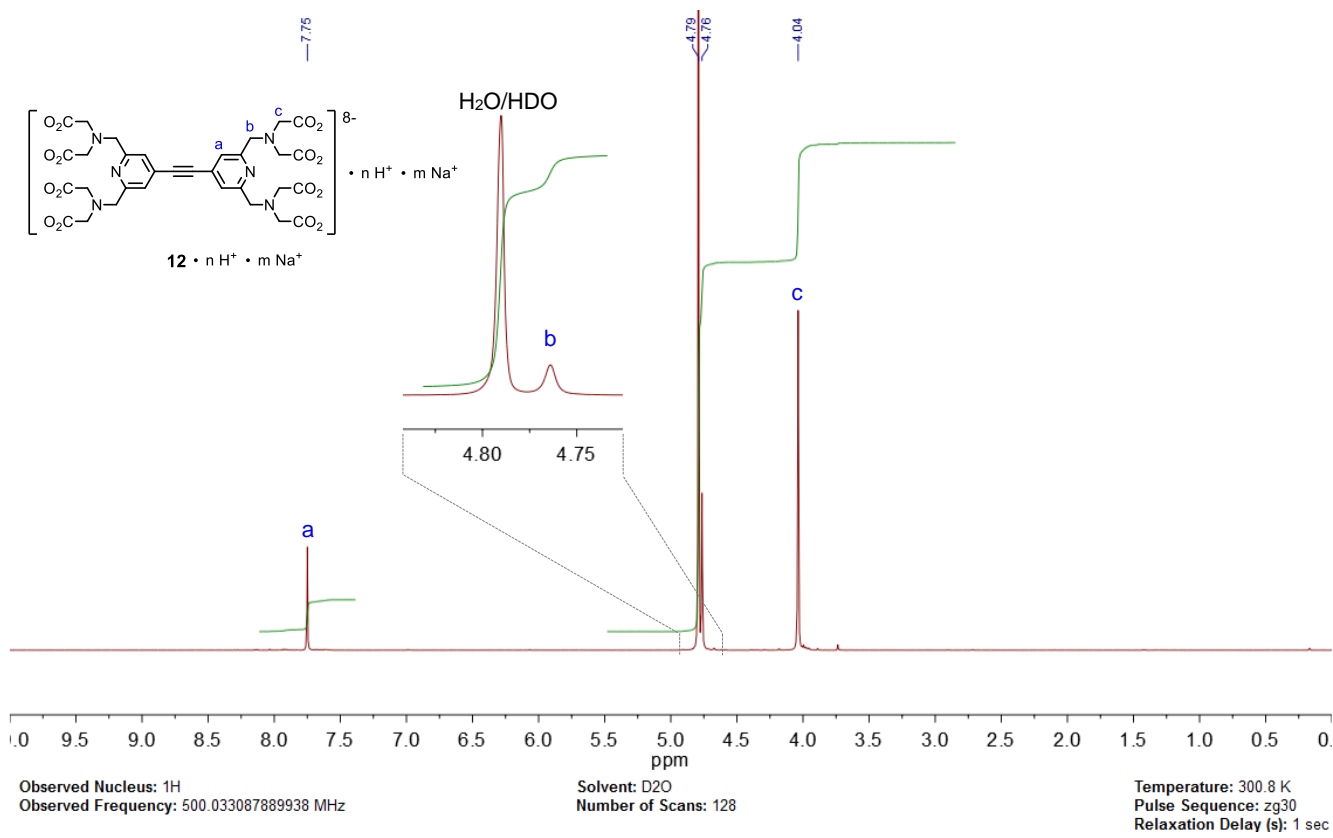
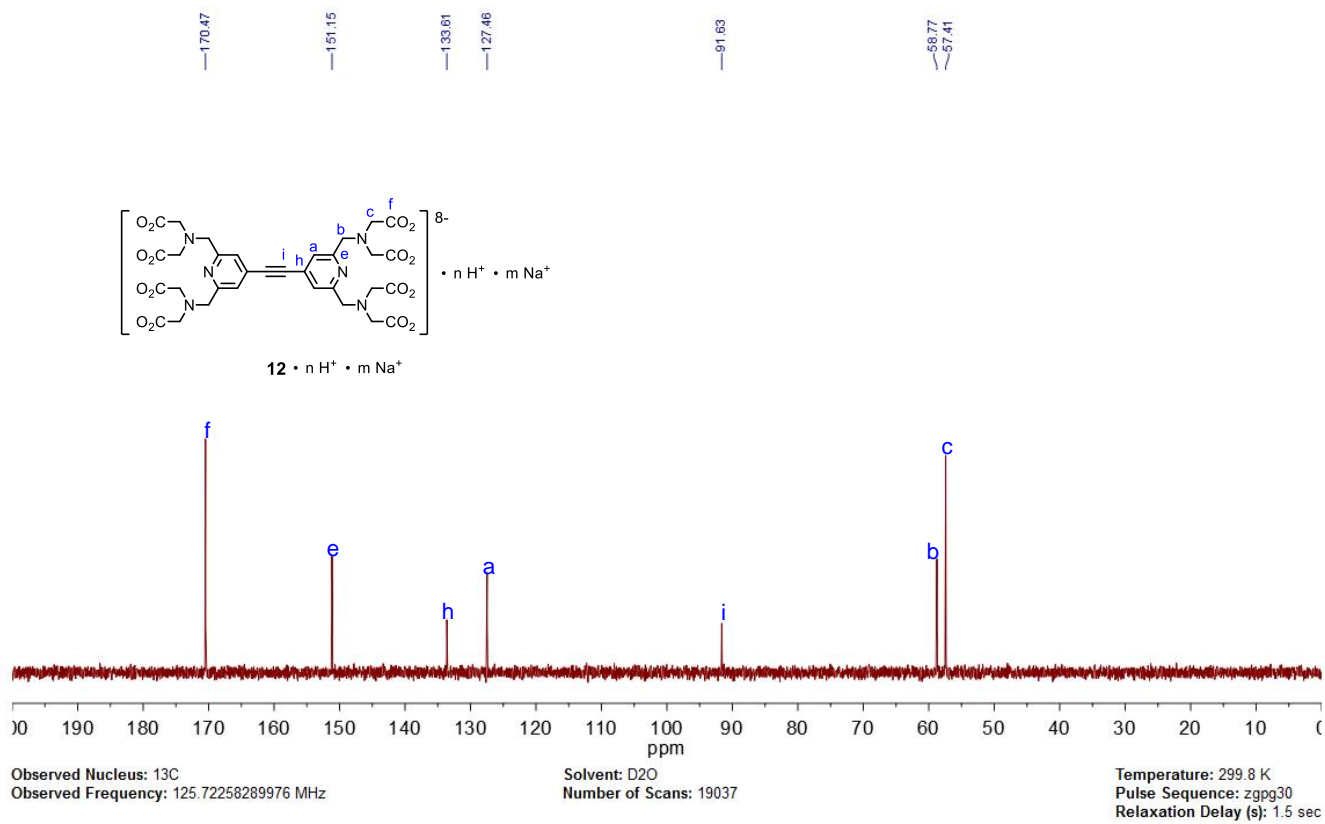


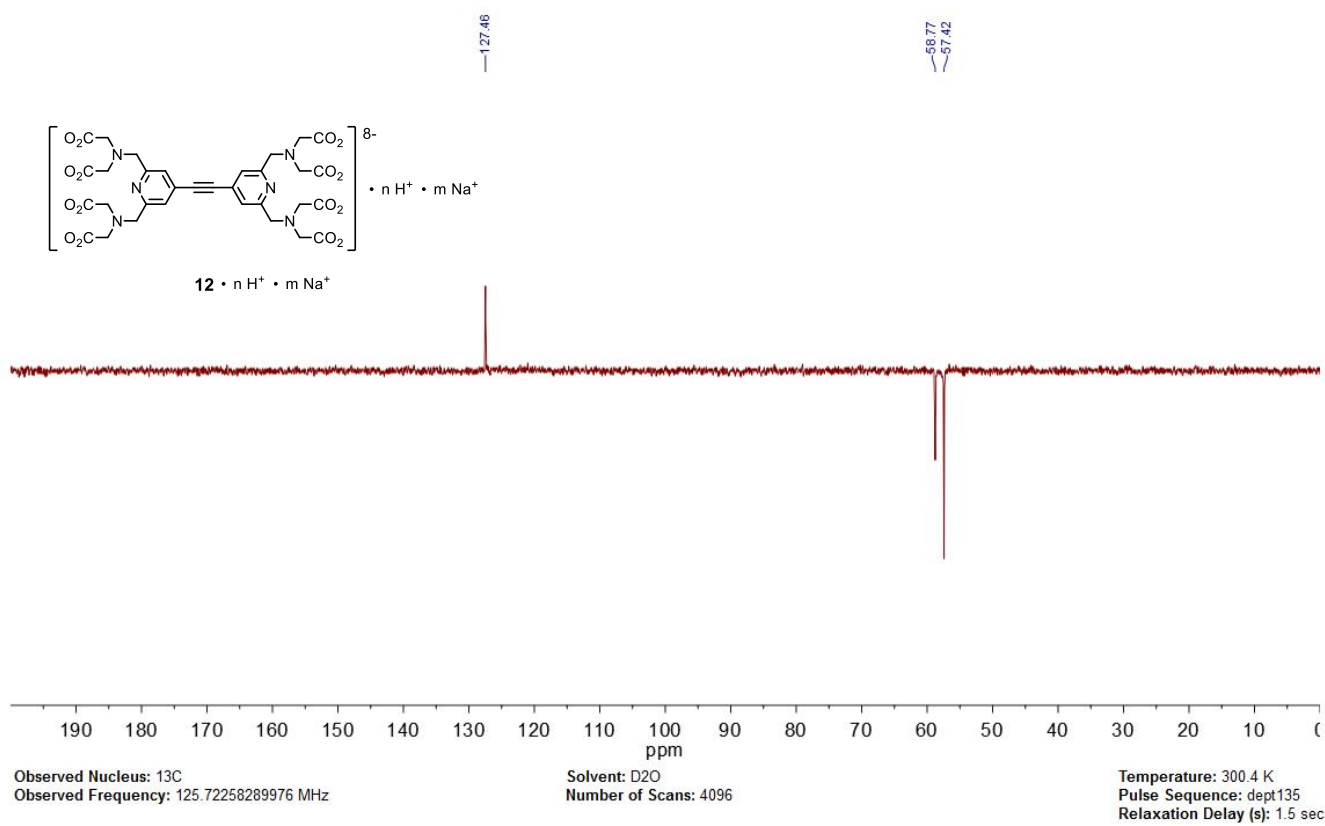
Figure S5e. HMBC NMR spectrum of ester **11**.



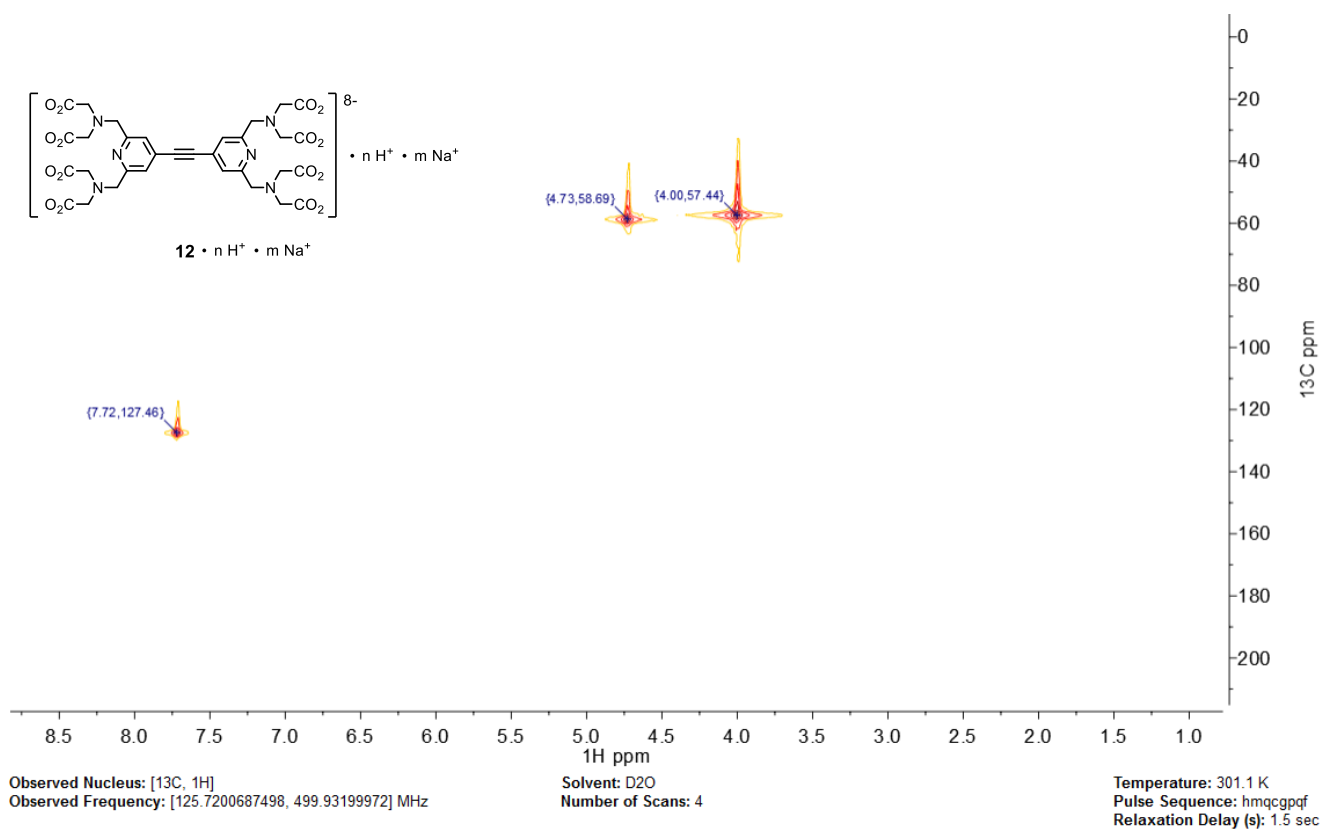
**Figure S6a.**  $^1\text{H}$  NMR spectrum of bisligand  $12 \cdot n \text{H}^+ \cdot m \text{Na}^+$ .



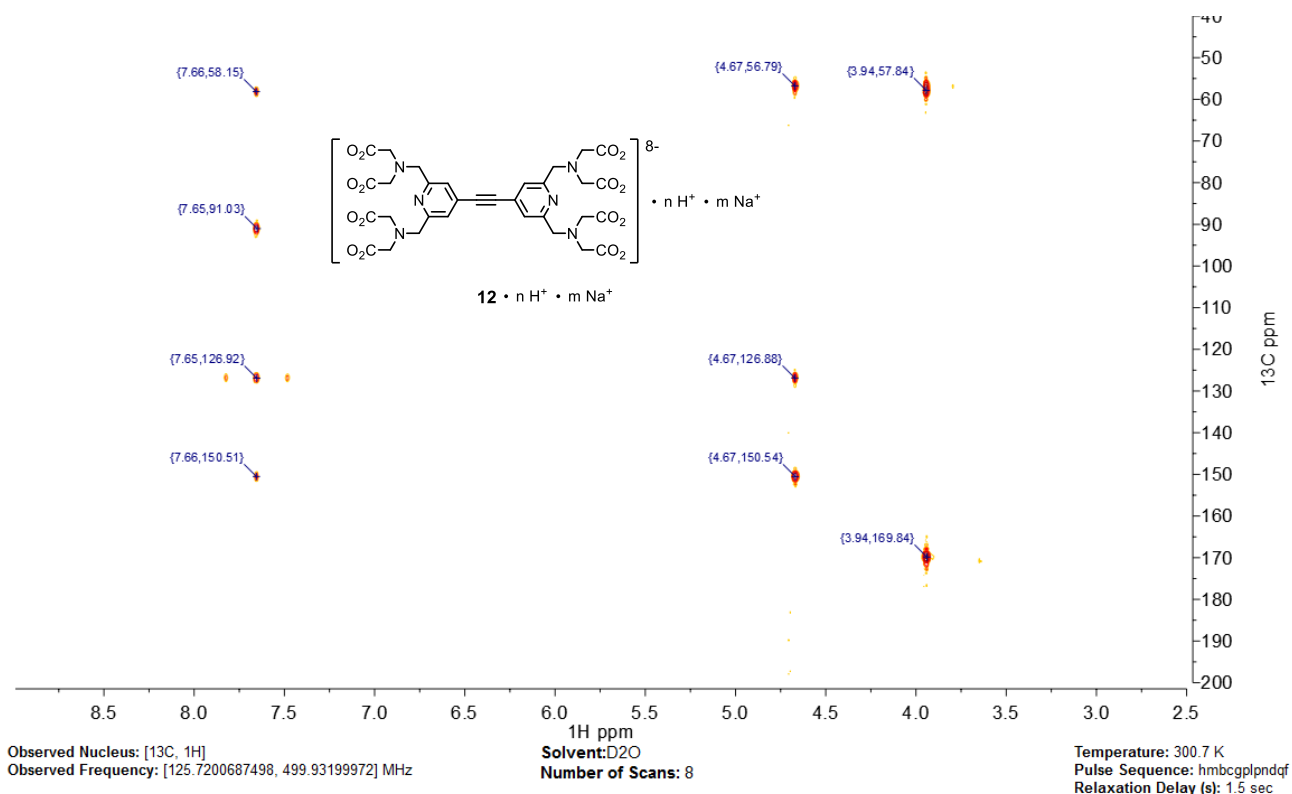
**Figure S6b.** <sup>13</sup>C NMR spectrum of bisligand **12**•n H<sup>+</sup>•m Na<sup>+</sup>.



**Figure S6c.**  $^{13}\text{C}$  DEPT 135 NMR spectrum of bisligand  $12 \cdot n \text{H}^+ \cdot m \text{Na}^+$ .



**Figure S6d.** HMQC NMR spectrum of bisligand **12**·n H<sup>+</sup>·m Na<sup>+</sup>.

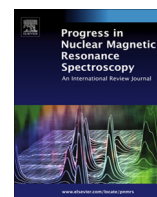


**Figure S6e.** HMBC NMR spectrum of bisligand **12**·n H<sup>+</sup>·m Na<sup>+</sup>.



Contents lists available at ScienceDirect

## Progress in Nuclear Magnetic Resonance Spectroscopy

journal homepage: [www.elsevier.com/locate/pnmrs](http://www.elsevier.com/locate/pnmrs)

# Dynamic nuclear polarization for sensitivity enhancement in modern solid-state NMR



Aany Sofia Lilly Thankamony<sup>1</sup>, Johannes J. Wittmann<sup>1</sup>, Monu Kaushik, Björn Corzilius\*

*Institute of Physical and Theoretical Chemistry, Institute of Biophysical Chemistry, and Center for Biomolecular Magnetic Resonance (BMRZ), Goethe University Frankfurt, Max-von-Laue-Str. 7–9, 60438 Frankfurt, Germany*

Edited by Geoffrey Bodenhausen and Beat Meier

## ARTICLE INFO

## Article history:

Received 27 February 2017

Accepted 8 June 2017

Available online 23 July 2017

## ABSTRACT

The field of dynamic nuclear polarization has undergone tremendous developments and diversification since its inception more than 6 decades ago. In this review we provide an in-depth overview of the relevant topics involved in DNP-enhanced MAS NMR spectroscopy. This includes the theoretical description of DNP mechanisms as well as of the polarization transfer pathways that can lead to a uniform or selective spreading of polarization between nuclear spins. Furthermore, we cover historical and state-of-the-art aspects of dedicated instrumentation, polarizing agents, and optimization techniques for efficient MAS DNP. Finally, we present an extensive overview on applications in the fields of structural biology and materials science, which underlines that MAS DNP has moved far beyond the proof-of-concept stage and has become an important tool for research in these fields.

© 2017 The Authors. Published by Elsevier B.V. This is an open access article under the CC BY-NC-ND license (<http://creativecommons.org/licenses/by-nc-nd/4.0/>).

## Contents

1. Introduction	122
1.1. Structure determination by solid-state NMR	122
1.2. Sensitivity issue	122
1.3. Concept of DNP	123
1.4. Scope of this review	123
2. Mechanisms and transfer pathways	124
2.1. Initial DNP transfer: DNP mechanisms	124
2.1.1. Solid effect	124
2.1.2. Cross effect	126
2.1.3. Overhauser effect in insulating solids	131
2.2. Integral DNP process: from electron spin to nuclear bulk	132
2.2.1. General concepts and early descriptions	132
2.2.2. Recent theoretical and experimental advances	135
2.3. Utilization of enhanced polarization	137
2.3.1. DNP build-up under microwave irradiation	137
2.3.2. Indirect vs. direct DNP	139
2.3.3. Active DNP pathways	139
2.3.4. Pulse sequences for indirect or direct DNP read-out	139
2.3.5. Simultaneous indirect and direct DNP	139
2.3.6. Examples of NMR pulse sequences used for MAS DNP	140

\* Corresponding author.

E-mail address: [corzilius@em.uni-frankfurt.de](mailto:corzilius@em.uni-frankfurt.de) (B. Corzilius).

<sup>1</sup> These authors contributed equally.

3.	Enhancement profiles	140
3.1.	Development of fundamental DNP theory	141
3.2.	Differences due to DNP mechanisms and polarizing agents	141
3.2.1.	Solid effect	141
3.2.2.	Cross effect	142
3.2.3.	Overhauser effect	143
3.2.4.	High-spin metal ions	145
3.3.	Information content	145
3.3.1.	Identification of DNP mechanism	145
3.3.2.	Multinuclear DNP	146
4.	Instrumentation	147
4.1.	High-frequency microwave sources	147
4.1.1.	Gyrotrons	147
4.1.2.	Other sources	147
4.2.	Control of DNP matching conditions	148
4.2.1.	Magnetic field variation	148
4.2.2.	Microwave frequency tunability	148
4.2.3.	Fast microwave frequency modulation	148
4.3.	Cryogenic MAS	148
4.3.1.	Nitrogen cooling	148
4.3.2.	Helium cooling	149
4.3.3.	Fast MAS and cryogenic temperatures	149
4.4.	DNP NMR probe and microwave transmission	150
4.4.1.	Cryogenic probe design	150
4.4.2.	Microwave transmission from source to sample	152
4.4.3.	Inside the sample chamber	152
5.	Polarizing agents	154
5.1.	Radicals with narrow EPR line for solid effect DNP	154
5.1.1.	BDPA-type radicals	154
5.1.2.	Trityl-type radicals	155
5.2.	Nitroxides and biradicals for cross effect DNP	155
5.2.1.	Monomeric radicals	156
5.2.2.	Nitroxide biradicals (and higher oligoradicals)	156
5.2.3.	Heterodimeric biradicals and mixtures	158
5.3.	Paramagnetic metal ions	161
5.3.1.	Ce(III) and Cr(V): early experiments	161
5.3.2.	Gd(III) and Mn(II) in chelate complexes	162
5.3.3.	Cr(III) in crystalline solids	162
6.	Practical aspects	163
6.1.	Build-up and depletion of the (enhanced) NMR signal	163
6.1.1.	Accelerated build-up of polarization during SE	163
6.1.2.	Depolarization by MAS	164
6.1.3.	The absolute sensitivity ratio	164
6.2.	Experimental parameters	165
6.2.1.	External (static) magnetic field	165
6.2.2.	MAS frequency	166
6.2.3.	Microwave power	167
6.2.4.	Sample temperature: enhancement factors and spectral resolution	167
6.3.	DNP sample preparation techniques	169
6.3.1.	DNP in a glass-forming matrix	169
6.3.2.	Alternative sample preparation techniques	169
6.3.3.	Matrix-free approaches	170
6.3.4.	Localized and targeted DNP	170
6.4.	Sample constitution	170
6.4.1.	Isotopic enrichment and depletion	170
6.4.2.	Polarizing agent concentration	171
6.4.3.	Interactions between polarizing agents and analytes	171
7.	Structure determination enabled by DNP enhancement	171
7.1.	Pioneering works on MAS DNP	171
7.1.1.	Early applications on polymers and diamonds	171
7.1.2.	Pioneering developments enabling biomolecular DNP	172
7.2.	Modern applications on biological systems	172
7.2.1.	Amyloid fibrils	172
7.2.2.	Membrane proteins	173
7.2.3.	Structure of biomolecules in large complexes	175
7.2.4.	Biomolecules embedded in complex environments	176
7.2.5.	Towards in-cell DNP	176
7.3.	Applications to materials research	178
7.3.1.	Enabling surface probing: DNP-SENS	179
7.3.2.	Materials embedded in organic glass-forming agents	181
7.3.3.	Impregnated microcrystals	181



7.4. Extending the NMR toolkit by DNP methods. . . . . 182  
 7.4.1. DNP of half-integer spin quadrupolar nuclei . . . . . 182  
 7.4.2. DNP of integer spin quadrupolar nuclei . . . . . 184  
 7.4.3. Wideline NMR ( $I = 1/2$ ). . . . . 184  
 8. Conclusions. . . . . 185  
 Acknowledgments . . . . . 186  
 References . . . . . 186

**1. Introduction**

*1.1. Structure determination by solid-state NMR*

Solid-state nuclear magnetic resonance (NMR) spectroscopy is a powerful technique for the identification of chemical compounds as well as for the determination of molecular structures and dynamics of various kinds of materials. This versatility is based on several interactions that provide information about the local electronic environment of the nuclei or inter-spin distances. Thus, invaluable information about connectivity and conformation can be obtained with atomic resolution.

Several (multidimensional) NMR experiments under magic-angle spinning (MAS) conditions [1,2] have been designed over the past decades that allow a tailored extraction of the desired structural information while providing high spectral resolution [3–9]. Since MAS NMR is not relying on rotational averaging of anisotropic interactions by fast molecular tumbling of the analyte molecule, the method is not limited by the molecular size as is the case with high-resolution NMR in solution. This makes MAS NMR especially amenable for atomistic structural investigations of large or insoluble biomolecules and biomolecular complexes. It can also provide structural insights into functional materials. In

particular, low-dimensional structures (e.g., fibrillar and 2-dimensional arrangements, surface layers), as well as arrangements lacking general long-range order (e.g., microcrystals, amorphous phases) are not accessible by means of X-ray crystallography and are therefore particularly interesting targets for MAS NMR.

Thus, it has been possible to address many problems in structural biology such as the arrangement of amyloidogenic peptides and proteins within (proto-)fibrils [10–14], large oligomeric complexes [15], membrane proteins [16,17], prokaryotic gas vesicles [18], etc. Currently, large strides are taken towards the investigation of such species within the environment of whole biological cells [19–21]. In materials science, MAS NMR has been applied to catalysis [22,23], glasses, functional materials [24,25], energy materials [26,27], biomass [28–31], soil [32–34], sediments [35], polymers [36–38], geomaterials [39–41], hybrid biomaterials [42–44], sol-gel materials [45,46], micro or macroporous materials (e.g., MOFs) [47–49], etc.

*1.2. Sensitivity issue*

However, the low intrinsic sensitivity of NMR caused by the small thermal population differences of the spin states restricts many possible applications due to unreasonably long measurement times. To a certain degree, lower experimental temperatures and/or higher external magnetic fields can improve the signal-to-noise ratio. If nuclei with low gyromagnetic ratio are to be detected, polarization transfer schemes from nuclei with large gyromagnetic ratios (high- $\gamma$  nuclei), such as  $^1\text{H}$  or  $^{19}\text{F}$ , are frequently exploited for increasing the sensitivity per unit time [50]. Recently, MAS with spinning frequencies beyond 100 kHz in combination with direct  $^1\text{H}$  detection has shown promising developments in terms of resolution and sensitivity [51,52].

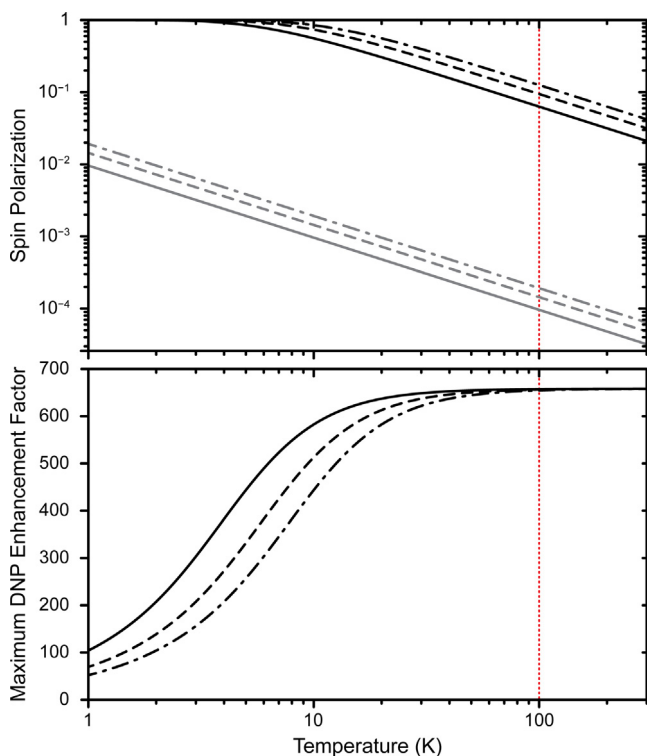


**Fig. 1.** Calculated absolute electron (black) and nuclear (gray) spin polarization following Eq. (1) (top) and maximum theoretical DNP enhancement factor after Eq. (2) (bottom) for a  $^1\text{H}$  nuclear spin coupled to an  $S = 1/2$  electron spin with  $g = 2$ . Magnetic fields are 9.4 T (solid line), 14.1 T (dashed line) and 18.8 T (dash-dotted line). The typical operational temperature of 100 K for MAS-DNP is marked by a vertical red dotted line.

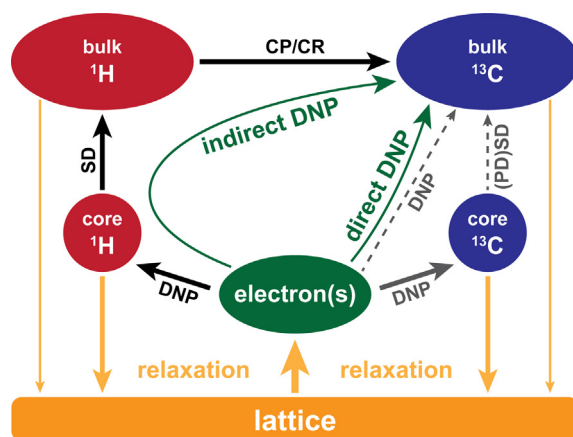


**Fig. 2.** Schematic representation of possible DNP transfer pathways in a system containing  $^1\text{H}$  and  $^{13}\text{C}$ . The latter nucleus was chosen for demonstration purposes; the scheme is valid for arbitrary low- $\gamma$  nuclei. Green arrows distinguish between indirect (e.g., via heteronuclear transfer from  $^1\text{H}$  to  $^{13}\text{C}$ ) and direct DNP transfer. (PD)SD and CP/CR stand for (proton-driven) spin diffusion and cross polarization/cross relaxation.

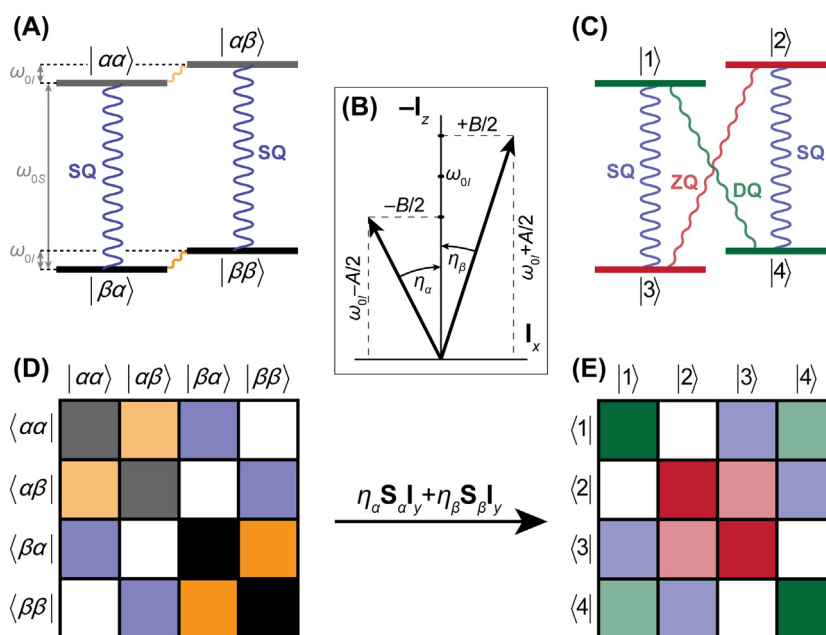


**Fig. 3.** (A) Energy scheme of a two-spin system with  $S = 1/2, I = 1/2$  in the Zeeman basis. SQ coherences excited by the  $\mu\text{W}$  field are depicted in blue, coherences introduced by the pseudo-secular HFI in orange. (B) Depiction of the eigenframe branching of the nuclear states in the different  $(\alpha, \beta)$  electron spin polarization subspaces. (C) Energy scheme in the eigenbasis of the static spin Hamiltonian (including HFI, but neglecting the  $\mu\text{W}$  field). SQ, DQ, and ZQ coherences are shown in blue, green, and red, respectively, as are eigenstates connected by the DQ or ZQ coherences. (D) Matrix representation of the Hamiltonian in the Zeeman basis [same color code as in (A)]. Neglecting  $\mu\text{W}$ -induced coherences the Hamiltonian is block-diagonal; the  $\beta$  electron spin subspace is shown in lighter colors. (E) Hamiltonian after diagonalization [same color code as in (C)].

Nevertheless, the overall gains are small as the signal intensity is governed by a thermal population difference, determined by the Boltzmann factor:

$$P = \tanh\left(\frac{\gamma\hbar B_0}{2k_B T}\right). \quad (1)$$

Here,  $P$  is the spin polarization,  $\gamma$  is its gyromagnetic ratio, and  $\hbar$  and  $k_B$  are the reduced Planck constant and the Boltzmann constant, respectively. Besides the variation of the external magnetic field  $B_0$ , and the temperature  $T$ , a much higher polarization gain is obtained if hyperpolarization techniques are employed, since they can generate much larger, non-thermal population differences. Among these are para-hydrogen induced polarization (PHIP) [53], chemically-induced dynamic nuclear polarization (CIDNP) [54], spin-exchange optical pumping (SEOP) [55], and dynamic nuclear polarization (DNP) [56,57]. The latter stands out due to its broad applicability in material science and biomolecular NMR spectroscopy. This is based on its capability to provide substantial nuclear hyperpolarization at high magnetic fields under MAS conditions (see Fig. 1).

### 1.3. Concept of DNP

As proposed by Overhauser in 1953 [56] and subsequently verified by Carver and Slichter [57], the much larger polarization of electron spins can be transferred to nuclear spins upon saturation of electron paramagnetic resonance (EPR) transitions by means of microwave ( $\mu\text{W}$ ) irradiation. In theory, a DNP enhancement factor,  $\varepsilon$ , equal to the ratio between the gyromagnetic ratios of the electron spin,  $S$ , and the nuclear spin,  $I$ , can be obtained:

$$\varepsilon_{\max} = \frac{P_S}{P_I} \left( \approx \frac{\gamma_S}{\gamma_I} \text{ for } \gamma_S \hbar B_0 \ll k_B T \right). \quad (2)$$

This factor is  $\sim 660$  for  $^1\text{H}$  and is accordingly larger for nuclei with smaller gyromagnetic ratios. In the decades following the initial discovery, several experimental and theoretical studies have

been performed pushing the achieved enhancement factors (*i.e.*, the intensity or integrated intensity ratio between spectra enhanced by  $\mu\text{W}$  irradiation and those in the absence of  $\mu\text{W}$ ) towards the theoretical maximum [58–64]. As the experimental time necessary for the accumulation of a required signal-to-noise ratio scales inversely with the square of the signal intensity and thus with the enhancement factor, tremendous time savings and novel possibilities for NMR spectroscopy can be achieved.

For most of the analytes under study, the application of DNP requires doping the (diamagnetic) sample with paramagnetic centers as sources of polarization. Usually, stable radicals fulfilling certain criteria serve as polarizing agents (PAs). These criteria are mainly governed by several possible mechanisms for DNP, besides other considerations regarding sample constitution. Furthermore, in order to provide the required  $\mu\text{W}$  irradiation and to match DNP conditions, specialized instrumentation (*i.e.*,  $\mu\text{W}$  source, DNP MAS NMR probe as well as cryogenic gas supply for MAS) has to be utilized. The theoretical and practical consequences of this broad scientific field, comprising specialized engineering, radical chemistry, EPR and state-of-the-art MAS NMR, create a scenario where all involved researchers are expected to intuitively understand the complex interplay between these fields.

### 1.4. Scope of this review

This review will provide an in-depth overview about the theoretical and practical aspects of DNP under MAS conditions at high magnetic fields. Here we will focus on topics of current state-of-the-art that have already proven applicability towards problems in structural biology and materials science.

In the following two sections, a detailed description of the theory of DNP mechanisms prominent under MAS conditions is given. Here, we will cover not only the quantum-mechanical description of the initial polarization transfer mechanisms but also the processes responsible for spreading and potential drainage of enhanced polarization within a large network of nuclear spins.

Furthermore, important methods of read-out and utilization of enhanced nuclear spin polarization by MAS NMR are described. In the same vein, we draw the connection between EPR properties of the PAs and the resulting DNP field- or frequency profiles. The specialized instrumentation required for MAS DNP, including modifications to existing MAS NMR instrumentation, is illustrated in Section 4. The focus lies on recent developments, for example, the development of high-power high-frequency  $\mu\text{w}$  sources and cryogenic MAS instrumentation, that played a crucial role for bringing DNP up to speed with contemporary NMR at high magnetic fields. In the subsequent Section 5, the development of the large variety of available PAs together with their DNP-relevant properties are covered. Concepts for optimizing various experimental parameters as well as sample preparation techniques proven for efficient DNP are reviewed in Section 6. Finally, the large potential of DNP for accelerating conventional NMR experiments and enabling novel experimental techniques is illustrated using several examples and applications in biology and materials research.

Especially in the last sections, it will become clear that DNP-enhanced MAS NMR has moved well beyond the proof-of-principle phase. However, the transition from a mostly explorative technique to a powerful method capable of providing invaluable structural data has only occurred very recently, in particular in the field of structural biology. This is underlined by the fact that of all published studies in which DNP enhancement substantially contributed to the extraction of structural information, more than 50% have been published just during the last two years. A similar boom has been observed in the field of materials research slightly earlier.

This review is limited in scope to principles relevant for MAS NMR and accompanying techniques such as (high-field) quadrupolar and wide-line NMR. For a detailed description of other DNP-based hyperpolarization techniques, including dissolution DNP for hyperpolarized NMR in solution or magnetic resonance imaging or spectroscopy (MRI/MRS) and related topics, we refer the reader to several other excellent reviews [65–73].

## 2. Mechanisms and transfer pathways

For a full understanding of DNP, we have to review the complete chain of polarization transfer from the electron spin of the PA to the nucleus where it is finally detected using typical MAS NMR schemes as illustrated in Fig. 2. We can generally separate the involved chain of events into three steps:

- (1) The initial DNP transfer
- (2) The propagation of the polarization to the nuclei of interest
- (3) The direct detection or heteronuclear transfer of polarization for indirect detection.

We will briefly describe these three steps and provide a thorough review in the following subsections.

For the first point, the usual approach is to restrict the number of considered spins to the bare minimum required in order to describe a specific mechanism. In this context, we have to consider the solid effect (SE), the cross effect (CE), and the Overhauser effect (OE). These mechanisms can be explained with a minimum of just two or three spins, allowing us to derive analytical solutions that describe the underlying quantum mechanics. For the description of SE (Section 2.1.1), we will review the situation of a static sample that can approximately describe PAs featuring (nearly) isotropic EPR spectra under MAS, and discuss the ramifications if the EPR spectrum of the PA features a significant anisotropy. The CE mechanism varies rather strongly when comparing samples under MAS

with the static case; we will focus on the MAS situation here (Section 2.1.2), but briefly review the steps required for description of static CE (Section 2.1.2.6). OE theory has not yet been described in detail for insulating solids, therefore, we review the general principles for electron–nuclear (e–n) cross-relaxation in Section 2.1.3. These general concepts are almost exclusively based on liquid-state DNP experiments, however, significant progress to describe OE-enabling dynamics in solids has been made recently. Thermal mixing (TM) is another mechanism that is closely related to CE when many electrons and nuclei interact strongly at low temperatures (typically  $T < 10$  K). As these conditions are generally not fulfilled during MAS DNP, we will not discuss TM in detail.

After the polarization has been transferred to the directly hyperfine-coupled nuclei, it has to propagate to the nuclei of interest, which are typically on molecules that are located at some distance from the PA. Therefore, this usually involves homonuclear spin diffusion (Section 2.2) through the cryoprotecting matrix and competes with the dynamic loss of polarization by spin-lattice relaxation.

Finally, the enhanced polarization is utilized on the nucleus of interest. This can happen in an indirect manner where advantage is taken of efficient spin diffusion through the  $^1\text{H}$  network. The polarization that has built up on  $^1\text{H}$  is then transferred to low- $\gamma$  nuclei for detection or further evolution. Alternatively, polarization that has built up directly on the low- $\gamma$  nuclear spins can be read out or used in typical MAS NMR schemes. This direct DNP approach is often favored for alternative transfer pathways and can result in complementary information as compared to indirect DNP experiments (see Section 2.3.2).

### 2.1. Initial DNP transfer: DNP mechanisms

#### 2.1.1. Solid effect

**2.1.1.1. Spin dynamics in static samples.** The solid effect in its simplest form is a two-spin process. It relies on the excitation of nominally forbidden electron–nuclear (e–n) double- and zero-quantum coherences by  $\mu\text{w}$  irradiation; these transitions are partly allowed due to a mixing of nuclear spin states. Like in common EPR techniques such as electron spin-echo envelope modulation (ESEEM) or electron–electron double resonance (ELDOR), the pseudo-secular hyperfine coupling is the driving interaction of such processes.

In the simplest case, a two-spin system of one  $S = 1/2$  electron spin and one  $I = 1/2$  nucleus can be described in a four-dimensional Hilbert space comprised of the Zeeman basis  $\{|\alpha\alpha\rangle, |\alpha\beta\rangle, |\beta\alpha\rangle, |\beta\beta\rangle\}$  (Fig. 3). Here  $\alpha$  and  $\beta$  symbolize the magnetic quantum number of each spin (i.e.,  $\alpha \rightarrow m_i = +1/2$  and  $\beta \rightarrow m_i = -1/2$ ). A dipolar coupling between the two spins introduces off-diagonal elements, perturbing this eigenbasis and introducing mixing between the Zeeman basis states. This can be deduced by the general spin Hamiltonian described by

$$\hat{H}_{\text{SE}} = \frac{\mu_{\text{B}}}{\hbar} \vec{B} \mathbf{g} \vec{S} - \frac{\mu_{\text{n}} g_{\text{n}}}{\hbar} \vec{B} \vec{I} + \vec{S} \mathbf{A} \vec{I}. \quad (3)$$

Here, the first two terms are the electron and nuclear Zeeman interactions while the last term is the hyperfine interaction (HFI). Using the typical convention for the definition of the laboratory frame defined by the external (static) magnetic field component with magnitude  $B_0$  oriented along  $z$  as well as the (linearly polarized)  $\mu\text{w}$  field component oriented along  $x$  and oscillating with frequency  $\omega_{\mu\text{w}}$ , the magnetic field vector is defined as

$$\vec{B} = \begin{pmatrix} 2B_1 \cos(\omega_{\mu\text{w}}t) \\ 0 \\ B_0 \end{pmatrix}, \quad (4)$$

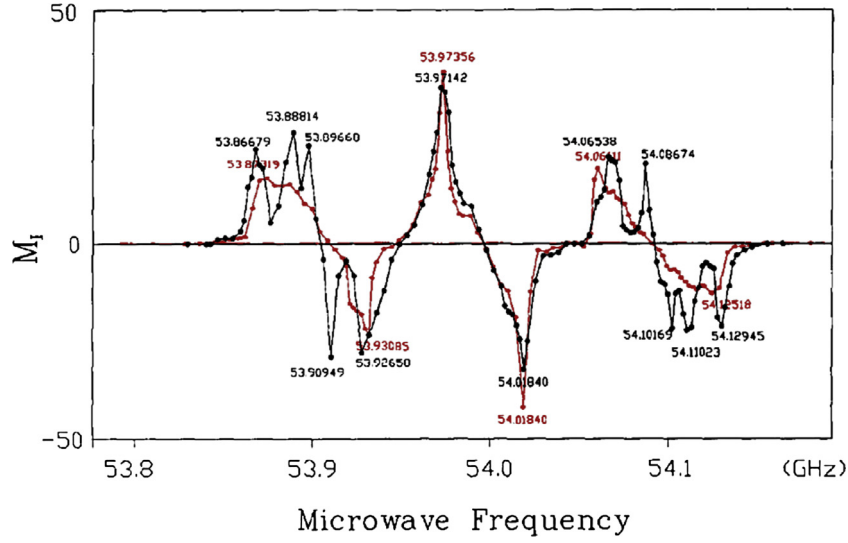


**Fig. 4.** Comparison between DNP-enhanced  $^{13}\text{C}$  signal intensity of diamond under static (black) and MAS (red) conditions. Data acquired at 1.9 T. The graph is an overlay of two figures from the original publication; reprinted with permission from [78].

the Hamiltonian can then be written as

$$\hat{H}_{SE} = \frac{\mu_B g_{zz}}{\hbar} B_0 \mathbf{S}_z + \frac{\mu_B g_{xx}}{\hbar} B_1 \cos(\omega_{\mu w} t) (\mathbf{S}_+ + \mathbf{S}_-) - \frac{\mu_n g_n}{\hbar} B_0 \mathbf{I}_z - \frac{\mu_n g_n}{\hbar} B_1 \cos(\omega_{\mu w} t) (\mathbf{I}_+ + \mathbf{I}_-) + \vec{\mathbf{S}} \mathbf{A} \vec{\mathbf{I}}. \quad (5)$$

Upon transformation of this Hamiltonian into the frame rotating with  $\omega_{\mu w}$  around z and truncation according to average Hamiltonian theory (AHT) after first order, the frequently used e-n Hamiltonian is obtained:

$$\hat{H}'_{SE} = \Omega_{0S} \mathbf{S}_z - \omega_{0I} \mathbf{I}_z + A_{zx} \mathbf{S}_z \mathbf{I}_x + A_{zy} \mathbf{S}_z \mathbf{I}_y + A_{zz} \mathbf{S}_z \mathbf{I}_z + \frac{\omega_{1S}}{2} (\mathbf{S}'_+ + \mathbf{S}'_-). \quad (6)$$

Prime symbols represent operators in the  $\mu w$  rotating frame;  $\Omega_{0S}$  is the frequency offset between  $\mu w$  and electron Zeeman frequency,  $\Omega_{0S} = \omega_{\mu w} - \omega_{0S}$ . Note that here and in the following, the nuclear Zeeman frequency,  $\omega_{0I}$ , is always considered to be positive; cases for nuclei with negative  $g_n$  value can be treated in a completely analogous manner. For simplification, the nuclear spin operators are transformed into a hybrid frame defined by the z-axis parallel to the static field and the dipolar HFI tensor frame, so that the e-n connection vector is pointing in the  $\mathbf{I}'_x$  direction (Fig. 3):

$$\hat{H}'_{SE} = \Omega_{0S} \mathbf{S}_z - \omega_{0I} \mathbf{I}_z + A \mathbf{S}_z \mathbf{I}_z + \frac{B}{2} \mathbf{S}_z (\mathbf{I}'_+ + \mathbf{I}'_-) + \frac{\omega_{1S}}{2} (\mathbf{S}'_+ + \mathbf{S}'_-). \quad (7)$$

Here, per definition,  $A = A_{zz}$  and  $B = \sqrt{A_{zx}^2 + A_{zy}^2}$ . Ignoring the  $\mu w$ -driven coherence [i.e., the last term in Eq. (7)] the Hamiltonian is block diagonal in each (i.e.,  $\alpha$  and  $\beta$ ) electron spin subspace. Therefore, each subspace can be independently diagonalized, resulting in an effective  $m_S$ -dependent state mixing.

**2.1.1.2. Definition of the eigenframe without  $\mu w$ .** Under the assumptions introduced above, the eigenframe of the static part of the Hamiltonian is tilted around its y-axis by the presence of the pseudo-secular HFI. Each electronic subspace is tilted as described by the respective branching angle

$$\eta_{\alpha/\beta} = \arctan\left(\frac{B}{A \mp 2\omega_{0I}}\right). \quad (8)$$

The mixed eigenstates deviate from the Zeeman basis. The new eigenbasis  $\{|1\rangle, |2\rangle, |3\rangle, |4\rangle\}$  is given by

$$\begin{aligned} |1\rangle &= p_\alpha |\alpha\alpha\rangle - q_\alpha |\alpha\beta\rangle \\ |2\rangle &= p_\alpha |\alpha\beta\rangle + q_\alpha |\alpha\alpha\rangle \\ |3\rangle &= p_\beta |\beta\alpha\rangle - q_\beta |\beta\beta\rangle \\ |4\rangle &= p_\beta |\beta\beta\rangle + q_\beta |\beta\alpha\rangle. \end{aligned} \quad (9)$$

With the mixing coefficients  $p_i = \cos(\frac{\eta_i}{2})$  and  $q_i = \sin(\frac{\eta_i}{2})$ . This state mixing of nuclear Zeeman states is a requirement for SE to occur.

At high field typically encountered in DNP-enhanced MAS NMR, the hyperfine coupling is about two or more orders of magnitude smaller than the nuclear Zeeman interaction. Therefore, the branching angles can be approximately simplified to

$$\eta_{\alpha/\beta} \approx \mp \frac{B}{2\omega_{0I}} \text{ for } |A|, |B| \ll \omega_{0I}. \quad (10)$$

In this case the mixing coefficients become:

$$\begin{aligned} p_{\alpha/\beta} &\approx 1 \\ q_{\alpha/\beta} &\approx \mp \frac{B}{4\omega_{0I}}. \end{aligned} \quad (11)$$

Subsequently, the Zeeman basis  $\{|\alpha\alpha\rangle, |\alpha\beta\rangle, |\beta\alpha\rangle, |\beta\beta\rangle\}$  as well as the quantum numbers  $m_S$  and  $m_I$  adequately describe the system due to the relatively weak mixing, while perturbing e-n coherences can still be excited by the  $\mu w$  field.

**2.1.1.3. SE matching and coherences excited by  $\mu w$ .** In order to induce SE mixing within the spin pair, an e-n zero-quantum (ZQ) or double-quantum (DQ) transition has to be excited. The respective coherences build up when the connected eigenstates are degenerate in the  $\mu w$  rotating frame. ZQ transitions occur between  $|2\rangle$  and  $|3\rangle$  (or  $|\alpha\beta\rangle$  and  $|\beta\alpha\rangle$  in the unperturbed basis), DQ transitions between  $|1\rangle$  and  $|4\rangle$  (or  $|\alpha\alpha\rangle$  and  $|\beta\beta\rangle$ ). Therefore, the respective matching conditions are fulfilled when

$$\omega_{\mu w} = \omega_{0S} \mp \omega_{0I}. \quad (12)$$

Here, the difference in Larmor frequencies corresponds to the DQ transitions, whereas the sum is relevant to the ZQ transitions.

The effective SE transition moments can be obtained by transforming the  $\mu\omega$  Hamiltonian

$$H'_{\mu\omega} = \frac{\omega_{1S}}{2} (\mathbf{S}'_+ + \mathbf{S}'_-) \quad (13)$$

into the eigenframe of the static Hamiltonian according to the difference in branching angles<sup>2</sup>:

$$\eta^- = \frac{\eta_\alpha - \eta_\beta}{2}. \quad (14)$$

Then the effective  $\mu\omega$  Hamiltonian is

$$H''_{\mu\omega} = \frac{\omega_{1S}}{2} \left\{ (\mathbf{S}'_+ + \mathbf{S}'_-) \cos \eta^- + \frac{1}{2} [(\mathbf{S}'_+ \mathbf{I}'_+ + \mathbf{S}'_- \mathbf{I}'_-) - (\mathbf{S}'_+ \mathbf{I}'_- + \mathbf{S}'_- \mathbf{I}'_+)] \sin \eta^- \right\}. \quad (15)$$

In the pseudo-high-field approximation ( $|A|, |B| \ll \omega_{0I}$ ),  $\eta^-$  can be simplified to

$$\eta^- \approx -\frac{B}{2\omega_{0I}}, \quad (16)$$

and subsequently the final, effective  $\mu\omega$  Hamiltonian is obtained:

$$H''_{\mu\omega} = \frac{\omega_{1S}}{2} \left\{ (\mathbf{S}'_+ + \mathbf{S}'_-) - \frac{B}{4\omega_{0I}} [(\mathbf{S}'_+ \mathbf{I}'_+ + \mathbf{S}'_- \mathbf{I}'_-) - (\mathbf{S}'_+ \mathbf{I}'_- + \mathbf{S}'_- \mathbf{I}'_+)] \right\}. \quad (17)$$

The EPR single-quantum (SQ) transition moment (first term) is practically unchanged while the e–n DQ and ZQ transition moments (second and third terms of Eq. (17), respectively) are introduced with an effective scaling factor,  $B/2\omega_{0I}$ , compared to the SQ transition. Due to the small magnitude of this factor, the transition probability is relatively low ( $\sim 10^{-4}$ – $10^{-8}$  relative to that of the SQ). Thus, large absolute  $\mu\omega$  field strengths are required in order to sufficiently drive these transitions and build up significant coherence.

As long as a SE transition is selectively excited (*i.e.*, the homogeneous linewidth of all possible transitions is small compared to the effective  $\mu\omega$  field strength), the system can be separated into the ZQ and DQ subspaces and evolution of the spin system can be described by a pseudo (doublet) spin following the simple Bloch equations [74]. Such a simplification will be useful for analysis of effective polarization transfer rates as is explained in more detail in Section 2.2.

**2.1.1.4. SE under MAS.** If the two-spin system exhibits a relatively large anisotropy, for example if a mono-nitroxide PA is considered, the spin eigenstates show significant periodic modulations due to MAS. In this case, electron SQ as well as e–n DQ and ZQ transitions can be induced transiently during level anti-crossings (LACs) [75]. These  $\mu\omega$ -driven LACs occur when the energy levels of connected spin states cross each other in the frame rotating with the  $\mu\omega$  frequency (see also below for a more detailed description in context of CE in Section 2.1.2 and Fig. 6). If the variations in eigenstate energy due to anisotropy is larger than  $\omega_{0I}$ , SQ as well as ZQ and/or DQ LACs will occur alternately. This situation is similar to the typically described differential SE (for further details see Sections 2.2.1.5 and 3.2.1), where enhancement by ZQ and DQ transitions partially cancel in a static sample with an inhomogeneously broadened EPR signal [76]. However, SQ LACs inflict a large saturation of the electron spin [75], which will reduce the polarization available for transfer to the nuclear spin [77].

In cases where the anisotropy is small compared to  $\omega_{0I}$  (*e.g.*, for trityl- and BDPA-type radicals), SE-enabling ZQ or DQ transitions can be selectively excited. Nevertheless, modulations in spin ener-

gies might still reduce the net excitation efficiency of the e–n ZQ or DQ transition of an individual spin-packet, however, virtually all spin-packets will experience a SE-inducing LAC during a rotor period. This might in fact increase the overall DNP enhancement under MAS as compared to the static case [75]. In a singular demonstration, Zhou and co-workers have compared DNP of natural and synthetic diamonds under static and MAS conditions within the same experimental setup at a rather low field of 1.9 T [78,79]. Interestingly, a splitting pattern—caused by anisotropic HFI to <sup>14</sup>N in nitrogen centered radicals—was observed in the DNP frequency profile for the static sample; that pattern was smeared out under MAS as is shown in Fig. 4. Unfortunately, the absolute <sup>13</sup>C enhancement factors could not be evaluated. Further experimental quantitative comparisons of these two cases (*i.e.*, static vs. MAS) with systems operating exclusively under SE have not been reported to our knowledge.

### 2.1.2. Cross effect

**2.1.2.1. Spin dynamics under MAS.** The theoretical description of the CE is considerably more complex than that of the SE. Not only does the required additional electron spin increase the dimensionality of the Hilbert space to at least 8, but the description of CE under MAS also differs significantly from that of a static sample. Recent quantum-mechanical descriptions of the spin dynamics have been given independently by Hu et al. [80] and Hovav et al. [81]. In both cases, the CE was treated as a static effect, where a  $\mu\omega$  field is applied to Zeeman states that are coupled by electronic and hyperfine interactions. As we will see, this situation relies on a peculiar set of matching conditions, where the difference in effective Larmor frequencies of the two electron spins matches the nuclear Zeeman frequency while at the same time one of the two electron spins is on resonance with the incident  $\mu\omega$  frequency:

$$(\Delta\omega_{0S} = |\omega_{0S,1} - \omega_{0S,2}| = \omega_{0I}) \quad \wedge \quad (\omega_{\mu\omega} = \omega_{0S,1} \vee \omega_{0S,2}) \quad (18)$$

In an ideal, hypothetical case, one could imagine a system of two electron spins with isotropic Zeeman interactions where the overall breadth of each EPR resonance is sufficiently small compared to  $\omega_{0I}$ . Such a gedankenexperiment has been elaborated in detail by Wollan [61]. In reality, finding two paramagnetic species which fulfil this condition is rather unpractical. A few serendipitous cases could be thought of, for example, a system of trityl- and BDPA-type radicals would roughly match the above condition for <sup>13</sup>C and allow CE within a radical mixture as Michaelis et al. have demonstrated at a field of 5 T [82]. However, even in this case the breadth of the trityl spectrum is of the same order as  $\omega_{0I}$ , which leads to anisotropy in CE matching.

A revolutionary description of CE under MAS has been proposed by Thurber and Tycko and almost simultaneously by Mentink-Vigier et al. in 2012 [75,83]. In their theory, the spin system periodically undergoes level anti-crossing (LAC) events, during which polarization can be exchanged between electron and nuclear spins. This model not only allows for a temporal separation of  $\mu\omega$  irradiation and CE matching events but also predicts the nuclear depolarization by MAS, which has recently been demonstrated experimentally [84–86]. A more detailed description of such LACs is given in Section 2.1.2.5 and practical aspects of nuclear depolarization are covered in Section 6.1.2.

As the simplest spin system capable of describing the CE, two electron spins ( $S_1 = 1/2$  and  $S_2 = 1/2$ ) and one nuclear spin have to be considered including electron–electron (e–e) coupling; the nucleus has to be hyperfine coupled to at least one of the electron spins:

$$\hat{H}_{CE} = \frac{\mu_B}{\hbar} \vec{B} (\mathbf{g}_1 \vec{S}_1 + \mathbf{g}_2 \vec{S}_2) - \frac{\mu_n g_n}{\hbar} \vec{B} \vec{I} + \vec{S}_1 \vec{D} \vec{S}_2 + (\vec{S}_1 \mathbf{A}_1 + \vec{S}_2 \mathbf{A}_2) \vec{I}. \quad (19)$$

<sup>2</sup> Due to the opposite signs of the two branching angles this difference corresponds to the full angle between the two nuclear spin quantization axes.

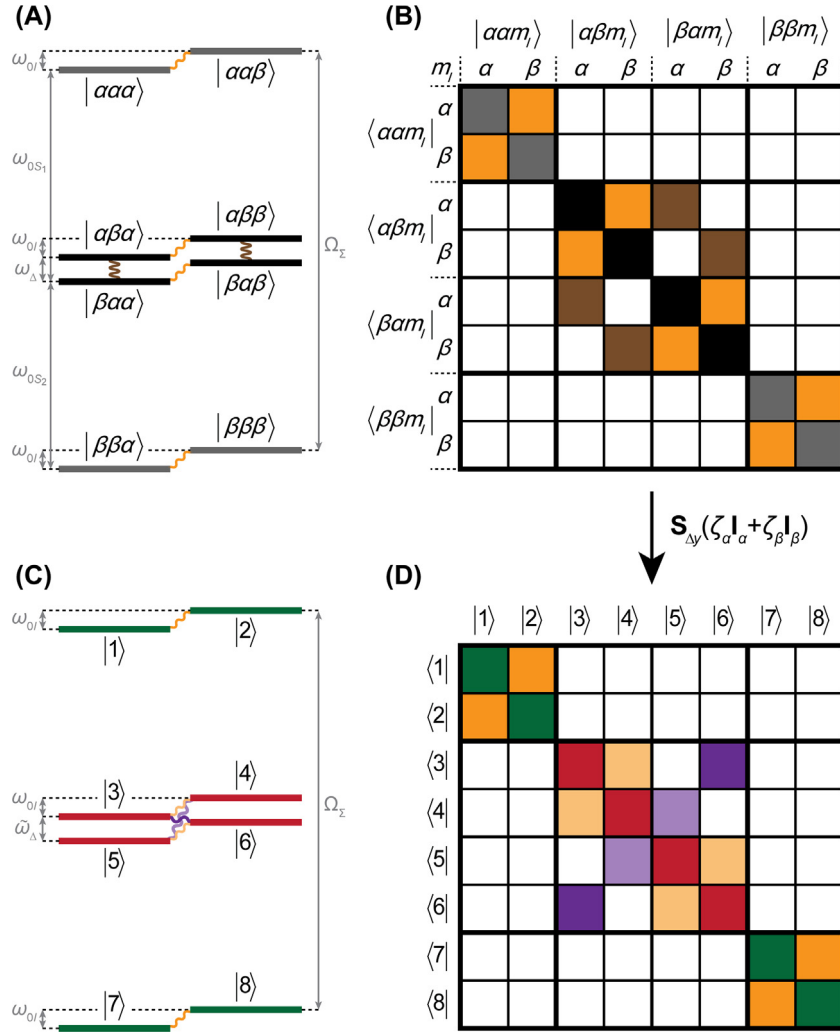


**Fig. 5.** (A) Energy scheme of the three-spin system containing two electron spins and one nuclear spin with  $S_1 = 1/2$ ,  $S_2 = 1/2$ , and  $I = 1/2$ , respectively. (B) Matrix representation of the Hamiltonian in the Zeeman basis. Electronic ZQ states are marked in black, electronic DQ states that do not participate in CE are shown in gray. Electronic ZQ coherences induced by e–e dipolar coupling are depicted in brown, coherences introduced by the pseudo-secular HFI in orange. (C) Energy scheme and (D) matrix representation in the eigenbasis of the combined Zeeman and e–e interaction (including HFI but neglecting the  $\mu w$  terms). Electronic DQ and ZQ states are shown in green and red, respectively; (part of) the pseudo-secular HFI (orange) is transformed into e–e–n flip-flop-flip coherences marked in purple within the ZQ subspace.

Upon rotating-frame truncation, according to the oscillating  $\mu w$  field in Eq. (4), the Hamiltonian is reduced to components commuting with  $\mathbf{S}_{iz}$ , and  $\mu w$ -driven SQ elements appear:

$$\begin{aligned} \hat{H}'_{CE} = & \Omega_{0S_1} \mathbf{S}_{1z} + \Omega_{0S_2} \mathbf{S}_{2z} - \omega_{0I} \mathbf{I}_z \\ & + d(3\mathbf{S}_{1z}\mathbf{S}_{2z} - \vec{\mathbf{S}}_1 \cdot \vec{\mathbf{S}}_2) - 2J\vec{\mathbf{S}}_1 \cdot \vec{\mathbf{S}}_2 \\ & + (A_{1zz}\mathbf{S}_{1z} + A_{2zz}\mathbf{S}_{2z})\mathbf{I}_z + (A_{1zx}\mathbf{S}_{1z} + A_{2zx}\mathbf{S}_{2z})\mathbf{I}_x + (A_{1zy}\mathbf{S}_{1z} + A_{2zy}\mathbf{S}_{2z})\mathbf{I}_y \\ & + \frac{\omega_{1S_1}}{2}\mathbf{S}'_{1x} + \frac{\omega_{1S_2}}{2}\mathbf{S}'_{2x}. \end{aligned} \quad (20)$$

The effective e–e dipole coupling,  $d = \frac{1}{2}D_{zz} - J$ , and the exchange-coupling constant,  $J = \frac{1}{3}(D_{xx} + D_{yy} + D_{zz})$ , can be extracted from the full e–e coupling tensor. We can conveniently separate diagonal and off-diagonal elements:

$$\begin{aligned} \hat{H}'_{CE} = & \underbrace{\Omega_{0S_1} \mathbf{S}_{1z} + \Omega_{0S_2} \mathbf{S}_{2z} - \omega_{0I} \mathbf{I}_z + D_0 \mathbf{S}_{1z} \mathbf{S}_{2z} + (A_1 \mathbf{S}_{1z} + A_2 \mathbf{S}_{2z}) \mathbf{I}_z}_{\hat{H}'_{CE, \text{on}}} \\ & + \underbrace{D_0 (\mathbf{S}'_{1x} \mathbf{S}'_{2x} + \mathbf{S}'_{1y} \mathbf{S}'_{2y}) + (A_{1x} \mathbf{S}_{1z} + A_{2x} \mathbf{S}_{2z}) \mathbf{I}_x + (A_{1y} \mathbf{S}_{1z} + A_{2y} \mathbf{S}_{2z}) \mathbf{I}_y + \omega_{1S_1} \mathbf{S}'_{1x} + \omega_{1S_2} \mathbf{S}'_{2x}}_{\hat{H}'_{CE, \text{off}}}. \end{aligned} \quad (21)$$

with  $D_d = 2(d - J)$ ,  $D_0 = -(d + 2J)$ , and  $A_i = A_{i,zz}$ ; we have also dropped one index 'z' from the pseudo-secular HFI coupling constants.

As mentioned above, Thurber and Tycko as well as Mentink-Vigier et al. have introduced a way to understand the CE under MAS by considering the time evolution of the anisotropic Hamiltonian during one rotor period. We can identify three separate events that occur periodically and generally do not coincide with each other:  $\mu w$  events, CE matching events, and e–e events. Accordingly, we will consider three cases:

- (1) the  $\mu w$  frequency is on resonance with one of the two electron spins and the frequency separation between the two electron spins is arbitrary;
- (2) the frequency separation of the two electron spins equals the nuclear Larmor frequency;
- (3) the Larmor frequency of the two electron spins is equal.

In the latter two cases, the  $\mu w$  frequency will be off-resonance with respect to both electron spins by an arbitrary value.

**2.1.2.2. Microwave (spin-flip) events.** In case (1), we assume that the  $\mu\omega$ -resonance condition is fulfilled for one electron spin,  $j$ . Furthermore, the other electron spin,  $i$ , shall be far off-resonance, so that  $|\Omega_{0S_{i \neq j}}| \gg |D_0|$ , and we neglect mixing of nuclear spin states by hyperfine couplings. Furthermore, we assume negligible differences in Rabi frequencies between the electrons, so that we can define a common Rabi frequency  $\omega_{1S}$ . In that case, we can drop all state mixing terms of the static Hamiltonian, so that solely the  $\mu\omega$  excitation acts on Zeeman states:

$$\hat{H}'_{\text{CE,SQ}} = \Omega_{0S_1} \mathbf{S}_{1z} + \Omega_{0S_2} \mathbf{S}_{2z} - \omega_{0I} \mathbf{I}_z + D_d \mathbf{S}_{1z} \mathbf{S}_{2z} + (A_1 \mathbf{S}_{1z} + A_2 \mathbf{S}_{2z}) \mathbf{I}_z + \frac{\omega_{1S}}{2} (\mathbf{S}'_{1+} + \mathbf{S}'_{1-} + \mathbf{S}'_{2+} + \mathbf{S}'_{2-}). \quad (22)$$

During evolution of anisotropic Zeeman and dipolar interactions, the  $\mu\omega$ -resonance condition is met if  $|\Omega_{0S_j}| = \frac{1}{2}|D_d \pm A_j|$ . The signs depend on the magnetic spin states of the off-resonance electron and the nucleus. This leads to equilibration of the connected Zeeman states and saturation of the respective EPR transition.

After such a resonance condition has been passed through during an LAC, the resulting change in polarization will decay slowly with  $T_{1S}$  and therefore is memorized by the system for a certain period. The non-equilibrium populations can subsequently be transferred to the other electron and the nucleus in a concerted fashion during a CE event, or only to the other electron during a dipolar flip-flop event. We will first describe a CE event, and then discuss the importance of e–e events.

**2.1.2.3. Cross-effect (flip-flop-flip) events.** In order to understand the actual CE transfer event under MAS, we have to transform the Hamiltonian into a frame in which the full e–e dipolar interaction is diagonal. The static Hamiltonian (excluding  $\mu\omega$  terms) is block diagonal with two outer  $2 \times 2$  blocks representing the e–e DQ subspace and one central  $4 \times 4$  block representing the corresponding ZQ subspace (Fig. 5). Thus, it can be rearranged as follows:

$$\hat{H}'_0 = \Omega_{\Sigma} \mathbf{S}_{\Sigma z} + \omega_{\Delta} \mathbf{S}_{\Delta z} - \omega_{0I} (\mathbf{S}_{\Sigma} + \mathbf{S}_{\Delta}) \mathbf{I}_z + \frac{D_d}{4} (\mathbf{S}_{\Sigma} - \mathbf{S}_{\Delta}) + D_0 \mathbf{S}_{\Delta x} + (A_{\Sigma} \mathbf{S}_{\Sigma z} + A_{\Delta} \mathbf{S}_{\Delta z}) \mathbf{I}_z + \mathbf{S}_{\Sigma x} (A_{\Sigma x} \mathbf{I}_x + A_{\Sigma y} \mathbf{I}_y) + \mathbf{S}_{\Delta x} (A_{\Delta x} \mathbf{I}_x + A_{\Delta y} \mathbf{I}_y), \quad (23)$$

with  $\mathbf{S}_{\Sigma z} = \frac{1}{2}(\mathbf{S}_{1z} + \mathbf{S}_{2z})$ ,  $\mathbf{S}_{\Delta z} = \frac{1}{2}(\mathbf{S}_{1z} - \mathbf{S}_{2z})$ ,  $\mathbf{S}_{\Sigma} = \mathbf{S}_1^z \mathbf{S}_2^z + \mathbf{S}_1^y \mathbf{S}_2^y$ ,  $\mathbf{S}_{\Delta} = \mathbf{S}_1^z \mathbf{S}_2^y + \mathbf{S}_1^y \mathbf{S}_2^z$ ,  $\mathbf{S}_{\Delta x} = \frac{1}{2}(\mathbf{S}'_{1+} \mathbf{S}'_{2-} + \mathbf{S}'_{1-} \mathbf{S}'_{2+})$ ,  $\Omega_{\Sigma} = \Omega_{0S_1} + \Omega_{0S_2}$ ,  $\omega_{\Delta} = \omega_{0S_1} - \omega_{0S_2}$ ,  $A_{\Sigma} = A_1 + A_2$ ,  $A_{\Delta} = A_1 - A_2$ ,  $A_{\Sigma a} = A_{1a} + A_{2a}$ , and  $A_{\Delta a} = A_{1a} - A_{2a}$  for  $a \in \{x, y\}$ . The  $\Sigma$  index denotes operators within the DQ space while  $\Delta$  marks operators confined to the ZQ space.

The tilting transformation below [Eq. (26)] acts exclusively on the ZQ subspace; thus we first separate that from the DQ subspace:

$$\hat{H}'_{\Sigma} = \Omega_{\Sigma} \mathbf{S}_{\Sigma z} - \omega_{0I} \mathbf{S}_{\Sigma} \mathbf{I}_z + \frac{D_d}{4} \mathbf{S}_{\Sigma} + \mathbf{S}_{\Sigma x} (A_{\Sigma x} \mathbf{I}_x + A_{\Sigma y} \mathbf{I}_y) + \mathbf{S}_{\Delta} \mathbf{I}_z + \frac{D_d}{4} \mathbf{S}_{\Delta} + D_0 \mathbf{S}_{\Delta x} + \mathbf{S}_{\Delta z} (A_{\Delta} \mathbf{I}_z + A_{\Delta x} \mathbf{I}_x + A_{\Delta y} \mathbf{I}_y). \quad (24)$$

Each of these can now be transformed into the eigenframe of the HFI acting in the respective subspace:

$$\hat{H}'_{\Sigma} = \Omega_{\Sigma} \mathbf{S}_{\Sigma z} - \omega_{0I} \mathbf{S}_{\Sigma} \mathbf{I}_z + \frac{D_d}{4} \mathbf{S}_{\Sigma} + A_{\Sigma} \mathbf{S}_{\Sigma z} \mathbf{I}_z + B_{\Sigma} \mathbf{S}_{\Sigma z} \mathbf{I}'_x + \omega_{\Delta} \mathbf{S}_{\Delta z} - \omega_{0I} \mathbf{S}_{\Delta} \mathbf{I}_z + \frac{D_d}{4} \mathbf{S}_{\Delta} + D_0 \mathbf{S}_{\Delta x} + A_{\Delta} \mathbf{S}_{\Delta z} \mathbf{I}_z + B_{\Delta} \mathbf{S}_{\Delta z} \mathbf{I}'_x, \quad (25)$$

with  $B_{\Sigma} = \sqrt{A_{\Sigma x}^2 + A_{\Sigma y}^2}$  and  $B_{\Delta} = \sqrt{A_{\Delta x}^2 + A_{\Delta y}^2}$ . The sole off-diagonal term which mixes the two electronic spin manifolds,  $D_0 \mathbf{S}_{\Delta x}$ , is located in the ZQ space. Thus, it can be eliminated by a transformation acting selectively on that space, using the unitary operator:

$$U_{\Delta} = \exp[i\mathbf{S}_{\Delta y} (\zeta_{\alpha} \mathbf{I}_x + \zeta_{\beta} \mathbf{I}_y)], \quad (26)$$

with  $\mathbf{S}_{\Delta y} = \frac{1}{2i}(\mathbf{S}'_{1+} \mathbf{S}'_{2-} - \mathbf{S}'_{1-} \mathbf{S}'_{2+})$ . The angles  $\zeta_i$  are derived from the e–e ZQ mixing coefficients as

$$\zeta_{\alpha, \beta} = \arctan\left(\frac{2D_0}{2\omega_{\Delta} \pm A_{\Delta}}\right). \quad (27)$$

The resulting Hamiltonian has the form:

$$\hat{H}''_{\Delta} = \tilde{\omega}_{\Delta} \mathbf{S}'_{\Delta z} - \omega_{0I} \mathbf{S}_{\Delta} \mathbf{I}_z + \frac{D_d}{4} \mathbf{S}_{\Delta} + \tilde{A}_{\Delta} \mathbf{S}'_{\Delta z} \mathbf{I}_z + (\tilde{B}_{\Delta} \mathbf{S}'_{\Delta z} + \tilde{K} \mathbf{S}'_{\Delta x}) \mathbf{I}'_x. \quad (28)$$

Alternatively, this can be expressed in terms of the raising and lowering operators as:

$$\hat{H}''_{\Delta} = \tilde{\omega}_{\Delta} \mathbf{S}'_{\Delta z} - \omega_{0I} \mathbf{S}_{\Delta} \mathbf{I}_z + \frac{D_d}{4} \mathbf{S}_{\Delta} + \tilde{A}_{\Delta} \mathbf{S}'_{\Delta z} \mathbf{I}_z + \left[ \frac{\tilde{B}_{\Delta}}{2} \mathbf{S}'_{\Delta y} + \frac{\tilde{K}}{4} (\mathbf{S}'_{1+} \mathbf{S}'_{2-} + \mathbf{S}'_{1-} \mathbf{S}'_{2+}) \right] (\mathbf{I}'_+ + \mathbf{I}'_-). \quad (29)$$

For simplicity, we assume that  $|\frac{A_{\Delta}}{2}| \ll |\omega_{\Delta}|$  at all times. This is a reasonable assumption except for the situation when  $\omega_{\Delta} \approx 0$ . Nevertheless, even in this case it is safe to assume that  $|\frac{A_{\Delta}}{2}| \ll |D_0|$ . Therefore, we can approximate that

$$\zeta_{\alpha} \approx \zeta_{\beta} \approx \zeta = \arctan\left(\frac{D_0}{\omega_{\Delta}}\right). \quad (30)$$

Under this assumption, we obtain the following simplified, effective frequencies:

$$\begin{aligned} \tilde{\omega}_{\Delta} &\approx \omega_{\Delta} \cos \zeta + D_0 \sin \zeta \\ \tilde{A}_{\Delta} &\approx A_{\Delta} \cos \zeta \\ \tilde{B}_{\Delta} &\approx B_{\Delta} \cos \zeta \\ \tilde{K} &\approx -B_{\Delta} \sin \zeta. \end{aligned} \quad (31)$$

We can interpret this situation as follows within a basis where the  $|\alpha\beta m_I\rangle$  and  $|\beta\alpha m_I\rangle$  Zeeman states in the ZQ subspace are mixed with the coefficients  $q_{\zeta} \approx \sin \frac{\zeta}{2}$  and  $p_{\zeta} \approx \cos \frac{\zeta}{2}$  due to e–e coupling:

$$\begin{aligned} |1\rangle &= |\alpha\alpha\alpha\rangle, & |2\rangle &= |\alpha\alpha\beta\rangle \\ |3\rangle &= p_{\zeta} |\alpha\beta\alpha\rangle - q_{\zeta} |\beta\alpha\alpha\rangle, & |4\rangle &= p_{\zeta} |\alpha\beta\beta\rangle - q_{\zeta} |\beta\alpha\beta\rangle \\ |5\rangle &= p_{\zeta} |\beta\alpha\alpha\rangle + q_{\zeta} |\alpha\beta\alpha\rangle, & |6\rangle &= p_{\zeta} |\beta\alpha\beta\rangle + q_{\zeta} |\alpha\beta\beta\rangle \\ |7\rangle &= |\beta\beta\alpha\rangle, & |8\rangle &= |\beta\beta\beta\rangle, \end{aligned} \quad (32)$$

Note that the states in the DQ subspace (i.e.,  $|1\rangle, |2\rangle, |7\rangle, |8\rangle$ ) remain unaffected.  $\tilde{\omega}_{\Delta}$ ,  $\omega_{0I}$ ,  $D_d$ , and  $\tilde{A}_{\Delta}$  determine the spin energies in the e–e ZQ subspace (i.e.,  $|3\rangle, |4\rangle, |5\rangle, |6\rangle$ ). Terms scaling with  $\tilde{B}_{\Delta}$  describe simultaneous e–n transitions connecting  $|3\rangle$  and  $|4\rangle$  as well as  $|5\rangle$  and  $|6\rangle$ , effectively representing the SE in this system. Finally, terms scaling with  $\tilde{K}$  describe e–e–n triple-spin transitions between  $|3\rangle$  and  $|6\rangle$  as well as  $|4\rangle$  and  $|5\rangle$ . Upon transformation of the off-diagonal terms into the interaction frame of the diagonal elements of the Hamiltonian in Eq. (29), we immediately find that all components that scale with  $\tilde{B}_{\Delta}$  (i.e., e–n transitions) oscillate with  $\omega_{0I}$ , but components proportional to  $\tilde{K}$  (i.e., e–e–n transitions) can become time independent when the CE matching condition is fulfilled:

$$\tilde{\omega}_{\Delta} = \pm \omega_{0I}. \quad (33)$$

For further simplification, in the typical case where  $|\tilde{\omega}_{\Delta}| = \omega_{0I} \gg |D_0|$ , we can conclude that  $\zeta_i$  is small:

$$\zeta = \arctan\left(\frac{D_0}{\omega_{\Delta}}\right) \approx \frac{D_0}{\omega_{\Delta}}. \quad (34)$$

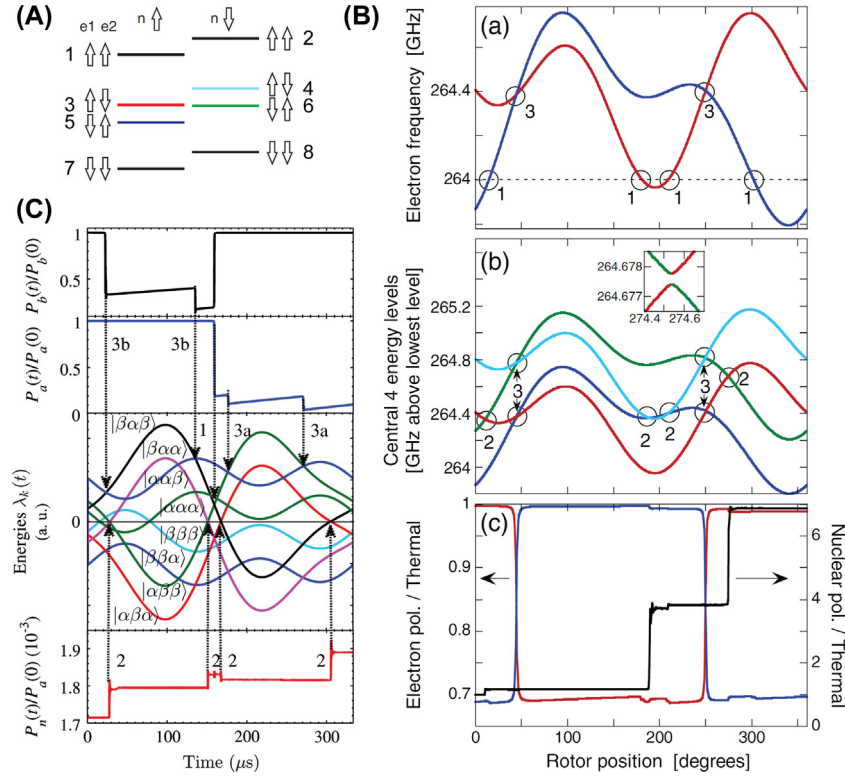


**Fig. 6.** Simulations of the evolution of spin eigenstates of an e–e–n system under MAS. (A) Definition of the spin states used by Thurber and Tycko [83]. Note, that numbers have been added in order to match the nomenclature in Eq. (32). (B) Evolution of SQ (EPR) excitation frequencies (a), eigenenergies of the four central (ZQ subspace) states (b), and spin polarizations (c) during one rotor period. Circles mark  $\mu\text{W}$  events (1), CE events (2), and e–e events (3) as described by Thurber and Tycko. (C) Similar depiction by Mentink-Vigier et al. [75] showing electron spin polarization, eigenenergies, and nuclear polarization (top to bottom). Further details are given in the original publications. (A) and (B) are reprinted with permission from [83], and (C) reprinted from [75].

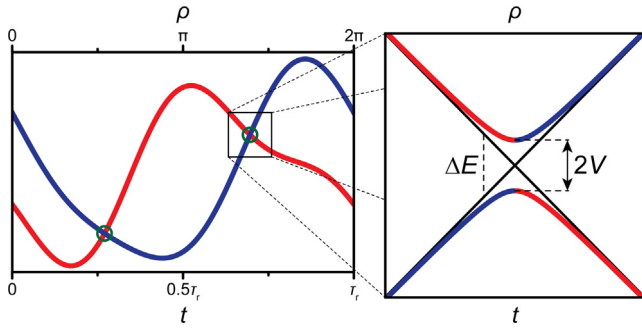


**Fig. 7.** Schematic representation of time and rotor-angle dependence of the eigenenergies of two arbitrary spin states (red and blue lines) over one rotor period. Green circles mark two occurring LACs. The black square delimits the area enlarged on the right. Close to the LAC, the rate of change in the energy difference  $\Delta E$  as well as in the mixing element  $V$  can often be neglected so that the Landau-Zener equation, Eq. (45), is applicable.

Therefore, we can approximate the effective frequencies by:

$$\begin{aligned} \tilde{\omega}_\Delta &\approx \omega_\Delta \left[ 1 + \left( \frac{D_0}{\omega_\Delta} \right)^2 \right] = \pm \omega_{0l} \approx \omega_\Delta \\ \tilde{A}_\Delta &\approx A_\Delta, \tilde{B}_\Delta \approx B_\Delta \\ \tilde{K} &\approx -\frac{B_\Delta D_0}{\omega_\Delta}, \end{aligned} \quad (35)$$

and we obtain the simplified Hamiltonian:

$$\begin{aligned} \hat{H}_\Delta^{\text{CE}} &\approx \omega_{0l} (\mathbf{S}_{\Delta z} - \mathbf{S}_\Delta \mathbf{I}_z) + \frac{D_d}{4} \mathbf{S}_\Delta + A_\Delta \mathbf{S}_{\Delta z} \mathbf{I}_z \\ &+ \frac{B_\Delta}{2} \left( \mathbf{S}_{\Delta z} \mp \frac{D_0}{2\omega_{0l}} (\mathbf{S}'_{1+} \mathbf{S}'_{2-} + \mathbf{S}'_{1-} \mathbf{S}'_{2+}) \right) (\mathbf{I}_+ + \mathbf{I}_-). \end{aligned} \quad (36)$$

In summary, the CE matching does not require any  $\mu\text{W}$  irradiation but is driven by a combination of the off-diagonal e–e coupling and pseudo-secular HFI. After a non-equilibrium polarization has been established on one electron spin during a  $\mu\text{W}$  event, the resulting polarization difference can now be transferred to the nucleus by a concerted e–e–n triple-spin flip. The transition moment of this event is approximately equal to  $D_0 B_\Delta / \omega_{0l}$ . By comparison of this CE transition moment with that of the SE,  $\omega_{15} B_\Delta / 2\omega_{0l}$ , we find that for CE the dipole coupling effectively takes the role of the  $\mu\text{W}$  field in SE. Therefore, considering typical dipole coupling constants and available  $\mu\text{W}$  field strengths, polarization transfer of the CE has a  $\sim 50\times$  larger transition moment and consequently a  $\sim 2500\times$  higher transition probability.

Due to the influence of the sign in the matching condition of Eq. (33)—which leads to opposite signs of the generated e–e–n coherences in Eq. (36)—it is important to distinguish which of the two electrons is saturated in the  $\mu\text{W}$  event. Finally, this results in the two lobes of opposite nuclear polarization enhancement in a field profile (see Section 3.2.2).

However, it is quite intuitive that the irradiated electron will at certain times switch places with the other electron in frequency space and that the second electron spin will at some time also undergo a  $\mu\text{W}$  event. Without adiabatic e–e events this would have two consequences: both electrons would become equally saturated and opposite CE transfers would occur with equal likelihood, effectively cancelling the net CE enhancement. Fortunately, e–e flip-flop events occur between these events, leading to polarization exchange of the two electron spins and ensuring that  $\mu\text{W}$  and CE events may result in the accumulation of a net nuclear polarization enhancement.



**2.1.2.4. Electron–electron (flip-flop) events.** An e–e flip-flop event occurs when the mixing between the connected states in the ZQ space is maximum so that e–e coherences can evolve. This is achieved when  $p_c = \sqrt{\frac{1}{2}}$  and occurs for

$$|D_0| \gg |\omega_\Delta|. \quad (37)$$

Therefore, we can intuitively expect that an e–e event occurs when two electron Zeeman states are nearly degenerate:

$$\omega_\Delta \approx 0 \quad (38)$$

In this strong coupling regime, the spin states are more appropriately expressed in their singlet/triplet eigenbasis:

$$\begin{aligned} |T_+\alpha\rangle &= |\alpha\alpha\alpha\rangle, & |T_+\beta\rangle &= |\alpha\alpha\beta\rangle \\ |S_0\alpha\rangle &= \frac{1}{\sqrt{2}}(|\alpha\beta\alpha\rangle - |\beta\alpha\alpha\rangle), & |T_0\beta\rangle &= \frac{1}{\sqrt{2}}(|\alpha\beta\beta\rangle - |\beta\alpha\beta\rangle) \\ |T_0\alpha\rangle &= \frac{1}{\sqrt{2}}(|\alpha\beta\alpha\rangle + |\beta\alpha\alpha\rangle), & |S_0\beta\rangle &= \frac{1}{\sqrt{2}}(|\alpha\beta\beta\rangle + |\beta\alpha\beta\rangle) \\ |T_-\alpha\rangle &= |\beta\beta\alpha\rangle, & |T_-\beta\rangle &= |\beta\beta\beta\rangle. \end{aligned} \quad (39)$$

In order to assess changes in Zeeman state populations, we have to consider the Hamiltonian in the Zeeman basis and treat the non-diagonal e–e coupling as a perturbation:

$$\hat{H}_\Delta^{e-e} = \omega_\Delta \mathbf{S}_{\Delta z} - \omega_{0l} \mathbf{S}_\Delta \mathbf{I}_z + \frac{D_d}{4} \mathbf{S}_\Delta + A_\Delta \mathbf{S}_{\Delta z} \mathbf{I}_z + \frac{D_0}{2} (\mathbf{S}'_{1+} \mathbf{S}'_{2-} + \mathbf{S}'_{1-} \mathbf{S}'_{2+}). \quad (40)$$

The e–e flip-flop terms become time-independent in the interaction frame when

$$\omega_\Delta = \pm \frac{A_\Delta}{2} \quad (41)$$

In practical terms, the HFI can be neglected and we arrive again at Eq. (38).

If this condition is fulfilled, polarization is exchanged efficiently between the two electron spins with a transition moment  $D_0$ . This exchange ensures that polarization is effectively swapped between all “opposing” CE events and between  $\mu w$  events that involve different electron spins. Therefore, given that e–e polarization exchange is quantitative, all opposing ( $\mu w$  or CE) events separated by e–e events act in a cumulative manner instead of mutually cancelling.

**2.1.2.5. Adiabaticity of events.** Up to now we have treated all events only in a static frame, where the state mixing is time independent and a certain equilibrium state would be reached after a sufficiently long time. Under MAS, however, eigenstates are evolving under the rotation of the interaction tensors (Zeeman, e–e, HFI) within the external magnetic field. This leads to periodic modulation of their energy separation and occurrence of typically several of the above-mentioned matching events during one rotor cycle, as shown in Fig. 6.

The transient crossing of these matching conditions constitutes a LAC event. If any state-mixing interaction would be absent during degeneracy of the states, then there were no possibility for the system to exchange populations between crossing states and an ideal level crossing event would be achieved. In contrast, if a sufficiently strong mixing interaction is present, populations can exchange adiabatically during the ideal LAC; the system remains in an eigenstate at all times.

For a quantitative description of the degree of adiabaticity of LACs, the rate with which the degeneracy is crossed as well as the mixing potential have to be considered. For a precise treatment, a quantum-mechanical propagation of the density operator yields the populations of all states during the rotor cycle. Typical DNP build-up time constants are more than four orders of magnitude longer than the MAS rotor period. Concurrently, the propaga-

tion under the Liouville-von Neumann equation has to be performed over very short time steps to account for the non-commuting properties of the Hamiltonian at different times. This leads to prohibitively time-consuming calculations. Certain scenarios can be investigated though, for example, a quasi-equilibrium where a periodic evolution is achieved by iterative propagation, or initial rates can be obtained based on given starting conditions.

For a semi-quantitative assessment, however, the Landau-Zener equation can be evoked:

$$P_{\text{LAC}} = 1 - \exp(-2\pi\Gamma), \quad (42)$$

with the adiabaticity parameter

$$\Gamma = \frac{V^2}{\partial\Delta E/\partial t}. \quad (43)$$

The Landau-Zener equation describes the adiabaticity of an LAC,  $P_{\text{LAC}}$ , under the condition that the crossing rate,  $\partial\Delta E/\partial t$ , as well as the mixing interaction,  $V$ , are time-independent during the crossing. The adiabaticity or probability to observe an ideal LAC reaches 1 for  $\Gamma \rightarrow \infty$  or  $|V| \gg |\partial\Delta E/\partial t|$ , or reaches 0 for  $\Gamma \rightarrow 0$  or  $|V| \ll |\partial\Delta E/\partial t|$ ; the latter case describes a level crossing.

For LACs that are relevant for CE, the crossing rate as well as the mixing interaction are time dependent. For typical modulation amplitudes during MAS (e.g., due to Zeeman anisotropy of >1 GHz in nitroxides) and relatively small dipole couplings (e.g., ~20 MHz), the above “Landau-Zener scenario” is sufficiently fulfilled in many cases (see Fig. 7); however, there are several situations where this approximation is clearly invalid. For example, for LACs that occur close to turning points of the eigenstate evolution or close to inversion points of the mixing interaction, this approximation is clearly violated. Nevertheless, we can gain insight and compare several situations with this analytical perturbation treatment.

The crossing rate can be expressed in terms of the rotor angle ( $\rho$ ) instead of time ( $t$ ):

$$\partial\rho = \omega_r \partial t, \quad (44)$$

which yields the MAS-dependent Landau-Zener equation

$$P_{\text{LAC}} = 1 - \exp\left(-\frac{2\pi V^2}{\omega_r \partial\Delta E/\partial\rho}\right). \quad (45)$$

The crossing rate for bis-nitroxides has been estimated to be in the range of  $\omega_r \partial(\Delta E/h)/\partial\rho \approx 20 \text{ THz s}^{-1}$  for typical  $\mu w$  events, and of  $\approx 30 \text{ THz s}^{-1}$  for CE and e–e events at an MAS frequency of 7 kHz [83]. In comparison, the mixing interaction is given for each case of CE-relevant LAC:

$$2V = \begin{cases} \omega_{15} & \text{for } \mu w \text{ event} \\ D_0 B/\omega_{0l} & \text{for CE event} \\ D_0 & \text{for e–e event} \end{cases} \quad (46)$$

Assuming typical values of  $\omega_{15}/2\pi \approx 1 \text{ MHz}$  [87],  $D_0/2\pi \approx 20 \text{ MHz}$ ,  $B_\Delta/2\pi \approx 1 \text{ MHz}$ , and  $\omega_{0l}/2\pi = 400 \text{ MHz}$ ,  $P_{\text{LAC}}$  of  $\mu w$  events is ~50%. This indicates significant saturation by  $\mu w$  irradiation over a few rotor cycles, considering typical electron spin–lattice relaxation time constants of  $T_{15} \approx 100\text{--}1000 \mu\text{s}$ . At the same time, e–e flip-flops are highly efficient, resulting in  $P_{\text{LAC}} \approx 1$ , ensuring that a net polarization difference is maintained between the two electrons. Nevertheless, a non-vanishing probability ( $\sim 10^{-6}$ ) for level crossings remains, so that over a few rotor periods a partial equilibration of polarization can accumulate. This results in a reduction of DNP efficiency, and also in dynamic nuclear depolarization in the absence of  $\mu w$  irradiation. The impact on practical aspects of this situation will be discussed in Section 6.1.2.

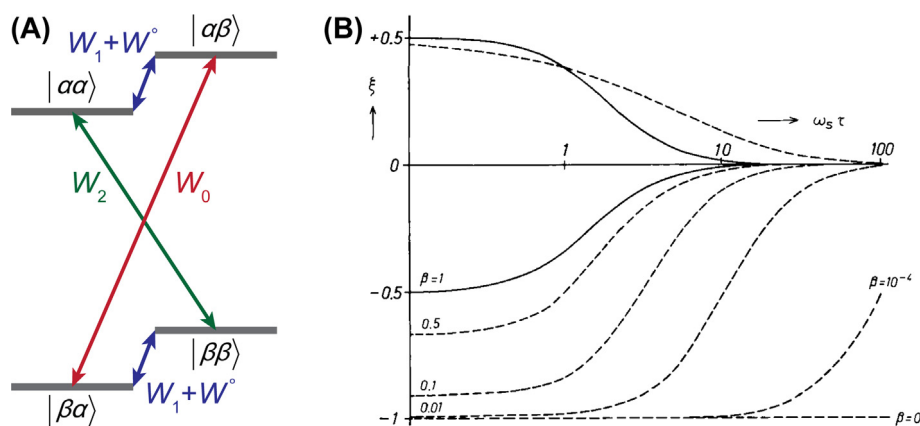


**Fig. 8.** (A) Definition of auto- and cross-relaxation rate constants responsible for OE in an e–n system with  $S = 1/2$ ,  $I = 1/2$ . (B) Coupling factor  $\xi$  for dipolar interactions (positive ordinate area) based on Solomon's equations for rotational (solid lines) and translational (dashed lines) diffusion [93]. The negative ordinate area contains coupling factors due to scalar interactions for different values of the parameters  $\beta$  which depends on the ratio of Heisenberg exchange and electronic relaxation rates. Reproduced with permission from [94].

CE events, on the other hand, show only a rather small adiabaticity factor on the order of 0.1%. This seems almost vanishingly small. However, nuclear spin–lattice relaxation occurs only on the order of  $\sim 10^3$ – $10^4$  rotor cycles, so that even small transfer steps (smaller than the thermal nuclear polarization) can accumulate in order to build up the large observed enhancement factors of  $\varepsilon > 10^2$ .

**2.1.2.6. Cross effect in static samples.** Under static conditions, CE matching [Eq. (33)] can only result in DNP when the  $\mu\omega$  resonance condition is fulfilled at the same time. In this case, the same diagonalization of the e–e interaction as after Eq. (26) can be performed so that the effective Hamiltonian, Eq. (29), is obtained. By subsequent transformation of the  $\mu\omega$  Hamiltonian into the frame of the diagonal part of Eq. (29), several cases of frequency matching can be deduced and effective transition moments can be obtained.

Of course, the requirement for simultaneous matching of CE and  $\mu\omega$  conditions reduces the number of actively contributing PA molecules randomly distributed within an amorphous frozen solution. However, DNP by CE can not only be driven “actively” by generation of  $\mu\omega$ -driven coherences, but can also “spontaneously” occur due to imbalances in spin polarization with respect to thermal equilibrium. This situation is similar to the individual CE events under MAS which are temporally decoupled from  $\mu\omega$  events. Such imbalances can be effectively caused by spectral diffusion of electron polarization upon  $\mu\omega$  irradiation, causing electron spin saturation to spread to spin packets that are off-resonance with respect to the  $\mu\omega$  frequency. These effects have been studied in detail and dubbed “indirect CE” by Vega and co-workers (see Section 2.2.2.3) [88].

### 2.1.3. Overhauser effect in insulating solids

The OE has been neglected in solid-state DNP (be it with or without MAS) until recently, because of its reliance on internal dynamics causing fluctuations of the HFI which in turn result in e–n cross-relaxation (see Fig. 8A). In conducting solids or liquid solutions, these dynamics can be provided by itinerant conduction electrons or molecular diffusion, respectively. In dielectrics, where mobile charge or spin carriers are absent, it was thought that no mechanism exists which can provide the required amplitude of the spectral density function at the relevant Larmor frequency combinations of e–n ZQ and DQ transitions. Nevertheless, the OE has been unquestionably identified in MAS DNP experiments. While the first report was an accidental observation in a  $^1\text{H}$  SE study of (water-soluble) sulfonated-BDPA (SA-BDPA) [89], the OE

was unambiguously proven shortly afterwards in a dedicated study of similar types of PAs [90]. Retroactively, hints of OE can be found in earlier published studies on BDPA [91], as well as in an investigation of the flavin mononucleotide (FMN) semiquinone radical that occurs as endogenous PA in flavodoxin [92].

OE DNP can simply be described by considering one electron spin and one nuclear spin. However, in contrast to the previously described SE, the nuclear spin has to experience a fluctuating scalar or dipolar HFI. Such fluctuations due to the presence of dynamics with characteristic correlation times on the order of  $\omega_{0S} \pm \omega_{0I}$  can bring about several (incoherent) transitions, namely electron and nuclear SQ as well as e–n DQ and ZQ transitions. These latter DQ and ZQ transitions result in additional electron relaxation pathways (i.e., e–n cross-relaxation) upon saturation of the EPR transition by  $\mu\omega$  irradiation, besides the most probable SQ relaxation. If there exists an imbalance between DQ and ZQ relaxation rates (described by rate constants  $W_0$  and  $W_2$ , respectively), nuclear hyperpolarization can be accumulated. In the case of  $^1\text{H}$  (or any nucleus with positive  $\gamma_I$ ), dominant ZQ relaxation leads to positive OE DNP enhancement; accordingly, larger rates of DQ relaxation to negative enhancement factors. Nuclear SQ relaxation, either being induced by the fluctuating HFI (rate constant  $W_1$ ) or caused by dynamics not related to the presence of the electron spin ( $W^\circ$ ) causes a reduction of the magnitude of enhancement. This situation is depicted in Fig. 8A.

For a quantitative description the simple Solomon equations [93],

$$\frac{\partial}{\partial t} \begin{pmatrix} P_S(t) \\ P_I(t) \end{pmatrix} = - \begin{pmatrix} \rho_S & \sigma_{SI} \\ \sigma_{SI} & \rho_I \end{pmatrix} \begin{pmatrix} P_S(t) - P_S^0 \\ P_I(t) - P_I^0 \end{pmatrix}, \quad (47)$$

can be solved for a steady-state solution of the nuclear spin polarization [94]:

$$\varepsilon_{\text{OE}} = 1 - \frac{\gamma_S}{\gamma_I} s \xi f. \quad (48)$$

Here,  $\varepsilon_{\text{OE}} = \frac{P_I^\infty}{P_I^0}$  and  $s = 1 - \frac{P_S^\infty}{P_S^0}$  are the OE enhancement and saturation factor, respectively. Superscript indices ‘ $\infty$ ’ mark parameters in the steady-state, while ‘0’ denotes parameters in thermal equilibrium.  $\rho_S$  and  $\rho_I$  are the electron and nuclear auto-relaxation rate constants, while  $\sigma_{SI}$  is the e–n cross-relaxation rate constant.  $\xi = \frac{\sigma_{SI}}{\rho_I} = \frac{W_2 - W_0}{W_0 + 2W_1 + W_2}$  and  $f = \frac{\rho_I}{\rho_I + W^\circ} = \frac{W_0 + 2W_1 + W_2}{W_0 + 2W_1 + W_2 + W^\circ}$  are the coupling and the leakage factors, respectively.

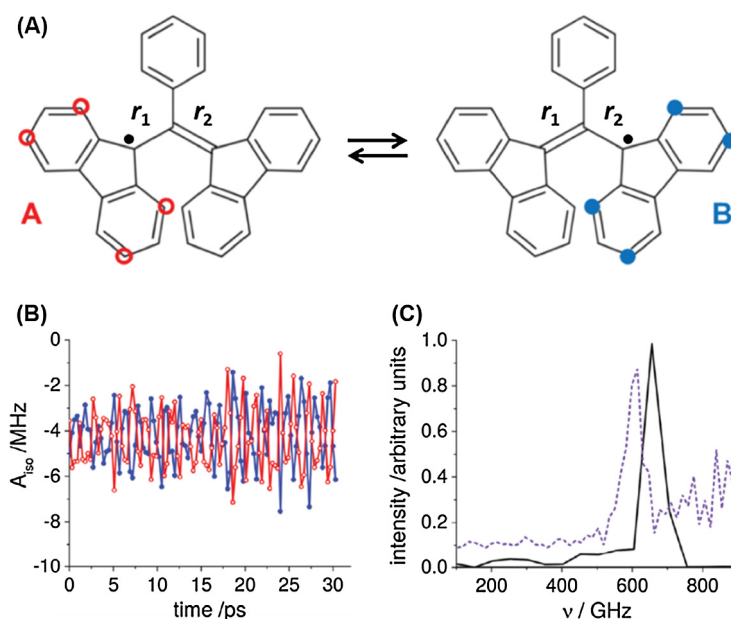


**Fig. 9.** (A) Two structures of BDPA showing two distinct sets of hydrogens (red and blue). Due to asymmetry in the distances between the fluorene groups and the central carbon ( $r_1 \neq r_2$ ), these structures are inequivalent and the two sets of  $^1\text{H}$  show different scalar HFI. (B) MD time trace of scalar HFI of the two sets of  $^1\text{H}$  (red and blue) in BDPA in vacuum, showing large amplitude of correlated fluctuations which occur out-of-phase with each other. (C) Fourier-transform of the time trace shown in (B), revealing a distinct frequency component near 650 GHz (black line); when embedded in amorphous OTP, this peak shifts slightly to lower frequency and broadens, leading to a wide background distribution. Figure reproduced with permission from [99].

$W_0$ ,  $W_2$ , as well as  $W_1$ , have to be derived from relaxation models based on dipolar or scalar HFI. In the seminal review of Hausser and Stehlik, several models have been described in detail, including intra- as well as intermolecular dynamics. For example, purely translational or rotational diffusion models lead to a dependence of the coupling factor on the electron Larmor frequency and the molecular correlations times as shown in Fig. 8B [94].

The saturation factor can be deduced in the simplest description from a steady-state solution of the Bloch equations under continuous wave (cw) irradiation [95]:

$$s = 1 - \frac{1 + \Omega_{0S}^2 T_{2S}^2}{1 + \Omega_{0S}^2 T_{2S}^2 + \omega_{1S}^2 T_{1S} T_{2S}}, \quad (49)$$

Here, it should be noted that, given sufficient  $\mu\text{W}$  power for significant saturation (i.e.,  $\omega_{1S}^2 T_{1S} T_{2S} > 1$ ), off-resonance excitation of the PA can also cause OE. This results in an expected broadening of the OE field profile with respect to the EPR line (see Section 3.2.3). Similar observations have been made in solution OE DNP given sufficient homogeneous broadening of the EPR line by Heisenberg exchange for off-resonance excitation [96].

Of course, rotational and translational diffusion models are generally not applicable in the solid-state. Nevertheless, by OE DNP using BDPA as PA, significant  $^1\text{H}$  signal enhancement factors on the order of 80 have been observed in an amorphous matrix of ortho-terphenyl (OTP) at a high field of 18.8 T [97]. Similarly, surprising experimental observations were made by Prisner and co-workers with high-field (9.2 T) OE DNP in solution. Here—even for small molecules such as water—rotational and translational correlation times are typically long compared to the inverse electron Larmor frequency ( $\omega_{0S}/2\pi = 259$  GHz). Therefore, based on the detailed description by Hausser and Stehlik, vanishing OE enhancement would be predicted at this high field as is seen in Fig. 8B [94]. However, a rather large  $\epsilon_{\text{OE}} \approx 100$  has been observed on  $^1\text{H}$  in water. As an explanation, the model by Hausser and Stehlik has been extended to include transient contacts between

the solvent and the PA with short correlation times which can be described by molecular dynamics (MD) simulations [72]. Very recently, similar findings have also been reported by Bennati and co-workers [98].

In the solid-state, the reason for OE-supporting fluctuations in the systems investigated so far is still vividly debated. A direct comparison between protonated and deuterated BDPA has identified the scalar-coupled protons on the BDPA molecule as responsible for the large, positive OE DNP enhancement. Furthermore, the unique field dependence—with increasing enhancement at higher external magnetic field (see Section 6.2.1)—might not only prove extremely valuable for DNP applications at fields of 18.8 T and above, but it was also expected to play an important role in solving this puzzle [90]. Very recently, Pylaeva et al. have presented a study of OE DNP based on classical and *ab initio* molecular dynamics (MD) simulations combined with spin dynamics simulations. According to their findings, two sets of protons (A and B, marked red and blue in Fig. 9A) show not only the largest scalar HFI, but also a very strong sensitivity of the scalar HFI to internal dynamics. Note that such fluctuations of the scalar HFI can contribute to the ZQ but not to the DQ and SQ rates mentioned above. The unique situation proposed is caused by the delocalization of the electron spin over the two fluorene rings *via* the bridging allyl. Asymmetry of the distance between the fluorene moieties and the central carbon atom then leads to an inequivalence of spin density on the two fluorenes and thus of the scalar HFI of the two sets of  $^1\text{H}$ . MD simulations have furthermore revealed that internal vibrational (ground state) dynamics cause a time-dependence of the distances  $r_1$  and  $r_2$ , which in turn leads to correlated fluctuations of the scalar HFI (Fig. 9B). Fourier-transformation of this time-dependence revealed a clear peak near 650 GHz for BDPA (Fig. 9C). While this study may explain the observed DNP enhancement from BDPA by OE in an intuitively comprehensible manner, no experimental evidence for such a vibrational mode has been provided thus far. Therefore it remains to be seen whether this hypothesis will be accepted as the valid theory for OE in dielectric solids.

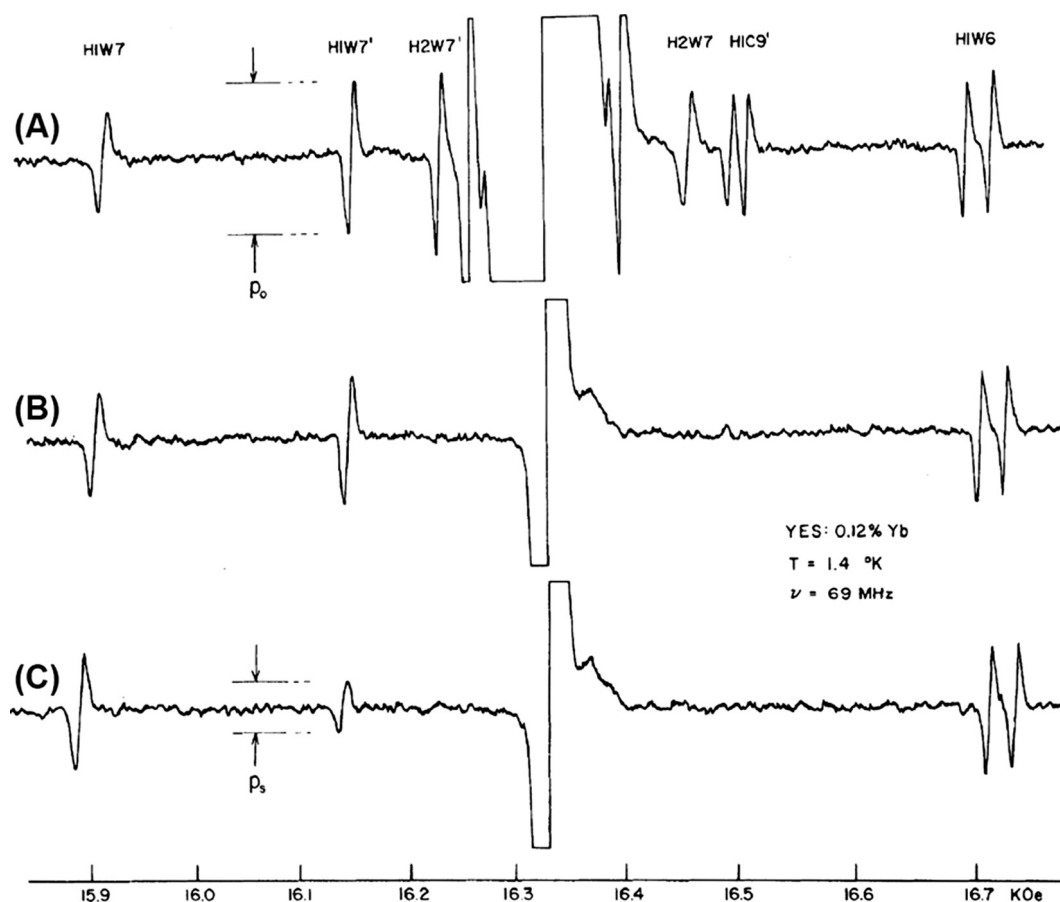


**Fig. 10.** Direct experimental observation of the spin-diffusion barrier in YES:Yb at 69 MHz  $^1\text{H}$  frequency and 1.4 K. Labeled signals correspond to protons within 6.2 Å of  $\text{Yb}^{3+}$  impurity; the bulk NMR signal at 16.33 kOe is  $1000 \times$  off-scale. (A)  $^1\text{H}$  spectrum in thermal equilibrium. (B) After irradiation of the bulk for 2–6 min, many  $^1\text{H}$  signals from outside the diffusion barrier are saturated by strong homonuclear coupling. (C) Only very few  $^1\text{H}$  signals inside the diffusion barrier remain at lattice temperature even after 100 min of bulk saturation. Figure reprinted with permission from [115].

## 2.2. Integral DNP process: from electron spin to nuclear bulk

### 2.2.1. General concepts and early descriptions

**2.2.1.1. Generation, accumulation and loss of enhanced nuclear polarization.** In the above sections we have reviewed several quantum-mechanical DNP transfer mechanisms. In all discussed cases of cw DNP, the effective rate of transfer (or the net polarization transferred per LAC event) is small [75,83,100]. For simple considerations, we are reminded that the magnitude of steady-state DQ or ZQ coherence would be small due to the almost vanishing transition moments of the SE. In this case—without any longitudinal relaxation—continuous excitation and concurrent decay of the built-up ZQ or DQ coherence would lead to slow but steady saturation of the connected polarization states. Within the isolated e–n spin pair, a maximum DNP enhancement factor of only  $0.5 \times \gamma_s/\gamma_1$  ( $\sim 330$  for  $^1\text{H}$ ) would be achieved even for complete saturation, contradicting Eq. (2). This is even exacerbated as one electron typically serves  $\sim 100$ – $10,000$  nuclear spins; the maximum enhancement factor would then scale with the e–n number ratio,  $N_s/N_1$ , resulting in negligible enhancement. The situation would be similar for CE due to the equilibration of the electron spin polarization difference by CE events [75,83,100].

However, large net enhancements can be achieved on all nuclei as electron spin polarization recovers by spin-lattice relaxation during or between the coherent transfer steps [101,102]. At the same time, nuclear polarization is also undergoing much slower spin-lattice relaxation leading to a reduction in steady-state polarization. The magnitude of the observed steady-state enhancement

depends on a rather complicated interplay between DNP transfer mechanism, homonuclear spin diffusion and effective electron and nuclear spin-lattice relaxation which in turn strongly depend on sample constitution and experimental conditions (see Section 6). Thus, only a semi-quantitative description for net observables has been derived for the SE which strongly relies on homonuclear spin diffusion (see below). A microscopic (quantum-mechanical) treatment is rather tedious and in most cases analytical derivations are impeded by the large number of spins to be taken into account. In Section 2.2.2.2, we review the general description of the problem, as well as several approaches including stark simplifications of the underlying problem and numerical simulations. However, we will first describe extensive studies from the early days of DNP, where attempts to understand the general processes involved in spreading of enhanced nuclear polarizations were made.

**2.2.1.2. The coupling between electron spins and the nuclear spin bath.** In simple and intuitive models, enhanced polarization is transferred only to nuclei in the direct vicinity of the electron spin(s), a model described early as the strict shell-of-influence or influence-sphere model [103,104]. Once directly transferred to a hyperfine-coupled nucleus, nuclear polarization is then expected to spread spatially by homonuclear spin diffusion [101,105,106]. This situation is in principle very similar to the relaxation of nuclear spins by paramagnetic dopants or impurities which has been exhaustively studied in the early days of magnetic resonance [101,107–111]. In fact, a paramagnetic species can act both as

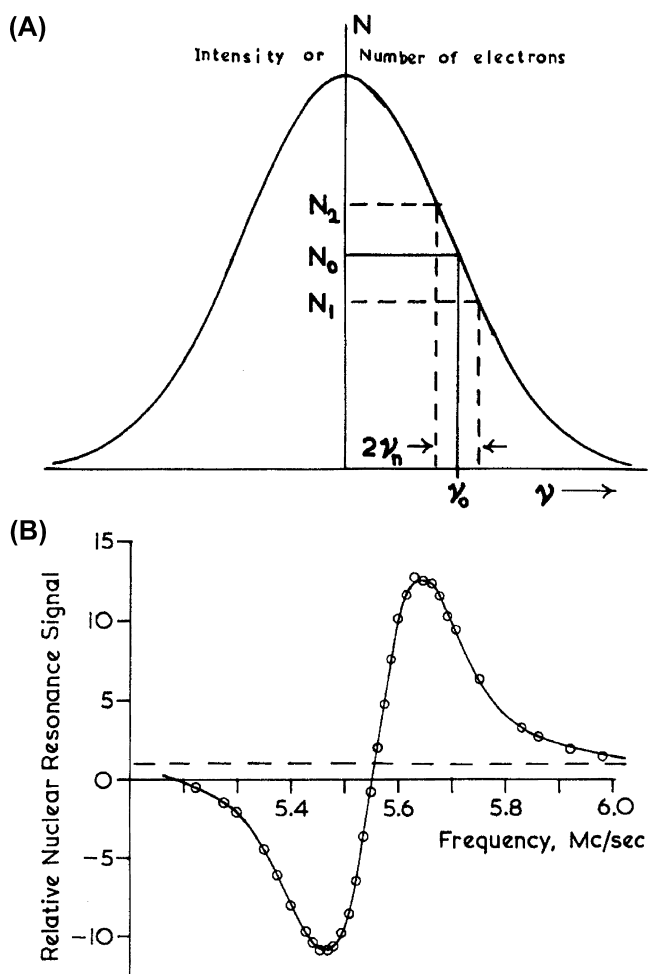


Fig. 11. Differential solid effect with an inhomogeneously broadened EPR line. Net signal enhancement results from imbalances in effective e–n ZQ and DQ transition intensity (A) and resembles the derivative of the EPR (SQ) absorption line (B). Figure reproduced from [76] with permission.

polarization source or as relaxation sink in DNP-active or DNP-inactive centers, respectively. This has been described previously in order to quantitatively predict steady-state nuclear enhancements [112,113].

2.2.1.3. Nuclear spin relaxation by paramagnetic sites and the diffusion barrier. In the above-mentioned models [101,107–111], paramagnetic centers are directly hyperfine-coupled to nuclear spins in close proximity. These core nuclei are subsequently communicating with the bulk lattice by homonuclear spin diffusion. Upon rf saturation of the bulk spins, their longitudinal magnetization is

mainly repleted by fast spin-lattice relaxation of the core nuclei. Therefore, two bottlenecks can be identified: (i) core nuclear spin relaxation is fast and bulk relaxation is limited by spin diffusion or (ii) spin diffusion is fast but core spin relaxation is the limiting factor [104]. Since spin diffusion relies on net energy conserving nuclear flip-flop transitions, large hyperfine couplings will offset the Larmor frequency of the core nuclei and quench diffusion to less hyperfine-shifted nuclear spins. The cut-off distance below which the effective communication between nuclei in dipolar contact to the electron spin (core nuclei) and nuclei that are virtually unaffected by the electron (bulk nuclei) ceases, is known as spin-diffusion barrier [114], and has been demonstrated (Fig. 10) by Wolfe on a sample of yttrium-ethyl-sulfate doped with ytterbium (YES:Yb) [115]. The very definition of the barrier can be based on the above-mentioned bottlenecks: nuclear spins that have a stronger coupling to the lattice phonons than to the bulk spins are within the spin-diffusion barrier, while spins that are strongly dipolar-coupled with the bulk homonuclear bath are outside of that barrier.

2.2.1.4. Spreading of enhanced nuclear polarization by spin diffusion. As already mentioned, the situation in DNP is rather similar to nuclear relaxation induced by paramagnetic centers where a repletion of bulk magnetization by core spins is following the rf saturation of the bulk; in DNP, core spins are hyperpolarized and the enhanced polarization is spread to the bulk by spin diffusion [101,106]. Therefore, all considerations derived for paramagnetic relaxation in the solid state should also be applicable to DNP. However, nuclear spins undergo spin-lattice relaxation at the same time as being hyperpolarized, either due to long-wavelength phonons, (local) temperature-activated dynamics in the bulk, or paramagnetic relaxation towards inactive PAs (e.g., those not fulfilling the DNP matching condition) acting as drain for hyperpolarization [108,116]. Consequently, a significant—and in many cases largest—amount of enhanced nuclear polarization is lost to the lattice [101].

2.2.1.5. Role of electron–electron interactions and spectral diffusion. Very early after the discovery of the SE [117–120] the effects of inhomogeneously broadened EPR lines, where the overall line width exceeds  $2\omega_{0f}$ , were studied by several groups [76,121,122]. In this general case, the differential solid effect (DSE) was formulated. It was theoretically predicted and experimentally confirmed that the DNP field profile is proportional to the first derivative of the EPR absorption line (see Fig. 11) [76]. Due to the cancellation of positive, (+), and negative, (–), enhancements simultaneously caused by ZQ and DQ transitions from different spin packets, the overall net enhancement can be reduced by one or more orders of magnitude with respect to the maximum enhancement that could be reached by selective saturation of the ZQ or DQ transition.

Given sufficient  $\mu\text{w}$  power to achieve a strong induction of the “forbidden” SE (DQ/ZQ) transitions, it has been shown that a significantly larger enhancement can be obtained than what would be

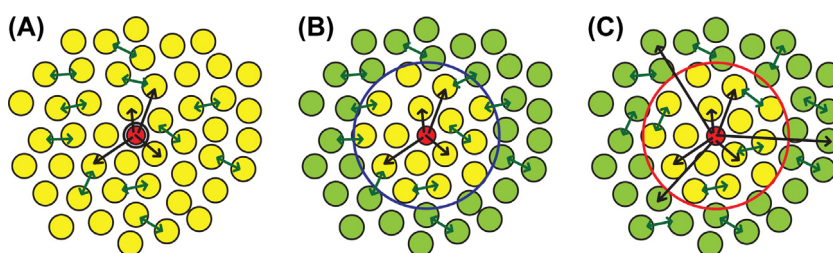
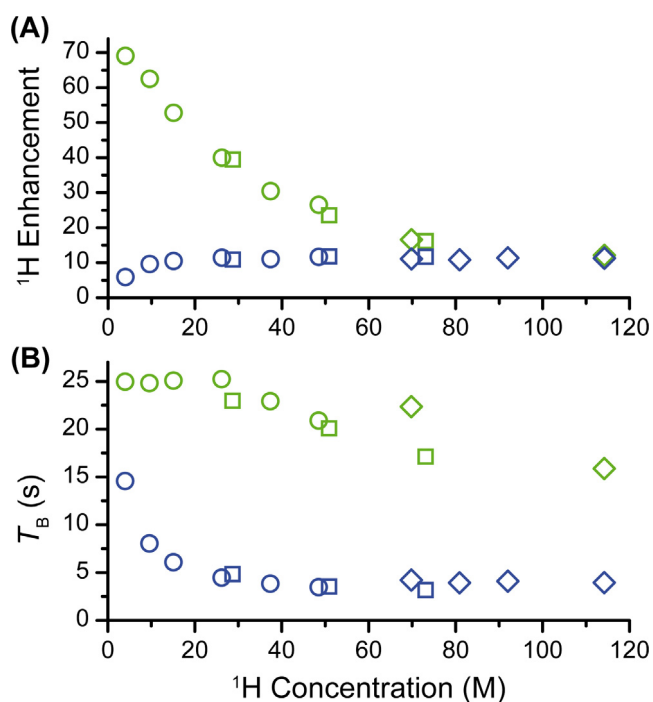


Fig. 12. Models utilized by Smith et al. for the description of transfer pathways between an electrons spin (red) and core nuclei (yellow) as well as bulk nuclei (green) as described in the text. A “soft” spin-diffusion barrier (slowly penetrable) is marked by a blue circle, a “hard” spin-diffusion barrier (impenetrable) by a red circle. The size of the spin-diffusion barrier and number of nuclei within it do not represent actual values. Reprinted from [77] with permission.



**Fig. 13.** Comparison of DNP enhancement factor (A) and build-up time constant (B) between 40 mM trityl OX063 (green) and 10 mM Gd-DOTA (blue) for various  $^1\text{H}$  concentrations in the matrix. Open circles represent samples prepared with  $d_8$ -glycerol, whereas open squares and diamonds correspond to samples prepared with  $d_5$ - and  $h_8$ -glycerol, respectively. The glycerol/water ratio was 60/40 (v/v) in all cases. All data points were recorded under 8 W microwave power at a temperature of  $\sim 86$  K. Reprinted from [74] with permission.

predicted from the slope of the inhomogeneously broadened EPR line [112]. This was explained by the expectation that electron spins switch their “state” between DNP-active (*i.e.*, irradiated by a  $\mu\text{W}$  field matching the SE frequency) and inactive (*i.e.*, irradiated with a  $\mu\text{W}$  field off-resonance with respect to the SE matching condition). This switch is induced by changes in the local field due to interactions with close-by nuclei or other electrons (*i.e.*, spectral diffusion). Thus, a larger fraction of electron spin packets can act as active PAs and contribute to an increase of net enhancement.

## 2.2.2. Recent theoretical and experimental advances

### 2.2.2.1. The role of spin diffusion in SE DNP.

The above-mentioned descriptions and problems have also been addressed in several modern approaches. Due to the large size of the spin system under consideration, a phenomenological treatment *via* effective rate equations provides a computationally less expensive way of describing the polarization transfer. As has been already elaborated in several works mentioned above [61,77,101,106], this situation can be classically described by a system of coupled differential equations as long as the magnitude of the coherences that may build up at any point in time is negligible:

$$\begin{aligned} \frac{dP_i^j}{dt} &= k_{\text{DNP}}^j (P_S - P_i^j) + \sum_{n=1}^{N_i} k_{\text{SD}}^{nj} (P_i^n - P_i^j) + \frac{1}{T_{1i}^j} (P_i^{\text{eq}} - P_i^j) \\ \frac{dP_S}{dt} &= -k_0 P_S + \sum_{n=1}^{N_i} k_{\text{DNP}}^n (P_i^n - P_S) + \frac{1}{T_{1S}} (P_S^{\text{eq}} - P_S). \end{aligned} \quad (50)$$

Here,  $P_S$  and  $P_i^j$  are the spin polarizations of the electron and the  $j^{\text{th}}$  nucleus;  $T_{1S}$  and  $T_{1i}^j$  are the electron and nuclear longitudinal relaxation time constants, respectively,  $k_{\text{DNP}}^j$  is the effective rate constant of DNP transfer to the  $j^{\text{th}}$  nucleus, and  $k_{\text{SD}}^{nj}$  describes the spin-

diffusion rate constant between the  $n^{\text{th}}$  and  $j^{\text{th}}$  nuclei. Finally,  $k_0$  is the rate constant of electron spin saturation due to off-resonance excitation of the SQ transition by the  $\mu\text{W}$  field.

Using this rather simple model, Smith et al. have compared three different scenarios (Fig. 12) [77]: (A) the polarization is transferred from the electron to the bulk and spin-diffusion rates between all nuclei are equal; in other words no spin-diffusion barrier exists; (B) the polarization can only be directly transferred to core nuclei and then has to cross a “soft” diffusion barrier before it can spread uniformly through the bulk; (C) the polarization is directly transferred in parallel to nuclei within and to those outside a “hard” spin-diffusion barrier with respective rate constants while no polarization is exchanged between the two baths. By experimental determination of three observables—the nuclear relaxation time constant without DNP, the buildup time constant under microwave irradiation and the net nuclear enhancement factor at infinite polarization time (for further details how these parameters are influenced by DNP see Section 6.1.1)—it was concluded that only model C is in qualitative agreement with experiment. However, a quantitative assessment of the size of the spin-diffusion barrier was not possible due to an insufficient set of experimental observables.

A semi-analytical definition of the barrier has been described by Hovav et al. based on the effective truncation of dipolar flip-flop terms by HFI: the transition between core and bulk nuclei can be found where the magnitude of the homonuclear flip-flop terms  $d_{ij}$  with all other nuclei become larger than the respective difference in hyperfine coupling to the electron  $\Delta A_{ij} = A_i - A_j$  [123]:

$$\zeta \left| \frac{d_{ij}}{2} \right| > |\Delta A_{ij}|. \quad (51)$$

The parameter  $\zeta$  describes paramagnetic quenching and results in the broadening of the nuclear flip-flop degeneracy condition due to faster nuclear decoherence. The vague character of this parameter also prohibited reliable analysis of the barrier’s dimensions in this case.

Further experimental indication of different bottlenecks governing the net transfer of polarization from the PA to the bulk has been provided by comparing  $^1\text{H}$  SE caused by trityl (OX063) and Gd-DOTA within otherwise identical samples (Fig. 13). By adjusting the protonation level of the solvent matrix a starkly different behavior has been observed: for trityl, enhancement factors are largest for maximum deuteration and decrease nearly hyperbolically with increasing  $^1\text{H}$  concentration while build-up rates show little variation; for Gd-DOTA the enhancement factor and build-up rates increase and level off at a protonation level of  $\sim 40\%$ . This difference is explained by rate-limiting DNP transfer but (relatively) fast spin diffusion through the bulk in the case of trityl, whereas for Gd-DOTA initial DNP is fast with subsequent rate-limiting spin diffusion.

The purely classical, diffusive treatment neglects any coherent interactions which might play a role in the spreading of polarization. This has been investigated by Brüscheweiler and Ernst, where a linear chain of spins was simulated quantum numerically and deviations from uniform spreading of polarization (which would be expected under steady-state diffusion without relaxation) were identified [124]. Nevertheless, such a quantum-mechanical treatment is extremely difficult to extend to a general network of  $N$  nuclear or electron spins. This stems from the fact, that—in order to include relaxation which is necessary for DNP—a transformation from Hilbert space (with a dimensionality scaling with  $2N$ ) to Liouville space is required. The resulting space with  $4N \times 4N$  elements makes solution of the Liouville-von Neumann equation very demanding.

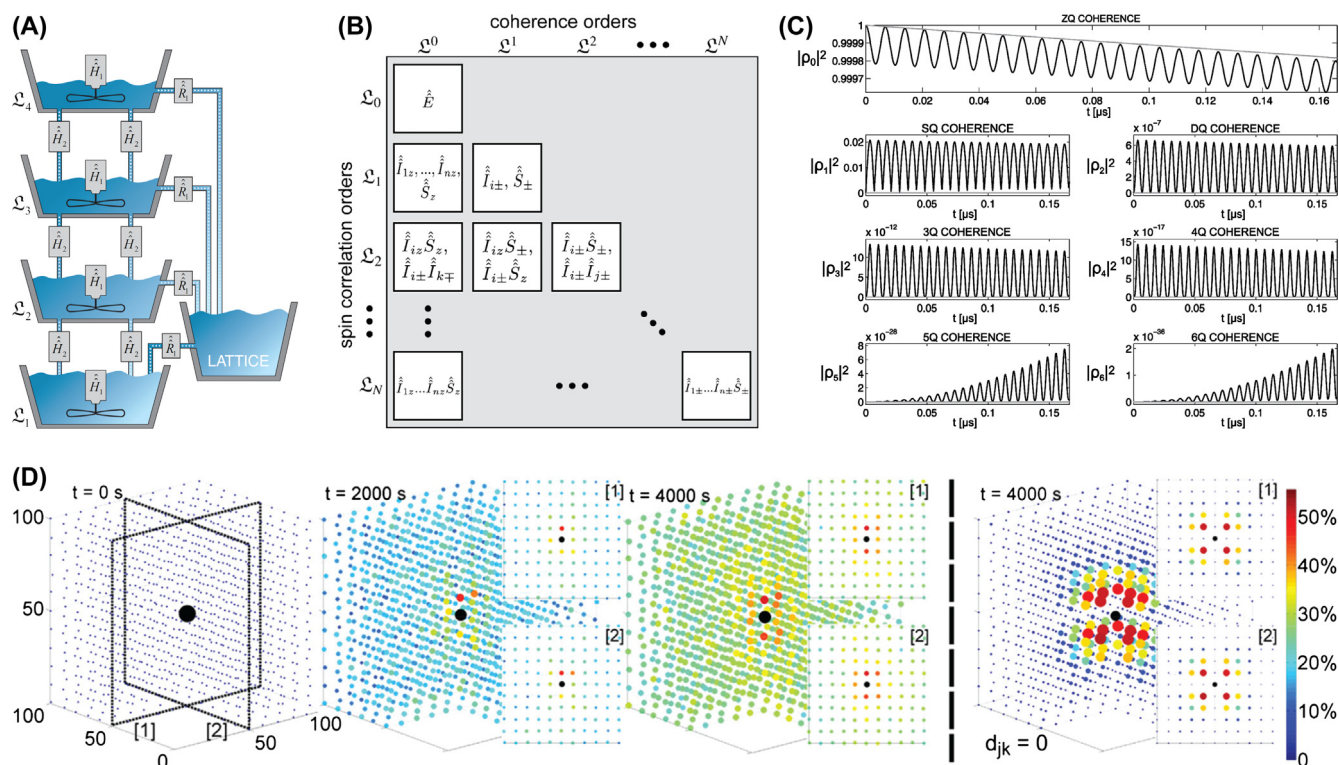


**Fig. 14.** Simulation of DNP on large spin systems. (A) Schematic illustration of the flow of the density matrix norm in the spin correlation order subspaces. Fast relaxation leaves high product order subspaces unpopulated. (B) Separation of the Liouville state space into subspaces of operators of equal spin correlation order (vertical axis) or coherence order (horizontal axis). (C) Time dependence of the norm of the ZQ coherence subspace and higher coherence subspaces. Only the norm for the ZQ coherence subspace is non-vanishing if the Krylov-Bogolyubov averaged Hamiltonian is used (gray line) while oscillations occur for all subspaces with the non-averaged Hamiltonian (black lines). (D) Simulation of the polarization dynamics of 1330 nuclear spins ( $^{13}\text{C}$ ) arranged on a regular grid in a cube around one central electron (black). The diameter and the color of the spheres indicate the nuclear spin polarization expectation value. The rightmost simulation shows the result with inhibited spin diffusion. Subfigure (A) reprinted from [128], (B) and (C) from [129], (D) from [130], with permission.

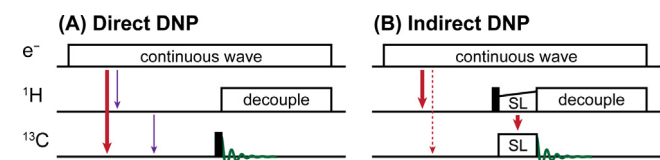


**Fig. 15.** (A) Polarization generated by direct DNP (thick red arrow) can be directly read out on the desired nuclei (e.g.,  $^{13}\text{C}$ ). Recently, it has been shown that incoherent polarization transfer pathways (cross relaxation from hyperpolarized proton spins; thin purple arrows) may contribute to the obtained spectra. (B) Pathway of polarization transfer for indirect DNP.  $^1\text{H}$  hyperpolarization generated by DNP is transferred to  $^{13}\text{C}$  by CP (thick red arrows). Depending on the width of the DNP resonance condition, a simultaneous direct polarization of the low- $\gamma$  nuclei can occur (dashed thin red arrow), which is filtered out by appropriate phase cycling.

Therefore, a hybrid treatment has been adapted towards DNP by Hovav et al. where they describe a linear chain of one electron spin and a few nuclear spins, while accounting for relaxation as well [123]. In this hybrid treatment, changes in spin population (not polarization) are modeled with effective rate equations which are based on a complete diagonalization of the spin Hamiltonian. By defining a direct hyperfine coupling only between the electron spin and the closest nuclear spin but allowing for dipolar evolution between all nuclei within the chain, it was found that direct transfer pathways exist between the electron spin and nuclei further removed along the chain. This result shows—from a theoretical viewpoint—that a classical treatment is insufficient for a complete description of the spreading of hyperpolarization. From a more practical viewpoint, it becomes clear that by a combination of

HFI and a strong dipolar-coupled network of core and bulk nuclear spins, additional transfer pathways exist which could alleviate the problem imposed by the spin-diffusion barrier. A more realistic description of a three-dimensional system, with much larger ratio of nuclei to electron spins would be highly desirable because this could allow for a quantitative comparison between theoretical prediction and experimental observation.

**2.2.2.2. Simulations of DNP with large nuclear/electron spin ratio.** Unfortunately, the model described in the section above is very difficult to generalize towards larger spin systems due to restrictions in computational power [123]. Recently, Kuprov has proposed the utilization of Fokker-Planck formalism in order to achieve higher efficiency of density operator propagation [125]. Even though the dimensionality of spin operators in Liouville space has to be extended by the spatial dimensions in Fokker-Planck space, the time slicing—necessary when the Hamiltonian is not self-commuting at all times—can be performed more efficiently particularly for situations involving complex spatial evolution of the spin Hamiltonian [126]. This can be beneficial for experiments under MAS. This formalism has been incorporated into the Spinach simulation library [127], which could lead to promising advances in theoretical modeling of complex situations for DNP under MAS.

Strides towards a general description of a system containing a rather large number of nuclear spins per electron spin have been taken by Köckenberger and co-workers (Fig. 14). For example, Karabanov et al. have shown that the large (Liouville) state-space can be effectively reduced because the norm of subspaces of higher spin-order does not significantly build up on the time scale of typical experiments (Fig. 14A). Therefore, only subspaces up to a

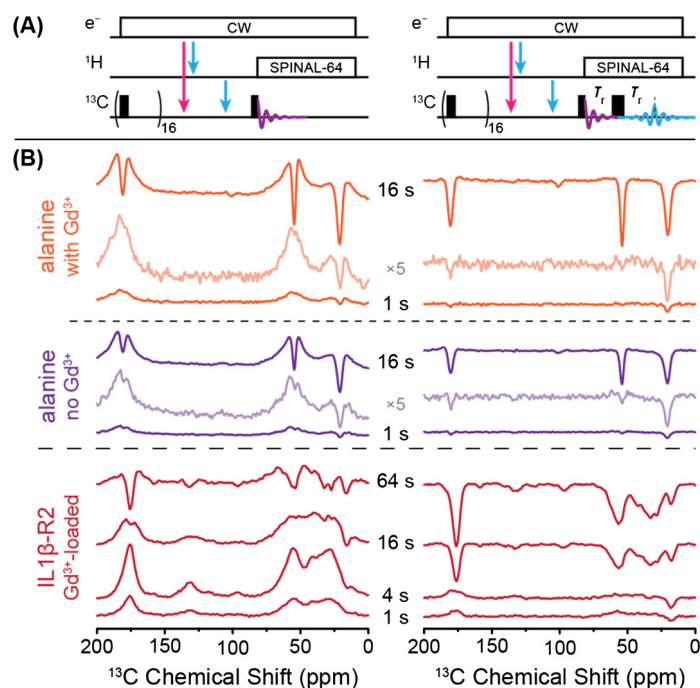


**Fig. 16.** (A) Pulse sequence for read-out of enhanced  $^{13}\text{C}$  polarization generated by direct DNP (magenta arrow) or generated indirectly by cross relaxation from DNP-enhanced  $^1\text{H}$  (cyan arrows). Read-out is performed by single-pulse excitation (left) or by Hahn echo (right). (B) MAS NMR spectra of three different samples ( $\text{U-}^{15}\text{N}, ^{13}\text{C}$ -IL1 $\beta$ -R2 protein loaded with  $\text{Gd}^{3+}$  as well as  $\text{U-}^{13}\text{C}$ -alanine in the presence or absence of  $\text{Gd}^{3+}$ ) doped with AMUPol, recorded using the pulse sequences in (A). Positive signals arise from direct  $^{13}\text{C}$  (+)-DNP whereas  $^1\text{H-}^{13}\text{C}$  cross-relaxation leads to negative signals. Reprinted with permission from [141].

certain spin-order have to be considered, leading to polynomial scaling instead of exponential scaling of the state-space with the number of spins. This facilitates simulations of large spin systems, even though the scaling power is still significant [128]. The same authors have also extended this state-space restriction approach by applying Krylov-Bogolyubov averaging of the fast oscillations during spin-evolution. Due to the presence of the electron spin and acceleration of higher spin-order decoherence, the state-space can be very effectively truncated for DNP-relevant systems (Fig. 14B and C). This allowed for simulations of SE [129] as well as CE [131] with a large number of nuclear spins up to  $10^3$ ; in such a large system, the SE DNP process is governed by kinetically constrained diffusion (Fig. 14D) [130]. Further extension of the theoretical model by incorporation of a kinetic Monte Carlo algorithm for the description of spin diffusion allowed the authors to predict that more efficient bulk hyperpolarization could be achieved by increasing the minimum distance between the electron spin and the closest nuclei [132]. This result is similar to the findings of Griffin and co-workers where it was concluded that a significant amount of nuclear spin polarization is lost to fast-relaxing core nuclei [74,77]. Although Köckenberger and co-workers have developed these models for conditions suitable for dissolution DNP (large  $^{13}\text{C}$  concentration, very low temperature), results could be qualitatively applicable to MAS DNP as well. However, in order to obtain quantitative predictions in the latter case, sample rotation under MAS would have to be explicitly included.

**2.2.2.3. Spectral diffusion in the context of DNP: direct vs. indirect CE.** Developments in high-field EPR spectroscopy have allowed to investigate the role of spectral diffusion which occurs under DNP-relevant conditions. A detailed study has been led at the Weizmann Institute (Rehovot, Israel) in a collaboration between the Goldfarb and Vega laboratories using an integral EPR/NMR/DNP spectrometer operating at W-band (94 GHz  $e^-$ , 140 MHz  $^1\text{H}$ , 3.4 T) [88,133]; this study has very recently been extended to a

field of 7 T (198 GHz  $e^-$ , 300 MHz  $^1\text{H}$ ) [134]. An additional (pump)  $\mu\text{W}$ -frequency source was used for ELDOR spectroscopy, allowing the measurement of electron (de-)polarization after off-resonance saturation [135]. A similar approach had been utilized by Granwehr and Köckenberger, however, their resonator-free setup in combination with longitudinal detection (LOD) of electron spin polarization is only suitable for experiments under TM conditions (i.e., at very low temperatures) [136].

The above-mentioned ELDOR experiments enabled the identification of spectral diffusion pathways active under typical DNP saturation. Using such a technique the authors have experimentally confirmed the correlation between differential polarization within the electron spin pair and the polarization of the coupled nucleus under CE (see Sections 2.1.2 and 6.1.2) [133]. Furthermore, it has been shown that the required selective electron depolarization can be inflicted either directly by  $\mu\text{W}$  irradiation of the spin packet of one of the electrons within the CE-matching pair, or indirectly by excitation of an off-resonance spin packet and subsequent spectral diffusion of electron polarization. These processes have been dubbed *direct CE* (dCE) and *indirect CE* (iCE) [88]. It should be noted that this distinction is highly relevant under static conditions where the narrow matching condition for dCE can be achieved only by a rather small number of active spin pairs whereas iCE can benefit from significantly increased fraction of actively polarizing pairs due to effective spectral diffusion. Under MAS, the spin packets modulate their Larmor frequency [75,83], which leads to a situation comparable to iCE (see above, Section 2.1.2).

## 2.3. Utilization of enhanced polarization

### 2.3.1. DNP build-up under microwave irradiation

Since DNP causes a build-up of longitudinal magnetization, this process is indistinguishable from the return to thermal polarization due to spin-lattice relaxation. Even though early experiments using DNP enhancement in combination with MAS utilized a gated



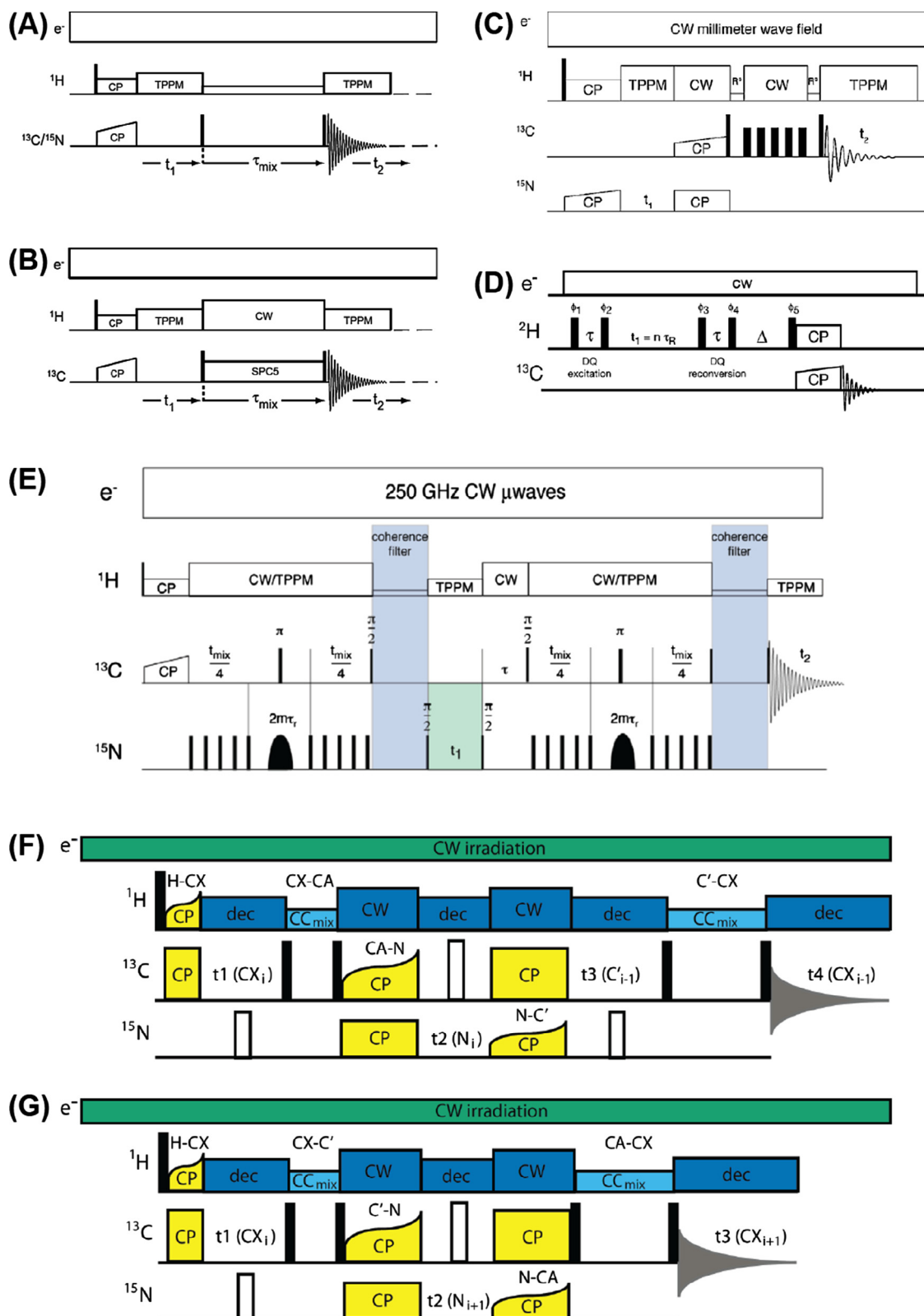


**Fig. 17.** Various MAS NMR pulse sequences employing DNP enhancement. (A) Homonuclear correlation spectroscopy by proton-driven spin diffusion and (B) by SPC5 double-quantum mixing; reprinted from [137] with permission. (C) Heteronuclear correlation spectroscopy by double CP in combination with homonuclear mixing; reprinted from [146] with permission. (D) Double-quantum (DQ)  $^2\text{H}$ - $^{13}\text{C}$  correlation spectroscopy; reproduced from [147] with permission. (E) Frequency-selective transferred-echo double resonance (FS-TEDOR); reprinted from [148] with permission. (F) “Backward” (4D  $\text{CX}(\text{C}\alpha)\text{N}(\text{C}')\text{CX } i \rightarrow i - 1$ ) and (G) “forward” (3D  $\text{CX}(\text{C}')\text{N}(\text{C}\alpha)\text{CX } i \rightarrow i + 1$ )  $\text{S}^3$  correlation experiments; reproduced from [149] with permission.

$\mu\text{W}$  irradiation where the acceleration voltage of the gyrotron  $\mu\text{W}$  source was cut right before NMR acquisition [91], it was shown that this instrumentation-taxing technique is unnecessary [137]. Consequently, experiments can be performed virtually unchanged from their “conventional” variants by allowing the polarization transfer chain explained earlier to occur during the regular recycle delay while the sample is continuously irradiated by  $\mu\text{W}$ . Thus, modification of typical MAS NMR pulse sequences is generally not required.

### 2.3.2. Indirect vs. direct DNP

As shown in Fig. 15, DNP can be performed either directly on the nuclear species to be detected (*i.e.*, low- $\gamma$  nucleus) or indirectly by first hyperpolarizing  $^1\text{H}$  and then transferring the enhanced polarization to the low- $\gamma$  nuclei for detection or further evolution/-transfer [91]. These scenarios are usually known as direct and indirect DNP.<sup>3</sup> Here, it should be noted that these definitions should generally be based on the pathway of enhanced polarization from the PA to the nuclear spin that is detected. In the following, we will see that there are several ways how this pathway can be controlled. In particular, experimental parameters such as field/frequency matching can be adjusted in favor of a specific DNP mechanism, or a suitable pulse sequence/phase cycle can be employed which allows a selective read-out of the sought-after polarization.

### 2.3.3. Active DNP pathways

In the case of bis-nitroxide PAs, the field profiles of  $^1\text{H}$  and low- $\gamma$  nuclei such as  $^{13}\text{C}$  are almost congruent (see Section 3.2.2). Consequently, both DNP transfer pathways are equally active, although they may occur with different rates. Polarization that has built up by unwanted transfer pathways has to be discarded by the pulse sequence used for read-out, however, in most cases, appropriate phase cycles are already implemented in the conventional pulse programs (*e.g.*, Hartmann-Hahn cross-polarization) in order to suppress spurious contributions.

In the case of PAs with narrow EPR lines, the SE mechanism allows for selection of the DNP transfer pathway. By choosing the respective SE matching condition, Eq. (12), either  $^1\text{H}$  or the low- $\gamma$  nuclear species can be selectively hyperpolarized while the other species remains close to thermal polarization (see Section 3.2.1). Therefore, in these cases, the DNP matching has to be adjusted when changing between indirect and direct DNP detection schemes by adjusting the magnetic field or the  $\mu\text{W}$  frequency.

### 2.3.4. Pulse sequences for indirect or direct DNP read-out

Most commonly performed is indirect DNP, where the polarization is generated on a suitable nuclear species, normally  $^1\text{H}$ , and is then transferred to the nuclear species of interest such as  $^2\text{H}$ ,  $^{13}\text{C}$ ,  $^{15}\text{N}$ ,  $^{17}\text{O}$ ,  $^{27}\text{Al}$ ,  $^{29}\text{Si}$ , etc. (Fig. 15). This transfer is typically performed by cross-polarization (CP), after which either the free induction decay (FID) is recorded or further magnetization transfer steps can be employed. Any potential polarization that has built up by direct DNP is filtered by an appropriate CP phase cycle, in the same way as the thermal polarization of the nuclear spins to be detected is discarded in a conventional CPMAS experiment. Indirect DNP has the advantage that by hyperpolarizing a strongly-coupled nuclear spin network, the DNP transfer process is very efficient and short build-up time periods as well as a uniform spreading of enhanced polarization can be achieved.

For direct DNP, on the other hand, no heteronuclear transfer step is involved and a simple single-pulse excitation is used for read-out of the FID or for further transfer. In the cases where

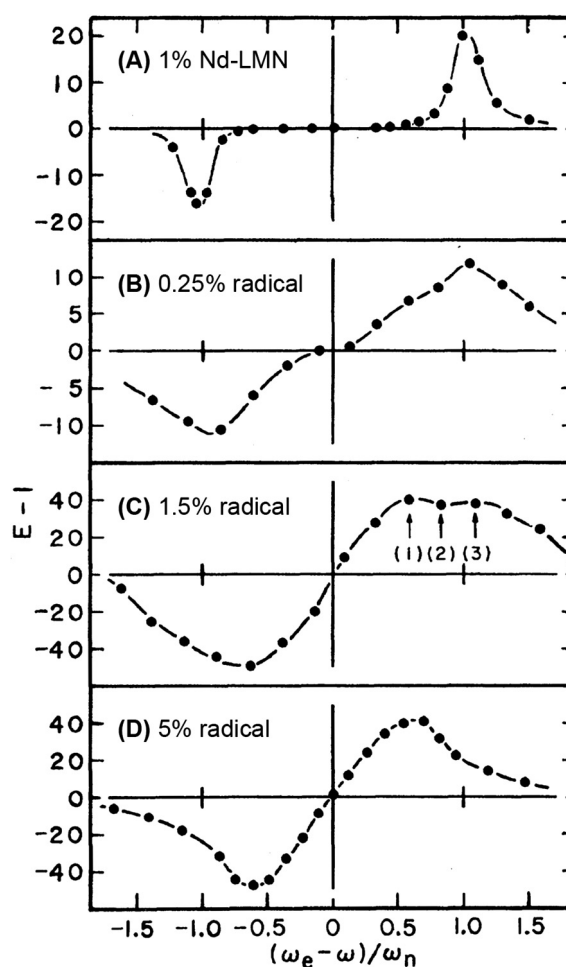


**Fig. 18.**  $^1\text{H}$  enhancements as function of static applied magnetic field at 4.2 K and 70 GHz: (A) 1%  $\text{Nd}^{3+}$  in LMN; (B), (C), and (D) 0.25, 1.5, and 5% Ley's radical in polystyrene, respectively. The magnetic field axis is shifted for comparison as  $g \approx 2.7$  for Nd-LMN, and  $g \approx 2.0$  for Ley's radical. Reprinted with permission from [59].

low- $\gamma$  nuclei are detected, the initial direct DNP transfer and the subsequent spreading through the bulk can be considerably slower and less efficient, especially when the local spin concentration is small. Therefore, spatial polarization gradients must be expected and have indeed been observed experimentally [138,139]. Also, increased line widths of the DNP-enhanced MAS NMR spectrum in comparison with the non-enhanced spectrum have been reported due to selective hyperpolarization of nuclei that are close to the paramagnetic PA [139–141]. Nevertheless, direct DNP can be performed in the absence of  $^1\text{H}$  (*i.e.*, where CP cannot be employed) [142], or where the direct transfer pathway is preferred, for example, in order to distinguish between surface and bulk sites [143,144] or to constrain enhanced polarization within a certain distance/volume around the PA [139,140].

### 2.3.5. Simultaneous indirect and direct DNP

Differentiation between direct and indirect DNP processes is only clear when no heteronuclear contact exists except the controlled (coherent) transfer pathway during the CP contact period. Recently, it has been shown that non-coherent transfer of polarization can also occur during DNP build-up between hyperpolarized  $^1\text{H}$  and  $^{13}\text{C}$  due to cross-relaxation (see Fig. 16) [139,141,145]. In this case, a negative signal enhancement is generated on  $^{13}\text{C}$  suggesting dipolar  $^1\text{H}$ – $^{13}\text{C}$  cross-relaxation dynamics to be responsi-

<sup>3</sup> Direct and indirect DNP as transfer pathways are not to be confused with direct and indirect CE as DNP mechanisms (dCE/iCE) which are described in Section 2.2.2.3.

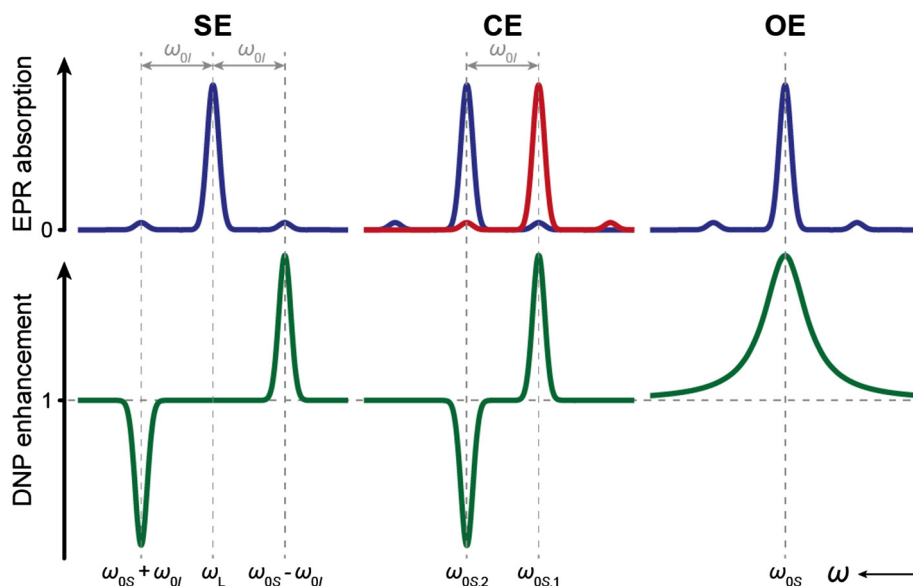


**Fig. 19.** Theoretically predicted DNP field profiles (green) of SE, CE, and OE, based on simple EPR line shapes (blue and red). Small satellite peaks at an offset corresponding to  $\omega_{0I}$  are the forbidden e–n DQ and ZQ transitions and are largely exaggerated in intensity. For CE, the EPR lines of two electron spins with ideal CE matching condition  $\Delta\omega_{OS} = \omega_{0I}$  are shown in different colors.

ble. For biomolecules, methyl groups have been identified as effective cross-relaxation promoters under DNP, even at temperatures of 100 K [141].

In the case of a bis-nitroxide PA, both nuclear species (*i.e.*,  $^1\text{H}$  and  $^{13}\text{C}$ ) are hyperpolarized at the same time. Subsequently, a combination of (+)-DNP enhancement by direct  $^{13}\text{C}$  DNP and of (–)-DNP by indirect DNP due to cross-relaxation is observed, partially cancelling each other. Nevertheless, due to the spatial selectivity of the two processes—direct DNP requires close vicinity of a PA while indirect DNP is emanating from methyl groups substantially removed from the PA—filtering schemes can be applied in the form of decoherence filters or  $^1\text{H}$  saturation schemes [141,145]. The former technique removes contributions from fast-decaying coherences of  $^{13}\text{C}$  nuclear spins in close vicinity of the PA while the latter suppresses the build-up of (–)-DNP by cross-relaxation from  $^1\text{H}$ . When the  $^1\text{H}$  SE condition can be induced selectively, enhancement due to indirect DNP by cross-relaxation can also be selectively observed without filtering techniques [139].

The additional selectivity provided by these methods is highly promising towards the generation of non-uniform and spatially constrained polarization which can potentially be utilized for spectral isolation of a sought-after molecular species within a complex mixture. First steps in this direction have been taken with the direct labeling of biomolecules with PA-tags (see also Section 6.3.4); the possibility of straightforward background removal by subtraction of non-enhanced ( $^1\text{H}$ -saturated) spectra underscores the importance of such methods.

### 2.3.6. Examples of NMR pulse sequences used for MAS DNP

Generally, most MAS NMR pulse sequences can be applied in combination with DNP without further modifications. Therefore, we will only present a small selection of NMR pulse sequences reported in combination with DNP which is based mostly on historical developments. However, the performance of pulse sequences—in particular those including long mixing periods—might be affected by the presence of the PAs which act as centers for enhanced longitudinal and transverse relaxation (see Section 6.4.2).

Many examples of DNP-enhanced multidimensional pulse sequences have been reported during the last years. Earliest reports included homonuclear chemical-shift correlation spectroscopy

[137], heteronuclear correlation spectroscopy by double CP (DCP) in combination with homonuclear mixing [146], double-quantum (DQ)  $^2\text{H}$ – $^{13}\text{C}$  correlation spectroscopy [147], and frequency selective TEDOR (FS-TEDOR) in combination with DNP [148] (see Fig. 17), as well as indirect detection of  $^{14}\text{N}$  by HMQC [150].

The large sensitivity gain by DNP has also stimulated the development and application of techniques that are otherwise not possible. For example, Märker et al. have applied a  $^{15}\text{N}$ – $^{13}\text{C}$  DCP-based heteronuclear correlation experiment (DCP-HETCOR) on a deoxyribonucleoside derivative in natural isotopic abundance which—in combination with  $^{13}\text{C}$ – $^{13}\text{C}$  *J*-refocused INADEQUATE—allowed for the complete assignment of  $^{13}\text{C}$  and  $^{15}\text{N}$  resonances despite the very low probability of direct one-bond contacts (*i.e.*, 10<sup>–2</sup>% for  $^{13}\text{C}$ – $^{13}\text{C}$  and 4 × 10<sup>–4</sup>% for  $^{13}\text{C}$ – $^{15}\text{N}$ ) [151]. Very recently, McDermott and co-workers have developed a novel 3D/4D sequential sidechain-sidechain (*S*<sup>3</sup>) correlation spectroscopy experiment (see Fig. 17F and G). This technique is only possible due to the large sensitivity gains by DNP and allows full assignment of protein resonances in a fraction of the experimental time required for conventional MAS NMR despite the frequently encountered inhomogeneous broadening and subsequent overlap of resonances at cryogenic temperatures [149]. A much more exhaustive description of experiments enabled by DNP is given in the context of relevant applications with DNP in Section 7.

## 3. Enhancement profiles

Polarization transfer from electron spins to nuclear spins can only take place at appropriate resonance conditions defined by the DNP mechanisms [*i.e.*, the DNP matching conditions as given by Eqs. (12) as well as (33)] and as explained in detail in Section 2.1. This can be achieved in two ways: either the magnetic field is shifted such that the electron and nuclear Zeeman interactions fulfil the matching condition with a fixed  $\mu\text{w}$  frequency, or—given a frequency-tunable  $\mu\text{w}$  source is available—the  $\mu\text{w}$  frequency can directly be adjusted. Thus obtained profiles of field- or frequency-dependent enhancement factors are commonly referred to as DNP field or frequency profiles, respectively; these two methods yield—except for the typical inversion of the abscissae—practi-

cally equivalent profiles. The oftentimes rich information contained in such profiles can be used to optimize DNP experiments or to investigate DNP mechanisms in more detail. Due to the widespread use of fixed-frequency gyrotron sources for MAS DNP (see Section 4.2.1), field profiles are most commonly recorded with sweepable NMR magnets which are now commercially available [152]. Alternatively, when a frequency-tunable  $\mu\text{W}$  source is utilized, the acquisition of frequency profiles is the most convenient method in a static DNP setup; however, the limited bandwidth of the  $\mu\text{W}$  resonating structure has been taken into account [153].

### 3.1. Development of fundamental DNP theory

Discussions of DNP field profiles have played a major role in the development of DNP theory. In fact, the very first hypothesis of CE was based on the observation of unexpected changes in the DNP field profiles at 2.5 T (70 GHz  $e^-$ ; 106 MHz  $^1\text{H}$ ) [58,59]. In these important experiments, Hwang and Hill observed a drastic change in the DNP enhancement profiles with varying concentration of Ley's radical [154] in polystyrene (see Fig. 18). SE was the only DNP mechanism known for solids at that time, and Jeffries and Schmutge had already established that (+)- and (-)-DNP enhancement peaks were then separated by  $2\omega_{0f}$ , based on the experiments on a lanthanum magnesium double nitrate crystal doped with 1%  $\text{Nd}^{3+}$  (Nd-LMN) [155]. With higher concentrations of Ley's radical in polystyrene, Hwang et al. observed a decrease in the separation of the (+)- and (-)-DNP extrema. This was attributed to the variation in e–e spin interactions and was dubbed *spin–spin effect*. Further experimental and theoretical research in this direction led to the establishment of CE as a viable DNP mechanism [61,62]. To date, CE is the most commonly employed mechanism when DNP is applied as structural investigation technique (see Section 7).

Analysis of DNP profiles of sample systems where SE is dominating—especially when differential SE was observed with inhomogeneously broadened EPR spectra—stipulated a deeper

understanding of the role of spatial and spectral spin diffusion (Section 2.3.2) to explain the efficient transfer of enhanced polarization to the nuclear spin bulk [76,101,106,121,122]. Consequently, the information obtained from DNP profiles led to the development of advanced theories of (integral) DNP mechanisms [156]. While DNP profiles due to SE can oftentimes be predicted quite accurately on basis of the EPR spectrum of the PA [157], CE is associated with much more complicated and less intuitive DNP profiles [158]. Furthermore, OE DNP was observed in insulating solids by analysis of DNP profiles [89,90,97]. In the following, we summarize the key points that characterize active DNP mechanisms (*i.e.*, SE, CE, and OE) under typical experimental conditions based on the theoretical discussion in Section 2.1.

### 3.2. Differences due to DNP mechanisms and polarizing agents

#### 3.2.1. Solid effect

SE is mainly observed with monomeric radicals featuring a relatively small EPR spectral breadth so that CE matching is inefficient; alternatively, also radicals with broad EPR linewidth can induce SE when their concentration is small and thus, intermolecular e–e interactions required for CE are negligible. In the simplest case, the shape of the DNP field profile can be directly deduced from the EPR spectrum of a PA [74,139,158]. According to Eq. (12), excitation of the e–n DQ or ZQ transitions leads to positive, (+), or to negative, (–), nuclear polarization enhancement, respectively. These conditions are separated by  $2\omega_{0f}$ . In the case of a narrow EPR spectrum—where ZQ and DQ transitions are sufficiently separated—the net (+)- and (–)-DNP enhancement peaks are well resolved and occur at frequencies  $\omega_{0s} - \omega_{0f}$  and  $\omega_{0s} + \omega_{0f}$ , respectively (see SE case in Fig. 19 and green spectrum in Fig. 20).

Inhomogeneous broadening of EPR spectra by typical mechanisms such as Zeeman anisotropy or unresolved HFI directly affects DNP field profiles as well. Even when the ZQ and DQ SE transitions are sufficiently separated (yellow spectrum in Fig. 20), the

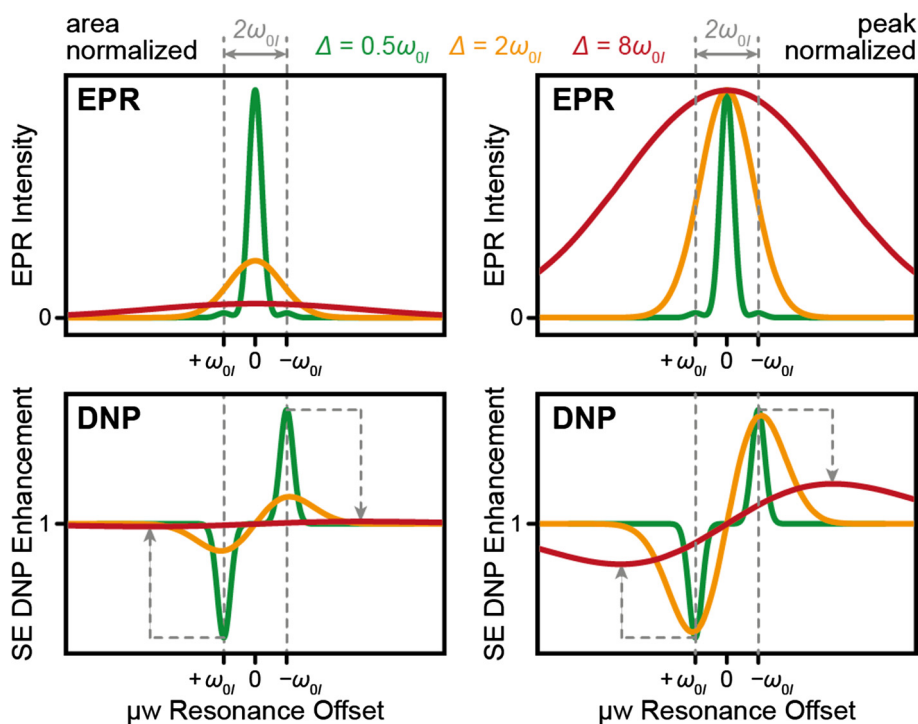


**Fig. 20.** Theoretical analysis of field profiles predicted by inhomogeneously broadened EPR spectra, demonstrating the transition from well-resolved SE (green) via partial overlap of ZQ and DQ transitions (orange) to differential SE (red). The left column shows spectra and profiles normalized to the full area under the EPR absorption spectrum while the right column data is normalized to the maximum peak absorption.

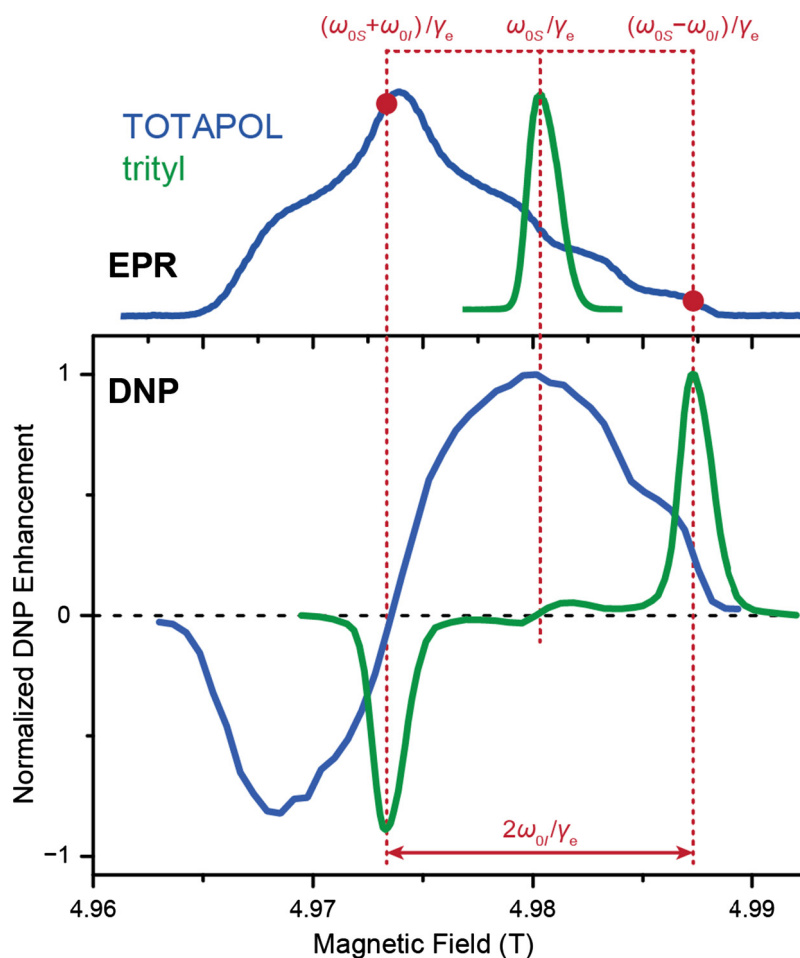


**Fig. 21.** Experimental DNP field profiles of TOTAPOL (blue) and trityl OX063 (green) in comparison with their respective EPR spectra at 140 GHz  $\mu\text{w}$  frequency. For trityl, DNP by SE is excited at the DQ and ZQ transitions of the EPR resonance (outer red dotted lines). For TOTAPOL, excitation of the SQ EPR transition of one spin packet (middle red line) leads to possible CE matching with spin packets resulting in opposite DNP sign, albeit with different probabilities (red dots).

resulting reduction of the excitation efficiency achievable with a fixed-frequency  $\mu\text{w}$  source leads to a proportional reduction of the maximum bulk signal enhancement due to a smaller number of spin-packets actively participating in SE induction [159]. This reduction can (in part) be compensated for by electron spectral diffusion [134,160], or—in the case of MAS DNP—rotor-angle dependent evolution of anisotropic interactions [75,83,156]. Also, frequency modulation has been shown to result in higher enhancement factors in static DNP [161–164]. In all of these cases, a larger number of electron spins were excited by  $\mu\text{w}$  irradiation as would be expected from the homogeneous linewidth of the spin packets as long as sufficient  $\mu\text{w}$  power was available for operation in the (partial) saturation limit of the SE. Unfortunately, this power requirement is usually not met for MAS DNP—even when a high-power gyrotron is used—due to the small transitions moments of the SE [74,89,139].

If the overall breadth due to inhomogeneous broadening of the EPR line exceeds  $2\omega_{0I}$  (red spectrum in Fig. 20), overlap of the ZQ and DQ transitions causes mutual cancellation of (+) and (–) enhancements and hence reduction of the net nuclear bulk polarization in addition to the less effective spin packet excitation described in preceding paragraph. As we have already explained in Section 2.2.1.5, for very large EPR line widths ( $\Delta \gg 2\omega_{0I}$ ), the DNP profile resembles the first derivative of the EPR spectrum [76]. Consequently, the separation between the maxima of (+)- and (–)-DNP peaks becomes greater than  $2\omega_{0I}$ .

A simple yet effective method for simulation of SE DNP profiles has been presented by Shimon et al. and is based on the differential (net) amplitude of DQ and ZQ transitions obtained by the EPR spectral shape function [158]. This method can easily be applied if the EPR spectrum is available (most preferably recorded with the same  $\mu\text{w}$  frequency used for DNP) and has proven highly useful in the identification of transitions between active DNP mechanisms [139,165], as is outlined in Section 3.3.1.

### 3.2.2. Cross effect

PAs with broad and anisotropic EPR spectra often favor the CE mechanism, given sufficient inter- or intramolecular e–e dipole coupling is provided. The shape of the CE field profile caused by such an inhomogeneous EPR line is difficult to understand or predict. As a *gedankenexperiment*, a spin system featuring two narrow lines which are separated by the nuclear Larmor frequency would achieve an ideally efficient CE [61]. In this case, the field profile would consist of two DNP peaks of different relative sign, separated by the nuclear Larmor frequency. These peaks coincide with the two EPR absorption lines: by direct excitation of either the low- or high-frequency EPR transition a CE three-spin-flip is induced, leading to either (+) or (–) nuclear enhancement, respectively (see CE case in Fig. 19). Such idealized systems are difficult to design due to the limitations on g-factor variation of available radicals; nevertheless, a mixture of BDPA and trityl type radicals

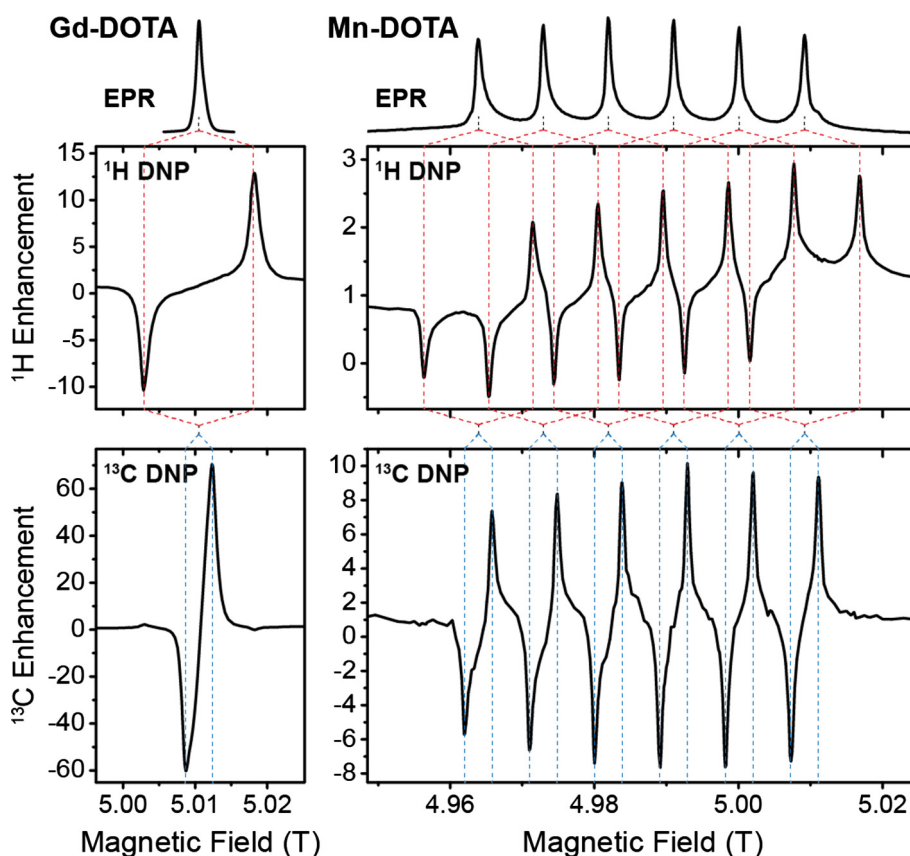


**Fig. 22.**  $^1\text{H}$  and  $^{13}\text{C}$  DNP field profiles of Gd-DOTA and Mn-DOTA PAs. EPR spectra shown on top of DNP profiles. All data recorded at 140 GHz  $\mu\text{w}$  frequency with 10 mM PA concentration in a 60/40 (vol%) glycerol/water solution at  $\sim 86$  K. Figure adapted with permission from [139].

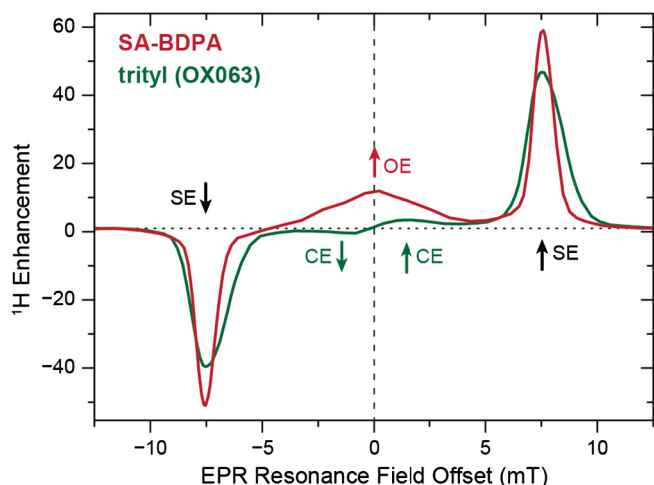


**Fig. 23.**  $^1\text{H}$  DNP enhancement field profiles of SA-BDPA (red) and trityl OX063 (green) measured at 140 GHz  $\mu\text{w}$  frequency (5 T) at 40 mM PA concentration in each case. Field profiles are centered around the EPR resonance maximum for each radical. Besides the prominent SE at the marked position, SA-BDPA shows significant OE with a saturation-broadened peak at the EPR transition; in contrast, trityl shows small contribution from CE with inflection of enhancement at the EPR transition. Data taken from [89].

can mimic such a scenario for DNP of low- $\gamma$  nuclei [82]. This situation is discussed in more detail in Section 5.2.3.

For strongly anisotropic, inhomogeneously broadened EPR lines (i.e.,  $\Delta > \omega_{0l} > \delta$ ), contributions from all spin packets within the spectral envelope have to be considered in a disordered sample.

Excitation of the absorption line at an arbitrary field/frequency combination will in most cases lead to both (+)- and (–)-DNP with concomitant partial cancellation. Subsequently, the DNP profile spreads across the whole EPR absorption spectrum and most importantly, no plateau occurs (Fig. 21). Under static conditions with randomly oriented monomeric radicals, a rather straightforward matching probability between spin packets can be evoked. Thus, for each point in field or frequency, the probabilities of finding matching partners separated by  $\Delta\omega_{0s} \approx \pm\omega_{0l}$  [see Eq. (33)] that result in (+) or (–) enhancement are weighted against each other, yielding a relative enhancement factor [158].

For a typical bis-nitroxide system, this analysis would have to account for the correlation between the molecular frames of the two interconnected radical moieties. The complexity is further exacerbated under MAS as explained in Section 2.1.2. As we have additionally laid out in Section 2.2.2, quantum-mechanical propagation of the full density operator in Liouville space is currently not feasible. Very recently, Mentink-Vigier et al. have introduced a semi-classical theory for simulation of such CE profiles under MAS, based on the solution of Bloch-like differential equations and numerical analysis of the adiabaticities of level anti-crossing (LAC) events within the Landau-Zener approximation [156].

### 3.2.3. Overhauser effect

As already discussed in Section 2.1.3, initially unexpected  $^1\text{H}$  signal enhancements by OE DNP have been reported in dielectric solids under MAS [89,90,97]. Since the OE operates by incoherent e–n cross relaxation, it can theoretically be driven by direct or indirect saturation of the EPR resonance line. Up to now, only direct saturation has been reported experimentally [89,90,97]; however, the slight asymmetry of maximum (+)- and (–)-DNP enhancement

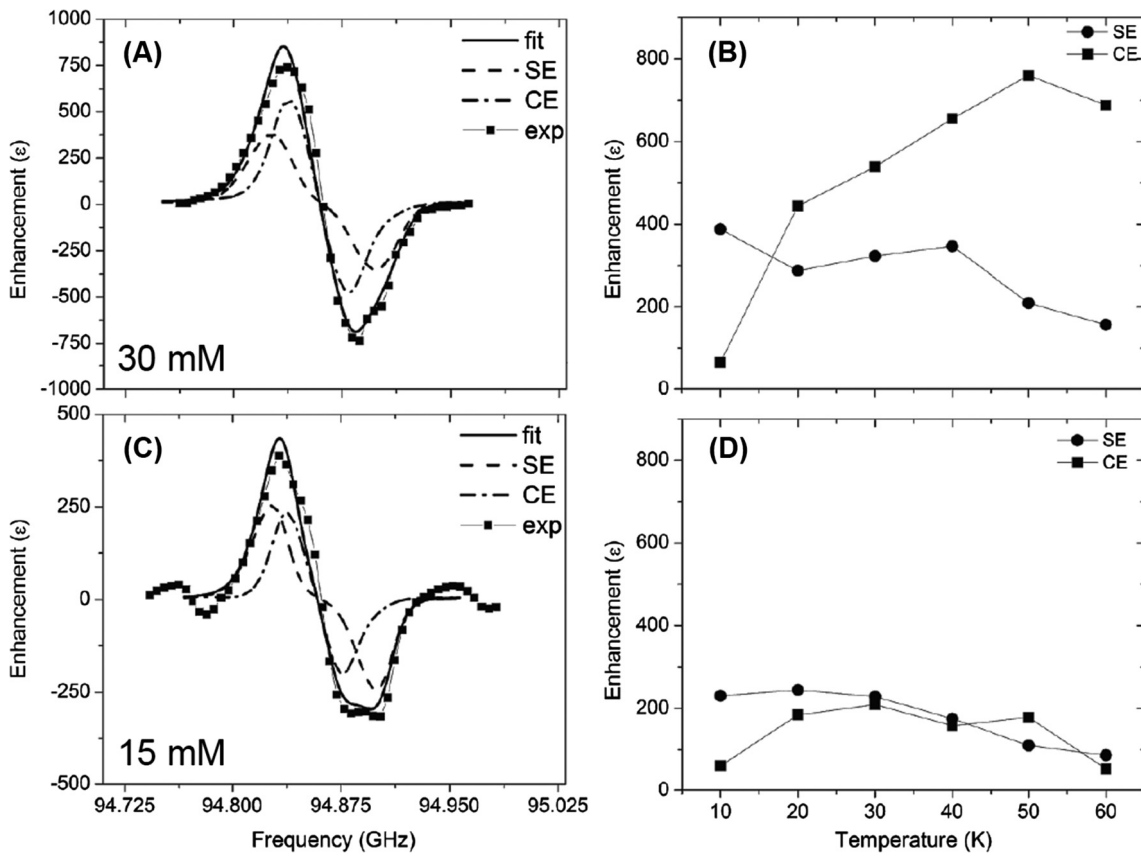


**Fig. 24.** (A) Experimental DNP frequency profile (squares) overlaid with the best-fit simulated  $^{13}\text{C}$  DNP profile (solid line) for 30 mM trityl at 30 K. The simulated DNP profile consists of the sum of simulated SE (dashed line) and CE (dash-dotted line) profiles. (B) relative contribution of SE (circles) and CE (squares) as a function of temperature for the same sample. (C) and (D) show corresponding data for 15 mM PA concentration. Reprinted from [169] with permission.

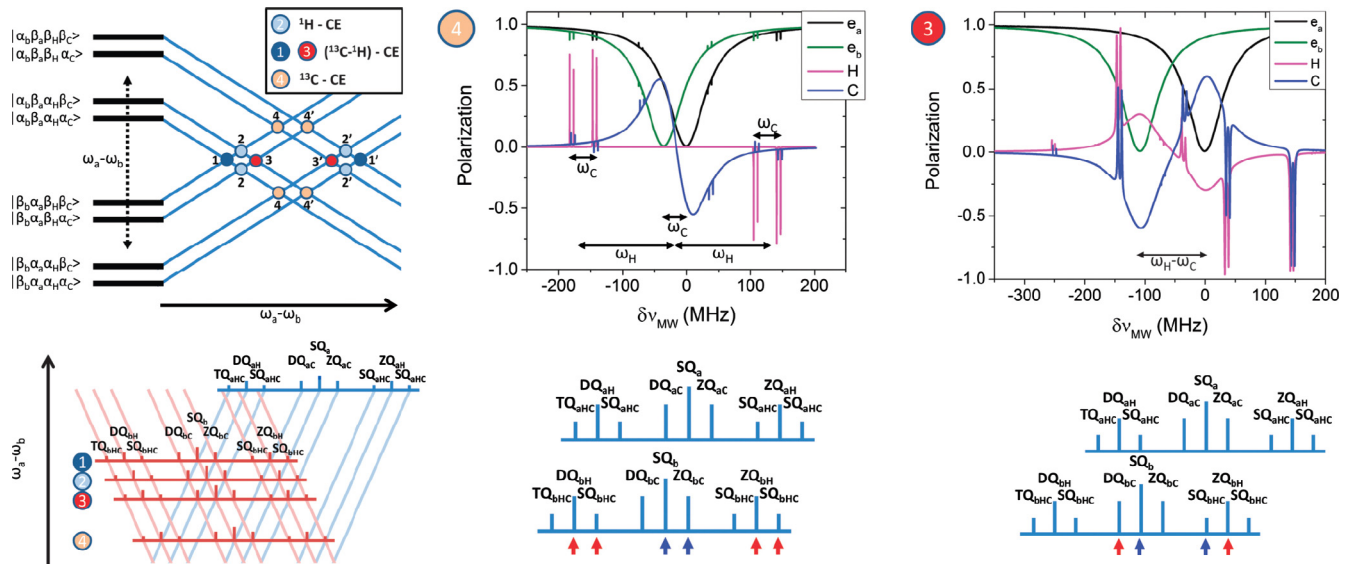


**Fig. 25.** Illustration of heteronuclear CE. Left: Eight central spin states of an  $e_1-e_2-^1\text{H}-^{13}\text{C}$  four-spin system as function of the electron Larmor frequency difference. Middle: Simulated electron and nuclear spin polarization profiles for the  $^{13}\text{C}$  CE matching condition; right: same polarization profiles at the  $^{13}\text{C}-^1\text{H}$  CE matching condition. Matching between the different possible spin transitions are shown in the lower depictions; for further details, the reader is referred to the original publication. Reproduced from [175] with permission.

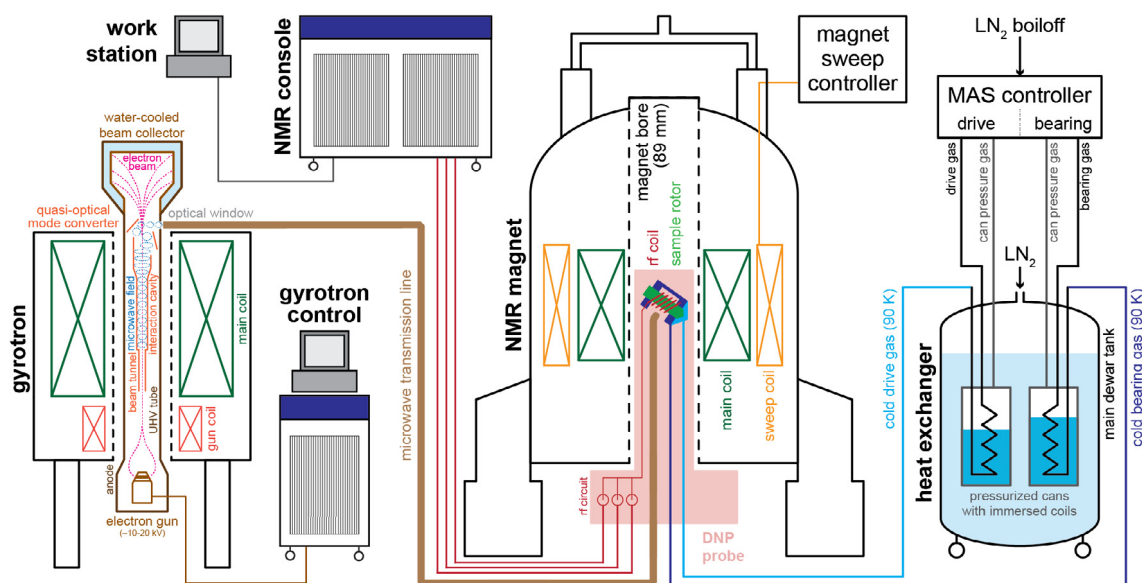


**Fig. 26.** Schematic representation of a typical experimental setup for DNP-enhanced MAS NMR spectroscopy. Besides the requirements for conventional solid-state NMR spectroscopy, microwaves generated by a gyrotron are transmitted into the probe. A cryo-MAS unit provides stable sample spinning at cryogenic temperatures.

factors observed at the SE conditions for trityl and SA-BDPA [74,89] might be attributable to an indirect saturation of the EPR line and subsequent OE by e–n cross relaxation.

DNP enhancement of one specific sign is theoretically expected and has been observed experimentally [89,166]. As shown in Fig. 19 (OE case), the DNP condition is centered around the EPR spectrum and generally resembles the EPR line shape. However, in all cases reported so far, a broadening of the OE DNP profiles with respect to the EPR spectrum has been observed. This is caused by a highly efficient saturation even at low  $\mu\text{W}$  power, so that off-resonance saturation has to be considered as is described in Section 2.1.3.

### 3.2.4. High-spin metal ions

The DNP mechanisms responsible for enhancement by high-spin metal ion PAs ( $\text{Gd}^{3+}$  and  $\text{Mn}^{2+}$ ) have been analyzed based on their field profiles [139,159,167]. Representative examples of field profiles are shown in Fig. 22. The theoretical description follows the same principles as laid out for PAs with  $S = 1/2$  in Section 2.1. However, the situation is not trivial due to the occurrence of multiple spin transitions with different properties. The EPR spectra of half-integer high spin systems often feature a narrow and isotropic (to first order) central transition (CT) and highly anisotropic satellite transitions (STs) spreading over a large field/frequency range due to zero-field splittings (ZFS.) As a result, the narrow CT evidently allows for SE [139], whereas the role of STs is still unclear. The large angular dependence of ZFS might support CE under MAS [167]. However, clear indications for such CE matching between STs or between a ST and the CT has not been presented yet. Therefore, for all examples of DNP with high-spin PAs presented thus far, a treatment of the CT alone is believed to be sufficient to explain occurrences of both SE and CE [139,168].

## 3.3. Information content

### 3.3.1. Identification of DNP mechanism

Even though knowledge of the sample composition and environment (e.g., PA type and concentration, temperature, external magnetic field) might already indicate the dominant DNP mechanism, the exact prediction is not straightforward; indeed, even a

transition from one dominant mechanism to another can occur when changing experimental parameters. As described in the preceding sections, the shape of the field profile can yield valuable information about the DNP mechanism active within a sample under certain experimental conditions.

Certain selection criteria have to be fulfilled for effective contribution of a specific DNP mechanism. CE requires a PA which allows for frequency matching according to Eq. (33) (i.e.,  $|\Delta\omega_{0s}| = \omega_{0l}$ ) while at the same time sufficient e–e dipole couplings have to be present. If one of those criteria is not met, CE is absent or inefficient. For example, SA-BDPA shows no sign of CE due to the small EPR line-width even though sufficient e–e dipole couplings are expected at the high concentration. In many cases two mechanisms can be observed to exist next to each other. For example, SA-BDPA shows OE being active besides SE; for trityl OX063, minor contributions from CE  $^1\text{H}$  DNP are evident along with major enhancements due to SE [74,89]. This situation is illustrated in Fig. 23.

Such a combination of different DNP mechanisms is much less obvious when PAs with EPR line widths exceeding the nuclear Larmor frequency are considered (i.e.,  $\Delta > \omega_{0l} > \delta$ ). Intuitively, efficient CE is expected if a dipolar coupling between electron spins is provided. However, SE can still contribute significantly to the observed DNP enhancement. This situation has been investigated in detail by the Vega group in the context of static DNP. Shimon et al. corroborated the relative contribution of CE and SE from TEMPOL in static samples and found a transition between the different mechanisms depending on experimental parameters such as sample temperature and incident  $\mu\text{W}$  power [158]. Interestingly, the absolute contribution of the  $^1\text{H}$  CE decreased at low temperatures (<30 K); this observation has also been reproduced by similar experiments with the biradical TOTAPOL [165] as well as with the monoradical trityl for  $^{13}\text{C}$  DNP [169]. The latter example is shown in Fig. 24. Significant extension of electron spin lattice relaxation at lower temperatures has been proposed as the possible explanation of this phenomenon. The decrease of CE efficiency when lowering the temperature is rather unexpected and not observed under MAS conditions. In contrast, under MAS overall DNP enhancements increase with decreasing temperatures; this has been experimentally shown down to 24 K [170]; furthermore, enhancement factors are higher than those obtained under static conditions [171]. How-



ever, to the best of our knowledge, no similar attempt to disentangle relative contributions of SE and CE has been undertaken so far for MAS DNP.

3.3.2. Multinuclear DNP

Another interesting effect has been reported already more than 40 years ago by Borghini, De Boer and Morimoto in relation to their analysis of <sup>1</sup>H and <sup>2</sup>H DNP enhancement profiles. They observed (weak) DNP features occurring at  $\omega_{\mu w} = \omega_{0S} \pm 2\omega_{0I} (^1H)$  as well as  $\omega_{\mu w} = \omega_{0S} \pm \omega_{0I} (^1H) \pm \omega_{0I} (^2H)$  at temperatures of 700 mK [172,173]. These features were identified as forbidden multi-spin SE transitions, where an electron spin flips together with two pro-

tons or one proton/deuteron pair in a concerted manner. Such multi-nuclear SE transitions with up to four protons flipping at the same time have also been observed indirectly by depletion of the electron spin polarization at 80 K by Smith et al.; however, no DNP enhancement by multi-nuclear flips could be observed at this temperature. Nominally, such multi-spin transitions are strongly forbidden, nevertheless, the large number of nuclear combinations paired with indirect homonuclear couplings introduced by strong HFI is expected to increase the effective transition probabilities [174].

The aforementioned heteronuclear multi-spin SE has also been observed for <sup>1</sup>H and <sup>13</sup>C in samples doped with 15 mM trityl at

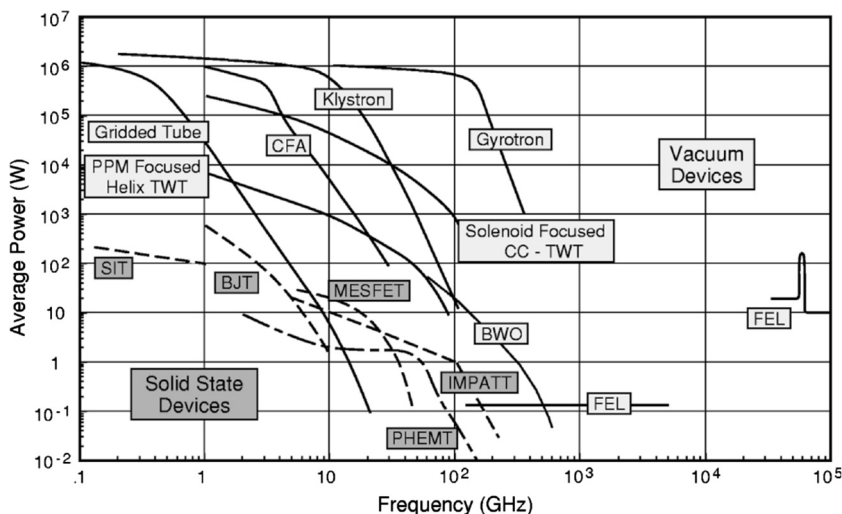


Fig. 27. Frequency dependence of the output power of different electronic devices capable of producing high-frequency electromagnetic irradiation. For abbreviations and further explanations, the reader is referred to the original publication. Reprinted with permission, from [185].

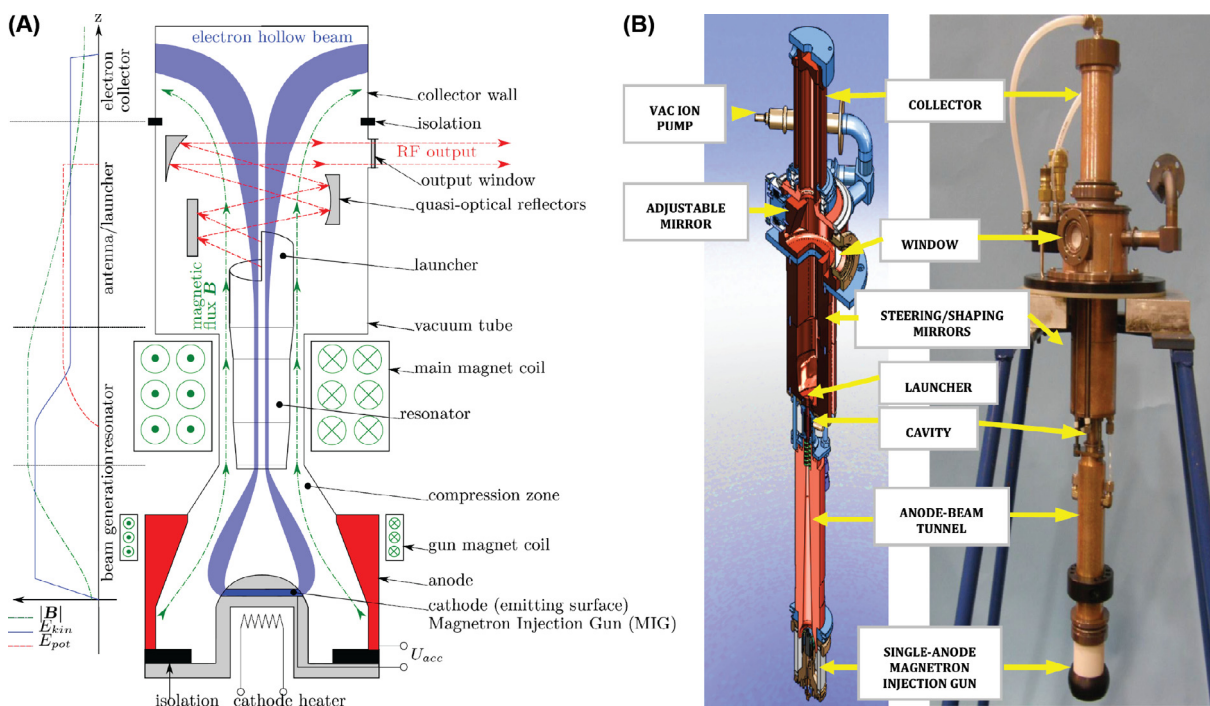


Fig. 28. (A) Schematic drawing of a gyrotron showing the essential components for  $\mu w$  generation; the left plot shows the qualitative profiles of magnetic field (green), electron beam kinetic energy (blue) and  $\mu w$  field potential energy (red). See text for further description. Figure is reproduced from [203] with permission. (B) Computer-generated model (left) and photograph (right) of a 395 GHz gyrotron commercially available from Bruker Biospin. Reprinted from [152] with permission.

temperatures of up to 30 K (see Fig. 24C) [169]. Shimon et al. have performed a detailed experimental analysis of this effect and have proposed several multi-spin transfer pathways to occur in parallel as direct (*i.e.*, coherently  $\mu\text{w}$ -driven) or indirect (*i.e.*, due to electron spin polarization depletion) DNP mechanisms (see also Fig. 25) [175]. Later, this model was extended to account for experimental observation of simultaneous heteronuclear CE between  $^1\text{H}$  and  $^2\text{H}$  [176]. For detailed explanation of these effects we refer the reader to the original publications.

#### 4. Instrumentation

Due to the unique experimental conditions (*i.e.*, high-power, high-frequency  $\mu\text{w}$  irradiation, cryogenic MAS), application of DNP requires significant modifications of existing MAS NMR instrumentation. Since 2009, specialized hardware has been offered commercially by Bruker Biospin for a magnetic field of 9.4 T [177]; recently the scope has been extended by instruments operating at fields of 14.1 and 18.8 T [152].

A schematic drawing of a typical DNP MAS setup is shown in Fig. 26. A short description of the most important components and their implication on effective DNP enhancements is given in the following. For an extensive treatment of the technical details of the individual components, the reader is referred to several excellent reviews [146,152,178–180].

##### 4.1. High-frequency microwave sources

###### 4.1.1. Gyrotrons

Until the mid of the 1990s, the available  $\mu\text{w}$  sources had been the limiting factor for the external magnetic field at which the DNP NMR experiments were conducted. Pioneered by Griffin and co-workers, [91,181,182] the introduction of gyrotrons as sources of high-power/high-frequency  $\mu\text{w}$  radiation dramatically extended this limit (see Fig. 27). Moderate- to high-field DNP setups are accessible today as a result of intensive research [152,177,183,184].

Gyrotrons were originally developed for plasma heating in Tokamak fusion experiments by producing pulsed outputs in the  $> 1$  MW power range; an excellent historical review on the general development of these devices has been written by Nusinovich et al. [186]. For DNP experiments, gyrotrons have been introduced as a truly continuous  $\mu\text{w}$  source by a combined effort of Richard Temkin at the Plasma Science and Fusion Center (PSFC) and Robert Griffin at the Francis Bitter Magnet Laboratory (FBML) at MIT [182]. While the original setup operated at 140 GHz, the scope has been extended by development of gyrotrons by academic research groups with purpose for DNP applications at 250, 330, and 460 GHz (MIT) [146,187–190], 400 and 460 GHz (Osaka) [191–193], 187 GHz (Warwick) [194], 200 GHz (WUSTL) [195], and 260–530 GHz (EPFL) [196–198]. Furthermore, gyrotrons for DNP applications have been developed or designed by Bruker Biospin/Communication & Power Industries (CPI) (263, 395, and 527 GHz) [152,177,199], Gycom (259 GHz) [200] and Bridge12 (395 GHz) [201].

Gyrotrons for continuous wave (cw) operation provide reliable monochromatic  $\mu\text{w}$  irradiation frequencies up to 1 THz and deliver continuous output power at the sample in the order of 10 W and higher. Such high power levels are necessary for MAS DNP as the size of the sample exceeds the  $\mu\text{w}$  wavelength several-fold; thus, the sample is not situated inside a  $\mu\text{w}$ -resonating structure. In contrast, for EPR and static DNP experiments a resonator is typically used, alleviating the requirement for large incident power by efficient conversion between incident  $\mu\text{w}$  power and field amplitude.

As electron cyclotron maser devices, gyrotrons rely on the acceleration of an annular-shaped electron beam—which is emit-

ted from an electron gun cathode—into a longitudinal magnetic field (see Fig. 28). Within this field, the electrons gyrate with their cyclotron resonance frequency and pass an interaction cavity. Here, the cyclotron maser instability causes transverse bunching of the electrons and an electromagnetic field is generated [202]. This field in turn interacts with the movement of the electrons in the beam, amplifying the bunching and allowing the extraction of transverse kinetic energy in the form of  $\mu\text{w}$  irradiation which is then guided into an overmoded, corrugated waveguide (see Section 4.4.2) by a quasi-optical mode converter.

Under stable operation conditions, up to 200 W of power can be extracted while the power from the overall kinetic energy of the beam is  $\sim 1.5$  kW. This results in an energy efficiency of  $\sim 10$ – $15\%$  [189]; this figure is considerably smaller ( $\sim 1\%$ ) when a high-frequency gyrotron operates at the second harmonic of the cyclotron condition (thus requiring a smaller magnetic field) [204]. This high power output is possible because a gyrotron operates as a fast-wave device with minimal power deposition in the highly-overmoded interaction cavity. Virtually all excess (waste) power is deposited within a water-cooled collector situated behind the quasi-optical mode converter. This situation is different for slow-wave devices which can also provide high frequencies, but are limited with respect to the output power because of significant power deposition within the small interaction structure (see section below).

For practical purposes, the cyclotron frequency must coincide with the Larmor frequency of the electron spins of the PA. Therefore, a second superconducting magnet of similar field strength as the NMR magnet (or an integer fraction thereof if overtones are used) is required. However, due to relativistic effects of electrons within the high-energy beam, the magnetic field of the gyrotron magnet has to be increased by  $\sim 2\%$  so that DNP matching conditions can be achieved with typical nitroxides or other radicals. There are plans to overcome this requirement for a second superconducting magnet—bearing significant cost and lab space

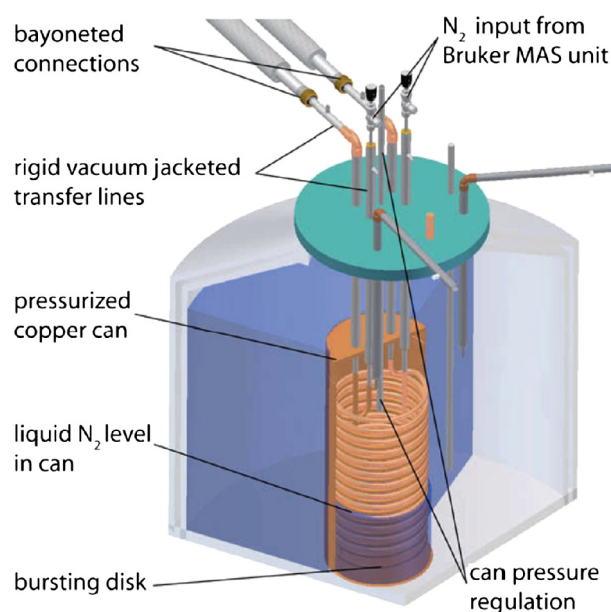


**Fig. 29.** Typical heat exchanger used for producing cold gas for sample spinning. A conventional MAS unit produces a regulated flow of gas, which is cooled to a target temperature inside a pressurized copper can. The output temperature of the cryogenic gas is controlled by the pressure of the inner can. Reprinted from [215] with permission.

burden—by a miniaturized gyrotron to be used inside a two-center magnet [205–208].

#### 4.1.2. Other sources

In addition to the above,  $\mu\text{W}$  irradiation generated by an extended interaction oscillator/klystron (EIO/EIK) [170,209], a backward wave oscillator (BWO) [206], or a solid-state source [162,163] has been employed for MAS DNP. EIKs and EIOs are linear-beam devices with high-power capability and a relatively large bandwidth that can either spontaneously generate the high-frequency  $\mu\text{W}$  field (EIOs) or amplify a low-power driving input (EIKs). In both cases, this is accomplished through interaction of the accelerated electron beam with a cavity, which can consist of a single gap (EIO) or can be constituted by multiple coupled gaps (EIK) [210]. However, the dimension of the interaction cavity of these “slow-wave” devices decreases with increasing frequency. If long life-time should be guaranteed, this restricts the achievable maximum powers.

Similar limitations are also faced in the case of BWOs. These are vacuum tube devices, where  $\mu\text{W}$  frequency oscillations are created by propagating a traveling wave backwards against the electron beam. Thus, the group velocity of the generated electromagnetic wave is opposite to the direction of the electron beam. BWOs have a broad tuning range and can in principle be operated in both cw and pulsed mode, however, output powers decrease rather quickly at frequencies higher than approximately 100 GHz [211].

Solid-state sources—which usually operate by up-conversion of a low  $\mu\text{W}$  frequency to the desired output—are robust, cheap and allow for control of the output power, frequency and phase in a simple way. Furthermore, employment of fast  $\mu\text{W}$  gating by PIN diode switches or mixers and frequency modulation by an arbitrary waveform generator (AWG) before up conversion allow the generation of simple rectangular or amplitude/frequency shaped pulses, similar to applications in modern pulsed EPR [153,162,212,213]. The major drawback is the extremely low maximum power tolerated by these solid-state devices in the range of a few tens of mW that typically requires a combination with a high-frequency amplifier based on the above-mentioned principles.

In these situations where MAS DNP enhancement factors are limited by insufficient  $\mu\text{W}$  power, lowering the experimental temperature to 20 K and below can alleviate the problem [163]. However, increasing demand by high-frequency DNP applications has already stimulated significant advances in maximum output power and frequency of these rather cheap and compact devices and further developments might make these sources viable alternatives to gyrotrons for common MAS DNP applications.

## 4.2. Control of DNP matching conditions

### 4.2.1. Magnetic field variation

A drawback of commercially available gyrotrons for DNP applications [152] is that they generate a fixed  $\mu\text{W}$  frequency. Therefore, the static external magnetic field of the NMR magnet is initially set to a certain value such that electron and nuclear Larmor frequencies are adjusted for optimum enhancement obtainable with typical nitroxide-based PAs.

A greater flexibility is obtained if the NMR magnet is equipped with an additional superconducting sweep coil. This allows for fine-tuning of the magnetic field and consequently, the matching conditions for maximum SE or CE enhancement [Eqs. (12) and (33), respectively] can be reached for other PAs as well. It is important to note that—in particular for PAs with narrow matching conditions—sweeping the field may be required to achieve (direct) DNP for different nuclei. Examples for such field-swept DNP enhancement profiles are illustrated in Section 3 as well as in Fig. 35.

Superconducting magnets with such tuning capabilities are now commercially available with fields up to 18.8 Tesla. However, the accessible field range is limited by the sustainable current limit of the sweep coil and the field can only be swept over a restricted range. Thus, the DNP conditions for certain radical–nuclei combinations may or may not be accessible depending on the type of PA (for details see Section 5) and magnet setup used. Furthermore, the sweep rate often is rather limited and temporary field instability/drift as well as changes in homogeneity following charging or discharging the sweep coil have to be considered.

### 4.2.2. Microwave frequency tunability

Accounting for these above-mentioned limitations, recently developed frequency-tunable gyrotrons have potential advantages and would simplify the experimental setup because they could alleviate the necessity for field sweepability of the NMR magnet. Rather small frequency tuning within a range of  $\sim 100$  MHz can be achieved by temperature-controlled changes in (single-mode) interaction cavity dimensions [177]. For a larger frequency range the interaction cavity has to be re-designed such that several longitudinal modes are accessible by magnetic field and/or beam voltage variation. Such devices have first been introduced for DNP operation at 460 and 330 GHz with a tuning range of up to 1.2 GHz [187,188]. However, the output power can vary significantly over the tuning range due to differences in efficiency and overlap of different interaction modes. More recently, tuning ranges of up to 3 GHz have been reported for several devices operating at frequencies between 200 and 530 GHz [189–192,195,196]. Nevertheless, such frequency tunability has barely been utilized yet in order to address varying matching conditions due to different DNP mechanisms or PAs, or for the acquisition of DNP frequency profiles under MAS [209].

### 4.2.3. Fast microwave frequency modulation

An interesting application of frequency tunability has first been demonstrated using solid-state sources under either static or MAS conditions: by modulation of the  $\mu\text{W}$  frequency in the kHz range, a significant increase in DNP enhancement was observed [161–164]. A modulation capability has henceforth been adopted for frequency-tunable gyrotrons, where variation of the beam voltage allows for fast modulation of output frequency [193].

In the context of static DNP, the effect can be easily explained by the increase of the number of directly excited spin packets within an inhomogeneously broadened EPR spectrum [161]. For MAS, the situation is more complex due to rotational evolution of the spin Hamiltonian (see Section 2.1.2) and an extended theoretical treatment of the problem still has to be developed in order to properly explain the effect.

## 4.3. Cryogenic MAS

A rigid dipolar-coupled spin network and sufficiently long electron and nuclear spin relaxation times are prerequisites for high DNP enhancements. Thus, typical MAS DNP of biomolecular samples or surface-wetted materials generally require cryogenic temperatures between 20 K [163] and 180 K [214]. The region between  $\sim 100$  and 180 K can rather easily be achieved with commercial instrumentation and liquid nitrogen ( $\text{LN}_2$ ) as cryogen. Custom instrumentation with optimized thermal insulation can reach temperatures as low as 80 K [215,216]. For even lower temperatures, cooling with liquid Helium (LHe) is necessary [170,178,217]. In both cases the liquid cryogens are also often used for *in-situ* generation of very pure MAS gas by evaporation.

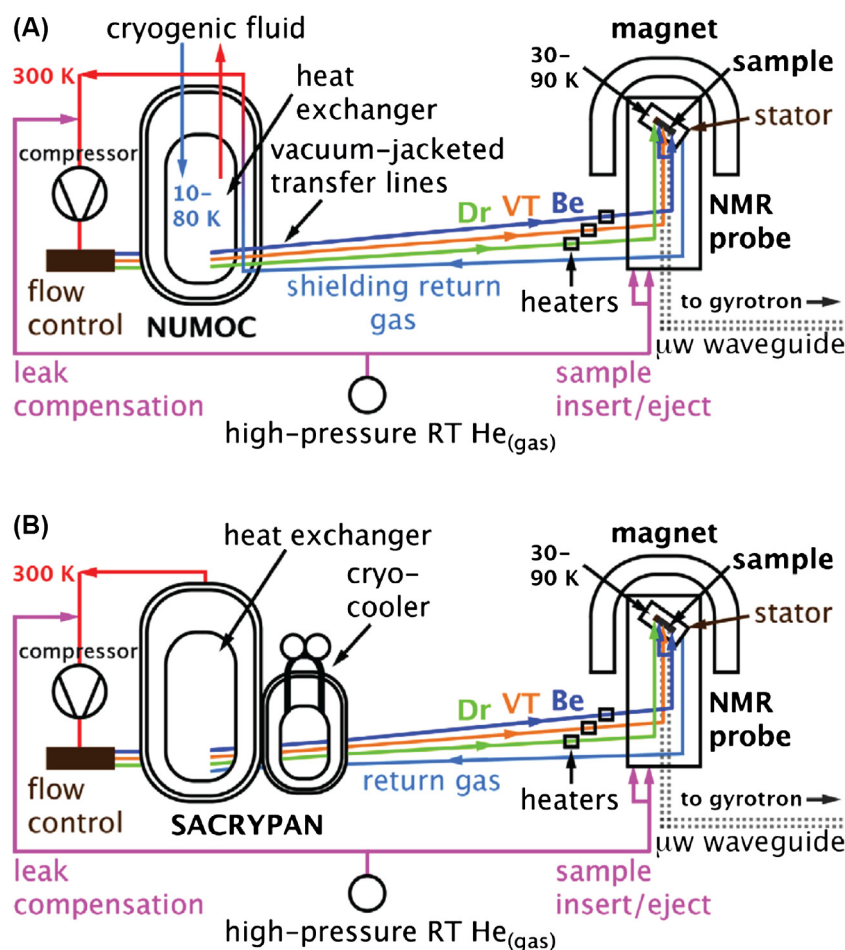


**Fig. 30.** Schematic drawing of a closed-loop system for helium- or  $N_2$ -cooled MAS with cooling by (A) cryogenic fluid (LHe or  $LN_2$ ) or (B) a cryo-cooler. Reprinted from [217] with permission.

#### 4.3.1. Nitrogen cooling

Several engineering challenges have been mastered to provide stable MAS with cryogenic gas, specifically nitrogen at favorable temperatures close to the liquefaction point [152,215]. A steady flow for each of the cold spinner gases (*i.e.*, bearing and drive with a gas flow in the order of 50–100 l/h [152]) has to be produced by external heat exchangers, which can be regulated according to the required spinning frequencies and sample temperature. A “coil-in-can design” has proven very effective for providing long-term stability and preventing liquefaction of the spinner gas to avoid major spinning instabilities [184,215]. This design relies on the spinner gas flowing through a coiled copper tube that is situated within a pressurized copper-can submerged in  $LN_2$  (see Fig. 29). By externally adjusting the pressure of  $N_2$  gas inside the can, the liquid level and thus the contact surface and heat transfer rate between coil and  $LN_2$  can be controlled. In early designs, both spinner gas lines were cooled within one can; more recent designs feature separate cans for bearing, drive and variable temperature (VT) gas lines, allowing for greater adjustability. Vacuum jacketed transfer lines then transport the cold gases to the DNP probe, entering the sample chamber either through the probe body, or from the top of the vertical magnet bore.

Use of  $LN_2$  for MAS feed gases (boil-off) and for cooling thereof results in significant costs of operation. In total, the consumption of  $LN_2$  adds up to several hundreds of liters per day for a typical setup described above. Recently, it has been shown that consumption of  $LN_2$  can be dramatically reduced by utilization of nitrogen generators and refrigerators [183,184].

#### 4.3.2. Helium cooling

Further reduction of the sample temperature can be desirable for increase in DNP enhancement, especially when available  $\mu w$  power is limited (see also Section 6.2.4). This can be achieved by using Helium as spinner gas for MAS [91,178,217,218]. In particular, due to the large running-costs associated with LHe, a low-consumption design is essential. For example, the return gas can be recycled in a closed-circle setup as shown in Fig. 30 [178,219].

Alternatively, LHe boil-off can be directly used to selectively cool the sample with the VT line, while MAS operation is provided with RT or precooled gas [170,220]. In this design, a rotor material with low thermal conductivity such as  $ZrO_2$  allows for anchoring the (axially) outer regions of the rotor at room temperature by the bearing and drive gas while the central region—separated from the bearing spaces by baffles—is cooled down to 20 K. However, this low temperature can only be reached if extra-long rotors are used so that the temperature gradient between bearing and sample region is reduced. Furthermore, recycling of the cost-expensive helium is not possible in this case.

#### 4.3.3. Fast MAS and cryogenic temperatures

Due to the increasing viscosity of  $N_2$  as temperatures approach the liquefaction point, maximum MAS rates are significantly reduced as compared to conventional MAS NMR experiments with room temperature gas. Originally, the instrumentation for cryogenic MAS has been developed for rotor diameters between 2.5 and 7 mm [91,184,215,218,221]. In these cases, spinning rates were limited to  $\sim 15$  kHz.

With the advent of fast MAS applications and  $^1\text{H}$  detection, fast-spinning MAS DNP probes have recently become available. This extended the available spinning frequencies up to 40 kHz at 100 K by using smaller diameter rotors (1.3 mm), allowing not only for mechanistic investigations of DNP under these conditions (see also Section 6.2.2) but also for higher sensitivity and resolution [86].

#### 4.4. DNP NMR probe and microwave transmission

##### 4.4.1. Cryogenic probe design

In addition to conventional solid-state NMR functionality, DNP probes have to be designed to account for  $\mu\text{W}$  transmission and

cryogenic MAS. The latter requires an air dielectric transmission line rf circuit design [222]. This allows for removing the tuning and matching elements from the cold rf coil and positioning of those within the probe box that is ideally stabilized at room temperature [215].

The large temperature gradient within the probe is typically sustained by incorporation of thermally insulated transfer lines for cold MAS gas as well as a VT line for additional sample cooling capacity. In order to prevent significant temperature reduction and subsequent condensation of humidity within the probe body, the exhaust line has to be thermally insulated as well; the cold exhaust can be used to pre-cool MAS/VT feed gases in order to reduce cryogen consumption [217]. Insulation can be provided by vacuum

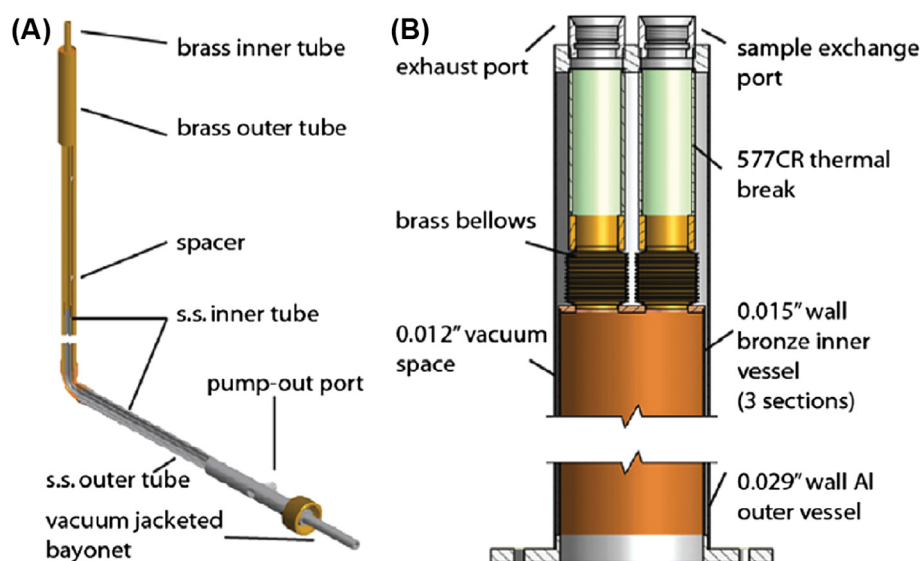


Fig. 31. (A) Model for the vacuum-jacketed, thermally insulated transfer lines inside the probe. Brass tubing is used for durable vacuum retention. (B) A vacuum-jacketed Dewar is incorporated with a sample exchange port and an exhaust port. Fiberglass and brass bellows act as thermal breaks. Reprinted from [184] with permission.

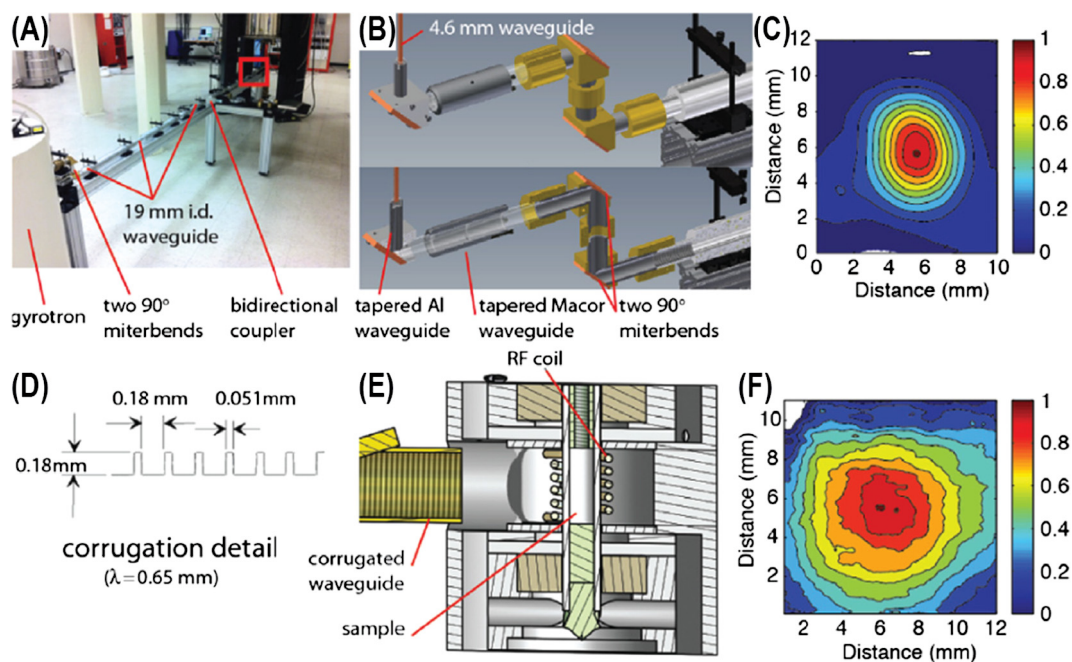
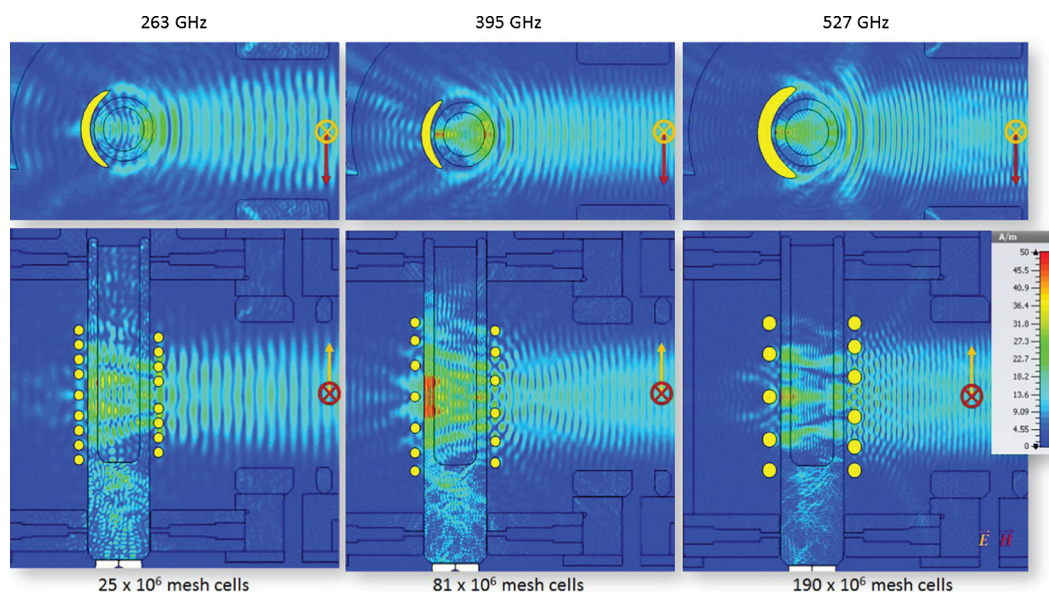
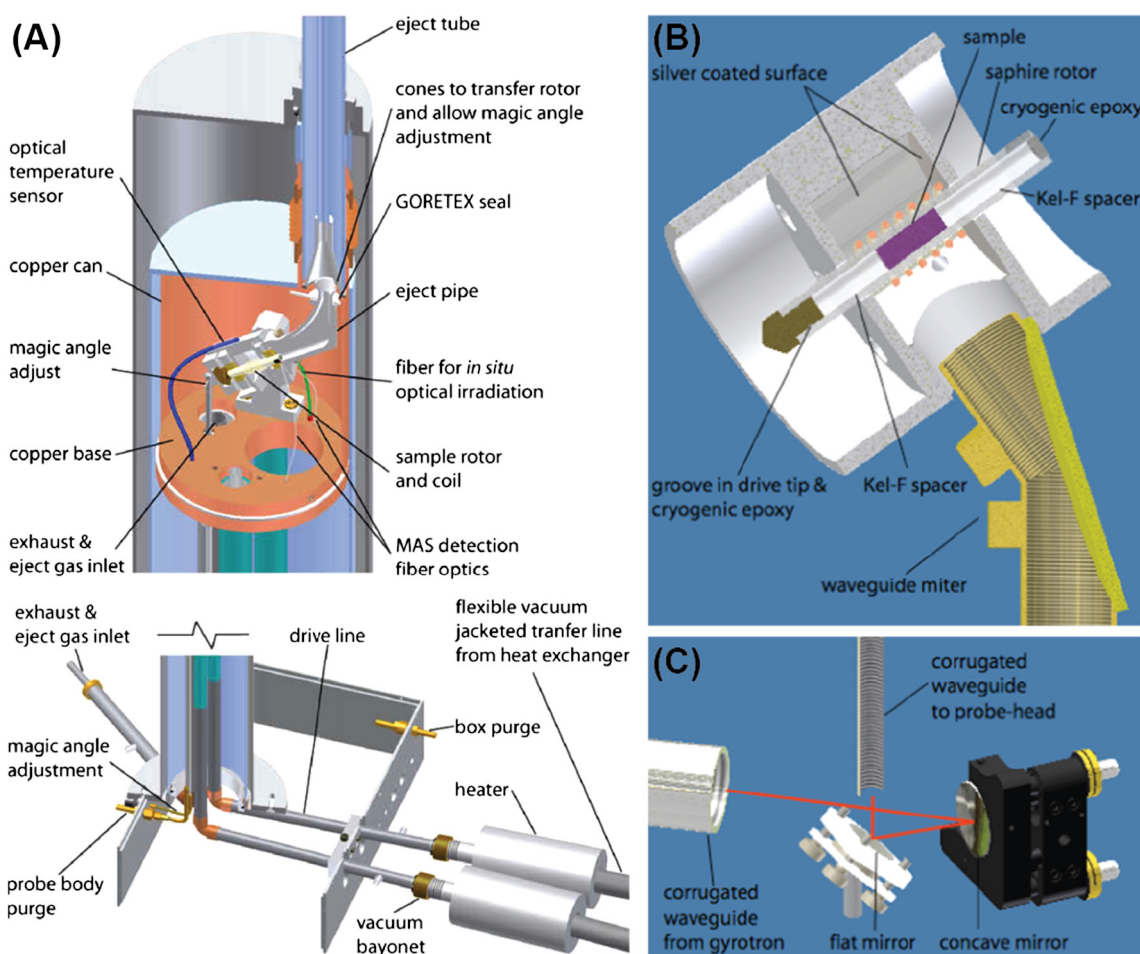


Fig. 32. (A) Photograph of the  $\mu\text{W}$  transmission line of a typical DNP setup. (B) Model of tapers and miter bends that are used to focus the microwave beam into the vertical waveguide leading to the stator. (C) Thermal image of the microwave beam in the middle of the wave guide. (D) Schematic drawing of the corrugations. Depth and spacing fulfil the  $\lambda/4$  condition. (E) Cross-section of the stator with the end of the waveguide directing the  $\mu\text{W}$  irradiation on the rotor. (F) Image of the beam leaving the wave guide towards the sample. Reprinted from [184] with permission.



**Fig. 33.** Simulated  $\mu\text{W}$  magnetic field magnitude distribution inside the coil of a 3.2 mM MAS probe at 263, 395 and 527 GHz. The microwave beam enters from the right side. Rows show views along the rotor axis (top) and in a plane perpendicular to this axis (bottom). Reprinted from [152] with permission.



**Fig. 34.** (A) Schematic drawing of a MAS DNP probe with possibility for *in-situ* optical irradiation. Further modifications to standard MAS NMR functionality are the angled eject tube for convenient cryogenic sample (un-)loading. (B) Enlarged view of the corrugated waveguide that transmits  $\mu\text{W}$  irradiation to the sample. (C) Quasi-optical system of mirrors delivers the microwaves from the gyrotron towards the stator. Reprinted from [215] with permission.

jacketing of coaxial tubes and employing materials with small thermal conductivity. Stainless steel fulfils these criteria, however, even “non-magnetic” austenitic steel alloys (e.g., 316, 321 series) tend to magnetize due to mechanical stress and repeated temperature cycling [215]. Therefore, stainless steel should not be used near to the homogeneous region of the magnetic field (i.e., the sweet spot). Fiberglass can be an alternative, but brass has proven superior vacuum retention properties as well as durability and can be easily soldered to the stainless-steel section of the transfer lines; in the same vein bronze has successfully been used for construction of the cryostat that shields the magnet bore from the cryogenic temperatures [184]. Such a design is shown in Fig. 31.

Additionally, a thermal break is incorporated within the electrically and thermally well-conducting copper transmission line. A section of stainless steel near the probe body can serve as such, but reduction of electrical conductivity of this part of the resonant circuit and subsequent loss of rf efficiency has to be compensated by a non-magnetic silver/gold plating with thickness on the order of the rf penetration depth [215].

4.4.2. Microwave transmission from source to sample

Usually, the  $\mu\text{w}$  beam is converted from its initial higher mode generated inside the gyrotron interaction cavity to a Gaussian mode of propagation by the use of a quasi-optical mode converter typically consisting of a Vlasov antenna [189,194]. The Gaussian beam then exits the gyrotron tube via a sapphire window optimized in thickness for minimal reflection losses and is guided into an overmoded circular waveguide for transmission in an  $\text{HE}_{11}$  mode (Fig. 32A). Due to the excellent coupling between a Gaussian beam propagating in free space and this hybrid mode propagating inside an overmoded waveguide, negligible insertion losses occur even in the absence of special coupling elements such as horns, given that the beam width is significantly smaller than the inner diameter of the waveguide. Corrugation of the inner waveguide surface further minimizes transmission losses so that  $<0.1 \text{ dB m}^{-1}$  attenuation [223] can be achieved (Fig. 32D); however, care has to be taken for good alignment of the waveguide. Miter bends are used for changes in propagation direction, for example for adjustment between differences in the gyrotron output window and the probe input port orientation, or if vertical level changes have to be accounted for.

Alternatively, also quasi-optical systems of transmission have been developed for DNP. These feature the advantage of extremely low transmission losses and simple manipulation of the  $\mu\text{w}$  polarization properties by a Martin-Puplett interferometer that can be utilized to increase power efficiency of spin excitation and larger DNP enhancements for a given output power [224]. However, due to the rather long wavelengths in the 0.6–2 mm range, the angular spread of the  $\mu\text{w}$  beam is significant. This requires a significant number of parabolic mirrors with large diameter and relatively short focal lengths so that the  $\mu\text{w}$  beam can be transmitted efficiently over the necessary distance [194]. Therefore, such a system can only be employed if space is not a limiting factor.

The  $\mu\text{w}$  beam enters the probe via one of the above-mentioned paths. Due to the space restriction within the longitudinal bore of the superconducting magnet, an efficient design can be achieved by utilizing the hollow inner conductor of the coaxial rf waveguide of the transmission line probe as the circular overmoded  $\mu\text{w}$  waveguide. Since this conductor is part of the rf resonant circuit, care has to be taken to provide electrical isolation between the externally connected end of the waveguide and the rf transmission line, for example by quasi-optical coupling between the elements [215]. Alternatively, the  $\mu\text{w}$  beam can also be coupled to the DNP probe from the top of the bore [194].

4.4.3. Inside the sample chamber

4.4.3.1. Microwave irradiation of the sample. In a typical design, a miter bend in close vicinity of the MAS stator changes the direction of propagation such that the  $\mu\text{w}$  beam is launched orthogonally to the rotor axis. The waveguide is terminated shortly before reaching the rf coil (Fig. 32E). As shown in Fig. 33, the wave fronts are significantly diffracted (and reflected) due to the rf coil featuring a pitch of similar magnitude as the wavelength. This can create a non-uniform distribution of the  $\mu\text{w}$  field amplitude and induce phase shifts across the sample.

The dielectric properties of typically used sapphire rotors improve the  $\mu\text{w}$ -field filling factor; at the same time MAS leads to a partial averaging of angular field inhomogeneity. Nevertheless, a field inhomogeneity with an amplitude variation of a factor  $\sim 3$

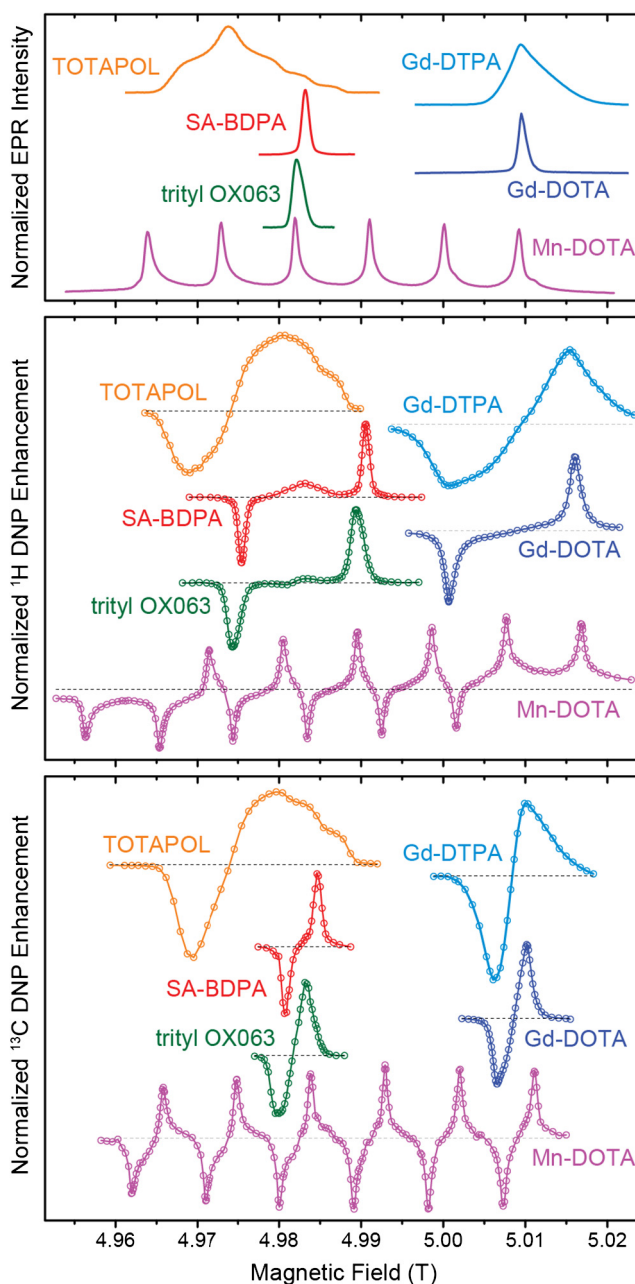


Fig. 35. Comparison of the EPR lineshapes and the corresponding  $^1\text{H}$  and  $^{13}\text{C}$  DNP field profiles of different PAs. Figure taken with permission from [139].

has to be accounted for [87]. Furthermore, thermal conductivity of sapphire is similar to that of copper at temperatures of around 100 K, which ensures efficient dissipation of heat deposited by dielectric losses within the sample during  $\mu\text{W}$  irradiation. Rotors made of  $\text{ZrO}_2$ —which are generally more robust and less expensive—have less favorable transmission/reflection properties at  $\mu\text{W}$  frequencies as well as lower thermal conductivity, so that reduced enhancement factors and increased sample heating is observed [177].

Efforts have been taken to improve the conversion factor (*i.e.*, the ratio between incident  $\mu\text{W}$  power and generated field amplitude) within the framework of an MAS stator, for example by addition of an astigmatic lens optimized for the cylindrical rotor shape [87], or by reflective coating of the inner stator surface so that a significant Q factor increase could be achieved [215]. Also, varying the rf coil pitch with larger separations in the central section has been tried in order to minimize diffraction interference [152]. Alternative approaches employ  $\mu\text{W}$  irradiation of the sample along the spinning axis [91,183,194]. Such a design does not require modification of a commercially available stator, prevents diffraction by the coil and potentially improves power conversion and irradiation efficiency, for example, by providing a reflective surface at the far end of the sample chamber [91]. However, in such a design, the presence of the waveguide or quasi-optical mirrors along the rotor axis introduces additional problems regarding sample ejection.

**4.4.3.2. Sample changing: injection and ejection of rotors.** Due to operation under cryogenic conditions, removal of the cold probe from the cryostat for access to the stator requires exposure to ambient environment. This in turn necessitates a full temperature cycling of the probe to room temperature and back to  $\sim 100$  K in order to remove any condensation. This procedure is not only time-consuming but also introduces the possibility of failure due to handling or thermomechanical wear. Therefore, modern DNP probes are usually equipped with a semi-automatic sample inject/eject system.

A model developed by the Griffin group at MIT is shown in Fig. 34 [215]. This design has been adapted by Bruker in their commercial instruments [177]. The rotor is injected either from the top of the bore or through the bottom of the probe and is pneumatically driven in and out of the stator by controlled pressure bursts of nitrogen gas. This greatly eases experiments, especially when a large number of samples is involved, such as for systematic investigations of optimal DNP conditions, or when screening sample-composition dependent parameters [225]. Under certain conditions it is also possible to inject pre-cooled rotors containing temperature-sensitive samples [177].

**4.4.3.3. Light-activation.** For the investigation of photo-activated processes, the DNP probe can be modified with a light irradiation channel (Fig. 34). This is typically achieved by introduction of an optical fiber that connects to a laser system outside the probe

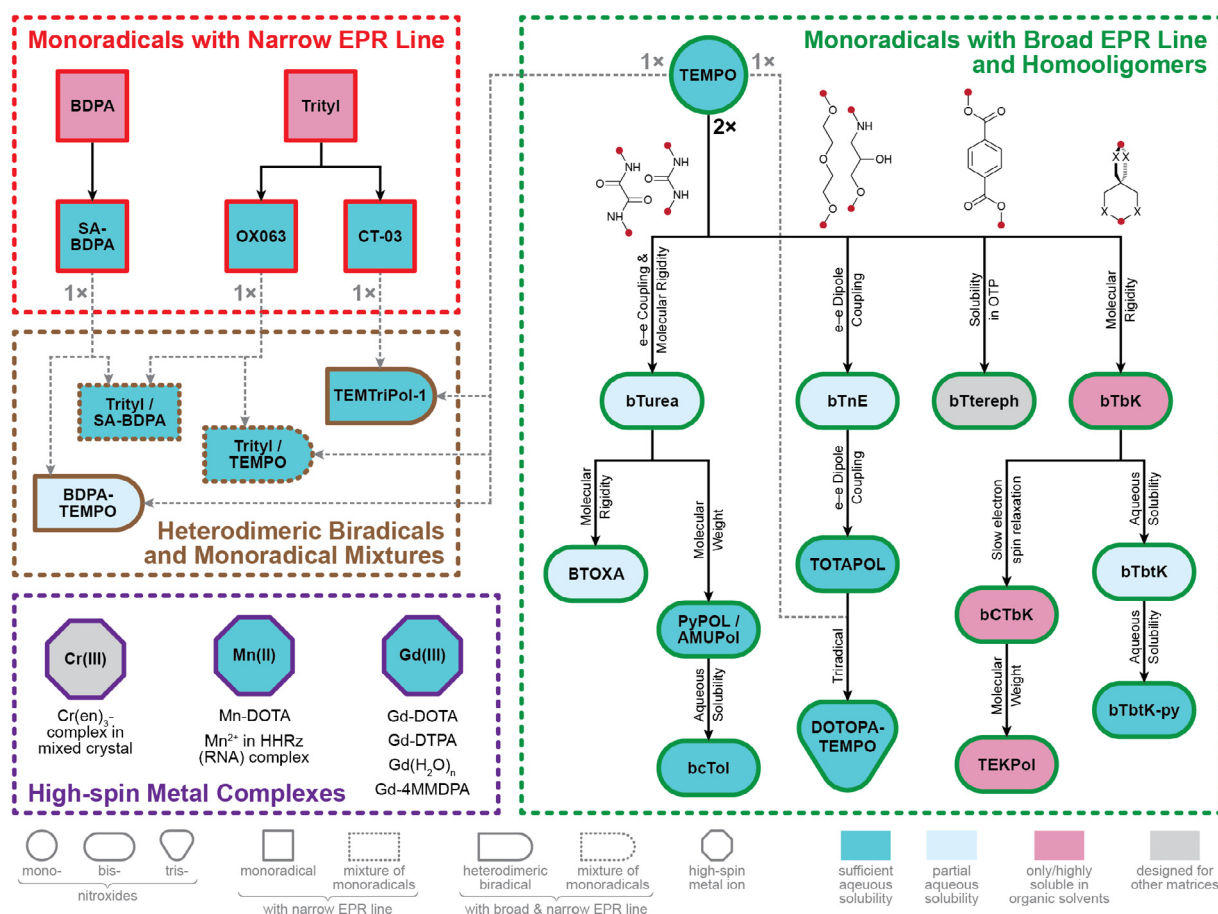


**Fig. 36.** Overview of the development of PAs for MAS DNP. The shape of the boxes encodes radical type, the number of unpaired electrons per PA molecule and distinguishes between narrow and wide EPR lineshapes; solubility of the individual families is color coded; for details see figure legend. Factors accompanying dashed arrows indicate the number and type of monoradicals that are chemically bonded to form bi- and triradicals. Chemical structures show molecular tethers connecting the TEMPO moieties at the positions indicated in red.



and is terminated inside the MAS stator. Such modifications have been employed, for example, to study temperature-trapped states within the photo-cycle of membrane proteins of the rhodopsin-family, such as bacteriorhodopsin [226,227] or channelrhodopsin [228]. For more details of these applications see Section 7.2.2.

## 5. Polarizing agents

DNP requires the presence of unpaired electrons in the form of free radicals or metal ions with an open d- or f-shell in order to enhance NMR signals by transferring polarization from electron spins to the nearby nuclear spins [229]. Therefore, such PAs play a very important role for DNP. Most commonly, PAs are exogenous (e.g., small paramagnetic molecules such as mono- or biradicals) which are added to the system (usually by dissolving the sample in—or impregnating it with—a radical-containing, glass-forming cryoprotecting mixture, see Section 6.3). Recently, endogenous PAs have come into focus, where stable radicals or paramagnetic metal ions are present in the analyte molecule [92,140]. This is further described in Section 6.3.4.

Generally, PAs are evaluated based on several parameters, as their efficiency is influenced by the solubility, concentration and electron spin properties at experimental temperatures. As illustrated in Fig. 35, the DNP mechanism evoked by PAs depends on several factors such as the homogeneous linewidth ( $\delta$ ) as well as the inhomogeneous breadth ( $\Delta$ ) of the EPR spectrum, its g-anisotropy, and the nuclear Larmor frequency ( $\omega_{0f}$ ). The development and design of new PAs for proficient DNP mechanisms under MAS and high magnetic field are growing areas of research.

In the following section, we describe different PAs used mainly for MAS DNP by exploiting SE and CE. In the case of the latter mechanism, we classify the PAs into two main classes: monomeric radicals (including mixtures thereof) as well as homo- and heterodimeric biradicals. Then, we will review the utilization of metal ions that can give rise to both SE and CE. Fig. 36 shows an overview of the developments in the design of PAs discussed in detail in this section.

### 5.1. Radicals with narrow EPR line for solid effect DNP

In order to satisfy the requirements for SE, PAs with a small homogeneous EPR linewidth ( $\delta$ ) and inhomogeneous breadth ( $\Delta$ ) in relation to the nuclear Larmor frequency (i.e.,  $\delta, \Delta < 2\omega_{0f}$ ) are considered. As already laid out in Section 2.2.1.5, excessive inhomogeneous or homogeneous broadening leads to differential SE with starkly reduced net enhancement.

At high magnetic fields, this limits the choice of suitable PAs due to the dominant Zeeman interaction, thus excluding the use of any radicals featuring significant g-anisotropy. To date, applications of MAS DNP using SE at high magnetic field ( $B_0 \geq 5$  T) have mostly been performed with two exogenous PA types, namely BDPA and trityl. Therefore, we will limit the description to these systems. Furthermore, a reduced flavin mononucleotide (FMN) semiquinone has been used in a single study as endogenous PA; this system will be discussed in Section 6.3.4.

#### 5.1.1. BDPA-type radicals

1,3-bisdiphenylene-2-phenyl allyl (BDPA, for chemical structure see Fig. 37) [230] was the first stable radical PA utilized for

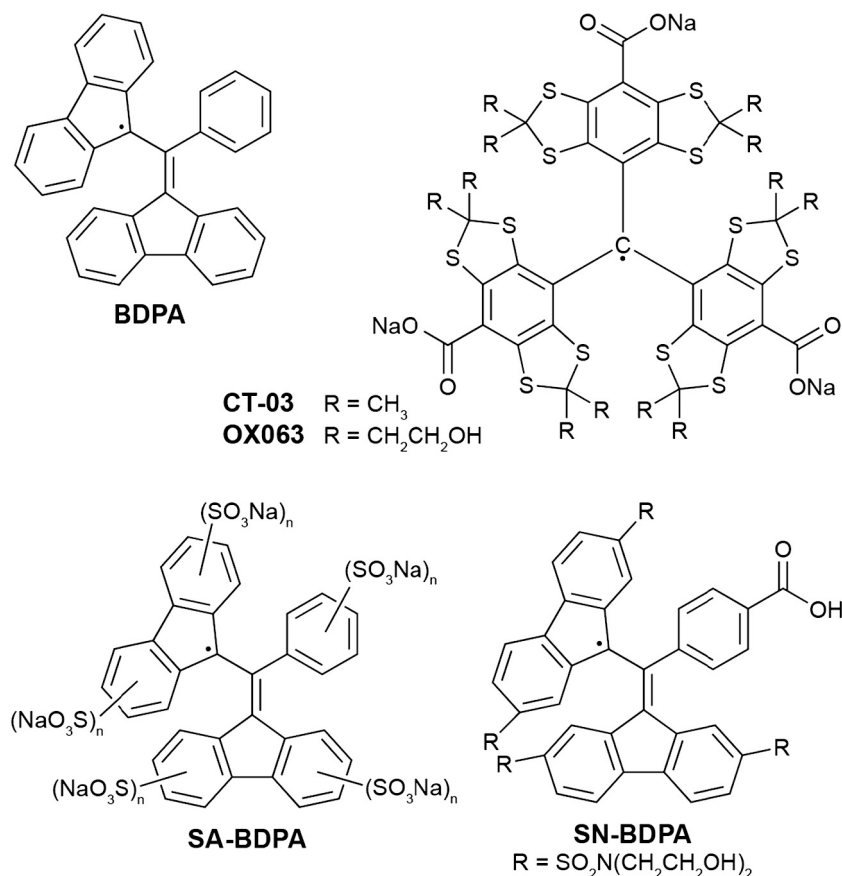


Fig. 37. Chemical structures of BDPA [230], its sulfonated (SA-BDPA) and sulfonamide (SN-BDPA) derivatives [89] and trityl-type radicals OX063 and CT-03 (the latter is also known as Finland trityl) [233,234].

DNP under MAS [63,91,231]. Its narrow EPR line width of 20 MHz [173,232] is caused by inhomogeneously broadening due to the HFI with the 21 protons on the aromatic rings. This width is maintained over a large external magnetic field range; only at a field of 9.4 T and higher, the  $g$ -anisotropy broadening becomes of similar magnitude [90]. The high chemical stability and ease of dilution in polystyrene makes BDPA an ideal sample for calibration purposes [63,91]. Even though BDPA is an excellent PA, its biological applications are limited due to its lack of solubility in aqueous mixtures.

Haze et al. expanded the potential biological applications of BDPA by synthesizing a highly water-soluble and air-stable derivative, sulfonated-BDPA (SA-BDPA) [89]. It has a narrow EPR line-width similar to BDPA, which makes SA-BDPA a very efficient PA for SE DNP. In the same study, a sulfonamide derivative (SN-BDPA) was introduced as well, which allows for highly modular chemical variability. In a 40 mM frozen solution of SA-BDPA in  $d_8$ -glycerol/ $D_2O/H_2O$ , a  $^1H$  enhancement factor of 110 was obtained for MAS experiments. The SE performance is slightly better as compared to trityl OX063 (see below), however, the slow electron spin-lattice relaxation ( $T_{1S} = 56$  ms at 80 K and 5 T) may cause saturation at moderate  $\mu W$  power [89]. This tendency of saturation in combination with the large number of HFI-coupled  $^1H$  spins in BDPA (and its derivatives) give rise to OE DNP in insulating solids as we have laid out in Sections 2.1.3 and 3.2.3.

### 5.1.2. Trityl-type radicals

A highly prominent group of water-soluble PAs with narrow EPR line width is based on triphenylmethyl (trityl) radical also known as triarylmethyl (TAM) radical (see Fig. 37). Towards the end of the 1990s, Ardenkjær-Larsen et al. investigated such radicals as probes for EPR oximetry. The requirements for good sensitivity towards oxygen-induced line broadening included high chemical stability, water solubility, narrow EPR spectra as well as an inherently small inhomogeneous linewidth [233].

One resulting trityl derivative, OX063, fulfils these requirements to a very large degree and shows efficient SE [233]. In OX063, all aromatic hydrogens are replaced by hydrophilic functional groups, providing not only chemical stability by steric hindrance and water-solubility but also removing the relatively large isotropic HFI. In contrast to another prominent trityl derivative, Finland trityl CT-03 [234], OX063 does not contain relaxation-promoting methyl groups, which alleviates the need for deuteration in order to reduce the homogeneous EPR linewidth [235]. The inhomogeneous linewidth of OX063 in frozen solution is  $\sim 50$  MHz (FWHM) at 5 T, and it scales linearly with the external field strength since the  $g$ -anisotropy is the major cause of broadening at high magnetic fields [139].

OX063 is a versatile PA for MAS, yielding a  $^1H$  enhancement factor of up to 91 (with a linear dependence on the  $\mu W$  power) [74]. The spin-lattice relaxation time is sufficiently fast ( $T_{1S} = 1.3$  ms at 80 K and 5 T), thus significant EPR saturation is avoided during SE DNP [74,77,89]; it has also been demonstrated as a powerful PA for DNP of nuclei with small gyromagnetic ratios such as  $^2H$  ( $\epsilon \geq 700$ ) [147],  $^{13}C$  ( $\epsilon = 480$ ) [82] and  $^{17}O$  ( $\epsilon \approx 115$ ) [236]. In all these latter cases, OX063 is the most efficient PA studied so far. This is explained by the fact that the EPR linewidth is of a similar magnitude as the nuclear Larmor frequencies, in fact allowing for CE to be efficient (see below).

Besides these applications as PA for MAS DNP, trityl OX063 is popular for its pivotal role in dissolution DNP [237]. Here, trityl greatly outperforms nitroxides when  $^{13}C$  is directly hyperpolarized within neat, amorphous pyruvic acid (doped with OX063) [238]. OX063 has been patented and is the sole approved PA for the commercial HyperSense dissolution DNP system [239]. In that context, two carbon centered perchloro-triphenylmethyl (chlorinated

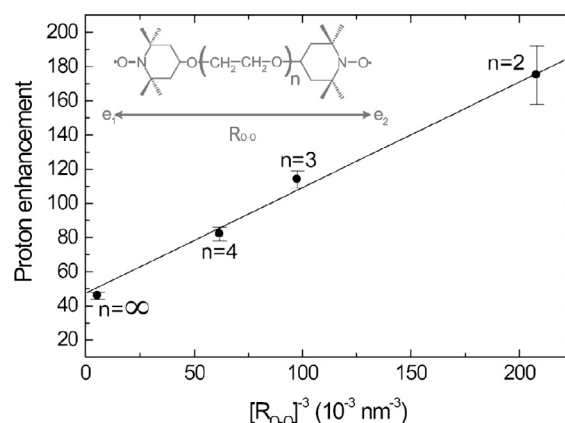


Fig. 38.  $^1H$  DNP enhancement factors in the bTnE series as a function of e–e dipole coupling. The inset shows the chemical structure of bTnE. Figure reprinted with permission from [254].

trityl) radicals aimed for dissolution DNP have been investigated [240]. The authors observed unexpected behavior including an inversion of enhanced NMR signals that was tentatively ascribed to hetero-nuclear effects due to the presence of magnetically active  $^{35}Cl$  and  $^{37}Cl$  nuclei (both  $I = 3/2$  with significant nuclear quadrupole interactions) within the PA. Further reports on such hetero-nuclear assisted DNP effects—where a  $^{35/37}Cl$ - $^{13}C$  transfer pathway has been postulated—are not conclusive [241].

### 5.2. Nitroxides and biradicals for cross effect DNP

So far, CE has been proven the most efficient polarization-transfer mechanism in DNP and is widely applied to materials and biological systems at high magnetic fields ( $>5$  T). It dominates over other potential mechanisms when the inhomogeneously broadened EPR linewidth (e.g., due to  $g$ -tensor anisotropy) is larger than the nuclear Larmor frequency (i.e.,  $\Delta > \omega_{0I} > \delta$ ). As described in Section 2.1.2, the CE is a three-spin process that requires significant dipolar coupling between the two electrons, which therefore have to be in close spatial relationship (generally at a distance  $< 25$  Å) [242,243]. This requirement can be fulfilled in two ways. On the one hand, a sufficiently high concentration of monomeric radicals eventually leads to intermolecular spatial proximity. On the other hand, two (or more) radical moieties interconnected by a molecular linker of particular length enable CE.

Besides the necessity of sufficient e–e coupling, the separation of the EPR resonance frequencies of the two electron spins has to match the nuclear Larmor frequency (i.e.,  $|\omega_{S,1} - \omega_{S,2}| = \omega_{0I}$ ). Therefore, the CE performance of individual (bis-)nitroxide radicals is strongly orientation-dependent because the Larmor frequency of the electron spin is dominated by the anisotropic  $g$ -tensor at high magnetic fields [244,245]. This anisotropy is the reason that the EPR frequency separation scales linearly with the external magnetic field and thus also with the nuclear Larmor frequency. This, on the other hand, ensures that the CE matching condition can be fulfilled at practically any NMR frequency or field.

Further advantages of these radicals are their solubility in aqueous or organic media (depending on the type of nitroxide used) and their chemical stability under a wide range of conditions [244]. Furthermore, nitroxides are extensively used for spin-labeling purposes and are therefore offered in a large variety of derivatives tailored for different applications and conditions [246–249].

Another important parameter for efficient CE DNP is electron-spin relaxation. Both, the spin-lattice relaxation time ( $T_{1S}$ ) and electron spin-spin relaxation time ( $T_{2S}$ ), play an important role in

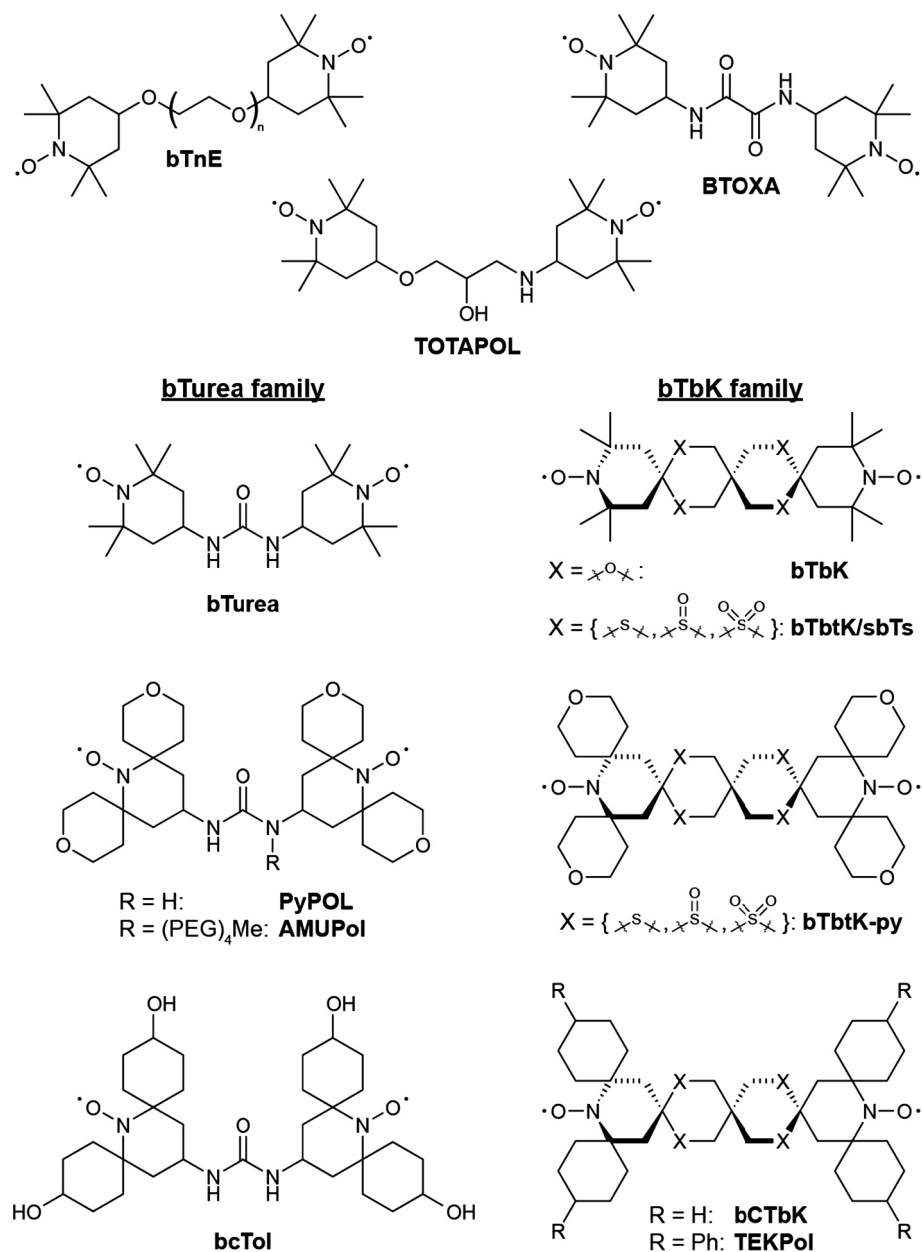


**Fig. 39.** Chemical structures of several bis-nitroxide PAs. See text for details and original publications where these PAs were introduced.

saturation of the EPR transition and excitation of CE under  $\mu\text{W}$  irradiation [81,250]. The electronic relaxation-time constants strongly depend on the molecular mass and polarity of the solvent, which has to be considered during PA design [251]. Systematic attempts to improve these parameters are further elaborated in the following sections.

### 5.2.1. Monomeric radicals

As we have laid out in Section 3.2.2, the first DNP experiments evoking the CE were reported in the early stages of DNP by Hwang et al. They described the CE in polystyrene doped with diphenylpicryl-hydrazyl (DPPH), galvinoxyl and Ley's radical [59,60]. In 1976, Wollan explained the theory of CE with  $^1\text{H}$  DNP experiments on erbium-doped yttrium ethyl sulfate (YES:Er) [61,62]. However, biological samples cannot be doped with these radicals for DNP, as they are typically prepared in aqueous media. Griffin and co-workers first utilized the nitroxide radical TEMPO (2,2,6,6-tetramethyl-1-piperidiny-1-oxyl) dissolved in glycerol/water (60/40 vol%)

solution and enhanced the  $^1\text{H}$  signals of glycine 185-fold at 5 T and 14 K [181]. It was also shown that large enhancements were obtained with 40 mM TEMPO concentration, demonstrated on the amino acid arginine and the 18.7 kD protein T4-lysozyme in MAS experiments [218]. Even though reasonable enhancement factors were obtained with these monomeric radicals, the high radical concentrations required can lead to paramagnetic quenching and line broadening in NMR spectra [225,252,253].

### 5.2.2. Nitroxide biradicals (and higher oligoradicals)

**5.2.2.1. The advent of bis-nitroxide PAs: BTnE and TOTAPOL.** Biradicals were introduced by Griffin, Swager and co-workers at MIT in order to reduce the required radical concentration and to improve the efficiency of CE by providing sufficient intramolecular e-e dipolar coupling. By the interconnection of two TEMPO molecules using di-, tri-, or tetra-ethylene glycol chains—yielding a series of bis-TEMPO-n-ethyleneglycol (BTnE) biradicals—Hu et al. demonstrated that the size of the e-e dipolar coupling

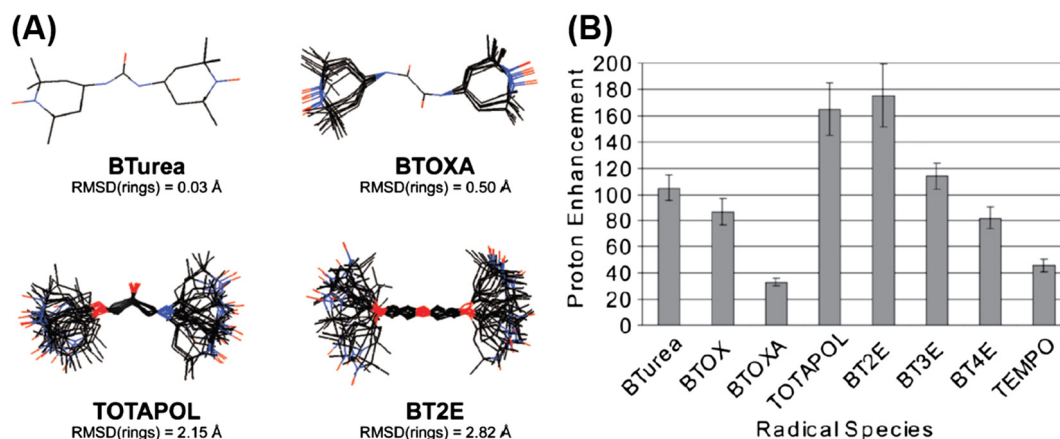


**Fig. 40.** (A) Structures of bTurea, BTOXA, TOTAPOL, and BT2E, refined using geometrical constraints obtained from EPR lineshapes, with given root-mean-square deviations (RMSD) for the atoms of the TEMPO rings. Reprinted from [244] with permission. (B)  $^1\text{H}$  DNP enhancement factors of several PAs (10 mM in electron spin concentration each) in standard solutions (2 M  $^{13}\text{C}$ -urea, 60/30/10 (w/w/w)  $\text{d}_6$ -DMSO/ $\text{D}_2\text{O}$ / $\text{H}_2\text{O}$ ) at 90 K and 5 T. Figure reprinted from [229] with permission.

directly affects the CE mechanism [see Fig. 38, also see Eq. (36) and Section 2.1.2.3]. However, those radicals were insoluble in a glycerol/water solution required for biomolecular studies [254].

This issue was overcome by the introduction of the water-soluble biradical 1-(TEMPO-4-oxy)-3-(TEMPO-4-amino)propan-2-ol (TOTAPOL), which was a milestone for the development of exogenous PAs in solid-state DNP NMR [221]. It has the ability to dissolve in aqueous media containing salt and glycerol and is highly stable at room temperature. Outstanding signal enhancements were obtained with TOTAPOL which is one of the most commonly used exogenous PAs for solid-state materials and biological systems to date [143,209,255–263].

**5.2.2.2. Tri-radicals and higher: the DOTOPA series.** In 2010, Thurber et al. introduced a new triradical DOTOPA-TEMPO. By increasing the number of nitroxide functionalities per molecule, the larger number of close e–e contacts suggest a higher probability of CE matching. The DNP performance of DOTOPA-TEMPO was compared with 4-amino TEMPO and TOTAPOL; even though large enhancements for  $^1\text{H}$  NMR signals of proteins in frozen glycerol/water solutions were observed in static samples with low  $\mu\text{W}$ -power, DOTOPA-TEMPO is less soluble in water [163]. Later on, the same group synthesized DOTOPA-TEMPO-based oligo triradicals, as well as nitroxide-based biradical and tetradical compounds; these radicals varied in e–e distances,  $T_{1S}$ , relative orientations of nitroxide groups and solubility. Among them, DOTOPA-TEMPO-based triradicals showed better water solubility and indirect DNP enhancement factors ( $\epsilon = 92$ –128) for  $^{15}\text{N}$ ,  $^{13}\text{C}$ -labeled melittin tetramer in partially protonated glycerol/water at 30 mM total nitroxide concentration. The experiments were performed under MAS in a temperature range of 25–30 K at 9.4 T and with an output  $\mu\text{W}$  power of approximately 0.8 W. The triradicals satisfied the requirements for CE, while tetradicals showed lower enhancements because of the poor solubility and longer e–e distances than the triradical, as well as rapid electronic spectral diffusion [264].

**5.2.2.3. Rigidity of the linker: bTurea, BTOXA, and the bTbK series.** In TOTAPOL, two TEMPO moieties are linked with a propan-2-ol group that is flexible and can adopt many molecular orientations (see Fig. 40A). In early attempts to shorten the tether, and also to study a more rigid alignment of the two nitroxides, Hu et al. introduced two novel linker groups, resulting in bis-TEMPO-urea (bTurea) and bis-TEMPO-oxalyl amide (BTOXA) [244]. Both biradicals failed to generate enhancement factors that can approach

those obtained with TOTAPOL or BT2E; in particular, BTOXA yielded virtually equal performance as TEMPO monoradicals. This was tentatively attributed to the possibility that the dipole coupling was too large in combination with an unfavorable mutual orientation, especially in the case of BTOXA where the two nitroxide  $g$ -tensor frames are almost collinear. A comparison of the enhancement factors obtained with the above PAs is shown in Fig. 40B.

At that point, in the first decade of the 2000s, PA design efforts were guided by the prediction that the ideal mutual orientation of two nitroxides for optimal CE matching efficiency were such that the  $x$ -axes of the  $g$ -tensor eigenframes of the two electron spins would have to be collinear, but that their  $z$ - and  $y$ -axes would have to be rotated by  $90^\circ$ . In this case, the EPR spectrum could be irradiated at the high-field side (corresponding to  $g_{zz}$  orientation)—where experimentally the largest DNP enhancement is observed—and each saturated electron spin would be accompanied by a nitroxide with a resonance frequency given by  $g_{yy}$ . This scenario would yield the most-efficient CE matching, see Eq. (33). From a molecular-geometry perspective, this condition would be found if the N–O bonds are collinear, while the C–N(O)–C planes of the two nitroxides are orthogonal to each other.

Such an arrangement was accomplished within a new biradical, bis-TEMPO-bisketal (bTbK) in which the two TEMPO moieties are linked by a spiro-center locking the radicals in the suitable relative orientation. With bTbK, NMR signal intensities were enhanced with  $\epsilon$  being 1.4-fold larger as compared to TOTAPOL [265]. However, the main limitation of bTbK was its poor solubility in aqueous media.

This triggered a search for water-soluble rigid biradicals incorporating the electron spin properties and DNP efficiency found in bTbK. One approach was the substitution of the oxygen atoms in the spiro-linker by more polarizable sulfur groups in mixed oxidation states. This resulted in a better water solubility of the resulting bis-TEMPO-bis-thioketal (bTbtK) biradicals in DMSO/water [266]. Solubility was further enhanced by Kiesewetter et al. by substitution of the protecting dimethyl groups by tetrahydropyran (THP) rings. The resulting bTbtK-py/SPIROPOL yielded an enhancement of 230 in glycerol/water solvent and finally outperformed TOTAPOL, which at that point seemed to have serendipitously fulfilled the most desirable properties of an ideal CE-efficient PA [267].

**5.2.2.4. The larger the better: bCTbK, PyPol/AMUPol, and the TEKPol series.** At the same time, the groups of Tordo and Ouari (Aix-Marseille University) were leading an extraordinary undertaking to probe the chemical space for possible improvements of PAs

[268,269]. This led to the development of a new rigid biradical for non-aqueous solvents. The bulky derivative of bTbK, bis-cyclohexyl-TEMPO-bisketal (bCTbK), was introduced by Zagdoun et al. by replacing the geminal dimethyl groups of bTbK by spiro-cyclohexyl moieties [270]. This increased the size and rigidity of the radical and resulted in slower electron spin relaxation. They have shown that  $T_{1S}$  of bCTbK in TCE impregnating a hybrid mesostructured silica material was twice as long and that larger enhancement factors were obtained compared to bTbK under similar conditions.

This approach was then extended towards two novel water-soluble radicals PyPol and AMUPol in 2013 by Sauvee et al. [271]. Structurally these are based on bTurea, and water solubility has been maximized by nitroxide-protecting THP rings and linker-decorating polyethyleneglycol (PEG) chains. The enhancement factors obtained for AMUPol in glycerol/water system were 3.5–4 times larger than for TOTAPOL at 9.4 and 14.1 T at a typical temperature of 97 K. The structural flexibility of the urea linker might seem to contradict this high efficiency. However, Michaelis et al. have also reported that larger conformational flexibility can improve DNP performance in a systematic study of several thiourea-type bis-nitroxides [272]. Very recently, it has also been shown that AMUPol exhibits a rather strong e–e exchange interaction of  $J/2\pi = 43$  MHz that is expected to support CE-enhancement and explain the significant advantage over TOTAPOL, particularly at high magnetic fields [273].

Furthermore, the non-aqueous soluble radical TEKPol—a heavier analog of bTbK—was also introduced [274]. Similar to AMUPol, large enhancement factors of more than 200 were obtained for TEKPol in TCE that was also ascribed to the slow electron spin relaxation. Interestingly, it also yielded relatively large DNP enhancement at higher temperatures (180–200 K). Current development of bTurea-based PAs is ongoing in systematic studies in order to improve DNP efficiency and solubility within several research groups and promising results have been recently published [275–277]. An example of such a systematic effort is shown in Fig. 41.

**5.2.2.5. Other approaches.** Alternative routes to achieve water-solubility of bTbK were demonstrated in the form of host-guest

complexes. Mao et al. have encapsulated bTbK in a cyclodextrin (Captisol) that resulted in improved water solubility of the PA and larger DNP efficiency as compared to TOTAPOL [278]. Later on, a related approach was used again to solubilize hydrophobic biradicals by surfactant encapsulation within micelles. Large signal enhancements were obtained by bTbK that was solubilized in a water/glycerol mixture with the help of deuterated surfactant sodium octyl sulfate [279] or by TEKPol that was incorporated into micelles formed by the protonated neutral surfactant polysorbate 80 (Tween-80) [280]. The solubilization in micelles preserves the glassy nature of the mixture and enables the DNP activity of the biradical.

Furthermore, systems such as OTP and the anti-inflammatory drug indomethacin have metastable amorphous phases but are not miscible with biradicals like TOTAPOL. Hence, Ong et al. introduced the novel organic biradical bis-TEMPO terephthalate (bTtereph), which has similar EPR and DNP properties as TOTAPOL. They succeeded in uniformly distributing bTtereph in OTP and indomethacin by a procedure that is common in pharmaceutical sample preparation (*i.e.*, in the absence of solvent) and obtained a  $^1\text{H}$  signal enhancement factor of 58 for the amorphous phase of OTP [281].

### 5.2.3. Heterodimeric biradicals and mixtures

The advantages of two specific radical types can be combined within heterodimeric biradicals where the respective radical moieties can differ in their EPR spectral and/or relaxation properties. For example, one radical with slow spin-lattice relaxation paired with another fast-relaxing radical can boost CE efficiency if the slow-relaxing radical species is irradiated by  $\mu\text{W}$  [82,229,282]. This leads to efficient saturation of this radical type, while the accompanying (fast-relaxing) radical ensures a large polarization differential to be transferred to the nuclei. Equally, irradiation of a radical moiety with a narrow EPR line causes similarly efficient EPR saturation; a paired radical with large spectral anisotropy can then provide efficient CE matching over a large range of molecular orientations.

A proof of concept has been demonstrated experimentally by Hu et al.; in a mixture of TEMPO and trityl (20 mM each), the DNP enhancement factor could be increased 4-fold as compared

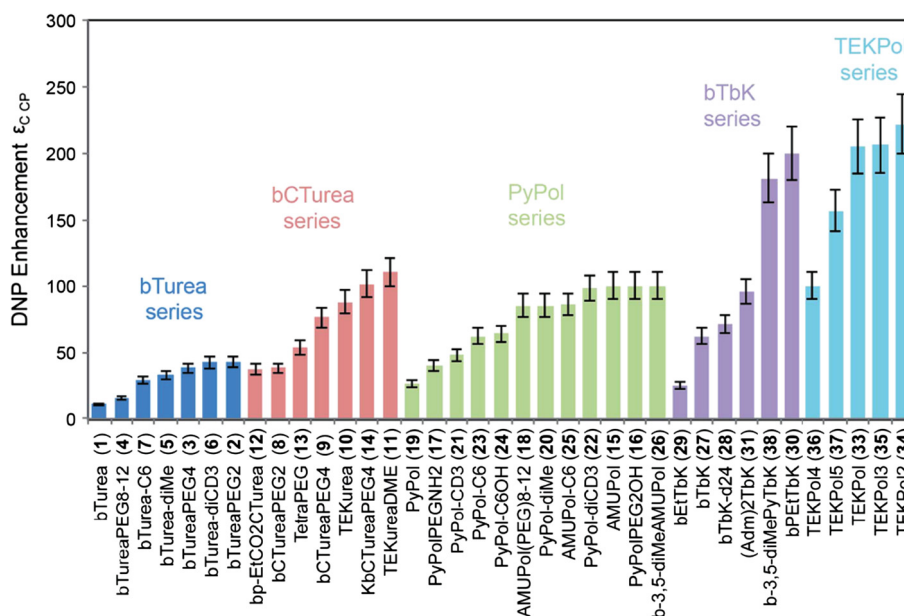


**Fig. 41.**  $^1\text{H}$  DNP enhancement factors from several bis-nitroxide PAs at a concentration of 16 mM in frozen solutions of TCE (9.4 T, 110–115 K). For chemical structure of selected PAs see Fig. 39; for structures of all given PAs see original publication. Figure taken with permission from [276].

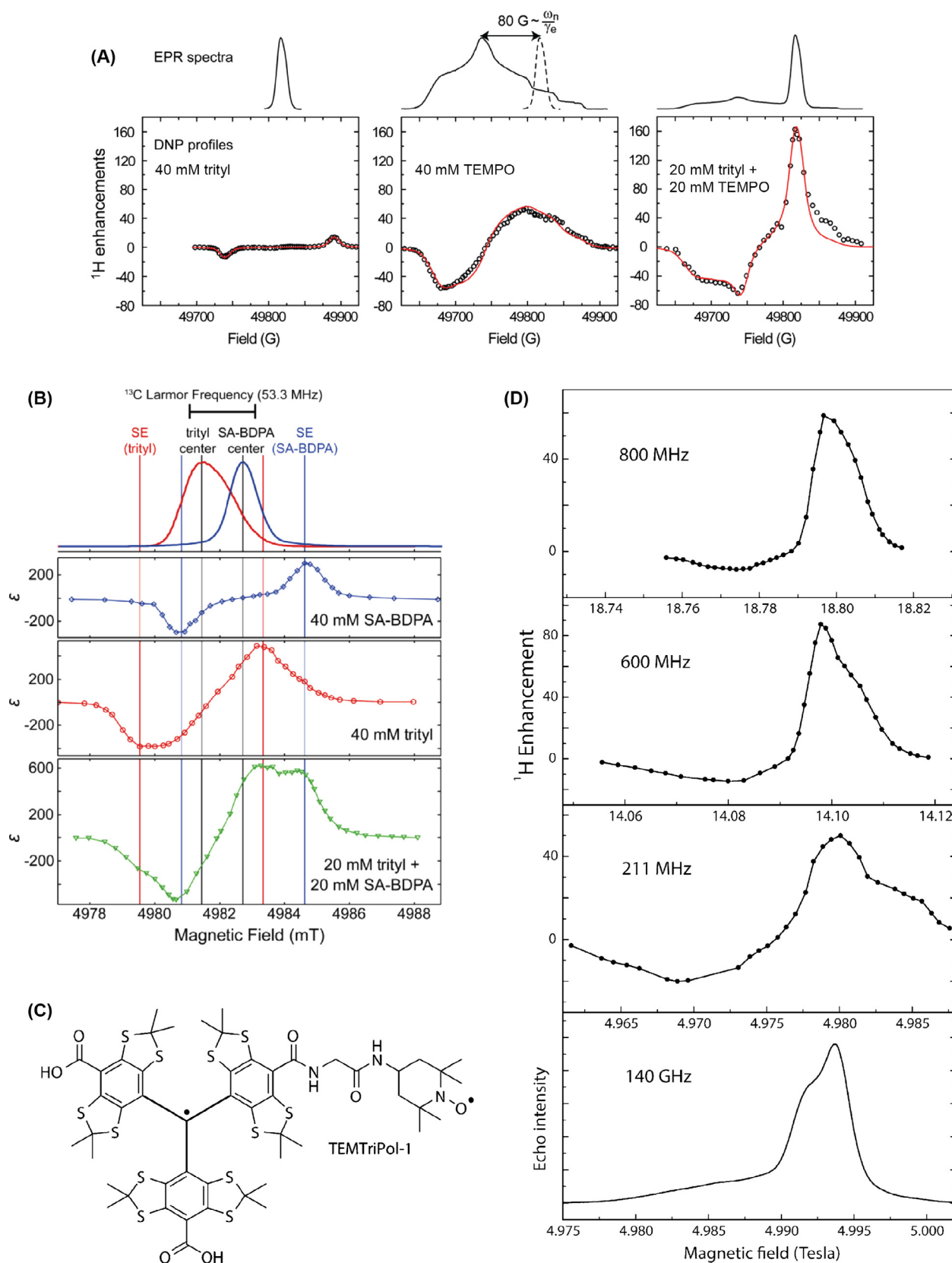


**Fig. 42.** DNP with radical mixtures or heterodimeric PAs. (A)  $^1\text{H}$  DNP with trityl/TEMPO mixture at 5 T (140 GHz  $e^-$ ; 211 MHz  $^1\text{H}$ ) [282]. (B)  $^{13}\text{C}$  DNP with trityl/SA-BDPA mixture at 5 T (140 GHz  $e^-$ ; 53 MHz  $^{13}\text{C}$ ) [82]. (C) Chemical structure of TEMTriPol-1 and (D)  $^1\text{H}$  DNP enhancements with that biradical at 18.8 T (527 GHz  $e^-$ ; 800 MHz  $^1\text{H}$ ), 14.1 T (395 GHz  $e^-$ ; 600 MHz  $^1\text{H}$ ), and 5 T (140 GHz  $e^-$ ; 211 MHz  $^1\text{H}$ ) in comparison with echo detected EPR spectrum at 140 GHz [283]. See original publications for further experimental details. Subfigures reprinted or adapted from the original publications with permissions.

to a TEMPO solution with equal PA concentration (40 mM) [282]. One of the most striking observations was that this advantage can only be achieved if the (narrow and slowly relaxing) trityl is directly excited by  $\mu\text{W}$ , while irradiation of the (broad and fast relaxing) TEMPO function gave no significant advantage (see Fig. 42A).

Another example of such a radical mixture has been provided by Michaelis et al. [82]. A 34 MHz difference (at 5 T) between the EPR absorption maxima of trityl OX063 and SA-BDPA potentially allows for CE matching of a large variety of nuclei with small gyromagnetic ratios. In fact,  $^{13}\text{C}$  (with a nuclear Larmor frequency of 53 MHz at 5 T) could be hyperpolarized with an enhancement factor of  $\varepsilon = 620$  at a concentration of 20 mM of each radical, significantly surpassing enhancement factors obtained with solutions containing only one of the two radicals at equal electron spin concentration of 40 mM ( $\varepsilon = 300$  for SA-BDPA;  $\varepsilon = 480$  for OX063), see Fig. 42B. Interestingly, spectral decomposition of the DNP field profile into all possible contributions allowed for unambiguous identification of the CE contribution which resulted from SA-BDPA/OX063 pairs [82].

However, efforts to create stable and water-soluble heterodimeric biradicals that encompass these advantages and alleviate the detrimental effects of the large paramagnetic concentration of a molecular mixture have been hampered by chemical difficulties. Problems intrinsic to radical chemistry are potentiated in the presence of two radicals with different redox potentials. Activity of both radicals has to be maintained throughout the synthetic

pathway, or one radical must be activated in the presence of the other. One combined effort of the Swager and Griffin labs resulted in the successful synthesis of a BDPA-TEMPO biradical that combined the advantages of a narrow and broad EPR line radical situated within one molecule, however, water-solubility was limited. Additionally, the chemical modification of the BDPA moiety resulted in a significant  $g$ -anisotropy that might partially invalidate the advantages of the otherwise very slowly relaxing spin with a narrow resonance line [284].

Nevertheless, a newly developed heterodimeric biradical that satisfies the CE matching condition with an electron pair featuring different electron relaxation rates has been successfully synthesized and tested for DNP efficiency at various field strengths by Mathies et al. [283]. TEMTriPol-1—in which a TEMPO nitroxide and a trityl radical are chemically interconnected (structure shown in Fig. 42C)—yielded a rather large  $^1\text{H}$  signal enhancement of 65 in a 10 mM glycerol/water solution at 18.8 T (527 GHz  $e^-$ , 800 MHz  $^1\text{H}$ ). Interestingly, TEMTriPol-1 showed an anomalous dependence on the external magnetic field, yielding its best performance (in relation to other PAs) at high field ( $\varepsilon = 65$  at 18.8 T;  $\varepsilon = 87$  at 14.1 T), whereas its efficiency dropped at lower field ( $\varepsilon = 50$  at 5 T), see Fig. 42D. This behavior has been explained by the strong exchange interaction ( $J/2\pi = 73$  MHz) between the nitroxide and trityl moieties that disturbs the CE mechanism when  $J$  is of a similar order of magnitude as the nuclear Larmor frequency (i.e., 211 MHz at 5 T; 600 MHz at 14.1 T; 800 MHz at 18.8 T) [283].

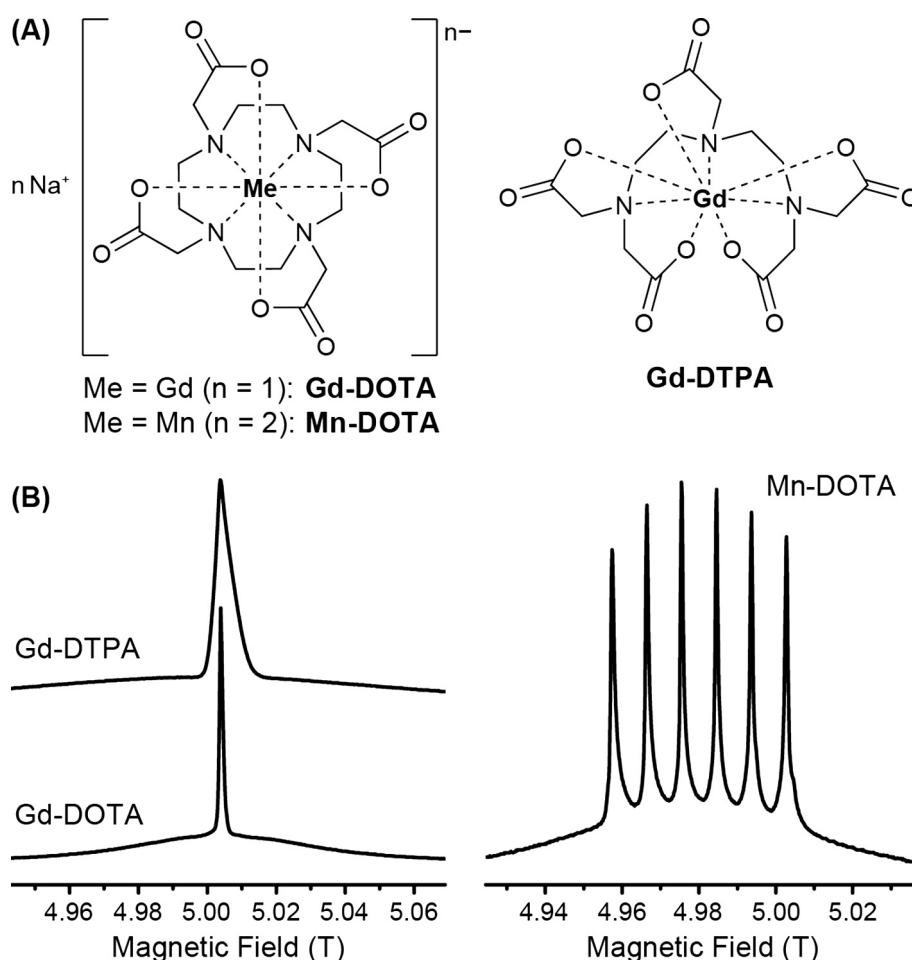
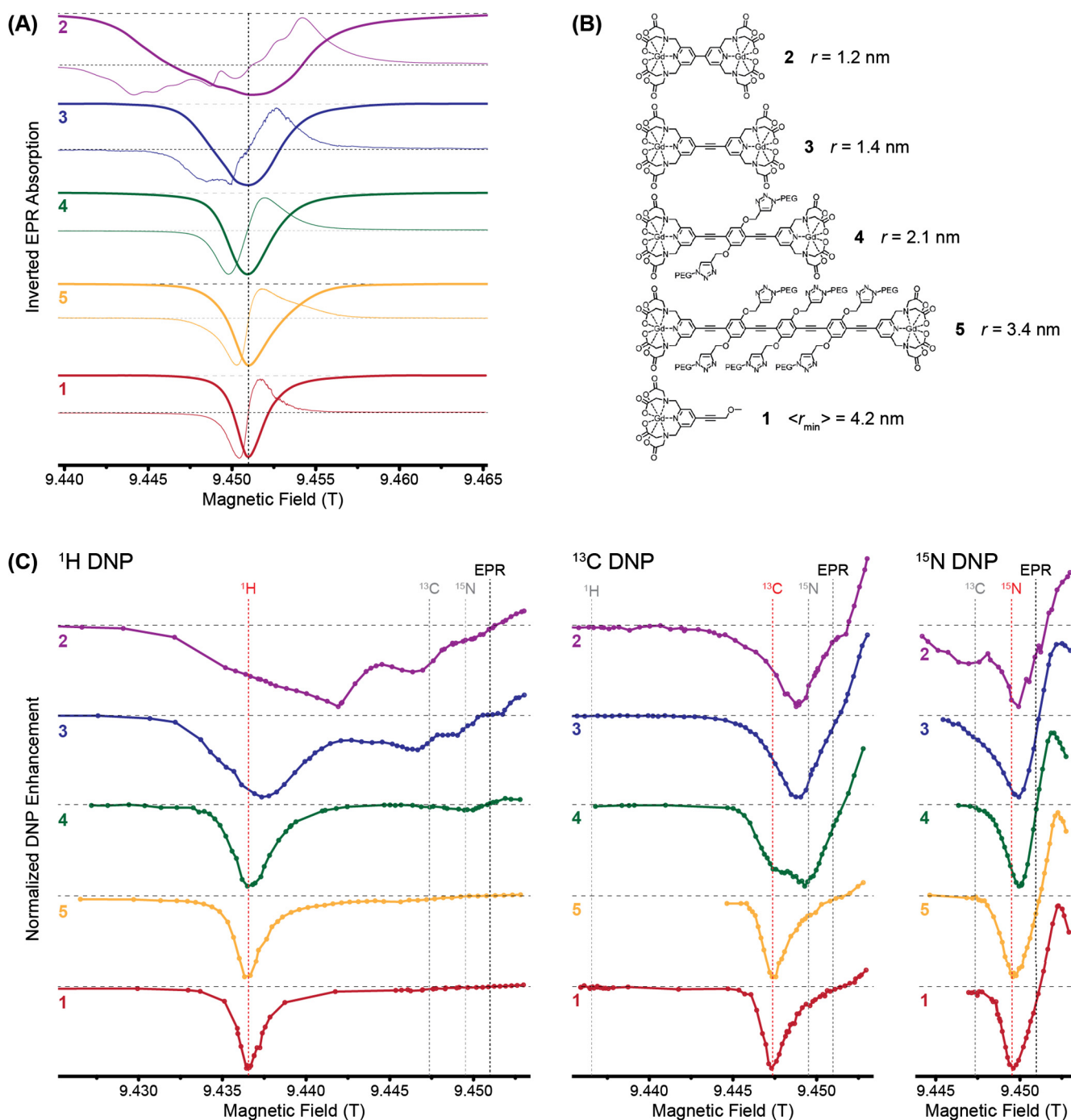


Fig. 43. (A) Chemical structures of the high-spin metal complexes Mn/Gd-DOTA and Gd-DTPA. (B) Field-swept EPR spectra of the metal complexes recorded at 1 mM in frozen solutions of  $d_8$ -glycerol/ $\text{D}_2\text{O}$  at 139.5 GHz and 80 K using a Hahn echo sequence. Subfigure (B) adapted with permission from [159].



**Fig. 44.** (A) 263 GHz cw EPR spectra (recorded as field derivatives in thin lines, integral/absorption spectra in thick lines) of frozen solutions of mono(Gd-chelate) **1** and bis(Gd-chelate)s **2–5**. Spectra are inverted for better comparison with DNP field profiles. (B) Chemical structures of the investigated complexes. (C) 263 GHz  $^1\text{H}$ ,  $^{13}\text{C}$ , and  $^{15}\text{N}$  DNP field profiles of the same samples as in (A). Data taken from [168]. For further information, see original publication.

### 5.3. Paramagnetic metal ions

#### 5.3.1. Ce(III) and Cr(V): early experiments

DNP using paramagnetic metal ions has first been reported immediately after the discovery of SE DNP. Abraham et al. studied Ce(III) as main constituent in  $\text{Ce}_2\text{Mg}_3(\text{NO}_3)_{12} \cdot 24 \text{H}_2\text{O}$  or as impurity in diamagnetic  $\text{La}_2\text{Mg}_3(\text{NO}_3)_{12} \cdot 24 \text{H}_2\text{O}$  (also known as LMN) and in  $\text{CaF}_2$ . Furthermore, they reported rather small enhancement factors by employing Cr(III) as impurity within synthetic sapphire ( $\alpha\text{-Al}_2\text{O}_3$ ) or utilizing ferric impurities in  $\text{K}_3\text{Co}(\text{CN})_6$  [76,113]. Later, Cr(V)—reduced *in situ* from Cr(VI) [285]—in complexes with diols

and glycerol has been extensively used as PA for spin-polarized targets in scattering experiments [286–290]. All these experiments have been performed at low field and very low temperatures. In the transition metal complex of Cr(V), a single unpaired electron is located in the 3d-shell, yielding a  $S = 1/2$  system with an isotropic  $g$ -factor ( $g_{\text{iso}} = 1.981$ ) in liquid ethylene glycol; upon freezing of the solution, only a very small anisotropy is observed [286]. The rare earth Ce(III) has a  $4f^1$  configuration with a free ion  $^2F$  ground state ( $S = 1/2$ ,  $L = 3$ , ground state  $J = 5/2$ ) [291]. In trigonal LMN, this situation results in a large spin-orbit coupling (SOC) and effective Zeeman anisotropy with a parallel principal



axis component (PAC)  $g_{\parallel} \approx 1.83$  and an almost vanishing perpendicular PAC  $|g_{\perp}| \leq 0.1$  [292,293]. In contrast to these  $S = 1/2$  systems, Cr(III) and Fe(III) feature high spin quantum numbers, leading to much more complex DNP enhancement profiles featuring more than one DNP condition as compared to what has been observed for doublet PAs [76].

### 5.3.2. Gd(III) and Mn(II) in chelate complexes

The increasing complexity of DNP parameters imposed by high-spin properties makes the prediction of DNP performance and the design of an efficient high-spin PA rather difficult [167]. Nevertheless, the search for efficient PAs for high-field MAS DNP constrains the space of possible PAs to a large degree. One of the most stringent requirements of a PA is the compatibility with current instrumentation, consisting of an NMR magnet without or with a limited sweep capability as well as a gyrotron, typically with a fixed-frequency output (see Section 4.2). This prohibits the use of metal ions or PAs that feature pronounced SOC, resulting in  $g$ -factors strongly deviating from the 'spin-only'  $g_e = 2.0023$  of the free electron. Unfortunately, many transition metal ions in low-spin complexes such as  $\text{Cu}^{2+}$ ,  $\text{Co}^{2+}$ ,  $\text{Fe}^{3+}$  experience significant SOC due to an admixture of (energetically low-lying) excited states and consequently show significant  $g$ -anisotropy [291]. This impedes DNP applications using such  $S = 1/2$  metal ions as PAs at high field despite exciting perspectives, given their relevance in biology and materials science.

A rather small group of high-spin transition-metal or rare-earth ions—including  $\text{Gd}^{3+}$  and  $\text{Mn}^{2+}$ —feature peculiar electron-spin properties. These are caused by the combination of a non-degenerate electronic ground state with no orbital momentum and (unpopulated) excited states lying high above the ground-state energy [291]. Half-filled electronic subshells quench the orbital momentum:  $\text{Mn}^{2+}$  has a  $3d^5$  configuration with a  ${}^6S$  ground state, whereas  $\text{Gd}^{3+}$  has 7 unpaired electrons in the highly screened  $f$ -shell ( $4d^7$  configuration with  ${}^8S$  state).<sup>4</sup> Despite their high-spin properties, the quenched SOC leads to a practically isotropic Zeeman interaction with  $g$ -values very close to  $g = 2.00$ , manifested in a rather narrow EPR central transition (CT) between the  $m_s = \pm 1/2$  states in the half-integer (Kramer's type) systems. Satellite transitions (*i.e.*, transitions where  $m_s$  changes its absolute value) are influenced by ZFS in first order, which results in a very broad spectral feature, especially when amorphous solutions of such high-spin complexes are considered [294].

Given a highly symmetric complex geometry, the ZFS constant is typically in the range of a few hundred MHz up to a few GHz. For example, in high-affinity chelate complexes, the CT is only affected to a small degree by second-order effects that are less pronounced and can even be negligible at high magnetic fields [295]. The compatibility with cellular environments [296,297]—also considering the inherent chemical stability of Gd(III) or Mn(II)—makes such complexes highly interesting PAs for MAS DNP [139,140].

$\text{Gd}^{3+}$  and  $\text{Mn}^{2+}$  bound in complexes of the chelators DOTA and DTPA (see Fig. 43) were first introduced as high-spin metal ion PAs for MAS DNP by Corzilius et al. in 2011. A very narrow EPR CT linewidth of 29 MHz at 5 T was observed for Gd-DOTA complex, which allowed induction of SE with an initially reported  ${}^1\text{H}$  enhancement factor of  $\sim 12$  in a urea model sample [159]. Due to the narrowing of the CT at higher magnetic fields, the detrimental field dependence of the SE transition probability proportional to  $B_0^{-2}$  [see Eq. (17)] is partially compensated for, leading to still sig-

nificant performance with  $\varepsilon = 8$  at 14.1 T. Direct DNP of low- $\gamma$  nuclei ( ${}^{13}\text{C}$  and  ${}^{15}\text{N}$ ) was reported with enhancement factors in excess of 100, potentially allowing for site-directed DNP on biomolecules using site-directed spin-labeling (SDSL) with metal chelate tags; furthermore, the contribution of CE mechanism was demonstrated [139].

The latter observation stimulated the groups of Corzilius (Frankfurt) and Godt (Bielefeld) to design several bis(Gd-complexes) in which two Gd-binding chelate moieties are interconnected by linkers of varying lengths [168]. This has not only led to an increase in DNP efficiency in analogy to what has been achieved with bis-nitroxide PAs [254], but also has resulted in further understanding of the inter-electronic distance dependence for CE DNP of different nuclear spins (see Fig. 44).

Due to the strong isotropic HFI to the  ${}^{55}\text{Mn}$  nucleus ( $I = 5/2$ , 100% natural abundance), Mn(II) suffers from a splitting of the EPR CT into a sextet with  $\sim 250$  MHz separation; this reduces the achievable enhancement factors equally  $\sim 6$ -fold with respect to Gd(III) [139,159]. Nevertheless, the high biological relevance of  $\text{Mn}^{2+}$  and structural similarity with the diamagnetic  $\text{Mg}^{2+}$  ion justifies further investigation as potential endogenous PA. Such a premise was demonstrated on an inactivated hammerhead ribozyme where one  $\text{Mn}^{2+}$  ion was specifically bound to RNA. In this case, intra-molecular DNP was used to directly hyperpolarize  ${}^{13}\text{C}$  within the same molecule [140].

### 5.3.3. Cr(III) in crystalline solids

$\text{Cr}^{3+}$  can have similar properties as the above-mentioned metal ions, despite its  $3d^3$  electronic configuration with atomic  ${}^4F$  ground-state term. In an octahedral ligand field, this state transforms into a (non-degenerate)  ${}^4A_{2g}$  ground state with  $L = 0$ , resulting in an isotropic Zeeman interaction and  $g \approx 2.0$ . However, significant deviation from ideal octahedral symmetry can reintroduce an excited-state admixture (mainly  ${}^4T_{2g}$ ) and lead to larger deviations from the free-electron  $g_e$  [298]. Small distortions of the ligand-field symmetry may still conserve the pure ground-state properties but manifest themselves in a moderate ZFS of up to several GHz, as can be found in ruby [299–301].

An ideal system featuring a high trigonal symmetry of the metal site is found in a crystalline sample of  $[\text{Co}(\text{en})_3\text{Cl}_3]_2 \cdot \text{NaCl} \cdot 6\text{H}_2\text{O}$  ( $\text{en} = \text{ethylenediamine}$ ,  $\text{C}_2\text{H}_8\text{N}_2$ , Fig. 45) paramagnetically doped with  $\text{Cr}^{3+}$  [303]; in this case,  $\text{Cr}^{3+}$  ( $S = 3/2$ ) and  $\text{Co}^{3+}$  (low-spin  $3d^6$ ,  $S = 0$ ) are structurally interchangeable due to the similarity

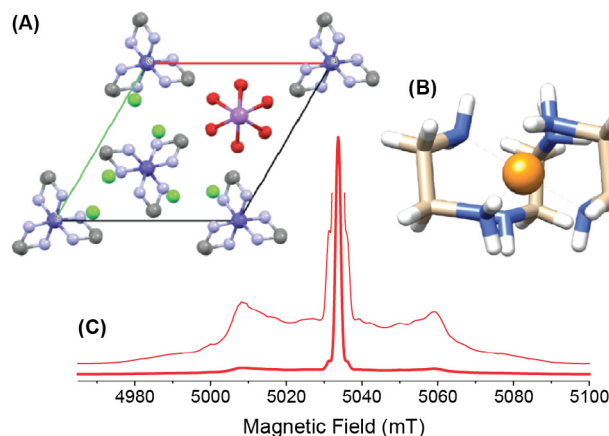


**Fig. 45.** (A) Crystallographic unit cell of  $[\text{Co}(\text{en})_3\text{Cl}_3]_2 \cdot \text{NaCl} \cdot 6\text{H}_2\text{O}$  ( $\text{en} = \text{ethylenediamine}$ ,  $\text{C}_2\text{H}_8\text{N}_2$ ). Projection of the crystal structure with the  $c$  axis perpendicular to the plane of the drawing. (B) Molecular unit with hydrogen atoms. (C) Field-swept 140 GHz EPR spectrum of 0.1% Cr(III)-doped  $[\text{Co}(\text{en})_3\text{Cl}_3]_2 \cdot \text{NaCl} \cdot 6\text{H}_2\text{O}$  using a Hahn echo sequence at a temperature of 80 K. Figure adapted from [302] with permission.

<sup>4</sup>  $\text{Eu}^{2+}$  and  $\text{Tb}^{4+}$  also exist in the same electronic configuration and show similar EPR spectroscopic properties, however, they are chemically less stable than  $\text{Gd}^{3+}$  and—as most lanthanides—tend to obtain a +3 oxidation state.

of ionic radii [304]. Therefore, paramagnetic doping with molar ratios between 0.1 and 3% can be achieved without effecting any change in the crystal structure [302]. The EPR spectrum (Fig. 45C) shows a narrow CT with practically isotropic  $g = 1.987$  and an axial ZFS with a constant of  $D = 740$  MHz at 80 K. By irradiation of the SE condition, a rather small  $^1\text{H}$  enhancement was observed in the fully-protonated sample. More interestingly, significant direct-DNP enhancement factors on the order of 20–30 have been observed for  $^{13}\text{C}$  and  $^{59}\text{Co}$  at high doping ratios of 3%, with a strong dependence on the latter parameter. This was surprising in several ways. First, the rather narrow CT linewidth of  $\sim 40$  MHz was relatively small compared to the  $^{13}\text{C}$  and  $^{59}\text{Co}$  Larmor frequencies (53 and 51 MHz, respectively); more importantly, any anisotropies resulting from ZFS or HFI would act equally on neighboring  $\text{Cr}^{3+}$  in the long-range ordered crystalline lattice, prohibiting the majority of matching conditions found in stochastically oriented (amorphous) samples [167]. This indicated that CE matching between the CT of one  $\text{Cr}^{3+}$  and a satellite transition of a neighboring ion might support DNP: while the former transition appears static, the latter are modulated by ZFS under MAS. As the second surprise, the nearest distance between a  $\text{Cr}^{3+}$  PA and  $^{59}\text{Co}$  nucleus is 7.7 Å, proving that direct DNP can act over rather large distances [302].

## 6. Practical aspects

The observed outcome of a DNP experiment, such as the generation of enhanced nuclear polarization or quenching of NMR signal due to the presence of the paramagnetic PA, is a result of the interplay between various microscopic processes. In turn, these processes themselves are dependent on experimental conditions (e.g., sample temperature,  $\mu\text{w}$  power, MAS frequency, etc.), the type of PA used, and the constitution of the sample. Clearly, sample preparation is a very important factor for DNP and can play a decisive role in the success of an experiment. For example, due to the complexity of samples in biomolecular as well as materials science applications, and the manifold molecular dynamics that determine the relaxation behavior, the overall enhancements are often found to be several-fold reduced as compared to model substances. An exception is the enhancement factor of 250 obtained for a ribozyme where relaxation-inducing methyl groups are absent in the purified sample [140]. Similarly, unfavorable freezing properties of the solvent can render a DNP experiment fruitless [281]. In the following, an overview is given about the influence of various parameters and guidelines for their optimization.

### 6.1. Build-up and depletion of the (enhanced) NMR signal

#### 6.1.1. Accelerated build-up of polarization during SE

In the case of SE the observed DNP-build-up rate (under  $\mu\text{w}$  irradiation) is expected to be larger than the spin-lattice relaxation rate (without  $\mu\text{w}$ ) [61,106,121]. Based on a simplified description, the effective bulk DNP rate,  $k_{\text{DNP}}^{\text{eff}}$ , and the observed relaxation rate,  $T_{1l}^{-1}$ , are additive towards the measured build-up rate,  $T_{\text{B}}^{-1}$  [77]:

$$\frac{1}{T_{\text{B}}} = k_{\text{DNP}}^{\text{eff}} + \frac{1}{T_{1l}}. \quad (52)$$

This is valid as long as spin diffusion within the bulk nuclear spin bath is faster than the effective transfer of polarization between electron spins and (observable) bulk nuclei. Then, the effective DNP rate depends on the  $\mu\text{w}$  field strength and accordingly on the incident  $\mu\text{w}$  power. Such an acceleration of longitudinal-polarization build-up is observed in experiments and potentially complicates the reliable measurement of DNP enhancement factors [62,74,77]. For a reproducible measurement,

the enhancement at infinite polarization time,  $\varepsilon_{\infty}$ , has to be measured. Practically this requires recording the DNP-enhanced signal intensity,  $I_{\text{DNP}}$ , while using a polarization build-up period,  $\tau$ , which is significantly longer than  $T_{\text{B}}$ . This is then compared to the thermal-polarization signal intensity,  $I_{\text{off}}$ , that must also be recorded at recycle delays much longer than  $T_{1l}$ :

$$\varepsilon_{\infty} = \frac{I_{\text{DNP}}(\tau \gg T_{\text{B}})}{I_{\text{off}}(\tau \gg T_{1l})}. \quad (53)$$

In a reasonable approximation, this can be achieved by choosing a polarization period or recycle delay approximately 5-fold longer than  $T_{\text{B}}$  or  $T_{1l}$ , respectively. More reliable is the acquisition of a full build-up curve after complete destruction of the polarization due to a pre-saturation train [225]. Exponential fitting allows for the extraction of a pre-exponential factor representing the polarization at infinite time. In many practical cases, an “instantaneous” DNP enhancement factor is provided by measuring DNP-enhanced signal intensity vs. thermal equilibrium at a finite build-up time well below the optimum  $\sim 5 \times T_{\text{B}}$ . For example, this can be due to prohibitively long build-up time constants typically encountered for (dilute) low- $\gamma$  nuclei, weak thermal signals that do not allow for the acquisition of a full time profile, or ineffective off-signal sensitivity at  $\sim 5 \times T_{1l}$ . In these cases, care has to be taken because the instantaneous  $\varepsilon(\tau)$  is a function of polarization time if  $T_{\text{B}} \neq T_{1l}$ :

$$\varepsilon(\tau) = \varepsilon_{\infty} \frac{1 - \exp(-\tau/T_{\text{B}})}{1 - \exp(-\tau/T_{1l})}. \quad (54)$$

Thus, the destruction of the residual magnetization using a pre-saturation train or the use of an adequate number of dummy scans is of great importance for a reproducible quantification of the enhancement.

On the other hand, the acceleration of the polarization build-up accounts for an additional sensitivity advantage not included in  $\varepsilon_{\infty}$  [305]:

$$\kappa = \sqrt{\frac{T_{1l}}{T_{\text{B}}}}. \quad (55)$$

This factor  $\kappa$  only represents the advantage in S/N gained by faster build-up of DNP-enhanced signal vs. longitudinal relaxation in the same sample without  $\mu\text{w}$  irradiation and thus does not account for paramagnetic relaxation enhancement (PRE), which can be caused by the presence of the paramagnetic PA:

$$\frac{1}{T_{1l}} = \frac{1}{T_{1l}^{\circ}} + \Gamma_{1l}^{\text{PRE}}. \quad (56)$$

$T_{1l}^{\circ}$  is the relaxation time constant of the diamagnetic (undoped) reference and is stringently larger than or equal to  $T_{1l}$  of the sample doped with PA, since the latter is accelerated by the PRE rate,  $\Gamma_{1l}^{\text{PRE}}$ . Therefore, a reference sample of equal composition but lacking PA has to be measured for the accurate determination of off-signal intensity and spin-lattice relaxation time constant. An effective  $\kappa^{\circ}$  is then obtained:

$$\kappa^{\circ} = \sqrt{\frac{T_{1l}^{\circ}}{T_{\text{B}}}}. \quad (57)$$

This additional acceleration due to PRE might indicate an additional increase in sensitivity at first glance, however, the SE enhancement strongly depends on the spin-lattice relaxation time constant of the bulk nuclear spins [74,77]:

$$\varepsilon_{\infty} \approx k_{\text{DNP}}^{\text{eff}} T_{1l}. \quad (58)$$

As soon as  $T_{1l} \ll T_{1l}^{\circ}$ , or from another viewpoint  $\Gamma_{1l}^{\text{PRE}} \gg (T_{1l}^{\circ})^{-1}$ , Eq. (58) shows that the bulk DNP enhancement factor scales inversely with the PRE rate:

$$\varepsilon_\infty \approx \frac{k_{\text{DNP}}^{\text{eff}}}{\Gamma_{11}^{\text{PRE}}} \quad (59)$$

Under the further assumption that  $k_{\text{DNP}}^{\text{eff}} \ll T_{11}$  (i.e., operation of the SE far from saturation),  $K^\circ$  then is simplified as

$$K^\circ = \sqrt{T_{11}^\circ \Gamma_{11}^{\text{PRE}}} \quad (60)$$

Here it becomes clear that the sensitivity loss due to reduction of DNP enhancement outweighs the benefit of faster acquisition due to PRE, so that a compromise has to be found. In most cases, typical SE PAs are quite poor PRE agents, so that sufficient DNP enhancement can be achieved with minimal reduction in  $T_{11}$  [225].

### 6.1.2. Depolarization by MAS

In comparison to SE, the situation is completely different when a CE-active PA is concerned. As we have described in Section 2.1.2, CE transitions do not require  $\mu\text{W}$  irradiation in order to transfer polarization between electron spins and nuclear spins. This leads—especially under MAS—to a strong link between the nuclear polarization,  $P_I$ , and the difference in electron polarization,  $\Delta P_S$ , between the two electron spins that in turn fulfil the CE matching condition Eq. (33). In thermal equilibrium  $P_I$  and  $\Delta P_S$  are equal; this can be simply derived from the respective Boltzmann factors. However, if there is an induced imbalance, the relatively large CE transition moments [see Eq. (36)] will lead to a very efficient polarization transfer. For example, under saturation or inversion of the nuclear spin polarization, the recovery towards equilibrium is greatly accelerated by the presence of PAs potentially fulfilling the CE condition [306]. This coherent repolarization process is experimentally indistinguishable from nuclear spin-lattice relaxation processes, however, it is not to be confused with incoherent processes typically responsible for relaxation.

Equivalently, the nuclear spin polarization will also follow  $\Delta P_S$  when the latter is perturbed. This effect is naturally sought-after during CE DNP by saturating the EPR spectrum at certain points within the spectral shape, so that the polarization differential  $\Delta P_S$  is maximized. On the other hand, reduction of this differential in electron spin polarization (up to complete equilibration) over all possible CE pairs will reduce the observable non-DNP-enhanced NMR signal amplitude (down to vanishing). Such a (complete or partial) equilibration can be induced by large homogeneous EPR linewidths or electron spectral diffusion, so that  $\mu\text{W}$ -saturation at one frequency also causes saturation of electron spins off-resonance by the nuclear Larmor frequency, or by MAS without  $\mu\text{W}$  irradiation. In both cases sufficiently long electron spin longitudinal relaxation time constants,  $T_{15}$ , are a prerequisite. In the latter case this condition can in many cases be quite easily fulfilled at intermediate-to-fast MAS frequencies, where  $T_{15}$  is of similar size than the rotational period,  $2\pi/\omega_r$ , or larger. In that case, any non-adiabaticity of the e–e flip-flop events (see Section 2.1.2.5) leads to non-ideal exchange of polarization accumulating over several rotor periods and therefore partial equilibration of electron spin polarization. This process causes effective dynamic nuclear depolarization driven by CE under MAS in the absence of  $\mu\text{W}$  irradiation [85].

This depolarization is unique to CE-enabling PAs and is difficult to distinguish from paramagnetic bleaching or quenching that can occur at the same time (see below). Nevertheless, both effects have starkly different consequences. In fact, nuclear depolarization rather strongly depends on the MAS frequency and can be reverted to a large extent by  $\mu\text{W}$ -driven selective saturation of the EPR spectrum so that a large polarization differential is induced. In contrast, assuming uniform enhancement of all observed nuclear spins, bleaching is affecting both the DNP-enhanced as well as the non-enhanced NMR spectrum (i.e., the on- and the off-spectrum, respectively). In the latter case (i.e., bleaching) the NMR signal

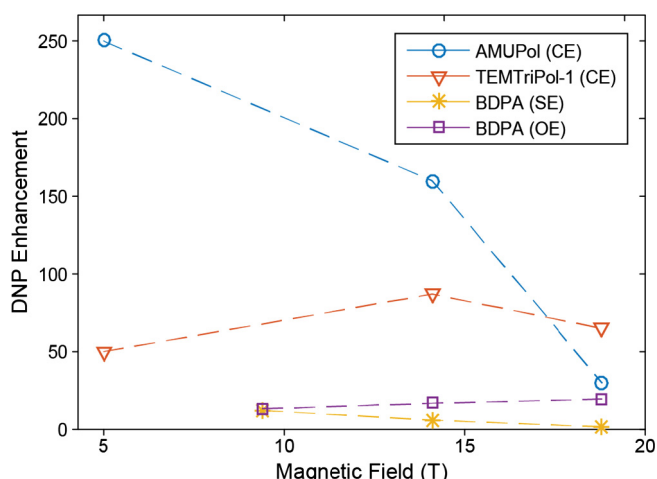


**Fig. 46.** Magnetic field dependence of  $^1\text{H}$  DNP enhancement factors for different PAs. Data taken from [283] (AMUPol, TEMTriPol-1) and [90] (BDPA). Enhancement factors obtained by SE and CE drop significantly with increasing values of  $B_0$ . Note, that the increase between 5 and 14.4 T observed for TEMTriPol-1 is due to a change in mechanism [283]. Only the OE in BDPA shows a favorable field dependence over the whole accessible range.

intensity might be greatly reduced even though large DNP enhancement factors would be measured, due to the reduced number of observable spins. In the former case (i.e., depolarization) the enhancement factor might be overestimated because the DNP-enhanced spectrum is compared to an off-spectrum that is not in thermal equilibrium but effectively at a much higher spin-temperature. This might even result in quite unexpected observations such as apparent enhancement factors that exceed the theoretically possible ratio of  $\gamma_S/\gamma_I$  [see Eq. (2)] as has already been demonstrated in experiment [217].

### 6.1.3. The absolute sensitivity ratio

The presence of the paramagnetic species causes a reduction of the number of detectable nuclear spins by bleaching effects in the vicinity of the electron spins. One possible reason for this is a broadening of NMR resonances due to increased transverse relaxation of nuclear spins (coherence quenching), possibly in combination with strong paramagnetic shifts. Furthermore, even when detected low- $\gamma$  nuclei are virtually unaffected by the PA, global  $^1\text{H}$  relaxation in the rotating frame can reduce efficiency of typically employed techniques such as heteronuclear CP.

These effects have been systematically studied in homogeneous frozen solutions using TOTAPOL as PA [252]. Furthermore, a direct comparison between different PAs and effective DNP mechanisms was presented [225]. Besides these experiments in environments relevant for biological studies, a quantitative study of  $^{29}\text{Si}$  CP and CP/CPMG experiments on hybrid mesoporous silica impregnated with aqueous biradical solutions was reported by Rossini et al. [253]. In all cases, a reduction of the non-enhanced ( $\mu\text{W}$ -off) signal intensity in the presence of radicals was observed. The ratio between the thermal polarization signal intensity of a DNP sample doped with PA,  $I_{\text{off}}$ , and that of diamagnetic reference sample,  $I^\circ$ , is therefore often given as a so-called bleaching or quenching factor  $\xi$ :

$$\xi = 1 - \frac{I_{\text{off}}}{I^\circ} \quad (61)$$

Together with the acceleration factor  $\kappa^\circ$  from Eq. (57), this can be combined into an effective DNP signal-to-noise enhancement  $E$ :

$$E = \varepsilon_\infty (1 - \xi) \kappa^\circ = \varepsilon_\infty \frac{I_{\text{off}}}{I^\circ} \sqrt{\frac{T_{11}^\circ}{T_B}} \quad (62)$$

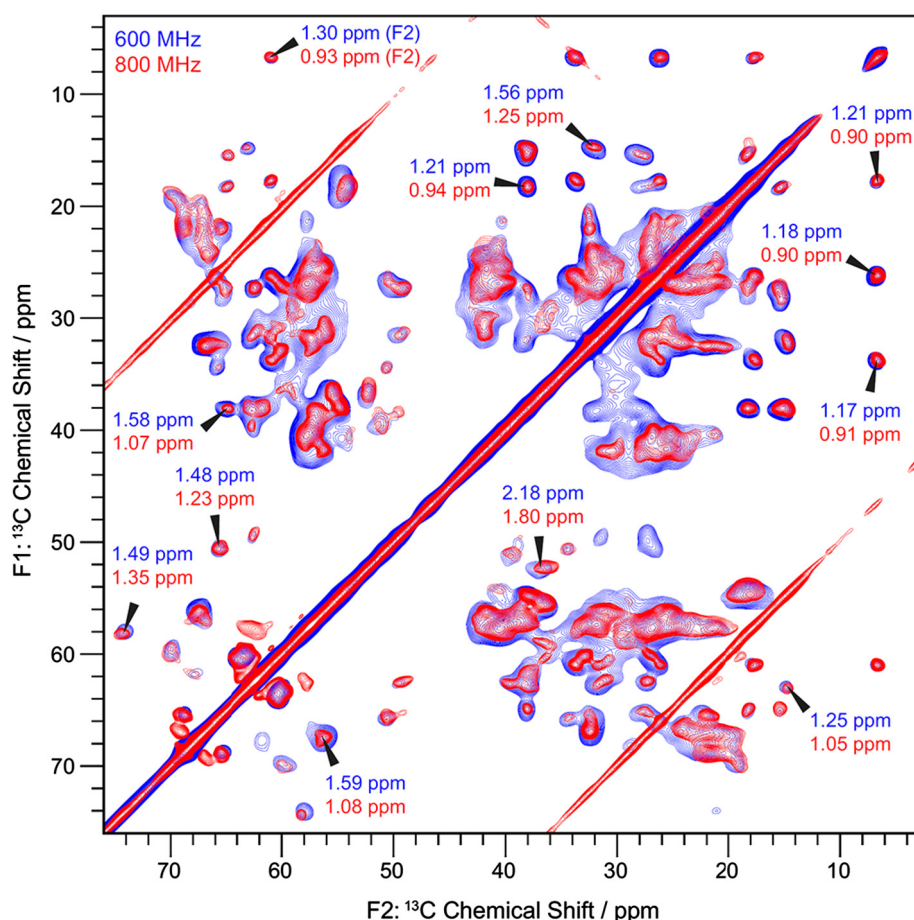


**Fig. 47.** Overlay of  $^{13}\text{C}$ - $^{13}\text{C}$  PDSO 2D NMR spectra of MxiH protein needles using DNP at 800 MHz (red, 8 kHz MAS, 95 K, 30 ms mixing time) and at 600 MHz (blue, 11 kHz MAS, 104 K, 20 ms mixing time). The full widths at half height (FWHM) in the direct dimension are annotated for some resolved peaks illustrating the increase in resolution at 800 MHz. Figure taken from [311] with permission.

However, from a practical viewpoint several aspects have not been considered here. For example, the groups of Lafon and Pruski have systematically analyzed the effective sensitivity enhancement (per unit time) in DNP-enhanced  $^{13}\text{C}$  and  $^{29}\text{Si}$  CPMAS on functionalized mesoporous silica nanoparticles and separated the contributions due to DNP, paramagnetic quenching/bleaching, the presence of frozen solvent, sample temperature (*i.e.*, the increased Boltzmann factor at lower temperatures) as well as the changes in relaxation and cross-polarization behavior [307]. In addition, Takahashi et al. have provided an even more comprehensive discussion of various factors, including experimental temperature, line broadening due to altered experimental conditions (different sample composition and/or temperature), reduced effective analyte concentration, signal loss by bleaching or reduction in transfer efficiencies in sophisticated NMR pulse sequences, as well as differences in equipment, which also come into play when comparing the full scope available for conventional MAS NMR with specialized instruments required for DNP [308]. Thus, for optimal performance, multiple and partially interconnected experimental parameters have to be considered.

## 6.2. Experimental parameters

### 6.2.1. External (static) magnetic field

From a basic NMR-spectroscopic point of view, higher external magnetic fields are beneficial in terms of sensitivity and resolution. Thus, most of the DNP-supported MAS experiments aiming at structural investigations are performed at fields  $\geq 9$  T. In contrast,

SE and CE decrease in efficiency due to a complex interplay between various factors [179]. Mainly, the increasing width of the EPR line associated with incomplete excitation and the lower transition probabilities of the driven  $e-n$  transitions at higher fields and Zeeman frequencies are the reason for this dependence. Furthermore, the significant field dependence of electron and nuclear spin relaxation as well as spin diffusion has to be considered. The theoretical description of the underlying interactions is rather complex, nevertheless the general dependence on the external magnetic field is confirmed experimentally [90,309].

As shown in Fig. 46, particular radicals allowing for CE DNP can yield significant signal enhancements at the highest currently available fields. Compared to SE, much larger absolute values of the CE transition probability explain this performance (see Section 2.1.2.3). Still, the loss in enhancement factors as compared to lower fields is tremendous. Differences in instrumental design, for example, the  $\mu\text{w}$ -power output of the gyrotron, different conversion factors due to shorter wavelength, and changes in effective sample temperature are likely contributing to this behavior as well. It should be noted that especially at high magnetic fields, the reduction in enhancement could be compensated for, provided larger  $\mu\text{w}$  power was available. This is predicted by theory due to the direct scaling of the SE transition moment with  $B_1$  field amplitude [74]; additionally, it was shown in experiment that the observed enhancement due to CE is far from saturation at the largest available power [184].

In view of routine DNP applications at high external fields, the development of novel radicals with narrow EPR lines and long

electronic relaxation times becomes highly desirable. Special interest lies in the further investigation and development of heterodimeric PAs for CE that have shown promising early results (see Section 5.2.3). Furthermore, PAs capable of performing OE DNP in solids might be a promising alternative, as the enhancement becomes more effective at high external magnetic fields [90]. Recent experiments have shown that under certain conditions, the enhancement obtained by OE (using BDPA as PA) can even exceed those generated by CE using highly efficient bis-nitroxide PAs [97]. As another alternative, pulsed transfer schemes are expected to be independent of the external field and could lead to improved enhancements provided that the necessary hardware requirements can be fulfilled [166,310].

Despite the ideally expected linear increase of spectral resolution with the external magnetic field, the exact dependence thereof in DNP-enhanced MAS NMR is still discussed in lively controversy. On the one hand, the introduction of paramagnetic species into the sample is a potential source of line broadening (Section 6.1.3). On the other hand, especially in biomolecular NMR, resolution losses due to the “protein glass transition” [312] have complex reasons that are still not fully understood, see also Section 6.2.4 for further discussion. As described in more detail in this sections, non-equivocal observations have been reported in the literature suggesting a potential conclusion that the line broadening processes may not only be strongly sample-dependent but also be determined by both homogeneous and heterogeneous broadening mechanisms. Due to the significant inhomogeneous contribution, the use of higher external magnetic field is not expected to increase the resolution in a linear fashion, even though substantial improvements have been demonstrated [261,311,313–315] as is shown exemplary in Fig. 47. It should also be noted that especially higher-dimensional correlation experiments suffer less from inhomogeneous broadening experienced at high fields and can be utilized in order to resolve overlapping signals without losing signal intensity [149].

### 6.2.2. MAS frequency

Resolution and sensitivity of NMR experiments also benefit from high MAS frequencies. From a mechanistic point of view, the MAS frequency can influence the DNP process during several stages. On the one hand, the adiabaticity of LAC during the CE polarization transfer, discussed in Section 2.1.2.5, depends on the MAS frequency, see Eq. (45). However, for a CE event the adiabatic-

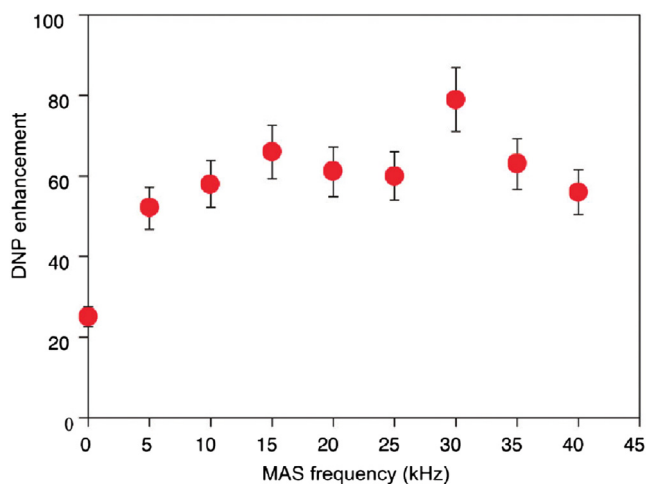


Fig. 48. MAS frequency dependence of the  $^1\text{H}$  DNP enhancement of 0.25 M proline in a typical glycerol/water mixture (DNP-juice) with 10 mM AMUPol at 115 K and 18.8 T. Reproduced with permission from [86].

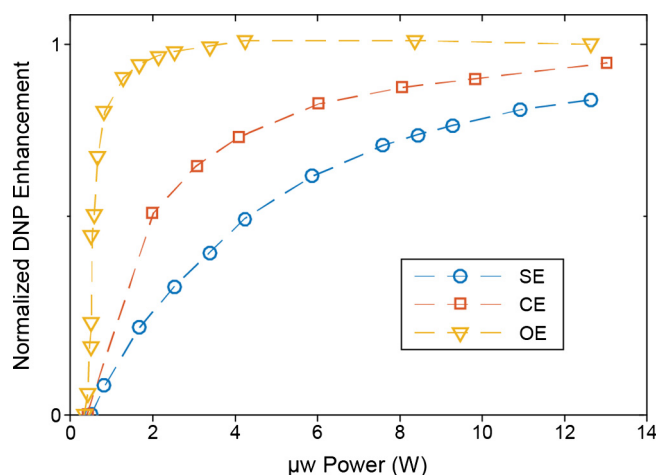


Fig. 49. Microwave power dependence of the normalized DNP enhancement for SE, CE and OE DNP. Data collected from [90,266].

ity parameter  $\Gamma$  is small and the Landau-Zener equation predicts an almost linear dependence of the adiabaticity with the MAS frequency in that range. Thus, a reduction of the transfer probability due to faster MAS is compensated for by the increased number of CE events per unit time [83]. Another potential influence of MAS on the observed global DNP enhancement is caused by the dependence of nuclear spin-diffusion processes on the MAS frequency [316–319]. Due to the scaling of the spin-diffusion rate constants with roughly the inverse of the spinning frequency, detrimental effects, such as a less uniform distribution of polarization over the sample, might be expected. However, if spin diffusion is the rate-limiting step for nuclear spin relaxation at the same time, the overall enhancement factor should remain unaffected [101].

Experimentally, Chaudhari et al. [86] reported only small variations of the  $^1\text{H}$  CE DNP enhancement factor between 5 and 40 kHz MAS at 18.8 T (Fig. 48), suggesting that  $^1\text{H}$  spin diffusion still seems to be fast enough to provide for a homogenous distribution of polarization over the whole sample. Rosay et al. performed an investigation for slow to intermediate MAS frequencies at an external field of 9.4 T. In contrast, they observed a significant influence of the MAS frequency on the  $^1\text{H}$  DNP enhancement, leading to a maximum of  $\epsilon = 80$  at 3 kHz MAS. The decreasing enhancements at MAS frequencies up to 14 kHz were, however, attributed to sample heating effects due to insufficient temperature control (see Section 6.2.4 for further information) [177].

The seemingly simple conclusion of DNP being unaffected by the MAS frequency might no longer be valid for direct DNP on dilute nuclei with small gyromagnetic ratios [318,319]. Here, spin diffusion is generally slower and large overall enhancements might be prohibited by the bottleneck of polarization distribution [138,139]. However, no systematic studies either supporting or refuting this prediction are known to the authors.

It is worth mentioning that in all aforementioned studies, increased enhancement factors were obtained under MAS conditions as compared to static experiments. This indicates significant mechanistic changes of the quantum-mechanic processes in rotating samples compared to static CE-based DNP experiments. Such changes are in line with the theory of CE under MAS by Thurber and Tycko as well as Mentink-Vigier et al. as discussed above and in great detail in Section 2.1.2.

### 6.2.3. Microwave power

An additional observation in the study of Chaudhari et al. is that the enhancement factors obtained for samples in smaller rotors (i.e., 1.3 mm instead of 3.2 mm outer diameter) are significantly

larger [86]. Similar findings have also been reported by Song et al. who compared the DNP efficiency in 4 mm and 2.5 mm rotors [221]. This was claimed to be caused by an improved  $\mu\text{w}$  penetration of the sample due to the reduced wall and sample thickness compared to the larger diameter rotors, finally leading to an increase in average  $\mu\text{w}$  field strength and thus larger enhancement factors [87]. In addition to wall thickness, the rotor material can have an influence on the obtained results, as we have explained in more detail in Section 4.4.3.1. Other experimental findings, where the  $\mu\text{w}$  field is enhanced inside the sample by the addition of diamagnetic particles [320], support such an explanation.

Fig. 49 shows the general trend of the dependence of the enhancement factor on the incident  $\mu\text{w}$  power for several DNP mechanisms. Significant differences can serve as indications to distinguish between the three DNP mechanisms [165]. For SE-type polarization transfer, DNP enhancement factors (as well as the build-up rate constants, see Section 6.1.1) increase almost linearly with increasing  $\mu\text{w}$  power. In contrast, maximum CE enhancements can be reached even with lower  $\mu\text{w}$  power. This is due to the fact that allowed electronic SQ instead of “forbidden” e–n DQ or ZQ transitions must be excited by  $\mu\text{w}$  in this case (see Sections 2.1.1 and 2.1.2). For (solid-state) OE DNP a very steep increase and an early saturation of the transferred polarization as a function of the  $\mu\text{w}$  field is observed, explained by efficient electronic SQ saturation due to long  $T_{1S}$  of the utilized BDPA in combination with efficient excitation of its narrow EPR line. This effect is especially interesting for cases where the  $\mu\text{w}$  power is limited by low-power sources.

In all cases, saturation or even a certain reduction of the enhancement is observed or predicted for very large  $\mu\text{w}$  power [74,152,162,163,177]. Sample heating, which leads to increased relaxation, is expected to play a significant role for a limitation of the maximum applied power [321].

#### 6.2.4. Sample temperature: enhancement factors and spectral resolution

A graphical summary of the DNP enhancement as a function of sample temperature is shown in Fig. 50 for various PAs, obtained from several reports [97,214,217,219,250,271,322]. The maximum enhancement factor measured under MAS up to date has been obtained on a sample doped with AMUPol, which yielded  $\epsilon = 680$  for  $^1\text{H}$  at 55 K [217].<sup>5</sup> A significant contribution towards this increase in DNP enhancement can be traced to the increase in nuclear longitudinal relaxation time constants with decreasing temperature which is important for more efficient accumulation of polarization (see Section 6.1 for further discussion). However, the details of the interplay between electron spin relaxation, nuclear spin-lattice relaxation and motional averaging of dipolar interactions that are responsible for the DNP transfer as well as for the propagation of enhanced nuclear polarization are still unclear, in particular with respect to vanishing enhancement near the glass transition temperature of the solvent [97].

Even though the tremendous increase in sensitivity at low temperature opens up several new fields of applications, the sample constitution under these cryogenic conditions can become an issue. Especially in the case of DNP on biomolecular systems, there has to be a compromise between signal enhancement and a loss of resolution induced by frozen-out dynamics at temperatures below the “protein glass transition” [312,323]. Such a signal broadening for protein samples can already be observed at temperatures that are easily accessible by nitrogen cooling (approximately at 200 K and below) and necessitates a tradeoff between enhancement

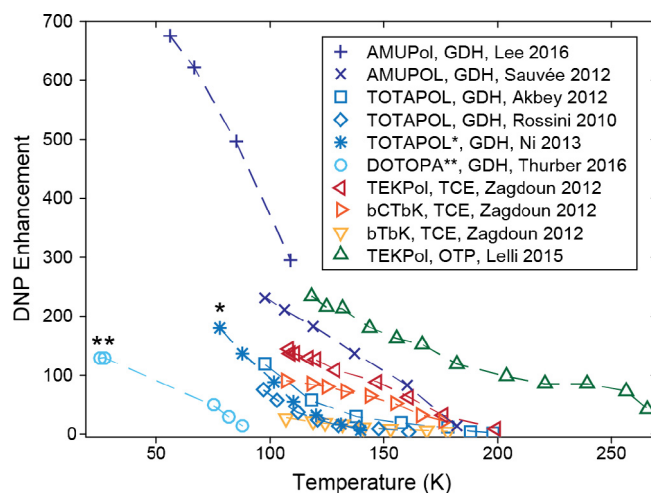


Fig. 50. Temperature dependence of  $^1\text{H}$  DNP enhancement for various PAs and under different experimental conditions. Data was collected from several studies at a  $^1\text{H}$  resonance frequency of 400 MHz [97,170,177,214,216,217,271,274]. The data marked with an asterisk (\*) were recorded at 380 MHz [216]; the data marked with double asterisk (\*\*) were recorded with a low-power  $\mu\text{w}$ . Source [170].

and desired resolution [324]. If higher temperatures are used to avoid these effects, the losses in DNP enhancement can partially be compensated for by faster signal accumulation due to the accelerated build-up of polarization; additionally, deuteration of the sample has shown to increase DNP enhancement factors especially at elevated temperatures (Fig. 51) [214,325]. However, the conditions are not yet sufficient to perform DNP experiments on biomolecules with significant enhancements at or near room temperature.

It is noteworthy that in OTP, significant enhancement factors of up to 20 have indeed been obtained close to room temperature, even at a field of 18.8 T [97]. This holds promise for molecules that are soluble in such a matrix as well as for surface-wetting of insoluble materials. Despite this intriguing observation, it is still unclear in how far the larger overall rigidity of the OTP matrix will alleviate resolution problems at these elevated temperatures.

Despite optimized sample preparation procedures to reduce the above-mentioned broadening [263], extraction of structural information under DNP may still be complicated, in particular for large, uniformly isotope-labeled systems prone to spectral crowding. Very recently, multi-dimensional correlation spectroscopy enabled by the large DNP sensitivity enhancement has been shown to overcome this issue and may be applicable in a general manner [149]. Also, selective isotope labeling has been successfully used to simplify the spectra so that sufficient resolution is retained. For example, several studies on retinal proteins such as bacteriorhodopsin [146,226,227], proteorhodopsin [326,327] and channelrhodopsin [228] have been reported. In order to study structural changes during their photo-cycle, the trapping of intermediate states at temperatures of approximately 100 K is an essential requirement of these experiments. This makes MAS DNP a method of choice even though a certain broadening of the resonances is observed. The interested reader is also referred to Section 7.2.2 for more details on these applications.

In the same vein, reduction of the temperature to cryogenic conditions may result in additional information that is otherwise not accessible. In some cases, the local environment can preserve the line widths of specific resonances so that sufficient resolution is obtained at low temperatures and high magnetic fields. Thus, the occurrence of well-resolved signals is also an indicator for structural or dynamical properties [311,313,328]. Furthermore, highly flexible parts of a macromolecule can be invisible in NMR

<sup>5</sup> The reader should note that this enhancement factor is larger than the theoretically predicted maximum from Eq. (2). This is explained by CE-induced depolarization of the off-signal ( $w/o \mu\text{w}$ ) and explained in more detail in Section 6.1.3.

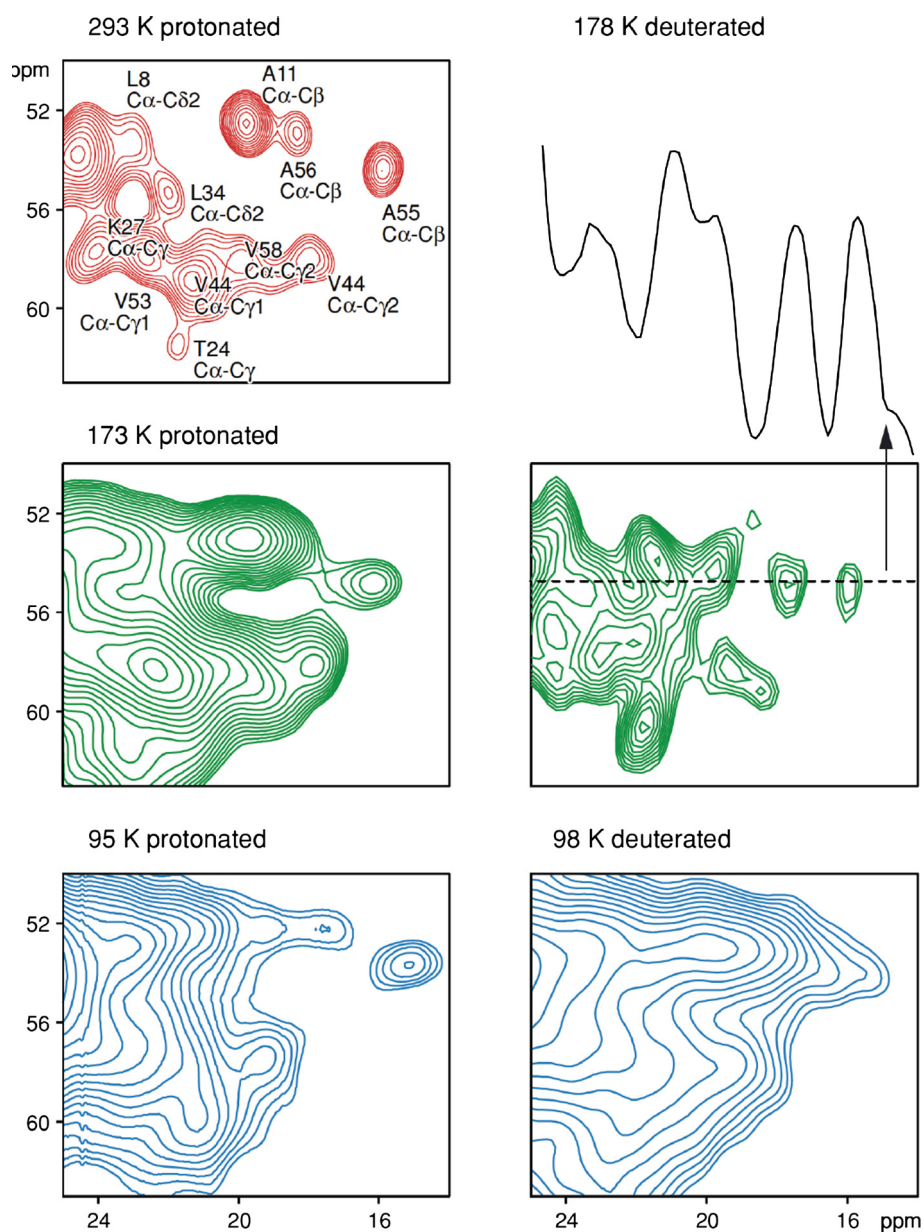


**Fig. 51.** Comparison of the resolution in 2D  $^{13}\text{C}$ - $^{13}\text{C}$  spectra of protonated and deuterated SH3 samples at different temperatures. The figure is reproduced from [214] with permission.

spectra recorded at room temperature and only observed under DNP conditions [261].

Similarly, side-chain dynamics can show distinct differences between room temperature and cryogenic conditions. Many aromatic functional groups show twofold symmetric flips that often interfere with NMR detection. At room temperature, this typically leads to rather broad or even undetectable resonances of aromatic side chain signals. Upon slowing down of the responsible interconversion at typical DNP-relevant temperatures of  $\sim 100$  K the resonances can be recovered [329], allowing for the extraction of a larger number of structural constraints, in particular if coupled with the sensitivity gains from DNP [330,331]. In contrast, three-fold symmetric methyl groups reorient rapidly at room temperature, which results in intrinsically narrow  $^{13}\text{C}$  resonances [332]. Under typical sample temperatures employed in DNP, these hopping dynamics approach an intermediate-exchange regime

and often lead to broad resonances and fast relaxation [324,333]. This situation, however, can give rise to interesting phenomena such as heteronuclear cross-relaxation during DNP (see Section 2.3.5) [141,145].

### 6.3. DNP sample preparation techniques

#### 6.3.1. DNP in a glass-forming matrix

For most DNP experiments, the PA is dissolved in a solvent at ambient temperatures to ensure a uniform distribution. The analyte can be co-dissolved in a homogeneous mixture or it can be heterogeneously dispersed within the solution. In the first case, solubility of all components in the solvent is obviously essential. In the latter case, the enhanced polarization has to diffuse into the phase containing the analyte, such as a lipid bilayer bearing the membrane protein of interest, or microcrystals. For small

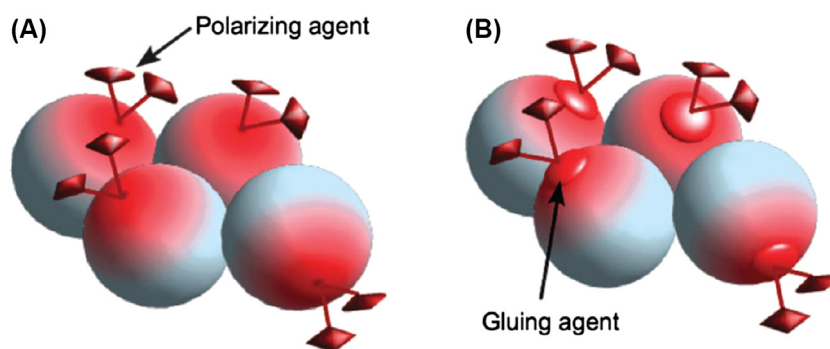


**Fig. 52.** Sketch of the basic principle behind matrix-free sample preparation. In order to avoid phase separation and aggregation upon freezing, the PA is either (A) covalently bonded to the analyte molecules or (B) a “gluing agent” is used to establish close spatial proximity. Figure reproduced from [342] with permission.

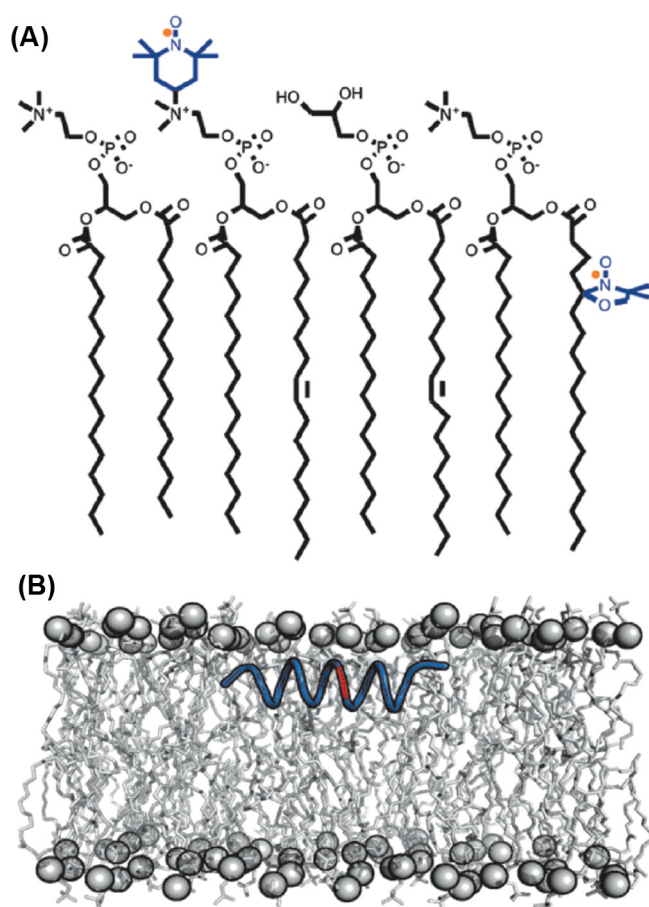


**Fig. 53.** Spatial proximity between PAs and analyte molecules can be guaranteed by covalently decorating the structure preserving matrix (e.g., lipids) with PA units. Figure adapted from [262] with permission.

nanoscopic systems, polarization can be uniformly spread throughout the analyte by  $^1\text{H}$  homonuclear spin diffusion, while for larger microscopic systems a polarization gradient is observed as a function of the distance from the surface [138,258].

Crystallization of the solvent upon freezing can cause phase separation between the PA and the analyte molecules, leading to strongly reduced enhancements [281]. For this reason, the solvent should be a good glass-forming agent and additionally offer cryoprotection of the analyte upon freezing. Especially biomolecules might undergo cold-denaturation processes or phase transitions

due to solvent crystallite formation. This may lead to heterogeneity of the sample and result in reduced spectral resolution or even to an irreversible adaption of non-functional structures that must be circumvented or minimized by the appropriate solvent. Often, the so-called “DNP-juice” ( $d_8$ -glycerol/ $\text{D}_2\text{O}/\text{H}_2\text{O}$ , 60:30:10%) or  $d_6$ -DMSO/water mixtures are used as glass-forming matrix for aqueous solutions [334,335]. While DMSO often provides better solubility for PAs, glycerol is favored for biomolecular systems due to their larger stability in this solvent. In the case of hydrophobic compounds, TCE or OTP can serve as good glass-forming agents [97,274,280,281,336].

### 6.3.2. Alternative sample preparation techniques

The addition of a large amount of cryoprotectant causes a reduction in sample filling factor and thus a significant reduction in signal intensity that has to be accounted for when assessing the absolute sensitivity ratio (see Section 6.1.3). Additionally, the matrix might disturb the properties of the analyte. In order to tackle these issues, alternative ways of preparing samples in order to achieve a homogenous radical distribution while avoiding any (excess) solvent matrix are being developed.

One such sample preparation technique is “incipient wetness impregnation” that is specifically suitable for porous samples that are insoluble in the PA-bearing solvent [255]. Here, the solution is added to the sample in such a small volume that the pores and the surface are saturated with solvent while excess volume is avoided to optimize the sample filling factor. Also, due to the altered physical properties of the solvent molecules upon direct contact with the surface, crystallization upon sample freezing is prevented.

Other techniques are co-sedimentation of large biomolecules [337,338], co-condensation for functionalization of mesoporous silica with nitroxide radicals [142], film casting of polymers, [339] or co-milling of solid samples with a matrix-forming agent [340]. In the special case of amorphous polymers, a solvent-free sample preparation is feasible. In order to avoid phase separation, the PA is covalently bonded to (a fraction of) the analyte molecules [341].

### 6.3.3. Matrix-free approaches

Recent approaches explore the possibility to study systems without the use of the typical glass-forming solvents. Aggregation and phase separation of the individual components of the sample upon removing the solvent can be avoided if the PA exhibits a certain binding affinity to the analyte (Fig. 52A). Otherwise, “gluing agents” establish contacts between PA and analyte (Fig. 52B) [342]. Such an approach is especially appealing in systems that are prepared in a structure-preserving matrix. For example, membrane proteins are usually reconstituted in a lipid matrix that mimics their native environment. For matrix-free DNP experiments,



such liposomes have been stabilized in combination with small amounts of alternative cryoprotectants like trehalose [343]. Furthermore, the PA can be bonded covalently to molecules in the environment (Fig. 53B) rather than distributed randomly over the whole sample [262,340,342,343]. A maximized filling factor of the NMR rotor and the close spatial proximity between PA and analyte lead to promising sensitivity gains compared to samples where the PAs are distributed statistically over the sample. Furthermore, under certain conditions, signal broadening was reported to be less severe than in the classic approach using bulk glass-forming agents [342].

In the context of applications to materials science, solvent-free DNP-enhanced NMR of an organic–inorganic hybrid material has been demonstrated on mesoporous silica functionalized with TEMPO moieties. Lilly Thankamony et al. incorporated TEMPO into porous inorganic silica materials by co-condensation, enhancing  $^{29}\text{Si}$  NMR signals by direct DNP. Due to the close vicinity between PA and nuclear spins, the  $^{29}\text{Si}$  signals rapidly build up in direct DNP experiments—which further improves the NMR sensitivity [142]. Later, Gajan et al. also demonstrated matrix-free DNP applications to insoluble hybrid organic–inorganic silica materials containing homogeneously distributed mono- or dinitroxide radicals [344]. Meanwhile, the fast acquisition of 2D  $^{13}\text{C}$ – $^{13}\text{C}$  NMR correlation spectra of natural abundance microcrystalline cellulose—in which the PA is again uniformly distributed without any solvent—was also reported by the group of Gaël de Paëpe [345]. Later, they also introduced a novel matrix-free sample preparation approach for the study of nanoassemblies such as diphenylalanine (FF) dipeptide [260].

#### 6.3.4. Localized and targeted DNP

More recently, several studies on localized or targeted DNP using site-directed spin labeling (SDSL) schemes or non-covalent labeling with PA-bearing tags or ligands have been reported. In the localized DNP approach, a close and well defined spatial proximity between PA and target molecules is achieved by specifically attaching the PA to native or point-mutated cysteine sites in proteins by SDSL [139,262,346–348], a technique often utilized in EPR spectroscopy or for PRE/PCS studies by NMR spectroscopy. In a very elegant demonstration, it has been shown that the contact interfaces of two proteins within a heterodimer can be probed, using CE DNP in combination with SDSL. By attaching one (mono-)nitroxide PA tag to each of the two subunits, CE DNP is only enabled if the complex adopts a closed conformation thus that the two nitroxides are in dipolar contact [348].

For targeted DNP, a modified ligand or paramagnetic metal ion is specifically bound to the biomolecule of interest [140,349,350]. Endogenous radicals such as the flavin mononucleotide semiquinone in the flavodoxin protein have also been shown to act as PA [92]. These approaches allow for selective DNP transfer to the analyte while loss of hyperpolarization due to spreading to the bulk can be prevented by deuteration of the latter [349,350], or by employing direct DNP of a biomolecule that is enriched with low- $\gamma$  nuclear isotopes [140]. Further information about the application of these techniques is provided in Section 7.2.

### 6.4. Sample constitution

#### 6.4.1. Isotopic enrichment and depletion

As mentioned above, the initial polarization transfer step from the electron spins to nearby “core” nuclear spins is followed by spin-diffusion processes that are responsible for a spatial distribution of the magnetization to bulk nuclei and thus play an important role for efficient DNP. The proton concentration of the matrix was found to have a strong impact on the DNP enhancement, hence the typically used ratios of deuterated and protonated components

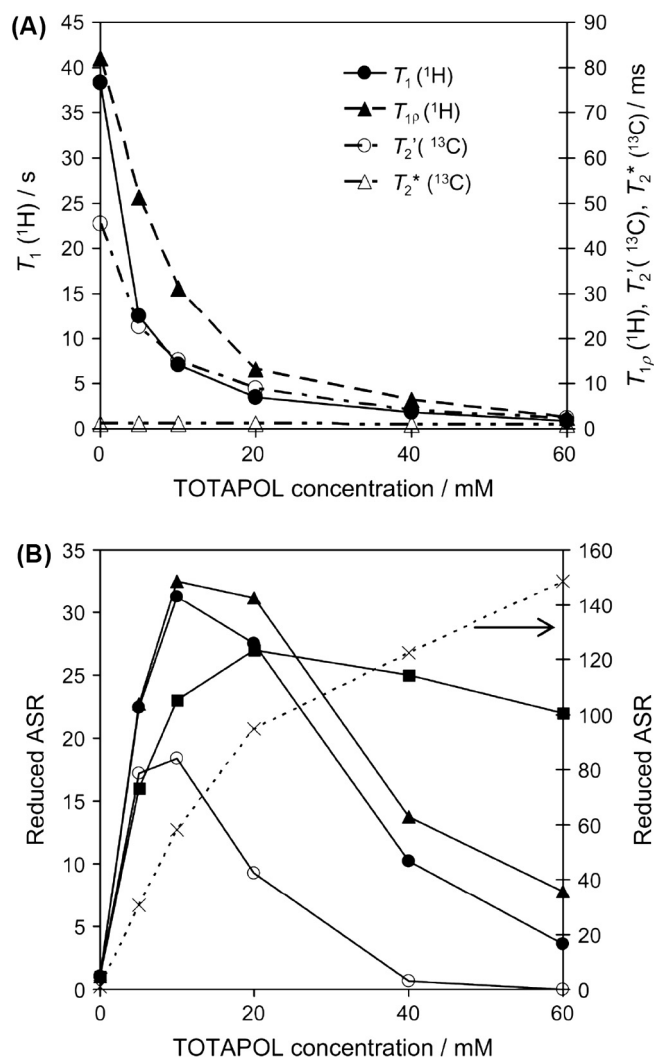


**Fig. 54.** (A) Influence of the concentration of TOTAPOL on  $^1\text{H}$  and  $^{13}\text{C}$  relaxation times on 2 M  $^{13}\text{C}$ -urea in  $d_6$ -DMSO/ $\text{D}_2\text{O}$ / $\text{H}_2\text{O}$  (60/30/10 vol%). (B) Resulting absolute sensitivity ratio (ASR) in a refocused INADEQUATE experiment, combining DNP and relaxation effects. Data show DNP enhancement factor only (squares), as well as cumulatively adding the following parameters: acceleration of experiment due to reduction of build-up time constants (crosses), loss of signal due to bleaching (triangles), reduced CP efficiencies due to increased relaxation in the rotating frame (full circles) and loss of signal during mixing due to increased transverse relaxation (open circles). The right ordinate axis is used for data represented by crosses. Reprinted from [308] with permission.

(see also Section 6.3.1) [335]. While a sufficiently high level of protonation has to be provided in order to guarantee efficient pathways for nuclear spin diffusion, the deuteration increases the electronic as well as nuclear relaxation times and in turn the DNP enhancements [74,351]. This depends strongly on the PA and DNP mechanism involved [74]. Also, recent reports have shown indications that no loss in DNP enhancement is observed even for fully protonated matrices when highly-efficient PAs such as AMUPol are used [141]. However, systematic studies are required to identify the optimal  $^1\text{H}$  bulk concentration over a large range of experimental parameters.

Additionally, deuteration of the PAs [250,352] and target molecules [325] has been shown to improve the DNP enhancement due to optimized relaxation properties. As proton detection may become feasible with the latest generation of commercially available fast-spinning DNP probes, a dilution of the strongly dipolar-coupled proton network has the obvious advantage of

improved resolution of  $^1\text{H}$  spectra [353]. Because in most DNP experiments to date the  $^1\text{H}$  magnetization is read out after CP to the respective nucleus, a certain degree of protonation is required for improved sensitivity [354]. Thus, optimal ratios under DNP-enhancement are expected to be dependent on the PA and the sample under study.

Similar arguments also hold for direct DNP of low- $\gamma$  nuclei. In that case, proton-driven spin diffusion leads to a significant distribution of the polarization, however, it requires sufficiently high concentration of the low- $\gamma$  nuclear species (e.g., upon isotopic enrichment). In contrast, certain parts of the sample (e.g., solvent matrix, linker) in natural abundance or even depleted in the magnetically active isotope can selectively block transfer pathways [139–141,349]. Trivially, isotope depletion of the solvent also eliminates background signals that otherwise might overlap with the spectrum of the analyte [337].

#### 6.4.2. Polarizing agent concentration

As should be clear from the discussion in the previous sections, the concentration of the PA has to be adjusted carefully such that optimal enhancement, sensitivity and resolution are obtained [252,308,340]. The underlying effects are complex, and in most cases difficult to predict.

On the one hand, a certain number of unpaired electrons need to be available, serving as source of polarization. Furthermore, the relative contributions of various DNP mechanisms depend on the radical concentration (see Section 3 for further information). In particular, e–e contacts required for the CE become more probable if monoradicals are used in high concentrations. For biradicals, this proximity is always given and a rather low concentration is generally sufficient to obtain sufficient enhancements by CE.

On the other hand, a high (global or local) concentration of radicals causes unfavorable quenching effects (Sections 6.1.2 and 6.1.3) resulting in reduced sensitivity and potentially in a loss of spectral resolution and information [85,225,253]. The increased relaxation rates may also cause losses in efficiency during recoupling and polarization transfer experiments [252,253]. However, the reduction of polarization build-up times (Fig. 54A) is beneficial as it allows for increased repetition rates.

Experimental findings (Fig. 54B) indicate optimum PA concentrations between 10 and 20 mM for homogeneous solutions. In particular cases, for example if long coherence decay times are necessary for efficient transfer of polarization between nuclei over intermediate/long distances, a reduced PA concentration can be beneficial [259]. In addition, it should be noted that in more complex samples, interactions between the analyte and the PA can result in larger effective, local concentration of paramagnetic centers around the nuclear spin systems of interest (see below). In this case, the global concentration has to be adjusted accordingly, such that excessive line broadening or quenching is avoided [355].

#### 6.4.3. Interactions between polarizing agents and analytes

In addition to an influence on electronic relaxation properties, the molecular size and geometry of the radicals may also have application-specific consequences. For example, larger radicals may not enter porous materials, which on the one hand may lead to lower signal enhancements but on the other hand cause less quenching. Thus, the dimensions of the radicals themselves can be a useful parameter to investigate [356], see more details in Section 7.3.2.

In any case, a possible interaction between the radical and the substrate has to be considered because a very large local concentration of PA can cause line broadening of the NMR resonances (see above section). For example, Ravera et al. exploited non-specific interactions for co-sedimentation of proteins and PAs [338]; furthermore, specific interactions with TOTAPOL have been

observed in BSA [337]. PAs have also been found to bind to amyloid surfaces [355] and active surface sites in porous materials [357]. Highly specific interactions between a PA-carrying ligand and a protein have been utilized deliberately to obtain selective hyperpolarization in the case of targeted DNP [349,350]; this approach is covered in more detail in Sections 6.3.4 and 7.2.5. Finally, possible reactions of the PA with other components of the sample—leading to a destruction of radical functionality and consequently to a loss of DNP (but possibly a gain in resolution)—have to be considered as well [358].

## 7. Structure determination enabled by DNP enhancement

MAS DNP has come a long way since the earliest pioneering applications on polymers and materials in the laboratories of Wind and Schaefer and the groundbreaking later works dominated by Griffin. Applications in the first  $\sim 2\frac{1}{2}$  decades (i.e., 1983–2009) were largely guided by the development of custom-built hardware. Furthermore, DNP applications towards biomolecular systems required a significant amount of proof-of-concept development in order to become interesting for the young, quickly developing field of biological MAS NMR.

Nevertheless, the commercialization of MAS DNP instrumentation around 2009—in combination with a quickly growing and highly creative community—paved the way for the popularity of MAS DNP today. This has led to a tremendous increase in reported state-of-the-art DNP applications towards structural problems from various research groups, first in the field of materials science, and more recently also in the field of structural biology. In the following, we will give an overview of these developments and of the diverse field of applications.

### 7.1. Pioneering works on MAS DNP

#### 7.1.1. Early applications on polymers and diamonds

Wind and coworkers introduced the instrumentation suitable for MAS DNP and presented the first DNP-enhanced MAS NMR of coal as well as BDPA-doped polystyrene as early as 1983 [359]. During the following years they applied the method to study the structural properties of various materials such as undoped trans-polyacetylene [360], doped polymers [361], coal [362], amorphous silicon [363], organic conducting polymers [364], ceramic fibers [365], and diamond films [366]. All of these experiments were performed at room temperature using an external magnetic field of 1.4 T (40 GHz  $e^-$ , 60 MHz  $^1\text{H}$ ).

The structural defects of undoped trans-polyacetylene were studied in detail by indirect  $^{13}\text{C}$  DNP NMR, using intrinsic defects (i.e., unpaired electrons in the material) as PA. Spectra recorded before and after air oxidation showed the formation of oxygen bridges, as well as epoxide, hydroxyl and carbonyl groups in  $^{13}\text{C}$  spectra [360]. It was also shown that direct and indirect DNP can probe the surface structure of  $^{13}\text{C}$ -enriched chemical-vapor-deposited diamond films [366]. Using indirect DNP ( $^1\text{H}$ - $^{13}\text{C}$  CPMAS), all carbon atoms in the sample were enhanced uniformly because of fast spin diffusion among  $^1\text{H}$ . This signal enhancement enabled the acquisition of spectra, which would require impossibly long measurement times under conventional MAS NMR conditions. Besides that, by employing  $^{13}\text{C}$  (direct) DNP in samples with natural isotopic abundance, only the rare  $^{13}\text{C}$  spins near to the radicals were enhanced [367]. An excellent overview of these pioneering works is given in a review by Wind et al. [63].

Later, the group of Schaefer studied heterogeneous blends of undoped polycarbonate (PC) and of polystyrene that was homogeneously doped with BDPA, by using indirect [231,368] and direct DNP of  $^{13}\text{C}$  [369]. Filtering to retain only enhanced NMR signals

of PC by comparing  $\mu\text{W}$  on- and off-signals allowed for selective detection of the polymer interface. As a result, it was possible to show that molecular dynamics of interface chains were retarded as compared to those within the PC bulk [370].

Another early effort towards MAS DNP was undertaken by the Zhou lab, using a custom-built 53 GHz (1.8 T) instrument. They were able to investigate the structures of different natural [78] and synthetic [79] diamonds using direct  $^{13}\text{C}$  DNP NMR. Such studies are usually prohibited by extremely long spin-lattice relaxation time constants; however, a DNP enhancement factor of  $\sim 1000$  allowed for acquisition of sufficient signal intensity after reasonable polarization times. Further studies involved hyperpolarization of pitch using the intrinsic unpaired electrons as PA [371].

### 7.1.2. Pioneering developments enabling biomolecular DNP

In the early days, the development required for DNP-enhanced MAS NMR spectroscopy on biological samples was almost exclusively driven by the pioneering work of Griffin and co-workers. In principle, NMR-sensitivity for most biomolecular systems is smaller than that of (bulk) materials or powdered systems because biomolecules form crystals with a high water content, or are embedded in conformation-stabilizing matrices such as lipids. Therefore, the first seminal demonstration of possible sensitivity enhancement by DNP transfer from a co-dissolved PA to a small biomolecule (1- $^{13}\text{C}$ -glycine) in frozen solution showed a way to overcome this problem. Shortly thereafter, Hall et al. hyperpolarized the amino acid L-arginine as well as  $^{15}\text{N}$ -Ala-labeled T4 lysozyme using TEMPO as PA and achieved DNP enhancements up to 50-fold, proving that protein structural biology by MAS NMR can benefit from a large sensitivity gain [218].

Subsequently, Rosay et al. extended the investigation to soluble and membrane proteins as well as to an intact bacteriophage, consisting of virus capsid and the contained genome. By analyzing the DNP enhancement factors of the coat protein and the single-stranded DNA core of fd bacteriophages, it was shown that  $^1\text{H}$  polarization can efficiently diffuse through the 20 Å thick coat layer, allowing for hyperpolarization of the encapsulated genome that is not in direct contact with the solvent [372]. Furthermore, it was demonstrated, that structurally relevant amino acid signals of (membrane) proteins can be resolved in the DNP-enhanced spectra even for uniformly isotope-labeled samples [373].

Another proof-of-principle has been provided by van der Wel et al. by hyperpolarization of GNNQQNY nanocrystals. This oligopeptide forms the core of the yeast prion protein Sup35p and can undergo fibrillization; consequently, it served as a test-bed for the investigations of amyloid fibrils that play a key role in many neurodegenerative diseases. DNP caused a polarization gradient within the relatively large nanocrystals that not only allowed for direct analysis of the spin-diffusion kinetics governing the spreading of enhanced  $^1\text{H}$  polarization, but also served as proof that heterogeneous, nanoscopic structures such as amyloid fibrils can be effectively investigated by DNP-enhanced NMR [258].

## 7.2. Modern applications on biological systems

Especially for large biomolecular systems like protein–protein complexes or membrane proteins, the intrinsically low sensitivity imposes challenges for structure elucidation by solid-state NMR. Thus, biomolecular NMR spectroscopy can benefit in several ways from the signal enhancements provided by DNP. Obviously, the increased signal-to-noise ratio allows for gathering the required information in less experimental time and the measurement of higher-dimensional spectra in fully labeled compounds becomes feasible which can provide additional structural information or simplify spectral assignment [149].

Furthermore, the required isotope labeling is often cost-expensive or the enriched samples can hardly be produced and purified in copious amounts. Provided the DNP enhancement is sufficiently large, multidimensional experiments of samples at natural abundance even in rather small amounts may be envisioned, as has been demonstrated for small organic molecules [138,151,342,374] and for a peptide embedded in bioinspired silica [375]. For samples at natural abundance, the structurally relevant long-distance restraints can be measured reliably, as no dipolar-truncation effects by strong dipolar couplings (e.g., between neighboring carbons) suppress the polarization transfer between weakly-coupled nuclei [376].

### 7.2.1. Amyloid fibrils

The principle of DNP on amyloid fibrils was demonstrated by Debelouchina et al. on GNNQQNY fibrils [330]; this system has already been described in above Section 7.1.2. Due to their structural rigidity amyloid fibrils are an ideal sample system for investigation by DNP-enhanced NMR. There is experimental evidence that for amyloid- $\beta$  ( $A\beta_{40}$ ), this can result in comparable line widths at room temperature and at cryogenic temperatures relevant for DNP [315].

The large sensitivity gains from DNP can greatly facilitate the measurement of medium- to long-range distances that typically require the acquisition of a large number of different mixing times. This advantage has been utilized by Bayro et al. for the generation of intermolecular constraints in order to elucidate the arrangement of  $\beta$ -strands within fibrils formed by the 86-residue SH3 domain of PI3 kinase (PI3-SH3). Under MAS DNP conditions, a significantly larger number of intermolecular constraints could be obtained that was attributed not only to the larger signal intensity due to DNP, but also due to the occurrence of resonances at cryogenic temperatures that are dynamically quenched at or near room temperature. Based on a total of 111 intermolecular  $^{13}\text{C}$ - $^{13}\text{C}$  and  $^{15}\text{N}$ - $^{13}\text{C}$  constraints, it was established that the PI3-SH3 protein strands are aligned in a parallel arrangement within the amyloid fibril [331].

Similarly, investigation of the higher-order structure of fibrils is a pivotal step towards understanding the extraordinary stability of the amyloid architecture. Debelouchina et al. succeeded in deriving the protofilament arrangement within fibrils formed by an eleven-residue segment of the amyloidogenic protein transthyretin. Due to large savings in acquisition time, it was possible to obtain a large number of quantitative distance and torsion-angle restraints in order to derive an accurate structure (Fig. 55) [377].

The formation of  $A\beta_{40}$  fibrils has been studied by Tycko and co-workers by DNP-enhanced MAS NMR at very low temperatures near 30 K. Potapov et al. were able to monitor intermediate steps of the self-assembly process of  $A\beta_{40}$  from monomers *via* oligomers and protofibrils to form fibrils by freeze-quenching the fibrillization process at different points of time [378]. They found that the supramolecular  $\beta$ -sheet structure only forms during the fibril stage, but that the molecular conformation is qualitatively similar at all stages [378].

Weirich et al. have elucidated the structure of amyloid fibrils formed from islet amyloid polypeptides that are a hallmark of type-2 diabetes mellitus and are known to be cytotoxic to pancreatic  $\beta$ -cells. Here, DNP-enhanced MAS NMR at cryogenic conditions supported the study of the conformational flexibility of the N-terminal residues [379].

An intriguing observation was made by Nagaraj et al. when investigating functional amyloids formed by CsgA protein. They found that TOTAPOL has the propensity to bind to the fibril surface, similar to the fluorescent dye thioflavin-T (ThT). DNP from only 0.25 mM TOTAPOL allowed for the extraction of long-range distance constraints, which were difficult to obtain without

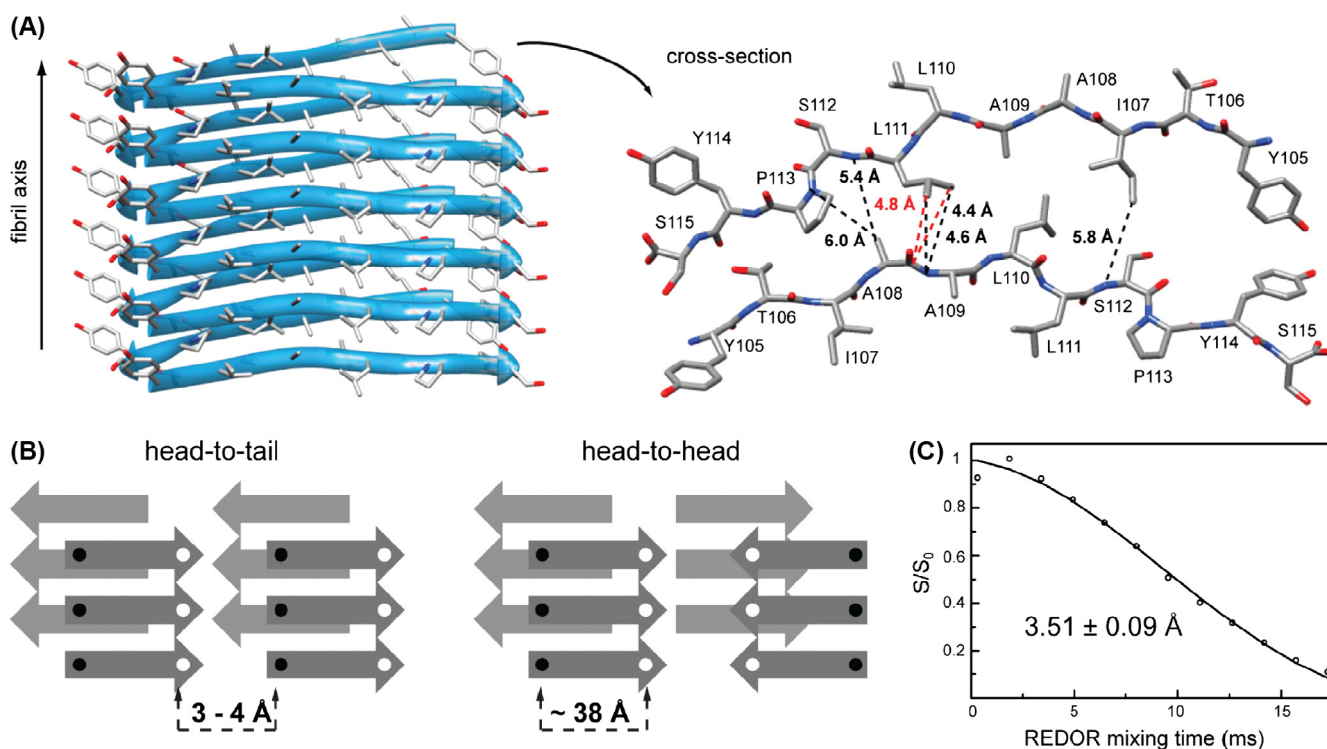


**Fig. 55.** (A) Structure of the amyloidogenic protein transthyretin TTR(105–115) protofibril (PDB ID: 2m5n). View along the fibril axis with an emphasis on the parallel, in-register  $\beta$ -strands within each  $\beta$ -sheet (left), and summary of the observed quantitative contacts that constrain the odd-even-odd-even antiparallel  $\beta$ -sheet interface (right). (B) Two possible arrangements of the protofilaments are head-to-tail and head-to-head arrangements. (C) DNP-enhanced  $^{15}\text{N}$ - $^{13}\text{C}$  experiment with REDOR mixing was used to measure the distance between the two labels. The fitted distance is  $3.51 \pm 0.09 \text{ \AA}$ , consistent with a head-to-tail protofibril organization. Figure adapted with permission from [377].

sensitivity enhancement. The small PA concentration reduced the line broadening occurring under conventional PA concentrations. Such affinity towards fibril surfaces is proposed to be a general feature of amyloids [355].

### 7.2.2. Membrane proteins

The function of membrane proteins is crucial in understanding many transport processes in biology that are often linked to diseases and their treatment. Therefore, they offer an intriguing target for solid-state NMR while being constituted within an immobilizing lipid bilayer. This, however, leads to a small effective protein concentration and thus typically low NMR sensitivity that can be overcome by DNP.

Interestingly, the requirement for cryogenic temperatures in order to conduct DNP experiments and the resulting freezing of biomolecular dynamics—which often imposes a substantial challenge due to signal broadening—also offers the possibility to access states that may otherwise be hidden in conventional NMR at or near room temperature. Such trapping of states has been impressively demonstrated with the first major biological application of MAS DNP. Griffin and co-workers have trapped several intermediate states of the photocycle of bacteriorhodopsin (bR) by photoactivation due to *in-situ* optical irradiation (see Section 4.4.3.3) and controlled thermal relaxation. The conformational ensemble is then conserved and spectroscopically accessible during the acquisition of DNP-enhanced MAS NMR spectra at cryogenic temperature. Such a technique has enabled the first observation of the early K state of bR by NMR. Mak-Jurkauskas et al. identified significant changes in retinal Schiff-base/counterion interactions between the light-adapted resting state (bR<sub>568</sub>), the K state, and the L state that is reached by thermal relaxation [226]. Furthermore, in a subsequent study by Bajaj et al., the interaction with the counterion was found to play a crucial role in the adoption of

several possible L-state conformations: out of a discrete set of four observed L substates, only one functional state with a very strong counterion interaction allows the further photocycle evolution towards the M state, while three shunt substates of L directly revert the system back to bR<sub>568</sub> [227].

Similar investigations have been conducted by Glaubitz and co-workers on the related retinal proteins proteorhodopsin (PR) and channelrhodopsin-2 (ChR2). By employing an *in-situ* light-irradiation technique similar to that used in the above-described studies, Becker-Baldus et al. have been able to investigate the conformation of retinal and its interactions within the active site in ChR2 (Fig. 56). They found three distinct intermediates of the photocycle; whereby two of those could be trapped by repeated illumination, freezing, and thermal relaxation, the third could only be detected during continuous illumination [228]. The same group has also applied ex-situ illumination in combination with freeze-quenching of photointermediates of PR, which allowed for the detailed analysis of photoactive-site interactions during the photocycle with DNP-enhanced MAS NMR [380]. Furthermore, Mao et al. were able to accurately determine the structural changes in the retinal that give rise to green/blue color switching caused by a single point mutation [326] and Maciejko et al. studied the contacts across protomers in PR oligomers. In the latter case, it was shown that one specific salt-bridge is responsible for the formation of pentamers or hexamers [327].

DNP is also a powerful tool for the investigation of ligand binding to (membrane) proteins where orthogonal labeling strategies (e.g.,  $^{13}\text{C}$ -ligand/ $^{15}\text{N}$ -protein or vice versa) allow for selective spectroscopy of ligand-protein contacts even in the presence of substantial line broadening. Such an approach was pursued by Andreas et al. for studying the binding of the small drug molecule rimantadine to the M2<sub>18–60</sub> proton transporter from influenza A virus. By employing a rather small TOTAPOL concentration of only

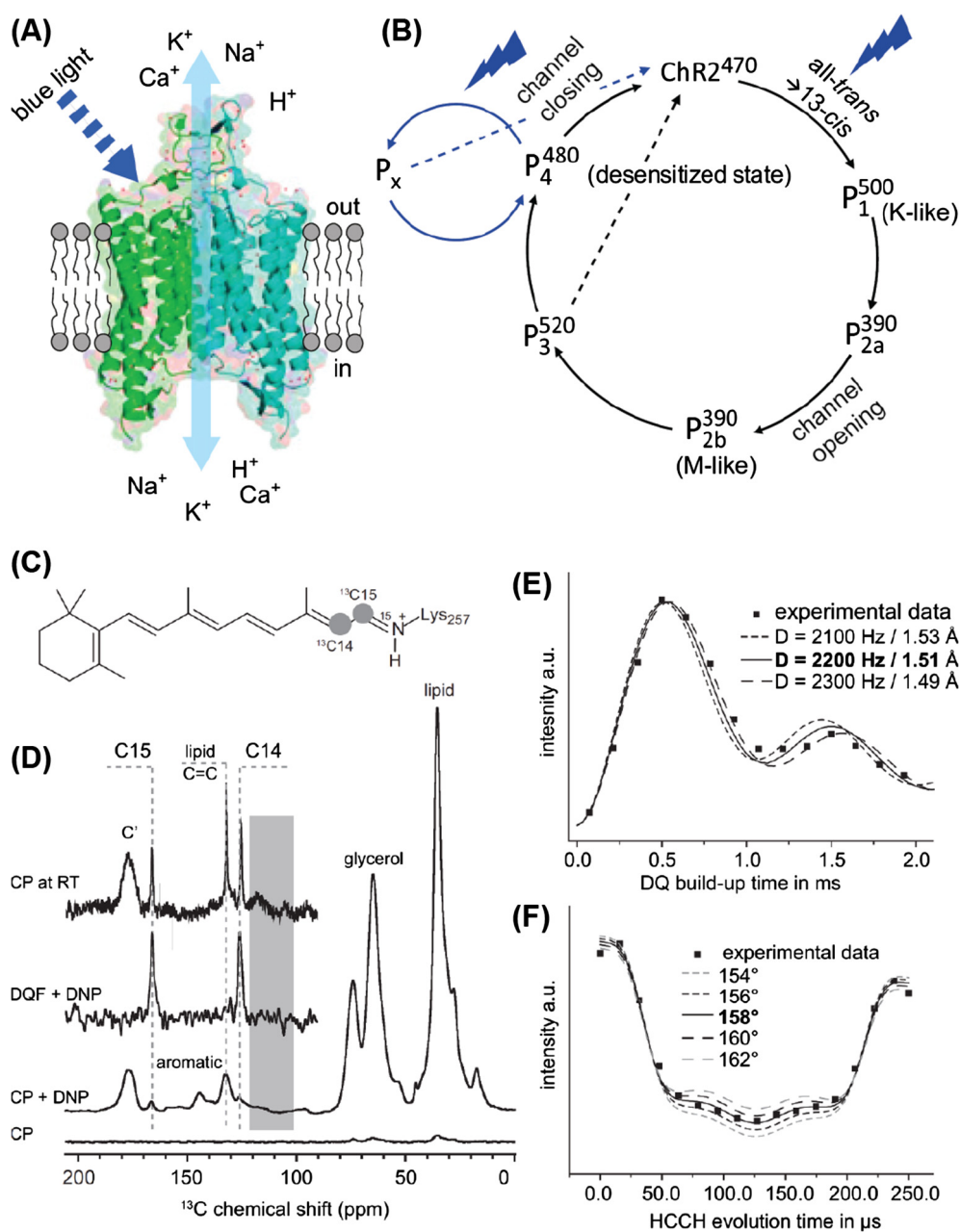


**Fig. 56.** (A) Visualization of dimeric ChR2 reconstituted into a lipid bilayer. Blue light illumination activates ChR2. (B) Single turnover (black arrows) and continuous illumination photocycle (blue arrows). (C) Chemical structure of 14,15-<sup>13</sup>C all-trans retinal. (D) DNP-enhanced MAS NMR of U-<sup>15</sup>N-ChR2 containing 14,15-<sup>13</sup>C retinal. A 62-fold signal enhancement is achieved for <sup>13</sup>C CP; the natural abundance background can be efficiently suppressed by a double-quantum filter (DQF). (E) <sup>13</sup>C14-<sup>13</sup>C15 double-quantum (DQ) build-up curve. (F) HCCH dephasing curves for the C14-C15 spin system in ChR2 reporting on the HCCH dihedral angle. Figure adapted from [228] with permission.

~5 mM, the measurement of intermediate/long-range distances of 4 Å and larger allowed for the localization of the binding site within the pore with an accuracy of 0.2 Å, and furthermore allowed for the observation of weak (dynamical) external binding sites [259]. In the same vein, Ong et al. investigated the binding of two different substrates to the secondary multidrug efflux pump EmrE by DNP-enhancement of homonuclear, intermolecular contacts between <sup>13</sup>C-labeled substrate and 2-<sup>13</sup>C-glycerol-labeled protein. It was possible to identify a common binding pocket occupied by both substrates while at the same time the bound ligand population showed some degree of heterogeneity [381].

Further DNP-supported studies of membrane proteins and membrane-embedded peptides include the assembly of a

correctly-folded and functional heptahelical membrane protein by protein trans-splicing [382], the observation of multiple conformations of lipid-anchored peptide vaccines [383], as well as the refinement of the membrane-embedded channel structure of a potassium channel (KcsA) [313]. The latter study by Koers et al. revealed conformational sub-states in two different stages of the channel's gating cycle.

Amongst very recent efforts, DNP has been explored by Glaubitz and co-workers as a method for the investigation of *E. coli* MsbA as a model ATP-binding cassette (ABC) transporter and signal enhancement factors of ~20 have been obtained [384]. Shortly thereafter, the same group has applied DNP-enhanced MAS NMR for studying the human transporter associated with antigen

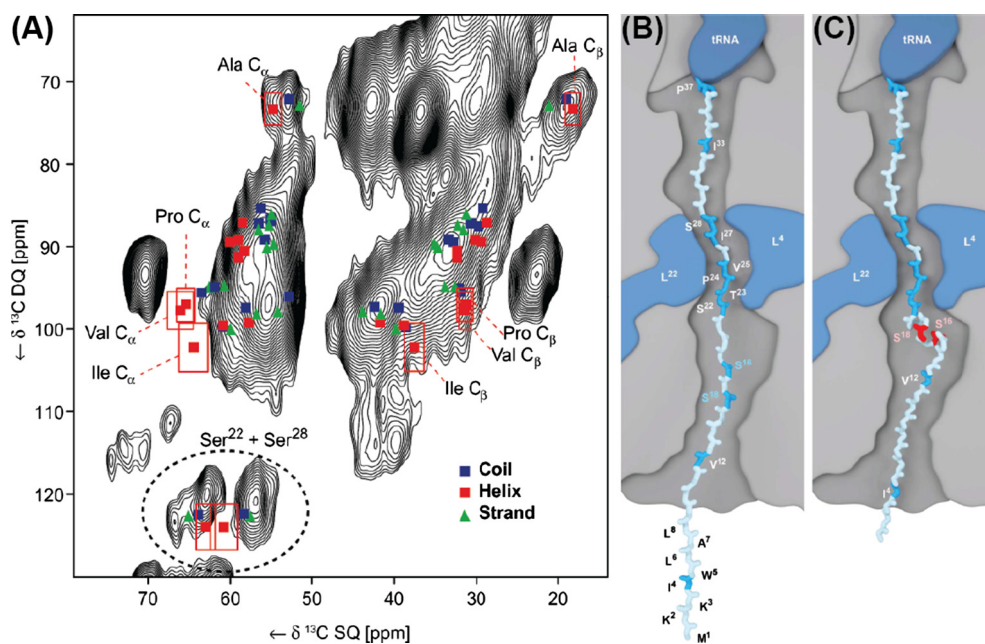


**Fig. 57.** (A) Comparison of DNP-enhanced POST-C7 DQ-SQ spectra of the ribosome embedded nascent chain S16A/S18A-DsbA-SecM overlaid with predicted chemical shifts for three different tertiary structures. (B + C) Structure models of nascent chains assuming a stretched (B) and a partial helical conformation (C). Reproduced from [387] with permission.

processing (TAP), a 150 kDa heterodimeric ABC transport complex. The successful identification of the binding cavity of an antigenic peptide as well as its backbone conformation and interactions with the protein is the first step to determine the structural basis for the function of TAP in human health [385].

### 7.2.3. Structure of biomolecules in large complexes

DNP has been intensively employed in the investigation of large biomolecular complexes that often suffer from potential spectral crowding and the small volume concentration of the sought-after species. For example, Oschkinat and co-workers have recently studied the structure of a chromophore in phytochrome photoreceptors. DNP-enhanced MAS NMR supported the localization of the positive charge of the phycocyanobilin (PCB) chromophore. Furthermore, the proximity of PCB ring nitrogen atoms and functionally relevant water molecules was also determined, both of which play a role in proton exchange pathways [386].

The same group has also investigated the structure of a signal sequence of disulfide oxidoreductase A (DsbA), stalled within the nascent chain exit tunnel of the ribosome. Such a situation not only imposes a selectivity problem due to the large background of the ribosome (>5000 a.a. vs. 37 a.a. of the peptide) but also a sensitivity problem due to the small effective concentration of the nascent peptide [387]. While the former problem can be compensated for by isotope labeling strategies, the latter problem can be overcome by DNP as has been first demonstrated by Bodenhausen and co-workers on a protein subunit within a ribosomal complex [388]. In the above-mentioned study, enhancement factors between 15 and 20 have allowed Lange et al. to investigate the conformational states of the peptide resembling the nascent chain. In conclusion, the chain adopts an extended structure in the ribosome with only minor populations of helical structure (Fig. 57) [387].

The epidermal growth factor receptor (EGFR) has been recently investigated in a collaborative effort headed by Baldus and van Bergen en Henegouwen. As one of the most common protein targets in anti-cancer therapy, its activation by epidermal growth factor (EGF) is of utmost interest. Therefore, Kaplan et al. studied the changes in EGFR dynamics upon binding of EGF (Fig. 58). By

employing DNP-supported MAS NMR they found that in the ligand-unbound state, the extracellular domain (ECD) is highly flexible, while the intracellular kinase domain (KD) is rigid. Upon binding of EGF, the ECD becomes restricted in its motions, which favors cooperative binding. The latter is required for receptor dimerization, which in turn causes allosteric activation of the intracellular tyrosine kinase [389].

Furthermore, the 36 MDa filamentous circular single-stranded DNA bacteriophage Pf1 has been studied by McDermott and co-workers. The virion consists of the genome (7.3 kb) distributed over two non-complementary DNA strands embedded within a capsid of  $\sim 2 \mu\text{m}$  in length. Due to the  $\sim 5$ -fold smaller signal intensity of NMR signals from DNA as compared to coat protein, the investigation of interactions between the genome strands as well as between DNA and the protein imposes a significant challenge. Nevertheless, Sergeyev et al. have succeeded in shedding light on the unusual structure of the DNA in uniformly  $^{13}\text{C}$ ,  $^{15}\text{N}$ -labeled Pf1 by analysis of chemical shifts made accessible by a  $\sim 22$ -fold DNP enhancement [390].

Very recently, the study of viral structure and function by DNP-enhanced MAS NMR has been extended towards human immunodeficiency virus (HIV-1) tubular assemblies of CA capsid protein in a collaborative effort. By achieving a DNP-enhancement factor of 64 at 14.1 T and a remarkable resolution of NMR spectra at 109 K, Gupta et al. were able to observe functionally relevant “invisible” species, such as dynamically disordered states, which are not detectable using other methods. Furthermore, it was concluded that within a CA-SP1 assembly, the SP1 spacer peptide is unstructured and in a random-coil conformation [391].

### 7.2.4. Biomolecules embedded in complex environments

The study of biomolecules that are embedded in their native environment (ideally within the complete cell/organism) is one of the major aims of structural biology. However, such studies are often impeded by similar problems as discussed in the above sections (*i.e.*, selectivity and sensitivity). First strides towards this aim in combination with DNP have been taken by Griffin and co-workers by reconstitution of bR in purple membrane

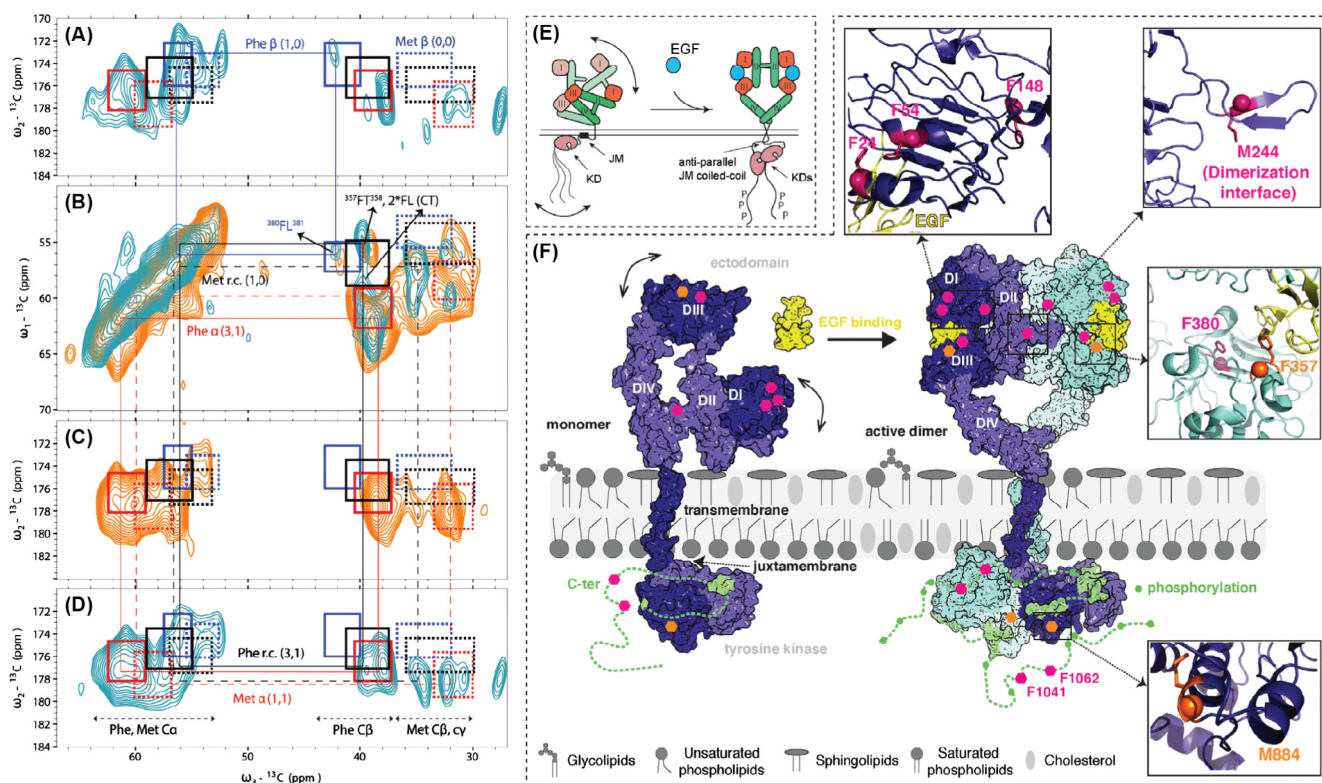


**Fig. 58.** (A, C, and D) 2D planes of 3D NCOCX spectra on EGFR before (C, orange) and after (A and D, cyan) addition of EGF shown at 124 ppm (A), and 120.5 ppm (C and D)  $^{15}\text{N}$  chemical shifts. (B) 2D N-edited  $^{13}\text{C}$ - $^{13}\text{C}$  experiment of cell membrane obtained with (cyan) and without (orange) EGF. (E) Model of EGFR activation via conformational selection in the ECD. (F) Various  $^{13}\text{C}$ -labeled residues act as NMR probes, revealing changes in the local dynamics of different domains of EGFR. Figure reproduced from [389] with permission.

[148,226,227]. Further explorative developments have been driven by Reif and co-workers by characterization of membrane proteins in isolated native cellular membranes: Jacso et al. have demonstrated that membranes can be directly isolated from *E. coli* cultures in which the membrane protein is over-expressed, without need for purification and reconstitution [392]. In a similar vein, Renault et al. have investigated the prospect of DNP-enhanced MAS NMR spectroscopy of whole cells as well as cellular envelope preparations [393]. This technique has been subsequently applied in order to investigate the structure of the type IV secretion system core complex (T4SScc) that is a 1-MDa part of a larger machine (T4SS) being embedded in both the inner and outer membranes of Gram-negative bacteria. DNP allowed for the study of T4SScc embedded in the cellular envelope of *E. coli* by 2D and 3D correlation spectroscopy (NCACX/NCOCX) at fields of 9.4 and 18.8 T. Kaplan et al. were able to confirm earlier structural models based on *in vitro* and *in silico* data, but also observed the folds of parts of the complex at the periplasmic surface that have evaded detection in purified complexes [394].

Hong and co-workers have studied the binding of expansin to plant cell walls. This protein plays a crucial role in loosening the cell wall, yet its course of action has been mostly unknown due to its presence in typically minute quantities during cell growth. By DNP-enhanced spin-diffusion and 2D  $^{13}\text{C}$  correlation spectroscopy, the authors have observed highly specific binding of expansin to cellulose domains enriched in xyloglucan. These bound domains in turn appear to have altered conformations, leading to the cell wall loosening [395].

A very recent field of interest made accessible by DNP is the study of biomacromolecules embedded within silica networks. In these hybrid organic/inorganic materials, the sought-after biomole-

cule is sparsely dispersed within the embedding matrix—similar to the examples given above—which makes NMR-spectroscopic investigation for structural biology difficult. Signal enhancement by DNP has allowed several groups to examine such systems, stimulated by a proof-of-concept demonstration by Ravera et al. on biosilica-entrapped enzymes [396]. Subsequent studies were able to determine the structure of the incorporated proteins and peptides in intact diatom biosilica [397] as well as of a silaffin-derived pentalysine peptide embedded in bioinspired silica [375].

### 7.2.5. Towards *in-cell* DNP

*In-cell* NMR holds the ultimate promise of observing biomolecules and investigating their structure and function within their native environment. It has been shown that processes such as ligand binding [398], protein-protein interactions [399], and even protein folding [400] strongly depend on the environment and can differ when observed within cells or in a “sterile” *in vitro* buffer. However, *in-cell* NMR significantly suffers from similar problems encountered for large complexes but to a much larger degree, leading to extremely weak sensitivity and poor selectivity in order to differentiate between sought-after molecules present in minute concentrations and large amounts of diverse cellular background components.

Strategies for the selective introduction of isotope-labeled proteins have been introduced to overcome the latter issue to some degree [401]. By application of multidimensional correlation spectroscopy or multiple-quantum filters, the selectivity can be improved by the appropriate power of the ratio of the isotopic enrichment (e.g.,  $\sim 10,000$ -fold by double-quantum filtering in the case of pairs of  $^{13}\text{C}$  nuclei). A similar approach was pursued by Frederick et al. who have been able to demonstrate that macro-

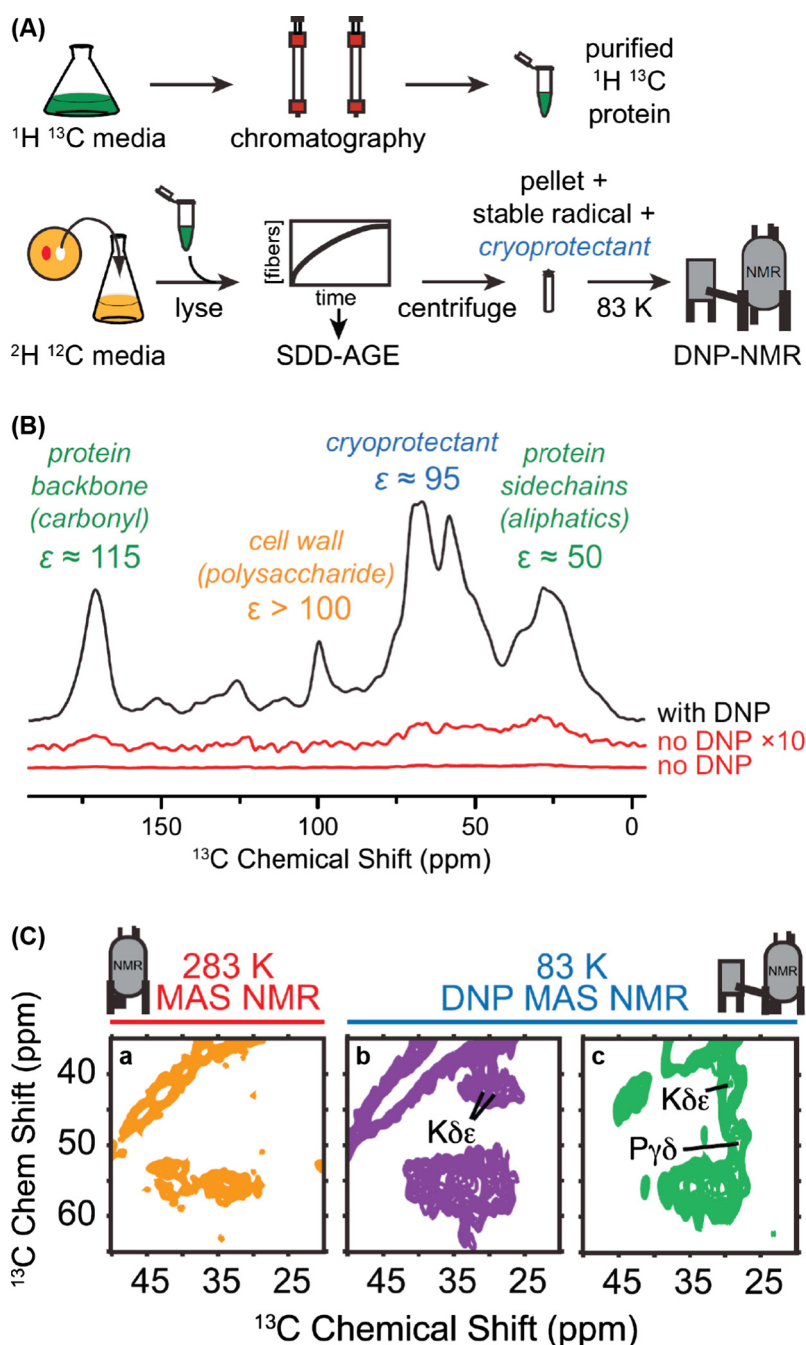


**Fig. 59.** (A) Preparation of samples for DNP MAS NMR of proteins at endogenous levels in biological environments. (B) 1D  $^{13}\text{C}$  CPMAS spectra both with (black) and without DNP. (C) Side chains of NM fibers in cellular lysates have a different chemical environment than *in vitro* templated NM. Aliphatic region of (a) purified NM fibers at 283 K in protonated assembly buffer (b) purified NM fibers at 83 K in 60%  $d_8$ -glycerol and (c) NM fibers at 83 K in 60%  $d_8$ -glycerol, templated into the amyloid form in the presence of cellular lysates. Figure adapted from [402] with permission.

molecular folding of proteins in fibrillar structures significantly differs when fibrillization occurs in cellular milieus (*i.e.*, from proteins in native concentration within eukaryotic cell lysates) as compared to induction in purified media (Fig. 59). In this case, selective detection of NMR signals from the analyte protein (NM domain of eukaryotic translation release factor Sup35) was achieved by introduction of isotope-enriched protein to the cell lysate upon which the amyloid formation was induced in the complex cellular milieu. By choosing appropriate NMR techniques using DNP-enhancement after adding TOTAPOL to the lysate, it was possible to provide evidence for significant structuring of the middle (M)

domain that otherwise adopted a disordered random-coil conformation *in vitro* [402].

As mentioned in Sections 6.3.3 and 6.3.4, an alternative approach providing high selectivity is the introduction of the PA in a “targeted” or “site-specific” manner. This promising technique has recently emerged in several independent and parallel demonstrations and has already been successfully applied within a cell lysate [349]. In general, a covalent bonding of the PA to the sample [139,346,347] or the surrounding structure-preserving matrix [262,343] ensures a close spatial proximity of the sources of polarization to the target molecules. Also a non-covalent binding affinity



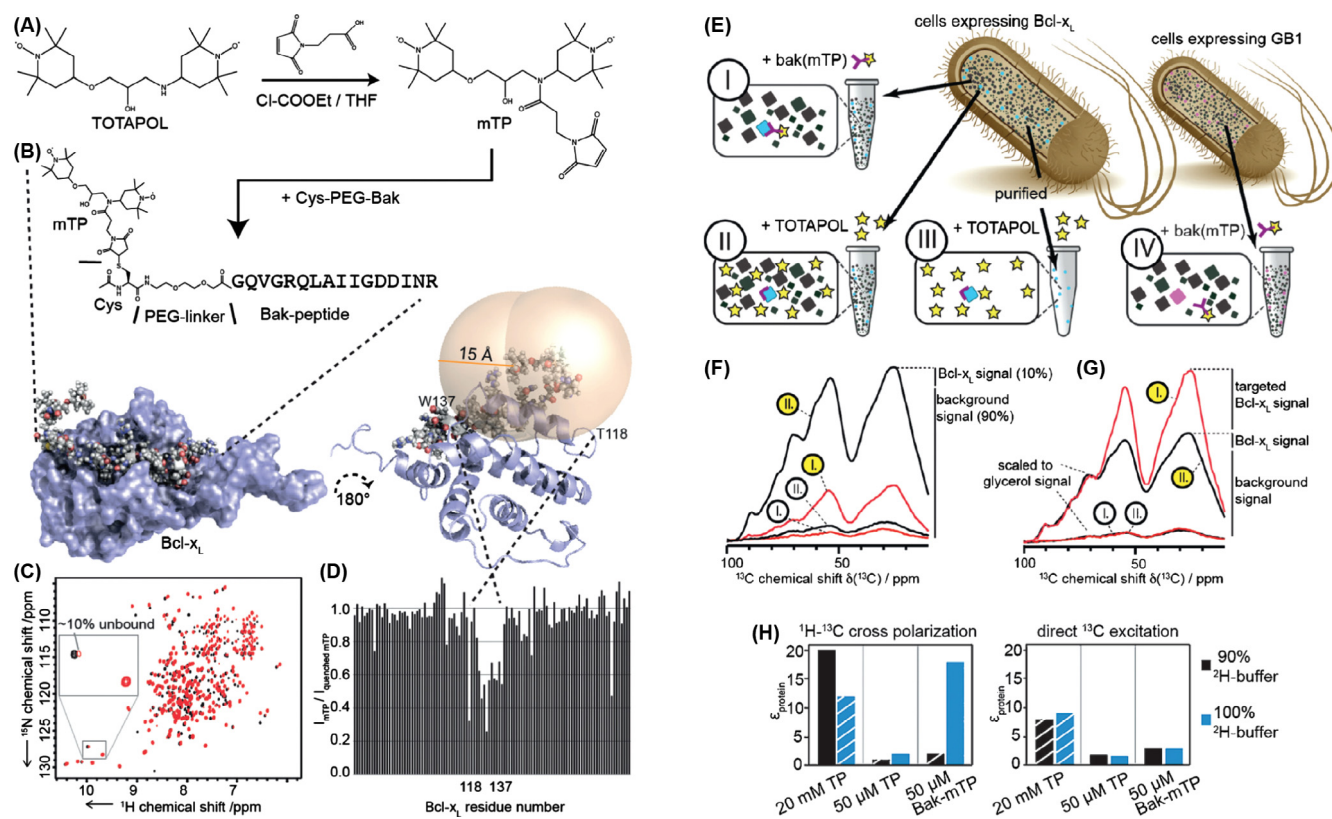


**Fig. 60.** Targeted DNP for structural investigation of Bak-peptide binding to the protein Bcl-x<sub>L</sub>. (A) TOTAPOL is linked to the peptide and (B) due to selective binding well defined spatial proximity is established. (C) <sup>15</sup>N–<sup>1</sup>H HSQC spectra of pure protein and protein-ligand complex confirm high binding affinity. (D) The binding position can be identified by PRE effects on close-by residues. (E) Schematic of used samples. (F) 1D spectra in the presence (yellow label) and absence (white label) of μw for the conventional (black) and targeted (red) setup. Expected signal contributions are indicated. (G) Same spectra as in (F), but scaled to the glycerol background. (H) Polarization by targeted DNP can be selectively confined to the protein in perdeuterated matrix. Reproduced from [349] with permission.

of the PA to the analyte can be exploited [140,349,350,355] In addition to the above, such an affinity has been introduced by a “gluing agent” such as trehalose [342].

A simplification of the spectra and an optimized ε is found experimentally as the enhancement of (parts of) the target molecules is favored over the enhancement of the matrix. Due to such a selective enhancement using protein-specific ligands, this approach would also facilitate in-cell NMR experiments [394] or experiments in systems, which are difficult to purify [392]. In a similar vein, Viennet et al. [349] and Rogawski et al. [350] independently obtained a localized position of the PA by docking a radical-carrying ligand to the target protein (Fig. 60). In both studies, enhancement factors on the order of ~20 were observed at a field of 14.1 T (600 MHz/395 GHz) using the protein-bound PA in stoichiometric concentration with respect to the protein. Interestingly, virtually no global quenching or bleaching of protein resonances was observed, despite the close vicinity of the paramagnet. A related approach was applied in the case of metal-binding biomolecules, such as RNA, where a native binding ion can be exchanged by a paramagnetic transition metal (e.g., Mg<sup>2+</sup> by Mn<sup>2+</sup>), introducing localized PA centers for DNP [140]. Also, molecules that contain endogenous radicals have been studied using DNP [92].

All these approaches have in common that the position of the radical is known *ab initio* or can be identified from paramagnetic relaxation effects (Fig. 60D) [403]. Thus, additional site-specific information can be deduced [313,347]. Future prospect could also be the analysis of site-specific DNP enhancement in order to obtain more quantitative distance information.

### 7.3. Applications to materials research

After the early MAS DNP studies had been reported as described in Section 7.1.1, it took more than a decade to develop the dedicated hardware technology that is now commercially available. This, however, led to an extraordinary interest in using DNP-enhanced NMR particularly to characterize inorganic and hybrid materials where isotope labeling is usually impossible or difficult. Also, due to the oftentimes already intrinsically inhomogeneously broadened signals encountered in solid materials, the incorporation of the analyte within a glass-forming matrix at cryogenic temperatures (see Section 6.3.1) was not accompanied by a further detrimental loss in resolution as had been observed for biological samples.

#### 7.3.1. Enabling surface probing: DNP-SENS

First applications of high-field DNP to materials were initiated by the groups of Emsley, Bodenhausen and Lafon. In 2010, Lesage et al. described the first surface-enhancement of hybrid organic silica materials with a 50-fold increase in the NMR sensitivity. They used TOTAPOL to enhance the <sup>13</sup>C CPMAS spectra of organic groups (phenol or imidazolium units) in natural isotopic abundance,<sup>6</sup> covalently attached to the surface of porous silica (Fig. 61) [255]. This general approach for enhancing the surface signals by DNP was dubbed “DNP surface-enhanced NMR spectroscopy”

<sup>6</sup> In the following, natural isotopic abundance is to be assumed if not stated otherwise.

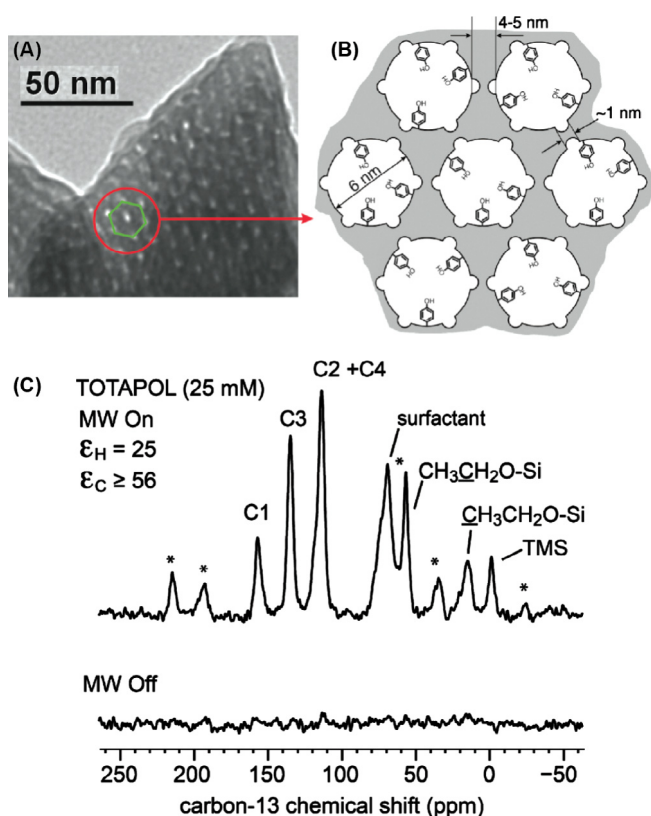


**Fig. 61.** (A) Transmission electronic microscopy image and (B) schematic representation of nanoporous silica functionalized with phenol moieties. (C)  $^{13}\text{C}$  CPMAS spectra with (top) and without (bottom)  $\mu\text{W}$  irradiation of the material impregnated with TOTAPOL solution, showing selective DNP enhancement of the surface phenol functional groups. Figure adapted from [255] with permission.

(DNP-SENS) and is applicable to porous materials impregnated by radical solutions. The PA occupies the pores of the material and hyperpolarizes the protons in the solvent. Efficient  $^1\text{H}$  spin diffusion aids in spreading the polarization towards the pore surface. The enhanced polarization is then transferred to the nuclei of interest within the material by CP. This method that allowed for selective enhancement of surfaces and surface-bound species in contrast to the larger amount of nuclear spins in bulk, was quickly recognized as a seminal step towards a broad field of applications [404].

For example, surface-enhanced  $^{29}\text{Si}$  DNP spectra served as evidence for the incorporation of functional groups on silica surfaces by identifying the surface Q- and T-sites in a functionalized silica material (Fig. 62); in addition, the large enhancement factors allowed the acquisition of 2D  $^1\text{H}$ - $^{29}\text{Si}$  correlation spectra in a short time [256]. Shortly thereafter, Lafon et al. presented the complementarities of direct and indirect DNP. Indirect DNP was found to be selective for surface sites, whereas direct DNP allows for the observation of both surface and subsurface sites. In particular, the  $^{29}\text{Si}$  NMR spectra of subsurface sites were enhanced by direct DNP with a 30-fold enhancement using TOTAPOL (Fig. 63) [143]. They also showed that dispersed nanoparticles of laponites can also be enhanced by indirect or direct  $^{29}\text{Si}$  DNP [144].

A further important demonstration of the applicability of DNP to mesoporous systems has been provided by Lafon et al. A one-dimensional  $^1\text{H}$  spin-diffusion model was employed to analyze the enhancement factors of an organic/inorganic hybrid material with surfactant (S-MSN) and without surfactant (Ex-MSN). It has been proven that DNP can be used to indirectly enhance the NMR signals of  $^{13}\text{C}$  and  $^{29}\text{Si}$  in S-MSN where the nuclei (within the pores) and the PA (trapped in the surrounding disordered

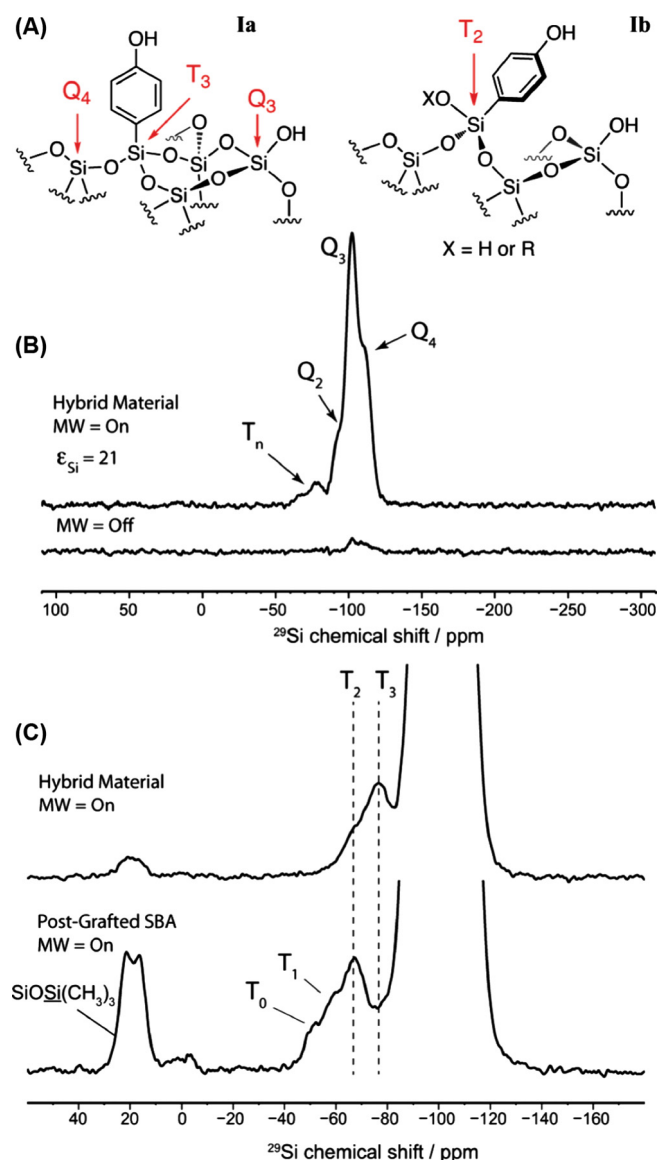


**Fig. 62.** (A) Structures of the  $\text{T}_3$  and  $\text{T}_2$  species that are present on phenol-functionalized silica surfaces. (B)  $^{29}\text{Si}$  CPMAS spectra of **I** with (top) and without (below) DNP enhancement. (C) DNP-enhanced  $^{29}\text{Si}$  CPMAS spectra of two different phenol functionalized mesoporous materials showing different ratios of surface species. Figure taken from [256] with permission.

water matrix) are spatially separated by several hundreds of nanometers (see Fig. 64). This is due to the diffusion of  $^1\text{H}$  spin hyperpolarization into the mesopores before it is being transferred to the rare spins by CP [356].

In 2014, Guo et al. exploited the signal enhancement of DNP by TOTAPOL to identify different amine sites and to quantify the binding of  $\text{Pt}^{2+}$  to a zirconium-containing metal-organic framework (MOF), UiO-66- $\text{NH}_2$  [405]. By  $^1\text{H}$ - $^{15}\text{N}$  CPMAS NMR in combination with X-ray absorption spectroscopy and density functional theory (DFT) calculations, they determined the stereoisomerism of  $\text{Pt}^{2+}$  binding and rationalized the lack of affinity of  $\text{Cu}^{2+}$  for the host material. It is worth mentioning that TOTAPOL is too large to enter the pores of the framework, so that the observed enhancement must be based on an efficient distribution of polarization by spin diffusion.

DNP has also been used to elucidate the binding sites in a catalyst constructed from dirhodium acetate dimer ( $\text{Rh}_2(\text{OAc})_4$ ) units covalently linked to amine- and carboxyl-bifunctionalized

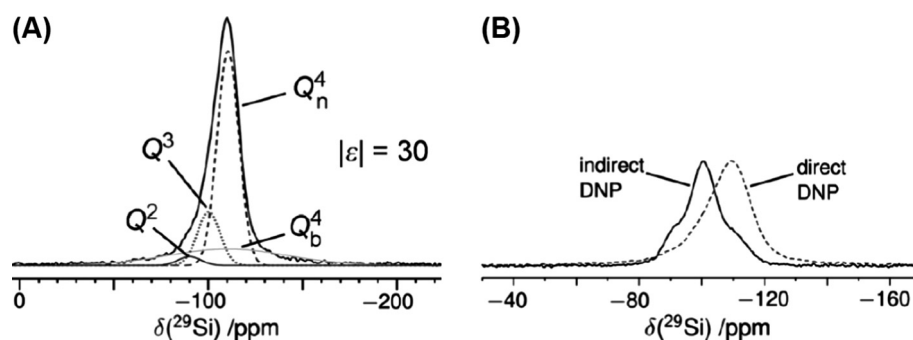


**Fig. 63.** (A) Direct DNP-enhanced  $^{29}\text{Si}$  NMR spectra of porous silica. The deconvolution of the direct DNP spectrum is also displayed. (B) Comparison between the  $^{29}\text{Si}$  NMR spectra obtained with direct DNP (dashed line) and indirect DNP via  $^1\text{H}$  (continuous line). Figure adapted from [143] with permission.

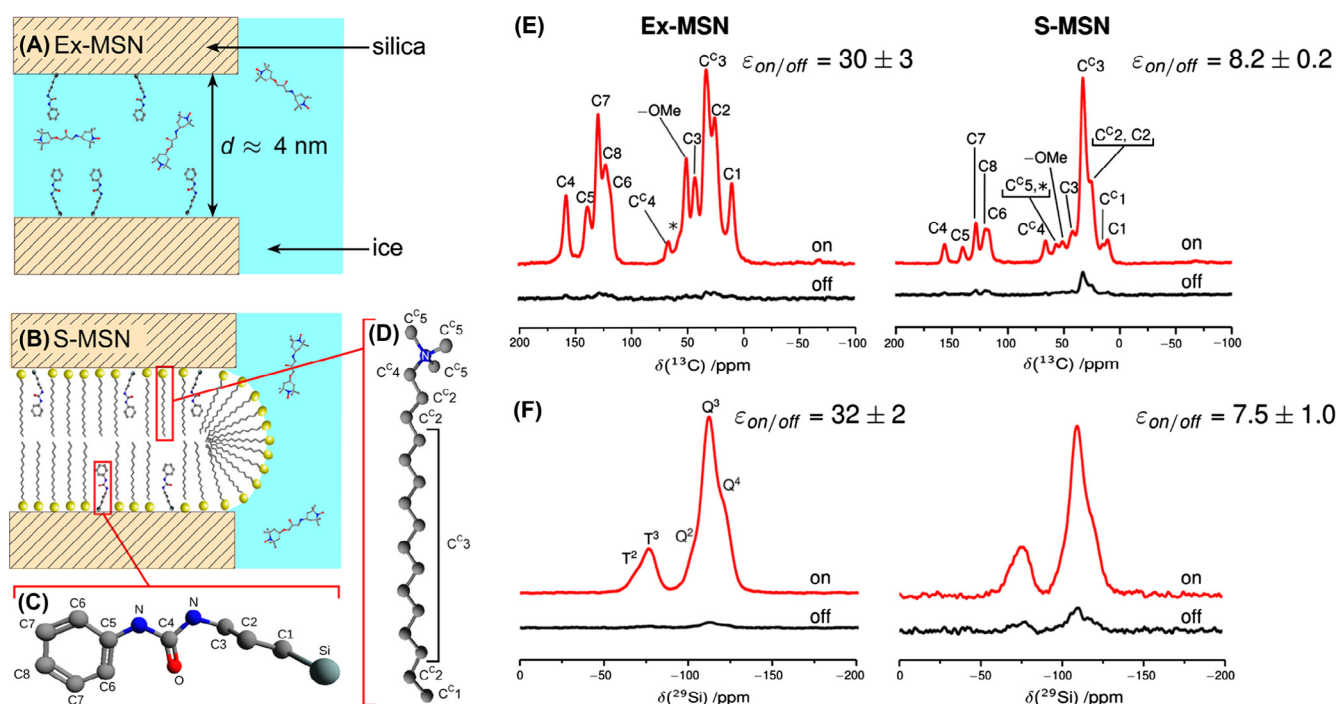


**Fig. 64.** (A and B) Sketches of (A) Ex-MSN (where the aqueous solution of TOTAPOL can penetrate into the mesopores) and of (B) S-MSN functionalized by covalently bound 3-(N-phenylureido)propyl (PUP) and impregnated with the surfactant cetyl trimethyl ammonium bromide (CTAB). (C and D) Numbering of carbon atoms in (C) PUP and (D) CTAB. (E and F) CPMAS spectra of (E)  $^{13}\text{C}$  and (F)  $^{29}\text{Si}$  in Ex-MSN (left) and S-MSN (right) impregnated with a 12.5 mM TOTAPOL in  $\text{H}_2\text{O}$ . Figure adapted from [356] with permission.

mesoporous silica (SBA-15-NH<sub>2</sub>-COOH) by Gutmann et al. The binding sites of carbonyl and amine groups were detected using DNP enhanced  $^{13}\text{C}$  and  $^{15}\text{N}$  CPMAS spectra within a short experimental time [406]. Furthermore,  $^{15}\text{N}$  CPMAS enhanced by DNP allowed the discrimination between covalently bound and adsorbed peptides on collagen-like peptides immobilized on carboxylate functionalized mesoporous silica (COOH/SiO<sub>x</sub>) [407].

DNP SENS using 1D and/or 2D NMR has also been applied for structural determination of various other materials, including silica (SiO<sub>2</sub>) nanoparticles [408,409], silica-supported zirconium catalyst [410], hybrid mesoporous silica [411], silicates [412], phenylpyridine-based periodic mesoporous organosilicate [413], nanostructured soft matter [414], alumina-supported metal nanoparticles [415,416], heterogeneous alkene metathesis catalysts [417], cellulose nanocrystals [418], aluminosilicates [419,420], lignocellulosic biomass [421], functional paper materials [422], organometallic complex supported on an amorphous silica [423], nitrogen-containing active pharmaceutical ingredients (APIs)

[424], polymorphs of theophylline [425], colloidal quantum dots [426], functionalized nanodiamonds [427], etc. In addition, thermolysis of ammonia borane was also explored by using  $^{15}\text{N}$  DNP NMR in combination with other spectroscopic techniques [428].

### 7.3.2. Materials embedded in organic glass-forming agents

In a search for DNP-supporting glass-forming agents other than the commonly employed glycerol/water mixtures, Zagdoun et al. tested the DNP enhancements on hybrid mesoporous materials for a series of non-aqueous solvents capable of dissolving the hydrophobic PA bTbK. They concluded that TCE is a promising organic solvent that can provide signal enhancements similar to aqueous solvents and can be used with hydrophobic materials for solid-state DNP [336]. Subsequently, the first application of DNP-enhanced  $^{15}\text{N}$  and  $^{13}\text{C}$  CPMAS NMR to an N-functionalized MOF was tested with bTbK in TCE solution (Fig. 65). A reduction of the experimental time by two orders of magnitude due to DNP

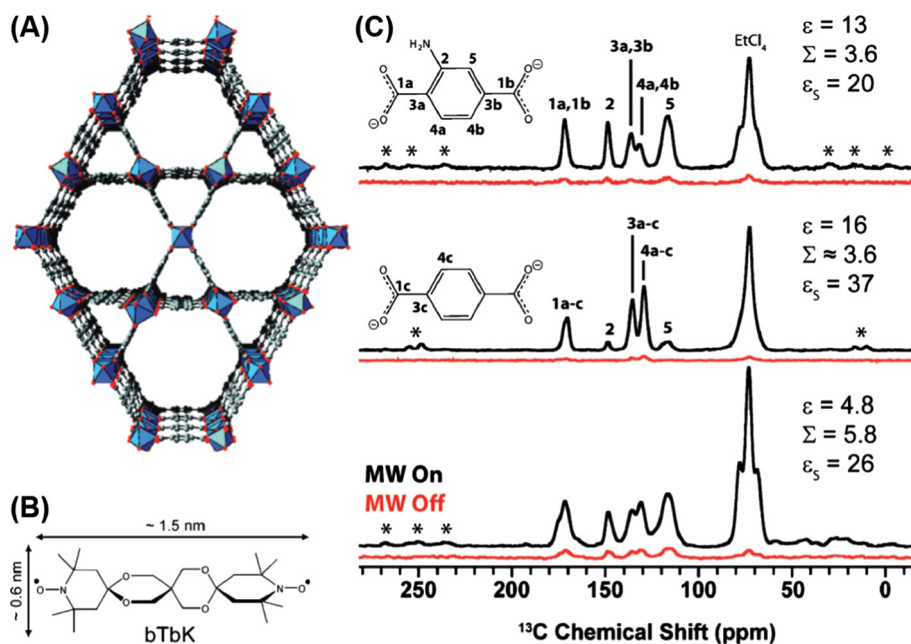


**Fig. 65.** (A) Crystal structure of the MOF used by Rossini et al. (B) Chemical structure and dimensions of the PA bTbK, indicating possible penetration of the pores. (C) 1D  $^{13}\text{C}$  CPMAS spectra of MOF samples impregnated with a 16 mM bTbK solution in TCE, recorded with (black) or without  $\mu\text{w}$  irradiation (red). Figure adapted from [429] with permission.

was found irregardless of the ability of bTbK to penetrate the small (1.6 nm) pores of the material [429].

A chemical application of DNP MAS NMR at 14.1 T was reported by Blanc et al. for the molecular structure determination of microporous organic polymers (MOP) using bCTbK as PA dissolved in TCE. A good signal-to-noise ratio of the  $^{13}\text{C}$  and  $^{15}\text{N}$  CP MAS NMR spectra due to  $\varepsilon \geq 10$  allowed for the detailed determination of molecular structure of the complex polymer networks of the MOP [430].

Rossini et al. demonstrated the atomic-level characterization of active pharmaceutical ingredients (API) in commercial pharmaceutical formulations (with API contents between 4.8 and 8.7 wt%). They determined the domain sizes of the API using DNP-enhanced  $^{13}\text{C}$  and  $^{15}\text{N}$  CPMAS spectra. The use of TCE as the solvent for the biradical PA TEKPol minimized potential perturbations of the API [431].

Apart from the DNP studies of nonporous or mesoporous nanoparticles, Lilly Thankamony et al. studied the trend of catalytic activity in a series of fibrous nanosilica oxynitrides with various nitrogen contents (KCC-1) using DNP-enhanced  $^{15}\text{N}$  NMR while the samples were impregnated with bTbK in TCE. The reduction of catalytic activity of KCC-1 upon preparation at higher nitridation temperatures was shown to correlate with the disappearance of primary amine sites and the formation of secondary amines [432].

### 7.3.3. Impregnated microcrystals

Van der Wel et al. demonstrated that microscopic dispersions of insoluble biomolecular assemblies can be hyperpolarized in a glycerol/water mixture doped with PA [258]. This concept had been extended by Rossini et al. towards microcrystalline solids that are soluble in aqueous glass-forming agents but can be dispersed as a solid in hydrophobic organic solvents. This was first demonstrated on powdered microcrystalline solids of small molecules such as glucose, sulfathiazole, and paracetamol that have been impregnated with bCTbK in tetrabromoethane [138]. Signal enhancements on the order of 100 were obtained, which allowed for the rapid acquisition of  $^{13}\text{C}$ – $^{13}\text{C}$  correlation spectra in natural abundance. Furthermore, it was shown that the analysis of DNP

enhancement factors and polarization dynamics can be directly used in order to obtain information about the crystal grain size due to rate-limiting spin diffusion through the crystal bulk [138], a concept that has also been applied to spherical silicon nanoparticles [257].

This impregnation technique has proven extremely valuable for the investigation of pharmaceutical formulations in order to assess the quality of the distribution of the API [431]. Furthermore, the sensitivity gain by DNP has allowed the extraction of quantitative structural constraints for organic powders at natural isotopic abundance by means of NMR crystallography which has been first demonstrated by Viel and co-workers [433]. Märker et al. have extended this approach for the crystal structure determination of molecular assemblies [151]. In particular, by avoiding dipolar truncation [376] in compounds in natural abundance, quantification of distances of up to 7 Å between pairs of  $^{13}\text{C}$  allowed for the identification of  $\pi$ -stacking in (nano-)self-assembled cyclic dipeptides [374]. In another demonstration, the structure elucidation of a complex organic framework has been supported by DNP-enhanced NMR crystallography [434].

### 7.4. Extending the NMR toolkit by DNP methods

Quadrupolar nuclei (see Table 1) often pose as a problem for solid-state NMR when the quadrupole interactions are large. In many cases, even the central transition of nuclei with half-integer spin quantum number experiences a second-order effect that can lead to inhomogeneous broadening with effective line widths that can be much larger than the MAS frequency. In the same vein, nuclei with  $I = 1/2$ , but featuring a rather large chemical shift anisotropy, can share similar problems with quadrupolar nuclei such as low sensitivity due to a large resonance dispersion and insufficient excitation/detection bandwidth. Combined with small gyromagnetic ratios and/or a low natural abundance of the nuclear species, the strongly reduced NMR sensitivity significantly limits the application of conventional NMR techniques. For this reason, DNP is a powerful method for the investigation of quadrupolar nuclei.

**Table 1**  
List of selected NMR-active nuclei.

Isotope	Spin S	Gyromagnetic ratio $\gamma/2\pi$ [MHz T <sup>-1</sup> ]	Quadrupole moment Q [fm <sup>2</sup> ]	Abundance [%]
<sup>1</sup> H	1/2	42.576	–	~100
<sup>2</sup> H	1	6.536	0.286	0.01
<sup>13</sup> C	1/2	10.708	–	1.07
<sup>14</sup> N	1	3.078	2.044	99.6
<sup>15</sup> N	1/2	4.317	–	0.37
<sup>17</sup> O	5/2	5.774	–2.56	0.038
<sup>27</sup> Al	5/2	11.103	14.66	100
<sup>29</sup> Si	1/2	8.466	–	4.68
<sup>35</sup> Cl	3/2	4.177	–8.17	75.8
<sup>43</sup> Ca	7/2	2.869	–4.08	0.14
<sup>51</sup> V	7/2	11.213	–4.3	99.8
<sup>59</sup> Co	7/2	10.077	+42	100
<sup>119</sup> Sn	1/2	15.966	–	8.59
<sup>195</sup> Pt	1/2	9.292	–	33.8
<sup>207</sup> Pb	1/2	9.034	–	22.1

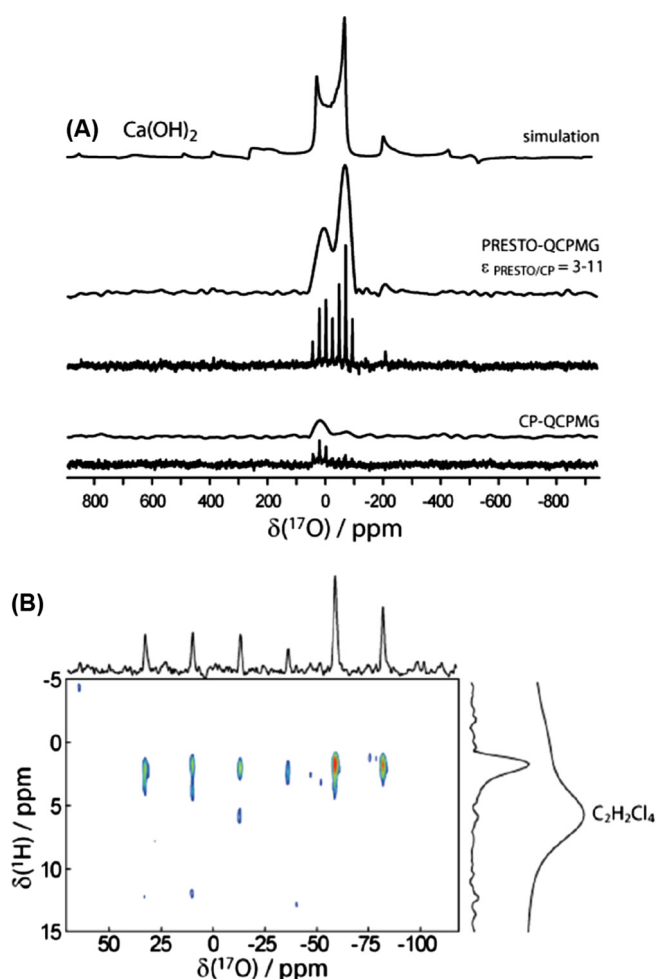


**Fig. 66.** (A) DNP-enhanced <sup>17</sup>O MAS NMR spectra of Ca(OH)<sub>2</sub> in natural abundance, acquired using CP-QCPMG (bottom) and PRESTO-QCPMG schemes (middle), as well as simulations of the PRESTO MAS spectra (top). (B) DNP-enhanced <sup>1</sup>H–<sup>17</sup>O MAS PRESTO QCPMG-HETCOR NMR spectra acquired in 4.5 h. Projections along the <sup>1</sup>H dimension show that polarization is transferred mainly from the hydroxyl proton and not the solvent. Figure adapted from [437] with permission.

#### 7.4.1. DNP of half-integer spin quadrupolar nuclei

**7.4.1.1. <sup>17</sup>O (*I* = 5/2) NMR.** <sup>17</sup>O is a rather challenging nucleus due to its relatively large quadrupolar moment, small gyromagnetic ratio, and particularly low natural abundance (see Table 1). Nevertheless,

the large chemical shift range and quadrupole coupling tensor can yield important information about the local environment of oxygen. Indirect and direct DNP of <sup>17</sup>O has first been demonstrated by Michaelis et al. on H<sub>2</sub><sup>17</sup>O in the glycerol/water matrix or on small molecules, while in all cases <sup>17</sup>O was partially enriched [236,435]. Shortly afterwards, Blanc et al. extended the method for detection of <sup>17</sup>O in natural isotopic abundance within the surface and subsurface sites of inorganic oxides and hydroxides [436].

Later, Perras et al. demonstrated the applicability of the PRESTO technique which can improve the sensitivity of <sup>17</sup>O DNP-SENS even further (Fig. 66). This technique is an alternative approach for the direct transfer of polarization from a spin-1/2 to a quadrupolar nucleus for DNP applications. PRESTO was used to distinguish between hydrogen-bonded and lone <sup>17</sup>O sites on the surface of the silica gels. Its use enabled undistorted line shape measurements, 2D <sup>1</sup>H–<sup>17</sup>O HETCOR NMR spectra, and accurate internuclear distance measurements [437]. They also demonstrated that PRESTO provides several advantages over conventional CP for a number of different quadrupolar nuclei, including <sup>11</sup>B, <sup>23</sup>Na, and <sup>27</sup>Al [438].

**7.4.1.2. <sup>27</sup>Al (*I* = 5/2) NMR.** The observation of homo- and heteronuclear proximities involving <sup>27</sup>Al is particularly challenging if diluted species such as surface sites or defects are studied. However, DNP enhancement compensates for the low sensitivity as well as for the small efficiency of cross polarization and dipolar recoupling due to the presence of the quadrupole interaction. This is a prerequisite for more sophisticated <sup>27</sup>Al–<sup>27</sup>Al correlation experiments that allow for probing spatial proximities and local environment. Thus, the local coordination sphere of <sup>27</sup>Al sites at the surface of the  $\gamma$ -alumina nanoparticles or mesoporous  $\gamma$ -alumina has been successfully probed using standard techniques for high-resolution NMR of bulk quadrupolar nuclei like MQ-MAS [439–441]. As shown in Fig. 67, 2D homonuclear dipolar correlation experiments were utilized to identify penta-coordinated Al sites that act as bridging units between interfacial tetra- and hexa-coordinated Al at the surface of mesoporous  $\gamma$ -alumina [440]. In these studies, spatial information is obtained by exploiting the fact that <sup>1</sup>H are located exclusively in hydroxyl groups at the surface. In addition to that, Lee et al. confirmed that penta coordinated Al<sup>3+</sup> ions are only present in this first surface layer by utilization of indirect DNP via <sup>1</sup>H–<sup>27</sup>Al CP [441].

Furthermore, Pourpoint et al. reported the first observation of <sup>27</sup>Al–<sup>13</sup>C proximities in Al-based MOFs impregnated with TOTAPOL using advanced NMR methods, such as dipolar-mediated HMQC (D-HMQC) and symmetry-based RESPDOR (S-RESPDOR), combined

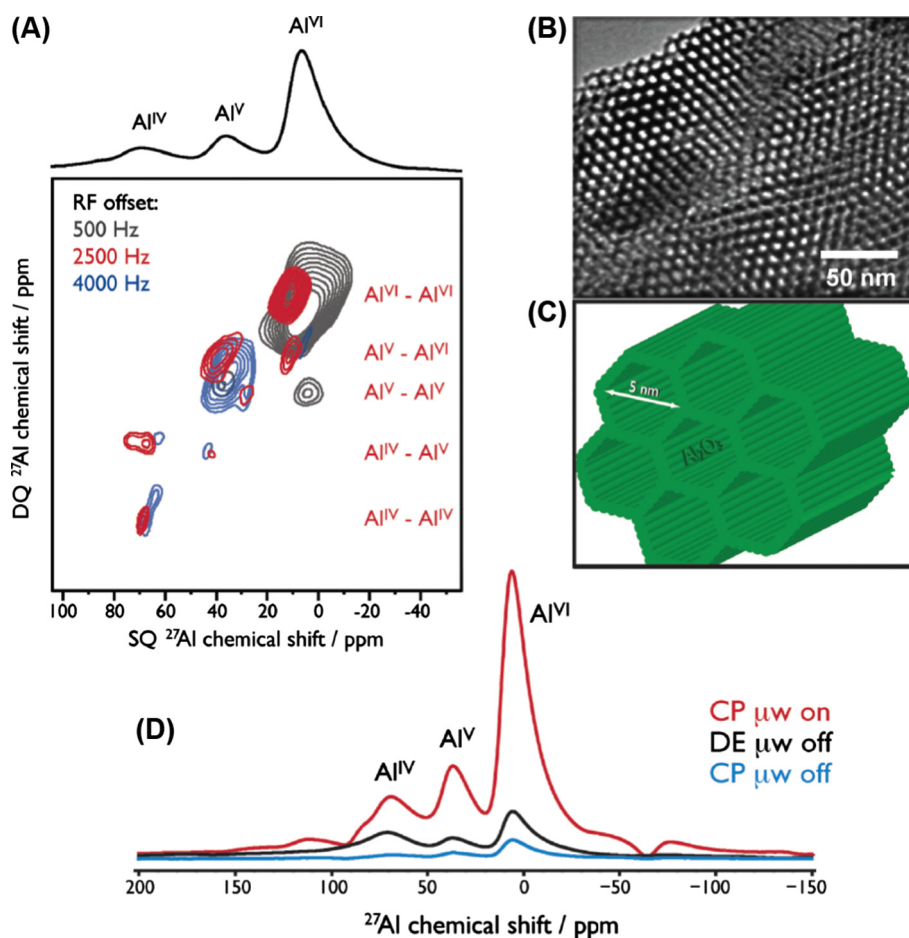


**Fig. 67.** (A) DNP-enhanced, interface-selective DQ-SQ  $^{27}\text{Al}$  homonuclear dipolar correlation spectra of mesoporous alumina. (B) Transmission electron micrograph and (C) schematic representation of ordered hexagonal mesoporous alumina. (D)  $^{27}\text{Al}$  NMR spectra of this sample. Figure adapted from [440] with permission.

with a frequency splitter so that the very similar Larmor frequencies of  $^{27}\text{Al}$  and  $^{13}\text{C}$  can be tuned simultaneously. EPR and DNP-enhanced NMR spectroscopy could prove that TOTAPOL enters the cavities of MOFs within a short timescale of  $\sim$ minutes even though these cavities are smaller than 0.88 nm [442]. They also investigated the complexity of a geological material using  $^{27}\text{Al}$  and  $^{13}\text{C}$  DNP NMR. The proximity between the aluminum ions and dissolved organic matter (DOM) from the Kochechum River (Central Siberia) was studied. The DNP sample was prepared by impregnating lyophilized DOM powder with a solution of 10 mM AMUPol in  $d_6$ -DMSO/ $\text{D}_2\text{O}/\text{H}_2\text{O}$ . The DNP-enhanced NMR spectra enabled the detection of proximities between the  $^{27}\text{Al}$  and  $^{13}\text{C}$  nuclei present in the DOM. They showed that  $\sim$ 8% of the carboxylate groups observed by NMR are connected to the  $\text{Al}^{3+}$  ions in the DOM sample and that aluminum ions exhibit a tetrahedral environment [443].

The practicality of targeted DNP characterization by varying the functional side groups of mono-radicals was demonstrated by Lund et al. in a systematic study of  $^{27}\text{Al}$  direct-DNP-enhanced solid-state NMR on surface-exposed acid sites of mesoporous alumina-silica (Al-SBA-15). By employing 4-amino TEMPO that is attracted to the negatively charged surface sites of Al-SBA-15 in its protonated form, a  $^{27}\text{Al}$  signal enhancement factor of 13 was obtained. This was compared to  $\epsilon = 3 - 4$  from other—neutral or negatively charged—mono-radicals that do not adsorb as strongly to Al-SBA-15. The differences in enhancement factors have been attributed to the local concentrations of the spin probes and their proximity to  $^{27}\text{Al}$  on the surface [357].

**7.4.1.3.  $^{35}\text{Cl}$  ( $I = 3/2$ ) NMR.** Hirsh et al. demonstrated DNP-enhanced  $^1\text{H}$ - $^{35}\text{Cl}$  broadband adiabatic inversion cross polarization (BRAINC-CP) experiments for the detection of APIs. In order to benefit from the significantly larger DNP enhancements under MAS while avoiding the acquisition of spinning side bands within the wide-line  $^{35}\text{Cl}$  NMR powder pattern, they have applied a technique called spinning-on spinning-off (SOSO) acquisition. During the polarization delay, MAS was applied for efficient DNP and rotation is stopped shortly before acquisition. This provided for an extra 2-fold intensity gain compared with purely static experimental DNP conditions. By impregnation of APIs with 15 mM TEKPol in TCE or 1,3-dibromobutane an overall DNP enhancement of 110 was obtained. This allowed for the molecular-level characterization of APIs in their bulk forms as well as in dosage forms with low Cl contents (0.45 wt%) [444].

**7.4.1.4.  $^{43}\text{Ca}$  ( $I = 7/2$ ) NMR.** Even though calcium is a very interesting and highly relevant element, its only NMR-active stable isotope,  $^{43}\text{Ca}$ , is extremely insensitive due to a combination of effects (see Table 1). Very recently, Lee et al. reported the first DNP application to  $^{43}\text{Ca}$  NMR. They demonstrated the differentiation of calcium environments in surface and core species of carbonated hydroxyapatite nanoparticles using  $^{43}\text{Ca}$  MAS DNP NMR in a short experimental time. They succeeded to record  $^1\text{H}$ - $^{43}\text{Ca}$  and  $^1\text{H}$ - $^{13}\text{C}$  2D correlation experiments at the very small natural isotopic abundance of only 0.14%. The analysis revealed that surface species ( $\text{Ca}^{2+}$  and carbonates) could be distinguished from the core entities [445].

7.4.1.5.  $^{51}\text{V}$  ( $I = 7/2$ ) NMR. Applications of DNP by directly and indirectly enhancing  $^{51}\text{V}$  signals on vanadyl sulfate samples under MAS conditions were reported by Perez Linde et al. DNP-enhanced  $^{51}\text{V}$  NMR spectra of vanadium species dissolved together with TOTAPOL in a glycerol/water mixture were recorded as a function of pH. The pH-dependent presence of vanadyl radicals was investigated and it was observed that at pH higher than 11,  $^1\text{H}$  can be most efficiently hyperpolarized by TOTAPOL and the enhanced polarization can be transferred to  $^{51}\text{V}$  nuclei through CP. Most interestingly, the presence of vanadyl sulfate resulted in a larger  $^1\text{H}$  enhancement factor as compared to solutions containing only TOTAPOL. This effect was attributed to the interactions between paramagnetic vanadyl species and the PA [446].

7.4.1.6.  $^{59}\text{Co}$  ( $I = 7/2$ ) NMR.  $^{59}\text{Co}$  has been directly hyperpolarized by employing  $\text{Cr}^{3+}$  as PA by Corzilius et al. The paramagnetic  $\text{Cr}^{3+}$  has been used to isostructurally substitute the diamagnetic  $\text{Co}^{3+}$  in crystalline  $[\text{Co}(\text{en})_3\text{Cl}_3]_2 \cdot \text{NaCl} \cdot 6 \text{H}_2\text{O}$  (see Section 5.3.3 and Fig. 45 for details on the sample system). A  $^{59}\text{Co}$  DNP enhancement factor of up to 16 was reported. This approach demonstrated the general feasibility of MAS DNP using PAs which have been doped into the host crystalline lattice without inducing structural changes [302].

#### 7.4.2. DNP of integer spin quadrupolar nuclei

7.4.2.1.  $^2\text{H}$  ( $I = 1$ ) NMR. Despite carrying an integer spin, the quadrupole moment of  $^2\text{H}$  is particularly small which results in a relatively narrow NMR spectrum. The concept of direct  $^2\text{H}$  MAS DNP on isotope-labeled compounds was first demonstrated by Maly et al. [147].

Recently, DNP-enhanced  $^1\text{H}$ - $^2\text{H}$  CPMAS of organic solids in natural abundance, such as histidine hydrochloride monohydrate, glycylglycine and theophylline, have been performed by Rossini et al. at 9.4 T and 100 K [353 1803]. Samples were impregnated with TEKPol in TCE; indirect DNP allowed for the acquisition of  $^2\text{H}$  CPMAS spectra within 1 h. The resolution of the acquired  $^2\text{H}$  spectra was comparable to that of  $^1\text{H}$  spectra obtained with state-of-the-art homonuclear decoupling techniques and provided direct access to hydrogen chemical shifts and  $^2\text{H}$  EFG (electric field gradient) tensor parameters.

7.4.2.2.  $^{14}\text{N}$  ( $I = 1$ ) NMR.  $^{14}\text{N}$  poses as an intriguing but challenging target for NMR studies due to its large natural abundance and relevance especially in biological context while at the same time suffering from an integer nuclear spin quantum number that does not give rise to a narrow CT. Although it shares the latter property with  $^2\text{H}$ , the quadrupole moment of  $^{14}\text{N}$  is about one order of magnitude larger which makes direct detection extremely difficult.

Indirect detection of  $^{14}\text{N}$  via single-quantum correlation (SQC) or double-quantum correlation (DQC) with an  $I = 1/2$  nucleus (e.g.,  $^{13}\text{C}$ ) in an HMQC-type experiment can yield correlation spectra under MAS with rather narrow lines [447,448]. Alternatively, excitation of the “forbidden”  $\Delta m_I = \pm 2$  transition at twice the nuclear Larmor frequency results in a narrow overtone (OT) NMR spectrum not influenced by the nuclear quadrupole interaction to first order [449,450]. This method has also been demonstrated in combination with MAS [451,452]. However, both techniques typically suffer from low efficiency and therefore DNP is an excellent method to counter that problem.

Indirect  $^{14}\text{N}$  detection by HMQC with DNP-enhancement has been demonstrated by Vitthum et al. [150], based on experiments introduced by the same group earlier without DNP [453]. Indirect  $^{13}\text{C}$  DNP enhancement with factors of  $\sim 40$  were achieved on U- $^{13}\text{C}$ -proline dissolved in glycerol/water together with 20 mM TOTAPOL. This allowed for the acquisition of  $^{13}\text{C}$ - $^{14}\text{N}$  correlation spectra within a few hours while experimental time on the order of at least one week were required without DNP. The detection

of DNP-enhanced  $^{14}\text{N}^{\text{OT}}$  MAS NMR spectra has been presented by Rossini et al. Indirect  $^{14}\text{N}$  DNP enhancements of around two orders of magnitude were achieved on model amino acids which were impregnated with 15 mM TEKPol in TCE. CP transfer from hyperpolarized  $^1\text{H}$  nuclei directly to the  $^{14}\text{N}$  overtone transition was demonstrated using a standard pulse sequence. It was also shown that DNP enhancement enables  $^1\text{H}$ - $^{14}\text{N}^{\text{OT}}$  HETCOR and  $^{13}\text{C}$ - $^{14}\text{N}^{\text{OT}}$  HMQC spectra to be obtained from samples in natural  $^{13}\text{C}$  abundance in a short time, proving that such correlation experiments can be used for observing H–N and C–N correlations in completely unlabeled samples [454].

#### 7.4.3. Wideline NMR ( $I = 1/2$ )

7.4.3.1.  $^{119}\text{Sn}$  NMR. Gunther et al. demonstrated the first DNP application to  $^{119}\text{Sn}$  NMR for characterizing microporous zeolites containing  $\sim 2$  wt% of natural abundance Sn in the catalytically active Sn- $\beta$ . They used TOTAPOL, bTbK, bCTbK, and SPIROPOL (i.e., bTbK-py) biradicals as PAs and obtained enhancement factors as large as 75 with bCTbK for indirect DNP of  $^{119}\text{Sn}$  which allowed the characterization of Sn- $\beta$  by more than  $\sim 2$  orders of magnitude reduced acquisition times [455].  $^{119}\text{Sn}$  DNP-SENS has also been applied to allyltritylstannane [ $\text{Bu}_3\text{Sn}(\text{allyl})$ ] to detect the minor surface species  $[(\text{RSiO})_2\text{SnBu}_2]$ , present in low density ( $< 0.1 \text{ nm}^{-2}$ ). Signal enhancements of 56 for  $^{119}\text{Sn}$  in combination with CPMG enabled the acquisition of a  $^1\text{H}$ - $^{119}\text{Sn}$  HETCOR spectrum in less than 6 h and showed the correlations between the two tin resonances and the protons of the butyl group [456].

Protesescu et al. showed that DNP-SENS selectively enhanced the weak  $^{119}\text{Sn}$  NMR signal of the natural oxide coating as well as of capping ligands on colloidal Sn/SnO<sub>x</sub> nanoparticles (NPs). By combining DNP-SENS with Mössbauer and X-ray absorption spectroscopies, they have determined a Sn/SnO/SnO<sub>2</sub> core/shell/shell-structure of the Sn-NPs. They have also shown that DNP-SENS experiments can be carried out for hydrophilic (ion-capped) surfaces and hydrophobic functionalities of surfaces capped by ligands with long hydrocarbon chains in various solvents [457]. At the same time, Wolf et al. presented framework Sn(IV)-active sites in an octahedral environment which are bound to three or four siloxy groups of a Sn- $\beta$  zeolite framework using DNP-SENS. It was concluded that there are two active sites of Sn(IV) present which have distinct NMR signatures: one site where two water molecules are coordinated to Sn (closed site), and another site where one of the water molecules has opened one of the Sn–O–Si bridges (open site) [458]. Later, they also studied the morphology and atomic-level structure of Sn- $\beta$  zeolites using DNP-enhanced NMR [459].

7.4.3.2.  $^{195}\text{Pt}$  NMR. Recently, Kobayashi et al. have demonstrated that DNP enhancement can be used in combination with BRAIN-CP from  $^1\text{H}$  and WURST-CPMG detection of wideline  $^{195}\text{Pt}$  solid-state NMR. The breadth of the  $^{195}\text{Pt}$  spectra reaches  $\sim 10,000$  ppm, therefore a combination of several sensitivity-enhancing methods was necessary to characterize the atomic-scale geometry of the  $\text{Pt}^{2+}$  ions coordinated by the linkers in MOFs. It was possible to separate the signals from cis- and trans-coordinated atomic  $\text{Pt}^{2+}$  species supported on the UiO-66-NH<sub>2</sub> MOF in the DNP-enhanced wideline NMR spectra (Fig. 68). Furthermore, the kinetic effects in the formation of  $\text{Pt}^{2+}$  complexes and the thermodynamic effects in their reduction to nanoparticles were also studied [460].

7.4.3.3.  $^{207}\text{Pb}$  NMR. DNP has been used by Kobayashi et al. to enhance the wideline  $^{207}\text{Pb}$  solid-state NMR spectra of lead white [lead carbonate,  $2 \text{ PbCO}_3 \cdot \text{Pb}(\text{OH})_2$ ], a model lead soap, and an aged lead-based paint film. The samples were impregnated with 16 mM TEKPol in a TCE/*d*<sub>4</sub>-methanol (96:4) mixture. They performed DNP-enhanced static wideline  $^1\text{H}$ - $^{207}\text{Pb}$  BRAIN-CP and  $^1\text{H}$ - $^{207}\text{Pb}$  CPMAS

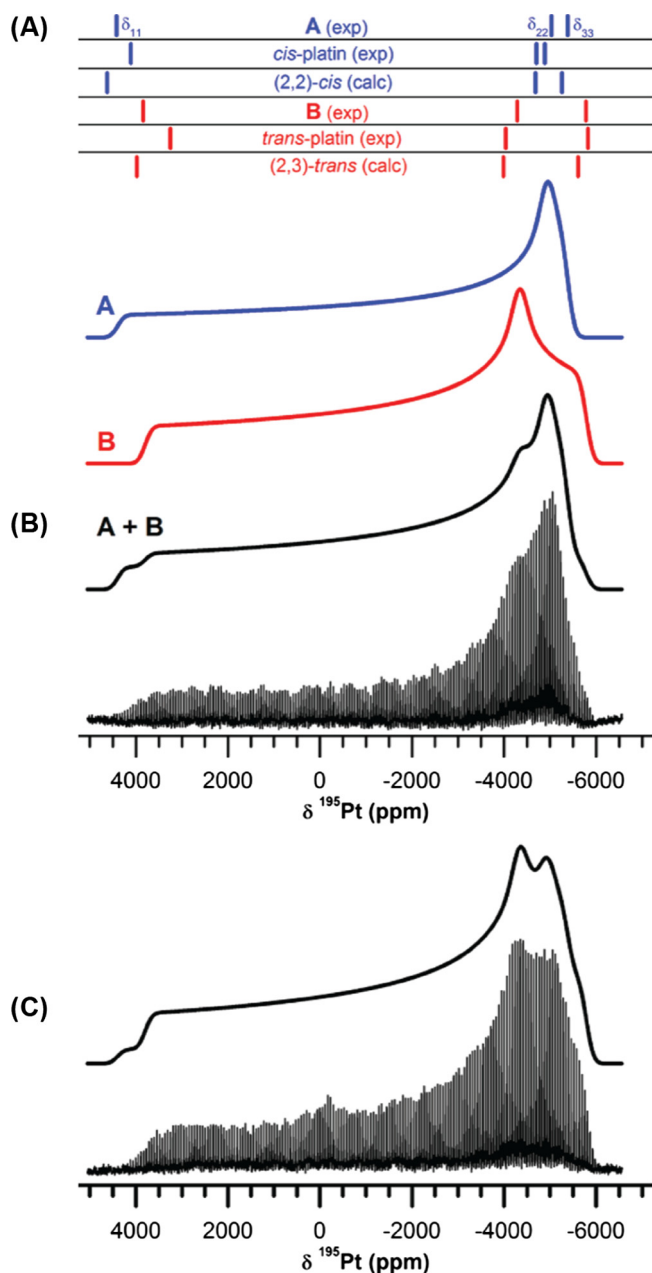


**Fig. 68.** (A) Simulated powder patterns for the cis and trans sites of  $\text{Pt}^{2+}/\text{UiO-66-NH}_2$ . (B-C) DNP-enhanced wide-line  $^{195}\text{Pt}$  BRAIN-CP spectra (B) prior and (C) post reductive treatment for 30 min at 150 °C in 10%  $\text{H}_2/\text{Ar}$ . The spectra consist of 14 subspectra acquired in 7.5 h. Figure adapted from [460] with permission.

experiments at a temperature of  $\sim 110$  K, and  $^{207}\text{Pb}$  WURST-CPMG experiments at temperatures ranging from 110 K to 308 K. By applying the above-mentioned set of methods and utilizing selective DNP enhancements of certain chemical components it was possible to disentangle the spectral contributions within the complex mixture. Thus, the formation of a lead soap upon aging could be detected within the paint film and the degradation mechanism of lead pigments in such films could be elucidated [461].

## 8. Conclusions

We have presented a comprehensive review about the theoretical concepts as well as instrumental and methodological progress in solid-state DNP NMR. Based on the continuously improving

theoretical understanding of the underlying microscopic processes and driven by interdisciplinary efforts—such as the development of advanced instrumentation, tailored polarizing agents and optimized sample preparation techniques—not only a tremendous boost in the available maximum enhancement factors but also a much broader general applicability has been reported over the past years. This progress allows for applications of hyperpolarization techniques to various problems in material science and biomolecular solid-state NMR. In this vein, DNP has enabled several investigations of structural properties of materials that would not have been possible without the outstanding gain in sensitivity due to signal enhancement by DNP.

Still, further improvements are to be expected in the next few years. DNP has become the driving force for the development of high-power high-frequency  $\mu\text{W}$  sources. Thus, promising developments on frequency-tunability of such sources are expected to simplify the experimental setup. The ongoing quest for sources operating at even higher frequencies is likely to extend the current limitations on the external magnetic fields faced by DNP. Furthermore, several revolutionary techniques that are still in the development/concept phase and have not been covered in this review might prove highly useful in the near future. Such developments include time-domain/pulsed DNP [166,310,462–464] potentially in combination with gyro amplifiers [465,466], frequency-swept techniques [467–469], electron decoupling [74,195,470], DNP of oriented membranes [471,472], or micro-MAS compatible with  $\mu\text{W}$  resonating structures [473]. Furthermore, temperature-jump [474–476] or rapid-melt techniques [477,478] which are both based on solid-state DNP could become applicable to signal enhancement in solution NMR.

Initially aimed to improve sensitivity on biomolecules, high-field MAS DNP demonstrated its versatility, in particular in applications to problems in material science. NMR investigations of low-density species, as well as of “challenging” nuclei with low gyromagnetic ratios, low natural isotopic abundance and/or large anisotropic interactions (chemical-shift anisotropy or quadrupolar interaction) were performed in a reasonable experimental time. Also, several methodological developments such as correlation experiments of heteronuclei at low natural isotopic abundance significantly extended the toolkit of conventional solid-state NMR.

Even though the full potential of DNP in biomolecular NMR spectroscopy has not yet been reached and mostly specialized questions are addressed at the moment, recent advances on tackling the resolution issue show promising results. Among these are improvements in sample preparation which allow for higher sample filling factors and reduce line-broadening effects due to the protein glass transition. Recent progress in localized/targeted DNP studies offers perspectives for further investigations of structural properties of selected species. Not only additional PRE restraints can be determined in such an approach; potentially, site-specific DNP enhancement might also provide quantitative structural information in the near future. Furthermore, the resolution issue can be tackled by multidimensional NMR experiments that become possible with large enhancement factors as well as DNP-accessible magnetic fields greater than 18 T.

## Acknowledgments

This work has been funded by the Deutsche Forschungsgemeinschaft through Emmy Noether grant CO802/2-1. BC is greatly indebted to R. G. Griffin for continuous inspiration, outstanding support, and transfer of knowledge; furthermore, ideas exchanged during inspiring discussions with many colleagues, regarding scientific or technical matters, have influenced this article in a direct or indirect way. In that regard, BC thanks in particular D. Akhmetzyanov, L. B. Andreas, A. B. Barnes, M. J. Bayro,



J. Becker-Baldus, J. A. Bryant, T. V. Can, M. A. Caporini, E. Daviso, G. T. Debelouchina, R. DeRoche, M. T. Eddy, A. Feintuch, C. Glaubitz, D. Goldfarb, Y. Hovav, S. Jannin, I. Kuprov, D. Lee, M. Lelli, A. Lesage, M. L. Mak-Jurkauskas, T. Maly, J. Mao, J. Mathies, Y. Matsuki, F. Mentink-Vigier, V. K. Michaelis, E. A. Nanni, Q. Z. Ni, G. Pintacuda, T. Prisner, E. Ravera, D. Ruben, H. Schwalbe, J. R. Sirigiri, D. Shimon, A. A. Smith, A. Thakkar, K. Thurber, A. C. Torrezan, S. Vega, J. J. Walsh, and P. P. Woskov. ASLT acknowledges O. Lafon for the inspiration, support and guidance, G. Buntkowsky for constant high support, and D. Carnevale, A. J. Perez Linde for useful discussions and technical assistance. MK expresses sincere gratitude towards G. De Paëpe and D. Lee for guidance, encouragement and continued support.

## References

- [1] I.J. Lowe, Free induction decays of rotating solids, *Phys. Rev. Lett.* 2 (1959) 285–287.
- [2] E.R. Andrew, A. Bradbury, R.G. Eades, Removal of dipolar broadening of nuclear magnetic resonance spectra of solids by specimen rotation, *Nature* 183 (1959) 1802–1803.
- [3] Y. Ishii, C-13-C-13 dipolar recoupling under very fast magic angle spinning in solid-state nuclear magnetic resonance: applications to distance measurements, spectral assignments, and high-throughput secondary-structure determination, *J. Chem. Phys.* 114 (2001) 8473–8483.
- [4] M.H. Levitt, Symmetry in the design of NMR multiple-pulse sequences, *J. Chem. Phys.* 128 (2008) 052205.
- [5] I. Scholz, J.D. van Beek, M. Ernst, Operator-based Floquet theory in solid-state NMR, *Solid State Nucl. Magn. Reson.* 37 (2010) 39–59.
- [6] A. Schuetz, C. Wasmer, B. Habenstein, R. Verel, J. Greenwald, R. Riek, A. Bockmann, B.H. Meier, Protocols for the sequential solid-state NMR spectroscopic assignment of a uniformly labeled 25 kDa protein: HET-s(1–227), *ChemBioChem* 11 (2010) 1543–1551.
- [7] G. De Paëpe, Dipolar recoupling in magic angle spinning solid-state nuclear magnetic resonance, *Annu. Rev. Phys. Chem.* 63 (63) (2012) 661–684.
- [8] T. Gullion, J. Schaefer, Rotational-echo double-resonance NMR, *J. Magn. Reson.* 81 (1989) 196–200.
- [9] P. Robery, B.H. Meier, R.R. Ernst, Radio-frequency-driven nuclear-spin diffusion in solids, *Chem. Phys. Lett.* 162 (1989) 417–423.
- [10] C. Wasmer, A. Lange, H. Van Melckebeke, A.B. Siemer, R. Riek, B.H. Meier, Amyloid fibrils of the HET-s(218–289) prion form a beta solenoid with a triangular hydrophobic core, *Science* 319 (2008) 1523–1526.
- [11] A.K. Schutz, T. Vagt, M. Huber, O.Y. Ovchinnikova, R. Cadalbert, J. Wall, P. Guntert, A. Bockmann, R. Glockshuber, B.H. Meier, Atomic-resolution three-dimensional structure of amyloid beta fibrils bearing the Osaka mutation, *Angew. Chem. Int. Ed.* 54 (2015) 331–335.
- [12] J.X. Lu, W. Qiang, W.M. Yau, C.D. Schwieters, S.C. Meredith, R. Tycko, Molecular structure of beta-amyloid fibrils in Alzheimer's disease brain tissue, *Cell* 154 (2013) 1257–1268.
- [13] M.T. Colvin, R. Silvers, Q.Z. Ni, T.V. Can, I. Sergeev, M. Rosay, K.J. Donovan, B. Michael, J. Wall, S. Linse, R.G. Griffin, Atomic resolution structure of monomeric Aβ42 amyloid fibrils, *J. Am. Chem. Soc.* 138 (2016) 9663–9674.
- [14] M.A. Walti, F. Ravotti, H. Arai, C.G. Glabe, J.S. Wall, A. Bockmann, P. Guntert, B. H. Meier, R. Riek, Atomic-resolution structure of a disease-relevant A beta(1–42) amyloid fibril, *Proc. Natl. Acad. Sci. U.S.A.* 113 (2016) E4976–E4984.
- [15] C.M. Quinn, T. Polenova, Structural biology of supramolecular assemblies by magic-angle spinning NMR spectroscopy, *Q. Rev. Biophys.* 50 (2017) e1.
- [16] S.A. Shahid, B. Bardiaux, W.T. Franks, L. Krabben, M. Habeck, B.J. van Rossum, D. Linke, Membrane-protein structure determination by solid-state NMR spectroscopy of microcrystals, *Nat. Methods* 9 (2012), 1212–U1119.
- [17] S.L. Wang, R.A. Munro, L.C. Shi, I. Kawamura, T. Okitsu, A. Wada, S.Y. Kim, K.H. Jung, L.S. Brown, V. Ladizhansky, Solid-state NMR spectroscopy structure determination of a lipid-embedded heptahelical membrane protein, *Nat. Methods* 10 (2013) 1007–1012.
- [18] E. Daviso, M. Belenky, R.G. Griffin, J. Herzfeld, Gas vesicles across kingdoms: a comparative solid-state nuclear magnetic resonance study, *J. Mol. Microbiol. Biotechnol.* 23 (2013) 281–289.
- [19] Z. Serber, L. Corsini, F. Durst, V. Dotsch, In-cell NMR spectroscopy, *Methods Enzymol.* 394 (2005) 17–41.
- [20] P. Selenko, G. Wagner, Looking into live cells with in-cell NMR spectroscopy, *J. Struct. Biol.* 158 (2007) 244–253.
- [21] L. Barbieri, E. Luchinat, L. Banci, Characterization of proteins by in-cell NMR spectroscopy in cultured mammalian cells, *Nat. Protoc.* 11 (2016) 1101–1111.
- [22] F. Deng, J. Yang, C. Ye, Solid state NMR characterization of solid surface of heterogeneous catalysts, in: G.A. Webb (Ed.), *Modern Magnetic Resonance*, Springer, Netherlands, Dordrecht, 2006, pp. 205–211.
- [23] A.S. Lilly Thankamony, A. Krishnan, M. Sankar, N.K. Kala Raj, P. Manikandan, P. R. Rajamohan, T.G. Ajithkumar, Immobilization of phosphotungstic acid (PTA) on imidazole functionalized silica: evidence for the nature of PTA binding by solid state NMR and reaction studies, *J. Phys. Chem. C* 113 (2009) 21114–21122.
- [24] T. Narasimhaswamy, M. Monette, D.K. Lee, A. Ramamoorthy, Solid-state NMR characterization and determination of the orientational order of a nematogen, *J. Phys. Chem. B* 109 (2005) 19696–19703.
- [25] N.M. Washton, S.L. Brantley, K.T. Mueller, Probing the molecular-level control of aluminosilicate dissolution: a sensitive solid-state NMR proxy for reactive surface area, *Geochim. Cosmochim. Acta* 72 (2008) 5949–5961.
- [26] T.-J. Park, S.H. Kim, G.H. Li, C.G. Cho, Y. Kim, <sup>31</sup>P solid-state NMR Characterization of poly(vinylphosphate-black-styrene) for DMFC membrane, *Macromol. Symp.* 249–250 (2007) 466–471.
- [27] G.J. Rees, S.T. Orr, L.O. Barrett, J.M. Fisher, J. Houghton, G.H. Spikes, B.R.C. Theobald, D. Thompsett, M.E. Smith, J.V. Hanna, Characterisation of platinum-based fuel cell catalyst materials using <sup>195</sup>Pt wide-line solid state NMR, *Phys. Chem. Chem. Phys.* 15 (2013) 17195–17207.
- [28] T. Komatsu, J. Kikuchi, Selective signal detection in solid-state NMR using rotor-synchronized dipolar dephasing for the analysis of hemicellulose in lignocellulosic biomass, *J. Phys. Chem. Lett.* 4 (2013) 2279–2283.
- [29] Y. Pu, B. Hallac, A.J. Ragauskas, Plant biomass characterization: application of solution- and solid-state NMR spectroscopy, in: C.E. Wyman (Ed.), *Aqueous Pretreatment of Plant Biomass for Biological and Chemical Conversion to Fuels and Chemicals*, John Wiley & Sons, Ltd, 2013, pp. 369–390.
- [30] R.L. Johnson, K. Schmidt-Rohr, Quantitative solid-state <sup>13</sup>C NMR with signal enhancement by multiple cross polarization, *J. Magn. Reson.* 239 (2014) 44–49.
- [31] O.D. Bernardinelli, M.A. Lima, C.A. Rezende, I. Polikarpov, E.R. deAzevedo, Quantitative <sup>13</sup>C MultiCP solid-state NMR as a tool for evaluation of cellulose crystallinity index measured directly inside sugarcane biomass, *Biotechnol. Biofuels* 8 (2015) 110.
- [32] C. Keeler, G.E. Maciel, Quantitation in the solid-state <sup>13</sup>C NMR analysis of soil and organic soil fractions, *Anal. Chem.* 75 (2003) 2421–2432.
- [33] N.J. Mathers, Z. Xu, Solid-state <sup>13</sup>C NMR spectroscopy: characterization of soil organic matter under two contrasting residue management regimes in a 2-year-old pine plantation of subtropical Australia, *Geoderma* 114 (2003) 19–31.
- [34] J. Mao, X. Kong, K. Schmidt-Rohr, J.J. Pignatello, E.M. Perdue, Advanced solid-state NMR characterization of marine dissolved organic matter isolated using the coupled reverse osmosis/electrodialysis method, *Environ. Sci. Technol.* 46 (2012) 5806–5814.
- [35] A.P. Deshmukh, B. Chefetz, P.G. Hatcher, Characterization of organic matter in pristine and contaminated coastal marine sediments using solid-state <sup>13</sup>C NMR, pyrolytic and thermochemolytic methods: a case study in the San Diego harbor area, *Chemosphere* 45 (2001) 1007–1022.
- [36] P.A. Mirau, Solid-state NMR characterization of polymer interfaces, in: G.A. Webb (Ed.), *Modern Magnetic Resonance*, Springer, Netherlands, Dordrecht, 2006, pp. 575–581.
- [37] K.M. Eldho, P.R. Rajamohan, R. Anto, N. Bulakh, A.K. Lele, T.G. Ajithkumar, Insights into the molecular dynamics in polysulfone polymers from <sup>13</sup>C solid-state NMR experiments, *J. Phys. Chem. B* 119 (2015) 11287–11294.
- [38] Y.-L. Hong, T. Miyoshi, Solid-state NMR characterization of polymer chain structure and dynamics in polymer crystals, in: S. Palsule (Ed.), *Encyclopedia of Polymers and Composites*, Springer, Berlin, Heidelberg, 2013, pp. 1–17.
- [39] J.B. Murdoch, J.F. Stebbins, I.S.E. Carmichael, High-resolution <sup>29</sup>Si NMR study of silicate and aluminosilicate glasses: the effect of network-modifying cations, *Am. Miner.* 70 (1985) 332–343.
- [40] H. Eckert, J.P. Yesinowski, L.A. Silver, E.M. Stolper, Water in silicate glasses: quantification and structural studies by <sup>1</sup>H solid echo and MAS-NMR methods, *J. Phys. Chem.* 92 (1988) 2055–2064.
- [41] C. Le Losq, B.O. Mysen, G.D. Cody, Water and magmas: insights about the water solution mechanisms in alkali silicate melts from infrared, Raman, and <sup>29</sup>Si solid-state NMR spectroscopies, *Prog. Earth Planet. Sci.* 2 (2015) 22.
- [42] N. Baccile, G. Laurent, C. Bonhomme, P. Innocenzi, F. Babonneau, Solid-state NMR characterization of the surfactant-silica interface in templated silicas: acidic versus basic conditions, *Chem. Mater.* 19 (2007) 1343–1354.
- [43] S. Abdullhussain, H. Breitzke, T. Ratajczyk, A. Grünberg, M. Srour, D. Arnaut, H. Weidler, U. Kunz, H.J. Kleebe, U. Bommerich, J. Bernarding, T. Gutmann, G. Buntkowsky, Synthesis, solid-state NMR characterization, and application for hydrogenation reactions of a novel Wilkinson's-type immobilized catalyst, *Chem. – Eur. J.* 20 (2014) 1159–1166.
- [44] A.S. Cattaneo, C. Ferrara, A.M. Marculescu, F. Giannici, A. Martorana, P. Mustarelli, C. Tealdi, Solid-state NMR characterization of the structure and thermal stability of hybrid organic-inorganic compounds based on a HLaNb<sub>2</sub>O<sub>7</sub> Dion-Jacobson layered perovskite, *Phys. Chem. Chem. Phys.* 18 (2016) 21903–21912.
- [45] C. Bonhomme, C. Coelho, N. Baccile, C. Gervais, T. Azaïs, F. Babonneau, Advanced solid state NMR techniques for the characterization of sol-gel-derived materials, *Acc. Chem. Res.* 40 (2007) 738–746.
- [46] F. Babonneau, C. Bonhomme, Solid-state NMR characterization of sol-gel materials: recent advances, in: D. Levy, M. Zayat (Eds.), *The Sol-Gel Handbook*, Wiley-VCH Verlag GmbH & Co. KGaA, 2015, pp. 651–672.
- [47] S.E. Ashbrook, S. Sneddon, New methods and applications in solid-state NMR spectroscopy of quadrupolar nuclei, *J. Am. Chem. Soc.* 136 (2014) 15440–15456.
- [48] A. Sutrisno, Y. Huang, Solid-state NMR: a powerful tool for characterization of metal-organic frameworks, *Solid State Nucl. Magn. Reson.* 49–50 (2013) 1–11.
- [49] G. Mali, Looking into metal-organic frameworks with solid-state NMR Spectroscopy, in: F. Zafar, E. Sharmin (Eds.), *Metal Organic Frameworks*, 2016, <http://dx.doi.org/10.5772/64134>, ISBN 978-953-51-2663-8, Print ISBN 978-953-51-2662-1.

- [50] S.R. Hartmann, E.L. Hahn, Nuclear double resonance in the rotating frame, *Phys. Rev.* 128 (1962) 2042–2053.
- [51] V. Agarwal, S. Penzel, K. Szeckely, R. Cadalbert, E. Testori, A. Oss, J. Past, A. Samoson, M. Ernst, A. Bockmann, B.H. Meier, De novo 3D structure determination from sub-milligram protein samples by solid-state 100 kHz MAS NMR spectroscopy, *Angew. Chem. Int. Ed. Engl.* 53 (2014) 12253–12256.
- [52] L.B. Andreas, K. Jaudzems, J. Stanek, D. Lalli, A. Bertarello, T. Le Marchand, D.C. D. Paepe, S. Kotelovica, I. Akopjana, B. Knott, S. Wegner, F. Engelke, A. Lesage, L. Emsley, K. Tars, T. Herrmann, G. Pintacuda, Structure of fully protonated proteins by proton-detected magic-angle spinning NMR, *Proc. Natl. Acad. Sci. U.S.A.* 113 (2016) 9187–9192.
- [53] S.B. Duckett, R.E. Mewis, Application of parahydrogen induced polarization techniques in NMR spectroscopy and imaging, *Acc. Chem. Res.* 45 (2012) 1247–1257.
- [54] R.G. Lawler, Chemically induced dynamic nuclear polarization (CIDNP). II. Radical-pair model, *Acc. Chem. Res.* 5 (1972) 25–33.
- [55] G.W. Thad, Fundamentals of spin-exchange optical pumping, *J. Phys.: Conf. Ser.* 294 (2011) 012001.
- [56] A.W. Overhauser, Polarization of nuclei in metals, *Phys. Rev.* 92 (1953) 411–415.
- [57] T.R. Carver, C.P. Slichter, Polarization of nuclear spins in metals, *Phys. Rev.* 92 (1953) 212–213.
- [58] C.F. Hwang, B.A. Hasher, D.A. Hill, F. Markley, The use of chemically doped polystyrene as a polarized proton target material, *Nucl. Instrum. Methods* 51 (1967) 254–256.
- [59] C.F. Hwang, D.A. Hill, New effect in dynamic polarization, *Phys. Rev. Lett.* 18 (1967) 110–112.
- [60] C.F. Hwang, D.A. Hill, Phenomenological model for new effect in dynamic polarization, *Phys. Rev. Lett.* 19 (1967) 1011–1014.
- [61] D.S. Wollan, Dynamic nuclear-polarization with an inhomogeneously broadened ESR line. 1. Theory, *Phys. Rev. B* 13 (1976) 3671–3685.
- [62] D.S. Wollan, Dynamic nuclear-polarization with an inhomogeneously broadened ESR line. 2. Experiment, *Phys. Rev. B* 13 (1976) 3686–3696.
- [63] R.A. Wind, M.J. Duijvestijn, C. van der Lugt, A. Manenschijn, J. Vriend, Applications of dynamic nuclear polarization in  $^{13}\text{C}$  NMR in solids, *Prog. Nucl. Magn. Reson. Spectrosc.* 17 (1985) 33–67.
- [64] M. Afeworki, J. Schaefer, Mechanism of DNP-enhanced polarization transfer across the interface of polycarbonate/polystyrene heterogeneous blends, *Macromolecules* 25 (1992) 4092–4096.
- [65] J.H. Ardenkjaer-Larsen, On the present and future of dissolution-DNP, *J. Magn. Reson.* 264 (2016) 3–12.
- [66] A. Bornet, S. Jannin, Optimizing dissolution dynamic nuclear polarization, *J. Magn. Reson.* 264 (2016) 13–21.
- [67] F. Jähnig, G. Kwiatkowski, M. Ernst, Conceptual and instrumental progress in dissolution DNP, *J. Magn. Reson.* 264 (2016) 22–29.
- [68] A. Comment, Dissolution DNP for in vivo preclinical studies, *J. Magn. Reson.* 264 (2016) 39–48.
- [69] J. van Bentum, B. van Meerten, M. Sharma, A. Kentgens, Perspectives on DNP-enhanced NMR spectroscopy in solutions, *J. Magn. Reson.* 264 (2016) 59–67.
- [70] M.D. Lingwood, S. Han, Solution-state dynamic nuclear polarization, in: A.W. Graham (Ed.), *Annu. Rep. NMR Spectrosc.*, Academic Press, 2011, pp. 83–126 (Chapter 3).
- [71] E. Ravera, C. Luchinat, G. Parigi, Basic facts and perspectives of Overhauser DNP NMR, *J. Magn. Reson.* 264 (2016) 78–87.
- [72] T. Prisner, V. Denysenkov, D. Sezer, Liquid state DNP at high magnetic fields: instrumentation, experimental results and atomistic modelling by molecular dynamics simulations, *J. Magn. Reson.* 264 (2016) 68–77.
- [73] J.-H. Ardenkjaer-Larsen, G.S. Boebinger, A. Comment, S. Duckett, A.S. Edison, F. Engelke, C. Griesinger, R.G. Griffin, C. Hilty, H. Maeda, G. Parigi, T. Prisner, E. Ravera, J. van Bentum, S. Vega, A. Webb, C. Luchinat, H. Schwalbe, L. Frydman, Facing and overcoming sensitivity challenges in biomolecular NMR spectroscopy, *Angew. Chem. Int. Ed.* 54 (2015) 9162–9185.
- [74] B. Corzilius, A.A. Smith, R.G. Griffin, Solid effect in magic angle spinning dynamic nuclear polarization, *J. Chem. Phys.* 137 (2012) 054201.
- [75] F. Mentink-Vigier, Ü. Akbey, Y. Hovav, S. Vega, H. Oschkinat, A. Feintuch, Fast passage dynamic nuclear polarization on rotating solids, *J. Magn. Reson.* 224 (2012) 13–21.
- [76] M. Abraham, M.A.H. McCausland, F.N.H. Robinson, Dynamic nuclear polarization, *Phys. Rev. Lett.* 2 (1959) 449–451.
- [77] A.A. Smith, B. Corzilius, A.B. Barnes, T. Maly, R.G. Griffin, Solid effect dynamic nuclear polarization and polarization pathways, *J. Chem. Phys.* 136 (2012) 015101.
- [78] J. Zhou, L. Li, H. Hu, B. Yang, Z. Dan, J. Qiu, J. Guo, F. Chen, C. Ye, Study of natural diamonds by dynamic nuclear polarization-enhanced  $^{13}\text{C}$  nuclear magnetic resonance spectroscopy, *Solid State Nucl. Magn. Reson.* 3 (1994) 339–351.
- [79] B. Yang, J. Zhou, H. Hu, L. Li, J. Qiu, J. Guo, P. He, J. Lu, C. Ye, Study of synthetic diamonds by dynamic nuclear polarization-enhanced  $^{13}\text{C}$  nuclear magnetic resonance spectroscopy, *Appl. Magn. Reson.* 9 (1995) 379–388.
- [80] K.N. Hu, G.T. Debelouchina, A.A. Smith, R.G. Griffin, Quantum mechanical theory of dynamic nuclear polarization in solid dielectrics, *J. Chem. Phys.* 134 (2011) 125105.
- [81] Y. Hovav, A. Feintuch, S. Vega, Theoretical aspects of dynamic nuclear polarization in the solid state – the cross effect, *J. Magn. Reson.* 214 (2012) 29–41.
- [82] V.K. Michaelis, A.A. Smith, B. Corzilius, O. Haze, T.M. Swager, R.G. Griffin, High-field  $^{13}\text{C}$  dynamic nuclear polarization with a radical mixture, *J. Am. Chem. Soc.* 135 (2013) 2935–2938.
- [83] K.R. Thurber, R. Tycko, Theory for cross effect dynamic nuclear polarization under magic-angle spinning in solid state nuclear magnetic resonance: the importance of level crossings, *J. Chem. Phys.* 137 (2012) 084508.
- [84] K.R. Thurber, R. Tycko, Perturbation of nuclear spin polarizations in solid state NMR of nitroxide-doped samples by magic-angle spinning without microwaves, *J. Chem. Phys.* 140 (2014) 184201.
- [85] F. Mentink-Vigier, S. Paul, D. Lee, A. Feintuch, S. Hediger, S. Vega, G. De Paepe, Nuclear depolarization and absolute sensitivity in magic-angle spinning cross effect dynamic nuclear polarization, *Phys. Chem. Chem. Phys.* 17 (2015) 21824–21836.
- [86] S.R. Chaudhari, P. Berruyer, D. Gajan, C. Reiter, F. Engelke, D.L. Silverio, C. Coperet, M. Lelli, A. Lesage, L. Emsley, Dynamic nuclear polarization at 40 kHz magic angle spinning, *Phys. Chem. Chem. Phys.* 18 (2016) 10616–10622.
- [87] E.A. Nanni, A.B. Barnes, Y. Matsuki, P.P. Woskov, B. Corzilius, R.G. Griffin, R.J. Temkin, Microwave field distribution in a magic angle spinning dynamic nuclear polarization NMR probe, *J. Magn. Reson.* 210 (2011) 16–23.
- [88] Y. Hovav, D. Shimon, I. Kaminker, A. Feintuch, D. Goldfarb, S. Vega, Effects of the electron polarization on dynamic nuclear polarization in solids, *Phys. Chem. Chem. Phys.* 17 (2015) 6053–6065.
- [89] O. Haze, B. Corzilius, A.A. Smith, R.G. Griffin, T.M. Swager, Water-soluble organic radicals as polarizing agents for high field dynamic nuclear polarization, *J. Am. Chem. Soc.* 134 (2012) 14287–14290.
- [90] T.V. Can, M.A. Caporini, F. Mentink-Vigier, B. Corzilius, J.J. Walsh, M. Rosay, W.E. Maas, M. Baldus, S. Vega, T.M. Swager, R.G. Griffin, Overhauser effects in insulating solids, *J. Chem. Phys.* 141 (2014) 064202.
- [91] L.R. Becerra, G.J. Gerfen, B.F. Bellew, J.A. Bryant, D.A. Hall, S.J. Inati, R.T. Weber, S. Un, T.F. Prisner, A.E. McDermott, K.W. Fishbein, K.E. Kreisler, R.J. Temkin, D.J. Singel, R.G. Griffin, A spectrometer for dynamic nuclear polarization and electron paramagnetic resonance at high frequencies, *J. Magn. Reson. Ser. A* 117 (1995) 28–40.
- [92] T. Maly, D. Cui, R.G. Griffin, A.-F. Miller,  $^1\text{H}$  dynamic nuclear polarization based on an endogenous radical, *J. Phys. Chem. B* 116 (2012) 7055–7065.
- [93] I. Solomon, Relaxation processes in a system of two spins, *Phys. Rev.* 99 (1955) 559–565.
- [94] K.H. Haussler, D. Stehlik, Dynamic nuclear polarisation in liquids, *Adv. Magn. Reson.* 3 (1968) 79.
- [95] F. Bloch, Nuclear induction, *Phys. Rev.* 70 (1946) 460–474.
- [96] N. Enkin, G. Liu, I. Tkach, M. Bennati, High DNP efficiency of TEMPONE radicals in liquid toluene at low concentrations, *Phys. Chem. Chem. Phys.* 16 (2014) 8795–8800.
- [97] M. Lelli, S.R. Chaudhari, D. Gajan, G. Casano, A.J. Rossini, O. Ouari, P. Tordo, A. Lesage, L. Emsley, Solid-state dynamic nuclear polarization at 9.4 and 18.8 T from 100 K to room temperature, *J. Am. Chem. Soc.* 137 (2015) 14558–14561.
- [98] G. Liu, M. Levien, N. Karschin, G. Parigi, C. Luchinat, M. Bennati, One-thousand-fold enhancement of high field liquid nuclear magnetic resonance signals at room temperature, *Nat. Chem.* 9 (2017) 676–680.
- [99] S. Pylaeva, K.L. Ivanov, M. Baldus, D. Sebastiani, H. Elgabarty, Molecular mechanism of Overhauser dynamic nuclear polarization in insulating solids, *J. Phys. Chem. Lett.* 8 (2017) 2137–2142.
- [100] F. Mentink-Vigier, Ü. Akbey, H. Oschkinat, S. Vega, A. Feintuch, Theoretical aspects of magic angle spinning – dynamic nuclear polarization, *J. Magn. Reson.* 258 (2015) 102–120.
- [101] G.R. Khutsishvili, Spin diffusion, *Sov. Phys. Uspekhi* 8 (1966) 743–769.
- [102] D.S. Wollan, J.W. Poulton, Dynamic proton polarization with an inhomogeneously-broadened ESR line, *Phys. Lett. A* 33 (1970) 33–34.
- [103] K.H. Langley, C.D. Jeffries, Theory and operation of a proton-spin refrigerator, *Phys. Rev.* 152 (1966) 358–376.
- [104] C.D. Jeffries, On nuclear relaxation in dilute paramagnetic crystals, *Proc. Phys. Soc.* 88 (1966) 257–258.
- [105] N. Bloembergen, On the interaction of nuclear spins in a crystalline lattice, *Physica* 15 (1949) 386–426.
- [106] A. Abragam, M. Goldman, Principles of dynamic nuclear polarisation, *Rep. Prog. Phys.* 41 (1978) 395–467.
- [107] P.G. de Gennes, Sur la relaxation nucléaire dans les cristaux ioniques, *J. Phys. Chem. Solids* 7 (1958) 345–350.
- [108] W.E. Blumberg, Nuclear spin-lattice relaxation caused by paramagnetic impurities, *Phys. Rev.* 119 (1960) 79–84.
- [109] H.E. Rorschach, Nuclear relaxation in solids by diffusion to paramagnetic impurities, *Physica* 30 (1964) 38–48.
- [110] M. Goldman, Impurity-controlled nuclear relaxation, *Phys. Rev.* 138 (1965) A1675–A1681.
- [111] J.I. Kaplan, Numerical solution of the equation governing nuclear magnetic spin-lattice relaxation in a paramagnetic-spin-doped insulator, *Phys. Rev. B* 3 (1971) 604–608.
- [112] P. Zegers, R. Van Steenwinkel, Strong solid state effect in an inhomogeneous electron spin system, *Physica* 33 (1967) 332–342.
- [113] A. Abragam, M. Borghini, P. Catillon, J. Coustham, P. Roubeau, J. Thirion, Diffusion de protons polarisés de 20 MeV par une cible de protons polarisés et mesure préliminaire du paramètre Cnn, *Phys. Lett.* 2 (1962) 310–311.
- [114] G.R. Khutsishvili, Spin diffusion and magnetic relaxation of nuclei, *Sov. Phys. JETP* 15 (1962) 909–913.
- [115] J.P. Wolfe, Direct observation of a nuclear spin diffusion barrier, *Phys. Rev. Lett.* 31 (1973) 907–910.

- [116] N. Bloembergen, E.M. Purcell, R.V. Pound, Relaxation effects in nuclear magnetic resonance absorption, *Phys. Rev.* 73 (1948) 679–712.
- [117] M. Abraham, R.W. Kedzie, C.D. Jeffries,  $\gamma$ -Ray anisotropy of  $\text{Co}^{60}$  nuclei polarized by paramagnetic resonance saturation, *Phys. Rev.* 106 (1957) 165–166.
- [118] C.D. Jeffries, Polarization of nuclei by resonance saturation in paramagnetic crystals, *Phys. Rev.* 106 (1957) 164–165.
- [119] E. Erb, J.L. Motchane, J. Uebbersfeld, Effet de polarisation nucléaire dans les liquides et les gaz adsorbés sur les charbons, *C.R. Hebd. Acad. Sci.* 246 (1958) 2121–2123.
- [120] A. Abragam, W.G. Proctor, Une nouvelle méthode de polarisation dynamique des noyaux atomiques dans les solides, *C.R. Hebd. Acad. Sci.* 246 (1958) 2253–2256.
- [121] O.S. Leifson, C.D. Jeffries, Dynamic polarization of nuclei by electron-nuclear dipolar coupling in crystals, *Phys. Rev.* 122 (1961) 1781–1795.
- [122] J.L. Motchane, *Ann. Phys. (Paris)* 7 (1962) 139.
- [123] Y. Hovav, A. Feintuch, S. Vega, Dynamic nuclear polarization assisted spin diffusion for the solid effect case, *J. Chem. Phys.* 134 (2011) 074509.
- [124] R. Brünschweiler, R.R. Ernst, Non-ergodic quasi-equilibria in short linear spin 12 chains, *Chem. Phys. Lett.* 264 (1997) 393–397.
- [125] I. Kuprov, Fokker-Planck formalism in magnetic resonance simulations, *J. Magn. Reson.* 270 (2016) 124–135.
- [126] P. Hodgkinson, L. Emsley, Numerical simulation of solid-state NMR experiments, *Prog. Nucl. Magn. Reson. Spectrosc.* 36 (2000) 201–239.
- [127] H.J. Hogben, M. Krzystyniak, G.T.P. Charnock, P.J. Hore, I. Kuprov, Spinach – a software library for simulation of spin dynamics in large spin systems, *J. Magn. Reson.* 208 (2011) 179–194.
- [128] A. Karabanov, I. Kuprov, G.T.P. Charnock, A.v.d. Drift, L.J. Edwards, W. Köckenberger, On the accuracy of the state space restriction approximation for spin dynamics simulations, *J. Chem. Phys.* 135 (2011) 084106.
- [129] A. Karabanov, A. van der Drift, L.J. Edwards, I. Kuprov, W. Köckenberger, Quantum mechanical simulation of solid effect dynamic nuclear polarization using Krylov-Bogolyubov time averaging and a restricted state-space, *Phys. Chem. Chem. Phys.* 14 (2012) 2658–2668.
- [130] A. Karabanov, D. Wiśniewski, I. Lesanovsky, W. Köckenberger, Dynamic nuclear polarization as kinetically constrained diffusion, *Phys. Rev. Lett.* 115 (2015) 020404.
- [131] A. Karabanov, G. Kwiatkowski, W. Köckenberger, Quantum mechanical simulation of cross effect DNP using Krylov-Bogolyubov averaging, *Appl. Magn. Reson.* 43 (2012) 43–58.
- [132] D. Wiśniewski, A. Karabanov, I. Lesanovsky, W. Köckenberger, Solid effect DNP polarization dynamics in a system of many spins, *J. Magn. Reson.* 264 (2016) 30–38.
- [133] Y. Hovav, I. Kaminker, D. Shimon, A. Feintuch, D. Goldfarb, S. Vega, The electron depolarization during dynamic nuclear polarization: measurements and simulations, *Phys. Chem. Chem. Phys.* 17 (2015) 226–244.
- [134] A. Leavesley, D. Shimon, T.A. Siaw, A. Feintuch, D. Goldfarb, S. Vega, I. Kaminker, S. Han, Effect of electron spectral diffusion on static dynamic nuclear polarization at 7 Tesla, *Phys. Chem. Chem. Phys.* 19 (2017) 3596–3605.
- [135] P. Schosseler, T. Wacker, A. Schweiger, Pulsed ELDOR detected NMR, *Chem. Phys. Lett.* 224 (1994) 319–324.
- [136] J. Granwehr, W. Köckenberger, Multidimensional low-power pulse EPR under DNP conditions, *Appl. Magn. Reson.* 34 (2008) 355–378.
- [137] V.S. Bajaj, C.T. Farrar, M.K. Hornstein, I. Mastovsky, J. Viereg, J. Bryant, B. Elena, K.E. Kreisler, R.J. Temkin, R.G. Griffin, Dynamic nuclear polarization at 9 T using a novel 250 GHz gyrotron microwave source, *J. Magn. Reson.* 160 (2003) 85–90.
- [138] A.J. Rossini, A. Zagdoun, F. Hegner, M. Schwarzwälder, D. Gajan, C. Copéret, A. Lesage, L. Emsley, Dynamic nuclear polarization NMR spectroscopy of microcrystalline solids, *J. Am. Chem. Soc.* 134 (2012) 16899–16908.
- [139] M. Kaushik, T. Bahrenberg, T.V. Can, M.A. Caporini, R. Silvers, J. Heiliger, A.A. Smith, H. Schwalbe, R.G. Griffin, B. Corzilius, Gd(III) and Mn(II) complexes for dynamic nuclear polarization: small molecular chelate polarizing agents and applications with site-directed spin labeling of proteins, *Phys. Chem. Chem. Phys.* 18 (2016) 27205–27218.
- [140] P. Wenk, M. Kaushik, D. Richter, M. Vogel, B. Suess, B. Corzilius, Dynamic nuclear polarization of nucleic acid with endogenously bound manganese, *J. Biomol. NMR* 63 (2015) 97–109.
- [141] D. Daube, V. Aladin, J. Heiliger, J.J. Wittmann, D. Barthelme, C. Bengs, H. Schwalbe, B. Corzilius, Heteronuclear cross-relaxation under solid-state dynamic nuclear polarization, *J. Am. Chem. Soc.* 138 (2016) 16572–16575.
- [142] A.S. Lilly Thankamony, O. Lafon, X. Lu, F. Aussenac, M. Rosay, J. Trébosc, H. Vezin, J.-P. Amoureux, Solvent-free high-field dynamic nuclear polarization of mesoporous silica functionalized with TEMPO, *Appl. Magn. Reson.* 43 (2012) 237–250.
- [143] O. Lafon, M. Rosay, F. Aussenac, X. Lu, J. Trébosc, O. Cristini, C. Kinowski, N. Touati, H. Vezin, J.-P. Amoureux, Beyond the silica surface by direct silicon-29 dynamic nuclear polarization, *Angew. Chem. Int. Ed.* 50 (2011) 8367–8370.
- [144] O. Lafon, A.S.L. Thankamony, M. Rosay, F. Aussenac, X.Y. Lu, J. Trébosc, V. Bout-Roumazailles, H. Vezine, J.P. Amoureux, Indirect and direct Si-29 dynamic nuclear polarization of dispersed nanoparticles, *Chem. Commun.* 49 (2013) 2864–2866.
- [145] M.M. Hoffmann, S. Bothe, T. Gutmann, F.-F. Hartmann, M. Reggelin, G. Buntkowsky, Directly vs indirectly enhanced  $^{13}\text{C}$  in dynamic nuclear polarization magic angle spinning NMR experiments of nonionic surfactant systems, *J. Phys. Chem. C* 121 (2017) 2418–2427.
- [146] V.S. Bajaj, M.K. Hornstein, K.E. Kreisler, J.R. Sirigiri, P.P. Woskov, M.L. Mak-Jurkauskas, J. Herzfeld, R.J. Temkin, R.G. Griffin, 250 GHz CW gyrotron oscillator for dynamic nuclear polarization in biological solid state NMR, *J. Magn. Reson.* 189 (2007) 251–279.
- [147] T. Maly, L.B. Andreas, A.A. Smith, R.G. Griffin, H-2-DNP-enhanced H-2-C-13 solid-state NMR correlation spectroscopy, *Phys. Chem. Chem. Phys.* 12 (2010) 5872–5878.
- [148] V.S. Bajaj, M.L. Mak-Jurkauskas, M. Belenky, J. Herzfeld, R.G. Griffin, DNP enhanced frequency-selective TEDOR experiments in bacteriorhodopsin, *J. Magn. Reson.* 202 (2010) 9–13.
- [149] I.V. Sergeev, B. Itin, R. Rogawski, L.A. Day, A.E. McDermott, Efficient assignment and NMR analysis of an intact virus using sequential side-chain correlations and DNP sensitization, *Proc. Natl. Acad. Sci. U.S.A.* (2017).
- [150] V. Vitzthum, M.A. Caporini, G. Bodenhausen, Solid-state nitrogen-14 nuclear magnetic resonance enhanced by dynamic nuclear polarization using a gyrotron, *J. Magn. Reson.* 205 (2010) 177–179.
- [151] K. Märker, M. Pingret, J.M. Mouesca, D. Gasparutto, S. Hediger, G. De Paëpe, A new tool for NMR crystallography: complete  $^{13}\text{C}/^{15}\text{N}$  assignment of organic molecules at natural isotopic abundance using DNP-enhanced solid-state NMR, *J. Am. Chem. Soc.* 137 (2015) 13796–13799.
- [152] M. Rosay, M. Blank, F. Engelke, Instrumentation for solid-state dynamic nuclear polarization with magic angle spinning NMR, *J. Magn. Reson.* 264 (2016) 88–98.
- [153] A. Feintuch, D. Shimon, Y. Hovav, D. Banerjee, I. Kaminker, Y. Lipkin, K. Zibener, B. Epel, S. Vega, D. Goldfarb, A dynamic nuclear polarization spectrometer at 95 GHz/144 MHz with EPR and NMR excitation and detection capabilities, *J. Magn. Reson.* 209 (2011) 136–141.
- [154] K. Ley, E. Müller, K. Scheffler, Zur Unterscheidung möglicher mesomere Grenz Zustände bei "Aroxylene", *Angew. Chem.* 70 (1958) 74–75.
- [155] T.J. Schmutge, C.D. Jeffries, High dynamic polarization of protons, *Phys. Rev.* 138 (1965) A1785–A1801.
- [156] F. Mentink-Vigier, S. Vega, G. De Paepe, Fast and accurate MAS-DNP simulations of large spin ensembles, *Phys. Chem. Chem. Phys.* 19 (2017) 3506–3522.
- [157] Y. Hovav, A. Feintuch, S. Vega, Theoretical aspects of dynamic nuclear polarization in the solid state – the solid effect, *J. Magn. Reson.* 207 (2010) 176–189.
- [158] D. Shimon, Y. Hovav, A. Feintuch, D. Goldfarb, S. Vega, Dynamic nuclear polarization in the solid state: a transition between the cross effect and the solid effect, *Phys. Chem. Chem. Phys.* 14 (2012) 5729–5743.
- [159] B. Corzilius, A.A. Smith, A.B. Barnes, C. Luchinat, I. Bertini, R.G. Griffin, High-field dynamic nuclear polarization with high-spin transition metal ions, *J. Am. Chem. Soc.* 133 (2011) 5648–5651.
- [160] T.A. Siaw, M. Fehr, A. Lund, A. Latimer, S.A. Walker, D.T. Edwards, S.-I. Han, Effect of electron spin dynamics on solid-state dynamic nuclear polarization performance, *Phys. Chem. Chem. Phys.* 16 (2014) 18694–18706.
- [161] Y. Hovav, A. Feintuch, S. Vega, D. Goldfarb, Dynamic nuclear polarization using frequency modulation at 3.34 T, *J. Magn. Reson.* 238 (2014) 94–105.
- [162] T.A. Siaw, A. Leavesley, A. Lund, I. Kaminker, S. Han, A versatile and modular quasi optics-based 200 GHz dual dynamic nuclear polarization and electron paramagnetic resonance instrument, *J. Magn. Reson.* 264 (2016) 131–153.
- [163] K.R. Thurber, W.M. Yau, R. Tycko, Low-temperature dynamic nuclear polarization at 9.4 T with a 30 mW microwave source, *J. Magn. Reson.* 204 (2010) 303–313.
- [164] A. Bornet, J. Milani, B. Vuichoud, A.J. Perez Linde, G. Bodenhausen, S. Jannin, Microwave frequency modulation to enhance dissolution dynamic nuclear polarization, *Chem. Phys. Lett.* 602 (2014) 63–67.
- [165] D. Shimon, A. Feintuch, D. Goldfarb, S. Vega, Static  $^1\text{H}$  dynamic nuclear polarization with the biradical TOTAPOL: a transition between the solid effect and the cross effect, *Phys. Chem. Chem. Phys.* 16 (2014) 6687–6699.
- [166] T.V. Can, J.J. Walsh, T.M. Swager, R.G. Griffin, Time domain DNP with the NOVEL sequence, *J. Chem. Phys.* 143 (2015) 054201.
- [167] B. Corzilius, Theory of solid effect and cross effect dynamic nuclear polarization with half-integer high-spin metal polarizing agents in rotating solids, *Phys. Chem. Chem. Phys.* 18 (2016) 27190–27204.
- [168] M. Kaushik, M. Qi, A. Godt, B. Corzilius, Bis-gadolinium complexes for solid effect and cross effect dynamic nuclear polarization, *Angew. Chem. Int. Ed. Engl.* 56 (2017) 4295–4299.
- [169] D. Banerjee, D. Shimon, A. Feintuch, S. Vega, D. Goldfarb, The interplay between the solid effect and the cross effect mechanisms in solid state  $^{13}\text{C}$  DNP at 95 GHz using trityl radicals, *J. Magn. Reson.* 230 (2013) 212–219.
- [170] K. Thurber, R. Tycko, Low-temperature dynamic nuclear polarization with helium-cooled samples and nitrogen-driven magic-angle spinning, *J. Magn. Reson.* 264 (2016) 99–106.
- [171] Y. Matsuki, K. Ueda, T. Idehara, R. Ikeda, I. Ogawa, S. Nakamura, M. Toda, T. Anai, T. Fujiwara, Helium-cooling and -spinning dynamic nuclear polarization for sensitivity-enhanced solid-state NMR at 14 T and 30 K, *J. Magn. Reson.* 225 (2012) 1–9.
- [172] M. Borghini, W. de Boer, K. Morimoto, Nuclear dynamic polarization by resolved solid-state effect and thermal mixing with an electron spin-spin interaction reservoir, *Phys. Lett. A* 48 (1974) 244–246.
- [173] W. de Boer, Dynamic orientation of nuclei at low temperatures, *J. Low Temp. Phys.* 22 (1976) 185–212.

- [174] A.A. Smith, B. Corzilius, O. Haze, T.M. Swager, R.G. Griffin, Observation of strongly forbidden solid effect dynamic nuclear polarization transitions via electron–electron double resonance detected NMR, *J. Chem. Phys.* 139 (2013) 214201.
- [175] D. Shimon, Y. Hovav, I. Kaminker, A. Feintuch, D. Goldfarb, S. Vega, Simultaneous DNP enhancements of  $^1\text{H}$  and  $^{13}\text{C}$  nuclei: theory and experiments, *Phys. Chem. Chem. Phys.* 17 (2015) 11868–11883.
- [176] I. Kaminker, D. Shimon, Y. Hovav, A. Feintuch, S. Vega, Heteronuclear DNP of protons and deuterons with TEMPOL, *Phys. Chem. Chem. Phys.* 18 (2016) 11017–11041.
- [177] M. Rosay, L. Tometich, S. Pawsey, R. Bader, R. Schauwecker, M. Blank, P.M. Borchard, S.R. Cauffman, K.L. Felch, R.T. Weber, R.J. Temkin, R.G. Griffin, W.E. Maas, Solid-state dynamic nuclear polarization at 263 GHz: spectrometer design and experimental results, *Phys. Chem. Chem. Phys.* 12 (2010) 5850–5860.
- [178] Y. Matsuki, T. Idehara, J. Fukazawa, T. Fujiwara, Advanced instrumentation for DNP-enhanced MAS NMR for higher magnetic fields and lower temperatures, *J. Magn. Reson.* 264 (2016) 107–115.
- [179] T. Maly, G.T. Debelouchina, V.S. Bajaj, K.N. Hu, C.G. Joo, M.L. Mak-Jurkauskas, J.R. Sirigiri, P.C.A. van der Wel, J. Herzfeld, R.J. Temkin, R.G. Griffin, Dynamic nuclear polarization at high magnetic fields, *J. Chem. Phys.* 128 (2008) 052211.
- [180] A.B. Barnes, G. De Paëpe, P.C.A. van der Wel, K.N. Hu, C.G. Joo, V.S. Bajaj, M.L. Mak-Jurkauskas, J.R. Sirigiri, J. Herzfeld, R.J. Temkin, R.G. Griffin, High-field dynamic nuclear polarization for solid and solution biological NMR, *Appl. Magn. Reson.* 34 (2008) 237–263.
- [181] G.J. Gerfen, L.R. Becerra, D.A. Hall, R.G. Griffin, R.J. Temkin, D.J. Singel, High frequency (140 GHz) dynamic nuclear polarization: Polarization transfer to a solute in frozen aqueous solution, *J. Chem. Phys.* 102 (1995) 9494–9497.
- [182] L.R. Becerra, G.J. Gerfen, R.J. Temkin, D.J. Singel, R.G. Griffin, Dynamic nuclear polarization with a cyclotron resonance maser at 5 T, *Phys. Rev. Lett.* 71 (1993) 3561–3564.
- [183] Y. Matsuki, H. Takahashi, K. Ueda, T. Idehara, I. Ogawa, M. Toda, H. Akutsu, T. Fujiwara, Dynamic nuclear polarization experiments at 14.1 T for solid-state NMR, *Phys. Chem. Chem. Phys.* 12 (2010) 5799.
- [184] A.B. Barnes, E. Markhasin, E. Daviso, V.K. Michaelis, E.A. Nanni, S.K. Jawla, E.L. Mena, R. DeRocher, A. Thakkar, P.P. Woskov, J. Herzfeld, R.J. Temkin, R.G. Griffin, Dynamic nuclear polarization at 700 MHz/460 GHz, *J. Magn. Reson.* 224 (2012) 1–7.
- [185] V.L. Granatstein, R.K. Parker, C.M. Armstrong, Vacuum electronics at the dawn of the twenty-first century, *Proc. IEEE* 87 (1999) 702–716.
- [186] G.S. Nusinovich, M.K.A. Thumm, M.I. Petelin, The gyrotron at 50: historical overview, *J. Infrared Millimeter Terahertz Waves* 35 (2014) 325–381.
- [187] A.C. Torrezan, S.T. Han, I. Mastovsky, M.A. Shapiro, J.R. Sirigiri, R.J. Temkin, A. B. Barnes, R.G. Griffin, Continuous-wave operation of a frequency-tunable 460-GHz second-harmonic gyrotron for enhanced nuclear magnetic resonance, *IEEE Trans. Plasma Sci.* 38 (2010) 1150–1159.
- [188] A.C. Torrezan, M.A. Shapiro, J.R. Sirigiri, R.J. Temkin, R.G. Griffin, Operation of a continuously frequency-tunable second-harmonic CW 330-GHz gyrotron for dynamic nuclear polarization, *IEEE Trans. Electron Dev.* 58 (2011) 2777–2783.
- [189] A.B. Barnes, E.A. Nanni, J. Herzfeld, R.G. Griffin, R.J. Temkin, A 250 GHz gyrotron with a 3 GHz tuning bandwidth for dynamic nuclear polarization, *J. Magn. Reson.* 221 (2012) 147–153.
- [190] S. Jawla, Q.Z. Ni, A. Barnes, W. Guss, E. Daviso, J. Herzfeld, R. Griffin, R. Temkin, Continuously tunable 250 GHz gyrotron with a double disk window for DNP-NMR spectroscopy, *J. Infrared Millimeter Terahertz Waves* 34 (2013) 42–52.
- [191] Y. Matsuki, K. Ueda, T. Idehara, R. Ikeda, K. Kosuga, I. Ogawa, S. Nakamura, M. Toda, T. Anai, T. Fujiwara, Application of continuously frequency-tunable 0.4 THz gyrotron to dynamic nuclear polarization for 600 MHz solid-state NMR, *J. Infrared Millimeter Terahertz Waves* 33 (2012) 745–755.
- [192] T. Idehara, Y. Tatematsu, Y. Yamaguchi, E.M. Khutoryan, A.N. Kuleshov, K. Ueda, Y. Matsuki, T. Fujiwara, The development of 460 GHz gyrotrons for 700 MHz DNP-NMR spectroscopy, *J. Infrared Millimeter Terahertz Waves* 36 (2015) 613–627.
- [193] T. Idehara, E.M. Khutoryan, Y. Tatematsu, Y. Yamaguchi, A.N. Kuleshov, O. Dumbrajs, Y. Matsuki, T. Fujiwara, High-speed frequency modulation of a 460-GHz gyrotron for enhancement of 700-MHz DNP-NMR spectroscopy, *J. Infrared Millimeter Terahertz Waves* 36 (2015) 819–829.
- [194] K.J. Pike, T.F. Kemp, H. Takahashi, R. Day, A.P. Howes, E.V. Kryukov, J.F. MacDonald, A.E.C. Collis, D.R. Bolton, R.J. Wylde, M. Orwick, K. Kosuga, A.J. Clark, T. Idehara, A. Watts, G.M. Smith, M.E. Newton, R. Dupree, M.E. Smith, A spectrometer designed for 6.7 and 14.1 T DNP-enhanced solid-state MAS NMR using quasi-optical microwave transmission, *J. Magn. Reson.* 215 (2012) 1–9.
- [195] D.E.M. Hoff, B.J. Albert, E.P. Saliba, F.J. Scott, E.J. Choi, M. Mardini, A.B. Barnes, Frequency swept microwaves for hyperfine decoupling and time domain dynamic nuclear polarization, *Solid State Nucl. Magn. Reson.* 72 (2015) 79–89.
- [196] S. Alberti, J.P. Ansermet, K.A. Avramides, D. Fasel, J.P. Hogge, S. Kern, C. Lievin, Y. Liu, A. Macor, I. Pagonakis, M. Silva, M.Q. Tran, T.M. Tran, D. Wagner, Design of a frequency-tunable gyrotron for DNP-enhanced NMR spectroscopy, in: 2009 34th International Conference on Infrared, Millimeter, and Terahertz Waves, 2009, pp. 1–2.
- [197] S. Alberti, J.-P. Ansermet, K.A. Avramides, F. Braunmueller, P. Cuanillon, J. Dubray, D. Fasel, J.-P. Hogge, A. Macor, E. de Rijk, M. da Silva, M.Q. Tran, T.M. Tran, Q. Vuillemin, Experimental study from linear to chaotic regimes on a terahertz-frequency gyrotron oscillator, *Phys. Plasmas* 19 (2012) 123102.
- [198] S. Alberti, F. Braunmueller, T.M. Tran, J. Genoud, J.P. Hogge, M.Q. Tran, J.P. Ansermet, Nanosecond pulses in a THz gyrotron oscillator operating in a mode-locked self-consistent Q-switch regime, *Phys. Rev. Lett.* 111 (2013) 205101.
- [199] M. Blank, P. Borchard, S. Cauffman, K. Felch, M. Rosay, L. Tometich, High-frequency gyrotrons for DNP-enhanced NMR applications, in: IEEE International Vacuum Electronics Conference, 2014, pp. 7–8.
- [200] V. Denysenkov, T. Prisner, Liquid state dynamic nuclear polarization probe with Fabry-Perot resonator at 9.2 T, *J. Magn. Reson.* 217 (2012) 1–5.
- [201] J.R. Sirigiri, T. Maly, L. Tarricone, A compact 395 GHz gyrotron for dynamic nuclear polarization, in: 2011 International Conference on Infrared, Millimeter, and Terahertz Waves, 2011, pp. 1–2.
- [202] S.P. Kuo, B.R. Cheo, Analysis of the electron cyclotron maser instability, *Phys. Lett. A* 103 (1984) 427–432.
- [203] A. Stock, A high-order particle-in-cell method for low density plasma flow and the simulation of gyrotron resonator devices, *Fakultät Luft- und Raumfahrttechnik und Geodäsie, Universität Stuttgart*, 2013.
- [204] M.K. Hornstein, V.S. Bajaj, R.G. Griffin, K.E. Kreisler, I. Mastovsky, M.A. Shapiro, J.R. Sirigiri, R.J. Temkin, Second harmonic operation at 460 GHz and broadband continuous frequency tuning of a gyrotron oscillator, *IEEE Trans. Electron Dev.* 52 (2005) 798–807.
- [205] R. Sirigiri, T. Maly, Integrated high-frequency generator system utilizing the magnetic field of the target application, in: Bridge12 Technologies, Inc. Framingham, MA, 2014.
- [206] V.L. Bratman, A.E. Fedotov, Y.K. Kalynov, P.B. Makhalov, A. Samoson, THz gyrotron and BWO designed for operation in DNP-NMR spectrometer magnet, *J. Infrared Millimeter Terahertz Waves* 34 (2013) 837–846.
- [207] V.L. Bratman, A.E. Fedotov, Y.K. Kalynov, P.B. Makhalov, V.N. Manuilov, Project of gyrotron for DNP applications based on NMR magnet, in: 2016 41st International Conference on Infrared, Millimeter, and Terahertz waves (IRMMW-THz), 2016, pp. 1–2.
- [208] H. Ryan, J. van Bentum, T. Maly, A ferromagnetic shim insert for NMR magnets – towards an integrated gyrotron for DNP-NMR spectroscopy, *J. Magn. Reson.* 277 (2017) 1–7.
- [209] T.F. Kemp, H.R. Dannatt, N.S. Barrow, A. Watts, S.P. Brown, M.E. Newton, R. Dupree, Dynamic nuclear polarization enhanced NMR at 187 GHz/284 MHz using an extended interaction klystron amplifier, *J. Magn. Reson.* 265 (2016) 77–82.
- [210] D. Berry, H. Deng, R. Dobbs, P. Horoyski, M. Hyttinen, A. Kingsmill, R. MacHattie, A. Roitman, E. Sokol, B. Steer, Practical aspects of EIK technology, *IEEE Trans. Electron Dev.* 61 (2014) 1830–1835.
- [211] J. Benford, J.A. Swegle, E. Schamiloglu, *High Power Microwaves*, third ed., CRC Press, 2015.
- [212] D.R. Bolton, P.S. Cruickshank, D.A. Robertson, G.M. Smith, Sub-nanosecond coherent pulse generation at millimetre-wave frequencies, *Electron. Lett.* 43 (2007) 346–348.
- [213] A.A. Smith, B. Corzilius, J.A. Bryant, R. DeRocher, P.P. Woskov, R.J. Temkin, R.G. Griffin, A 140 GHz pulsed EPR/212 MHz NMR spectrometer for DNP studies, *J. Magn. Reson.* 223 (2012) 170–179.
- [214] Ü. Akbey, A.H. Linden, H. Oshkinat, High-temperature dynamic nuclear polarization enhanced magic-angle-spinning NMR, *Appl. Magn. Reson.* 43 (2012) 81–90.
- [215] A.B. Barnes, M.L. Mak-Jurkauskas, Y. Matsuki, V.S. Bajaj, P.C.A. van der Wel, R. DeRocher, J. Bryant, J.R. Sirigiri, R.J. Temkin, J. Lugtenburg, J. Herzfeld, R.G. Griffin, Cryogenic sample exchange NMR probe for magic angle spinning dynamic nuclear polarization, *J. Magn. Reson.* 198 (2009) 261–270.
- [216] Q.Z. Ni, E. Daviso, T.V. Can, E. Markhasin, S.K. Jawla, T.M. Swager, R.J. Temkin, J. Herzfeld, R.G. Griffin, High frequency dynamic nuclear polarization, *Acc. Chem. Res.* 46 (2013) 1933–1941.
- [217] D. Lee, E. Bouleau, P. Saint-Bonnet, S. Hediger, G. De Paëpe, Ultra-low temperature MAS-DNP, *J. Magn. Reson.* 264 (2016) 116–124.
- [218] D.A. Hall, D.C. Maus, G.J. Gerfen, S.J. Inati, L.R. Becerra, F.W. Dahlquist, R.G. Griffin, Polarization-enhanced NMR spectroscopy of biomolecules in frozen solution, *Science* 276 (1997) 930–932.
- [219] E. Bouleau, P. Saint-Bonnet, F. Mentink-Vigier, H. Takahashi, J.F. Jacquot, M. Bardet, F. Aussenac, A. Pura, F. Engelke, S. Hediger, D. Lee, G. De Paëpe, Pushing NMR sensitivity limits using dynamic nuclear polarization with closed-loop cryogenic helium sample spinning, *Chem. Sci.* 6 (2015) 6806–6812.
- [220] K.R. Thurber, R. Tycko, Biomolecular solid state NMR with magic-angle spinning at 25 K, *J. Magn. Reson.* 195 (2008) 179–186.
- [221] C. Song, K.-N. Hu, C.-G. Joo, T.M. Swager, R.G. Griffin, TOTAPOL: a biradical polarizing agent for dynamic nuclear polarization experiments in aqueous media, *J. Am. Chem. Soc.* 128 (2006) 11385–11390.
- [222] R.A. McKay, *Probes for special purposes*, eMagRes, John Wiley & Sons, Ltd, 2007.
- [223] E.A. Nanni, S.K. Jawla, M.A. Shapiro, P.P. Woskov, R.J. Temkin, Low-loss transmission lines for high-power terahertz radiation, *J. Infrared Millimeter Terahertz Waves* 33 (2012) 695–714.
- [224] B.D. Armstrong, D.T. Edwards, R.J. Wylde, S.A. Walker, S. Han, A 200 GHz dynamic nuclear polarization spectrometer, *Phys. Chem. Chem. Phys.* 12 (2010) 5920–5926.
- [225] B. Corzilius, L.B. Andreas, A.A. Smith, Q.Z. Ni, R.G. Griffin, Paramagnet-induced signal quenching in MAS-DNP experiments on frozen homogeneous solutions, *J. Magn. Reson.* 240 (2014) 113–123.

- [226] M.L. Mak-Jurkauskas, V.S. Bajaj, M.K. Hornstein, M. Belenky, R.G. Griffin, J. Herzfeld, Energy transformations early in the bacteriorhodopsin photocycle revealed by DNP-enhanced solid-state NMR, *Proc. Natl. Acad. Sci. U.S.A.* 105 (2008) 883–888.
- [227] V.S. Bajaj, M.L. Mak-Jurkauskas, M. Belenky, J. Herzfeld, R.G. Griffin, Functional and shunt states of bacteriorhodopsin resolved by 250 GHz dynamic nuclear polarization-enhanced solid-state NMR, *Proc. Natl. Acad. Sci. U.S.A.* 106 (2009) 9244–9249.
- [228] J. Becker-Baldus, C. Bamann, K. Saxena, H. Gustmann, L.J. Brown, R.C.D. Brown, C. Reiter, E. Bamberg, J. Wachtveitl, H. Schwalbe, C. Glaubitz, Enlightening the photoactive site of channelrhodopsin-2 by DNP-enhanced solid-state NMR spectroscopy, *Proc. Natl. Acad. Sci. U.S.A.* 112 (2015) 9896–9901.
- [229] K.N. Hu, Polarizing agents and mechanisms for high-field dynamic nuclear polarization of frozen dielectric solids, *Solid State Nucl. Magn. Reson.* 40 (2011) 31–41.
- [230] C.F. Koelsch, Syntheses with triarylvinylmagnesium bromides.  $\alpha,\gamma$ -Bisdiphenylene- $\beta$ -phenyllallyl, a stable free radical, *J. Am. Chem. Soc.* 79 (1957) 4439–4441.
- [231] M. Afeworki, R.A. McKay, J. Schaefer, Selective observation of the interface of heterogeneous polycarbonate/polystyrene blends by dynamic nuclear polarization carbon-13 NMR spectroscopy, *Macromolecules* 25 (1992) 4084–4091.
- [232] C.T. Farrar, D.A. Hall, G.J. Gerfen, S.J. Inati, R.G. Griffin, Mechanism of dynamic nuclear polarization in high magnetic fields, *J. Chem. Phys.* 114 (2001) 4922–4933.
- [233] J.H. Ardenkjær-Larsen, I. Laursen, I. Leunbach, G. Ehnholm, L.G. Wistrand, J.S. Petersson, K. Golman, EPR and DNP properties of certain novel single electron contrast agents intended for oximetric imaging, *J. Magn. Reson.* 133 (1998) 1–12.
- [234] T.J. Reddy, T. Iwama, H.J. Halpern, V.H. Rawal, General synthesis of persistent trityl radicals for EPR imaging of biological systems, *J. Org. Chem.* 67 (2002) 4635–4639.
- [235] I. Dhimitruka, O. Grigorieva, J.L. Zweier, V.V. Khrantsov, Synthesis, structure, and EPR characterization of deuterated derivatives of Finland trityl radical, *Bioorg. Med. Chem. Lett.* 20 (2010) 3946–3949.
- [236] V.K. Michaelis, B. Corzilius, A.A. Smith, R.G. Griffin, Dynamic nuclear polarization of  $^{17}\text{O}$ : direct polarization, *J. Phys. Chem. B* 117 (2013) 14894–14906.
- [237] J.H. Ardenkjær-Larsen, B. Fridlund, A. Gram, G. Hansson, L. Hansson, M.H. Lerche, R. Servin, M. Thaning, K. Golman, Increase in signal-to-noise ratio of  $>10,000$  times in liquid-state NMR, *Proc. Natl. Acad. Sci. U.S.A.* 100 (2003) 10158–10163.
- [238] J.H. Ardenkjær-Larsen, S. Macholl, H. Jóhannesson, Dynamic nuclear polarization with trityls at 1.2 K, *Appl. Magn. Reson.* 34 (2008) 509–522.
- [239] S. Anderson, K. Golman, F. Rise, H. Wikström, L.-G. Wistrand, Free radicals, in: *U.S. patent, 5,530,140*, 1996.
- [240] C. Gabellieri, V. Mugnaini, J.C. Paniagua, N. Roques, M. Oliveros, M. Feliz, J. Veciana, M. Pons, Dynamic nuclear polarization with polychlorotriphenylmethyl radicals: supramolecular polarization-transfer effects, *Angew. Chem. Int. Ed.* 49 (2010) 3360–3362.
- [241] F. Mentink Vigier, D. Shimon, V. Mugnaini, J. Veciana, A. Feintuch, M. Pons, S. Vega, D. Goldfarb, The  $^{13}\text{C}$  solid DNP mechanisms with perchlorotriphenylmethyl radicals – the role of  $^{35,37}\text{Cl}$ , *Phys. Chem. Chem. Phys.* 16 (2014) 19218–19228.
- [242] E.J. Hustedt, A.I. Smirnov, C.F. Laub, C.E. Cobb, A.H. Beth, Molecular distances from dipolar coupled spin-labels: the global analysis of multifrequency continuous wave electron paramagnetic resonance data, *Biophys. J.* 72 (1997) 1861–1877.
- [243] E.J. Hustedt, A.H. Beth, Nitroxide spin-spin interactions: applications to protein structure and dynamics, *Annu. Rev. Biophys. Biomol. Struct.* 28 (1999) 129–153.
- [244] K.N. Hu, C. Song, H.H. Yu, T.M. Swager, R.G. Griffin, High-frequency dynamic nuclear polarization using biradicals: a multifrequency EPR lineshape analysis, *J. Chem. Phys.* 128 (2008) 052302.
- [245] V.N. Parmon, A.I. Kokorin, G.M. Zhidomirov, The interpretation of the polycrystalline ESR spectra of nitroxide biradicals, *J. Magn. Reson.* 28 (1977) 339–349.
- [246] N.E. Shepherd, R. Gamsjaeger, M. Vandevenne, L. Cubeddu, J.P. Mackay, Site directed nitroxide spin labeling of oligonucleotides for NMR and EPR studies, *Tetrahedron* 71 (2015) 813–819.
- [247] S.A. Shelke, G.B. Sandholt, S.T. Sigurdsson, Nitroxide-labeled pyrimidines for non-covalent spin-labeling of abasic sites in DNA and RNA duplexes, *Org. Biomol. Chem.* 12 (2014) 7366–7374.
- [248] S.A. Shelke, S.T. Sigurdsson, Site-directed nitroxide spin labeling of biopolymers, in: C.R. Timmel, J.R. Harmer (Eds.), *Structural Information from Spin-Labels and Intrinsic Paramagnetic Centres in the Biosciences*, Springer, Berlin, Heidelberg, 2013, pp. 121–162.
- [249] G. Audran, E.G. Bagryanskaya, P. Bremond, M.V. Edeleva, S.R.A. Marque, D.A. Parkhomenko, O.Y. Rogozhnikova, V.M. Tormyshev, E.V. Tretyakov, D.V. Trukhin, S.I. Zhivetyeva, Trityl-based alkoxyamines as NMP controllers and spin-labels, *Polym. Chem.* 7 (2016) 6490–6499.
- [250] M.-A. Geiger, M. Orwick-Rydmark, K. Marker, W.T. Franks, D. Akhmetzyanov, D. Stoppler, M. Zinke, E. Specker, M. Nazare, A. Diehl, B.-J. van Rossum, F. Aussenac, T. Prisner, U. Akbey, H. Oschkinat, Temperature dependence of cross-effect dynamic nuclear polarization in rotating solids: advantages of elevated temperatures, *Phys. Chem. Chem. Phys.* 18 (2016) 30696–30704.
- [251] H. Sato, V. Kathirvelu, A. Fielding, J.P. Blinco, A.S. Micallef, S.E. Bottle, S.S. Eaton, G.R. Eaton, Impact of molecular size on electron spin relaxation rates of nitroxyl radicals in glassy solvents between 100 and 300 K, *Mol. Phys.* 105 (2007) 2137–2151.
- [252] S. Lange, A.H. Linden, Ü. Akbey, W.T. Franks, N.M. Loening, B.-J. van Rossum, H. Oschkinat, The effect of biradical concentration on the performance of DNP-MAS-NMR, *J. Magn. Reson.* 216 (2012) 209–212.
- [253] A.J. Rossini, A. Zagdoun, M. Lelli, D. Gajan, F. Rascon, M. Rosay, W.E. Maas, C. Coperet, A. Lesage, L. Emsley, One hundred fold overall sensitivity enhancements for silicon-29 NMR spectroscopy of surfaces by dynamic nuclear polarization with CPMG acquisition, *Chem. Sci.* 3 (2012) 108–115.
- [254] K.N. Hu, H.H. Yu, T.M. Swager, R.G. Griffin, Dynamic nuclear polarization with biradicals, *J. Am. Chem. Soc.* 126 (2004) 10844–10845.
- [255] A. Lesage, M. Lelli, D. Gajan, M.A. Caporini, V. Vitzthum, P. Miéville, J. Alauzun, A. Roussey, C. Thieuleux, A. Mehdi, G. Bodenhausen, C. Copéret, L. Emsley, Surface enhanced NMR spectroscopy by dynamic nuclear polarization, *J. Am. Chem. Soc.* 132 (2010) 15459–15461.
- [256] M. Lelli, D. Gajan, A. Lesage, M.A. Caporini, V. Vitzthum, P. Miéville, F. Héroguel, F. Rascón, A. Roussey, C. Thieuleux, M. Boualleg, L. Veyre, G. Bodenhausen, C. Coperet, L. Emsley, Fast characterization of functionalized silica materials by silicon-29 surface-enhanced NMR spectroscopy using dynamic nuclear polarization, *J. Am. Chem. Soc.* 133 (2011) 2104–2107.
- [257] U. Akbey, B. Altin, A. Linden, S. Ozelik, M. Gradzielski, H. Oschkinat, Dynamic nuclear polarization of spherical nanoparticles, *Phys. Chem. Chem. Phys.* 15 (2013) 20706–20716.
- [258] P.C.A. van der Wel, K.N. Hu, J. Lewandowski, R.G. Griffin, Dynamic nuclear polarization of amyloidogenic peptide nanocrystals: GNNQQNY, a core segment of the yeast prion protein Sup35p, *J. Am. Chem. Soc.* 128 (2006) 10840–10846.
- [259] L.B. Andreas, A.B. Barnes, B. Corzilius, J.J. Chou, E.A. Miller, M. Caporini, M. Rosay, R.G. Griffin, Dynamic nuclear polarization study of inhibitor binding to the M218–60 proton transporter from influenza A, *Biochemistry* 52 (2013) 2774–2782.
- [260] H. Takahashi, B. Viverge, D. Lee, P. Rannou, G. De Paëpe, Towards structure determination of self-assembled peptides using dynamic nuclear polarization enhanced solid-state NMR spectroscopy, *Angew. Chem. Int. Ed.* 52 (2013) 6979–6982.
- [261] P. Fricke, J.P. Demers, S. Becker, A. Lange, Studies on the MxiH protein in T3SS needles using DNP-enhanced ssNMR spectroscopy, *ChemPhysChem* 15 (2014) 57–60.
- [262] A.N. Smith, M.A. Caporini, G.E. Fanucci, J.R. Long, A method for dynamic nuclear polarization enhancement of membrane proteins, *Angew. Chem. Int. Ed.* 54 (2015) 1542–1546.
- [263] S.Y. Liao, M. Lee, T. Wang, I.V. Sergeev, M. Hong, Efficient DNP NMR of membrane proteins: sample preparation protocols, sensitivity, and radical location, *J. Biomol. NMR* 64 (2016) 223–237.
- [264] W.-M. Yau, K.R. Thurber, R. Tycko, Synthesis and evaluation of nitroxide-based oligoradicals for low-temperature dynamic nuclear polarization in solid state NMR, *J. Magn. Reson.* 244 (2014) 98–106.
- [265] Y. Matsuki, T. Maly, O. Ouari, H. Karoui, F. Le Moigne, E. Rizzato, S. Lyubanova, J. Herzfeld, T. Prisner, P. Tordo, R.G. Griffin, Dynamic nuclear polarization with a rigid biradical, *Angew. Chem. Int. Ed.* 48 (2009) 4996–5000.
- [266] E.L. Dane, B. Corzilius, E. Rizzato, P. Stocker, T. Maly, A.A. Smith, R.G. Griffin, O. Ouari, P. Tordo, T.M. Swager, Rigid orthogonal bis-TEMPO biradicals with improved solubility for dynamic nuclear polarization, *J. Org. Chem.* 77 (2012) 1789–1797.
- [267] M.K. Kiesewetter, B. Corzilius, A.A. Smith, R.G. Griffin, T.M. Swager, Dynamic nuclear polarization with a water-soluble rigid biradical, *J. Am. Chem. Soc.* 134 (2012) 4537–4540.
- [268] C. Ysacco, E. Rizzato, M.-A. Virolleaud, H. Karoui, A. Rockenbauer, F. Le Moigne, D. Siri, O. Ouari, R.G. Griffin, P. Tordo, Properties of dinitroxides for use in dynamic nuclear polarization (DNP), *Phys. Chem. Chem. Phys.* 12 (2010) 5841–5845.
- [269] C. Ysacco, H. Karoui, G. Casano, F. Le Moigne, S. Combes, A. Rockenbauer, M. Rosay, W. Maas, O. Ouari, P. Tordo, Dinitroxides for solid state dynamic nuclear polarization, *Appl. Magn. Reson.* 43 (2012) 251–261.
- [270] A. Zagdoun, G. Casano, O. Ouari, G. Lapadula, A.J. Rossini, M. Lelli, M. Baffert, D. Gajan, L. Veyre, W.E. Maas, M. Rosay, R.T. Weber, C. Thieuleux, C. Coperet, A. Lesage, P. Tordo, L. Emsley, A slowly relaxing rigid biradical for efficient dynamic nuclear polarization surface-enhanced NMR spectroscopy: expeditious characterization of functional group manipulation in hybrid materials, *J. Am. Chem. Soc.* 134 (2012) 2284–2291.
- [271] C. Sauvée, M. Rosay, G. Casano, F. Aussenac, R.T. Weber, O. Ouari, P. Tordo, Highly efficient, water-soluble polarizing agents for dynamic nuclear polarization at high frequency, *Angew. Chem. Int. Ed.* 52 (2013) 10858–10861.
- [272] V.K. Michaelis, T.-C. Ong, M.K. Kiesewetter, D.K. Frantz, J.J. Walsh, E. Ravera, C. Luchinat, T.M. Swager, R.G. Griffin, Technical developments in high-field dynamic nuclear polarization, *Isr. J. Chem.* 54 (2014) 207–221.
- [273] P. Gast, D. Mance, E. Zurlò, K.L. Ivanov, M. Baldus, M. Huber, A tailored multifrequency EPR approach to accurately determine the magnetic resonance parameters of dynamic nuclear polarization agents: application to AMUPol, *Phys. Chem. Chem. Phys.* 19 (2017) 3777–3781.

- [274] A. Zagdoun, G. Casano, O. Ouari, M. Schwarzwaldler, A.J. Rossini, F. Aussenac, M. Yulikov, G. Jeschke, C. Coperet, A. Lesage, P. Tordo, L. Emsley, Large molecular weight nitroxide biradicals providing efficient dynamic nuclear polarization at temperatures up to 200 K, *J. Am. Chem. Soc.* 135 (2013) 12790–12797.
- [275] C. Sauvee, G. Casano, S. Abel, A. Rockenbauer, D. Akhmetzyanov, H. Karoui, D. Siri, F. Aussenac, W. Maas, R.T. Weber, T. Prisner, M. Rosay, P. Tordo, O. Ouari, Tailoring of polarizing agents in the bTurea series for cross-effect dynamic nuclear polarization in aqueous media, *Chem. – Eur. J.* 22 (2016) 5598–5606.
- [276] D.J. Kubicki, G. Casano, M. Schwarzwaldler, S. Abel, C. Sauvee, K. Ganesan, M. Yulikov, A.J. Rossini, G. Jeschke, C. Coperet, A. Lesage, P. Tordo, O. Ouari, L. Emsley, Rational design of dinitroxide biradicals for efficient cross-effect dynamic nuclear polarization, *Chem. Sci.* 7 (2016) 550–558.
- [277] A.P. Jagtap, M.-A. Geiger, D. Stoppler, M. Orwick-Rydmark, H. Oschkinat, S.T. Sigurdsson, bcTol: a highly water-soluble biradical for efficient dynamic nuclear polarization of biomolecules, *Chem. Commun.* 52 (2016) 7020–7023.
- [278] J. Mao, D. Akhmetzyanov, O. Ouari, V. Denysenkov, B. Corzilius, J. Plackmeyer, P. Tordo, T.F. Prisner, C. Glaubitz, Host-guest complexes as water-soluble high-performance DNP polarizing agents, *J. Am. Chem. Soc.* 135 (2013) 19275–19281.
- [279] M.K. Kiesewetter, V.K. Michaelis, J.J. Walsh, R.G. Griffin, T.M. Swager, High field dynamic nuclear polarization NMR with surfactant sheltered biradicals, *J. Phys. Chem. B* 118 (2014) 1825–1830.
- [280] M. Lelli, A.J. Rossini, G. Casano, O. Ouari, P. Tordo, A. Lesage, L. Emsley, Hydrophobic radicals embedded in neutral surfactants for dynamic nuclear polarization of aqueous environments at 9.4 Tesla, *Chem. Commun.* 50 (2014) 10198–10201.
- [281] T.-C. Ong, M.L. Mak-Jurkuskas, J.J. Walsh, V.K. Michaelis, B. Corzilius, A.A. Smith, A.M. Clausen, J.C. Cheetham, T.M. Swager, R.G. Griffin, Solvent-free dynamic nuclear polarization of amorphous and crystalline ortho-terphenyl, *J. Phys. Chem. B* 117 (2013) 3040–3046.
- [282] K.N. Hu, V.S. Bajaj, M. Rosay, R.G. Griffin, High-frequency dynamic nuclear polarization using mixtures of TEMPO and trityl radicals, *J. Chem. Phys.* 126 (2007) 044512.
- [283] G. Mathies, M.A. Caporini, V.K. Michaelis, Y. Liu, K.-N. Hu, D. Mance, J.L. Zweier, M. Rosay, M. Baldus, R.G. Griffin, Efficient dynamic nuclear polarization at 800 MHz/527 GHz with trityl-nitroxide biradicals, *Angew. Chem. Int. Ed.* 54 (2015) 11770–11774.
- [284] E.L. Dane, T. Maly, G.T. Debelouchina, R.G. Griffin, T.M. Swager, Synthesis of a BDPA-TEMPO Biradical, *Org. Lett.* 11 (2009) 1871–1874.
- [285] N.S. Garif'yanov, B.M. Koz'yev, V.N. Fedotov, Width of the EPR line of liquid solutions of ethylene glycol complexes for even and odd chromium isotopes, *Dokl. Phys.* 13 (1968) 107.
- [286] H. Glättli, M. Odehnal, J. Ezratty, A. Malinovski, A. Abragam, Polarisation dynamique des protons dans le glycol ethylique, *Phys. Lett. A* 29 (1969) 250–251.
- [287] A.P. Stepanov, V.N. Fedotov, V.I. Baldin, N.B. Yunosov, Dynamic polarization of protons in Cr(V) and Mo(V) complex compound solutions in weak magnetic fields, *Dokl. Akad. Nauk SSSR* 194 (1970) 871.
- [288] M. Borghini, T.O. Niinikoski, F. Udo, P. Weymuth, Dynamic polarization and relaxation of protons in 1,6-hexanediol and 1,8-octanediol: a feasibility study for a frozen spin polarized target, *Nucl. Instrum. Methods* 105 (1972) 215–220.
- [289] W. De Boer, High proton polarization in 1,2-propanediol at <sup>3</sup>He temperatures, *Nucl. Instrum. Methods* 107 (1973) 99–104.
- [290] J. Svoboda, Dynamic polarization and relaxation of protons in the glycerol:Cr (V) complex, *J. Phys. C: Solid State Phys.* 7 (1974) L144.
- [291] A. Abragam, B. Bleaney, *Electron Paramagnetic Resonance of Transition Metal Ions*, Oxford University Press, Oxford, 1970.
- [292] K.D. Bowers, J. Owen, Paramagnetic resonance II, *Rep. Prog. Phys.* 18 (1955) 304–375.
- [293] R.H. Ruby, H. Benoit, C.D. Jeffries, Paramagnetic resonance below 1°K: spin-lattice relaxation of Ce<sup>3+</sup> and Nd<sup>3+</sup> in lanthanum magnesium nitrate, *Phys. Rev.* 127 (1962) 51–56.
- [294] A.M. Raitisimring, A.V. Astashkin, O.G. Poluektov, P. Caravan, High-field pulsed EPR and ENDOR of Gd<sup>3+</sup> complexes in glassy solutions, *Appl. Magn. Reson.* 28 (2005) 281–295.
- [295] M. Benmelouka, J. Van Tol, A. Borel, M. Port, L. Helm, L.C. Brunel, A.E. Merbach, A high-frequency EPR study of frozen solutions of Gd-III complexes: straightforward determination of the zero-field splitting parameters and simulation of the NMRD profiles, *J. Am. Chem. Soc.* 128 (2006) 7807–7816.
- [296] M. Qi, A. Groß, G. Jeschke, A. Godt, M. Drescher, Gd(III)-PyMTA label is suitable for in-cell EPR, *J. Am. Chem. Soc.* 136 (2014) 15366–15378.
- [297] A. Martorana, G. Bellapadrona, A. Feintuch, E. Di Gregorio, S. Aime, D. Goldfarb, Probing protein conformation in cells by EPR distance measurements using Gd<sup>3+</sup> spin labeling, *J. Am. Chem. Soc.* 136 (2014) 13458–13465.
- [298] H. Kamimura, Anisotropic spin-orbit coupling of d<sup>3</sup> and d<sup>8</sup> solutes in corundum, *Phys. Rev.* 128 (1962) 1077–1084.
- [299] S. Sugano, Y. Tanabe, Absorption spectra of Cr<sup>3+</sup> in Al<sub>2</sub>O<sub>3</sub> part A. Theoretical studies of the absorption bands and lines, *J. Phys. Soc. Jpn.* 13 (1958) 880–899.
- [300] S. Sugano, I. Tsujikawa, Absorption spectra of Cr<sup>3+</sup> in Al<sub>2</sub>O<sub>3</sub> part B. Experimental studies of the zeeman effect and other properties of the line spectra, *J. Phys. Soc. Jpn.* 13 (1958) 899–910.
- [301] H. Klein, U. Scherz, M. Schulz, H. Setyono, K. Wiszniewski, Temperature dependence of the EPR spectrum of ruby, *Z. Phys. B* 28 (1977) 149–157.
- [302] B. Corzilius, V.K. Michaelis, S.A. Penzel, E. Ravera, A.A. Smith, C. Luchinat, R.G. Griffin, Dynamic nuclear polarization of <sup>1</sup>H, <sup>13</sup>C, and <sup>59</sup>Co in a tris (ethylenediamine)cobalt(III) crystalline lattice doped with Cr(III), *J. Am. Chem. Soc.* 136 (2014) 11716–11727.
- [303] B.R. McGarvey, Spin Hamiltonian for Cr III complexes. Calculation from crystal field and molecular orbital models and ESR determination for some ethylenediammine complexes, *J. Chem. Phys.* 41 (1964) 3743–3758.
- [304] R.D. Shannon, Revised effective ionic radii and systematic studies of interatomic distances in halides and chalcogenides, *Acta Crystallogr. Sect. A* 32 (1976) 751–767.
- [305] R.R. Ernst, G. Bodenhausen, A. Wokaun, *Principles of Nuclear Magnetic Resonance in One and Two Dimensions*, Oxford University Press, Oxford, 1987.
- [306] A.J. Perez Linde, S. Chinthalapalli, D. Carnevale, G. Bodenhausen, Rotation-induced recovery and bleaching in magnetic resonance, *Phys. Chem. Chem. Phys.* 17 (2015) 6415–6422.
- [307] T. Kobayashi, O. Lafon, A.S. Lilly Thankamony, I.I. Slowing, K. Kandel, D. Carnevale, V. Vitzthum, H. Vezin, J.-P. Amoureux, G. Bodenhausen, M. Pruski, Analysis of sensitivity enhancement by dynamic nuclear polarization in solid-state NMR: a case study of functionalized mesoporous materials, *Phys. Chem. Chem. Phys.* 15 (2013) 5553–5562.
- [308] H. Takahashi, C. Fernández-de-Alba, D. Lee, V. Maurel, S. Gambarelli, M. Bardet, S. Hediger, A.-L. Barra, G. De Paëpe, Optimization of an absolute sensitivity in a glassy matrix during DNP-enhanced multidimensional solid-state NMR experiments, *J. Magn. Reson.* 239 (2014) 91–99.
- [309] D. Mance, P. Gast, M. Huber, M. Baldus, K.L. Ivanov, The magnetic field dependence of cross-effect dynamic nuclear polarization under magic angle spinning, *J. Chem. Phys.* 142 (2015) 234201.
- [310] G. Mathies, S. Jain, M. Reese, R.G. Griffin, Pulsed dynamic nuclear polarization with trityl radicals, *J. Phys. Chem. Lett.* 7 (2016) 111–116.
- [311] P. Fricke, D. Mance, V. Chevelkov, K. Giller, S. Becker, M. Baldus, A. Lange, High resolution observed in 800 MHz DNP spectra of extremely rigid type III secretion needles, *J. Biomol. NMR* 65 (2016) 121–126.
- [312] K.L. Ngai, S. Capaccioli, N. Shinyashiki, The protein “glass” transition and the role of the solvent, *J. Phys. Chem. B* 112 (2008) 3826–3832.
- [313] E.J. Koers, E.A.W. van der Cruysen, M. Rosay, M. Weingarth, A. Prokofyev, C. Sauvé, O. Ouari, J. van der Zwan, O. Pongs, P. Tordo, W.E. Maas, M. Baldus, NMR-based structural biology enhanced by dynamic nuclear polarization at high magnetic field, *J. Biomol. NMR* 60 (2014) 157–168.
- [314] M.M. Maricq, J.S. Waugh, NMR in rotating solids, *J. Chem. Phys.* 70 (1979) 3300–3316.
- [315] J.-M. Lopez del Amo, D. Schneider, A. Loquet, A. Lange, B. Reif, Cryogenic solid state NMR studies of fibrils of the Alzheimer's disease amyloid- $\beta$  peptide: perspectives for DNP, *J. Biomol. NMR* 56 (2013) 359–363.
- [316] A. Kubo, C.A. McDowell, Spectral spin diffusion in polycrystalline solids under magic-angle spinning, *J. Chem. Soc., Faraday Trans. 1* 84 (1988) 3713–3730.
- [317] Z. Jia, L. Zhang, Q. Chen, E.W. Hansen, Proton spin diffusion in polyethylene as a function of magic-angle spinning rate. A phenomenological approach, *J. Phys. Chem. A* 112 (2008) 1228–1233.
- [318] J.-N. Dumez, L. Emsley, A master-equation approach to the description of proton-driven spin diffusion from crystal geometry using simulated zero-quantum lineshapes, *Phys. Chem. Chem. Phys.* 13 (2011) 7363–7370.
- [319] J.J. Wittmann, L. Hendriks, B.H. Meier, M. Ernst, Controlling spin diffusion by tailored rf-irradiation schemes, *Chem. Phys. Lett.* 608 (2014) 60–67.
- [320] D.J. Kubicki, A.J. Rossini, A. Pura, A. Zagdoun, O. Ouari, P. Tordo, F. Engelke, A. Lesage, L. Emsley, Amplifying dynamic nuclear polarization of frozen solutions by incorporating dielectric particles, *J. Am. Chem. Soc.* 136 (2014) 15711–15718.
- [321] P. Miéville, V. Vitzthum, M.A. Caporini, S. Jannin, S. Gerber-Lemaire, G. Bodenhausen, A spinning thermometer to monitor microwave heating and glass transitions in dynamic nuclear polarization, *Magn. Reson. Chem.* 49 (2011) 689–692.
- [322] K.R. Thurber, A. Potapov, W.-M. Yau, R. Tycko, Solid state nuclear magnetic resonance with magic-angle spinning and dynamic nuclear polarization below 25 K, *J. Magn. Reson.* 226 (2013) 100–106.
- [323] A.B. Siemer, K.-Y. Huang, A. McDermott, Protein linewidth and solvent dynamics in frozen solution NMR, *PLoS One* 7 (2012) e47242.
- [324] A.H. Linden, W.T. Franks, U. Akbey, S. Lange, B.J. van Rossum, H. Oschkinat, Cryogenic temperature effects and resolution upon slow cooling of protein preparations in solid state NMR, *J. Biomol. NMR* 51 (2011) 283–292.
- [325] Ü. Akbey, W.T. Franks, A. Linden, S. Lange, R.G. Griffin, B.J. van Rossum, H. Oschkinat, Dynamic nuclear polarization of deuterated proteins, *Angew. Chem. Int. Ed.* 49 (2010) 7803–7806.
- [326] J. Mao, N.N. Do, F. Scholz, L. Reggie, M. Mehler, A. Lakatos, Y.S. Ong, S.J. Ullrich, L.J. Brown, R.C. Brown, J. Becker-Baldus, J. Wachtveitl, C. Glaubitz, Structural basis of the green-blue color switching in proteorhodopsin as determined by NMR spectroscopy, *J. Am. Chem. Soc.* 136 (2014) 17578–17590.
- [327] J. Maciejko, M. Mehler, J. Kaur, T. Lieblein, N. Morgner, O. Ouari, P. Tordo, J. Becker-Baldus, C. Glaubitz, Visualizing specific cross-protomer interactions in the homo-oligomeric membrane protein proteorhodopsin by dynamic-nuclear-polarization-enhanced solid-state NMR, *J. Am. Chem. Soc.* 137 (2015) 9032–9043.

- [328] T. Bauer, C. Dotta, L. Balacescu, J. Gath, A. Hunkeler, A. Bockmann, B.H. Meier, Line-broadening in low-temperature solid-state NMR spectra of fibrils, *J. Biomol. NMR* 67 (2017) 51–61.
- [329] A.B. Barnes, B. Corzilius, M.L. Mak-Jurkauskas, L.B. Andreas, V.S. Bajaj, Y. Matsuki, M.L. Belenky, J. Lugtenburg, J.R. Sirigiri, R.J. Temkin, J. Herzfeld, R.G. Griffin, Resolution and polarization distribution in cryogenic DNP/MAS experiments, *Phys. Chem. Chem. Phys.* 12 (2010) 5861–5867.
- [330] G.T. Debelouchina, M.J. Bayro, P.C.A. van der Wel, M.A. Caporini, A.B. Barnes, M. Rosay, W.E. Maas, R.G. Griffin, Dynamic nuclear polarization-enhanced solid-state NMR spectroscopy of GNNQQNY nanocrystals and amyloid fibrils, *Phys. Chem. Chem. Phys.* 12 (2010) 5911–5919.
- [331] M.J. Bayro, G.T. Debelouchina, M.T. Eddy, N.R. Birkett, C.E. MacPhee, M. Rosay, W.E. Maas, C.M. Dobson, R.G. Griffin, Intermolecular structure determination of amyloid fibrils with magic-angle spinning and dynamic nuclear polarization NMR, *J. Am. Chem. Soc.* 133 (2011) 13967–13974.
- [332] O.B. Peersen, S.O. Smith, Rotational resonance NMR of biological membranes, *Concepts Magn. Reson.* 5 (1993) 303–317.
- [333] Q.Z. Ni, E. Markhasin, T.V. Can, B. Corzilius, K.O. Tan, A.B. Barnes, E. Daviso, Y. Su, J. Herzfeld, R.G. Griffin, Peptide and protein dynamics and low-temperature/DNP magic angle spinning NMR, *J. Phys. Chem. B* 121 (2017) 4997–5006.
- [334] A. Baudot, L. Alger, P. Boutron, Glass-forming tendency in the system water-dimethyl sulfoxide, *Cryobiology* 40 (2000) 151–158.
- [335] M.M. Rosay, Sensitivity Enhanced Nuclear Magnetic Resonance of Biological Solids, Chemistry, Massachusetts Institute of Technology, Cambridge, MA, 2001.
- [336] A. Zagdoun, A.J. Rossini, D. Gajan, A. Bourdolle, O. Ouari, M. Rosay, W.E. Maas, P. Tordo, M. Lelli, L. Emsley, A. Lesage, C. Coperet, Non-aqueous solvents for DNP surface enhanced NMR spectroscopy, *Chem. Commun.* 48 (2012) 654–656.
- [337] E. Ravera, B. Corzilius, V.K. Michaelis, C. Luchinat, R.G. Griffin, I. Bertini, DNP-Enhanced MAS NMR of bovine serum albumin sediments and solutions, *J. Phys. Chem. B* 118 (2014) 2957–2965.
- [338] E. Ravera, B. Corzilius, V.K. Michaelis, C. Rosa, R.G. Griffin, C. Luchinat, I. Bertini, Dynamic nuclear polarization of sedimented solutes, *J. Am. Chem. Soc.* 135 (2013) 1641–1644.
- [339] D. Le, G. Casano, T.N.T. Phan, F. Ziarelli, O. Ouari, F. Aussenac, P. Thureau, G. Mollica, D. Gimes, P. Tordo, S. Viel, Optimizing sample preparation methods for dynamic nuclear polarization solid-state NMR of synthetic polymers, *Macromolecules* 47 (2014) 3909–3916.
- [340] E. Elisei, M. Filibian, P. Carretta, S.C. Serra, F. Tedoldi, J.F. Willart, M. Descamps, A. Cesaro, Dynamic nuclear polarization of a glassy matrix prepared by solid state mechanochemical amorphization of crystalline substances, *Chem. Commun.* 51 (2015) 2080–2083.
- [341] V. Vitzthum, F. Borcard, S. Jannin, M. Morin, P. Miéville, M.A. Caporini, A. Sienkiewicz, S. Gerber-Lemaire, G. Bodenhausen, Fractional spin-labeling of polymers for enhancing NMR sensitivity by solvent-free dynamic nuclear polarization, *ChemPhysChem* 12 (2011) 2929–2932.
- [342] H. Takahashi, S. Hediger, G. De Paëpe, Matrix-free dynamic nuclear polarization enables solid-state NMR  $^{13}\text{C}$ - $^{13}\text{C}$  correlation spectroscopy of proteins at natural isotopic abundance, *Chem. Commun.* 49 (2013) 9479–9481.
- [343] C. Fernández-de-Alba, H. Takahashi, A. Richard, Y. Chenavier, L. Dubois, V. Maurel, D. Lee, S. Hediger, G. De Paëpe, Matrix-free DNP-enhanced NMR spectroscopy of liposomes using a lipid-anchored biradical, *Chem. – Eur. J.* 21 (2015) 4512–4517.
- [344] D. Gajan, M. Schwarzwälder, M.P. Conley, W.R. Grüning, A.J. Rossini, A. Zagdoun, M. Lelli, M. Yulikov, G. Jeschke, C. Sauvée, O. Ouari, P. Tordo, L. Veyre, A. Lesage, C. Thieuleux, L. Emsley, C. Copéret, Solid-phase polarization matrices for dynamic nuclear polarization from homogeneously distributed radicals in mesostructured hybrid silica materials, *J. Am. Chem. Soc.* 135 (2013) 15459–15466.
- [345] H. Takahashi, D. Lee, L. Dubois, M. Bardet, S. Hediger, G. De Paëpe, Rapid natural-abundance 2D  $^{13}\text{C}$ - $^{13}\text{C}$  correlation spectroscopy using dynamic nuclear polarization enhanced solid-state NMR and matrix-free sample preparation, *Angew. Chem. Int. Ed.* 51 (2012) 11766–11769.
- [346] M.A. Voinov, D.B. Good, M.E. Ward, S. Millikisyan, A. Marek, M.A. Caporini, M. Rosay, R.A. Munro, M. Ljumovic, L.S. Brown, V. Ladizhansky, A.I. Smirnov, Cysteine-specific labeling of proteins with a nitroxide biradical for dynamic nuclear polarization NMR, *J. Phys. Chem. B* 119 (2015) 10180–10190.
- [347] E.A.W. van der Crujisen, E.J. Koers, C. Sauvée, R.E. Hulse, M. Weingarth, O. Ouari, E. Perozo, P. Tordo, M. Balduis, Biomolecular DNP-supported NMR spectroscopy using site-directed spin labeling, *Chem. – Eur. J.* 21 (2015) 12971–12977.
- [348] B.J. Wylie, B.G. Dzikowski, S. Pawsey, M. Caporini, M. Rosay, J.H. Freed, A.E. McDermott, Dynamic nuclear polarization of membrane proteins: covalently bound spin-labels at protein–protein interfaces, *J. Biomol. NMR* 61 (2015) 361–367.
- [349] T. Viennet, A. Viegas, A. Kuepper, S. Arens, V. Gelev, O. Petrov, T.N. Grossmann, H. Heise, M. Etkorn, Selective protein hyperpolarization in cell lysates using targeted dynamic nuclear polarization, *Angew. Chem. Int. Ed.* 55 (2016) 10746–10750.
- [350] R. Rogawski, I.V. Sergeev, Y. Li, M.F. Ottaviani, V. Cornish, A.E. McDermott, Dynamic nuclear polarization signal enhancement with high-affinity biradical tags, *J. Phys. Chem. B* 121 (2017) 1169–1175.
- [351] A. Zagdoun, A.J. Rossini, M.P. Conley, W.R. Grüning, M. Schwarzwälder, M. Lelli, W.T. Franks, H. Oschkinat, C. Copéret, L. Emsley, A. Lesage, Improved dynamic nuclear polarization surface-enhanced NMR spectroscopy through controlled incorporation of deuterated functional groups, *Angew. Chem. Int. Ed.* 52 (2013) 1222–1225.
- [352] F.A. Perras, R.R. Reing, I.I. Slowing, A.D. Sadow, M. Pruski, Effects of biradical deuteration on the performance of DNP: towards better performing polarizing agents, *Phys. Chem. Chem. Phys.* 18 (2016) 65–69.
- [353] A.J. Rossini, J. Schlagnitweit, A. Lesage, L. Emsley, High-resolution NMR of hydrogen in organic solids by DNP enhanced natural abundance deuterium spectroscopy, *J. Magn. Reson.* 259 (2015) 192–198.
- [354] Ü. Akbey, S. Lange, W.T. Franks, R. Linsler, K. Rehbein, A. Diehl, B.-J. van Rossum, B. Reif, H. Oschkinat, Optimum levels of exchangeable protons in perdeuterated proteins for proton detection in MAS solid-state NMR spectroscopy, *J. Biomol. NMR* 46 (2010) 67–73.
- [355] M. Nagaraj, T.W. Franks, S. Saeidpour, T. Schubeis, H. Oschkinat, C. Ritter, B.-J. van Rossum, Surface binding of TOTAPOL assists structural investigations of amyloid fibrils by dynamic nuclear polarization NMR spectroscopy, *ChemBioChem* 17 (2016) 1308–1311.
- [356] O. Lafon, A.S.L. Thankamony, T. Kobayashi, D. Carnevale, V. Vitzthum, Slowing II, K. Kandel, Vezin H., J.P. Amoureux, G. Bodenhausen, M. Pruski, Mesoporous silica nanoparticles loaded with surfactant: low temperature magic angle spinning C-13 and Si-29 NMR enhanced by dynamic nuclear polarization, *J. Phys. Chem. C* 117 (2013) 1375–1382.
- [357] A. Lund, M.F. Hsieh, T.A. Siaw, S.I. Han, Direct dynamic nuclear polarization targeting catalytically active Al-27 sites, *Phys. Chem. Chem. Phys.* 17 (2015) 25449–25454.
- [358] A.H. Linden, S. Lange, W.T. Franks, Ü. Akbey, E. Specker, B.-J. van Rossum, H. Oschkinat, Neurotoxin II bound to acetylcholine receptors in native membranes studied by dynamic nuclear polarization NMR, *J. Am. Chem. Soc.* 133 (2011) 19266–19269.
- [359] R.A. Wind, F.E. Anthonio, M.J. Duijvestijn, J. Smidt, J. Trommel, G.M.C. de Vette, Experimental setup for enhanced  $^{13}\text{C}$  NMR spectroscopy in solids using dynamic nuclear polarization, *J. Magn. Reson.* 52 (1983) 424–434.
- [360] R.A. Wind, M.J. Duijvestijn, J. Vriend, Structural defects in undoped trans-polyacetylene, before and after air oxidation, studied by DNP-enhanced  $^{13}\text{C}$  NMR, *Solid State Commun.* 56 (1985) 713–716.
- [361] R.A. Wind, N. Zumbulyadis, R.H. Young, Y. Hung, L. Li, R.H.D. Nuttall, G. Maciel, EPR and  $^1\text{H}$  and  $^{13}\text{C}$  dynamic nuclear polarization studies of a molecularly doped polymer: bisphenol A polycarbonate doped with trianisylamine and trianisylammonium perchlorate, *Solid State Nucl. Magn. Reson.* 1 (1992) 55–65.
- [362] R.A. Wind, M.J. Duijvestijn, C. van der Lugt, J. Smidt, H. Vriend, An investigation of coal by means of e.s.r.,  $^1\text{H}$  n.m.r.,  $^{13}\text{C}$  n.m.r. and dynamic nuclear polarization, *Fuel* 66 (1987) 876–885.
- [363] H. Lock, R.A. Wind, G.E. Maciel, N. Zumbulyadis,  $^{29}\text{Si}$  dynamic nuclear polarization of dehydrogenated amorphous silicon, *Solid State Commun.* 64 (1987) 41–44.
- [364] R.A. Wind, H. Lock, M. Mehring,  $^{13}\text{C}$  knight shift saturation and  $^1\text{H}$  dynamic nuclear polarization in a polycrystalline sample of the organic conductor (fluoranthenyl)2PF<sub>6</sub>, *Chem. Phys. Lett.* 141 (1987) 283–288.
- [365] R.H. Lewis, R.A. Wind, G.E. Maciel, Investigation of cured hydridopolysilazane-derived ceramic fibers via dynamic nuclear polarization, *J. Mater. Res.* 8 (1993) 649–654.
- [366] H. Lock, R.A. Wind, G.E. Maciel, C.E. Johnson, A study of  $^{13}\text{C}$ -enriched chemical vapor deposited diamond film by means of  $^{13}\text{C}$  nuclear magnetic resonance, electron paramagnetic resonance, and dynamic nuclear polarization, *J. Chem. Phys.* 99 (1993) 3363–3373.
- [367] M.J. Duijvestijn, R.A. Wind, J. Smidt, A quantitative investigation of the dynamic nuclear polarization effect by fixed paramagnetic centra of abundant and rare spins in solids at room temperature, *Physica B+C* 138 (1986) 147–170.
- [368] M. Afeworki, R.A. McKay, J. Schaefer, Dynamic nuclear polarization enhanced nuclear magnetic resonance of polymer-blend interfaces, *Mater. Sci. Eng., A* 162 (1993) 221–228.
- [369] M. Afeworki, S. Vega, J. Schaefer, Direct electron-to-carbon polarization transfer in homogeneously doped polycarbonates, *Macromolecules* 25 (1992) 4100–4105.
- [370] M. Afeworki, J. Schaefer, Molecular dynamics of polycarbonate chains at the interface of polycarbonate/polystyrene heterogeneous blends, *Macromolecules* 25 (1992) 4097–4099.
- [371] J. Zhou, B. Yang, J. Hu, H. Hu, L. Li, J. Qiu, F. Zeng, C. Ye, Investigation of a naphthalene pitch by high-resolution solid-state dynamic nuclear polarization, *Solid State Nucl. Magn. Reson.* 6 (1996) 127–133.
- [372] M. Rosay, A.-C. Zeri, N.S. Astrof, S.J. Opella, J. Herzfeld, R.G. Griffin, Sensitivity-enhanced NMR of biological solids: dynamic nuclear polarization of Y21M fd bacteriophage and purple membrane, *J. Am. Chem. Soc.* 123 (2001) 1010–1011.
- [373] M. Rosay, J.C. Lansing, K.C. Haddad, W.W. Bachovchin, J. Herzfeld, R.J. Temkin, R.G. Griffin, High-frequency dynamic nuclear polarization in MAS spectra of membrane and soluble proteins, *J. Am. Chem. Soc.* 125 (2003) 13626–13627.
- [374] K. Märker, S. Paul, C. Fernández-de-Alba, D. Lee, J.-M. Mouesca, S. Hediger, G. De Paëpe, Welcoming natural isotopic abundance in solid-state NMR: probing  $\pi$ -stacking and supramolecular structure of organic nanoassemblies using DNP, *Chem. Sci.* 8 (2017) 974–987.

- [375] Y. Geiger, H.E. Gottlieb, U. Akbey, H. Oschkinat, G. Goobes, Studying the conformation of a silaffin-derived pentylsine peptide embedded in biosilica using solution and dynamic nuclear polarization magic-angle spinning NMR, *J. Am. Chem. Soc.* 138 (2016) 5561–5567.
- [376] M.J. Bayro, M. Huber, R. Ramachandran, T.C. Davenport, B.H. Meier, M. Ernst, R.G. Griffin, Dipolar truncation in magic-angle spinning NMR recoupling experiments, *J. Chem. Phys.* 130 (2009) 114506.
- [377] G.T. Debelouchina, M.J. Bayro, A.W. Fitzpatrick, V. Ladizhansky, M.T. Colvin, M.A. Caporini, C.P. Jaroniec, V.S. Bajaj, M. Rosay, C.E. MacPhee, M. Vendruscolo, W.E. Maas, C.M. Dobson, R.G. Griffin, Higher order amyloid fibril structure by MAS NMR and DNP spectroscopy, *J. Am. Chem. Soc.* 135 (2013) 19237–19247.
- [378] A. Potapov, W.-M. Yau, R. Ghirlando, K.R. Thurber, R. Tycko, Successive stages of amyloid- $\beta$  self-assembly characterized by solid-state nuclear magnetic resonance with dynamic nuclear polarization, *J. Am. Chem. Soc.* 137 (2015) 8294–8307.
- [379] F. Weirich, L. Gremer, E.A. Mirecka, S. Schiefer, W. Hoyer, H. Heise, Structural characterization of fibrils from recombinant human islet amyloid polypeptide by solid-state NMR: the central FGAILS segment is part of the  $\beta$ -sheet core, *PLoS One* 11 (2016) e0161243.
- [380] M. Mehler, F. Scholz, Sandra J. Ullrich, J. Mao, M. Braun, Lynda J. Brown, Richard C.D. Brown, Sarah A. Fiedler, J. Becker-Baldus, J. Wachtveitl, C. Glaubitz, The EF Loop in green proteorhodopsin affects conformation and photocycle dynamics, *Biophys. J.* 105 (2013) 385–397.
- [381] Y.S. Ong, A. Lakatos, J. Becker-Baldus, K.M. Pos, C. Glaubitz, Detecting substrates bound to the secondary multidrug efflux pump EmrE by DNP-enhanced solid-state NMR, *J. Am. Chem. Soc.* 135 (2013) 15754–15762.
- [382] M. Mehler, C.E. Eckert, A. Busche, J. Kulhei, J. Michaelis, J. Becker-Baldus, J. Wachtveitl, V. Dötsch, C. Glaubitz, Assembling a correctly folded and functional heptahelical membrane protein by protein trans-splicing, *J. Biol. Chem.* 290 (2015) 27712–27722.
- [383] E.J. Koers, M.P. López-Deber, M. Weingarth, D. Nand, D.T. Hickman, D. Mlaki Ndao, P. Reis, A. Granet, A. Pfeifer, A. Muhs, M. Baldus, Dynamic nuclear polarization NMR spectroscopy: revealing multiple conformations in lipid-anchored peptide vaccines, *Angew. Chem. Int. Ed.* 52 (2013) 10905–10908.
- [384] H. Kaur, A. Lakatos, R. Spadaccini, R. Vogel, C. Hoffmann, J. Becker-Baldus, O. Ouari, P. Tordo, H. McHaourab, C. Glaubitz, The ABC exporter MsbA probed by solid state NMR – challenges and opportunities, *Biol. Chem.* 396 (2015) 1135–1149.
- [385] E. Lehnert, J. Mao, A.R. Mehdipour, G. Hummer, R. Abele, C. Glaubitz, R. Tampé, Antigenic peptide recognition on the human ABC transporter TAP resolved by DNP-enhanced solid-state NMR spectroscopy, *J. Am. Chem. Soc.* 138 (2016) 13967–13974.
- [386] D. Stöppler, C. Song, B.-J. van Rossum, M.-A. Geiger, C. Lang, M.-A. Mroginski, A.P. Jagtap, S.T. Sigurdsson, J. Matysik, J. Hughes, H. Oschkinat, Dynamic nuclear polarization provides new insights into chromophore structure in phytochrome photoreceptors, *Angew. Chem. Int. Ed.* 55 (2016) 16017–16020.
- [387] S. Lange, W.T. Franks, N. Rajagopalan, K. Döring, M.A. Geiger, A. Linden, B.-J. van Rossum, G. Kramer, B. Bukau, H. Oschkinat, Structural analysis of a signal peptide inside the ribosome tunnel by DNP MAS NMR, *Sci. Adv.* 2 (2016) e1600379.
- [388] I. Gelis, V. Vitzthum, N. Dhimole, M.A. Caporini, A. Schedlbauer, D. Carnevale, S.R. Connell, P. Fucini, G. Bodenhausen, Solid-state NMR enhanced by dynamic nuclear polarization as a novel tool for ribosome structural biology, *J. Biomol. NMR* 56 (2013) 85–93.
- [389] M. Kaplan, S. Narasimhan, C. de Heus, D. Mance, S. van Doorn, K. Houben, D. Popov-Celeketić, R. Damman, E.A. Katrukha, P. Jain, W.J.C. Geerts, A.J.R. Heck, G.E. Folkers, L.C. Kapitein, S. Lemeer, P.M.P. van Bergen en Henegouwen, M. Baldus, EGFR dynamics change during activation in native membranes as revealed by NMR, *Cell* 167 (2016) 1241–1251.
- [390] I.V. Sergeev, L.A. Day, A. Goldbourt, A.E. McDermott, Chemical shifts for the unusual DNA structure in Pfl bacteriophage from dynamic-nuclear-polarization-enhanced solid-state NMR spectroscopy, *J. Am. Chem. Soc.* 133 (2012) 20208–20217.
- [391] R. Gupta, M. Lu, G. Hou, M.A. Caporini, M. Rosay, W. Maas, J. Struppe, C. Suiter, J. Ahn, I.J. Byeon, W.T. Franks, M. Orwick-Rydmark, A. Bertarello, H. Oschkinat, A. Lesage, G. Pintacuda, A.M. Gronenborn, T. Polenova, Dynamic nuclear polarization enhanced MAS NMR spectroscopy for structural analysis of HIV-1 protein assemblies, *J. Phys. Chem. B* 120 (2016) 329–339.
- [392] T. Jacso, W.T. Franks, H. Rose, U. Fink, J. Broecker, S. Keller, H. Oschkinat, B. Reif, Characterization of membrane proteins in isolated native cellular membranes by dynamic nuclear polarization solid-state NMR spectroscopy without purification and reconstitution, *Angew. Chem. Int. Ed.* 51 (2012) 432–435.
- [393] M. Renault, S. Pawsey, M.P. Bos, E.J. Koers, D. Nand, R. Tommassen-van Boxtel, M. Rosay, J. Tommassen, W.E. Maas, M. Baldus, Solid-state NMR spectroscopy on cellular preparations enhanced by dynamic nuclear polarization, *Angew. Chem. Int. Ed.* 51 (2012) 2998–3001.
- [394] M. Kaplan, A. Cukkemane, G.C.P. van Zundert, S. Narasimhan, M. Daniels, D. Mance, G. Waksman, A.M.J.J. Bonvin, R. Fronzes, G.E. Folkers, M. Baldus, Probing a cell-embedded megadalton protein complex by DNP-supported solid-state NMR, *Nat. Methods* 12 (2015) 649–652.
- [395] T. Wang, Y.B. Park, M.A. Caporini, M. Rosay, L. Zhong, D.J. Cosgrove, M. Hong, Sensitivity-enhanced solid-state NMR detection of expansin's target in plant cell walls, *Proc. Natl. Acad. Sci. U.S.A.* 110 (2013) 16444–16449.
- [396] E. Ravera, V.K. Michaelis, T.-C. Ong, E.G. Keeler, T. Martelli, M. Fragai, R.G. Griffin, C. Luchinat, Biosilica-entrapped enzymes studied by using dynamic nuclear-polarization-enhanced high-field NMR spectroscopy, *ChemPhysChem* 16 (2015) 2751–2754.
- [397] A. Jantschke, E. Koers, D. Mance, M. Weingarth, E. Brunner, M. Baldus, Insight into the supramolecular architecture of intact diatom biosilica from DNP-supported solid-state NMR spectroscopy, *Angew. Chem. Int. Ed.* 54 (2015) 15069–15073.
- [398] J.A. Hubbard, L.K. MacLachlan, G.W. King, J.J. Jones, A.P. Fosberry, Nuclear magnetic resonance spectroscopy reveals the functional state of the signalling protein CheY in vivo in *Escherichia coli*, *Mol. Microbiol.* 49 (2003) 1191–1200.
- [399] D.S. Burz, K. Dutta, D. Cowburn, A. Shekhtman, Mapping structural interactions using in-cell NMR spectroscopy (STINT-NMR), *Nat. Meth.* 3 (2006) 91–93.
- [400] M.M. Dedmon, C.N. Patel, G.B. Young, G.J. Pielak, FlgM gains structure in living cells, *Proc. Natl. Acad. Sci. U.S.A.* 99 (2002) 12681–12684.
- [401] L.A. Baker, M. Daniëls, E.A.W. van der Cruisen, G.E. Folkers, M. Baldus, Efficient cellular solid-state NMR of membrane proteins by targeted protein labeling, *J. Biomol. NMR* 62 (2015) 199–208.
- [402] K.K. Frederick, V.K. Michaelis, B. Corzilius, T.C. Ong, A.C. Jacavone, R.G. Griffin, S. Lindquist, Sensitivity-enhanced NMR reveals alterations in protein structure by cellular milieu, *Cell* 163 (2015) 620–628.
- [403] C.P. Jaroniec, Structural studies of proteins by paramagnetic solid-state NMR spectroscopy, *J. Magn. Reson.* 253 (2015) 50–59.
- [404] R.G. Griffin, Spectroscopy: clear signals from surfaces, *Nature* 468 (2010) 381–382.
- [405] Z. Guo, T. Kobayashi, L.-L. Wang, T.W. Goh, C. Xiao, M.A. Caporini, M. Rosay, D. D. Johnson, M. Pruski, W. Huang, Selective host-guest interaction between metal ions and metal-organic frameworks using dynamic nuclear polarization enhanced solid-state NMR spectroscopy, *Chem. – Eur. J.* 20 (2014) 16308–16313.
- [406] T. Gutmann, J. Liu, N. Rothermel, Y. Xu, E. Jaumann, M. Werner, H. Breitzke, S. T. Sigurdsson, G. Buntkowsky, Natural abundance  $^{15}\text{N}$  NMR by dynamic nuclear polarization: fast analysis of binding sites of a novel amine-carboxyl-linked immobilized dirhodium catalyst, *Chem. – Eur. J.* 21 (2015) 3798–3805.
- [407] M. Werner, A. Heil, N. Rothermel, H. Breitzke, P.B. Groszewicz, A.S. Thankamony, T. Gutmann, G. Buntkowsky, Synthesis and solid state NMR characterization of novel peptide/silica hybrid materials, *Solid State Nucl. Magn. Reson.* 72 (2015) 73–78.
- [408] D. Lee, G. Monin, N.T. Duong, I.Z. Lopez, M. Bardet, V. Mareau, L. Gonon, G. De Paëpe, Untangling the condensation network of organosiloxanes on nanoparticles using 2D  $^{29}\text{Si}$ – $^{29}\text{Si}$  solid-state NMR enhanced by dynamic nuclear polarization, *J. Am. Chem. Soc.* 136 (2014) 13781–13788.
- [409] T. Kobayashi, D. Singappuli-Arachchige, Z. Wang, I.I. Slowling, M. Pruski, Spatial distribution of organic functional groups supported on mesoporous silica nanoparticles: a study by conventional and DNP-enhanced  $^{29}\text{Si}$  solid-state NMR, *Phys. Chem. Chem. Phys.* 19 (2017) 1781–1789.
- [410] N. Eedugurala, Z.R. Wang, U. Chaudhary, N. Nelson, K. Kandel, T. Kobayashi, Slowling II, M. Pruski, A.D. Sadow, Mesoporous silica-supported amidozirconium-catalyzed carbonyl hydroboration, *ACS Catal.* 5 (2015) 7399–7414.
- [411] M.P. Conley, R.M. Drost, M. Baffert, D. Gajan, C. Elsevier, W.T. Franks, H. Oschkinat, L. Veyre, A. Zagdoun, A. Rossini, M. Lelli, A. Lesage, G. Casano, O. Ouari, P. Tordo, L. Emsley, C. Copéret, C. Thieuleux, A well-defined Pd hybrid material for the Z-selective semihydrogenation of alkynes characterized at the molecular level by DNP SENS, *Chem. – Eur. J.* 19 (2013) 12234–12238.
- [412] R.P. Sangodkar, B.J. Smith, D. Gajan, A.J. Rossini, L.R. Roberts, G.P. Funkhouser, A. Lesage, L. Emsley, B.F. Chmelka, Influences of dilute organic adsorbates on the hydration of low-surface-area silicates, *J. Am. Chem. Soc.* 137 (2015) 8096–8112.
- [413] W.R. Gruning, A.J. Rossini, A. Zagdoun, D. Gajan, A. Lesage, L. Emsley, C. Copéret, Molecular-level characterization of the structure and the surface chemistry of periodic mesoporous organosilicates using DNP-surface enhanced NMR spectroscopy, *Phys. Chem. Chem. Phys.* 15 (2013) 13270–13274.
- [414] R. Graf, M.R. Hansen, D. Hinderberger, K. Muennemann, H.W. Spiess, Advanced magnetic resonance strategies for the elucidation of nanostructured soft matter, *Phys. Chem. Chem. Phys.* 16 (2014) 9700–9712.
- [415] R.L. Johnson, F.A. Perras, T. Kobayashi, T.J. Schwartz, J.A. Dumesic, B.H. Shanks, M. Pruski, Identifying low-coverage surface species on supported noble metal nanoparticle catalysts by DNP-NMR, *Chem. Commun.* 52 (2016) 1859–1862.
- [416] F.A. Perras, H. Luo, X. Zhang, N.S. Mosier, M. Pruski, M.M. Abu-Omar, Atomic-level structure characterization of biomass pre- and post-lignin treatment by dynamic nuclear polarization-enhanced solid-state NMR, *J. Phys. Chem. A* 121 (2017) 623–630.
- [417] T.C. Ong, W.C. Liao, V. Mougél, D. Gajan, A. Lesage, L. Emsley, C. Copéret, Atomic description of reaction intermediates for supported metathesis catalysts enabled by DNP SENS, *Angew. Chem. Int. Ed.* 55 (2016) 4743–4747.
- [418] L. Zhao, W. Li, A. Plog, Y. Xu, G. Buntkowsky, T. Gutmann, K. Zhang, Multi-responsive cellulose nanocrystal-rhodamine conjugates: an advanced structure study by solid-state dynamic nuclear polarization (DNP) NMR, *Phys. Chem. Chem. Phys.* 16 (2014) 26322–26329.
- [419] A.R. Mouat, C. George, T. Kobayashi, M. Pruski, R.P. van Duyne, T.J. Marks, P.C. Stair, Highly dispersed  $\text{SiO}_x/\text{Al}_2\text{O}_3$  catalysts illuminate the reactivity of isolated silanol sites, *Angew. Chem. Int. Ed.* 54 (2015) 13346–13351.



- [420] M. Valla, A.J. Rossini, M. Caillot, C. Chizallet, P. Raybaud, M. Digne, A. Chaumonnot, A. Lesage, L. Emsley, J.A. van Bokhoven, C. Coperet, Atomic description of the interface between silica and alumina in aluminosilicates through dynamic nuclear polarization surface-enhanced NMR spectroscopy and first-principles calculations, *J. Am. Chem. Soc.* 137 (2015) 10710–10719.
- [421] F.A. Perras, J.D. Padmos, R.L. Johnson, L.-L. Wang, T.J. Schwartz, T. Kobayashi, J. H. Horton, J.A. Dumesic, B.H. Shanks, D.D. Johnson, M. Pruski, Characterizing substrate-surface interactions on alumina-supported metal catalysts by dynamic nuclear polarization-enhanced double-resonance NMR spectroscopy, *J. Am. Chem. Soc.* 139 (2017) 2702–2709.
- [422] T. Gutmann, B. Kumari, L. Zhao, H. Breitzke, S. Schöttner, C. Rüttiger, M. Gallei, Dynamic nuclear polarization signal amplification as a sensitive probe for specific functionalization of complex paper substrates, *J. Phys. Chem. C* 121 (2017) 3896–3903.
- [423] P. Berruyer, M. Lelli, M.P. Conley, D.L. Silverio, C.M. Widdifield, G. Siddiqi, D. Gajan, A. Lesage, C. Copéret, L. Emsley, Three-dimensional structure determination of surface sites, *J. Am. Chem. Soc.* 139 (2017) 849–855.
- [424] S.L. Veinberg, K.E. Johnson, M.J. Jaroszewicz, B.M. Kispal, C.R. Mireault, T. Kobayashi, M. Pruski, R.W. Schurko, Natural abundance  $^{14}\text{N}$  and  $^{15}\text{N}$  solid-state NMR of pharmaceuticals and their polymorphs, *Phys. Chem. Chem. Phys.* 18 (2016) 17713–17730.
- [425] A.C. Pinon, A.J. Rossini, C.M. Widdifield, D. Gajan, L. Emsley, Polymorphs of theophylline characterized by DNP enhanced solid-state NMR, *Mol. Pharm.* 12 (2015) 4146–4153.
- [426] L. Piveteau, T.-C. Ong, A.J. Rossini, L. Emsley, C. Copéret, M.V. Kovalenko, Structure of colloidal quantum dots from dynamic nuclear polarization surface enhanced NMR spectroscopy, *J. Am. Chem. Soc.* 137 (2015) 13964–13971.
- [427] C. Presti, A.S.L. Thankamony, J.G. Alauzun, P.H. Mutin, D. Carnevale, C. Lion, H. Vezin, D. Laurencin, O. Lafon, NMR and EPR characterization of functionalized nanodiamonds, *J. Phys. Chem. C* 119 (2015) 12408–12422.
- [428] T. Kobayashi, S. Gupta, M.A. Caporini, V.K. Pecharsky, M. Pruski, Mechanism of solid-state thermolysis of ammonia borane: a  $^{15}\text{N}$  NMR study using fast magic-angle spinning and dynamic nuclear polarization, *J. Phys. Chem. C* 118 (2014) 19548–19555.
- [429] A.J. Rossini, A. Zagdoun, M. Lelli, J. Canivet, S. Aguado, O. Ouari, P. Tordo, M. Rosay, W.E. Maas, C. Copéret, D. Farrusseng, L. Emsley, A. Lesage, Dynamic nuclear polarization enhanced solid-state NMR spectroscopy of functionalized metal-organic frameworks, *Angew. Chem. Int. Ed.* 51 (2012) 123–127.
- [430] F. Blanc, S.Y. Chong, T.O. McDonald, D.J. Adams, S. Pawsey, M.A. Caporini, A.I. Cooper, Dynamic nuclear polarization NMR spectroscopy allows high-throughput characterization of microporous organic polymers, *J. Am. Chem. Soc.* 135 (2013) 15290–15293.
- [431] A.J. Rossini, C.M. Widdifield, A. Zagdoun, M. Lelli, M. Schwarzwälder, C. Copéret, A. Lesage, L. Emsley, Dynamic nuclear polarization enhanced NMR spectroscopy for pharmaceutical formulations, *J. Am. Chem. Soc.* 136 (2014) 2324–2334.
- [432] A.S. Lilly Thankamony, C. Lion, F. Pourpoint, B. Singh, A.J. Perez Linde, D. Carnevale, G. Bodenhausen, H. Vezin, O. Lafon, V. Polshettiwar, Insights into the catalytic activity of nitrated fibrous silica (KCC-1) nanocatalysts from  $^{15}\text{N}$  and  $^{29}\text{Si}$  NMR spectroscopy enhanced by dynamic nuclear polarization, *Angew. Chem. Int. Ed.* 54 (2015) 2190–2193.
- [433] G. Mollica, M. Dekhil, F. Ziarelli, P. Thureau, S. Viel, Quantitative structural constraints for organic powders at natural isotopic abundance using dynamic nuclear polarization solid-state NMR spectroscopy, *Angew. Chem. Int. Ed.* 54 (2015) 6028–6031.
- [434] J. Leclaire, G. Poisson, F. Ziarelli, G. Pepe, F. Fotiadu, F.M. Paruzzo, A.J. Rossini, J.-N. Dumez, B. Elena-Herrmann, L. Emsley, Structure elucidation of a complex  $\text{CO}_2$ -based organic framework material by NMR crystallography, *Chem. Sci.* 7 (2016) 4379–4390.
- [435] V.K. Michaelis, E. Markhasin, E. Daviso, J. Herzfeld, R.G. Griffin, Dynamic nuclear polarization of oxygen-17, *J. Phys. Chem. Lett.* 3 (2012) 2030–2034.
- [436] F. Blanc, L. Sperrin, D.A. Jefferson, S. Pawsey, M. Rosay, C.P. Grey, Dynamic nuclear polarization enhanced natural abundance  $^{17}\text{O}$  spectroscopy, *J. Am. Chem. Soc.* 135 (2013) 2975–2978.
- [437] F.A. Perras, T. Kobayashi, M. Pruski, Natural abundance O-17 DNP two-dimensional and surface-enhanced NMR spectroscopy, *J. Am. Chem. Soc.* 137 (2015) 8336–8339.
- [438] F.A. Perras, T. Kobayashi, M. Pruski, PRESTO polarization transfer to quadrupolar nuclei: implications for dynamic nuclear polarization, *Phys. Chem. Chem. Phys.* 17 (2015) 22616–22622.
- [439] V. Vitzthum, P. Mieville, D. Carnevale, M.A. Caporini, D. Gajan, C. Coperet, M. Lelli, A. Zagdoun, A.J. Rossini, A. Lesage, L. Emsley, G. Bodenhausen, Dynamic nuclear polarization of quadrupolar nuclei using cross polarization from protons: surface-enhanced aluminium-27 NMR, *Chem. Commun.* 48 (2012) 1988–1990.
- [440] D. Lee, H. Takahashi, A.S.L. Thankamony, J.-P. Dacquin, M. Bardet, O. Lafon, G. D. Paëpe, Enhanced solid-state NMR correlation spectroscopy of quadrupolar nuclei using dynamic nuclear polarization, *J. Am. Chem. Soc.* 134 (2012) 18491–18494.
- [441] D. Lee, N.T. Duong, O. Lafon, G. De Paëpe, Primostrato solid-state NMR enhanced by dynamic nuclear polarization: pentacoordinated  $\text{Al}^{3+}$  ions are only located at the surface of hydrated  $\gamma$ -alumina, *J. Phys. Chem. C* 118 (2014) 25065–25076.
- [442] F. Pourpoint, A.S.L. Thankamony, C. Volkringer, T. Loiseau, J. Trébosc, F. Aussenac, D. Carnevale, G. Bodenhausen, H. Vezin, O. Lafon, J.-P. Amoureux, Probing  $^{27}\text{Al}$ - $^{13}\text{C}$  proximities in metal-organic frameworks using dynamic nuclear polarization enhanced NMR spectroscopy, *Chem. Commun.* 50 (2014) 933–935.
- [443] F. Pourpoint, J. Templier, C. Anquetil, H. Vezin, J. Trébosc, X. Trivelli, F. Chabaux, O.S. Pokrovsky, A.S. Prokushkin, J.-P. Amoureux, O. Lafon, S. Derenne, Probing the aluminum complexation by Siberian riverine organic matter using solid-state DNP-NMR, *Chem. Geol.* 452 (2017) 1–8.
- [444] D.A. Hirsh, A.J. Rossini, L. Emsley, R.W. Schurko,  $^{35}\text{Cl}$  dynamic nuclear polarization solid-state NMR of active pharmaceutical ingredients, *Phys. Chem. Chem. Phys.* 18 (2016) 25893–25904.
- [445] D. Lee, C. Leroy, C. Crevant, L. Bonhomme-Coury, F. Babonneau, D. Laurencin, C. Bonhomme, G. De Paëpe, Interfacial  $\text{Ca}^{2+}$  environments in nanocrystalline apatites revealed by dynamic nuclear polarization enhanced  $^{43}\text{Ca}$  NMR spectroscopy, *Nat. Commun.* 8 (2017) 14104.
- [446] A.J. Perez Linde, D. Carnevale, P. Miéville, A. Sienkiewicz, G. Bodenhausen, Dynamic nuclear polarization enhancement of protons and vanadium-51 in the presence of pH-dependent vanadyl radicals, *Magn. Reson. Chem.* 53 (2015) 88–92.
- [447] Z. Gan, Measuring amide nitrogen quadrupolar coupling by high-resolution  $^{14}\text{N}/^{13}\text{C}$  NMR correlation under magic-angle spinning, *J. Am. Chem. Soc.* 128 (2006) 6040–6041.
- [448] S. Cavadini, A. Lupulescu, S. Antonijevic, G. Bodenhausen, Nitrogen-14 NMR spectroscopy using residual dipolar splittings in solids, *J. Am. Chem. Soc.* 128 (2006) 7706–7707.
- [449] R. Tycko, S.J. Opella, Overtone NMR spectroscopy, *J. Chem. Phys.* 86 (1987) 1761–1774.
- [450] M. Bloom, M.A. LeGros, Direct detection of two-quantum coherence, *Can. J. Phys.* 64 (1986) 1522–1528.
- [451] L.A. O'Dell, C.I. Ratcliffe,  $^{14}\text{N}$  magic angle spinning overtone NMR spectra, *Chem. Phys. Lett.* 514 (2011) 168–173.
- [452] L.A. O'Dell, A. Brinkmann,  $^{14}\text{N}$  overtone NMR spectra under magic angle spinning: experiments and numerically exact simulations, *J. Chem. Phys.* 138 (2013) 064201.
- [453] S. Cavadini, A. Abraham, G. Bodenhausen, Coherence transfer between spy nuclei and nitrogen-14 in solids, *J. Magn. Reson.* 190 (2008) 160–164.
- [454] A.J. Rossini, L. Emsley, L.A. O'Dell, Dynamic nuclear polarization enhanced  $^{14}\text{N}$  overtone MAS NMR spectroscopy, *Phys. Chem. Chem. Phys.* 16 (2014) 12890–12899.
- [455] W.R. Gunther, V.K. Michaelis, M.A. Caporini, R.G. Griffin, Y. Roman-Leshkov, Dynamic nuclear polarization NMR enables the analysis of Sn-beta zeolite prepared with natural abundance Sn-119 precursors, *J. Am. Chem. Soc.* 136 (2014) 6219–6222.
- [456] M.P. Conley, A.J. Rossini, A. Comas-Vives, M. Valla, G. Casano, O. Ouari, P. Tordo, A. Lesage, L. Emsley, C. Coperet, Silica-surface reorganization during organotin grafting evidenced by Sn-119 DNP SENS: a tandem reaction of gem-silanol and strained siloxane bridges, *Phys. Chem. Chem. Phys.* 16 (2014) 17822–17827.
- [457] L. Protesescu, A.J. Rossini, D. Krieger, M. Valla, A. de Kergommeaux, M. Walter, K.V. Kravchik, M. Nachttegaal, J. Stangl, B. Malaman, P. Reiss, A. Lesage, L. Emsley, C. Copéret, M.V. Kovalenko, Unraveling the core-shell structure of ligand-capped Sn/SnO<sub>x</sub> nanoparticles by surface-enhanced nuclear magnetic resonance Mössbauer, and X-ray absorption spectroscopies, *ACS Nano* 8 (2014) 2639–2648.
- [458] P. Wolf, M. Valla, A.J. Rossini, A. Comas-Vives, F. Núñez-Zarur, B. Malaman, A. Lesage, L. Emsley, C. Copéret, I. Hermans, NMR signatures of the active sites in Sn- $\beta$  zeolite, *Angew. Chem. Int. Ed.* 53 (2014) 10179–10183.
- [459] P. Wolf, M. Valla, F. Nunez-Zarur, A. Comas-Vives, A.J. Rossini, C. Firth, H. Kallas, A. Lesage, L. Emsley, C. Coperet, I. Hermans, Correlating synthetic methods, morphology, atomic-level structure, and catalytic activity of Sn-beta catalysts, *ACS Catal.* 6 (2016) 4047–4063.
- [460] T. Kobayashi, F.A. Perras, T.W. Goh, T.L. Metz, W. Huang, M. Pruski, DNP-enhanced ultrawide-line solid-state NMR spectroscopy: studies of platinum in metal-organic frameworks, *J. Phys. Chem. Lett.* 7 (2016) 2322–2327.
- [461] T. Kobayashi, F.A. Perras, A. Murphy, Y. Yao, J. Catalano, S.A. Centeno, C. Dybowski, N. Zumbulyadis, M. Pruski, DNP-enhanced ultrawide-line  $^{207}\text{Pb}$  solid-state NMR spectroscopy: an application to cultural heritage science, *Dalton Trans.* 46 (2017) 3535–3540.
- [462] A. Henstra, P. Dirksen, J. Schmidt, W.T. Wenckebach, Nuclear-spin orientation via electron-spin locking (NOVEL), *J. Magn. Reson.* 77 (1988) 389–393.
- [463] C.T. Farrar, D.A. Hall, G.J. Gerfen, M. Rosay, J.H. Ardenkjær-Larsen, R.G. Griffin, High-frequency dynamic nuclear polarization in the nuclear rotating frame, *J. Magn. Reson.* 144 (2000) 134–141.
- [464] V. Weis, M. Bennati, M. Rosay, R.G. Griffin, Solid effect in the electron spin dressed state: a new approach for dynamic nuclear polarization, *J. Chem. Phys.* 113 (2000) 6795–6802.
- [465] H.J. Kim, E.A. Nanni, M.A. Shapiro, J.R. Sirigiri, P.P. Woskov, R.J. Temkin, Amplification of picosecond pulses in a 140-GHz gyrotron-traveling wave tube, *Phys. Rev. Lett.* 105 (2010) 135101.
- [466] E.A. Nanni, S.M. Lewis, M.A. Shapiro, R.G. Griffin, R.J. Temkin, Photonic-band-gap traveling-wave gyrotron amplifier, *Phys. Rev. Lett.* 111 (2013) 235101.
- [467] A. Henstra, P. Dirksen, W.T. Wenckebach, Enhanced dynamic nuclear polarization by the integrated solid effect, *Phys. Lett. A* 134 (1988) 134–136.
- [468] I. Kaminker, A. Potapov, A. Feintuch, S. Vega, D. Goldfarb, Population transfer for signal enhancement in pulsed EPR experiments on half integer high spin systems, *Phys. Chem. Chem. Phys.* 11 (2009) 6799–6806.
- [469] A. Doll, S. Pribitzer, R. Tschaggel, G. Jeschke, Adiabatic and fast passage ultra-wideband inversion in pulsed EPR, *J. Magn. Reson.* 230 (2013) 27–39.

- [470] E.P. Saliba, E.L. Sesti, F.J. Scott, B.J. Albert, E.J. Choi, N. Alaniva, C. Gao, A.B. Barnes, Electron decoupling with dynamic nuclear polarization in rotating solids, *J. Am. Chem. Soc.* 139 (2017) 6310–6313.
- [471] E. Salmikov, M. Rosay, S. Pawsey, O. Ouari, P. Tordo, B. Bechinger, Solid-state NMR spectroscopy of oriented membrane polypeptides at 100 K with signal enhancement by dynamic nuclear polarization, *J. Am. Chem. Soc.* 132 (2010) 5940–5941.
- [472] E.S. Salmikov, O. Ouari, E. Koers, H. Sarrouj, T. Franks, M. Rosay, S. Pawsey, C. Reiter, P. Bandara, H. Oschkinat, P. Tordo, F. Engelke, B. Bechinger, Developing DNP/solid-state NMR spectroscopy of oriented membranes, *Appl. Magn. Reson.* 43 (2012) 91–106.
- [473] A. Brinkmann, S.K. Vasa, H. Janssen, A.P.M. Kentgens, Proton micro-magic-angle-spinning NMR spectroscopy of nanoliter samples, *Chem. Phys. Lett.* 485 (2010) 275–280.
- [474] C.-G. Joo, K.-N. Hu, J.A. Bryant, R.G. Griffin, In situ temperature jump high-frequency dynamic nuclear polarization experiments: enhanced sensitivity in liquid-state NMR spectroscopy, *J. Am. Chem. Soc.* 128 (2006) 9428–9432.
- [475] C.-G. Joo, A. Casey, C.J. Turner, R.G. Griffin, In situ temperature-jump dynamic nuclear polarization: enhanced sensitivity in two dimensional  $^{13}\text{C}$ - $^{13}\text{C}$  correlation spectroscopy in solution, *J. Am. Chem. Soc.* 131 (2009) 12–13.
- [476] D. Yoon, M. Soundararajan, C. Caspers, F. Braunmueller, J. Genoud, S. Alberti, J.-P. Ansermet, 500-fold enhancement of in situ  $^{13}\text{C}$  liquid state NMR using gyrotron-driven temperature-jump DNP, *J. Magn. Reson.* 270 (2016) 142–146.
- [477] M. Sharma, G. Janssen, J. Leggett, A.P.M. Kentgens, P.J.M. van Bentum, Rapid-melt dynamic nuclear polarization, *J. Magn. Reson.* 258 (2015) 40–48.
- [478] P.J.M. van Bentum, M. Sharma, S.G.J. van Meerten, A.P.M. Kentgens, Solid effect DNP in a rapid-melt setup, *J. Magn. Reson.* 263 (2016) 126–135.

## Glossary of abbreviations

- AHT: average Hamiltonian theory  
 AMUPol: Aix-Marseille Université polarizing agent  
 API: active pharmaceutical ingredient  
 ASR: absolute sensitivity ratio  
 AWG: arbitrary waveform generator  
 bCTbK: bis-cyclohexyl-TEMPO-bisketal  
 BDPA: 1,3-bisdiphenylene-2-phenyl allyl  
 BRAIN-CP: broadband adiabatic inversion cross polarization  
 BT2E: bis-TEMPO-2-ethyleneglycol  
 bTbK: bis-TEMPO-bisketal  
 bTbtK: bis-TEMPO-bis-thioketal  
 bTbtK-py: bis-TEMPO-bis-thioketal-tetra-tetrahydropyran  
 BTnE: bis-TEMPO-n-ethyleneglycol  
 BTOXA: bis-TEMPO-oxalyl amide  
 bTtereph: bis-TEMPO terephthalate  
 bTurea: bis-TEMPO-urea  
 BWO: backward wave oscillator  
 CE: cross effect  
 ChR: channelrhodopsin  
 CIDNP: chemically induced dynamic nuclear polarization  
 CP: cross polarization  
 CPMG: Carr Purcell Meiboom Gill  
 CR: cross relaxation  
 CT: central transition  
 CTAB: cetyl trimethyl ammonium bromide  
 cw: continuous wave  
 dCE: direct cross effect  
 DCP: double cross polarization  
 DFT: density functional theory  
 D-HMQC: dipolar-mediated HMQC  
 DMSO: dimethyl sulfoxide  
 DNP: dynamic nuclear polarization  
 DNP-SENS: dynamic nuclear polarization surface enhanced NMR spectroscopy  
 DOM: dissolved organic matter  
 DOTA: 1,4,7,10-tetraazacyclododecane-1,4,7,10-tetraacetic acid  
 DOTOPA-TEMPO: 4-[N,N-di-(2-hydroxy-3-(TEMPO-4'-oxy)-propyl)]-amino-TEMPO  
 DPPH: diphenyl-picryl-hydrazyl  
 DQ: double quantum  
 DQC: double-quantum correlation  
 DQF: double-quantum filter  
 DsbA: disulfide oxidoreductase A  
 ECD: extracellular domain  
 EFG: electric field gradient  
 EGF: epidermal growth factor  
 EGFR: epidermal growth factor receptor  
 EIK: extended interaction klystron  
 EIO: extended interaction oscillator  
 ELDOR: electron–electron double resonance  
 EPR: electron paramagnetic resonance  
 ESEEM: electron spin echo envelope modulation  
 Ex-MSN: surfactant extracted mesoporous silica nanoparticle  
 FID: free induction decay  
 FMN: flavin mononucleotide  
 FS-TEDOR: frequency-selective transferred-echo double resonance  
 FWHH: full width at half height  
 HETCOR: heteronuclear correlation  
 HFI: hyperfine interaction  
 HMQC: heteronuclear multiple-quantum correlation  
 HSQC: heteronuclear single-quantum correlation  
 iCE: indirect cross effect  
 INADEQUATE: incredible natural abundance double quantum transfer experiment  
 KCC-1: fibrous nanosilica oxynitrides synthesized in KAUST Catalysis Center  
 KD: kinase domain  
 LAC: level anti crossing  
 LHe: liquid helium  
 LMN: lanthanum magnesium double nitrate  
 LN2: liquid nitrogen  
 MAS: magic-angle spinning  
 MD: molecular dynamics  
 MOF: metal-organic framework  
 MOP: microporous organic polymers  
 MQMAS: multiple-quantum MAS  
 MRI: magnetic resonance imaging  
 MRS: magnetic resonance spectroscopy  
 MSN: mesoporous silica nanoparticles  
 NMR: nuclear magnetic resonance  
 NQI: nuclear quadrupole interaction  
 OE: Overhauser effect  
 OT: overtone  
 OTP: ortho-terphenyl  
 PA: polarizing agent  
 PALI-melittin: Pro14-, Ala15-, Leu16-, and Ile17-isotopically-labeled peptide melittin  
 PC: polycarbonate  
 PCB: phycocyanobilin  
 PCS: pseudo-contact shift  
 PDS: proton-driven spin diffusion  
 PEG: polyethyleneglycol  
 PHIP: para-hydrogen induced polarization  
 P13-SH3: SH3 domain of the P13 kinase  
 PMO: periodic mesoporous organosilicate  
 POST-C7: permutationally offset stabilized C7  
 PR: proteorhodopsin  
 PRE: paramagnetic relaxation enhancement  
 PRESTO: phase-shifted recoupling effects a smooth transfer of order  
 QCPMG: quadrupolar Carr Purcell Meiboom Gill  
 REDOR: rotational echo double resonance  
 RESPDOR: resonance echo saturation pulse double resonance  
 rf: radio frequency  
 SA-BDPA: sulfonated BDPA  
 SD: spin diffusion  
 SDSL: site-directed spin labeling  
 SE: solid effect  
 SEOP: spin-exchange optical pumping  
 S-MSN: mesoporous silica nanoparticles with surfactant  
 SN-BDPA: sulfonamide BDPA  
 SOSO: spinning-on spinning-off  
 SPCS: supercycled POST C5  
 SPIROPOL: bTbtK-py (bis-TEMPO-bis-thioketal-tetra-tetrahydropyran)  
 SQ: single quantum  
 SQC: single-quantum correlation  
 S-RESPDOR: symmetry based RESPDOR  
 ST: satellite transition  
 TAM: triarylmethyl  
 TAP: transporter associated with antigen processing  
 TCE: 1,1,2,2-tetrachloroethane  
 TEDOR: transferred echo double resonance  
 TEKPol: tetrakis(phenylcyclohexyl) TEMPO-bisketal  
 TEMPO: 2,2,6,6-tetramethyl-1-piperidiny-1-oxyl  
 TEMPOL: 4-hydroxy-TEMPO  
 TEMTriPol: TEMPO/trityl polarizing agent  
 THP: tetrahydropyran  
 ThT: thioflavin-T  
 TM: thermal mixing  
 TOTAPOL: 1-(TEMPO-4-oxy)-3-(TEMPO-4-amino)propan-2-ol  
 VT: variable temperature  
 WURST: wideband uniform rate and smooth truncation  
 YES: yttrium ethyl sulfate  
 ZFS: zero-field splitting  
 ZQ: zero quantum  
 $\mu\text{w}$ : microwave



## Acknowledgments

I have learned invaluable lessons from all the names that appear in the following text. I would like to take this opportunity to express my heartfelt gratitude. These learning years of my life have been influenced by many talented people around me. The major source of inspiration, encouragement, and guidance has been my PhD supervisor Dr. Bjorn Corzilius. I am indebted to him for providing me the courage to try new ideas while keeping the safety net of his expertise in place. It has been a unique opportunity to have him as an immediate, ever-present source of motivation.

I am grateful to Prof. Thomas Prisner for his insightful comments, advice, support, inspiration and encouragement. I am thankful to Prof. Clemens Glaubitz for his support and spontaneous discussions. I thank the whole Glaubitz group for being welcoming and encouraging.

I am very thankful to Dr. Vasyl Denysenkov for helping in the times of instrument-failure or software-crash. I appreciate his patience and optimism immensely. I am grateful to Dr. Burkhard Endeward for his support with hardware related issues. I appreciate Dr. Jörn Plackmeyer for providing DOTA, and his help with chemistry related questions. I would also like to thank Dr. Johanna Becker-Baldus (AK Glaubitz) and Dr. Torsten Gutmann (AK Gerd Buntkowsky) for their much needed help at DNP spectrometers in Frankfurt and TU Darmstadt.

I would like to take this opportunity to express my gratitude towards my collaborators. Dr. Mian Qi and Prof. Adelheid Godt are appreciated for a fruitful collaboration on bis-metal polarizing agents. I would like to thank Dr. Anil Jagtap, Dr. Nitin Kunjir, and Prof. Snorri Sigurdson (Iceland) for providing various polarizing agent samples. Michel Geiger and Prof. Hartmut Oshkinat (Berlin) are acknowledged for collaboration on nitroxide radicals. I would like to thank Dr. Dorothea Wissser and Prof. Anne Lesage (ENS Lyon) for a nice collaboration and giving me an opportunity to work on the state-of-art 800 MHz spectrometer in their facility. Dr. Xiaoling Wang and Prof. Joanna Long (Florida) are gratefully acknowledged for collaboration on high-field DNP topic.

Simone Kobylka, Sigrid Kämmerer, and Silke Schneider are wholeheartedly appreciated for their administrative assistance. I would like to thank Bisera Krstić and Bernhard Thiem for their input to technical questions and supportive attitude.

I am grateful to Corzilius and Prisner groups for creating a nourishing environment. I appreciate Dr. Johannes Wittmann for patiently explaining theoretical aspects of NMR in detail. I am thankful to Dr. Dmitry Akhmetzyanov for suggestions and critical reading of this thesis. I am

very thankful to Jörg Heiliger, Victoria Aladin, and Denise Schuetz for their help with the German summary of this thesis. Dr. Alice Bowen, Dr. Alberto Callauto, and Dr. Benesh Joseph are thanked for their positive influence and useful insights. I am grateful to Thilo Hetzke, Denise Schuetz, Claudia Grytz, Eva Jaumann, Phillip Van Os, Nicole Erlenbach, and Markus Graenz for their support. I would like to thank my office-mates Dr. A.S.L. Thankamany and Diane Daube for their support, understanding, and creating a productive atmosphere. Christian Bengs is thanked for stimulating discussions over tea. I would like to thank Vica for making LaTeX-learning and thesis-writing process fun. I cherish the support and friendship I received from the group. The ease of discussions, stash of chocolates, and multi-lingual jokes are highly appreciated.

I feel privileged to have been introduced to the field of MAS DNP by two excellent mentors. I am grateful to Dr. Daniel Lee and Dr. Gael de Paepe (Grenoble) for their continuous support and encouragement.

My support system, my friends, and my family have contributed directly to the completion of my thesis. I consider myself fortunate to have Hundeeep Kaur and Varun Kumar as my constant support through ups and downs. They have been my pillars of strength, source of wisdom, and meme suppliers. I am thankful to Sneha Gupta for all the endless belly-laughes, adventures, and anecdotes. A big thank you to Hundeeep for being an awesome travel-sports-study partner, these four years would have been lot less colorful without her.

I couldn't have come this far without the encouragement of my family, for that, I am grateful to *The Kaushiks*. Thanks are due to my Grandma for her love and pride in my smallest achievements. I admire my nephews and nieces for being my chirpy little celebrations. I am very thankful to my siblings and cousins: Sandeep, Sonu and Sonia for their counsel and encouragement; Kamna, Prince, Rahul, and Ashish for always being there for me (with novelty food every time!); Priya and Priyanka for being my strength and confidants. I admire and appreciate my aunts and uncles for believing in me. This section is incomplete without thanking my mom for her love and world's best laddu. Thank you.

This thesis is dedicated to my parents Geeta and Mohanlal Kaushik.

# MONU KAUSHIK

First Name: Monu  
Family Name: Kaushik  
Date of birth: 15 July 1991  
Place of birth: Sonapat, India  
Nationality: Indian  
Address: Spielsgasse 16, Frankfurt, D-60439  
Email: [kaushik@em.uni-frankfurt.de](mailto:kaushik@em.uni-frankfurt.de)  
Phone No.: +4917672643074



## RESEARCH EXPERIENCE

### **Doctoral Research**

**Goethe University Frankfurt, DE**

Supervisor: Dr. Björn Corzilius

Sept 2013 – present

- High-frequency, 263 GHz EPR spectroscopy, dynamic nuclear polarization (DNP)
- Method development and simulations
- Extensive experimental experience on field-sweep NMR setup

### **Master Thesis**

**University Joseph Fourier, Grenoble, FR**

Supervisor: Dr. Gaël de Paëpe

2013

- Synthesis and characterization of dipeptide nanoparticles by SEM and solid-state NMR
- Density functional theory to predict NMR chemical shifts of functionalized silica nanoparticles

### **Master Internships**

**Institute of cryogenics (INAC, CEA)**

**University Joseph Fourier, Grenoble, FR**

- Solid-state NMR of functionalized silica nanoparticles
- PTM radical synthesis for DNP NMR

### **Department of physics**

**University of Delhi, New Delhi, IN**

- Investigation of polyoxometalates for incorporation of transition metal ions
- Synthesis of nanosized copper oxide with different synthetic routes
- Collection and interpretation of data from various characterization techniques

### **International Centre for Materials Science (ICMS)**

**JNCASR, Bengaluru, IN**

- CdSe, CdS, and ZnSe quantum dots synthesis using Schlenk line apparatus
- Calculation of particle size from UV-Vis spectra and PXRD data

## EDUCATION

### **Ph.D. Candidate, Chemistry**

Goethe University Frankfurt

Sept 2013-Nov 2017

Frankfurt am Main, DE

### **Master of Nanoscience and Nanotechnology**

2010-2013

### **Specialization: Nanochemistry**

2011-2012

University of Delhi (DU)

New Delhi, IN

Université Joseph-Fourier (UJF-Grenoble)

Grenoble, FR

### **Bachelor of Science**

2007-2010

Maharshi Dayanand University (MDU)

Haryana, IN

## ACHIEVEMENTS

- Ernst award 2017 from *Gesellschaft Deutscher Chemiker (GDCh)* at joint German-French conference on magnetic resonance, Bayreuth, DE
- First prize in 'NMR is art' contest organized by CIL laboratories at international conference ENC 2016 Pittsburgh, USA
- Poster prize at magnetic resonance conference EUROMAR 2014, Zurich, CH

## SCHOLARSHIPS/FELLOWSHIPS

- Completion scholarship 2017 from Goethe University, sponsored by *Deutscher Akademischer Austauschdienst (DAAD)*
- Short-Term Scientific Mission fellowship 2014 from (EU-COST) for research in CERM Florence, Italy
- ARCANÉ *Laboratoires d'excellence* fellowship for masters' thesis (Jan-June 2013)
- Campus-France scholarship for an academic year in France (2011-2012)
- Rajiv Gandhi Sciences Talent Research Fellowship (2011)
- Department of science and technology (DST, India) funding for Masters (2010-2013)
- Bachelor's funded by university scholarship for meritorious students (2007-2010)

## TEACHING AND DUTIES

- Teaching assistant: B.Sc. physical chemistry practical, Electrochemistry (2013-present)
- Maintenance of sample preparation lab and long-storage facility (2015-present)

## SUPERVISION ROLES

- Master internships:
  - Annabell Peters (July 2014)
  - Erhan Cetiner (August 2014)
  - Lukas Tapmeyer (February 2015)
- Bachelor thesis: Nahomie Philemon (June 2016)

## LANGUAGES

Hindi: Native

English: Near Native

German: Intermediate

French: Beginner

## PEER-REVIEWED PUBLICATIONS

- A. S. L. Thankamony, J. J. Wittmann, M. Kaushik, B. Corzilius. "Dynamic nuclear polarization for sensitivity enhancement in modern solid-state NMR." *Prog. Nucl. Magn. Reson. Spectr.* 102-103, 120-195 (2017)
- M. Kaushik, M. Qi, A. Godt, B. Corzilius. "Bis-Gadolinium Complexes for Solid Effect and Cross Effect Dynamic Nuclear Polarization." *Angew. Chem.*, 56, 15, 4295–4299 (2017)
- M. Kaushik, T. Bahrenberg, T. V. Can, M. A. Caporini, R. Silvers, J. Heiliger, A. A. Smith, H. Schwalbe, R. G. Griffin, and B. Corzilius. "Gd(III) and Mn(II) complexes for dynamic nuclear polarization: small molecular chelate polarizing agents and applications with site-directed spin labeling of proteins." *Phys. Chem. Chem. Phys.* 18, 27205-27218 (2016)
- P. Wenk, M. Kaushik, D. Richter, M. Vogel, B. Suess, and B. Corzilius. "Dynamic Nuclear Polarization of Ribonucleic Acid with Endogenously Bound Manganese." *J. Biomol. NMR* 63, 97-109 (2015)
- D. Lee, M. Kaushik, R. Coustel, Y. Chenavier, M. Chanal, M. Bardet, L. Dubois, H. Okuno, N. Rochat, F. Duclairoir, J.-M. Mousesca, and G. De Paëpe, "Solid-State NMR and DFT Combined for the Surface Study of Functionalized Silicon Nanoparticles." *Chem. Eur. J.*, 21, 16047–16058 (2015)

## JOURNAL PUBLICATION(S)

- M. Kaushik, D. Richter, and B. Corzilius. "Dynamic Nuclear Polarization in Solid-state NMR." *G.I.T. Laboratory Journal Europe* 1-2, 20 (2016)

## CONTRIBUTIONS TO INTERNATIONAL CONFERENCES

- 39<sup>th</sup> Joint Conference of the French and German Magnetic Resonance Societies, September 2017, Bayreuth (Germany) **Awarded talk**
- 10<sup>th</sup> Alpine conference on solid-state NMR, September 2017, Chamonix-Mont Blanc (France) **Short presentation**
- Ringberg Meeting 2016: Connecting EPR, ssNMR and DNP for the study of complex biomolecules, December 2016, Kreuth (Germany) **Invited talk**



- 38<sup>th</sup> FGMR Discussion Meeting of the German Magnetic Resonance Society, September 2016, Düsseldorf (Germany) **Presentation**
- 58<sup>th</sup> Annual Rocky Mountain Conference on Magnetic Resonance, July 2016, Breckenridge (Colorado, USA) **Selected presentation + poster**
- 37<sup>th</sup> FGMR Discussion Meeting of the German Magnetic Resonance Society, September 2015, Darmstadt (Germany) **poster**
- 5<sup>th</sup> International DNP symposium, August 2015, Egmond aan Zee (The Netherlands) **Presentation + poster**
- European Conference on Magnetic Resonance (EUROMAR), July 2014, Zürich (Switzerland) **Poster**
- COST Annual Meeting: Spin Hyperpolarisation in NMR and MRI, June 2014, Zürich (Switzerland) **Poster**
- EMBO practical course: solution and solid-state NMR of paramagnetic molecule, July 2014, Sesto Fiorentino (Italy) **Poster**